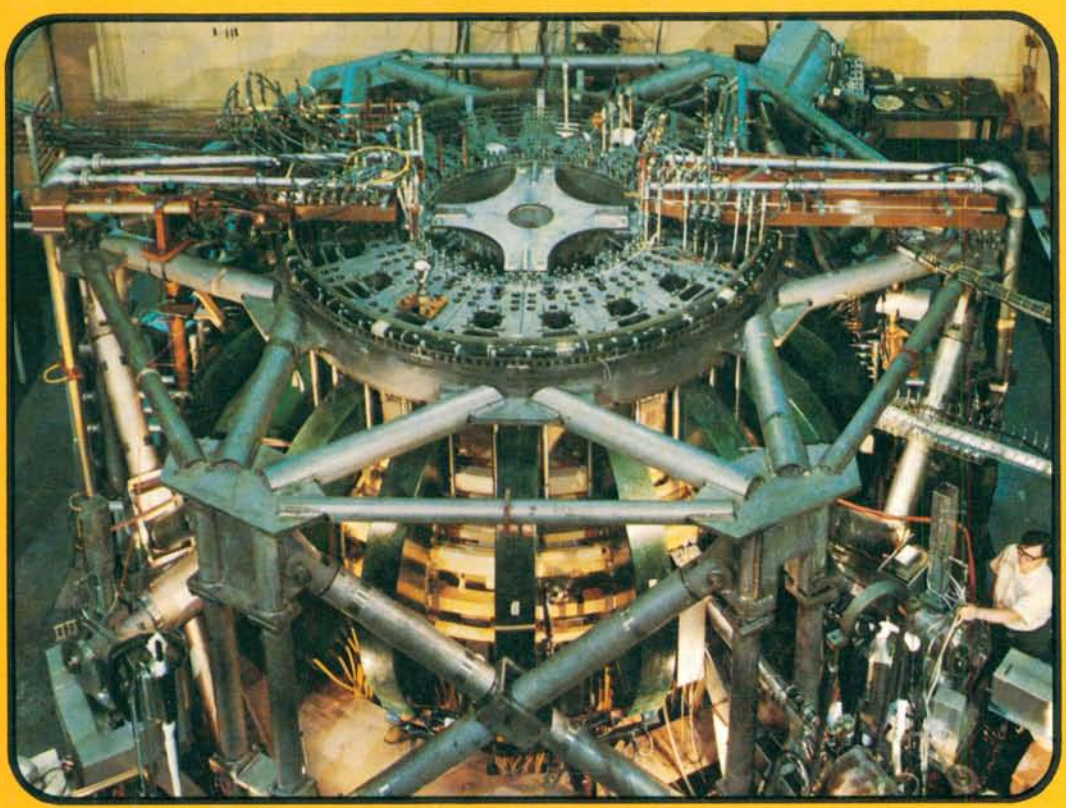
PLASMA PHYSICS AND CONTROLLED NUCLEAR FUSION RESEARCH 1978

VOL. II

Seventh Conference Proceedings, Innsbruck, 23-30 August 1978

NUCLEAR FUSION, SUPPLEMENT 1979



INTERNATIONAL ATOMIC ENERGY AGENCY, VIENNA, 1979

PLASMA PHYSICS AND CONTROLLED NUCLEAR FUSION RESEARCH 1978 VOL. II

The following States are Members of the International Atomic Energy Agency:

AFGHANISTAN
ALBANIA
ALGERIA
ARGENTINA
AUSTRALIA
AUSTRIA
BANGLADESH
BELGIUM
BOLIVIA
BRAZIL
BULGARIA
BURMA
BYELORUSSIAN SOVIET SOCIALIST REPUBLIC
CANADA
CHILE
COLOMBIA
COSTA RICA
CUBA
CYPRUS
CZECHOSLOVAKIA
DEMOCRATIC KAMPUCHEA
DEMOCRATIC PEOPLE'S REPUBLIC OF KOREA
DENMARK
DOMINICAN REPUBLIC
ECUADOR
EGYPT
EL SALVADOR
ETHIOPIA
FINLAND
FRANCE
GABON
GERMAN DEMOCRATIC REPUBLIC
GERMANY, FEDERAL REPUBLIC OF
GHANA
GREECE
GUATEMALA
HAITI
HOLY SEE
HUNGARY
ICELAND
INDIA
INDONESIA
IRAN
IRAQ
IRELAND
ISRAEL
ITALY
IVORY COAST
JAMAICA
JAPAN
JORDAN
KENYA
KOREA, REPUBLIC OF
KUWAIT
LEBANON
LIBERIA
LIBYAN ARAB JAMAHIRIYA
LIECHTENSTEIN
LUXEMBOURG
MADAGASCAR
MALAYSIA
MALI
MAURITIUS
MEXICO
MONACO
MONGOLIA
MOROCCO
NETHERLANDS
NEW ZEALAND
NICARAGUA
NIGER
NIGERIA
NORWAY
PAKISTAN
PANAMA
PARAGUAY
PERU
PHILIPPINES
POLAND
PORTUGAL
QATAR
ROMANIA
SAUDI ARABIA
SENEGAL
SIERRA LEONE
SINGAPORE
SOUTH AFRICA
SPAIN
SRI LANKA
SUDAN
SWEDEN
SWITZERLAND
SYRIAN ARAB REPUBLIC
THAILAND
TUNISIA
TURKEY
UGANDA
UKRAINIAN SOVIET SOCIALIST REPUBLIC
UNION OF SOVIET SOCIALIST REPUBLICS
UNITED ARAB EMIRATES
UNITED KINGDOM OF GREAT BRITAIN AND NORTHERN IRELAND
UNITED REPUBLIC OF CAMEROON
UNITED REPUBLIC OF TANZANIA
UNITED STATES OF AMERICA
URUGUAY
VENEZUELA
VIET NAM
YUGOSLAVIA
ZAIRE
ZAMBIA

The Agency's Statute was approved on 23 October 1956 by the Conference on the Statute of the IAEA held at United Nations Headquarters, New York; it entered into force on 29 July 1957. The Headquarters of the Agency are situated in Vienna. Its principal objective is "to accelerate and enlarge the contribution of atomic energy to peace, health and prosperity throughout the world".

© IAEA, 1979

Permission to reproduce or translate the information contained in this publication may be obtained by writing to the International Atomic Energy Agency, Kärntner Ring 11, P.O. Box 590, A-1011 Vienna, Austria.

Printed by the IAEA in Austria
May 1979

NUCLEAR FUSION SUPPLEMENT 1979

PLASMA PHYSICS AND CONTROLLED NUCLEAR FUSION RESEARCH 1978

PROCEEDINGS OF THE
SEVENTH INTERNATIONAL CONFERENCE ON PLASMA PHYSICS
AND CONTROLLED NUCLEAR FUSION RESEARCH
HELD BY THE
INTERNATIONAL ATOMIC ENERGY AGENCY
AT INNSBRUCK, 23 – 30 AUGUST 1978

In three volumes

VOL.II

INTERNATIONAL ATOMIC ENERGY AGENCY
VIENNA, 1979

PLASMA PHYSICS AND CONTROLLED NUCLEAR FUSION RESEARCH 1978
IAEA, VIENNA, 1979
STI/PUB/495
ISBN 92–0–130179–0

FOREWORD

Impressive progress towards the demonstration of the scientific feasibility of controlled fusion and the design and construction of a controlled thermonuclear power reactor was reported at the Seventh IAEA Conference on Plasma Physics and Controlled Nuclear Fusion Research. The three volumes of these Proceedings contain the contributed papers, summaries and discussions on the magnetic confinement approaches to fusion, inertial confinement fusion and fusion reactor engineering. These Conferences are now being held every two years to keep pace with the rapid progress being made, the previous one being held in Berchtesgaden, Federal Republic of Germany, in 1976.

The Seventh Conference was held by the IAEA in Innsbruck, Austria, from 23 to 30 August 1978. More than 500 participants and 38 observers from 32 countries and three international organizations attended. A total of 150 papers were presented at the technical sessions. The first session, on tokamak experiments, was called the Artsimovich Memorial Session to commemorate the contributions of Lev Andreevich Artsimovich to fusion research and to international co-operation in scientific endeavours.

The Proceedings are published in English as a supplement to the IAEA journal "Nuclear Fusion".

The Agency promotes close international collaboration among plasma and fusion physicists of all countries by regularly organizing conferences on controlled nuclear fusion and by holding seminars, workshops and specialists' meetings on selected topics. The activities will, it is hoped, contribute to the rapid use of this new source of energy to meet the world's future energy requirements.

EDITORIAL NOTE

The papers and discussions have been edited by the editorial staff of the International Atomic Energy Agency to the extent considered necessary for the reader's assistance. The views expressed and the general style adopted remain, however, the responsibility of the named authors or participants. In addition, the views are not necessarily those of the governments of the nominating Member States or of the nominating organizations.

Where papers have been incorporated into these Proceedings without resetting by the Agency, this has been done with the knowledge of the authors and their government authorities, and their cooperation is gratefully acknowledged. The Proceedings have been printed by composition typing and photo-offset lithography. Within the limitations imposed by this method, every effort has been made to maintain a high editorial standard, in particular to achieve, wherever practicable, consistency of units and symbols and conformity to the standards recommended by competent international bodies.

The use in these Proceedings of particular designations of countries or territories does not imply any judgement by the publisher, the IAEA, as to the legal status of such countries or territories, of their authorities and institutions or of the delimitation of their boundaries.

The mention of specific companies or of their products or brand names does not imply any endorsement or recommendation on the part of the IAEA.

Authors are themselves responsible for obtaining the necessary permission to reproduce copyright material from other sources.

CONTENTS OF VOLUME II

HIGH BETA I (Session E)

LASL toroidal reversed-field pinch programme (IAEA-CN-37/E-1-1) 3
D.A. Baker, C.J. Buchenauer, L.C. Burkhardt, C.K. Chu, J.N. DiMarco, J.N. Downing, A. Haberstich, R.B. Howell, A.R. Jacobson, H.J. Karr, P.C. Liewer, E.M. Little, M.D. Machalek, W. Park, A.E. Schofield, A.G. Sgro, K.S. Thomas, P.C.T. Van der Laan

Theoretical and experimental studies of the reversed-field pinch (IAEA-CN-37/E-1-2) 23
P.G. Carolan, C.W. Gowers, D.C. Robinson, M.R.C. Watts, H.A.B. Bodin

Studies on plasma formation, relaxation and heating in a reversed-field pinch (IAEA-CN-37/E-1-3) 37
M. Bagatin, A. Buffa, R. De Angelis, G. Malesani, S. Ortolani

Discussion on papers E-1-1 to E-1-3 53

Experimental and computational studies of high-beta tokamaks and reversed-field pinches (IAEA-CN-37/E-2) 55
T. Tamaru, K. Sugisaki, K. Hayase, T. Shimada, Y. Hirano, Y. Maejima, K. Ogawa, K. Hirano, S. Kitagawa, K. Sato, M. Wakatani, S. Yamada, H.Arimoto, Y. Kita, S. Yamaguchi, A. Nagata, S. Ido, I. Kawakami

Z-pinches of intense energy density driven by high-voltage storage lines (IAEA-CN-37/E-3) 69
P. Choi, A.E. Dangor, A. Folkierski, E. Kahan, D.E. Potter, P.D. Slade, S.J. Webb

Discussion 79

Tormac confinement, theory and experiment (IAEA-CN-37/E-4) 81
M.A. Levine, H.L. Berk, I.G. Brown, J. Coonrod, B. Feinberg, M. Greenwald, J. Hammer, W.B. Kunkel, B.R. Myers, R.A. Niland, A. Sessler, W. Sharp, R. Shaw, L. Soroka, M. Vella, A.H. Boozer, M.A. Mostrom, N.T. Gladd

Discussion 92

Experimental and theoretical liner fusion studies (IAEA-CN-37/E-5) 93
D.L. Book, R.L. Burton, A.L. Cooper, R.D. Ford, B. Hui, D.J. Jenkins, P.C. Liewer, A.E. Robson, P.J. Turchi, S. Hamasaki, N.A. Krall, L. Mascheroni, R. Shanny, E.L. Cantrell, R.A. Gerwin, I. Henins, T.R. Jarboe, R.C. Malone, J. Marshall, R.W. Moses, G.A. Sawyer, A.R. Sherwood, B.R. Suydam, C.E. Swannack

HIGH BETA II (Session U)

Experimental and theoretical studies of high-beta tokamaks (IAEA-CN-37/U-1) 105
A. Aydemir, C.K. Chu, G. Georgiou, R.A. Gross, H.C. Lui, J. Marsen, T.C. Marshall, Z. Mucha, G.A. Navratil, P.G. Weber, J. Busnardo-Neto, Y.G. Chen, C. Chin-Fatt, Y.P. Chong, A.W. DeSilva, G.C. Goldenbaum, H.R. Griem, R.A. Hess, P.C. Liewer, R.L. Merlino, D.P. Murphy, A.G. Sgro, R.N. Byrne
Discussion 113
Classical transport in Belt-Pinch II a (IAEA-CN-37/U-2) 115
G. Becker, O. Gruber, H. Krause, F. Mast, R. Wilhelm
Discussion 122
Recent progress in 1-MJ plasma focus dynamics and scaling for neutron production (IAEA-CN-37/U-3-1) 123
C. Gourlan, H. Kroegler, C. Maisonnier, J.P. Rager, B.V. Robouch, A. Gentilini
Neutron emission parameters in plasma focus devices (IAEA-CN-37/U-3-2) 135
G. Decker, H. Herold, H.J. Kaeppeler, W. Kies, W. Maysenhölder, B. Nahrath, T. Oppenländer, G. Pross, B. Rückle, A. Sauerbrunn, P. Schilling, H. Schmidt, M. Shakhatre, M. Trunk, K. Steinmetz, H. Bruhns, J. Ehrhardt, K. Hübner, P. Kirchesch, G. Mechler
Energy spectra of deuteron and electron beams from focused discharges and optimization criteria (IAEA-CN-37/U-3-3) 143
V. Nardi, W.H. Bostick, J. Feugeas, W. Prior, C. Cortese
Turbulence caused by the interaction between plasma and electric current in the Focus experiment (IAEA-CN-37/U-3-4) 159
A. Bernard, J.P. Garçonnet, A. Jolas, J.P. Le Breton, J. De Mascureau
Recent plasma focus research (IAEA-CN-37/U-3-5) 173
A. Bañuelos, H. Bruzzone, R. Delellis, J. Gratton, R. Gratton, H. Kelly, M. Milanese, J. Pouzo, F. Rodríguez Trelles
Discussion on papers U-3-1 to U-3-5 185
Principles of plasma heating and confinement in a compact toroidal configuration (IAEA-CN-37/U-4-1) 187
A.G. Es'kov, R.Kh. Kurtmullaev, A.P. Kreshchuk, Ya.N. Laukhin, A.I. Malyutin, A.I. Markin, Yu.S. Martyushov, B.N. Mironov, M.M. Orlov, A.P. Proshletsov, V.N. Semenov, Yu.B. Sosunov
Study of linear theta pinch with strong and fast-rising magnetic field (IAEA-CN-37/U-4-2) 205
V.A. Burtsev, A.B. Berezin, A.P. Zhukov, L.A. Zelenov, V.A. Kubasov, V.N. Litunovskij, B.V. Lyublin, A.G. Smirnov, V.G. Smirnov

End plugging of a hot linear theta pinch (IAEA-CN-37/U-4-3) 217
H. Azodi, M. Naraghi, H. Tahsiri, A. Torabi-Fard
Discussion 227
Recent developments in linear theta-pinch and laser-heated solenoid research (IAEA-CN-37/U-5) 229
K.F. McKenna, R.R. Bartsch, R.J. Commisso, C.A. Ekdahl, K.B. Freese, R.F. Gribble, F.C. Jahoda, G. Miller, R.E. Siemon, J.U. Brackbill, J.P. Freidberg, S.P. Gary, H.R. Lewis, A.G. Sgro, L. Turner, D. Winske, A.L. Hoffman, E.A. Crawford, D.D. Lowenthal, D.C. Quimby, G.C. Vlases, H.W. Hoida, Z.A. Pietrzyk
Discussion 246

NON-AXISYMMETRIC SYSTEMS I (Session H)

Heating, confinement and fluctuations in the CLEO stellarator (IAEA-CN-37/H-1) 251
D.W. Atkinson, J.E. Bradley, A.N. Dellis, P.C. Johnson, D.J. Lees, P.J. Lomas, W. Millar, A.C. Selden, L.E. Sharp, P.A. Shatford, P.R. Thomas
Discussion 263
Energy and particle confinement in the Ohmically heated W VII-A stellarator (IAEA-CN-37/H-2) 265
B. Cannici, G. Cattanei, A. Cavallo, D. Dorst, A. Elsner, G. Grieger, H. Hacker, J. How, H. Jäckel, R. Jaenicke, P. Javel, J. Junker, M. Kick, F. Leuterer, C. Mahn, S. Marlier, G. Müller, W. Ohlendorf, F. Rau, H. Renner, H. Ringler, J. Saffert, J. Sapper, P. Smeulders, M. Tutter, O. Vollmer, A. Weller, E. Würsching, H. Wobig
Discussion 275
Investigation of the m = 2 mode at q-values around 2 in the W VII-A stellarator (IAEA-CN-37/H-3) 277
B. Cannici, G. Cattanei, A. Cavallo, D. Dorst, A. Elsner, G. Grieger, H. Hacker, J. How, H. Jäckel, R. Jaenicke, P. Javel, J. Junker, M. Kick, F. Leuterer, C. Mahn, S. Marlier, G. Müller, W. Ohlendorf, F. Rau, H. Renner, H. Ringler, J. Saffert, J. Sapper, P. Smeulders, M. Tutter, O. Vollmer, A. Weller, E. Würsching, H. Wobig, M. Zippe
Discussion 286
Current equilibrium and effective ion charge in L-2 stellarator plasma (IAEA-CN-37/H-4(A)) 287
D.K. Akulina, Eh.D. Andryukhina, G.S. Voronov, M.S. Berezhetskij, S.E. Grebenshchikov, I.S. Danilkin, B.I. Kornev, O.I. Fedyanin, I.S. Sbitnikova, Yu.V. Khol'nov, I.S. Shpigel'

Injection of a solid hydrogen pellet into the L-2 stellarator (IAEA-CN-37/H-4(B)) 303
N.P. Donskaya, M.S. Rabinovich, G.S. Voronov
Discussion on papers H-4(A) and H-4(B) 307
Analytical investigations of equilibrium and stability in three-dimensional MHD configurations (IAEA-CN-37/H-5) 309
D. Lortz, J. Nührenberg
Discussion 320

NON-AXISYMMETRIC SYSTEMS II (Session L)

RF heating experiments on Heliotron devices and analysis of equilibrium and stability of straight helical Heliotron plasma (IAEA-CN-37/L-1) 323
K. Uo, A. Iiyoshi, H. Akimune, T. Obiki, S. Morimoto, M. Wakatani, A. Sasaki, K. Kondo, O. Motojima, M. Sato, T. Mutoh, I. Ohtake, M. Nakasuga, T. Mizuuchi, S. Kinoshita, K. Hanatani, T. Amano, S. Hamada
Discussion 334
A three-dimensional MHD code (IAEA-CN-37/L-2) 335
R. Chodura, A. Schlüter, M. Kaufmann, W. Lotz
Discussion 344
New results in high-beta MHD theory (IAEA-CN-37/L-3-1) 345
D.C. Barnes, J.U. Brackbill, T.E. Cayton, R.Y. Dagazian, J.P. Freidberg, W. Schneider, L.S. Hall, H. Grad, W. Grossmann, D.C. Stevens, E. Turkel, S. Wollman
Stabilizing effects of $\ell = 2,3$ helical fields on high-beta stellarator configurations (IAEA-CN-37/L-3-2) 355
F. Herrnegger, O. Betancourt, P. Garabedian
Discussion on papers L-3-1 and L-3-2 363
Experimental and theoretical studies of the ELMO Bumpy Torus (EBT) (IAEA-CN-37/L-4) 365
R.A. Dandl, F.W. Baity, Jr., K.H. Carpenter, J.A. Cobble, H.O. Eason, J.C. Glowienka, G.R. Haste, M.E. Hesse, S. Hiroe, N.H. Lazar, B.H. Quon, T. Uckan, T.L. White, Heavy Ion Beam Group, UV Spectroscopy Group, C.L. Hedrick, D.B. Batchelor, L. Deleano, R.C. Goldfinger, E.F. Jaeger, L.W. Owen, D.A. Spong, J.S. Tolliver, J.B. McBride, N.A. Krall, A.L. Sulton, Jr.
Discussion 372
Plasma stability control in a toroidal system by feedback and HF fields (IAEA-CN-37/L-5) 373
R.A. Demirkhanov, A.G. Kirov, V.P. Sidorov, L.F. Ruchko, S.N. Lozovskij, A.V. Sukachov, A.V. Nyushkov
Discussion 386

OPEN SYSTEMS I (Session J)

2XIIB plasma confinement experiments (IAEA-CN-37/J-1) 389
T.C. Simonen, J.F. Clauser, F.H. Coensgen, D.L. Correll, W.F. Cummins, R.P. Drake, J.H. Foote, A.H. Futch, R.K. Goodman, D.P. Grubb, A.L. Hunt, G. Melin, A.W. Molvik, W.E. Nexsen, B.W. Stallard, W.C. Turner
Discussion 399
RF plugging of laser-produced plasma in a cusp field (IAEA-CN-37/J-2) 401
T. Sato, R. Kumazawa, K.N. Sato, T. Watari, S. Okamura, M. Ichimura, S. Hidekuma, T. Fukagawa, T. Aoki, T. Kawamoto, K. Adati, S. Hiroe, H. Obayashi, T. Hatori, T. Watanabe, K. Takayama, S. Okada, R. Yoshino, H. Saito, S. Sudo, T. Sekiguchi
Discussion 410
Transverse particle losses in axially asymmetrical open traps (IAEA-CN-37/J-3) 411
M.E. Kishinevskij, P.B. Lysyanskij, D.D. Ryutov, G.V. Stupakov, B.M. Fomel', B.V. Chirikov, G.I. Shul'zhenko
Discussion 426
Studies of tandem mirror confinement (IAEA-CN-37/J-4) 427
D.E. Baldwin, R.H. Cohen, J.H. Foote, L.S. Hall, T.B. Kaiser, B.G. Logan, L.D. Pearlstein, T.D. Rognlien, J. Kesner
Discussion 435
Plasma confinement in GAMMA 6 (tandem mirror) (IAEA-CN-37/J-5) 437
S. Miyoshi, K. Yatsu, T. Kawabe, K. Ishii, A. Itakura, H. Ishizuka, S. Hagiwara
Discussion 443

OPEN SYSTEMS II (Session S)

Field reversal experiments (FRX) (IAEA-CN-37/S-1-1) 447
R.K. Linford, W.T. Armstrong, D.A. Platts, E.G. Sherwood
Field reversal in mirror machines (IAEA-CN-37/S-1-2) 457
L.D. Pearlstein, D.V. Anderson, D.E. Baldwin, J.A. Byers, B.I. Cohen, R.H. Cohen, W.C. Condit, T.K. Fowler, R.P. Freis, T.B. Kaiser, R.F. Post, M.E. Rensink, G.R. Smith, A.H. Boozer
Discussion on papers S-1-1 and S-1-2 467
Experimental studies of loss mechanism under the influence of cyclotron instabilities in a rarefied plasma (IAEA-CN-37/S-2) 469
V.A. Zhil'tsov, P.M. Kosarev, V.Kh. Likhtenshtejn, D.A. Panov, A.A. Skovoroda, A.G. Shcherbakov
Discussion 481

Drift wave stability and transport theory in fusion systems
(IAEA-CN-37/S-3) 483
N.A. Krall, S. Hamasaki, J.B. McBride, N.T. Gladd, P.H. Ng, H.H. Chen, J.D. Huba, R.C. Davidson, R.E. Aamodt, Y.-C. Lee, C.S. Liu, D.R. Nicholson, M.N. Rosenbluth, D. Chernin
Discussion 495
Recent results and work on field-reversing E- and P-layers
(IAEA-CN-37/S-4) 497
M. Tuszewski, D.J. Rej, S.C. Luckhardt, R.V. Lovelace, D.A. Larrabee, R.E. Kribel, H.H. Fleischmann, A. Drobot, J. Golden, C.A. Kapetanakos, R.A. Mahaffey, S.J. Marsh, J.A. Pasour, P.L. Dreike, A. Friedman, M. Greenspan, D.A. Hammer, S. Humphries, Jr., A. Mankofsky, R.N. Sudan
Discussion 508
Reversed magnetic fields induced by a rotating E-beam
(IAEA-CN-37/S-5) 509
C.W. Roberson, A. Fisher, J. Hubbard, W. Peter, S. Robertson, N. Rostoker, G. Saenz, D. Tzach, J.D. Sethian, K.A. Gerber, D.N. Spector, G.C. Goldenbaum, D.A. Hammer, A.E. Robson
Discussion 518

PLASMA HEATING I (Session G)

Lower hybrid resonance cones in tokamaks (IAEA-CN-37/G-1(A)) 521
M. Brambilla
Stochastic ion heating by an electrostatic wave in a sheared magnetic field
(IAEA-CN-37/G-1(B)) 527
Y. Gell, R. Nakach
Discussion on papers G-1(A) and G-1(B) 533
Ohmic pumping by means of externally driven tearing modes
(IAEA-CN-37/G-2) 535
M. Bonnedal, E. Canobbio
Discussion 541

PLASMA HEATING II (Session Q)

Transit time magnetic pumping in the Petula tokamak
(IAEA-CN-37/Q-1) 545
R. Bardet, M. Bernard, G. Briffod, M. Clément, A. Gauthier, M. Grégoire, P. Grelot, G. Haste, F. Parlange, D. Pinet, E. Porrot, G. Rey, B. Taquet, J. Weisse
Discussion 556

Parametric instabilities induced by a low-frequency heating wave in a magnetically confined plasma (IAEA-CN-37/Q-2) 559
D. Moreau
Discussion 568
Progress in heating of fusion plasmas with Alfvén waves and magneto-acoustic oscillations (IAEA-CN-37/Q-3) 569
J.L. Shohet, J.N. Talmadge, J.A. Tataronis, W. Grossmann, A. Hasegawa, L. Chen, E. Holzhauer, G. Janzen, F. Moser, G. Müller, E. Räuchle, E. Schneider, P.G. Schüller
Discussion 580
Fast-magnetosonic-wave excitation in large-tokamak plasmas (IAEA-CN-37/Q-4) 583
A.V. Longinov, K.N. Stepanov, V.A. Tsurikov
Discussion 605

PLASMA HEATING III (Session Y)

Plasma production and heating by glass-CO_2-hybrid laser system for magnetic traps (IAEA-CN-37/Y-1) 609
K.N. Sato, S. Okada, T. Sekiguchi, T. Fukagawa, M. Aizawa, H. Yasuda, R. Yoshino, H. Saito
Discussion 621
Investigation of plasma heating by powerful relativistic electron beams (IAEA-CN-37/Y-2) 623
A.V. Arzhannikov, A.V. Burdakov, B.N. Brejzman, A.S. Burmasov, L.N. Vyacheslavov, V.S. Kojdan, V.V. Konyukhov, V.A. Kornilov, Eh.P. Kruglyakov, V.N. Luk'yanov, K.I. Mekler, A.A. Podyminogin, A.I. Rogozin, D.D. Ryutov
Discussion 637
Plasma heating by current-driven turbulence in the tokamak TORTUR I (IAEA-CN-37/Y-4-1) 639
H. De Kluiver, C.J. Barth, H.J.B.M. Brocken, J.J.L. Caarls, B. De Groot, H.W. Kalfsbeek, H.W. Piekaar, A. Ravestein, W.R. Rutgers, B. De Stigter, H.W.H. Van Andel, H.W. Van der Ven
Experiments on hot-ion production in toroidal plasmas by applying pulsed electric fields along and across the toroidal magnetic field (IAEA-CN-37/Y-4-2) 649
T. Ishimura, N. Hosogane, S. Ohi, T. Yamamoto, M. Ichimura, N. Inoue, K. Yamazaki, Y. Ogawa, M. Kikuchi, A. Ozaki, T. Uchida
Discussion on papers Y-4-1 and Y-4-2 661

Summary on informal meetings on stellarators, plasma focus and tandem mirrors 663

Chairmen of Sessions 671

Secretariat of the Conference 671

Session E

HIGH BETA I

Chairman

H. DREICER
USA
Papers E-1-1 to E-1-3 were presented
by H.A.B. Bodin as Rapporteur

LASL TOROIDAL REVERSED-FIELD PINCH PROGRAMME*

D.A. BAKER, C.J. BUCHENAUER, L.C. BURKHARDT,
C.K. CHU,** J.N. DiMARCO, J.N. DOWNING, A. HABERSTICH,
R.B. HOWELL, A.R. JACOBSON, H.J. KARR, P.C. LIEWER,†
E.M. LITTLE, M.D. MACHALEK, W. PARK, ** A.E. SCHOFIELD,
A.G. SGRO, K.S. THOMAS, P.C.T. VAN DER LAAN§
Los Alamos Scientific Laboratory,
Los Alamos, New Mexico,
United States of America

Abstract

LASL TOROIDAL REVERSED-FIELD PINCH PROGRAMME.

The determination of the absolute energy loss due to radiation from impurities in the LASL toroidal reversed-field pinch experiment ZT-S is reported. The measurements show that over half the energy loss is accounted for by this mechanism. Thomson-scattering electron density measurements indicate only a gradual increase in temperature as the filling pressure is reduced, indicating an increased energy loss at lower pressures. Cylindrical and toroidal simulations of the experiment indicate either that a highly radiative pinch boundary or anomalous transport is needed to match the experimental results. New effects on the equilibrium due to plasma flows induced by the toroidal geometry are predicted by the toroidal simulations. The preliminary results on the low-temperature discharge cleaning of the ZT-S torus are reported. A description of the upgrade of the ZT-S experiment and the objectives, construction and theoretical predictions for the new ZT-40 experiment are given.

I. INTRODUCTION

The toroidal reversed-field pinch approach continues to be motivated by its promise of high-beta, stable equilibrium configuration with the possibility of ohmic heating to ignition with moderate magnetic fields. Further advantages stem from the freedom of choice of aspect ratio that gives an escape from possible adverse trapped-particle effects and can lead to a simpler modular construction with easier access as compared to a compact torus.

The Los Alamos program is currently centered around the 15-cm bore ZT-S experiment (a modification of the earlier 10-cm bore ZT-I experiment) and the 40-cm bore ZT-40 experiment presently under construction. Studies between the ZT-I and ZT-S experiments showing the confinement time scaling proportional to the square of the minor diameter are reported in Ref. [1].

---

* Work performed under the auspices of the US Department of Energy.

** Columbia University, New York, NY, USA.

† University of Maryland, College Park, MD, USA.

§ Present address: EEg Group EHO, Eindhoven University of Technology, Eindhoven, The Netherlands.

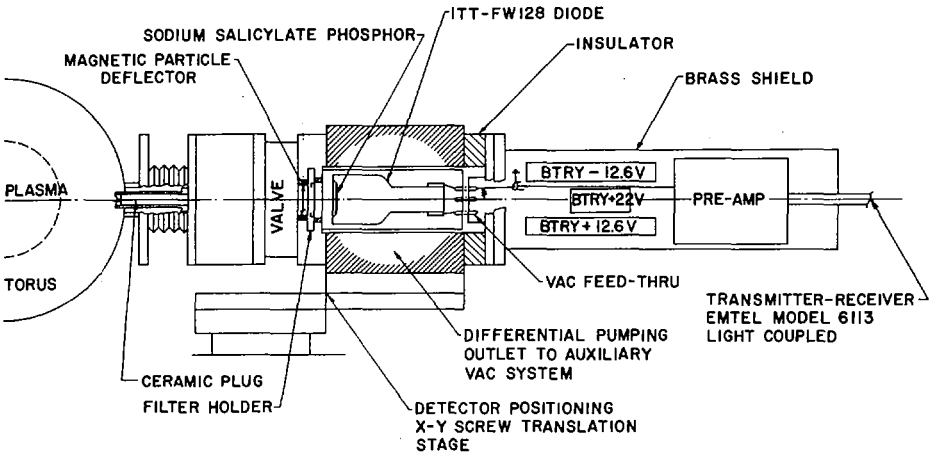


FIG.1. Schematic of photodiode radiation detector.

More recent efforts on the ZT-S experiment have been concentrated on the measurement of the radiation loss from impurities and in the study of the raising of the electron temperature by operating at lower filling pressure and by the use of low-temperature discharge cleaning.

The ZT-40 experiment is expected to begin preliminary physics in calendar year 1979. The experiment has been designed to allow versatility in its range of risetimes (2.5 μs-1 ms). It will allow the study of programmed reversed-field profiles as well as configurations obtained by self-reversal. The general aim of ZT-40 is to obtain physics information needed to predict the optimum design of subsequent larger devices.

II. ZT-S

A. General

A chief factor limiting the confinement time in the ZT-S reversed-field experiment after favorable plasma-field profiles are produced is the degeneration of the stability of the configuration with time due to resistive effects [1]. The measured electron temperatures are low and field diffusion rates are high. The general objectives have been to: (1) determine the nature and magnitude of the radiation loss; (2) operate at lower filling pressures in an attempt to raise electron temperatures; (3) design and test a discharge cleaning scheme; (4) design, build and test a power crowbar circuit to lengthen useful time of the field. The experiment was then upgraded to improve the following: vacuum cleanliness; versatility in the changing of the field programming; and diagnostics.

B. Radiation Loss Measurements

1. Nature and Level of Impurities. Spectroscopic and mass analyser measurements of the ZT-S discharge have shown that the main impurity is oxygen, with smaller amounts of carbon and nitrogen. The impurity number density is in the range from ~ 0.3% to ~ 1% of the deuterium fill.

Theoretical calculations [2] predict serious energy losses that can cause limitations on the electron temperatures for the current and plasma densities being studied.

2. Absolute Measurements of the Radiation Loss

(a) Method. A survey of the impurity lines was made spectroscopically to determine the spectral range of the line radiation emitted from the ZT-S plasma. The wavelength region containing the substantial portion of radiation is between 200-1000 Å. A fast system that was sensitive to vacuum ultraviolet radiation was arranged to view the ZT-S pinch through a pump port. A schematic of the detector arrangement is shown in Fig. 1. Basically the detecting system consists of a fast, linear photodiode of wide dynamic range. The detector is sensitive to visible wavelengths and is used with a sodium salicylate phosphor wavelength shifter that intercepts the photons emerging from the plasma. The fluorescence emission spectrum of the phosphor varies by a factor of 1.45 from 2500 Å to 1200 Å and then is flat down to 200 Å. The fluorescence spectrum centers at ~ 4200 Å well within the high sensitivity range of the photodiode.

The radiation from the plasma in the ZT-S discharge passes through the aperture in the alumina plug inserted into the pump port and then through two successive 1-cm-dia. apertures to the detector. The last two apertures are covered with a wire mesh grid to improve the detector shielding against electrical noise. The signal from the detector is amplified and then transmitted to an oscilloscope display.

(b) Results. The analysis and interpretation of the results of the measurements involve several factors: (1) the calibration of the detector; (2) the source and detailed solid-angle corrections; (3) the determination of mean photon energy. Since the measurement was made through a single port, assumptions about the source distribution are needed to make determinations of the absolute value of the total radiative energy loss. Toroidal symmetry is assumed and comparisons with a variety of reasonable radial source distributions show these alter the deduced loss over a range of about a factor of two.

For an assumed source distribution having a sharp boundary plasma with a flat emission profile, the measurements give a radiative loss of 5 to 8 MW per meter length during the ~ 30 μs stable time of the discharge. The total energy balance for a sample discharge is shown in Fig. 2. The two curves show the energy input and energy content per meter of length (plasma + field energy) of the discharge as a function of time as deduced from current, voltage and magnetic probe data. For comparison, the difference between the two curves, which represents the energy loss, is shown in Fig. 3 along with the radiation loss as deduced from the above detector measurements. The same radiation loss curve is compared with the calculated ohmic heating for T_e = 15 eV in Fig. 4. These curves indicate that essentially all of the loss is due to the radiation. In view of the factor of ~ 2 uncertainty in the absolute radiation measurement mentioned earlier, this agreement is fortuitous. The measurement does indicate however that the radiation contributes half or more of the energy loss.

For plasma temperatures of 15-20 eV, as measured for ZT-S from Thomson scattering (see next section) and spectral impurity ionization state measurements, a calculation of the theoretical radiation loss rate gives values of 8-10 MW per meter. The radiation loss rates were computed for assumed values of T_e using Ortolani's POWRAD code [2] based on McWhirter's radiation loss equation [3] with a multiplying factor of 5 as suggested by the Maryland Group results [4]. This agreement is better than expected in view of the uncertainties in the measurements and the approximations made

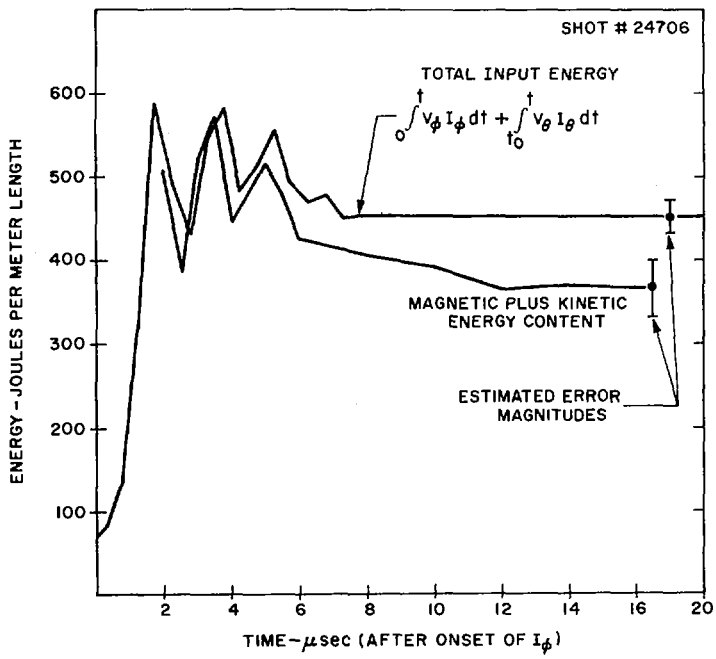


FIG.2. Energy input and content versus time in ZT-S.

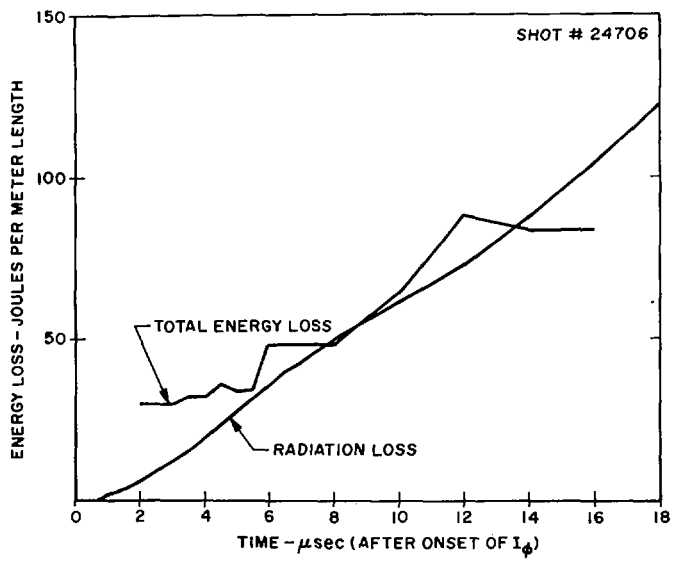


FIG.3. Curves comparing measured radiation loss with that deduced from energy balance shown in Fig. 2.

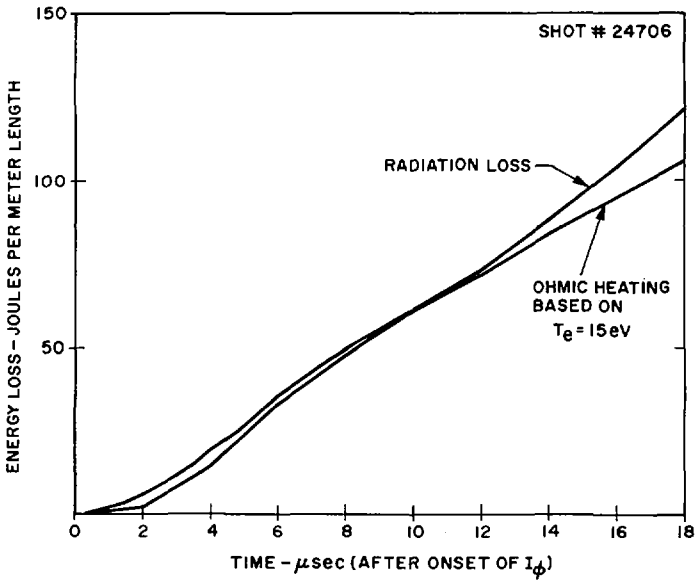


FIG.4. Curves comparing the measured radiation loss with the calculated Ohmic input.

in the functions used in determining the ionization, excitation and emission processes.

(c) Conclusions. The conclusions of these studies are as follows. For ZT-S operating at I = 60 kA and a filling pressure of 20 mtorr; (1) the radiation loss is $\gtrsim$ 50% of the energy loss; (2) the radiation is primarily in the vacuum uv with a mean energy of ~ 30 eV (λ ~ 400 Å); (3) the chief impurities are oxygen and carbon; (4) these losses are comparable to those predicted by theory.

C. Electron Temperature Measurement

1. General. Thomson-scattering measurements of electron temperature at filling pressures of 18 and 34 mtorr in ZT-S have been reported earlier [1]. Operation was studied at lower fill pressures to see if higher electron temperatures and lower diffusion rates can be obtained. Earlier measurements at lower densities were then hampered by instrumental scattering. This problem has been resolved by the addition of two 6943-Å notch filters to the scattered spectrum detector. The width at half maximum of each filter is 10.2 Å. The overall sensitivity of the detector is reduced by a factor of 2, whereas the instrumental scattering signal is down by a factor of 15. Good data have been obtained at filling pressures of 10 mtorr. Data acquisition at 5 mtorr is limited by the reproducibility of the pinch rather than by the sensitivity of the diagnostic. The field diffusion at $\leq$ 5 mtorr gas fill and lower was observed to be very rapid.

2. Results. The temperature measurements shown in Fig. 5 have been obtained with a filling pressure of D_2 of 10 mtorr and a peak toroidal current of 60 kA with an initial rise of 35 kA/μs. The initial bias field

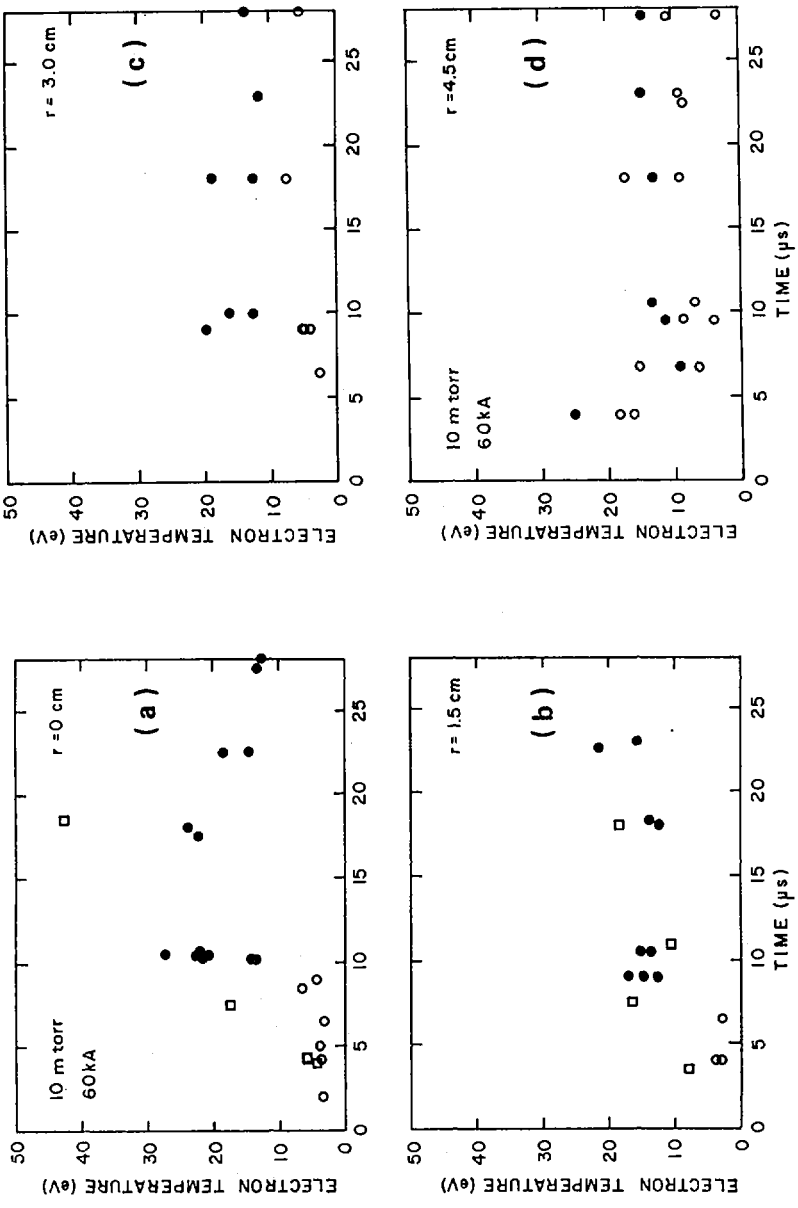


FIG. 5. Thomson-scattering measurement of electron temperature at (a) 0, (b) 1.5, (c) 3.0 and (d) 4.5 cm radius. Peak toroidal current 60 kA; filling pressure 10 mtorr of D_2.

was set at 0.064 T and the toroidal field at the wall reversed to -0.079 T in about 8.5 μs. The postimplosion plasma radius as estimated from pressure profiles was of the order of 4 cm.

The square data points have been obtained with a polychromator dispersion of 33 Å/mm and the circles with a dispersion of 66 Å/mm. The solid circles are the result of a least squares fit to 7 polychromator channels. The open circles are based on the same data, but using the two closest channels only on each side of the 6943 Å channel. The difference between the two analyses is relatively minor at late time in the discharges (> 10 μs). At early times, however, the analysis based on 4 data points gives a much lower temperature and, perhaps, a better representation of the main body of the electron distribution than the 7-point analysis.

Figure 5(a) shows a peak central value of T_e of 25 eV which then decays gradually to 15 eV at 25 μs. The electron temperature at 1.5- and 3-cm radii levels off at about 15 eV. There is an indication of a higher temperature sheath at $r \gtrsim 4.5$ cm at early times.

3. Conclusions. Comparison of this result with the previous T_e measurements indicates only a small increase of the electron temperature as the filling pressures decrease. The peak values of T_e reported earlier [1] were 12 eV at 34 mtorr and 15 eV at 18 mtorr. The operation at lower filling pressures does not show temperatures scaling inversely with the fill density as simple models would predict. A possible explanation is that there is either enhanced thermal transport or more wall impurities released at the lower fill pressure operation.

D. Discharge Cleaning Studies

1. Motivation. The foregoing radiation loss and T_e studies indicate the need for determining if suitable discharge cleaning methods can be developed in order to reduce the impurity level to acceptable limits. A preliminary investigation was made to determine the usefulness of the low temperature discharge technique [5] for the removal of the loosely bound surface impurities from an alumina discharge vessel. Previous work in this area has been limited to metal-walled systems. It is known, however, from the results of the Petula group at Grenoble that the replacement of a tungsten limiter with an alumina one can reduce the oxygen in the discharge a factor of three to four in the Petula tokamak [6].

2. Discharge Cleaning Circuit. The discharge cleaning circuit consists of capacitor and switching circuit capable of delivering ~ 110 J per pulse to a series connection of the toroidal and poloidal field circuits. This arrangement forms a 2-kA screw pinch and is capable of producing one to five pulses per second. The circuit can be quickly removed from the experiment by the use of a pair of pneumatically operated switches, thus minimizing the time between the cleanup discharges and the normal firing of ZT-S.

The energy input per pulse varied from 50 J at 0.7 mtorr to 160 J at 40 mtorr gas fill.

The confirmation of the required low electron temperature of the plasma during discharge cleaning was obtained by two methods. First the resistivity of the plasma was calculated from the voltage and current traces. Using the Spitzer equation and obtaining the plasma radius from the streak pictures, we find ~ 2-3 eV for the filling pressures of 1, 10 and 20 mtorr. The second method was a line-to-continuum measurement using Dβ 4861 Å. From this we found 3.0 eV at 10 mtorr and 2.0 eV at 1 mtorr.

3. Results. The mass analyser has been used to observe the gases that are pumped from the torus before and during discharge cleaning. The principal mass numbers observed are 14, 16, 18, 19, 20 and 28. These correspond to N, O or CH_4, H_2O, HDO, D_2O, and CO or N_2. The ambiguity between D_2O and CD_4 was resolved by comparing results between hydrogen and deuterium discharges.

The mass analyser was used to monitor the D_2O line during the discharge cleaning. With the turn-on of discharge cleaning there is an increase in D_2O. The amplitude of this signal decreases rapidly in the first few minutes and then levels off. When the discharge cleaning is terminated, the D_2O decreases immediately. When the gas flow is terminated the D_2O further decreases, usually below the initial level present.

4. Conclusions.

(1) Oxygen impurity was converted to water generated by the 2-5 eV plasma and is pumped from the system, as has been observed with metal systems [5]. This was done without overheating the polyethylene electrical insulation of ZT-S.

(2) Five hours of discharge cleaning reduced the effective outgassing rate by a factor of two or more. Further reductions in total outgassing rate were limited by the torus construction (see Sec. E below).

(3) In addition to water, the next most abundant impurity observed on the mass spectrograph was found to be mass 28 (CO or N_2).

(4) A simple capacitive discharge circuit allowing immediate switching between discharge cleaning and normal high-voltage operation has been demonstrated to be practical for ZT-S.

E. ZT-S Upgrade

1. Description of Upgrade

Since impurity radiation losses may be dominating the physics of the plasma behavior, it was decided to upgrade the cleanliness of the vacuum system. The alumina torus was made from ninety segments joined using viton O-rings. Although these O-rings were well protected from the plasma, they do constitute a significant outgassing load which cannot be corrected by discharge cleaning. Ideally one would solve this problem by using a solid torus. Although the procurement of such a torus with adequate diagnostic windows may be a future prospect, it is not possible on a short time basis. Instead, the number of O-rings can be significantly reduced by a special glass-joining technique [7]. The elements of the present ZT-S upgrade were as follows:

(a) Improved Vacuum System. (1) Reduction of number of O-rings in the system from 90 to 24. (2) No vacuum grease permitted. (3) The use of a new air bearing totally oil-free turbomolecular pump. (4) Improved effective pumping speed a factor of three. (5) Use of a quick change-over low-temperature discharge cleaning system.

(b) Improved Circuitry. (1) Power crowbar system. (2) New toroidal field circuit allowing more flexibility in setting up the RFP configuration.

(c) Improved Diagnostics. (1) New small, high-resolution magnetic probes. (2) New improved data acquisition system. (3) Newly developed five channel interferometer [8]. This will allow the measurement of the integrated electron density along five parallel chords simultaneously. A schematic of the arrangement is shown in Fig. 6.

At the time of this writing the upgraded machine has just become operational.

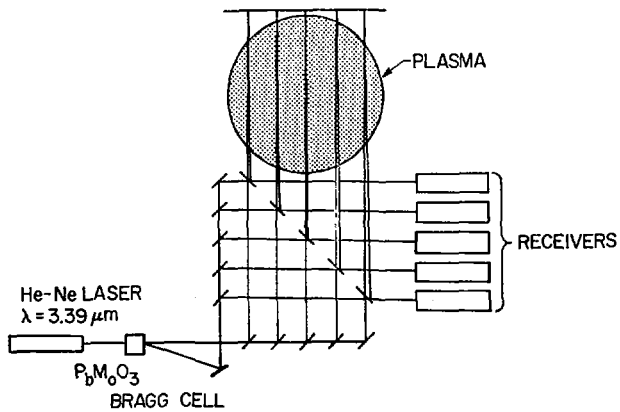


FIG. 6. Schematic of the five-channel interferometer.

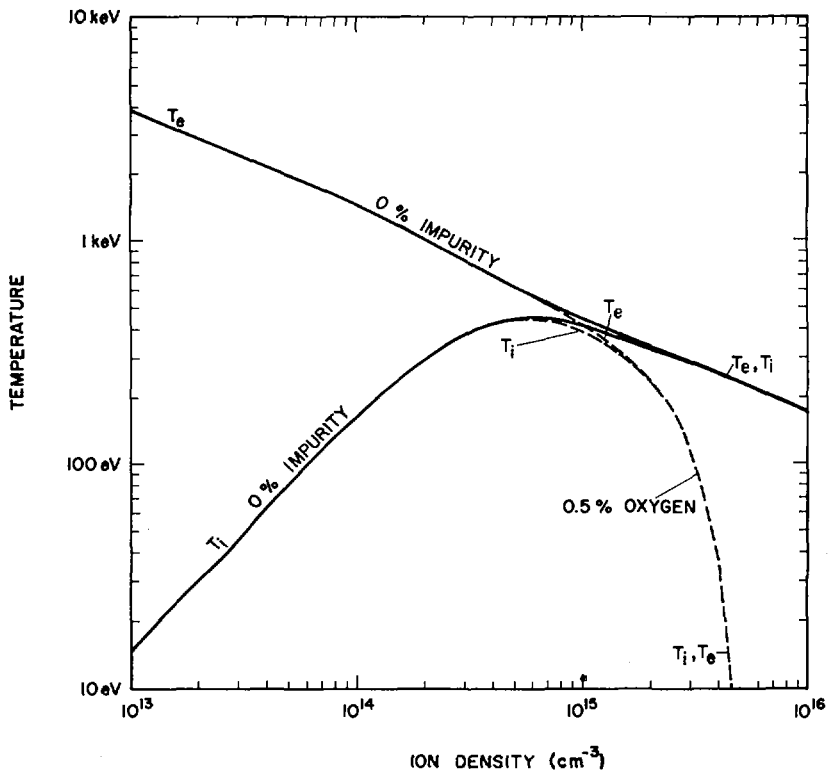


FIG. 7. Ion and electron temperatures at 3 ms predicted by IMPRAD code for a uniform total current density of 3 kA/cm² which rises in 1 ms and decays with an e-folding time of 10 ms.

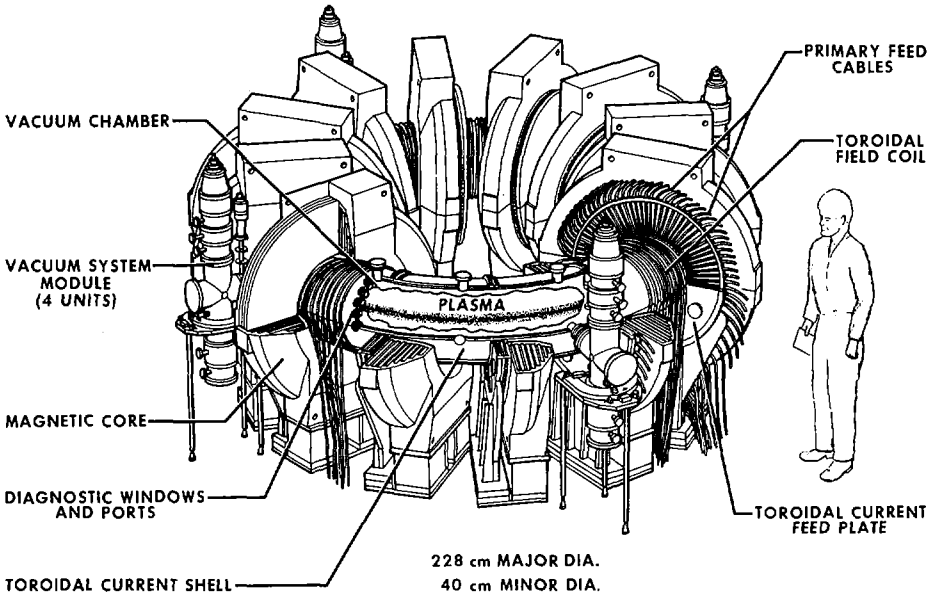


FIG.8. Artist's sketch of the front end of ZT-40.

IV. ZT-40

A. Objectives

The ZT-40 experiment is the next step beyond the ZT-S in the Reverse Field Pinch program at LASL. The initial objective of ZT-40 will be to demonstrate confinement time scaling from the results of ZT-I and ZT-S. If the confinement time scales as the square of the minor bore, ZT-40 will be stable for at least 150 to 200 μs. A second objective will be to operate in a regime clean enough to overcome the impurity radiation barrier and raise the temperature to at least $T_i = T_e \sim 100$ to 200 eV. The actual temperatures achievable will depend upon the useful upper limit on current density, the lower limit of the operating plasma density and the losses. If the diffusion coefficient becomes lower due to the higher T_e values longer confinement times can be expected. The power-crowbarred fields of ZT-40 can be sustained for ~ 3.5 ms. An upper limit on T_i and T_e to be expected, assuming classical ohmic heating and good confinement for 3 ms for various ion densities, can be seen from the curves in Fig. 7 obtained from the Imprad code [2]. Shown also is the effect of 0.5% oxygen impurity. No thermal transport losses are included. To maximize the ion temperature, an operating density of 5×10^{14}-10^{15} cm^{-3} is indicated. In addition, ZT-40 will be used to determine the ranges of the current and electron densities which allow the production of stable configurations. Of particular interest is to determine whether there are any microinstabilities which impose an upper limit on the usable ohmic heating current. Another objective is to operate with reduced rates of rise of current in order to establish the time scale over which the stability can be controlled by programming of external currents. The self-reversal method of production of reversed-field configurations will be studied as a function of risetime.

An overall objective of the studies is to determine the optimum operation between the generally competing reactor requirements of slow risetime and low start-up energy losses.

B. Description

ZT-40 has a 40-cm minor bore torus with plasma aspect ratio of 5.7. The torus can be fed at a maximum of 12 points and has 12 magnetic cores equally spaced about the torus. A drawing of the ZT-40 experiment is shown in Fig. 8. The maximum number of feedplates allowed in the design was determined by the requirement that the minimum allowable initial risetime of the current be the same as ZT-S (2.5 μs). The current risetime is lengthened to ~ 20 μs by removing feedplates and shorting the respective toroidal feed points, and by series-paralleling the poloidal field windings. Very slow operation (up to 1 ms) can be attained by removing all feedplates and inducing the toroidal current by means of toroidal windings on the outside of the primary or by energizing the field only with the power crowbar banks.

The initial experiments on ZT-40 will utilize a ceramic discharge tube. Further experiments with metal tubes are planned for the slower experiments if their use can be shown to lead to cleaner discharges. The discharge tube is located inside a 2-cm-thick aluminum stabilizing shell which serves as the primary conductor of a transformer with the plasma as the secondary.

The vacuum system has been designed to be oil-free and allows rapid pulse discharge cleaning and in situ baking of the vacuum chamber.

The basic machine parameters for ZT-40 are given in Table I.

TABLE I
ZT-40 DESIGN PARAMETERS

Major Radius	$R = 114$ cm
Minor Vacuum Chamber Radius	$a = 20$ cm
Gas Fill (D_2)	$p = 5\text{-}30$ mtorr
Electron Density	$n_e = 10^{14}\text{-}10^{16}$ cm^{-3}
Toroidal Current	$I\phi \sim 150\text{-}600$ kA
Mean Toroidal Current Density	$J\phi \leq 2$ kA/cm^2
Initial (Toroidal) Field	$B\phi = 0.2 - 0.6$ T
Reversed-Toroidal Field	$B\phi_R = \leq - 0.5$ T
Poloidal Field	$B\theta = \leq 0.6$ T
Range of Plasma Current Risetime	$\tau = 2.5$ μs to 1 ms
Base Pressure	$p_o \sim 10^{-8}$ torr

V. THEORY

A. One-Dimensional Hybrid Simulations

The LASL one-dimensional hybrid code [9,10] has been used to study the evolution of the magnetic field and temperature profiles of the ZT-S experiment. Anomalous bulk transport coefficients were required to achieve agreement with the measured profiles. The anomalous electrical resistivity used in previous calculations of ZT-I [9] were found to adequately describe the implosion and early post-implosion field diffusion in ZT-S (i.e. up to

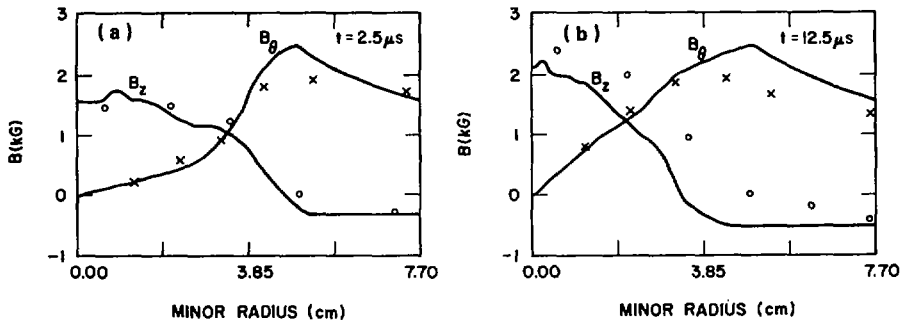


FIG.9. Comparison of the ZT-S fields theoretical calculations with the hybrid 1-D code. The x's are the experimental poloidal field data (to be compared with the B_θ of the cylindrical model) and the o's are the toroidal field data (compare with B_z). (a) Fields 2.5 μs after pinch current onset; (b) 12.5 μs after current onset.

3 μs), as illustrated in Fig. 9(a). Also as found for ZT-I [9], classical resistivity alone did not account for the observed diffusion because the heating in the low density outer portion of the sheath caused the resistivity to drop, inhibiting further diffusion. Including oxygen impurity radiation with the assumption that the oxygen density is either proportional to the compressed deuterium density or constant (the latter intended to mock-up wall emission of oxygen) lowers T_e in the dense core of the plasma but does not eliminate the high temperature (~ 100 eV) in the sheath. It presumably would be possible to devise, with much trial and error computing, a wall emission rate that would load the region with oxygen in such a way as to reduce the high sheath temperature. Except for the latter possibility, the observed field diffusion must be a result of anomalous effects.

A large anomalous resistivity is required to fit the field data during the implosion. However, at later times the resistivity must decrease. A calculation using the Chodura formula with the same coefficients throughout the calculation showed that the axial field profile collapsed to about 30 to 50% of the observed field at 10 μs and remained much lower than the observed field thereafter. In addition it is found that $T_e \geq 100$ eV everywhere in the plasma at 15 μs, whereas the observed T_e is less than 30 eV. Theoretically this drop in anomalous resistivity is expected, since the high velocities and steep gradients which may drive the turbulence during the implosion decrease afterward. In fact, measurements by Commisso and Griem [11] demonstrated a factor of 5 to 10 decrease in the turbulent fluctuation energy and resistivity after the implosion on the University of Maryland θ-pinch. Field profiles at 12.5 μs from a ZT-S calculation, with Chodura coefficients decreased by a factor of five after the first peak compression are compared with experiment in Fig. 9(b). Note that now the height of the axial field profile agrees with experiment (although the width of the profile is a bit too narrow) and the experimental and theoretical θ-profiles show a similar structure. In this calculation radiation from oxygen impurities having a constant density profile with a value 0.7% of fill density was included. In a previous calculation without the radiative loss, the plasma temperature reached 100 eV everywhere at 15 μs (although the field profiles were similar to those in Fig. 9(b)). In Fig. 10, T_e at 1.5 cm is plotted as a function of time for the calculation

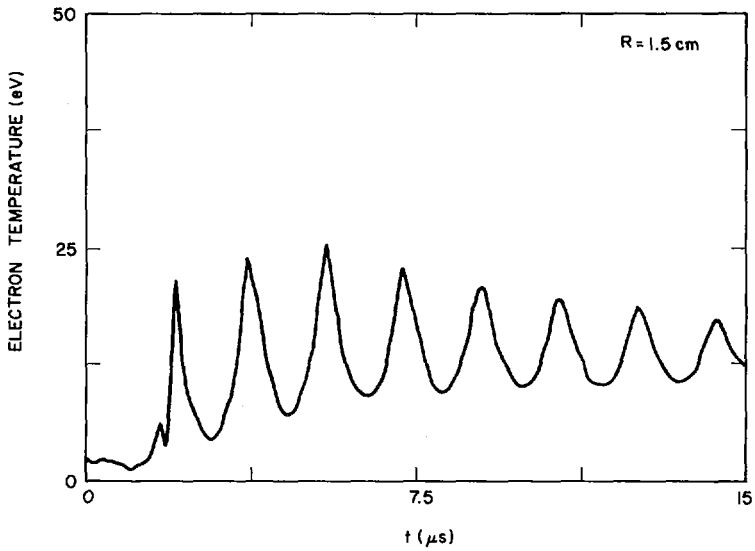


FIG.10. Electron temperature as calculated at R = 1.5 cm in ZT-S.

which included losses. Note that these temperatures are quite consistent with the measurements in Fig. 5(b). During the 15 μs a power loss of about 10 MW per meter was calculated, which is comparable to the average measured power loss reported in Sec. II(b).

In conclusion, the anomalous resistivity used to model the early time behavior of ZT-I also describes the early time field diffusion in ZT-S. The later time behavior of ZT-S, with its enhanced confinement time, also can be modeled provided that the resistivity is decreased at late time to account for the expected decrease in the turbulent fluctuation energy. When impurity radiation from oxygen is included in the calculation, and the oxygen density is chosen to be within its experimentally determined range, the calculated and measured T_e are comparable.

Simulations with this code have also been done for ZT-40 parameters. The predicted field distributions for a 20-μs current rise and a programmed reversed field are shown in Fig. 11. Chodura anomalous resistivity is used. The simulations show that sheath thickness is comparable to those found in the previous ZT experiments so that, with the larger radius of ZT-40, the poloidal field is well excluded from the main body of the pinch for well over 20 μs. The calculations indicate initial mean temperatures on the order of 100 eV. Further programming and studies of the stability of the resulting equilibrium profiles are in progress.

B. Time-Dependent Toroidal MHD Simulations

1. General. Two-dimensional MHD simulations of the LASL reversed field pinches ZT-I, ZT-S and ZT-40 have been made.

The model used is the single-fluid, time-dependent, axisymmetric magnetohydrodynamic equations with dissipation. Initial conditions assume a fully ionized low-temperature plasma at rest, with appropriate bias toroidal field. The equations are driven by time-dependent boundary

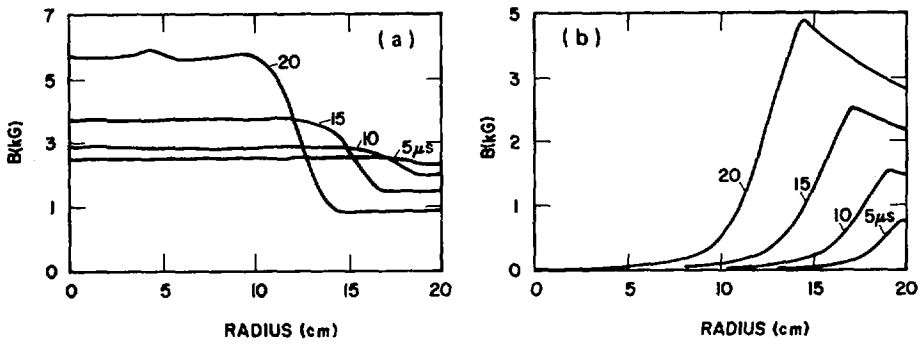


FIG.11. 1-D hybrid code predictions of the field profile for ZT-40 with reversed-field programming.
(a) Axial field; (b) azimuthal field.
Conditions: current risetime 20 μs; initial deuterium ion density 2.5 X 10^{15} cm^{-3}; initial bias field 3 kG; peak pinch current 600 kA.

conditions: the toroidal field and the poloidal flux are prescribed as functions of time in agreement with the experimental conditions. The poloidal flux is indirectly extrapolated from the prescribed toroidal current.

The only adjustable transport and dissipation parameters were the following:

(1) Electrical conductivity--both scalar classical Spitzer conductivity and Chodura [12] anomalous values were studied.

(2) Thermal conductivity--a constant value about equal to the classical parallel heat conductivity for a 4-eV plasma accounts for anomalous effects as well as radiation, not otherwise accounted for explicitly. Remarkably, the same constant value (2 x 10^6 cgs units) was found to apply to both ZT-I and ZT-S (as well as the Italian RFP ETA-BETA and the Dutch screw-pinch SP-1) in the sense that the predicted mean temperatures agree reasonably with experimental values.

(3) Numerical viscosity was used in momentum equations to give stability, but is small in effect compared to other dissipations.

(4) Low density cut-off in vacuum region equal to 5% of initial filling density.

The equations are solved numerically in an Eulerian grid in toroidal-polar coordinates, and the standard ADI method is used [13-15].

2. Results for ZT-I and ZT-S

(a) Field-penetration. The diffusion of the magnetic field is more directly controlled by the electrical conductivity than by the other transport coefficients, and it is instructive to examine different experiments at the same time. Figures 12 and 13 show B_ϕ and B_θ as functions of position at different time instants for ZT-I and ZT-S respectively. The dashed lines in Fig. 12 are obtained for a purely classical resistivity with a low T_e due to the anomalous thermal conductivity used. One concludes that for the temperature and current

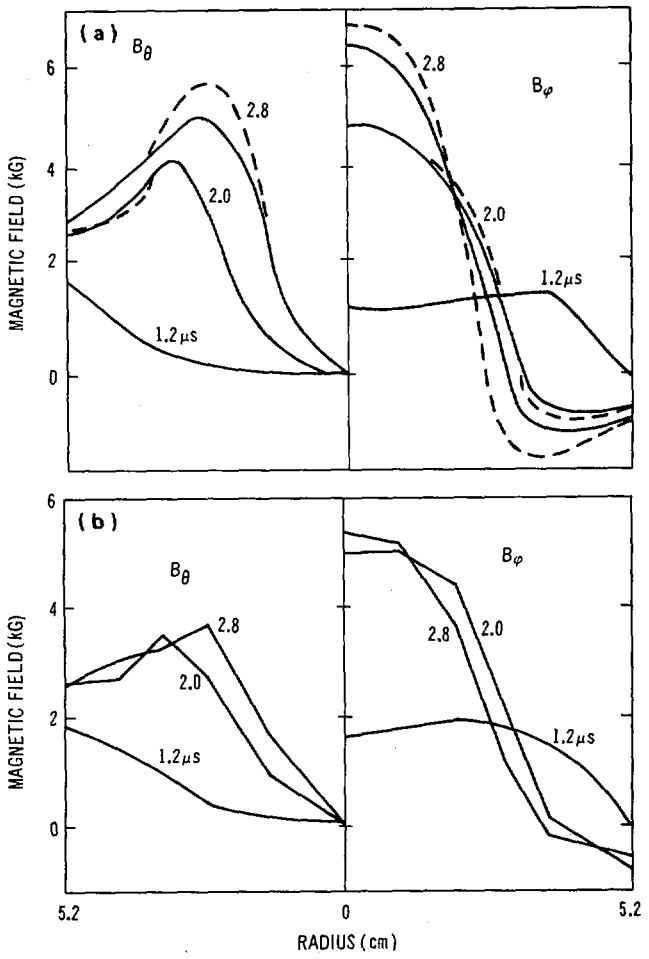


FIG.12. ZT-I toroidal and poloidal field profiles: (a) 2-D toroidal calculation results with classical resistivity (– – –), and with the anomalous resistivity (——); (b) Experimental curves (straight lines are drawn between data points).

density ranges of these experiments, both classical (with anomalously low T_e) and Chodura resistivity give reasonable agreement, although during the initial setting up phase, the Chodura resistivity gives somewhat better comparisons.

(b) Longer time behavior. The simulation runs are carried out to near-equilibrium. For this later phase the anomalous resistivity gave poor comparisons and the actual resistivity appears to be close to classical. For ZT-S the radial oscillations in the calculation damped in ~ 6 μs in agreement with observation.

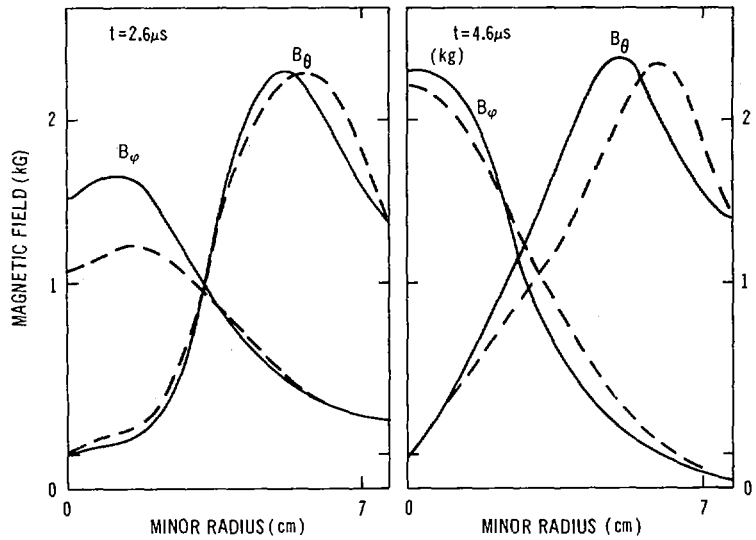


FIG.13. Toroidal and poloidal field profiles on the vertical radius ($\theta = \pi/2$) of the poloidal plane are compared between the toroidal 2-D calculation (——) and experiment (– – –) at 2.6 μs and 4.6 μs for ZT-S.

(c) Toroidal effects. This simulation does not have the same detailed physics as in many 1-D simulations, but it does give all toroidal effects automatically. The following particularly interesting toroidal phenomena should be noted. Figure 14(a) shows the toroidal shift of the magnetic axis versus time, and Fig. 14(b) shows the widely different current profiles along a vertical diameter and along a horizontal diameter of the poloidal plane, as a consequence of the toroidal shift. The toroidal shift is ~ 1 cm, about twice the shift computed assuming static equilibrium. This larger shift is evidently due to the toroidal plasma flow that can be seen in Fig. 15. These differences are important in interpreting measured results from experiments. In Fig. 15(a) are shown the three components of velocity in toroidal coordinates as functions of time at the two points indicated in Fig. 15(b). Prominently visible is a shear flow in the toroidal direction, induced by the $\vec{j} \times \vec{B}$ force in the poloidal plane (the toroidal curvature causes $\vec{j}$ and $\vec{B}$ to be not exactly parallel in the poloidal plane). It would be interesting to observe this flow in actual experiments.

3. Predictions for ZT-40

Figure 16 shows the predicted early time field profiles for ZT-40 using Chodura resistivity. The temperature at early times is about 70 eV. In this case, the present method of calculation can at best give the correct initial behavior and dynamics but the correct late time behavior must be obtained from quasi-equilibrium type of diffusion calculations.

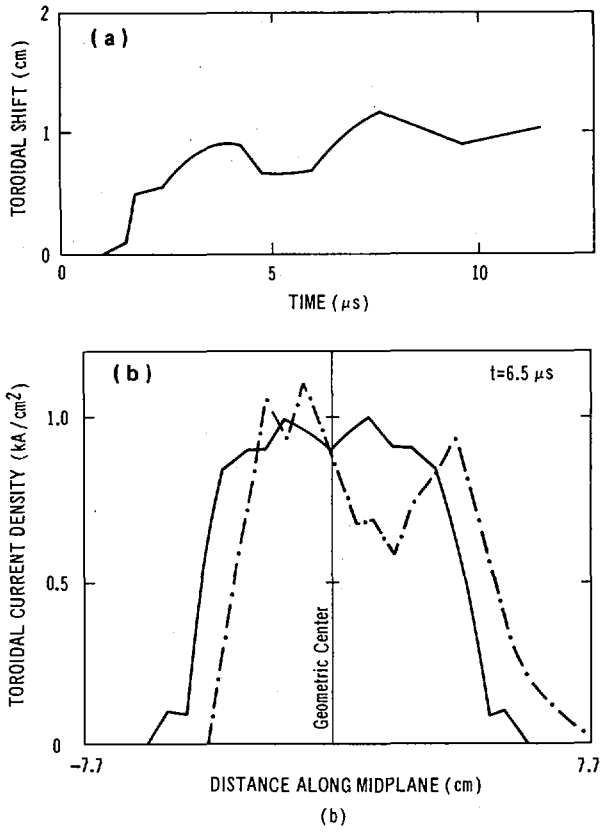


FIG.14. (a) Time trace of the toroidal shift of the magnetic axis (ZT-S). (b) Calculated toroidal current-density profiles at 6.5 μs. The solid line represents the values on the vertical diameter $\theta = \pm \pi/2$ of the poloidal plane, and the dotted-and-dashed line the values on the horizontal diameter (ZT-S).

For comparison, the dashed curves are the field profiles at 10 μs predicted by the LASL 1-D hybrid code with the same initial conditions and boundary fields. In contrast to the above 1-D calculations, which assume vacuum fields outside the pinch, in this calculation it is assumed that a low-density plasma filled the region between the imploded plasma column and the wall. This assumption corresponds to the situation in the two dimensional code. As may be seen, the agreement of the field profiles is quite good. However, the absence of anomalous cross field thermal conduction in the one dimensional calculation results in higher temperatures, with $T_i + T_e \approx 180$ eV at 10 μs.

If the low density halo is replaced by a vacuum, then all the applied current flows in the main plasma, resulting in a stronger implosion and different final equilibrium. The nature of the region between the imploded

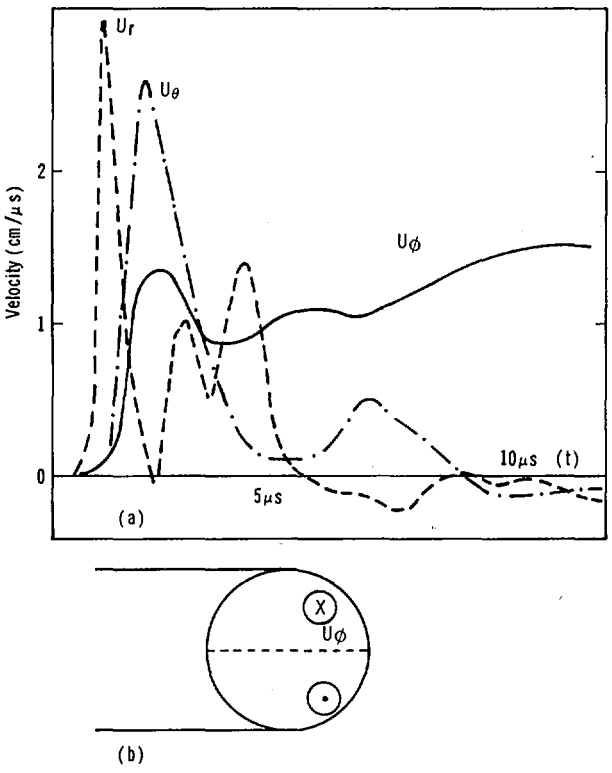


FIG.15. Time traces of the radial (U_r), azimuthal (U_θ) and toroidal velocities (U_ϕ at the point depicted in (b)) (ZT-S).

plasma column and the wall, be it vacuum fields or current-carrying plasma, is an input to the computational models rather than a prediction of them. Clarification of this issue must await more detailed measurements in the region near the wall.

ACKNOWLEDGMENTS

The authors wish to thank the LASL engineering group under the direction of C. F. Hammer for supplying the engineering for ZT-S upgrade and the ZT-40 design and construction. Thanks are also extended to R. Gerwin, L. W. Mann and L. Turner, who have supplied support in theoretical and computational areas.

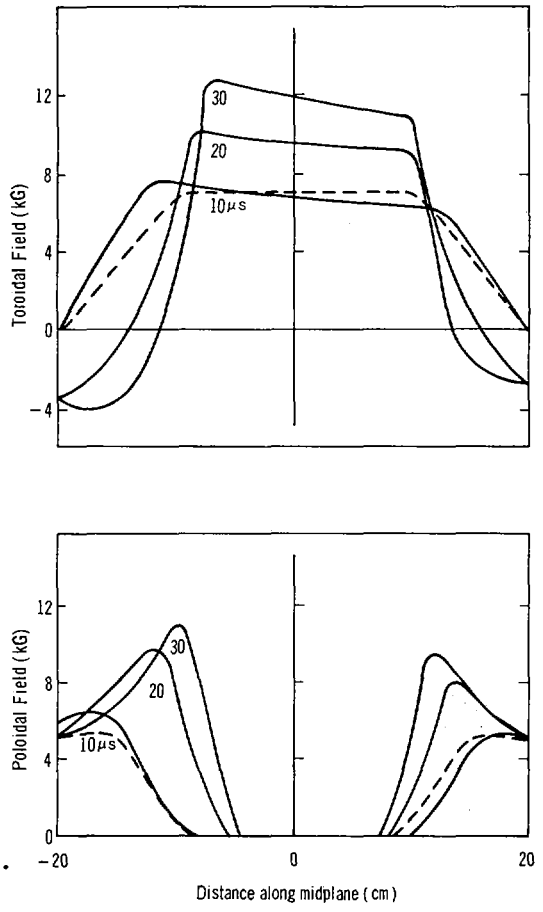


FIG.16. Predicted fields for ZT-40 for reversed-field programming as calculated with the 2-D code. Current risetime 10 μs; initial deuterium ion density 1.50 X 10^{15} cm^{-3}; initial toroidal bias field 3 kG; peak current 500 kA. Dashed curves show the corresponding fields at 10 μs for the 1-D hybrid simulation.

REFERENCES

[1] BAKER, D.A., et al., "Current temperature and confinement time scaling in toroidal reversed-field pinch experiments ZT-I and ZT-S", Plasma Physics and Controlled Fusion Research 1976 (Proc. 6th Int. Conf. Berchtesgaden,1976) Vol. 1, IAEA, Vienna (1977) 419.

[2] COSTA, S., ORTOLANI, S., Study of the Impurity Radiation Losses in a Pinch Discharge, Univ. of Padova Rep. UPEE 75/06 (1975).

[3] McWHIRTER, R.W.P., "Spectral intensities", Plasma Diagnostics Techniques (HUDDLESTONE, R.H., LEONARD, S.L., Eds), Academic Press, New York (1965), Chap. V, pp. 201–263.
[4] DMFE, Newsletter, Atomic Data for CTR (July 1975).
[5] OREN, L., TAYLOR, R.J., Nucl. Fusion **17** (1977) 1143.
[6] BARDET, R., et al., "The Petula tokamak experiment: effects of low-Z materials on plasma characteristics", Plasma Physics and Controlled Fusion Research 1976 (Proc. 6th Int. Conf. Berchtesgaden, 1976) Vol. 2, IAEA, Vienna (1977) 259.
[7] HAUTH, W.E., III, STODDARD, S.D., J. Am. Ceram. Soc. **57** (1978) 181.
[8] JACOBSON, A.R., A Novel Interferometer for the Measurement of Plasma Density, Los Alamos Scientific Lab. Rep. LA-6727-MS (1977).
[9] SGRO, A.G., NIELSON, C.W., Phys. Fluids **19** (1976) 126.
[10] SGRO, A.G., Phys. Fluids **21** (1978) 1410.
[11] COMMISSO, R.J., GRIEM, H.R., Phys. Fluids **20** (1977) 44.
[12] CHODURA, R., Nucl. Fusion **15** (1975) 55.
[13] LUI, H.C., CHU, C.K., Phys. Fluids **18** (1975) 1277.
[14] PARK, W., CHU, C.K., Nucl. Fusion **17** (1977) 1100.
[15] PARK, W., Ph. D. Thesis, to appear as Columbia Univ. Lab. Rep. No. 75.

THEORETICAL AND EXPERIMENTAL STUDIES OF THE REVERSED-FIELD PINCH

P.G. CAROLAN, C.W. GOWERS*, D.C. ROBINSON,
M.R.C. WATTS, H.A.B. BODIN
Culham Laboratory,
(Euratom/UKAEA Fusion Association),
Abingdon, Oxon.,
United Kingdom

Abstract

THEORETICAL AND EXPERIMENTAL STUDIES OF THE REVERSED-FIELD PINCH.

Recent studies of the reversed-field pinch (RFP) are presented. Stability theory has been extended to include both growth rate and marginal analyses of the tearing mode. The localized resistive interchange instability (g-mode) has been investigated numerically in cylindrical geometry. It is found that there are tearing-mode stable configurations with $\beta \lesssim 17\%$, but the stabilizing effects of ion viscosity and finite Larmor radius on the g-mode are less effective than previously found in a slab model and these modes are hard to suppress at high-β. A simple zero-dimensional code which simulates the setting up of RFP distributions by self-reversal is described in which Ohmic heating is balanced against radiation and turbulent losses using experimentally based values to describe these effects. Agreement is found with data from Zeta and the code is used to predict the performance of a new RFP experiment. Experimental studies of the mechanism of self-reversal on HBTXI for compressed and weakly compressed pinches are discussed and measurements presented in which the risetime is longer than the characteristic time for relaxation. In compressed pinches self-reversal is produced by a single large-amplitude m = 1 kink instability, whereas in weakly compressed discharges it is due to the cumulative effect of a number of small-amplitude m = 1 modes which grow successively. The magnitude of the observed change in B_ϕ is explained on this basis. A universal F-θ curve and sustained reversal are observed. The parameters of the next generation of RFP devices are discussed. Reactor studies highlight some problems peculiar to the RFP, but establish it as a viable alternative to the tokamak, with advantages if Ohmic ignition and high-β can be realized.

1. Introduction

In this paper theoretical and experimental results on the RFP obtained at Culham since the Berchtesgaden Conference are reviewed [1][2]. Theoretical studies of the tearing mode and numerical studies of the g-mode, for tearing-mode stable configurations, are described. A simple 0-D numerical code has been developed to simulate the setting-up phase of experiments with slow rise times in which the field configuration is generated by self-reversal. Numerical results are compared with data from Zeta [3] and predictions made for new experiments. Experimental measurements from HBTXI [2]

* AWRE Aldermaston, Berkshire, UK.

on the mechanism of self-reversal in compressed and weakly compressed pinches are presented and discussed. New data are reported in which the rise time of the current is longer than the characteristic time for relaxation, including the observation of a universal F-θ curve ($F = B_\phi wall/B_\phi (average)$; $\theta = B_\theta wall/B_\phi (average)$) and sustained reversal. The parameters and objectives of next-generation RFP experiments are briefly discussed and some recent reactor studies [4][5][6] summarised.

2. Theoretical Studies of Tearing and Resistive Interchange Modes

The reversed-field pinch can be stable to ideal hydromagnetic modes at high average β ($\bar{\beta} \gtrsim 30\%$). At zero β it can also be stable to resistive tearing modes with a vacuum region between the plasma and the conducting wall [7]. This wall is necessary to give stability to instabilities with poloidal mode numbers, m = 0 and 1. The introduction of a pressure gradient produces resistive interchanges and their properties have been investigated in some detail [8][9].

Analytic work is restricted to low and high magnetic Reynolds numbers, S ($= \tau_R/\tau_{Alfvén}$ where τ_R = resistive diffusion time), in slab geometry but intermediate values are more appropriate to many experiments. The calculations have been performed with numerical codes [10], which treat the resistive equation of motion in cylindrical geometry as an initial value problem and make no assumption as to the existence of a resistive layer. The equations include the Hall effect and a full stress tensor. Results have been obtained with a tearing-mode stable reversed-field pinch configuration in which the pressure gradient is generated so that it satisfies the Suydam criterion everywhere. This criterion can be written:

$$\frac{dp}{dr} = c_1 \, f(r) r B_\phi^2 \left(\frac{dP}{dr}/P\right)^2 \qquad (1)$$

where p, B_ϕ and P are the pressure, longitudinal field and the pitch - rB_ϕ/B_θ respectively; f(r) is an arbitrary function of r; c_1 is a constant. (When $c_1 f(r) \leq 0.125$ the Suydam criterion is satisfied.) The resulting configuration obtained by either holding the radial variation of pitch or parallel current constant as the pressure is increased is stable to ideal MHD modes for beta on axis = $\beta(o) < 17\%$ ($\beta_\theta \leq 0.5$).

The growth rate, p (normalised to the field diffusion time) is expressed in terms of S, and the most unstable mode number, m, is found to increase with S [8]. For m = 0, p is approximately given by $p \propto S^\nu$, $\nu \sim \frac{3}{4}$ for $S > 5 \times 10^3$. The slow interchange ordering gives $\nu = 2/3$ but this is only valid for $\beta \to 0$. As m increases so the velocity perturbation becomes more

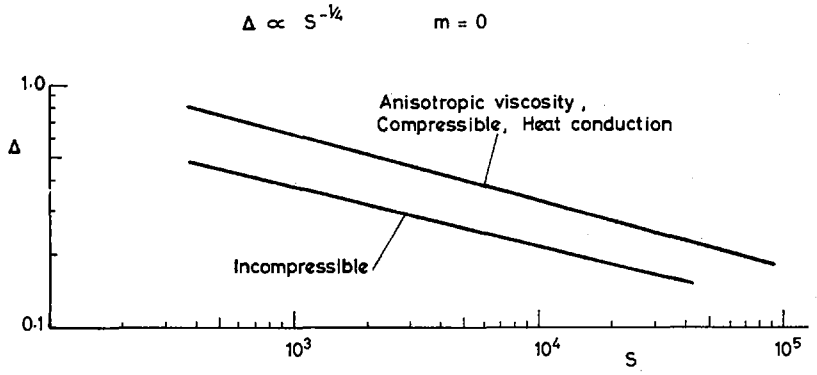


FIG.1. Resistive layer thickness as a function of S for m = 0 from a calculation assuming incompressibility and from a calculation including anisotropic viscosity, compressibility and heat conduction.

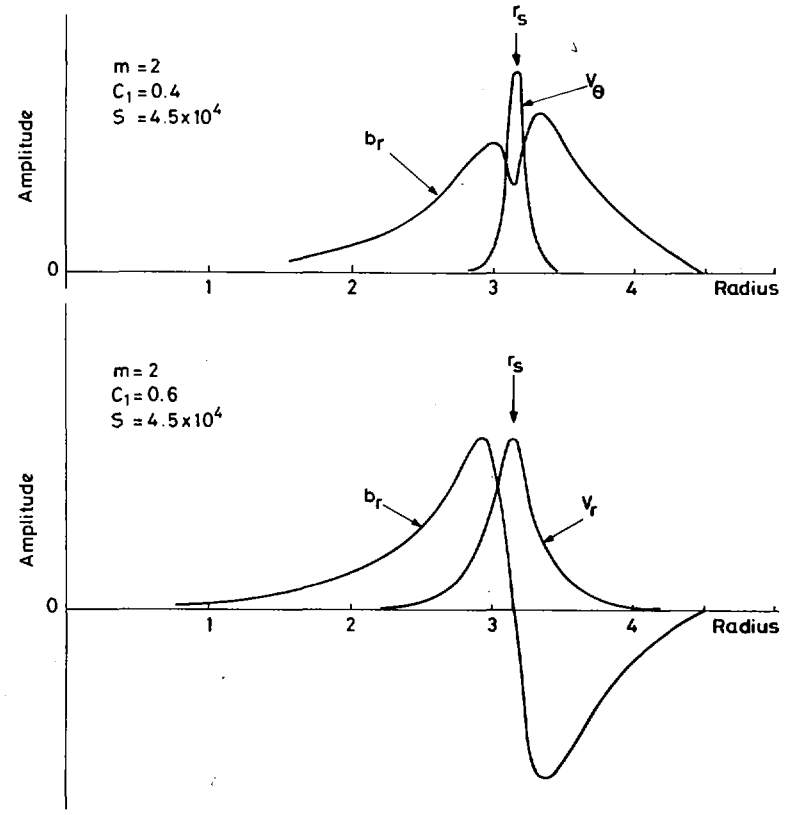


FIG.2. Calculated mode structure of the m = 2 resistive interchange as it evolves into a Suydam mode when the pressure gradient exceeds four times the Suydam gradient.

localised and $p \propto S^{\mu}$, $\mu \lesssim 1.0$ for $m \geq 3$. This appears to be the transition to the fast interchange ordering where the growth is at the hydromagnetic rate, though the criterion for this ordering, $\frac{1}{m} < \frac{\Delta}{R}$, is not satisfied. (We have taken Δ as the full width at half height of the azimuthal velocity perturbation. R is the radius of the singular surface.) The velocity perturbation is found to be localised within a resistive layer. The mode localisation for the m = 0 mode varies with S as shown in Fig.1, and is much the same if one includes viscosity and heat conduction, although Δ is larger.

Results obtained by varying f(r) in equation (1) establish that only the local pressure gradient gives rise to the growth. If the value of $c_1 f(r)$ is increased locally for S = 45 000, the ideal MHD Suydam mode eventually dominates (the radial field changes sign at the singular surface r_s), as shown in Fig.2 for m = 2. This occurs, for this value of S, when the pressure gradient exceeds the 'Suydam gradient' by four times. At higher values of S, e.g. 4.5×10^8, the ideal mode dominates at three times the Suydam gradient.

Though these interchange modes are not as well coupled to the magnetic field as tearing modes, the resultant field perturbations lead to the formation of magnetic islands [8]. If these islands overlap, which could occur as there are many rational surfaces present in the RFP, this could lead to substantial losses at high-β. Whether saturation of the 'g' modes arises as a result of island formation, as with the tearing mode, or as a result of removal of the local pressure gradient by convection is not yet clear. Non-linear calculations are in progress.

The inclusion of anisotropic viscosity, thermal conductivity, compressibility but not finite Larmor radius terms, does not affect this picture significantly. The resistive layer is broadened (Fig.1) and the growth rate is reduced by up to a factor of two.

When $\Delta < c/\omega_{pi}$ - the ion collisionless skin depth - the inclusion of the Hall effect and magnetic viscosity or finite Larmor radius terms is necessary. In this case the equations do not reduce simply to those of slab geometry, and B_θ curvature effects are dominant. In particular, the parallel viscosity survives in leading order with a term which is zero in slab geometry and small in tokamak ordering. Inclusion of the Hall effect alone makes the interchanges more unstable, but the resistive layer thickness is then limited by the ion collisionless skin depth. A rapid reduction in growth rate is observed for short-wavelength modes with m = 0, 1, 2. Long-wavelength m = 0 modes have their growth rate reduced somewhat but remain strongly unstable.

At low values of c_1 f(r), i.e. central values of $\beta \sim 4\%$, the parallel viscosity is found to have a stabilising effect and gives rise to a critical local pressure gradient depending on the shear. However, the region of strongest shear where the field reverses has essentially zero pressure gradient as the parallel viscosity does not stabilise the m = 0 mode. This gives rise to a critical pressure profile which for the RFP has $\bar{\beta} \lesssim 10\%$.

Our calculations show that reversed-field pinch configurations which are grossly stable to ideal and resistive tearing modes will be unstable to resistive interchanges growing on hybrid and hydromagnetic time scales. The most unstable mode number, m, increases with S and the velocity perturbation becomes increasingly localised. As the resistive layer depth becomes comparable with the ion collisionless skin depth a rapid reduction in growth rate is observed for short-wavelength modes.

3. Numerical Studies of Setting Up of RFP Distributions by Self-Reversal

A zero-dimensional code was developed to simulate the gross behaviour of the ZETA machine and to predict the behaviour of future reversed-field pinch devices. The code includes the electrical circuit and various loss mechanisms such as impurity radiation and turbulent energy convection from field fluctuations. Low-Z impurities were represented by oxygen, which was treated in a time-dependent manner, and high-Z by iron, which was assumed to be in coronal equilibrium. Turbulent field fluctuations were assumed to give rise to an equivalent diffusion [11][12] of $D = u.\Lambda$ where u is the random velocity of the turbulence ($= \delta B(\mu_o \rho)^{\frac{1}{2}}$) and Λ the transverse correlation length. Internal probe measurements in ZETA showed that $\Lambda \simeq a/10$ [12]. Computations for a plasma similar to ZETA (and applicable to a new planned RFP experiment called HBTXIA with R = 0.8m, a = 0.26m) show that the resultant energy confinement time is given by $\tau_E \approx a^2/10D$.

Fig.3 shows a comparison between the time variation of the calculated and observed [3] plasma current and electron temperature of a ZETA discharge. The observed values of the electron density, which decreased by a factor of 3 (owing to 'pump-out') to 5×10^{19} m^{-3} at the time of peak current and the field fluctuation levels which were reduced from $\delta B/B = 1\%$ to 0.1% (owing to 'quiescence') after the peak current were used in the code. An iron impurity density of 5×10^{16} m^{-3} was assumed to account for the observed total radiation. Satisfactory agreement is seen between calculated and observed values of T_e and I_{plasma} although the increase in T_e observed in the experiment towards the end of quiescence still remains to be explained.

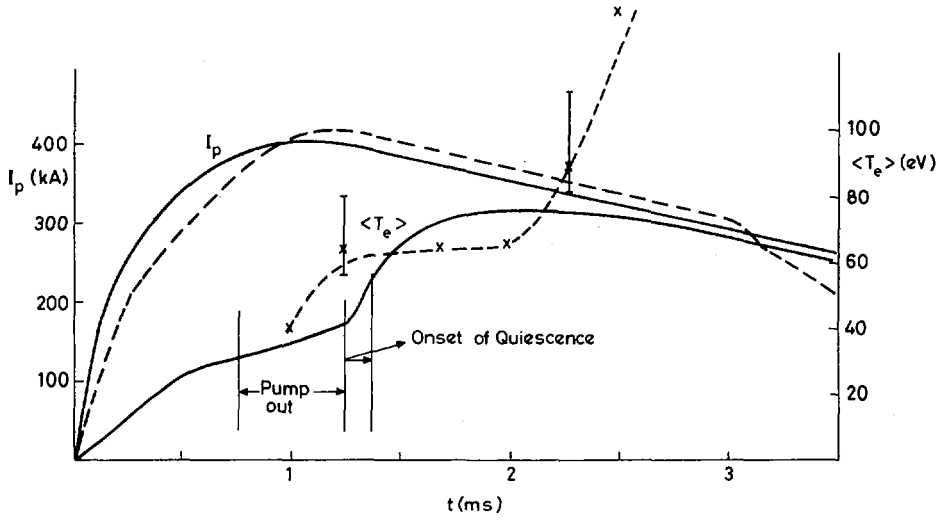


FIG.3. Comparison of calculated plasma current (I_p) and average electron temperature (T_e) with measured values (broken line) for ZETA.

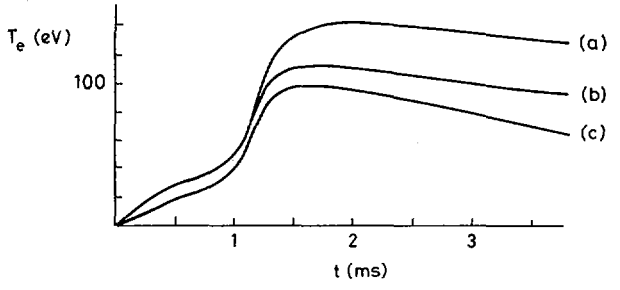


FIG.4. Predicted evolution of electron temperature for HBTXIA with various impurity concentrations: (a) 1% oxygen; (b) 1% oxygen + 0.1% iron; (c) 2% oxygen + 0.1% iron.

The circuit parameters used for HBTXIA were V_{bank} = 40kV, C_{bank} = 1mF, with a transformer turns ratio of 20 and an iron core that saturates at 0.45 volt-sec. The same field fluctuation levels, line density and pump-out factor as in the Zeta case were used. Calculations for different impurity concentrations gave peak currents in the range 440-500kA. The time variation of the electron temperature is shown in Fig.4, where it is seen that average temperatures exceeding 150eV are reached, decaying in $\gtrsim$ 5ms. The values of β_θ corresponding to the peak electron temperature range from 15%

to 19%. The poloidal magnetic Reynolds number ($= \tau_{diff}/\tau_{A\theta}$) at the current peak was in excess of 2.4×10^4 for all cases during the turbulent phase. This is expected to be high enough for 'quiescence' to occur, with a consequent reduction in the fluctuation level and a rise in the energy confinement time; therefore the assumption that $\delta B/B$ was reduced should be justified ($\delta B/B \propto S^{-\frac{1}{2}}$ - see section 4).

4. Recent Experiments on HBTXI

Detailed studies have been made on the production of reversed B_ϕ field in the HBTXI experiment (R = 100cm, a = 6.5cm, I_ϕ = 40-250kA, pulse duration $\sim$ 50μs). The self-reversal of B_ϕ in pinches with conserved toroidal flux can be explained as the non-linear effect of instabilities [2]. The change in B_ϕ is given by

$$\Delta B_\phi\ (r_w) = \frac{(m^2 + kr_w^2)\ b_\phi^m(r_w)^2}{(kr_w(mB_\theta(r_w) + kr_w B_\phi(r_w)))} \qquad (2)$$

where $\Delta B_\phi\ (r_w)$ is the change in the average B_ϕ field at the conducting wall, r_w, produced by an MHD or resistive instability of toroidal and poloidal mode numbers k and m, perturbed field, b_ϕ^m, mean field distribution, B_θ, B_ϕ. The reversal in HBTXI is produced by a single large-amplitude instability at high θ ($= B_{\theta wall}/B_{\phi average}$) and by the cumulative effect of a series of lower amplitude ($\sim$ 5%) m = 1 instabilities at low θ. If the current is maintained further m = 1 activity sustains the reversed field [2] as shown in Fig.5.

The characteristic time, τ_{rev}, for the reversal mechanism to operate is the instability growth time, $\tau_{instability}$. In discharges with a current rise time which is long compared with $\tau_{instability}$, the reversed-field ratio F is found to be a unique function of θ within experimental error. This is shown in Fig.6: F:θ diagrams for 11 discharges on HBTXI are shown superimposed in Fig.6(a) and an F:θ diagram calculated from results published from ALPHA [13] in Fig.6(b). ZETA gave similar results [14]. This behaviour is consistent with relaxation to a minimum energy state; the dashed line on Fig.6(a) represents the F:θ curve for the Bessel function distribution [15]. If the B_θ or B_ϕ field is programmed on a time $\ll \tau_{instability}$, the discharge can be driven to a state away from the minimum energy F:θ curve to which it returns with a large-amplitude instability.

The rate of production of reversed field, from (2), is $B_\phi \propto 1/\tau_{instability}\ (\delta B/B)^2$. Hence the fluctuation level necessary to maintain the reversed-field profile against diffusion may be estimated,

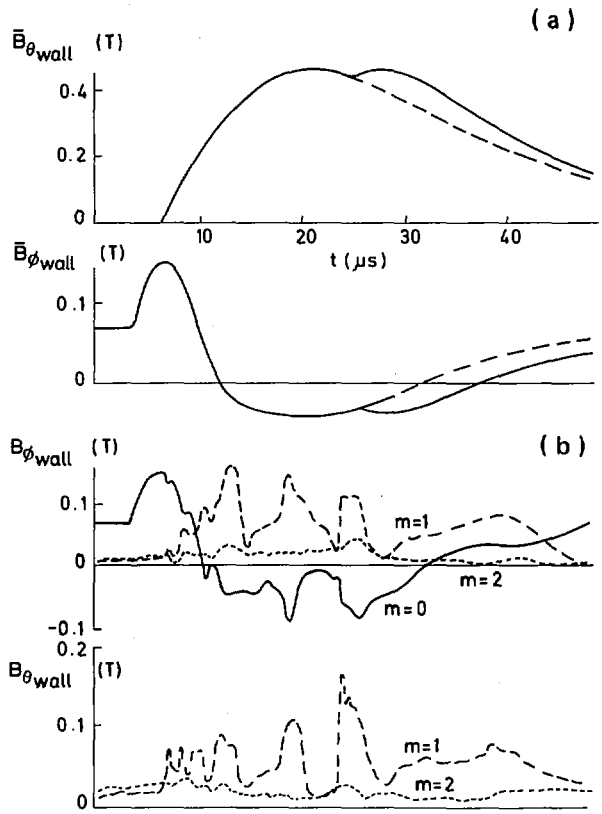


FIG.5. When the current is maintained on HBTXI, m = 1 activity sustains the reversed field. (a) $B_{\theta wall}$ ($\propto I_{plasma}$), showing secondary current rise, and $B_{\phi wall}$. (b) Mode structure of instabilities associated with sustained reversal.

$\delta B/B \propto (\tau_{instability}/\tau_{diffusion})^{\frac{1}{2}}$; thus $\delta B/B \propto S^{-\frac{1}{2}}$ (where S = magnetic Reynolds number) for ideal MHD instabilities. Similarly the fluctuation level to be expected during the current rise is $\delta B/B \propto (\tau_{instability}/\tau_{current\ rise})^{\frac{1}{2}}$.

An RFP may be set up by programming the B_θ and B_ϕ field from t = 0 so that the pinch follows the minimum energy curve on the F:θ diagram [1]. At 60kA the pinch is observed to be weakly unstable. The instabilities for the measured field configuration and magnetic Reynolds number, S, of such a pinch are predicted by an initial value calculation to be resistive interchanges driven by the pressure gradient and not ideal MHD modes or tearing modes. The radial profiles of the radial field have been measured but cannot be used to distinguish between ideal and resistive modes in this case since

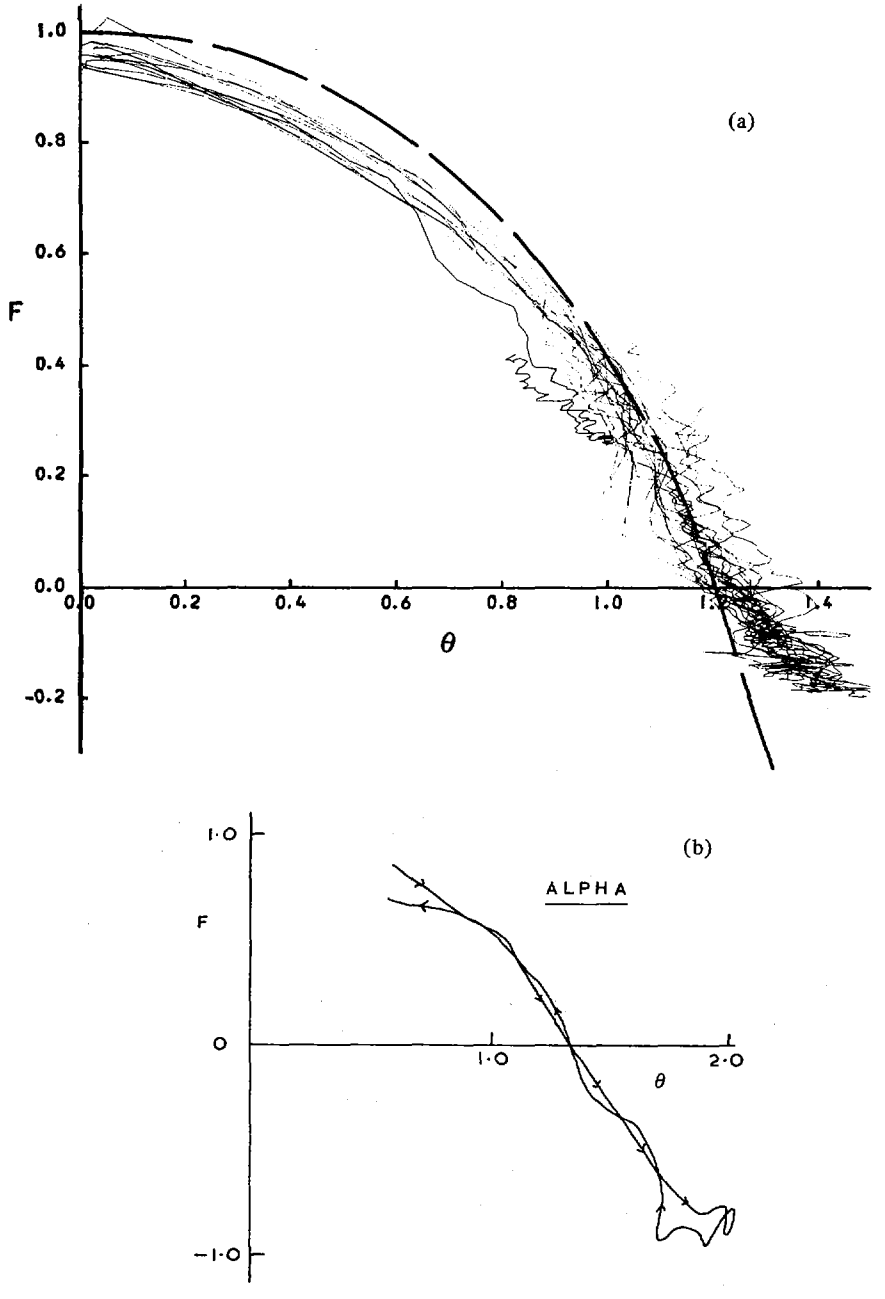


FIG.6. (a) F:θ diagrams for 11 discharges on HBT XI and (dashed) F:θ for the Bessel function model.
(b) F:θ diagram for ALPHA [13].

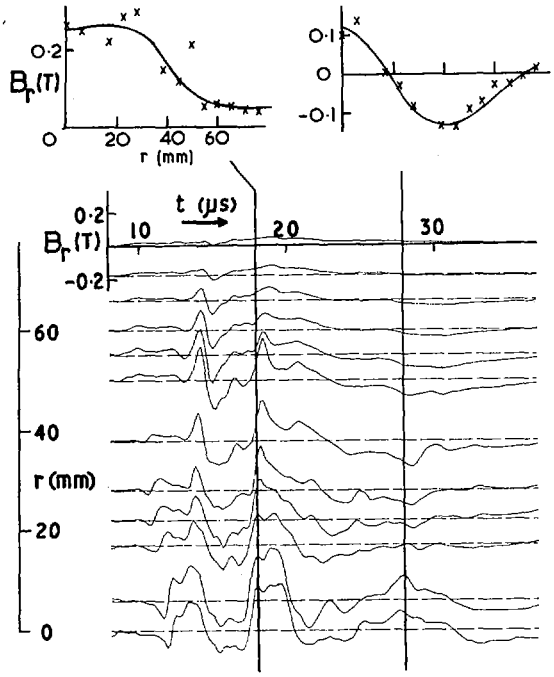


FIG.7. Evolution of the radial field, B_r, at 12 radial positions in a sustained pinch set up by field reversal. The insets show the radial profile at t = 18 μs and 28 μs.

at the low value of S of the 60kA pinch the perturbed field profiles from the two types of mode are similar. The measured field configuration of a 150kA sustained pinch has been analysed and is predicted to be unstable to MHD modes and resistive interchanges with $kr_w \sim 1.5$, and growth times of 3-4μs. Detailed information on the instabilities associated with the m = 1 activity has been obtained with an inserted magnetic probe and small coils at the quartz wall. The measured mean field configuration shows that the externally measured values of k are resonant between the magnetic axis and a radius of 3cm. If the activity is due to ideal MHD modes $b_r = 0$ at the resonant surface. Fig.7 shows the radial field structure for a single discharge. In general the radial field perturbation does not change sign, as in the left-hand inset; however, occasionally b_r changes sign with radius, as in the right-hand inset. The singular surface in these cases is at r ≈ 3cm. From these measurements it is deduced that the activity is a mixture of ideal and resistive pressure-driven modes for this low-θ discharge in which $\bar{\beta} \leq 10\%$, central $\beta \lesssim 5\%$.

TABLE I. ENGINEERING PARAMETERS OF NEXT-GENERATION RFP EXPERIMENTS AT CULHAM

	HBTXIA (building)	RFX (designed)
Major radius (cm)	80	180
Minor radius (cm)	26	60
Peak current I_ϕ (MA)	0.4	0.7–1 (1.5–2)[a]
Rise time (ms)	0.1–0.5	2–10 (10–50)
Decay time (ms)	1–5	10–20 (50–100)

[a] Stage II; same toroidal assembly, increased power supplies.

TABLE II. PARAMETERS FOR REVERSED-FIELD PINCH REACTORS WITH NORMAL AND SUPERCONDUCTING MAGNETIC FIELD WINDINGS

	Normal	Superconducting
Net output power (MW(e))	600	600
Gross thermal power (MW(th))	2500	1900
First wall radius (m)	1.75	1.5
Major radius (m)	16	14.5
Toroidal plasma current (MA)	19	17
Duration of burn (s)	27	25
Duration of full cycle (s)	40	37
Energy multiplication factor, Q	5.9	11.8
Recirculating power fraction, ε (%)	42	21

5. Next-Generation RFP Experiments

The main future objective is to obtain, by means of self-reversal aided by field control, stable high-β plasmas with low fluctuation levels and good confinement at high values of the magnetic Reynolds number, in metal-walled systems using slow-rising currents.

The first new experiment is the HBTXIA machine, now under construction, which utilises the HBTX capacitor bank suitably modified with a new load

assembly; this device was discussed in Section 3. A second device, known as RFX, has been designed whose main objective is to set up and sustain for times of 10ms or more (using additional field control) RFP distributions with plasma parameters [16] higher than those obtained hitherto at high-β. The machine parameters of these two devices are listed in Table I.

6. RFP Reactor Studies

It has been shown previously [17] that, because of the high-β (giving low values of magnetic field near external conductors), the possibility of ohmic ignition and the free choice of aspect ratio, the RFP Reactor might have advantages compared with other systems. Recently more detailed studies by a joint UK/Italian group [4] of a pulsed non-superconducting reactor established the RFP as a fully credible system. Quasi-DC operation is also possible, as in tokamaks, using sustained reversal; the need for a conducting shell was identified as the main engineering problem. However, the Q-value was found to be rather low, typically 5–7, in agreement with earlier estimates [18], because of the high recirculating power. The pulsed power supplies could be built by modest extrapolations of existing technology.

A substantial improvement in Q is to be expected [18] [5] by using superconducting windings, with a cost reduction of perhaps 20–30% compared with the non-superconducting variant, giving about £750/kW(e) for the station cost for a 600-MW(e) system. The main parameters of the normal and superconducting reactors are given in Table II. More detailed studies of the superconducting reactor are described in these Proceedings [6].

7. Conclusions

(1) Theoretically there are tearing-mode stable configurations with $\beta(o) \lesssim 17\%$. The resistive interchange mode (g-mode) is hard to suppress in cylindrical geometry with $\bar{\beta} > 10\%$, even when the full dissipative equations and the Hall and finite Larmor radius terms are included. Magnetic islands form and non-linear calculations are under way to estimate the saturation levels.

(2) The setting-up phase on Zeta, during which a stable RFP distribution is formed by self-reversal, has been simulated numerically using a simple 0-D code including losses from radiation and turbulent convection based on experimentally observed values. This code has been used to make performance predictions for a new machine.

(3) On HBTXI in compressed high-θ plasmas, self-reversal involves a single large-amplitude kink, while at low-θ it is due to the cumulative effect of several low-amplitude $m = 1$ modes which grow successively. When the current rise time is slower than the $m = 1$ growth time, the distribution remains close to a relaxed state as the current rises and falls and a universal F-θ

curve is observed. The reversed field can be sustained as long as the current is maintained (provided that $\theta \gtrsim 1.3$).

(4) The pulsed RFP Reactor is a credible scheme. Its principal disadvantage is the need for a stabilising shell. However, if ohmic ignition and high-β can both be realised, it has significant advantages in terms of engineering simplicity and cost.

(5) Emphasis in future RFP experiments will be placed on setting up distributions by means of aided reversal, at the highest possible values of magnetic Reynolds number and with slow rising currents, in HBTXIA and RFX.

ACKNOWLEDGEMENTS

The authors wish to thank S. Ortolani for assistance in the theoretical work on the resistive interchange mode with finite Larmor radius, and their colleagues at Culham for assistance with the experimental work.

REFERENCES

[1] GOWERS, C.W., et al., "An experimental, 3-D numerical and analytical study of reversed-field pinches (RFP)", Plasma Physics and Controlled Nuclear Fusion Research 1976 (Proc. 6th Int. Conf. Berchtesgaden, 1976) Vol. 1, IAEA, Vienna (1977) 429.

[2] BUNTING, C.A., et al., Proc. 8th European Conf. Controlled Fusion and Plasma Physics, Prague, 1977, Vol. 1 (1977) 79.

[3] ROBINSON, D.C., KING, R.E., "Factors influencing the period of improved stability in Zeta", Plasma Physics and Controlled Nuclear Fusion Research (Proc. Int. Conf. Novosibirsk, 1968) Vol. 1, IAEA, Vienna (1969) 263.

[4] HANCOX, R., et al., Fusion Reactor Design Concepts, (Proc. Tech. Committee Mtg. and Workshop, Madison, 1977), IAEA, Vienna (1978) 319.

[5] ROSTAGNI, G., NEWTON, A.A., private communication.

[6] HANCOX, R., WALTERS, C.R., paper IAEA-CN-37-I-1, these Proceedings.

[7] ROBINSON, D.C., Nucl. Fusion **18** (1978) 939.

[8] ROBINSON, D.C., Proc. 8th European Conf. Controlled Fusion and Plasma Physics, Prague, 1977, Vol. 1 (1977) 78.

[9] ORTOLANI, S., ROBINSON, D.C., Bull. Am. Phys. Soc. **22** (1977) 1190.

[10] KILLEEN, J., in Computational Problems in Plasma Physics and Controlled Thermonuclear Research, Plenum Press, New York (1970) 202.

[11] ROBINSON, D.C., in Proc. 3rd Topical Conference on Pulsed High-Beta Plasmas, Culham, 1975, Pergamon, Oxford (1976) 273.

[12] ROBINSON, D.C., et al., Plasma Phys. **10** (1968) 1005.

[13] GLUKHIKH, V.A., et al., Sov. Phys. – Tech. Phys. **5** (1961) 1331.

[14] ROBINSON, D.C., Plasma Phys. **11** (1969) 893.

[15] TAYLOR, J.B., Proc. 3rd Topical Conf. on Pulsed High-Beta Plasmas, Culham, 1975, Pergamon, Oxford (1976) 59.

[16] CHRISTIANSEN, J.P., ROBERTS, K.V., Proc. 8th European Conf. Controlled Fusion and Plasma Physics, Prague, 1977, Vol. 1 (1977) 82.
[17] BODIN, H.A.B., et al., "The pulsed reversed-field pinch reactor", Plasma Physics and Controlled Nuclear Fusion Research 1974 (Proc. 5th Int. Conf. Tokyo, 1974), Vol. 3, IAEA, Vienna (1975) 631.
[18] JAMES, T.E., NEWTON, A.A., BODIN, H.A.B., Proc. BNES Conf. on Nuclear Fusion Reactors, Culham, 1969, pp. 255 and 282.

STUDIES ON PLASMA FORMATION, RELAXATION AND HEATING IN A REVERSED-FIELD PINCH

M. BAGATIN, A. BUFFA, R. DE ANGELIS,
G. MALESANI, S. ORTOLANI
Centro di Studio sui Gas Ionizzati
del Consiglio Nazionale delle Ricerche
e dell'Università di Padova,
(Associazione Euratom-CNR),
Padua, Italy

Abstract

STUDIES ON PLASMA FORMATION, RELAXATION AND HEATING IN A REVERSED-FIELD PINCH.

Some problems relevant for the formation, relaxation and heating of a comparatively slow pinch have been investigated. The spontaneous relaxation of the pinch to a reversed-field pinch (RFP) configuration has been studied under various conditions of the ratio of the current rise-time (τ_I) to the MHD time (τ_A). For large τ_I/τ_A the tendency of the pinch to evolve along a universal patch is more evident; the stability analysis and the axial flux amplification phenomenon are discussed. Ionization and start-up problems are shown to be important with reference to experiments performed on ETA-BETA I with long ($\sim 160\mu s$) current risetimes and to zero-dimensional calculations of the ionization and formation phases. The steady-state and time-dependent power balance of the pinch is studied, with reference to a proposed RFP reactor, including impurity line radiation losses. Conditions for ignition are briefly discussed.

1. INTRODUCTION

The reversed-field pinch (RFP) is an axisymmetric configuration which is stabilized by the shear of the magnetic field and by the conducting wall, has $q < 1$ and can then operate with higher current densities than a conventional tokamak of the same size leading to high-β and high temperature by Ohmic heating [1].

Studies on RFP configurations are at present concentrated on further analysis of the results obtained in the small-size fast experiments recently developed [2–5], while larger experiments will be operating within a few months. Results of RFP studies on ETA-BETA I ($r = 5$ cm; $R = 40$ cm; $I = 50$–200 kA; $T/4 \cong 1$–$10\ \mu s$) have been previously reported [5, 6].

One way of producing the configuration is field programming, which consists in driving the toroidal field at the wall to reverse during the toroidal current rise.

An alternative way of producing the configuration is the phenomenon of self-reversal, by which the plasma spontaneously generates the RFP by relaxation to lower energy states. This method is particularly interesting in view of the difficulties of field programming in large-scale experiments and of controlling the energy losses during setting-up to produce stable profiles. However the method involves instabilities and plasma/wall interactions, and is not fully understood even if it is similar to the setting up of a tokamak configuration.

Setting up by field programming is by definition relatively fast because it aims to compete with the instabilities during the formation phase to confine the plasma away from the wall; setting up by self-reversal is slow in order to minimize the dynamic effects during the power input and it allows the MHD relaxation phenomena to dominate.

A new experiment (ETA-BETA II: r = 12.5 cm; R = 65 cm; I = 300 kA; $T/4 \cong 2-130$ μs) is being assembled in Padua [7] and will operate by the end of 1978. The first series of experiments will be performed to study the formation of the pinch by natural relaxation and the plasma heating and energy losses in a system with long current risetimes ($\cong$ 130 μs) and metal liner. We have therefore investigated some problems which are relevant in the context of the slow setting up by spontaneous reversal, and we refer in particular to:

(a) Experimental studies on ETA-BETA I with current risetime of about 10 μs to investigate the time evolution and stability of a self-reversed pinch under conditions of large τ_I/τ_A.

(b) Experiments performed on ETA-BETA I with current risetimes of $\sim$ 160 μs to study the ionization and formation phases under conditions of low applied electric field.

TABLE I. CHARACTERISTIC PARAMETERS OF FIVE DISCHARGES AT VARIOUS PRESSURES

p_0 (mtorr)	80	40	20	10	5
$\hat{I}_z$ (kA)	90	80	75	60	40
τ_A (μs)	0.5	0.4	0.3	0.25	0.25
τ_I/τ_A	20	25	33	40	40
θ_1	2.8	2.7	1.9	1.9	1.0
θ_2	1.4	1.1	1.1	1.6	1.5
$\Delta\theta = \theta_1 - \theta_2$	1.4	1.6	0.8	0.3	0.5

Notes:
θ_1 and θ_2 are the values of θ which define the beginning and the end of the reversal phase.
τ_A is calculated from the filling density and peak current.

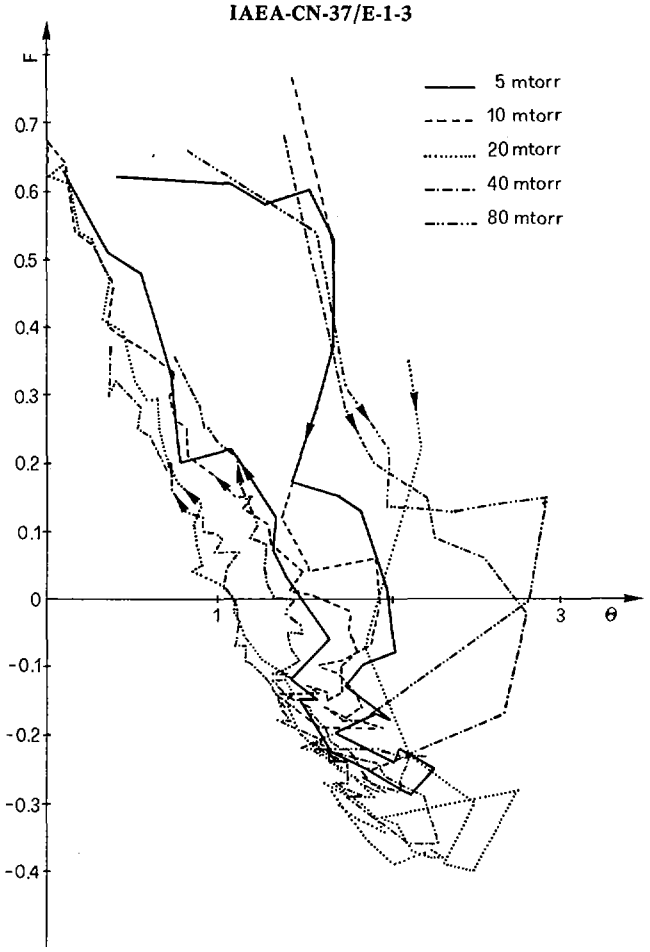


FIG.1. Field-reversal ratio F as a function of pinch ratio θ at pressures ranging from 5 mtorr to 80 mtorr of H_2. Arrows indicate increasing times.

(c) Steady-state and time-dependent calculations on the plasma power balance also accounting for impurity radiation losses. This study gives critical values for some plasma parameters necessary to Ohmically heat the pinch and achieve ignition in a proposed RFP reactor scheme [8].

2. SELF-REVERSAL STUDIES

Results previously reported [9] have shown that when the ratio of the current risetime to the MHD time τ_I/τ_A increases, the self-reversal is no longer associated with one clear particular instability, and high-frequency fluctuations

are present during the entire time of the discharge. The possibility of obtaining a self-reversal not violently produced, as was observed in the large ZETA experiment, supports the idea of crossing the reversal phase without too large wall contacts and losses. Furthermore, experiments performed on HBTX I [10] have shown the tendency of the plasma to evolve along a universal curve on the F-θ plane ($F = B_{z\ \text{wall}}/B_{z\ \text{average}}$; $\theta = B_{\theta\ \text{wall}}/B_{z\ \text{average}}$) independently of the initial conditions and the field programming, as long as $\tau_I \gg \tau_A$.

On ETA-BETA I a set of discharges with plasma current risetime of about 10 μs and filling pressures varying from 5 mtorr to 80 mtorr has been studied in terms of the time evolution on the F-θ diagram, of MHD stability properties and of the magnetic flux interchanges between azimuthal and axial field components.

2.1. Time evolution

Some characteristic parameters of five discharges at various pressures are given in Table I; in Fig. 1 the time history on the F-θ plane is drawn. From the figure and the table the formation phase (until after the field reversal) is seen to be characterized by larger fluctuations in the F-θ curve than the remainder of the curve. This observation confirms that once the energy input is terminated, the plasma relaxes according to natural MHD phenomena and tends to evolve along a universal path; this same tendency also appears during the formation phase for the larger values of τ_I/τ_A. Figure 2 draws the width of the path $\Delta\theta = \theta_1 - \theta_2$, and θ_1 and θ_2 as a function of τ_I/τ_A; $\Delta\theta$ substantially decreases as τ_I/τ_A increases, and this behaviour is mainly associated with the decrease in θ_1 whereas θ_2 varies little with τ_I/τ_A.

Also shown in Fig. 2 is the time at which the reversal is generated. At high τ_I/τ_A ($\geqslant 33$; $p_0 \leqslant 20$ mtorr), the constant θ_1 corresponds to an approximately constant plasma current at the reversal; the field reverses earlier because the current reaches the corresponding value earlier. With lower τ_I/τ_A the reversal appears later at higher θ-values, which confirms that the energy input delays the natural relaxation. The 20-mtorr discharge ($\tau_I/\tau_A = 33$) seems to individualize the transition between the relative dominance of the energy input and of the natural MHD relaxation.

From these considerations we can conclude that there is evidence in ETA-BETA I of the tendency of the pinch to evolve on the F-θ diagram along a curve corresponding to the minimum energy configurations. This behaviour is more evident when MHD phenomena dominate the field programming ($\tau_I \gg \tau_A$).

2.2. MHD stability analysis

The ideal MHD stability properties of the measured profiles have been studied at many different times during the discharge by computing the linear

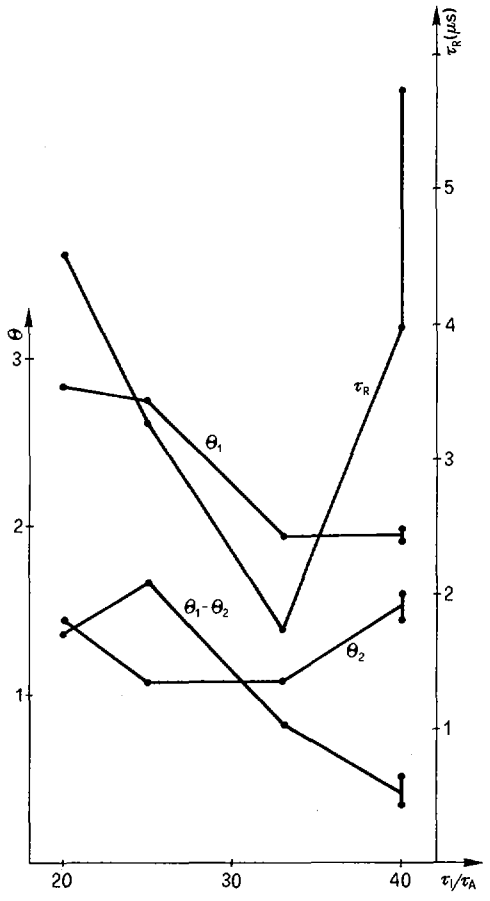


FIG.2. Values of θ at the beginning (θ_1), at the end (θ_2) of the reversal phase, and their difference $\Delta\theta = \theta_1 - \theta_2$ plotted versus the ratio of current risetime to MHD time (τ_I/τ_A). The time τ_R at which the reversal appears is also shown.

growth rates and perturbations of the unstable modes. We have discarded short-wavelength localized modes because of their dependence on the details of the equilibrium profiles and we discuss here the behaviour of some relatively long-wavelength ($k = 20–50\ m^{-1}$) modes. The formation of the RFP configuration is in all cases associated with fast-growing kink modes originating in the central regions of the pinch where most of the current flows. A qualitative difference appears in the time dependence of the growth rates in the various cases. For the high-pressure discharges in particular, after the reversal a more stable phase is found which eventually evolves to a new instability.

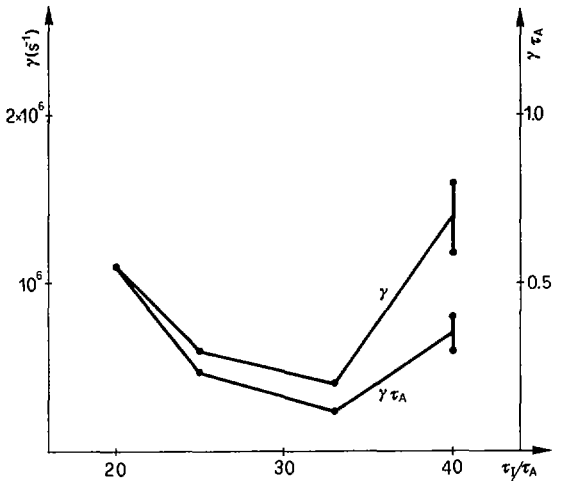


FIG.3. Instability growth rate just before reversal at various τ_I/τ_A. Also shown is the product $\gamma\tau_A$, where τ_A is the Alfvén time.

For the low-pressure discharges, the analysis predicts instability characteristics almost independent of time. These differences in the time evolution of the stability of the various cases is consistent with the behaviour of the fluctuations in the F-θ diagram and with previous observations [9]. Figure 3 shows the growth rates just before the reversal. As the filling pressure decreases from 80 mtorr to 20 mtorr (τ_I/τ_A = 20–33), we notice a decrease in the growth rate and the mode localization. At lower pressures the growth rate increases again and the modes are wider. The same results scaled to the Alfvén time are also given in Fig. 3 to show that it is not just the MHD scaling which determines the observed differences. The initial improvement of the stability with increasing τ_I/τ_A is consistent with the decrease in θ_1 (i.e. plasma compression) as shown in Fig. 2, but this behaviour is reversed, further increasing τ_I/τ_A and, at constant θ_1, there is a new increase in the growth rate associated with a wider region of excessive pressure gradient (Suydam violated) in the interior of the pinch.

2.3. Axial flux amplification

Evidence of the different characteristics of the various discharges considered is also found by examining the time variation of the azimuthal and axial magnetic field fluxes

$$\phi_z = \int_0^{rw} B_z\, 2\pi r dr, \qquad \phi_\theta = 2\pi R \int_0^{rw} B_\theta\, dr$$

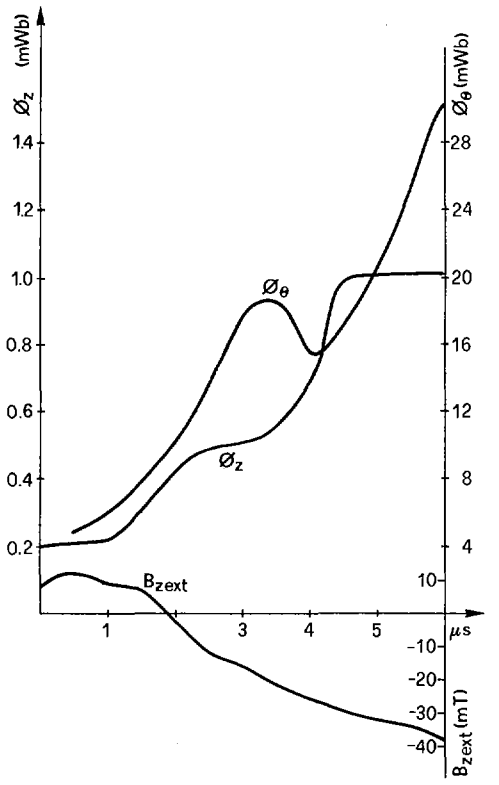


FIG.4. Measured time evolution of the poloidal and toroidal fluxes together with the axial field at the wall.

At high pressure, sharp axial flux amplifications are observed associated with fast decreases of the axial field at the plasma wall. These axial flux amplifications can be time-correlated with a decrease of the azimuthal flux, and if an effective wavelength for the interchange of the fluxes is introduced to give

$$\frac{\lambda}{2\pi R}\,|\Delta\phi_\theta| = |\Delta\phi_z|$$

we find typically $\lambda \cong 20$–30 cm. This picture of the flux amplification phenomenon [11] agrees well with the wavelength of the unstable modes discussed in Section 2.2.

An example of the measured fluxes versus time is given in Fig. 4 for the 20-mtorr discharge: the increase of ϕ_θ with the current is broken off by a sudden drop just when a fast ϕ_z amplification appears. It is more difficult to distinguish

these phenomena clearly at the beginning of the discharges when the energy input dominates or when their characteristic frequency becomes higher and their amplitude smaller (lower pressure).

3. IONIZATION AND FORMATION STUDIES

When operating with longer risetimes and relatively lower electric field than in a programmed RFP, problems such as the ionization and breakdown of the gas and the formation (start-up) of the discharge become more important and the power losses during the energy input phase can dominate and prevent the current rise. These problems have been investigated on a modified version of ETA-BETA I to operate with a quarter of a period of the applied voltage of ~ 160 μs and an initial electric field of ~ 500 $V \cdot m^{-1}$.

The breakdown has also been investigated by means of an ionization model which considers a volume ionization rate in electric field as indicated in Ref. [12] and simultaneously solves the density, energy and circuit equations. In the conditions considered, for a filling pressure higher than 2 mtorr, and starting from an initial electron density of 10^{10} m^{-3}, the model shows that a voltage drop appears after 3–5 μs, while the current reaches ~ 1 kA and the ionization degree is 10^{-3}. The experimentally measured breakdown times, defined as the times when the current reaches ~ 1 kA, are in the same range of 3–5 μs, confirming therefore the result that, for filling pressure higher than 2 mtorr, the gas ionization and breakdown is not a major problem.

The plasma formation phase has also been studied by a zero-dimensional time-dependent model which accounts for the processes of thermal ionization (initial ionization 1%), electron-ion equipartition, bremsstrahlung, oxygen line radiation by solving the time-dependent corona model rate equations [13], iron steady-state radiation and Ohmic heating by coupling the circuit equations to the electron energy equation. The computed time dependence of the plasma current is shown in Fig. 5 at 40 mtorr of filling pressure with various oxygen concentrations and compared with the experimental results. Note that both the experimental and computed currents go to zero at about the same time as the voltage. The ionization losses determine the first slowing-down of the current rise; afterwards, radiation losses dominate in determining the high resistance ($T \sim 2$–4 eV) and current decay. Oxygen relative concentrations of a few per cent are quite reasonable in ETA-BETA I [5] when the plasma continuously interacts with the walls.

We think it is important to show evidence that a quite reasonable radiation process can explain the observed start-up failure.

Experimentally, the filling pressure has been reduced with the aim of heating the plasma to higher temperatures. In Fig. 6 the plasma currents at various filling pressures (5–40 mtorr) are shown. Radiation losses can still explain the

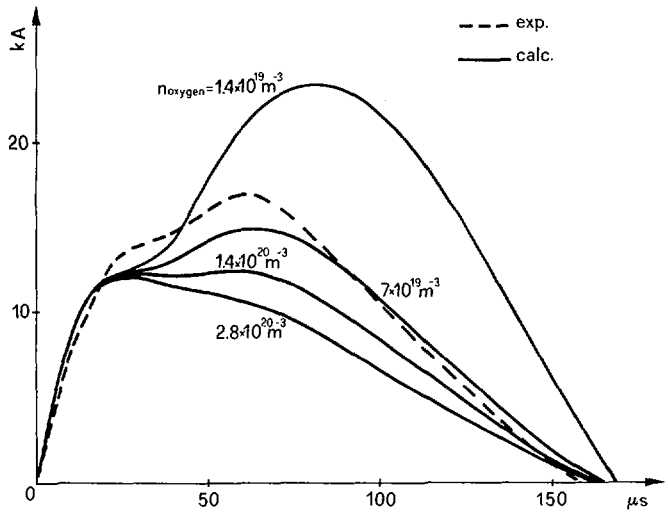


FIG.5. Measured and computed time evolution of the plasma current at 40 mtorr with various oxygen impurity concentrations.

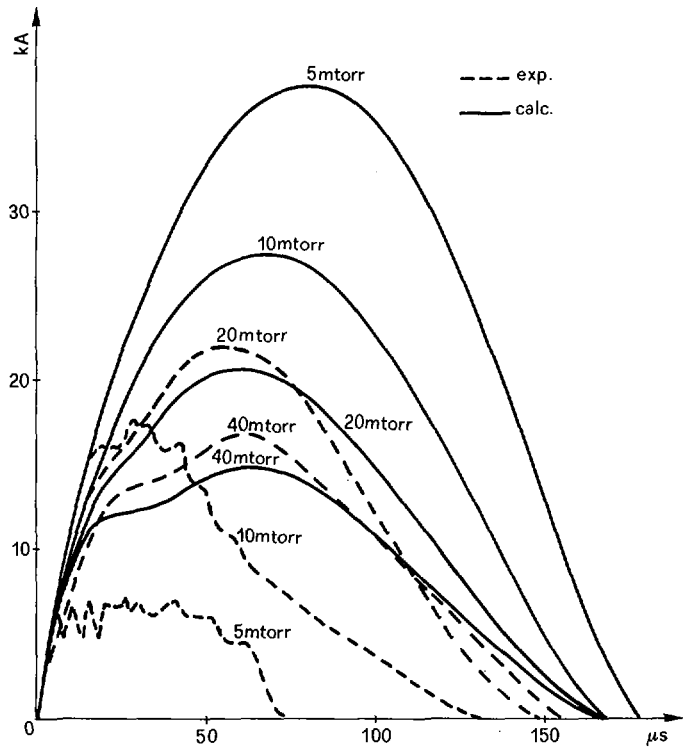


FIG.6. Comparison between measured and computed ($n_{oxygen} = 7 \times 10^{19}\ m^{-3}$) plasma current time evolution at filling pressure ranging from 5 mtorr to 40 mtorr.

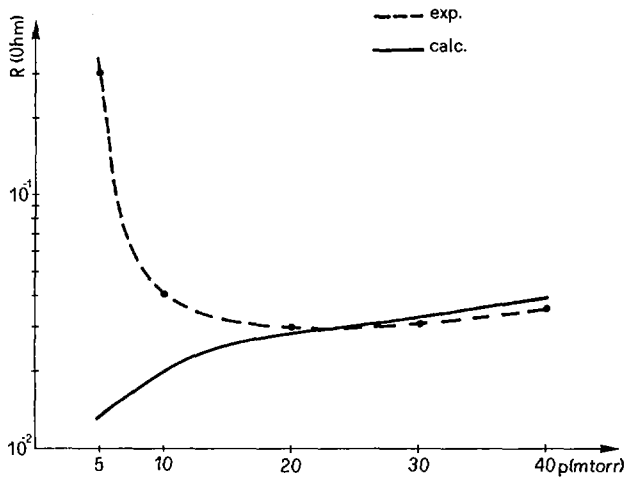


FIG. 7. Measured and computed ($n_{oxygen} = 7 \times 10^{19}$ m^{-3}) plasma resistance at current maxima as a function of filling pressure.

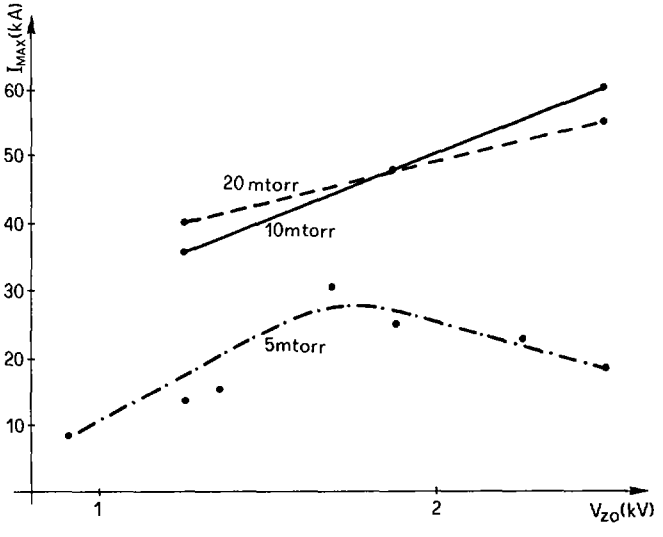


FIG. 8. Experimental dependence of the current maxima on the voltage initially applied.

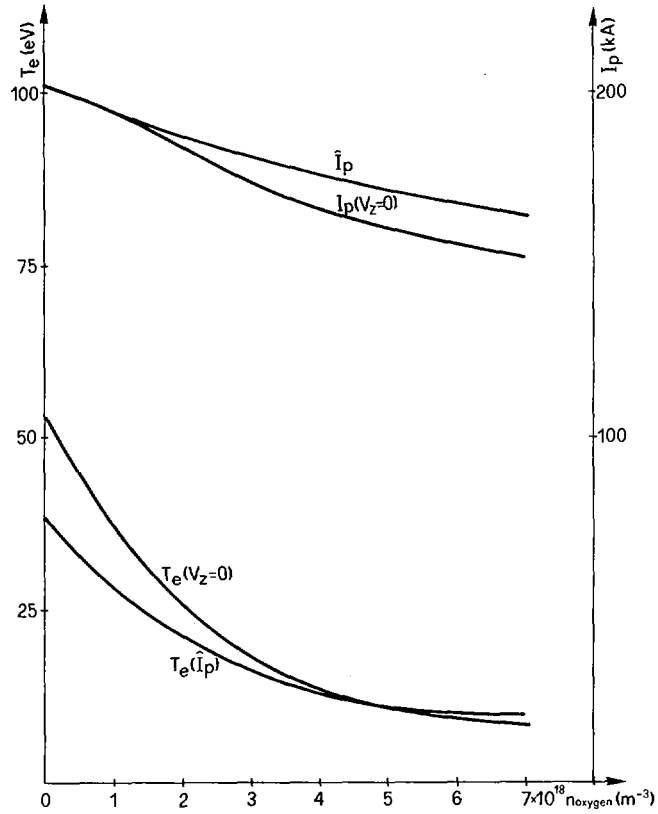


FIG.9. Comparison between temperatures and currents at the end of the energy input and at the current maximum as computed by the zero-dimensional model at p = 10 mtorr and V_{z0} = 30 kV versus oxygen content.

behaviour at 20 mtorr, but at lower pressures experimentally the plasma current decreases very rapidly and the physical processes considered in the model cannot account for increasing losses with decreasing density. A comparison of the measured and computed plasma resistance at maximum current is shown in Fig. 7. The experimental increase of the resistance at low filling pressures and the observation of a negative differential resistance with increasing applied voltage (see Fig. 8) are explained as due to increased losses. Runaway phenomena have been considered in order to explain the increased losses, because in the low-pressure discharges the applied electric field becomes comparable with the runaway critical field if the same percentage of ionization is assumed. In any case, no direct measurements are available.

These results stress the importance of start-up problems in the slow setting up and show that even low impurity concentration (see e.g. the upper curve in Fig. 5) can prevent plasma formation. We must, however, emphasize that ETA-BETA I is a device designed to operate with fast field programming and has a very small minor bore and high resistance. In ETA-BETA II the geometry will be more favourable in this respect because of the increased minor radius, and the energy at the same voltage will be about twice that in ETA-BETA I. Nevertheless, impurities must be kept at very low levels to achieve high currents and temperatures.

An example of the calculated performances is shown in Fig. 9 at 10 mtorr of filling pressure and with half of the available energy (V_z = 30 kV). In this figure the plasma temperature and current at the end of the energy input (zero voltage) are drawn as a function of the oxygen concentration; the comparison with $\hat{I}_p$ (current maxima) and with the temperature $T_e(\hat{I}_p)$ at the same time shows that the impurities now produce negligible current decay.

4. OHMIC HEATING AND PLASMA POWER BALANCE

Because of the higher currents ($I^2 \propto \beta\bar{\theta}^1$) which are possible, the RFP can in principle achieve higher temperatures by Ohmic heating than a tokamak of the same size. A RFP reactor scheme has recently been studied [8] and ignition by Ohmic heating alone has been considered on the assumption of bremsstrahlung as the only plasma energy loss [14].

The simple steady-state calculation has been extended to account for oxygen and iron impurity radiation losses. At the temperature where the Ohmic and the α-particle heating are equal (which is a good approximation, a little pessimistic, of the ignition temperature [14]) we can write for the ignition criterion:

$$2\,P_\alpha - P_{brem} - P_{imp} > 0$$

By taking a scaling as T^4 for the α-particle heating [14] and a variation as $T^{1/2}$ for the impurity radiation loss term in the vicinity of the ignition temperature (which for oxygen and iron is a reasonable approximation – see e.g. Ref. [15]), we can write the following criterion for the ratio of the current density[1] to the plasma density:

$$\frac{J}{n} > \left(\frac{J}{n}\right)_0 \frac{(1 + c_1\, f_{imp})^{11/14}}{(Z_{eff})^{1/2}}$$

[1] The current density here must be intended to include a resistance form factor due to the current distribution and it is then equal to the uniform axial current density times the square root of the form factor.

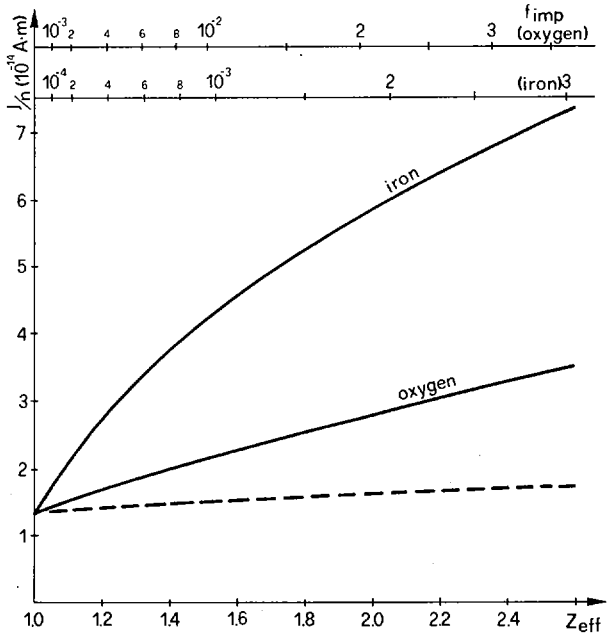


FIG.10. Ignition criterion for the ratio J/n as a function of Z_{eff} when oxygen or iron impurities are considered.

where f_{imp} is the impurity fractional content and

$$c_I \cong \begin{cases} 5 \times 10^3 & \text{for iron} \\ 1.4 \times 10^2 & \text{for oxygen} \end{cases}$$

and

$$\left(\frac{J}{n}\right)_0 \cong 1.33 \times 10^{-14}\ \text{A·m}$$

Obviously, when the line radiation is completely negligible we have $1 + c_I\ f_{imp} \approx Z_{eff}$ and we obtain the expression given in Ref. [14]:

$$\frac{J}{n} > \left(\frac{J}{n}\right)_0 (Z_{eff})^{2/7}$$

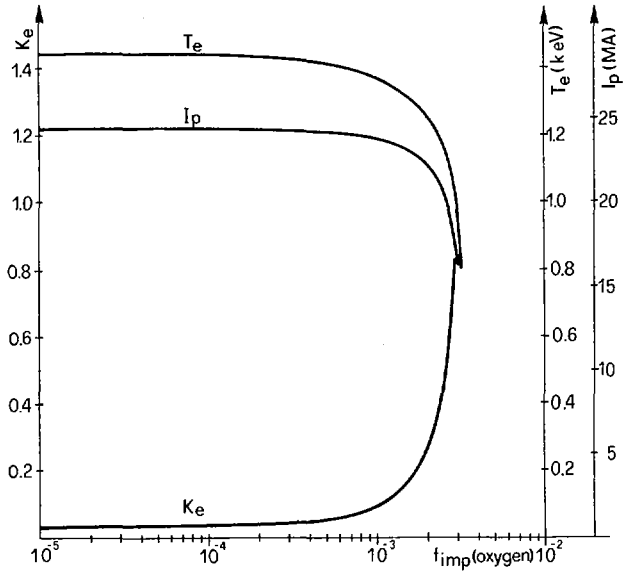


FIG.11. Computed electron temperature and plasma current at the end of the current rise versus oxygen fractional concentration. The ratio K_e of the dissipated energy to the magnetic energy in the plasma is also shown.

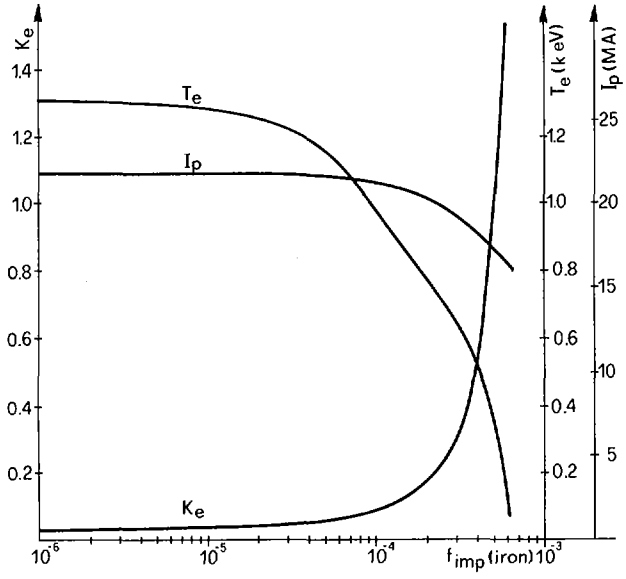


FIG.12. T_e, I_p and K_e at the end of the current rise versus iron fractional concentration as computed by the zero-dimensional model.

The critical J/n values for oxygen and iron are drawn as a function of Z_{eff} in Fig. 10 which, for comparison, also shows the curve without impurity line radiation (broken line) and the scales for the fractional contents of oxygen and iron.

The time-dependent study of the current rise and heating phases of the proposed RFP reactor was made with the zero-dimensional model described in Section 3.

The goal of the proposed reactor is to achieve 19 MA at the end of the current rise with a ratio of the dissipated energy to the magnetic energy in the plasma $K_e = \int R_p I_p^2 \, dt/((1/2) L_p I_p^2)$ of $\sim 50\%$. We have studied the conditions compatible with reaching these parameters when small fractions of oxygen and iron are present. In Figs 11 and 12, K_e, T_e ($\approx T_i$) and I_p at the end of the current rise are drawn as a function of the fractional content of oxygen and iron respectively. We see that $K_e \sim 50\%$ and plasma current of 19 MA correspond to $\sim 2.5 \times 10^{-3}$ of oxygen or to $\sim 4 \times 10^{-4}$ of iron. These values do not seem too unrealistic to invalidate the assumed efficiency ratio K_e. However, we also notice that the quantities drawn in Figs 11 and 12 vary rapidly around the $K_e \sim 50\%$ value and then small increases in the concentration of the considered impurities would prevent the achievement of the required parameters and ignition.

We also notice that, for oxygen, higher temperatures are reached at the end of the current rise phase corresponding to lower losses than for iron.

When α-particle heating is also considered, and the computation is extended beyond the setting-up phase with a constant current, ignition ($T_e \sim 3.5$ keV) will be reached in about 7 seconds.

5. CONCLUSIONS

The effect of a few relevant parameters on the slow setting up of RFP configurations has been investigated in ETA-BETA I in various experimental conditions which might be relevant to the larger and slower experiment ETA-BETA II.

Spontaneous relaxations of pinches to RFP configurations have been produced under various ratios between the current risetime and the MHD time.

At larger τ_I/τ_A the evolution on the F-θ diagram shows a tendency to be on a universal curve independent of the current programming.

The wavelength of the computed unstable modes and the one deduced on the assumption that the observed variation of azimuthal and axial flux occurs with conservation of the total helical flux are in good agreement.

Experiments with long current risetimes (~ 160 μs) in ETA-BETA I have shown that the formation (start-up) of the plasma at low power input can become a serious problem. A zero-dimensional time-dependent model of the plasma formation phase can explain the observed start-up failure with small amounts of oxygen impurity.

At the lower pressures (5–10 mtorr) the resistance increases rapidly, and runaway electrons could contribute to the observed behaviour.

Ohmic heating could be a valid mechanism in a pinch to achieve high temperatures. The steady-state and time-dependent power balance has been studied. The critical values of the ratio of the current density to the plasma density necessary to achieve ignition in a RFP reactor depend strongly on impurity concentrations.

By extending the results obtained to the conditions of the forthcoming ETA-BETA II experiment, a more favourable range of plasma performance is expected which appear suitable for a good understanding of the mechanisms involved in the slow setting up of RFPs.

REFERENCES

[1] BODIN, H.A.B., 3rd Topical Conf. on Pulsed High-Beta Plasmas, Culham, 1975, Pergamon, Oxford (1976), Paper B 1.1

[2] BAKER, D.A., et al., "Current, temperature and confinement time scaling in toroidal reversed-field pinch experiments ZT-I and ZT-S", Plasma Physics and Controlled Nuclear Fusion Research 1976 (Proc. 6th Int. Conf. Berchtesgaden, 1976) Vol. 1, IAEA, Vienna (1977) 419.

[3] GOWERS, C.W., et al., "An experimental, 3-D numerical and analytical study of reversed-field pinches", ibid. 429.

[4] SHIMADA, T., et al., "Reversed-field pinch experiments on TPE-1", ibid. 463.

[5] BUFFA, A., et al., "Heating diffusion and stability of reverse-field pinch configurations", ibid. 447.

[6] BUFFA, A., et al., "Reverse-field-pinch experiments in the ETA-BETA device", Plasma Physics and Controlled Nuclear Fusion Research 1974 (Proc. 5th Int. Conf. Tokyo, 1974) Vol. 3, IAEA, Vienna (1975) 431.

[7] FELLIN, L., MASCHIO, A., STELLA, A., in Proc. 10th Symp. on Fusion Technology, Padua, Sep. 1978.

[8] HANCOX, R., et al., "A 600 MW(e) reversed field pinch reactor study", Fusion Reactor Design Concepts (Proc. Tech. Committee Meeting and Workshop, Madison, 1977), IAEA, Vienna (1978) 319.

[9] BUFFA, A., et al., 8th Europ. Conf. on Controlled Fusion and Plasma Physics, Prague, 1977, Vol. 2 (1977) 81.

[10] GOWERS, C.W., et al., in Proc. 19th Annual Meeting, Am. Phys. Soc.,Plasma Physics Div., Atlanta, 1977.

[11] VERHAGE, A.J.L., FURZER, A.S., ROBINSON, D.C., Nucl. Fusion **18** (1978) 457.

[12] BUFFA, A., MALESANI, G., NALESSO, G.F., Phys. Rev. **A3** (1971) 955.

[13] COSTA, S., ORTOLANI, S., Univ. Padua Rep. UPee 75/06 (1975).

[14] LAWSON, J.D., Culham Lab. Rep. CLM-R 171 (1977).

[15] POST, D.E., et al., Princeton Plasma Phys. Lab. Rep. PPPL-1352 (1977).

DISCUSSION

ON PAPERS E-1-1 TO E-1-3

H. ZWICKER: In the long run the success of the reversed-field pinch system will be determined by diffusion. There are fairly high density gradients, however. My question, therefore, is whether you think one can exclude the possibility of lower hybrid drift modes increasing the diffusion strongly and thus destroying the configuration.

H.A.B. BODIN: This mode was not discussed much in the papers I have surveyed. It could cause anomalous diffusion, but, as I understand the situation from the work of Davidson and co-workers, because of the high shear the lower hybrid drift mode may not be dangerous in the reversed-field pinch, especially in the slow mode of operation.

However – and this is important – should diffusion cause the profile to change and become unstable, the instability will drive the relaxation process and stability will be recovered. What we do not know is the fluctuation level associated with this process. In my talk I showed that, experimentally, the fluctuation level becomes lower as the current rise becomes slower; also, the Culham paper IAEA-CN-37/E-1-2 indicates that it should become lower at high values of magnetic Reynolds number.

EXPERIMENTAL AND COMPUTATIONAL STUDIES OF HIGH-BETA TOKAMAKS AND REVERSED-FIELD PINCHES

T. TAMARU, K. SUGISAKI, K. HAYASE, T. SHIMADA,
Y. HIRANO, Y. MAEJIMA, K. OGAWA
Electrotechnical Laboratory,
Tanashi, Tokyo

K. HIRANO, S. KITAGAWA, K. SATO, M. WAKATANI*,
S. YAMADA, H. ARIMOTO, Y. KITA, S. YAMAGUCHI, A. NAGATA
Institute of Plasma Physics,
Nagoya University, Nagoya

S. IDO
Department of Nuclear Engineering,
University of Tokyo, Tokyo

I. KAWAKAMI
Atomic Energy Research Institute,
College of Science and Technology,
Nihon University, Tokyo,
Japan

Abstract

EXPERIMENTAL AND COMPUTATIONAL STUDIES OF HIGH-BETA TOKAMAKS AND REVERSED-FIELD PINCHES.

Experimental and computational studies of circular and non-circular high-β tokamaks and reversed-field pinches are summarized. STP-2 at Nagoya University is operated as a high-β tokamak in fast- and slow-compression modes. The preliminary results show the effectiveness of fast compression in removing the plasma from the wall. The non-circular screw pinch ETL-TPE-1a has T = 10 eV, n = 10^{15} cm^{-3}, B_t = 4 kG, an elongation of e = 3 and β = 5% in the confinement phase of 60 μs; MHD activities are measured in detail. ETL-TPE-1R is a modified version of ETL-TPE-1 and shows an improved reversed-field pinch (RFP) confinement by its doubled bore and flat-top of the Z-current. For example, long-time (over 60 μs) sustaining of high plasma current (160 kA) in the RFP configuration has been obtained. On the other hand, in STP-1 at Nagoya University, a good result has been obtained by the new programming for setting up RFP. The numerical calculations were performed at the University of Tokyo and at Nihon University. The 2D calculation shows an evident agreement with ETL-TPE-1 RFP experiments in its setting-up phase, and 3D MHD code has been developed to study the non-linear evolution of helical instability in a finite-β tokamak.

---

* Present address; Plasma Physics Laboratory, Kyoto University, Kyoto.

This paper summarizes the experimental studies of circular and non-circular high-β tokamaks and reversed-field pinches (RFP) carried out at the Electrotechnical Laboratory and the Plasma Physics Laboratory of Nagoya University and the computational studies of the reversed-field pinch and a finite-β tokamak performed at Nihon University and the University of Tokyo. The object of this research work is to study the confinement of high-β plasma in order to contribute to an increase of the β-value in axisymmetric toroidal systems.

STP-2 AT NAGOYA UNIVERSITY

(K. Hirano, S. Kitagawa, K. Sato, M. Wakatani, S. Yamada, H. Arimoto, S. Yamaguchi, A. Nagata)

The fast- and slow-compression modes in high-β tokamak experiments have been tested in this device. A schematic representation of the two modes is shown in Fig. 1; Table I gives the main parameters of the present experiment. The fast-compression mode has been studied in view of its ability to remove the plasma from the wall quickly and to minimize unfavourable plasma-wall interaction rather than to heat up the plasma by shock compression [1]. The slow-compression mode is somewhat similar to that appearing in TUMAN [2], except that the plasma current also increases with the toroidal field. For the fast-mode operation, some evidence of compressional magnetic limiter action has been observed in streak photographs, CO_2 interferometry and impurity line radiation. As is seen in Fig. 2, the oxygen neutral-line radiation disappears quickly as soon as the fast-rising current pulse is applied and appears again when the plasma current goes down to zero. On the other hand, for the slow mode, the oxygen neutral line does not disappear during the entire plasma current life.

NON-CIRCULAR TOROIDAL PINCH ETL-TPE-1a [3]

(K. Sugisaki, K. Hayase, T. Tamaru)

Experimental studies to find stable confinement conditions in a high-β, non-circular toroidal plasma were carried out in this device under various filling-gas pressures, $P = 2.5–20$ mtorr of D_2, a plasma current $I_p = 10–80$ kA and a bias field $B_0 = 0–0.7$ kG for a maximum magnetic field of $B_t = 4$ kG. Figure 3 shows a typical time evolution of B_t, I_p, loop voltage V_p, the electron density averaged over the medium plane, N_e, and a streak picture of a plasma column. It has been reported [4] that, for $q < 3$ operation, the plasma was subject to MHD instabilities with a growth time of 3–15 μs. Stable confinement conditions depend on the magnitude of B_0 and I_p, on which, mainly, β and q depend.

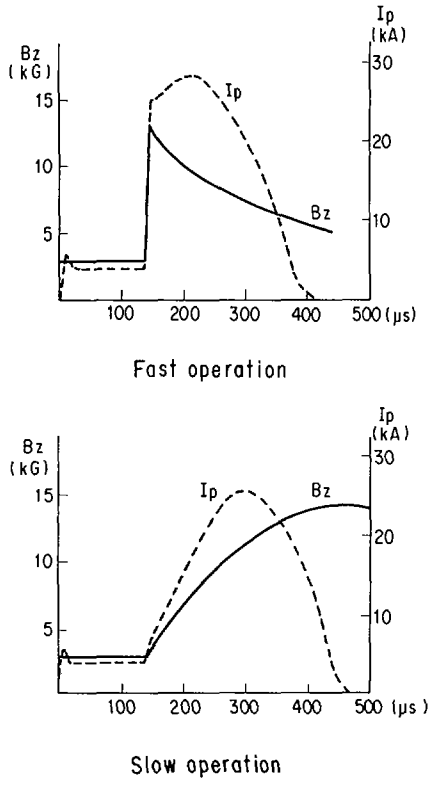


FIG.1. Field and current programming mode of STP-2 (HBT). B_z: toroidal field, I_p: plasma current.

TABLE I. MAIN PARAMETERS OF STP-2 (HBT) AND STP-1 (RFP)

		R (cm)	b (cm)	B_t (kG)	τ_B (μs)	I_p (kA)	τ_I (μs)
SPT-2	Fast compression	25	9	13.3	7	35	7
	Slow compression			14.1	310	30	160
SPT-1		12	4.2	7.7	6	110	2.6

R is the major radius, b the minor radius, B_t the maximum toroidal field strength, τ_B the rise-time of the toroidal field, $I_p$the maximum plasma current, and τ_I the rise-time of the plasma current.

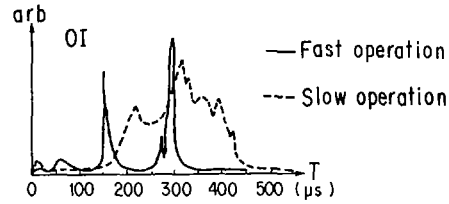


FIG.2. Typical time evolution of O I line intensity for fast- and slow-compression mode operation.

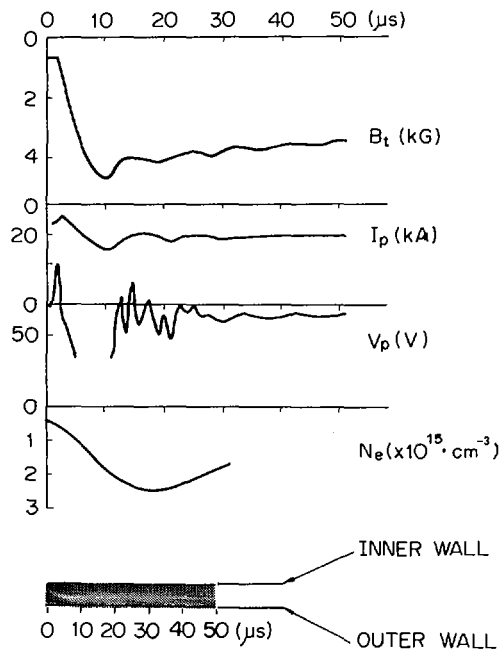


FIG.3. Typical time evolution of magnetic field B_t, plasma current I_p, loop voltage V_p, electron density averaged over the medium plane, N_e, and axially taken streak picture of plasma.

These are shown in Fig. 4 for 10 mtorr of D_2 where q* is the safety factor defined on the boundary surface of the current channel, and β^* is the peak value. These values were determined from the magnetic-field profiles in the plasma at 5 μs for β^* and at 10 μs for q*, considering the growth time of MHD instabilities. To investigate MHD instabilities in detail, the axial profiles of the poloidal field were measured along the inner wall of the discharge chamber with the probes A and B in Fig. 5. The results are shown in Fig. 6, and the conditions of operation

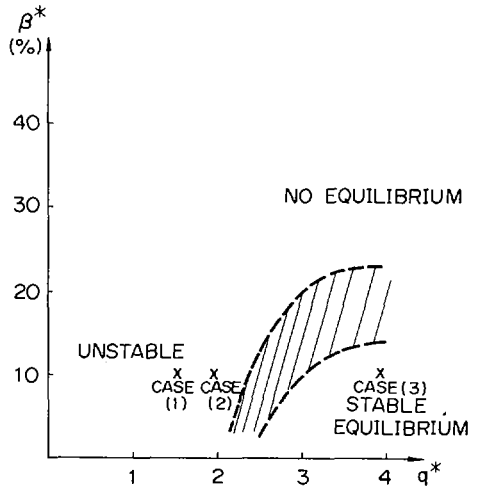


FIG.4. Stable-confinement conditions. The shaded area is a transient region.

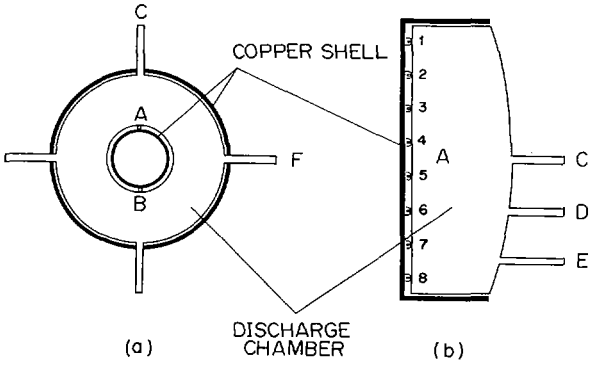


FIG.5. Magnetic probe positions in TPE-1a. (a) Horizontal medium plane viewed from top; (b) cross-section at A-C.

are indicated in Fig. 4. The difference in the magnetic-field profiles of A and B is due to MHD instabilities; the profiles are shown in Fig. 7 for two typical unstable cases. For the strongly unstable case (1), the distortion of the magnetic field extends over the whole discharge chamber, and high m modes (perhaps, m = 2) are observed together with the dominant m = 1 mode. The streak picture also shows pronouncedly turbulent behaviour of the plasma column accompanied with strong distortion and splitting. This mode is regarded as an external kink

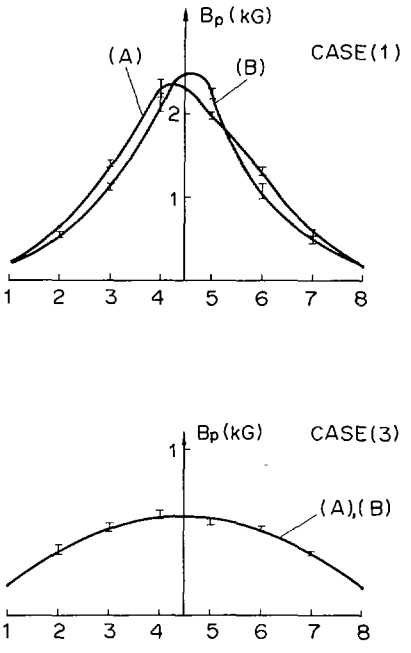


FIG. 6. Axial profiles of poloidal magnetic field along inner wall of discharge chamber at 5 μs. Numbers 1–8 are shown in Fig. 5. Operation conditions are given in Fig. 4.

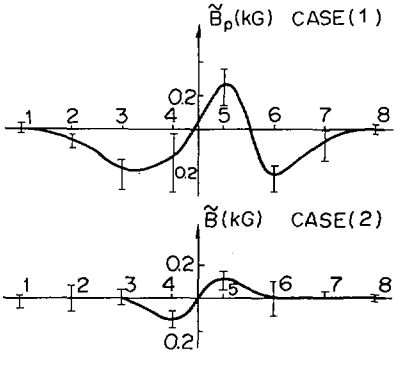


FIG. 7. Magnetic-field activities along inner wall.

mode. For the weakly unstable case (2), the magnetic-field distortion is localized near the medium plane and the dominant mode is obviously m = 1. The streak picture also shows that the gross behaviour of the plasma column is not so turbulent as in case (1). Magnetic-field measurement in the plasma indicates that the safety factor near the magnetic axis, q_0, is 1/2 to 1/2.5 of q*. This indicates that $q_0 \cong 1$ for marginally stable conditions. This mode is considered to be an m = 1 internal mode. Magnetic-field measurement also indicates that the current profile in lower-pressure operation is more peaked than in higher-pressure operation and q_0 is lower at a fixed value of q*. In conclusion, we can say that stable confinement conditions are found experimentally in high-β, non-circular plasma. The confinement condition seems to be limited by the appearance of a q = 1 singular surface in the plasma. For P = 10 mtorr, the ratio of q* to q_0 was about 2 to 2.5, and the marginal q was almost equal to that of a conventional tokamak. For higher-pressure operation, the current profile is broader and higher β is obtained, while a more peaked current profile for low-pressure operation leads to lower β.

REVERSED-FIELD PINCH, ETL-TPE-1R

(T. Shimada, Y. Hirano, K. Ogawa, Y. Maejima, T. Tamaru)

Previous work [5, 6] has reported that the RFP experiment on TPE-1 was successfully carried out (a) to obtain an MHD-stable RFP configuration by fast field programming and (b) to establish a technique of maintaining a stable RFP plasma in a range of plasma current of 50 to 70 kA by choosing the optimum values of the B_z field reversal ratio and the time delay between Z- and θ-currents by controlling the external coil currents. The confinement time of this stable configuration was limited by the field decay, which was comparable to the decay time of the external coil currents. In TPE-1R, the main modifications are that the size of the discharge tube is doubled and the rise-time and the duration of the flat top of the Z-current are increased by factors of 2.5 and 3, respectively. Table II gives the electrical parameters of the TPE-1R capacitor banks. If the configuration time is limited by resistive field diffusion, both the confinement time of the plasma and the electron temperature should be expected to have values increased by a factor 4. The preliminary computer calculation, whose codes have been developed on the basis of a point model including the external circuits, plasma convection losses, thermal conduction losses, radiation losses including impurities, charge-exchange losses and the input power of Joule heating, supports the above expectations and shows, as an example, plasma parameters as follows: maximum plasma current 250 kA; electron temperature 60 eV; ion temperature 50 eV; energy confinement time 100 μs; β-value 0.3 at 50 μs from start of current in ZETA mode operation with field programming.

TABLE II. ELECTRICAL PARAMETERS OF CAPACITOR BANKS OF ETL-TPE-1R (R/rs = 50/11.8, in cm)

	Energy (kJ)	Voltage (kV)	Peak value (kA)	Rise-time (μs)	Decay time (μs)
Pre-ionization					
Fast Z-pinch	0.3	40	7	0.3	
Slow Z-pinch	10	5	30	50	
Slow B_z					
(Bias)	180	5	700	100	
(Power crowbar)	30	5	180	60	
Fast B_z	100	40	1500	5	250
Fast I_z	40	40	300	10	
Slow I_z					
(Power crowbar)	50	5	350	50	

Preliminary results of the experiments are shown in Figs 8 and 9 in the case of D_2, 10 mtorr. Figure 8 shows $B_{z\,wall}$, toroidal flux, plasma current and toroidal one-turn voltage; Fig. 9 shows a typical F-θ diagram. The values of poloidal beta, β_p, obtained by MHD equilibrium analyses, are 0.2 to 0.3 at 40 μs after the start of the current. This suggests a plasma pressure ($nT_e + nT_i$) of up to 100 to 150×10^{15} eV·cm^{-3}.

REVERSED-FIELD PINCH STP-1 AT NAGOYA UNIVERSITY

(K. Hirano, Y. Kita)

A new mode of programming for RFP has been studied by using the small STP-1 apparatus. The operational parameters are shown in Table I. Care has been taken to prevent the plasma from contacting the wall during the setting-up phase. The new mode of operation starts from the screw pinch, and then the external field is reversed just as in the programming studied by Verhage [7]. The plasma current is, however, kept continuously increasing during the entire setting-up phase in order to compensate for the decrease of the external toroidal field so that pressure equilibrium across the minor radius is ensured. It is found that the trapped toroidal flux of this operation is larger by about a factor of two than the usual previous mode, which will give better MHD stability conditions.

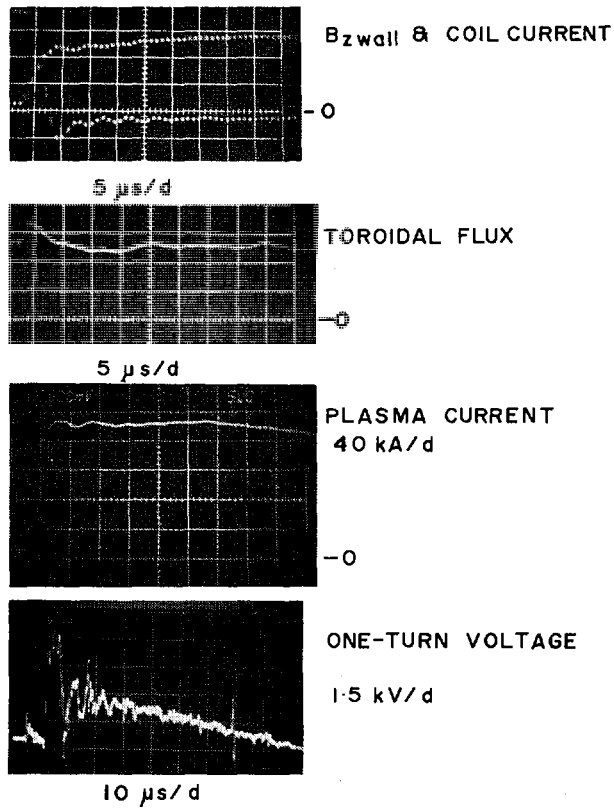


FIG.8. Time evolution of $B_{z,wall}$, toroidal flux Φ, plasma current I_p and toroidal one-turn voltage V_p in the case of D_2 and 10 mtorr.

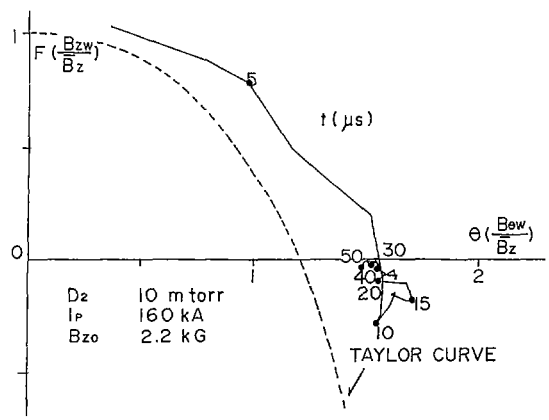


FIG.9. Typical F-θ diagram of TPE-1R.

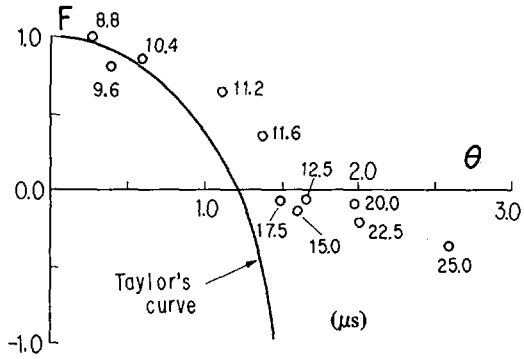


FIG.10. Typical F-θ diagram of new RFP programming in STP-1.

A typical F-θ diagram of the new program is given in Fig. 10. As can be seen, the program is controlled so that the θ-value should not very much exceed 2. At a plasma current of 58 kA, a stable operation of 13 μs is achieved with a density of 3.5×10^{15} cm^{-3} and a temperature of 20 eV. Higher-current operation of 110 kA results in a high plasma temperature of 40 eV and a density of 5.6×10^{15} cm^{-3}. Stable operation, however, was limited to 10 μs in spite of expected longer confinement time with high temperature.

NUMERICAL CALCULATIONS

(S. Ido, I. Kawakami)

2D and 3D MHD codes [8] (named 'ORION', written as an OLYMPIAN [9]) have been developed to study the dynamics of toroidal pinches as an initial value problem. Transport coefficients are assumed to be classical and a one-fluid model is used.

2D simulations

The setting-up and confinement phases of fast programmed RFP of ETL-TPE-1 [6] have been investigated by means of the 2D code. Typical parameters are: $a = 5$ cm, $R = 40$ cm, $n_0 = 4 \times 10^{15}$ cm^{-3}, $T_0 = 1$ eV, $B_{bias} = 2.4$ kG, changing time of $B_t = 3$ μs. Figure 11 shows the plasma current I_p and the toroidal flux Φ. The boundary condition of the toroidal field ($B_{t,wall}$) is also shown. The diffusion time of Φ is about 20 μs, agreeing with the experimental results. Figure 12 shows the F-θ diagram for two different values of field reversal (−0.2 kG and −1.0 kG), which do not have an obvious effect on

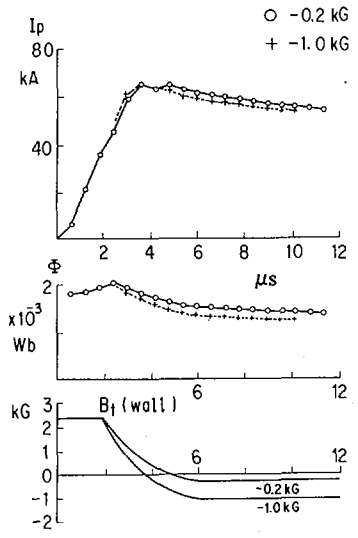


FIG.11. Boundary condition B_t (at wall) and results: plasma current I_p and toroidal flux Φ. The bias field is 2.4 kG at the plasma centre [2D results].

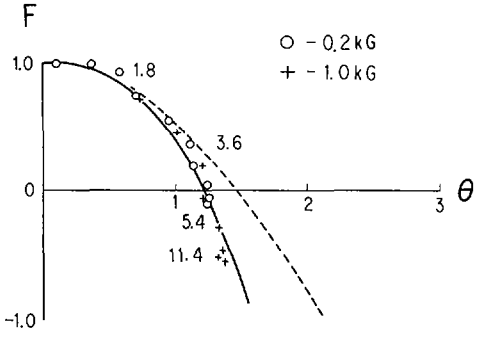


FIG.12. F-θ diagram for two values of field reversal at wall, −0.2 kG and −1.0 kG [2D results].

setting up RFP in the simulation. The sequence of computation points in the setting-up phase follows the line predicted by Taylor's Bessel function model in the F-θ diagram [10]. When the plasma current is sufficiently large and the toroidal flux is well conserved, a stationary confinement is observed after the setting-up (Fig. 12), as is observed in recent experiments of TPE-1R. However, when the plasma current is less than 30–40 kA, the RFP plasma is not confined and is cooled down at the wall. The toroidal flux then diffuses fast, and the

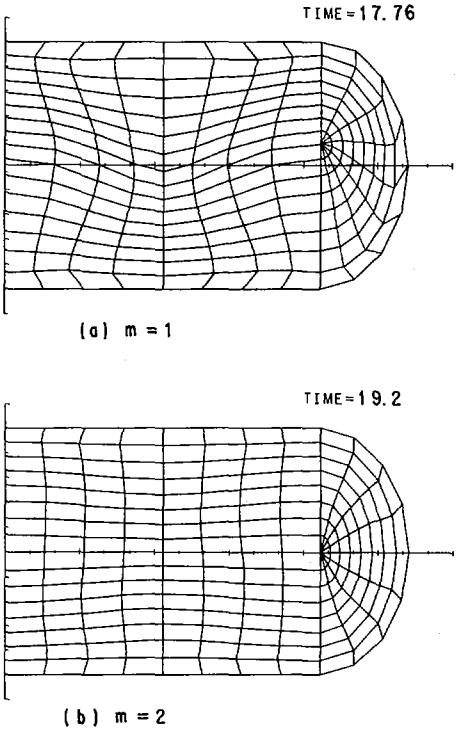


FIG.13. Pure Lagrangian mesh net-works for (a) m = 1 and (b) m = 2. Safety factor on plasma surface q_a is (a) 1.5 and (b) 2.5. The distortion is due to non-linear growth of the initial perturbation.

values of θ become anomalously large (> 4), which attests to unsuccessful setting-up. This shows that BFM is a good approximation for RFP in some conditions, such as large I_p, and that the force-free state leading to an RFP configuration can be readily produced by a well-programmed discharge, independent of details of field reversal dynamics in the setting-up phase.

3D MHD simulations

A 3D MHD code of the cylindrical geometry is developed and applied to a study of the non-linear evolution of MHD instability in a finite-β tokamak geometry as an initial value problem. The method is developed by modifying Pracht's [11] and Brackbill's [12] methods. The number of meshes is 8 X 16 X 8 in the r-, θ- and z-directions. To avoid non-essential numerical complications, it is assumed that the resistivity η is constant. Helical perturbation (n = 1, m = 1 and/or 2) is introduced initially. The parameters used are: a = 5 cm, R = 20 cm,

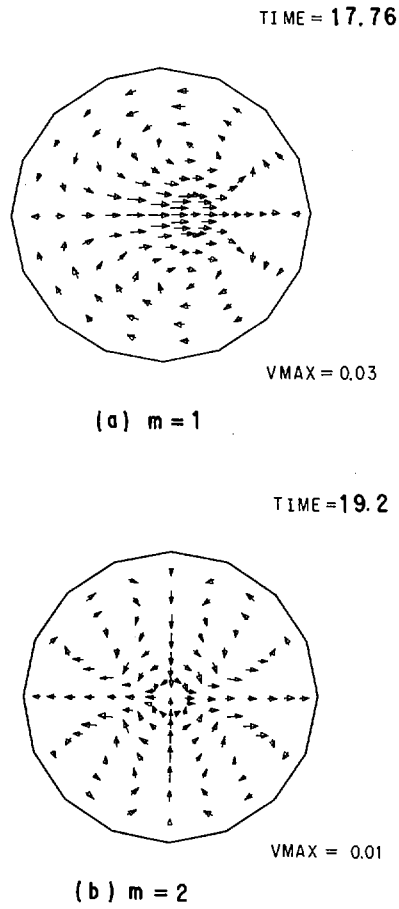


FIG.14. Poloidal velocity vector at z = 0 for (a) m = 1 and (b) m = 2 [3D results.].

$n_0 = 1 \times 10^{15}$ cm^{-3}, $T_0 = 20$ eV, $B_{t0} = 2.4$ kG, $\beta = 28\%$. Figure 13 shows the Lagrangian mesh network when m = 1 and m = 2 MHD modes grow sufficiently. The scale in the z-direction is 1/7 of those in other directions. Time is normalized by a/V_{TA}, ($V_{TA} = B_{t0}/\sqrt{\mu_0 \rho_0}$). Figure 14 shows the poloidal velocity vortices at z = 0, where 2 m vortices are observed for m = 1 and m = 2. In these cases, the current is initially distributed as $j(r) = j_0(1 - r^2/q^2$; $(q_a/q_0)_{t=0} = 2)$, and $I_p = 10$ kA, $q_a = 1.5$ for m = 1 and $I_p = 6$ kA, $q_a = 2.5$ for m = 2. Helical displacement of the plasma and growth of internal MHD modes in a finite-β plasma are clearly shown in these figures. In another simulation ($q_a = 1.15$), the m = 1 mode becomes active in a drastical way, showing the crucial effect of q_a.

REFERENCES

[1] HIRANO, K., et al., in Plasma Physics and Controlled Nuclear Fusion Research (Proc. 6th Int. Conf. Berchtesgaden, 1976), Vol. 1, IAEA, Vienna (1977) 503.
[2] GOLANT, V.E., in Controlled Fusion and Plasma Physics (Proc. 8th Europ. Conf. Prague, 1977) Vol. 2 (1977) 63.
[3] TAMARU, T., et al., in Plasma Physics and Controlled Nuclear Fusion Research (Proc. 6th Int. Conf. Berchtesgaden, 1976) Vol. 1, IAEA, Vienna (1977) 471.
[4] SUGISAKI, K., in Controlled Fusion and Plasma Physics (Proc. 8th Europ. Conf. Prague, 1977) Vol. 1 (1977) 74.
[5] OGAWA, K., et al., in Pulsed High Beta Plasma (Proc. 3rd Top. Conf. 1975) 255.
[6] SHIMADA, T., et al., in Plasma Physics and Controlled Nuclear Fusion Research (Proc. 6th Int. Conf. Berchtesgaden, 1976) Vol. 1, IAEA, Vienna (1977) 463.
[7] VERHAGE, A.J.L., Culham Laboratory Report, CLM-R161 (1976).
[8] IDO, S., Thesis at University of Tokyo (1978).
[9] ROBERTS, K.V., Comput. Phys. Commun. 7 (1974) 237.
[10] TAYLOR, J.B., Plasma Physics and Controlled Nuclear Fusion Research (Proc. 5th Conf. Tokyo, 1974) Vol. 1, IAEA, Vienna (1975) 161.
[11] PRACHT, W.E., J. Computer Phys. Commun. 17 (1975) 132.
[12] BRACKBILL, J.U., "Numerical magnetohydrodynamics for high-beta plasmas", in Methods in Computational Physics Vol. 16, Academic Press (1976).

Z-PINCHES OF INTENSE ENERGY DENSITY DRIVEN BY HIGH-VOLTAGE STORAGE LINES

P. CHOI, A.E. DANGOR, A. FOLKIERSKI,
E. KAHAN, D.E. POTTER, P.D. SLADE,
S.J. WEBB
Blackett Laboratory, Imperial College,
London, United Kingdom

Abstract

Z-PINCHES OF INTENSE ENERGY DENSITY DRIVEN BY HIGH-VOLTAGE STORAGE LINES.

Experimental, theoretical and computational results are presented of a study of the z-pinch as a hybrid magnetic-inertial containment device. In these preliminary experiments a current of 100 kA from a 600-kV storage line passes through a fast, small-radius pinch for 100 ns. A stationary pinch of radius ~ 0.3 of wall radius is observed. No bounce, oscillation, or current restrike at the wall occurs during the times of interest. Temperatures of 0.2 to 1.0 keV are measured with estimated number densities up to 2×10^{24} m^{-3}. The experimental results are compared with the predictions of the "slug" model which, unlike the snowplough, predicts a finite final radius and no bounce, and also with a radial simulation, in which ion viscosity plays a significant role. Scaling suggests that a plasma of small volume and intense energy density of thermonuclear interest can be produced with powerful storage lines.

1. INTRODUCTION

The technological advances of high-voltage storage lines now allow new regimes in the z-pinch to be considered. In this paper, we envisage the z-pinch as a hybrid magnetic-inertial containment device with containment times limited by convection losses arising from magnetohydrodynamic instability. Analysis of the scaling of such a pinch in meeting the Lawson criterion suggests that the $n\tau$ value depends solely on the power input per unit length. A power source of 10^{14} watts might be sufficient to produce breakeven conditions in deuterium-tritium.

In a series of pilot experiments reported here, the plasma and current are rapidly detached from the insulating walls at voltages of 600 kV and current of 100 kA. Historical problems of current restrike and insulator breakdown do not occur at these high voltages and during the short timescales of 120 ns. The parameters of the pinch obtained are comparable to those in the dense plasma focus, though in contrast to the latter experiments scaling of the device is now possible.

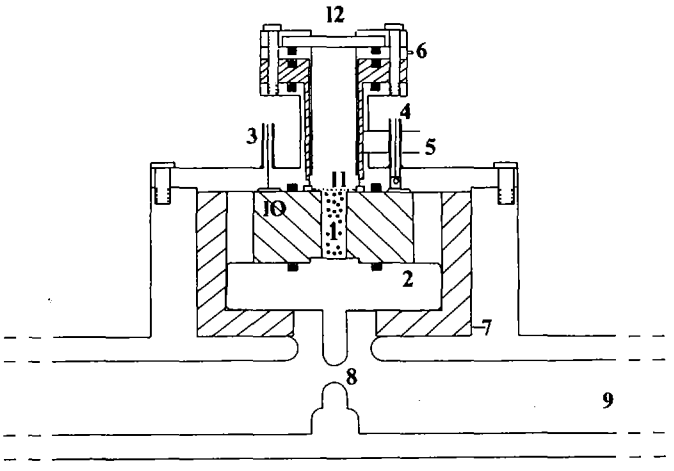


FIG.1. Pinch device. 1) plasma; 2) live electrode; 3) lead to voltage probe; 4) lead to magnetic dI/dt probe; 5) pumping port; 6) lead to pre-ionizing electrode; 7) PTFE insulating spacer; 8) water spark gap; 9) storage line; 10) perspex pinch tube; 11) mesh earthy electrode.

In Section 2, we present experimental results of the formation and properties of these very fast pinches. These results are compared with numerical simulations (Sec. 3), and with the results of an heuristic theoretical slug model, which gives reasonable agreement with experiment (Sec. 4). Some properties of stability, losses and scaling in such pinches are further discussed in Section 4.

2 EXPERIMENTAL RESULTS

A diagram of the experimental configuration is shown in Fig. 1. The pinch is fed from a high-voltage, storage, pulse-forming transmission line with water dielectric. The results described here were obtained on two devices. In the original (Mark I) device, the line operates at 200 kV and yields a current of 80 kA over a pulse-duration of 150 ns. The quartz discharge tube 10 cm long, internal radius 2 cm, operates with filling pressures of 30 - 100 mtorr of hydrogen. The Mark II device is a 600 kV line giving 100 kA for 120 ns into a pinch tube 3 cm long and filled to pressures of 0.1 - 8 torr of H_2. In the latter, two sizes of perspex tube have been used, 0.5 and 1 cm radius. To preionize the gas, a fraction of the line charging current is passed through the pinch tube.

A range of diagnostic techniques is in use. Results on the formation of the pinch, consistent for both devices, are obtained from electrical measurements and streak photography. In the Mark I device, operating at lower density,

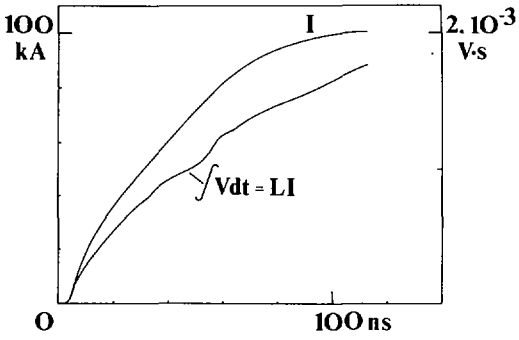


FIG.2. Current and integral of voltage curves. These were obtained from dI/dt and V oscillogrammes by averaging out ringing and computer integration. $\rho_0 = 2$ *torr* H_2; $r_0 = 0.5$ *cm.*

the electron temperature is determined from X-ray emission of targets. Further the evolution of plasma temperature can be inferred from the appearance of different stages of ionization of nitrogen impurity. The higher density in the Mark II device leads to intense soft X-ray emission by the plasma, which is examined by pinhole photography.

2.1 Electrical measurements. Typical waveforms of current through the discharge and integral of voltage across it are shown in Fig. 2. The current rises quasi-exponentially due to spark-gap inductance and then remains approximately constant during the times of interest (100 ns). By analysing the voltage and current traces, the variation of the inductance is obtained. Assuming that this inductance is due to a single moving current shell, its radius $r_p(t)$ can be found as function of time. For typical traces this is shown in Fig. 3. The results suggest that the current is carried in a sheet which propagates inwards typically to a radius of 0.3 of the wall radius; the radius of the current sheet appears to remain approximately constant for a further 100 ns, during which there is no significant expansion and oscillation or current restrike at the wall. The precision obtainable from the voltage trace is, however, limited by a large oscillation (period 8 ns) which is probably due to capacitive effects in the line - electrode configuration.

2.2 Streak photography. A typical streak photograph from the Mark II device is shown in Fig. 4. Comparable photographs are obtained over a reasonably wide range of parameters. Their interpretation is illustrated in the annotated diagram of Fig. 5. In the formation stage, the fastest observed line is interpreted as a shock which meets the axis after $\approx$ 50 ns and which propagates typically with a velocity of 3×10^5 ms^{-1}. The slower line is interpreted as a piston or current sheet, and this forms a final pinch of radius a $\approx 0.3\ r_0$. There is no apparent sign of a reflected shock or

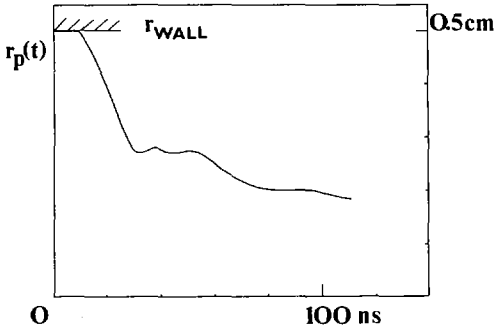


FIG.3. Position of current-carrying sheath obtained from data of Fig.2.

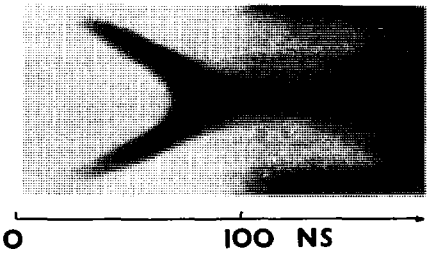


FIG.4. Streak photograph for conditions of Fig.2.

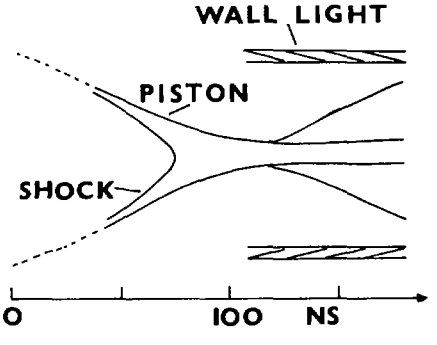


FIG.5. Diagram of Fig.4. When voltage from the line reverses at 120 ns, pinch expands and a second collapse begins at the wall.

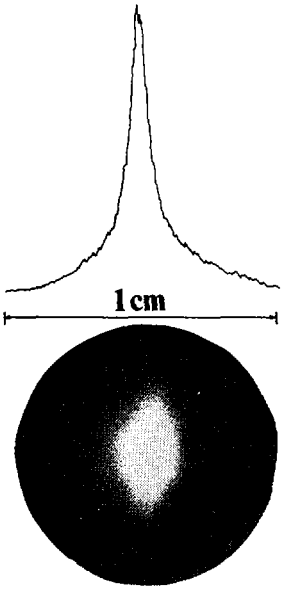


FIG. 6. X-ray pinhole photograph and its microdensitometer trace.

of radial oscillation of the pinch (1,2). The emission visible to the camera (> λ 4000 Å) falls significantly as the pinch is formed, and thereafter gradually reappears. At later times (∿ 150 ns), when the voltage from the line reverses, there is evidence of a second sheath forming at the wall. At the same time the pinch expands.

2.3 Target X-ray emission. In the Mark I device operating at low densities, small targets are introduced on axis. The solid matter decelerates hot electrons yielding X-rays. This emission is analysed using pinhole photography and various absorber foils. The technique perfected for the purpose by one of us (P.C.), has yielded an electron temperature T_e = 1.0 ± 0.2 keV for a filling pressure of 30 mtorr hydrogen.

2.4 Soft X-rays. The higher densities in the Mark II device give rise to soft X-ray emission from the pinch plasma; this is observed axially by pinhole photography (Fig. 6). The emission is most intense on the pinch axis, the hot region having a radius of approx. 1 mm.

Using various absorber foils, an electron temperature, in the axial region, of 0.2 ± 0.1 keV was inferred from the pinhole photographs. This is not unreasonable for the 3 Torr filling pressure used, in terms of the Bennett relation.

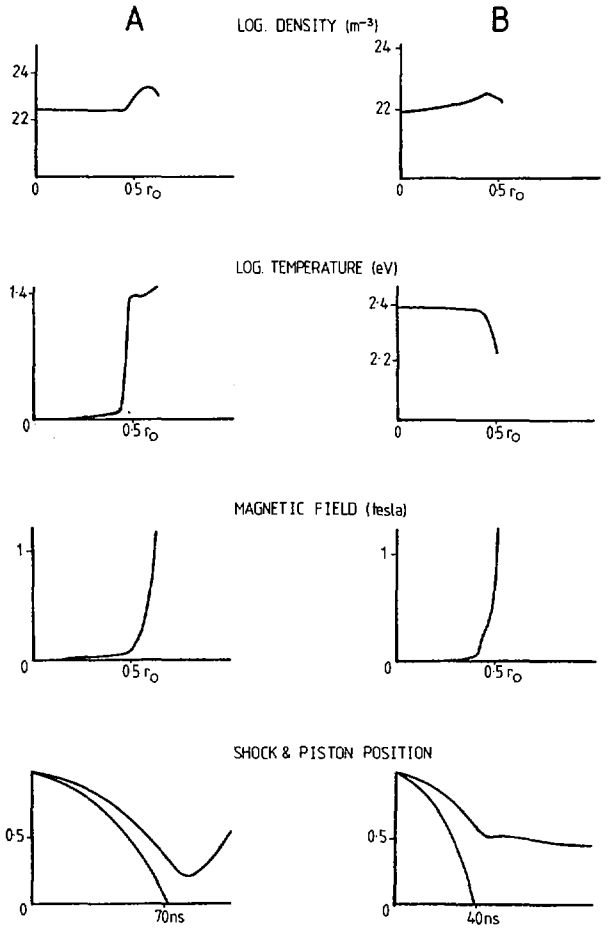


FIG. 7. Numerical solutions of plasma behaviour, in two cases, for the Mark-II device, $r_0 = 1$ cm:
A: filling pressure $\rho_0 = 300$ mtorr, Reynolds number $R \gg 1$.
B: $\rho_0 = 80$ mtorr, $R \cong 1$.
Typical profiles of density temperature and B_θ are plotted at particular instants during collapse (A: $t = 55$ ns, B: $t = 40$ ns).

3 NUMERICAL SIMULATION OF THE PINCH

The formation and structure of the pinch have been examined with a radial, time-dependent numerical code. The plasma is described by the magnetohydrodynamic equations. Equal ion and electron temperatures are assumed but classical resistive diffusion, ion and electron heat conduction and ion viscosity are included. The current is either pre-programmed or coupled to an appropriate circuit.

Detailed results have been obtained for the experimental configurations defined above. Two regimes have been distinguished which depend on the ion Reynold's number. In the Mark I device and at higher densities in the Mark II device, it is found that the Reynold's number significantly exceeds unity, that a well-defined shock is produced and that the shock reflects from the axis producing large oscillations in the piston position (Fig. 7).

At lower filling densities, however, the heating per particle becomes larger. Due to the strong dependence of the thermal conductivity and viscosity on temperature, the Reynold's number approaches unity. This results in the rapid conduction of heat to the axis, in the diffusion of the shock and in the viscous damping of the flow (Fig. 7). As a result there is little or no reflexion of the shock from the axis and as the pinch is formed the piston comes uniformly to rest. No oscillation of the pinch radius occurs. The final pinch radius is $a = 0.4\ r_o$ and the density and temperature are uniform across the pinch.

4 THEORY OF THE FORMATION AND PROPERTIES OF THE PINCH

4.1 The formation.. Existing theories of the formation of the pinch are not consistent in several important respects with what is observed in these very fast pinches. The snow-plough model (3) describes no structure in space and suggests a singular infinite compression on axis. Shock models (4) on the other hand do not describe cylindrical effects and suggest a sharp reflexion of the shock and expansion of the plasma. No equilibrium is therefore described or predicted.

In the ideal MHD limit, three regimes in the formation of a pinch have been distinguished (2), according to the rate at which the driving current is applied. With the pulse-forming lines used, the current rises very rapidly in a short time (30 ns) and thereafter remains constant at its plateau value I. In these circumstances a shock (radius $r_s(t)$) is propagated radially inwards, and the current is carried on a thin sheet - the piston - radius $r_p(t)$. During the time of collapse, sound waves can propagate both ways between the piston and shock. A heuristic model is presented in (2) in which it is assumed that the plasma pressure p(t) is uniform in space between shock and piston. This in turn implies that no reflexion of the shock will occur and therefore no expansion of the piston, as is consistent with experimental observations.

The Rankine-Hugoniot conditions for a strong shock are used to define the pressure, velocity and density of the plasma immediately behind the shock in terms of the filling density ρ_o, shock velocity v_s and ratio of specific heats γ. Using the adiabatic law and the equality of plasma and magnetic pressures at the piston, a simple relationship for the piston radius in terms of the shock radius is obtained

$$r_p = r_o \left(\frac{\gamma}{\gamma+1 - r_s^2/r_p^2} \right)^{\frac{\gamma}{\gamma-1}}$$

where r_o is the radius of the wall. Thus in the limit when the shock meets the axis, $r_s \to 0$, the final pinch radius is

$$a = r_o \left(\frac{\gamma}{\gamma+1} \right)^{\frac{\gamma}{\gamma-1}}$$

The equations are solved to give the positions of piston and shock in time (Fig. 8). The final pinch radius is a $\approx$ 0.31 r_o for $\gamma = 5/3$, no reflexion of the shock occurs and the piston comes to rest. The time to pinch is

$$t_p = 0.38 \left(\frac{16\pi^2 \rho_o}{\mu_o} \right)^{\frac{1}{2}} \frac{r_o^2}{I}$$

The results of this model are in close agreement with experimental observations (Sec. 2).

4.2 Properties of the pinch. Using a Lagrangian technique for each cylindrical element in the slug, analytic solutions for the profile of density and temperature in the equilibrium pinch are obtained:

$$\rho = \frac{\gamma+1}{\gamma-1} \rho_o \left(\frac{\gamma+1}{2\gamma} + \sqrt{\frac{(\gamma+1)^2}{4\gamma^2} + \frac{r^2-r_p^2}{\gamma r_p^2}} \right)^{\frac{2}{\gamma-1}}$$

Since the pressure is uniform in this model, the temperature is the inverse of this function. These profiles of density and temperature are plotted in Fig. 9. Heat conduction is limited to the region within the pinch, due to strong magnetic field,and will have the effect of diffusing the temperature and density profiles,while not altering the radius of the pinch. The parameters for typical conditions in the pinch according to the slug model are summarised in Table I.
By programming the current in time, regimes of singular compression by a coincident train of waves, and of adiabatic compression can be produced, resulting in greatly enhanced densities (2).

4.3 Plasma losses in the equilibrium. Several mechanisms limit, in principle, the containment time. Energy loss can occur by radial and axial conduction and by radiation (5). The predominant loss, however, will arise through radial convection due to MHD instabilities.

The linear theory of ideal MHD instability relates the linear growth time τ_s of the fastest modes to the radial transit time of sound waves, and so to the radial transit time

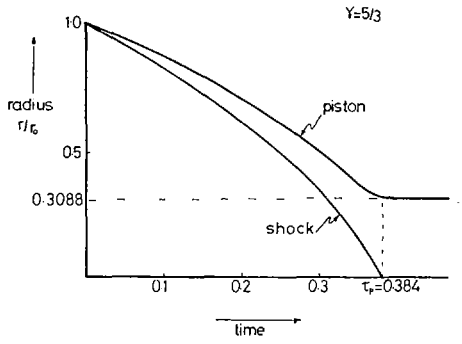


FIG.8. Solutions from the slug model for the piston and shock radii as functions of time, for the case $\gamma = 5/3$. The piston comes uniformly to rest as the shock approaches the axis.

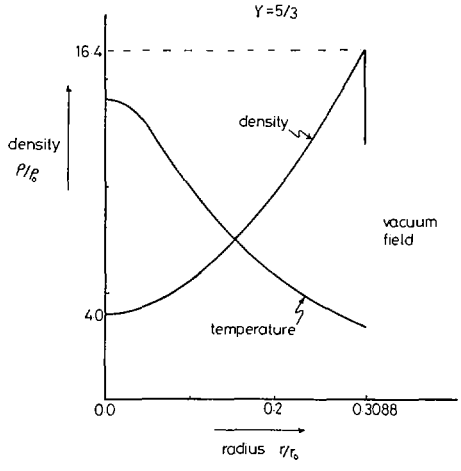


FIG.9. Solutions for the density and temperature as functions of radius r normalized to the wall radius r_0. The temperature is peaked on the axis, whereas the density has a hollow structure.

TABLE I. SLUG MODEL PARAMETERS FOR FILLING DENSITY OF 3 TORR, $r_0 = 0.5$ cm

current	I =	120 kA
maximum density	n_m =	$3 \times 10^{18} cm^{-3}$
peak temperature	T_m =	0.8 keV
pinch radius	a =	1.5 mm

of thermal ions. The radial convection loss time τ_c can therefore be written as

$$\tau_c = M\tau_s \approx Ma\sqrt{m_i/kT}$$

where M is a number in excess of unity.

In determining the parameter M, ideal MHD theory is not appropriate. At these high temperatures and small scale lengths, ion viscosity is a dominant effect in reducing the growth rate (6). Furthermore in the regime considered the Larmor radius of the ions relative to the pinch radius is of the order of unity. Linear theory suggests that finite Larmor radii have a stabilising effect on the pinch (7). In summary therefore we may expect the stability of the pinch to be enhanced over the inertial time τ_s by some unknown but significant multiple.

4.4 Scaling. Using the Bennett relation and the containment time τ_c, the Lawson product may be expressed as:

$$n\tau = \frac{\mu_o m_i^{\frac{1}{2}}}{8\pi^2} \frac{M}{(kT)^{3/2}} \frac{I^2}{a} \quad s.m^{-3}$$

Clearly to maximise this product, the radius a must be minimised. The radius obtainable is ultimately limited by the applied voltage V and hence,

$$n\tau = \frac{m_i}{4\pi (kT)^2} \cdot M \frac{IV}{z} \quad s.m^{-3}$$

where z is the length of the pinch. Thus the Lawson product which can be achieved is proportional to the power per unit length available from the electromagnetic source. Taking typical values for deuterium-tritium of $n = 10^{20}$ $s.m^{-3}$ $z = 5$ cm, $kT = 5$ keV and $M = 100$, the electromagnetic power required is 10^{14} watts.

5 CONCLUSION

The technology of high voltage storage lines has been successfully used to power a pinch. The plasma formed during the initial collapse remains confined for $\sim$ 100ns. This is an order of magnitude longer than the estimated growth-time of MHD instabilities, giving $M \sim 10$. The duration of the confined phase appears to be limited by the duration of the current pulse. When the voltage from the line reverses, the pinch begins to expand, and a new sheath converges from the wall.

The pinch has a finite radius which agrees with the "slug" model. Numerical simulation also predicts this, but for a smaller range of parameters than observed. It does not predict a radial temperature profile within the pinch, which the soft X-rays measurements indicate.

It is envisaged that the quasi steady-state pinch described above will be used as the initial state of an adiabatic compression, leading to temperatures and densities of thermonuclear interest.

REFERENCES

1 BODIN, H.A.B., NEWTON, A.A., PEACOCK, N.J., Nucl.Fusion 1 (1960) 54.
2 POTTER, D., Nucl.Fusion 18 6 (1978) 813.
3 ROSENBLUTH, M., GARWIN, R., ROSENBLUTH, A., Los Alamos Report - LA - 1850 (1954).
4 ALLEN, J.E., Proc.Phys.Soc. 70 (1957) 24.
5 HAINES, M.G., to be published in J.Phys.D: Appl.Phys. 11 (1978).
6 POTTER, D.E., Phys.Fluids 14 (1971) 1911.
7 WRIGHT, R.J., POTT, D.F.R., HAINES, M.G., Plasma Phys. 18 (1976) 1.

DISCUSSION

I. ALEXEFF: How do you pre-ionize the pinch?

D.E. POTTER: During the changing of the line from the Marx, a portion of the current is taken through a high resistance to create a small discharge at one end of the pinch tube (see Fig.1). The ionization spreads uniformly through the pinch tube.

R.N. SUDAN: Is it not true that the stabilization factor you quote for the pinch is valid only for wavelengths shorter than the betatron wavelength, which in your case is of the order of the pinch radius?

D.E. POTTER: I did not quote a stabilization factor. As far as I am aware, the stability of such a pinch, in which the ion Larmor radius or ion skin depth equals the radius, is unknown. The nearest analysis we have involves ideal MHD with finite-Larmor-radius effects included as a correction (Larmor radius/radius is a small parameter). This indeed suggests stabilization of the short-wavelength modes. The further extrapolation to these conditions remains unclear.

TORMAC CONFINEMENT, THEORY AND EXPERIMENT*

M.A. LEVINE, H.L. BERK, I.G. BROWN,
J. COONROD, B. FEINBERG, M. GREENWALD,
J. HAMMER, W.B. KUNKEL, B.R. MYERS,
R.A. NILAND, A. SESSLER, W. SHARP,
R. SHAW, L. SOROKA, M. VELLA
Lawrence Berkeley Laboratory,
University of California,
Berkeley, California

A.H. BOOZER, M.A. MOSTROM
Plasma Physics Laboratory,
Princeton University,
Princeton, New Jersey

N.T. GLADD
University of Maryland,
College Park, Maryland,
United States of America

Abstract

TORMAC CONFINEMENT, THEORY AND EXPERIMENT.

Tormac (Toroidal Magnetic Line Cusp) is a high-β absolute minimum-B plasma confinement system. A bicusp version of Tormac has been examined experimentally and tests of magneto-acoustic heating have been carried out. In this geometry, the support of the plasma pressure depends on the containment of particles in a sheath region on open magnetic field lines. A theoretical calculation of the stability of such containment as a function of β and shear predicts microturbulence in the region where the sheath must be operated. The implications of this turbulence are discussed in terms of reactor scaling.

Tormac Concept

Tormac (Toroidal Magnetic Cusp), first proposed by Levine,[1] is a stuffed toroidally symmetric line cusp. As a cusp, it possesses an absolute minimum-B with the advantage that it is MHD-stable at high beta. For a fusion reactor, several economies and simplifications result from this advantage.

* Work supported by US Department of Energy.

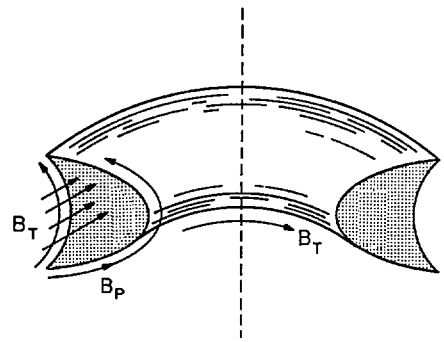


FIG.1. Toroidal bicusp.

In Tormac a high-β plasma is held by a cusp magnetic field at the surface. An absolute minimum-B geometry can be realized if the plasma pressure is held on open field lines at the plasma edge.

A crucial feature of Tormac is the containment of particles on these open field lines. On the open lines, particles are trapped between collisions by a canonical invariant[2] and an adiabatic invariant.[3] These invariants combine to give mirror-like trapping in the sheath rather than cusp scaling. The only way a particle can escape from Tormac is along an open field line, so that the loss rate is determined by the sheath. In the ideal case, the sheath loss is due to interparticle collisions. These collisions scatter particles into the loss cone. Since the probability of loss is then about equal to the probability of cross field diffusion, the sheath thickness is about an ion gyroradius, r_i. The containment time for such a system is then given by

$$n\tau = 0.1\ (R_p/r_i)(n/n_s)(P/P_s)n\tau_i \qquad (1)$$

where τ_i is the ion collision time in the sheath, R_p the characteristic plasma minor radius, r_i the ion gyroradius, and n/n_s the ratio of inside to sheath density, and P/P_s the ratio of inside pressure to the sheath pressure. The factor 0.1 includes geometric factors and the mirror logarithmic factor.

The question of how small the internal magnetic field can be in Tormac is tied to the drift problem. Fortunately, it is only the particles whose velocities are most closely aligned with the magnetic field that are lost from the open field lines.[3] Computer orbit calculations show that all particles whose orbits include at least 15% closed field lines were saved. This implies that a small but finite closed poloidal field is required.

The implementation of the internal magnetic field can be best discussed in terms of a specific example.[4] In the current Tormac experiments the toroidal bicusp shown in Fig. 1 is used. In this shape the radius of curvature of the open magnetic field lines in the surface of the plasma is negative, as required for an absolute minimum-B geometry. This is accomplished by having the magnetic field lines at small major radius dominated by the toroidal component of field and the intensity of the field lines at the outer toroidal radius dominated by the poloidal field component of field.

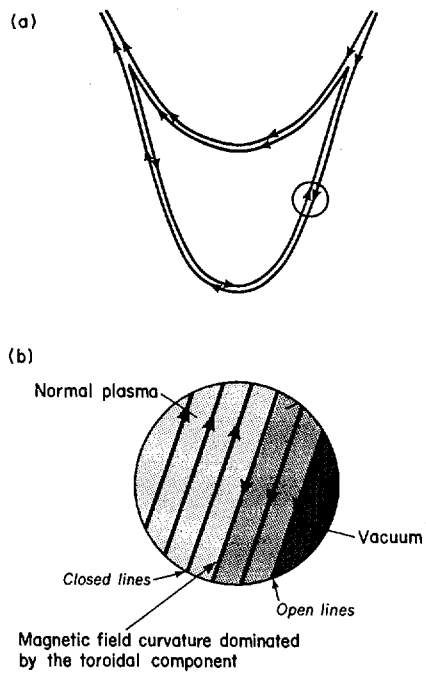


FIG.2. Cross-section of bicusp with internally closed poloidal field.

Limiting the number of cusps to two, as shown in the bicusp, has several advantages over the shapes with a larger number of cusps. Experimentally, fewer cusps reduce the complexity of the device and make it easier to produce the required magnetic field shaping without bringing the coils too close to the plasma. Theoretically, the bicusp reduces the particle loss cone and optimizes the volume-to-surface ratio.

A possible configuration for a bicusp with closed poloidal lines inside is given in Fig. 2. There is indicated in Fig. 2 a poloidal field reversal in the sheath. It should be remembered in considering this diagram that the toroidal magnetic field is present everywhere. What appears as a region of field reversal is only a mild field shear.

Stability considerations require that the closed poloidal magnetic field be confined to within a few gyroradii of the cusp magnetic field.

The use of closed poloidal magnetic field lines to support part of the plasma pressure in the bicusp limits particle drifts and improves $n\tau$.

Experiment

There are three experiments at Lawrence Berkeley Laboratory investigating various aspects of the Tormac problem: Tormac IV, Tormac V and Tormac PI. In addition, the 2XIIB experiments give vital information on the Tormac sheath. In this paper we discuss only Tormac IV.

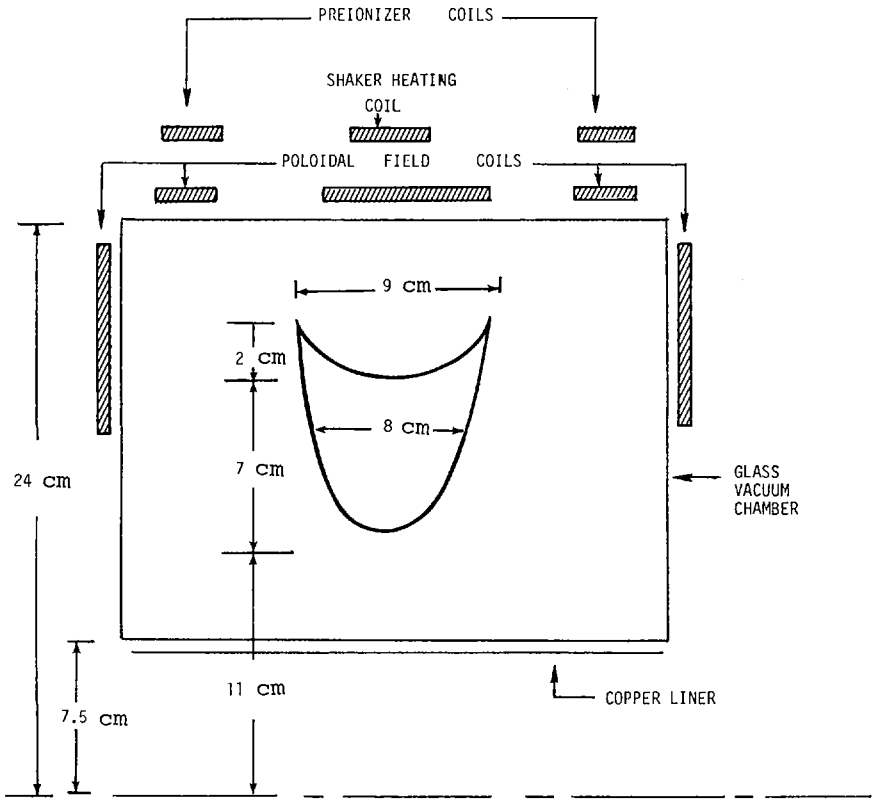


FIG.3. Schematic representation of Tormac IV with bicusp plasma in the calculated equilibrium position. The system is toroidally symmetric.

Tormac IV is a relatively small pulsed experiment. A cross-section with dimensions is shown in Fig. 3. The magnetic field e-folding decay time is 80 μs and the magnetic field intensity at the surface of the plasma has a maximum value of 6.5 kG. Plasma densities are of the order of $10^{15}/cm^3$.

Spectral data in Tormac IVA indicate an ion temperature of 150 eV. In Tormac IV, it should be noted that ion temperatures measured using spectral broadening are subject to effects such as turbulence which can mask the true plasma parameters. Recently, Tormac IVC was constructed to include Thomson scattering. Measurements in IVC give an electron temperature of 5 eV. The optical and electrical signal responses in these two devices have differences that are still to be resolved.

To further heat the plasma, 'shaker heating' or magneto-acoustic (M-A) waves are used. These waves are carried over a wide range of frequencies in a toroidally symmetric mode perpendicular to the magnetic field. This means that these waves do not affect the containment properties of Tormac and they

offer flexibility in the choice of frequency as well. Thus, in Tormac IV while the particle pressure changes substantially, the frequency of the heating system is kept constant at about 0.5 MHz.

Jacobson et al.[5] have demonstrated the use of M-A waves in resonant mode to heat a θ-pinch plasma. A general treatment of non-linear effects for Alfvén waves and M-A modes has been considered by Tataronis and Grossman.[6]

Coupling to the plasma can be expressed in terms of $Q = E/\Delta E$, where E is the total stored circuit energy and ΔE the change energy/radian due to the plasma. Small values of Q represent efficient coupling.

The problem of competing requirements of many wavelengths within the plasma for absorption and low-frequency long wavelengths for coupling is resolved by wave trapping. Wave trapping occurs when the coupling to the plasma is via a mode not near the normal modes of the plasma. To illustrate this and evaluate the low-frequency limit for shaker heating, the model shown in Fig. 3 is used. In this figure a magneto-acoustic wave is launched into the upper surface of the bicusp, driven by the one-turn coil. Ray tracing is used to illustrate a typical wave path through the plasma. After the first bounce from the lower surface the wave returns to the driven surface on a relatively short path.

From scaling arguments one then arrives at the relation

$$Q \sim \frac{\omega}{\omega_0} \ell n\left(\frac{s}{a}\right)\left(1 - \frac{\lambda}{8\pi R_p} \sin \frac{8\pi R_p}{\lambda}\right) \qquad (2)$$

where s is the distance from the coil to the plasma, a the length of the coil, and $\omega_0 = \omega/s$ where ω is the M-A wave velocity in the plasma. After the second bounce from the driven surface the wave travels a much longer and less regular path before again returning to the driven surface.

A small (0.360 joules) capacitor bank is 'rung down' through a coil encircling the major axis of the plasma. The energy in the system was adjusted by varying the charging voltage of the capacitors. The ringing frequency was set by the number of capacitors in the bank and a variable inductor in series with the heater coil, and can be varied between 180 and 350 kHz.

In Fig. 4, the measured circuit Q as a function of frequency is plotted along with Q from Eq.(2). The data fit did not appear adequate. Equation(2) was derived on the basis of a linear theory. If it is assumed that the absorption is not complete in the plasma but is amplitude-dependent, then the Q is a function of both ω and I. To test this hypothesis Q x I is plotted as a function of ω in Fig. 5. On the same plot, the value of Q x I derived from Eq.(2) is also plotted. These results would seem to indicate that a non-linear theory is a better fit of the data.

Microinstability

Since ions in the sheath are confined on open field lines by magnetic mirroring, the plasma is subject to the same loss-cone instabilities[7] found in mirror machines. In particular, the drift cyclotron loss-cone (DCLC) instability[8] is important because it is an absolute instability for propagation along the magnetic field lines. The Tormac sheath differs from conventional

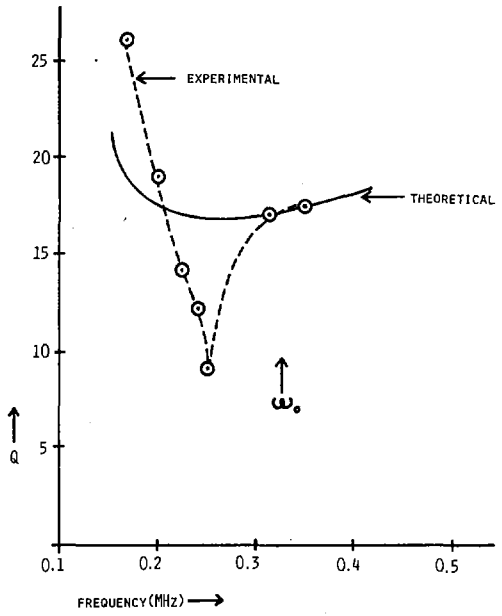


FIG.4. Predicted and measured absorption curve for shaker heating (linear).

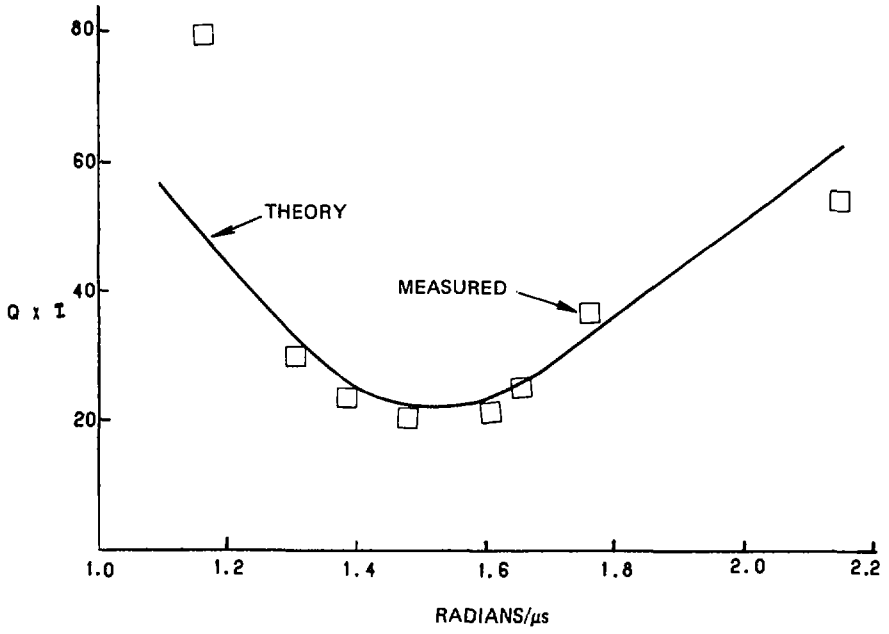


FIG.5. Predicted and measured absorption curve for shaker heating (non-linear). Q X I *versus frequency. Solid line represents normalized theory.*

mirror machines principally in having large magnetic shear, with a shear length of the order of an ion Larmor radius. Here, we investigate the effect of strong magnetic shear on the stability of the DCLC mode.

For the analysis we treat the electrons as a cold fluid and the ions in the straight line orbit approximation. We model the sheath by a plasma slab with spatial variation in the x direction only. The magnetic field is taken to be

$$\underset{\sim}{B} = B_0(x)\left(\hat{z}\cos\frac{x}{L_s} + \hat{y}\sin\frac{x}{L_s}\right) \tag{3}$$

and we seek modes localized to a region $\frac{|x|}{L_s} \ll 1$.

To model the loss-cone ion distribution, we choose a velocity distribution that is depleted in low perpendicular velocity particles. A convenient ion distribution is

$$F_i = \frac{\exp\left(\dfrac{-V_y - \int_0^x dx\,\omega_{cz}}{\omega_{co}\,R_p}\right)}{\pi\left[V_H^2\exp(\alpha_H^2) - \Delta\,V_h^2\exp(\alpha_h^2)\right]}\left[\exp\left(\frac{-V_\perp^2}{V_H^2}\right) - \Delta\exp\left(\frac{-V_\perp^2}{V_h^2}\right)\right] \tag{4}$$

where $\omega_{cz} = q\,B_z(x)/M_i c$; $\omega_{co} = q\,B_z(0)/M_i c$; $\alpha_H = V_H/2\omega_{co}R_p$; and $\alpha_h = V_h/2\omega_{co}R_p$. The plasma scale length R_p is related to the density gradient by

$\frac{1}{n}\frac{dn}{dx} = -\frac{\omega_{cz}}{\omega_{co}}\frac{1}{R_p}$, and the parameter Δ simulates the loss-cone filling factor, with $\Delta = 1$ roughly modeling an empty loss cone and $\Delta = 0$ corresponding to a filled loss cone. Because the Tormac sheath thickness is comparable with an ion Larmor radius, the overlapping of gyration orbits gives some loss-cone filling and makes the appropriate Δ somewhat less than unity.

An appropriate local dispersion equation is obtained by treating the ion response as purely electrostatic, while using an electrostatic response with electromagnetic corrections for the electrons.[9,10] Near x = 0 this dispersion relation is

$$\varepsilon(\omega, k_\perp^2, k_y, k_\parallel^2) \equiv$$

$$k_\perp^2\left(1 + \frac{\omega_{pe}^2}{\omega_{ce}^2}\right) - \frac{k_y\,\omega_{pi}^2}{R_p\omega\,\omega_{co}}\left(1 + \frac{R_p}{B}\frac{dB}{dx}\right) + \frac{\omega_{pe}^4}{\omega_{ce}^2 c^2} - \frac{\omega_{pe}^2}{\omega^2}\,\frac{k_\perp^2 k_\parallel^2 c^2}{\omega_{pe}^2 + k_\perp^2 c^2}$$

$$+ \frac{2\,\omega_{pi}^2}{V_H^2 - \bar{\Delta}\,V_h^2}\left[1 - \bar{\Delta} + \left(\frac{\omega-\omega_H^*}{k_\perp V_H}\right)Z\left(\frac{\omega-\omega_H^*}{k_\perp V_H}\right) - \bar{\Delta}\left(\frac{\omega-\omega_h^*}{k_\perp V_h}\right)Z\left(\frac{\omega-\omega_h^*}{k_\perp V_h}\right)\right]$$

$$= 0 \tag{5}$$

where $k_\perp^2 \equiv k_x^2 + k_y^2$; $\bar{\Delta} \equiv \Delta \exp(\alpha_h^2 - \alpha_H^2)$; $\omega_H^* \equiv -k_y V_H \alpha_H$; and $\omega_h^* \equiv -k_y V_h \alpha_h$. We note from pressure balance that

$$\frac{R_p}{B}\frac{dB}{dx} = \frac{\beta}{2}$$

at $x = 0$, where $\beta \equiv 8\pi\, n(0) M_i V_x^2 / B_o^2(0)$ and $V_x^2 \equiv \dfrac{V_H^4 - \bar{\Delta} V_h^4}{2(V_H^2 - \bar{\Delta} V_h^2)}$

is the mean square perpendicular velocity. For our analysis we choose $k_\parallel = 0$ and $x = 0$ and account for magnetic shear by taking $k_\parallel = k_y x / L_s$. We assume that the $k_\parallel$ term in Eq.(5) gives the dominant spatial dependence and neglect other x dependences. The eigenfrequency is then obtained by the WKB method and satisfies the phase integral condition

$$\int_{-x_t}^{x_t} dx\, k_x(x,\omega) = (n + \tfrac{1}{2})\pi \tag{6}$$

where $k_x(x,\omega)$ is a solution of Eq.(5) for fixed k_y and ω, and $\pm x_t$ are points where $k_x = 0$. An approximate solution of this phase integral relation is

$$\omega = \omega_o + \delta\omega$$

where ω_o satisfies the standard DCLC mode dispersion relation

$$\epsilon(\omega_o, k_y^2, k_y, 0) = 0 \tag{7}$$

and

$$\delta\omega = -(2n + 1)\frac{k_y}{L_s}\frac{\left(\dfrac{\partial\epsilon}{\partial k_\perp^2}\dfrac{\partial\epsilon}{\partial k_\parallel^2}\right)^{1/2}}{\dfrac{\partial\epsilon}{\partial\omega}} \tag{8}$$

with all derivatives evaluated at ω_o, $k_\perp^2 = k_y^2$, and $k_\parallel = 0$. This approximate solution is justified when $|\delta\omega/\omega_o| \ll 1$, and hence valid for a sufficiently large shear length. In Eq.(8) the sign of the square root is determined by requiring that the wave amplitude vanish at infinity, giving the condition

$$\mathrm{Re}\left[\frac{k_y}{\dfrac{\partial\epsilon}{\partial k_\perp^2}}\left(\frac{\partial\epsilon}{\partial k_\perp^2}\frac{\partial\epsilon}{\partial k_\parallel^2}\right)^{1/2}\right] > 0 \tag{9}$$

When $\mathrm{Im}(\delta\omega) < 0$, the critical shear length is readily obtained from the condition $\mathrm{Im}(\omega) = 0$. The shortest critical shear length is found by taking $n = 0$ and varying k_y to minimize $L_s\,\mathrm{Im}(\delta\omega)$. Except at small Δ, modes with $k_y \approx 0$ give the smallest critical shear length.

Typical plots of critical shear as a function of β are shown in Fig. 6 for several values of Δ. Solid curves are used where the frequency shift at marginal stability satisfies $|\delta\omega/\omega_0| < 0.3$, while the dashed curves give results where this validity criterion is violated. For $\Delta \gtrsim 1$ the increase in R_p/L_s as β decreases indicates a weakening of shear stabilization, and for sufficiently low β, the growth rate shift $\mathrm{Im}(\delta\omega)$ becomes positive, indicating destabilization due to shear. This result is found over a wide range of a_i/R_p and is confirmed by an accurate evaluation of $\delta\omega$ using Eq.(6).

Shear stabilization is seen at high β, but for $\Delta \gtrsim 1$ shear lengths much less than R_p are needed for stability. Only at lower Δ values does stabilization occur for attainable shear lengths and moderate β.

Reactor Considerations

The above stability analysis suggests that a Tormac configuration may have to operate with an externally imposed gas to partially fill the loss cone, in a manner similar to the 2XIIB experiment. When enhanced ion scattering loss is taken into account, the quasi-linear theory[11] for the loss-cone model predicts that optimal energy containment occurs when the electron temperature is about 300 eV. For low electron temperatures, electron drag shortens the containment time, while for higher electron temperatures the energy of the ions filling the ion loss region and transiting out of the system causes a shorter containment time. The optimum temperature is derived in reference 12 and is

$$T_e^{(opt)} = 350 \frac{N^{1/4} L^{1/4}}{A^{1/8}} T_i^{1/2} \text{ eV} \qquad (10)$$

where N is the particle density normalized to 10^{14}cm^{-3}, and L is the length of the shear in meters along the field line; T_i is the ion temperature normalized to 10 keV, and A is the atomic mass. Note that $T_e^{(opt)}$ is fairly insensitive to precise plasma parameters. The theory also indicates that the actual electron temperature is somewhat less than $T_e^{(opt)}$. For this discussion we shall assume Tormac can contain an electron temperature of 300 eV in the sheath.

Even with such a low electron temperature, conditions for a Tormac reactor can still be fulfilled. In a quiescent Tormac, with a sheath width of two ion Larmor radii, the sheath losses are due to the Coulomb ion-ion scattering rate, which implies a containment scaling law

$$T_i\, n\tau = 2.0 \times 10^{12}\, R\, B\, T_i^2 \left(\frac{n_p}{n_{sh}}\right)^2 \qquad (11)$$

where n_p and n_{sh} are the plasma density in the bulk of the plasma and the plasma sheath respectively, R is the minor radius in meters, B the magnetic field in Tesla, and T_i the ion temperature in keV. If $T_e < 0.1\, T_i$ in the sheath, due to either thermal conduction or loss-cone modes being present so that $T_e < T_e^{(opt)}$, then electron drag determines containment. If we assume that electron temperature is appreciably below the ion temperature only in the plasma sheath, we find the containment scaling law is then

$$T_i\, n\tau = 7 \times 10^{13}\, R\, B\, T_e^{3/2}\, T_i^{1/2} \left(\frac{n_p}{n_{sh}}\right)^2 \qquad (12)$$

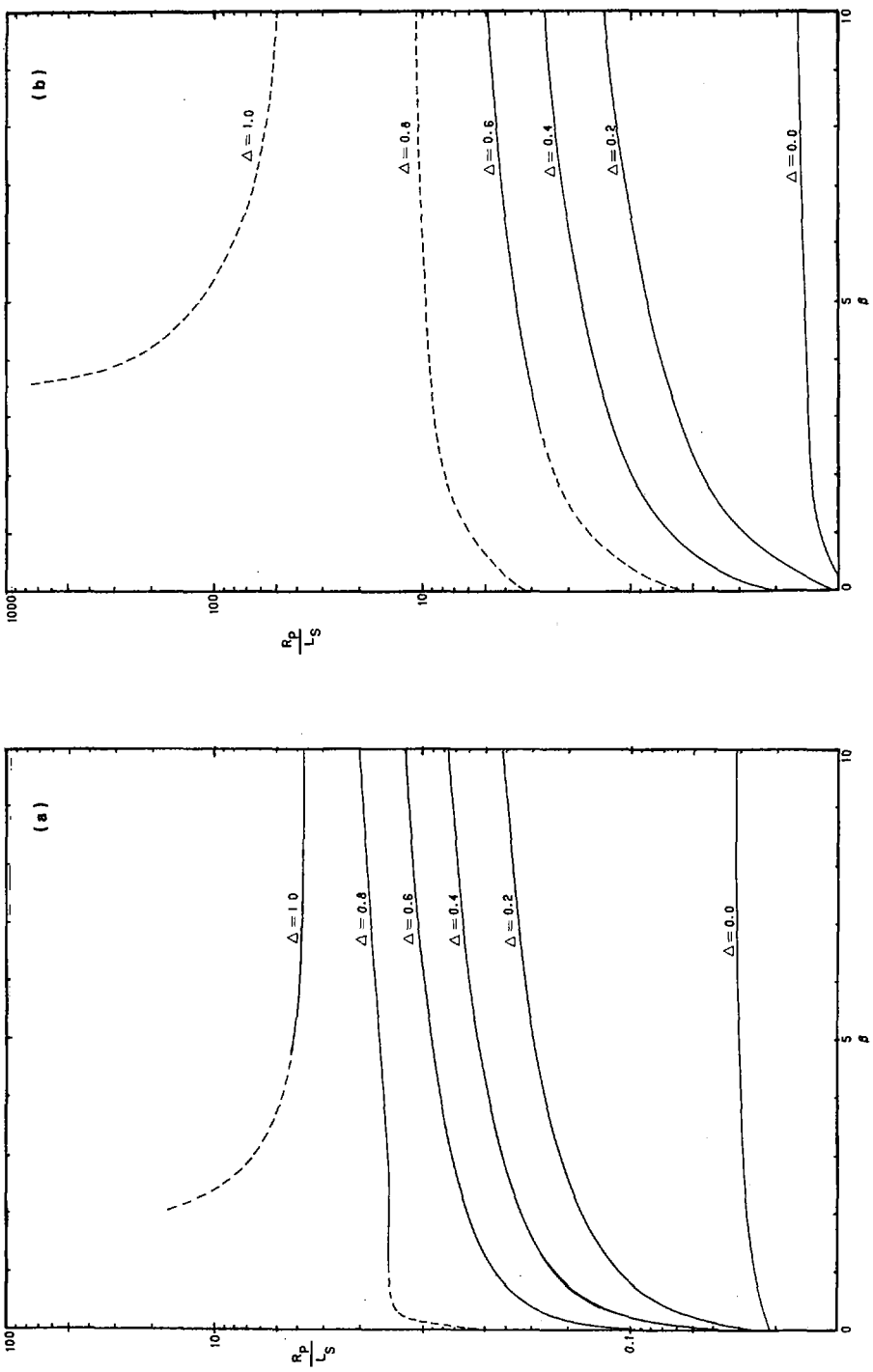


FIG. 6. Variation of critical shear with β for several values of the loss-cone factor Δ when $V_H^2/V_h^2 = 2.0$. *The approximations of the calculations are fulfilled only where the curves are solid. (a)* $a_i/R_p = 0.1$; *(b)* $a_i/R_p = 0.5$.

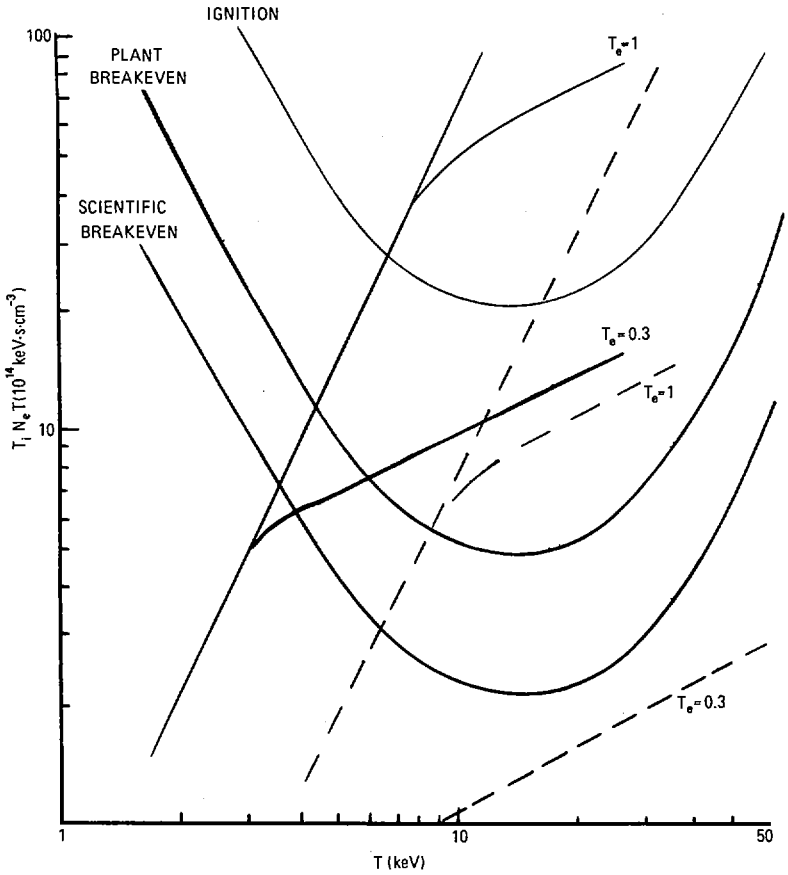


FIG. 7. Tormac scaling, RB = 3 (T_e *in keV).*

In both Eqs 11 and 12 we see that an appreciable gain arises if a Tormac configuration can operate with $n_{sh}/n_p < 1$.

As an example, in Fig. 7 we indicate the containment regime needed to achieve fusion conditions.[13] We choose RB = 3 and plot the Tormac T_i $n\tau$ for $n_p/n_{sh} = 3$ and $n_p/n_{sh} = 1$. The straight lines, corresponding to a quiescent Tormac, readily scale into the ignition regime for both $n_p/n_{sh} = 3$ and 1. A plasma with 300 eV electron temperature in the sheath almost achieves breakeven for $n_p/n_{sh} = 1$. For $n_p/n_{sh} = 3$ it is possible to operate in an economic energy-generating mode.

We are also interested in an alternative method of operation, where electrons are heated to near relativistic energies in the sheath. The purpose is two-fold:

1. Several experiments[14, 15] have observed that instabilities are suppressed in the presence of hot electrons;

2. The quiescent containment time, which may be achievable with hot electrons, is enhanced by a factor $(n_p/n_{sh})^2$ which from pressure balance can be as large as $(T_{eh}/T_i)^2$ where T_{eh} is the hot electron temperature.

REFERENCES

[1] GRAD, H., New York Univ., Inst. of Mathematical Science Rep. NYO 7969 (1957).
[2] LEVINE, M.A., BOOZER, A.H., KALMAN, G., BAKSHI, P., Phys. Rev. Lett. **28** (1972) 1323.
[3] BOOZER, A.H., LEVINE, M.A., Phys. Rev. Lett. **31** (1973) 1287.
[4] LEVINE, M.A., BROWN, I.G., GALLAGHER, C.C., Plasma Phys. Suppl., Pulsed High-Beta Plasmas (1976).
[5] JACOBSON, A.R., BUCHENAUER, C.J., DOWNING, H.J., THOMAS, K.S., Phys. Rev. Lett. **37** (1976) 897.
[6] TATARONIS, J.A., GROSSMAN, W., Nucl. Fusion **16** (1976) 667.
[7] ROSENBLUTH, M.N., POST, R.F., Phys. Fluids **8** (1965) 547.
[8] POST, R.F., ROSENBLUTH, M.N., Phys. Fluids **9** (1966) 730.
[9] BALDWIN, D.E., et al., "Loss-cone modes in inhomogeneous mirror machines", Plasma Physics and Controlled Nuclear Fusion Research 1971 (Proc. 4th Int. Conf. Madison, 1971) Vol.2, IAEA, Vienna (1971) 735.
[10] DAVIDSON, R.C., GLADD, N.T., WU, J.D., HUGA, J.D., Phys. Fluids **20** (1977) 301.
[11] BALDWIN, D.E., BERK, H.L., PEARLSTEIN, L.D., Phys. Rev. Lett. **36** (1976) 1051.
[12] BERK, H.L., CORRELL, D.L., GORMEZANO, C., RENSINK, M.E., Nucl. Fusion **18** (1978) 1379.
[13] McNALLY, J.Rand, Jr., Nucl. Fusion **17** (1977) 1273.
[14] IOFFE, M.S., KANAEV, B.I., PASTUKOV, V.P., YUSHMANOV, E.E., Sov. Phys.-JETP **40** (1974) 1064.
[15] KLINKOWSTEIN, R.E., SMULLIN, L.D., Phys. Rev. Lett. **40** (1978) 771.

DISCUSSION

T. SEKIGUCHI: This account of your work gives me a good opportunity to comment on the confinement properties of the high-beta cusp, a subject on which we recently reported (J. Phys. D **11** (1978) 1057). We found experimentally that the size of the (line-) cusp loss aperture for the spindle cusp is very sensitive to the plasma beta value. For this experiment we used a laser-produced high-beta plasma. When beta is higher than about 0.6, the loss aperture size is very near to what we call the "hybrid Larmor radius" – i.e. the geometrical mean of the electron and ion Larmor radii. However, it increases quickly to the ion Larmor radius if the beta drops to about 0.3. Therefore, if we can maintain a higher plasma beta value in the cusp container, we can expect good confinement properties (with a loss aperture an order of magnitude smaller than the ion Larmor radius in the case of a deuterium plasma).

EXPERIMENTAL AND THEORETICAL LINER FUSION STUDIES

D.L. BOOK, R.L. BURTON*, A.L. COOPER,
R.D. FORD, B. HUI**, D.J. JENKINS,
P.C. LIEWER, A.E. ROBSON, P.J. TURCHI
Naval Research Laboratory,
Washington, DC

S. HAMASAKI, N.A. KRALL, L. MASCHERONI,
R. SHANNY
Science Applications, Inc.,
Laboratory for Applied Plasma Studies,
La Jolla, California

E.L. CANTRELL, R.A. GERWIN, I. HENINS,
T.R. JARBOE, R.C. MALONE, J. MARSHALL,
R.W. MOSES, G.A. SAWYER, A.R. SHERWOOD,
B.R. SUYDAM, C.E. SWANNACK
Los Alamos Scientific Laboratory,
Los Alamos, New Mexico,
United States of America

Abstract

EXPERIMENTAL AND THEORETICAL LINER FUSION STUDIES.

The two US facilities currently engaged in imploding liner experimental programmes have adopted contrasting approaches. In both, the liner implosion heats plasma by adiabatic compression. The NRL Linus concept uses a rotationally stabilized thick liquid metal liner hydrodynamically imploded at subsonic speeds, compressing a magnetically confined plasma, then rebounding without loss of integrity. The LASL Fast Liner Experiment employs thin solid-metal liners, electromagnetically imploded at supersonic speeds, compressing a wall-confined ($\beta > 1$) magnetically insulated plasma, with subsequent destruction of the liner. Results of recent experiments, theoretical liner dynamics and plasma physics calculations, and considerations relevant to reactor designs are presented.

---

* JAYCOR, Alexandria, Virginia 22304, USA.

** Science Applications, Inc., McLean, Virginia 22101, USA.

I. SLOW LINERS

In the NRL approach the thick liner serves also as the first wall and blanket surrounding the reacting plasma. Stabilization against Rayleigh-Taylor modes of the liquid liner surfaces is achieved by means of the centrifugal force produced by rotation on the inside and by employing gas-driven pistons on the outside [1]. This means the energy transfer to the plasma is nearly reversible, so that the thermonuclear gain Q required for self-sustaining reactors need only be of order unity.

Early experiments, using up to 32 free cylindrical pistons driven radially by pulsed application of high pressure ($\sim$ 10 atm) helium demonstrated the basic implosion-reexpansion cycle with aqueous liners compressing trapped air in a hydrodynamic model apparatus. Low mode number azimuthal surface asymmetries were observed, however, because of the discreteness of the fluid injection and the lack of mechanical synchronization of the free-piston array [1]. Present experiments employ an annular piston surrounding the implosion chamber and displaced axially to implode the rotating liner. Complete azimuthal symmetry is obtained in this manner, providing excellent implosion quality, as indicated in Fig. 1, which shows a pattern of lines reflected by the liner inner surface during implosion and reexpansion.

With insufficient rotation, the optical quality of the surface is destroyed near minimum radius, indicating the onset of high frequency Rayleigh-Taylor instability (although the overall implosion may appear grossly stable). In Fig. 2, a stability parameter $s = 1 - r\ddot{r}/v^2$, calculated from the free surface trajectory at minimum radius, is plotted versus the radial compression ratio α. Comparison of observed surface quality with the marginal stability line ($s = 0$) indicates excellent correlation of experiment with the theoretical criterion for rotational stabilization [2].

In these experiments, the peak pressures were sufficiently low that the liner behaved as an incompressible fluid. Theoretical calculations of thick liner implosions at pressures of interest in the Linus concept ($\gtrsim$ 10 kbar) indicate that liner compressibility causes energy to be absorbed in material compression and, owing to the finite speed of sound, prevents communication of the energy in the outer regions of the liner to the plasma on the timescale of the turnaround. Both these effects reduce the efficiency ε of energy transfer from the driving source to the plasma. Studies have been carried out with the incompressible model used previously [3], modified to include the effect of finite sound transit time through the use of an "effective liner thickness," which is less than its true thickness. This model permits rapid surveys of parameter space at small dimensionless final pressures $\zeta_f = p_f/\rho c_s^2$, where ρ is the density and c_s the speed of sound in the liner.

In this model the ratio Q of the fusion energy per unit length released in one cycle to the energy E per unit length of the liner is

$$Q = \langle \beta^2 \rangle \varepsilon \, (\rho \varepsilon E)^{\frac{1}{2}} \, G(b^*) \tag{1}$$

where $\langle \beta^2 \rangle$ is the average of β^2 over the plasma cross-section and G is a function of b^*, the effective liner thickness in units of the minimum radius. Since E is obtained from a driving pressure p_d displacing the liner through $\sim \pi R^2$, where R is its initial inner radius, and since ε and b^* are both functions only of $\zeta_d = p_d/\rho c_s^2$ and the radial compression ratio α, we may write

$$Q = \langle \beta^2 \rangle \, R p_d^{\frac{1}{2}} \rho^{\frac{1}{2}} F(\alpha, \zeta_d) \tag{2}$$

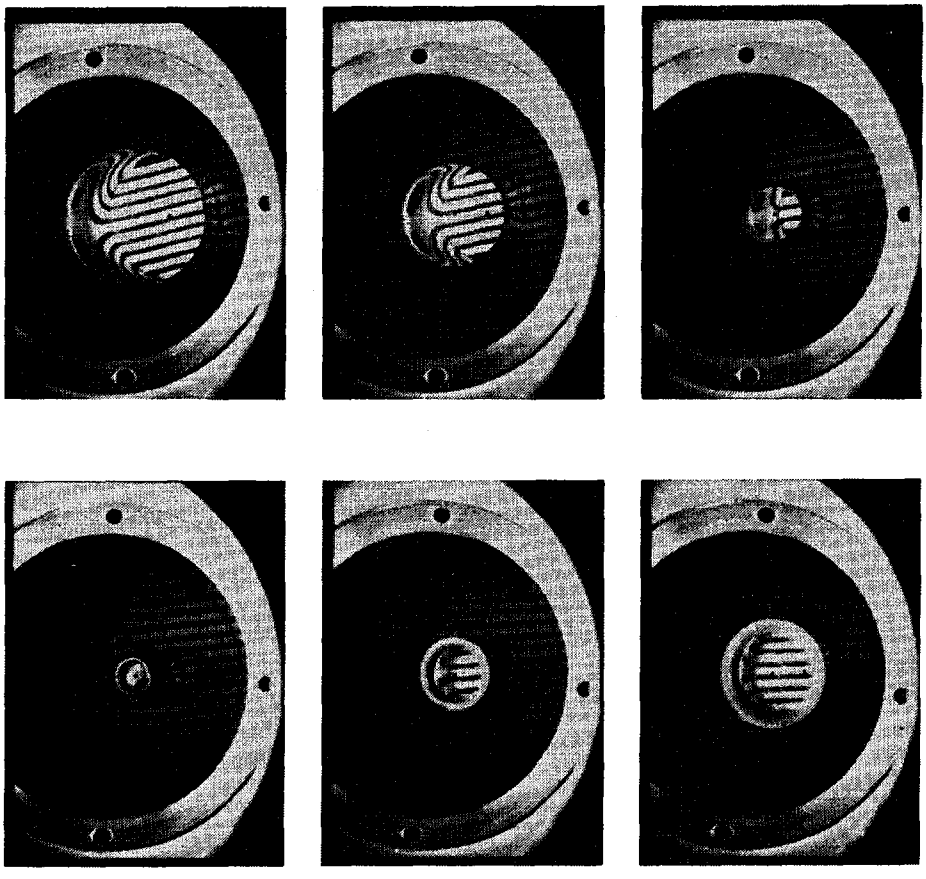


FIG.1. Stabilized implosion driven by annular piston. This sequence was photographed off-axis, showing the fiduciary lines reflected on the left- and (through the liner) right-hand sides of the inner surface.

In Fig. 4 F is plotted as a function of α with ζ_d as parameter. F becomes a sharply decreasing function of these arguments when the effects of compressibility become manifest, and for given R, p_d, and ρ, Q is maximized when the sound transit time through the liner is somewhat shorter than the turnaround time.

The compressible fluid equations have been solved numerically to survey the operation of rotationally stabilized thick imploding liners. Figure 5 shows Q as a function of the dimensionless final pressure $\zeta_f = p_f/\rho c_s^2$, for three different values of the radial compression ratio α_f. While no maximum appears in Q as a function of ζ_f, considerations of the total system size necessary to achieve higher pressures suggest that the optimum value of ζ_f is no higher than about 0.1, which for a lead-lithium liner with c_s = 1600 m/sec corresponds to p_f = 20 kbar.

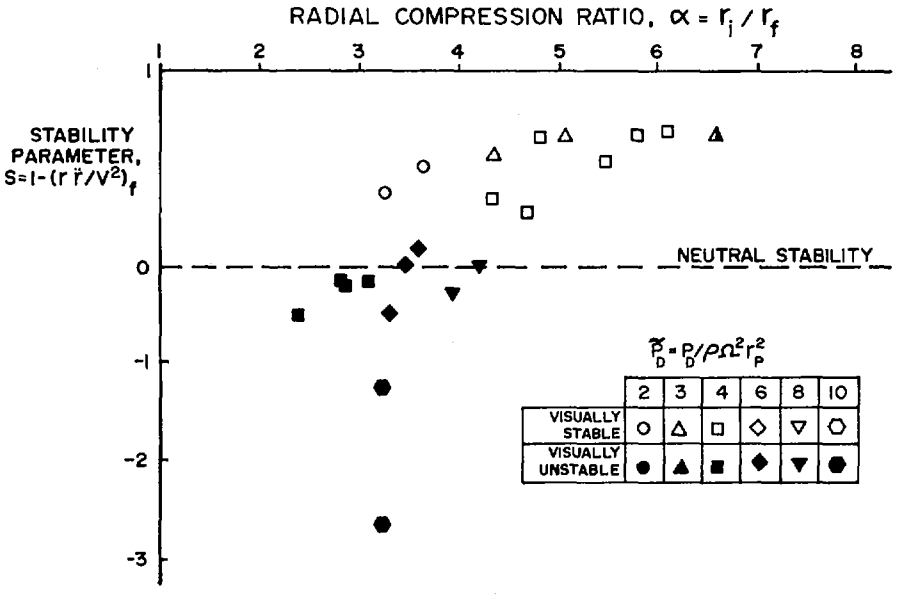


FIG.2. Stability parameter versus radial compression ratio. (Note the scale change at s = 0). $\tilde{P}_D$ is the drive pressure P_D scaled with the water density ρ, the rotation frequency Ω and the annular piston outer radius r_p.

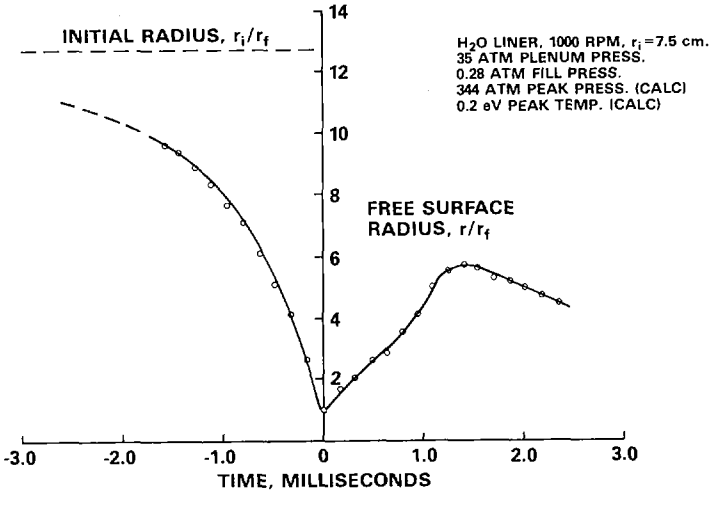


FIG.3. Helius trajectory, showing the reduced free surface radius versus time for a radial compression α = 12.7.

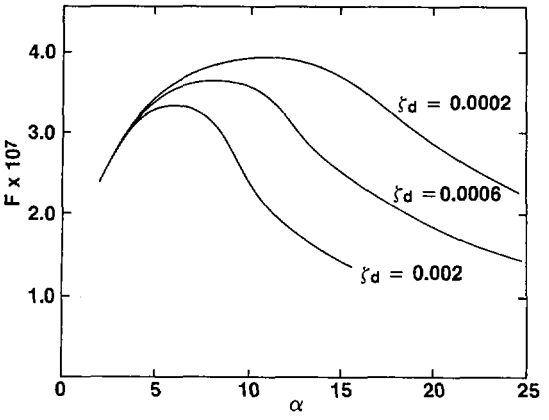


FIG.4. F as a function of α with ζ_d as parameter.

To study the dynamics of thick, compressible liners experimentally, a higher-pressure, slightly larger version of the previously used hydrodynamic model apparatus has been constructed. Called Helius, it has a 150 atm helium gas drive, which displaces an annular piston to implode rotating liners of either water or liquid sodium-potassium alloy (eutectic NaK). Trapped gas is the primary payload, as before, but provision has been made to compress magnetic flux using NaK liners. Fig. 3 shows the trajectory of an imploding rotationally stabilized water liner obtained with the Helius system. The radial compression ratio is 12:1 (initial radius, 7.5 cm) and a peak payload pressure corresponding to $\zeta_f = 0.015$ is attained. The overall implosion quality is similar to that achieved in the lower pressure experiments ($\zeta_f < 0.001$).

The effect of finite viscosity on the implosion dynamics has been shown theoretically to be generally negligible, except in a thin boundary layer at the free surface [4].

The relatively slow liners considered here require that the plasma be contained in a closed magnetic field configuration. Creation of such configurations inside liners using the currents induced by rotating relativistic electron beams is described in another paper [5]. Their compression by liners has been studied by means of a 1D quasi-equilibrium code which includes classical and anomalous transport processes. The latter incorporate drift ion cyclotron and lower-hybrid instabilities with fluctuation amplitudes limited by shear and finite-beta stabilization [6] and nonlinear processes. The average β decreases during compression, and since the fusion reaction rate scales as $<\beta^2>$ the fusion output in one cycle is strongly influenced by the pressure profile in the initial plasma. The principal classical loss, associated with cross-field ion thermal conductivity, sets a lower limit to the initial plasma temperature of several hundred eV, which in turn limits the maximum radial compression ratio to $\sim 10 - 20$.

Two versions of the code (written independently at SAI and NRL) give identical results for adiabatic compression and successfully reproduce the traces of B_θ and B_z measured in the NRL Seebie experiment [5]. The SAI code was used to study transport under conditions like those expected to occur in a Linus reactor, using an MHD equilibrium having an initial radius of 150 cm and plasma-to-total energy ratio $\eta = 0.66$, compressed by a liner with energy of 7×10^5

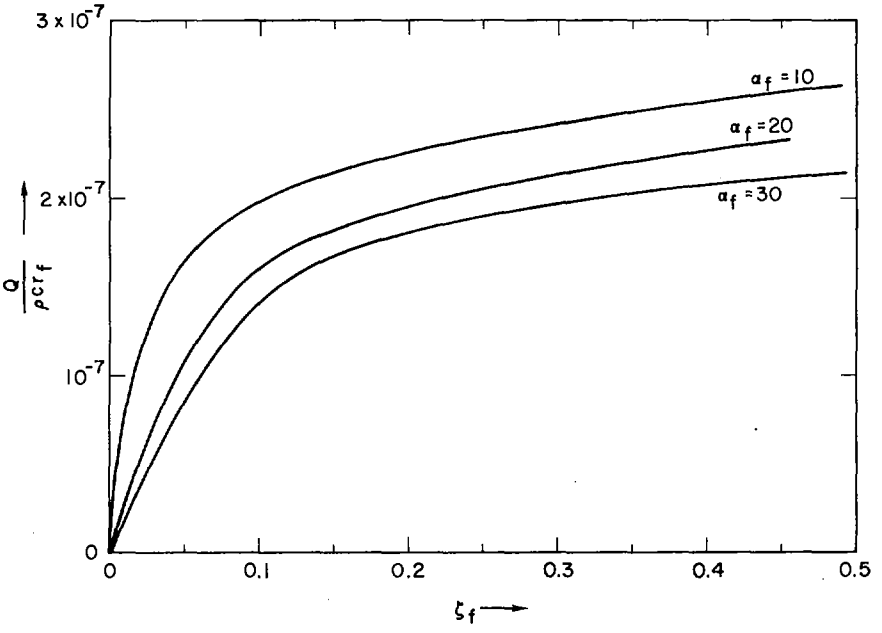


FIG.5. Q, scaled by $\rho c_s r_f$, versus ζ_f with α_f (= α) as parameter.

J/cm and initial velocity $v_L = 5 \times 10^3$ cm/sec, corresponding to an implosion time $t_o = 30$ msec and total compression $\alpha \approx 12$. The initial and final profiles are shown in Fig. 6. In general, anomalous transport effects including the shear and finite-beta cutoffs changed the results very little. Additional conclusions were as follows:

(i) B_θ increases more slowly than B_z, so that in the final state $B_\theta \leq 0.05\, B_z$, i.e., B_θ becomes almost negligible. Transport processes enhance the disparity.

(ii) The energy ratio η always decreases from its initial value to ~ 0.4. Turning on transport enhances the final value by 5-10%. Turning off the finite-beta cutoff on the lower-hybrid-drift modes, however, dramatically increases resistive heating in the center of the plasma, more than doubling peak temperatures.

(iii) The final interior profiles are insensitive to wall temperature, i.e., to whether or not heat is allowed to escape.

(iv) Heat conduction produces a characteristic broad flat-topped profile for both T_e and T_i. Since pressure profiles change only slightly, the density peaks up in the center, becoming up to 30% larger than in the case of adiabatic compression.

(v) Reducing initial radius and liner energy by factors of 5 and 25, respectively, leads to slight enhancement of classical transport effects. With anomalous transport, however, essentially all the heat is lost to the walls.

(vi) A high-field low-density buffer region near the wall is effective as a heat insulator provided the field is sheared there. Thus starting with a

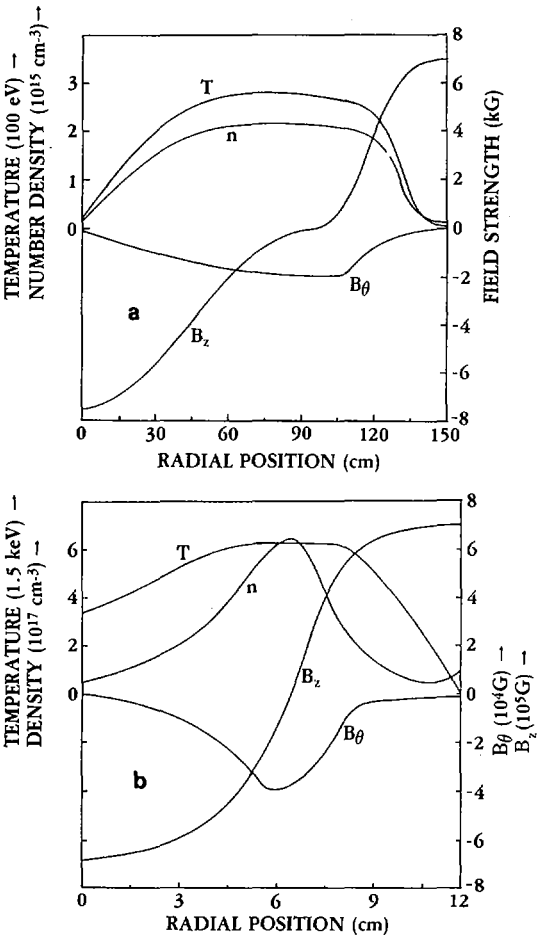


FIG.6. a) Initial profiles for reactor transport studies, showing temperature T, number density n, and magnetic field strength as functions of r; b) Final profiles corresponding to a), showing the effect of 12-fold radial compression with classical and anomalous transport.

flatter temperature and more peaked density leads to little change in η. With flat density and peaked temperature, however, heat flows rapidly to the walls and the density builds up to very large values in the outermost cell.

(vii) Particle and heat diffusion rates calculated from profiles generated by adiabatic compression accurately predict the profile broadening observed in the simulations.

II. FAST LINERS

The LASL Fast Liner Experiment (FLX) is exploring the imploding liner approach to fusion in the 10^6 cm/s liner velocity regime. A thin, cylindrical, metallic liner is driven by a Z-pinch magnetic field. Material end plugs are

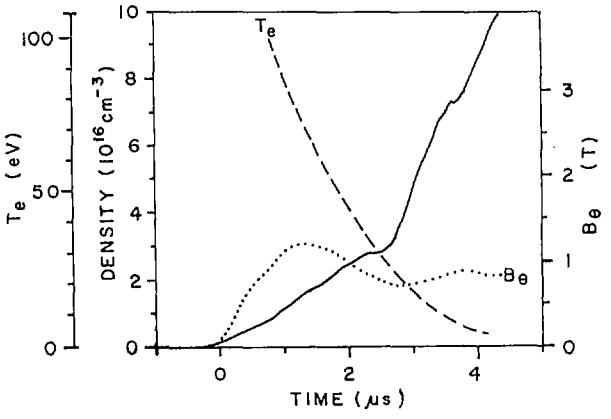


FIG. 7. Plasma temperature, density and magnetic field measured in the simulated FLX "liner" region.

employed. The initial plasma must be warm and dense ($n_o \sim 10^{17} - 10^{18}$ cm^{-3}; $T_o \sim$ 100-500 eV). An embedded magnetic field is required to protect against thermal losses.

Initial liner implosion experiments have been done without plasma on one-fifth of the Scyllac bank (1.75 MJ), with planned future expansion to 3.5 MJ. A typical liner is an aluminum cylinder 10 cm long, 5 cm in diameter, having 1-mm wall thickness. The diagnostics being employed include voltage and current measurements, flux compression, framing camera pictures, and breakable optic fibers.

Separate plasma preparation experiments, based on a coaxial plasma gun approach, have produced a plasma having $T \gtrsim 50$ eV, $B_\theta \gtrsim 10$ kG, and 10^{16} cm$^{-3} \leqslant n \leqslant 10^{18}$ cm^{-3} in an implodable geometry. The plasma is injected into a 9.6-cm-i.d., 10-cm-long cylindrical volume through a 1.3-cm-wide annulus. Implosion of the liner would close the annulus, trapping the plasma. The diagnostics used to measure the plasma properties in the "liner" region are Thomson scattering, quadrature interferometry, and metal-walled magnetic probes. Figure 7 shows the density, temperature, and magnetic field as a function of time for typical conditions. At $t \approx 2$ μs the plasma conditions are within the desired range, but the rate of fall of temperature is considerably faster than simple cross-field conduction would imply, perhaps owing to impurity radiation.

To study the buckling instability of the liner, we follow Abrahamson and Goodier[7] but include the effect of the restoring force of the driving magnetic field, B_θ. Thus the equation of motion for the perturbation of the shell displacement contains the destabilizing hoop stress term, a stabilizing term from the bending moment induced by work hardening, and the stabilizing term from the perturbed magnetic pressure. A sufficient condition for stability of thin shells is

$$\frac{B_\theta^2}{8\pi} > \frac{\sigma}{3\sqrt{6}} \left(\frac{12\sigma}{E_h}\right)^{1/2} \tag{3}$$

where σ is the yield modulus and E_h is the work hardening modulus. This implies stability if B_θ exceeds 125 kG for aluminum and 150 kG for copper.

TABLE I. SIMULATION OF LINER IMPLOSIONS WITH 1/5 SCYLLAC BANK

R_o(cm)	ℓ(cm)	v_{max}(cm/s)	τ_{impl}(μs)	ε_{kin}	ε_{load}	I_{max}(MA)
2	10	0.82	5.4	0.47	0.22	12.0
2.5	10	0.70	6.8	0.51	0.29	13.6
3	10	0.64	8.3	0.50	0.35	15.2
4	10	0.48	12.2	0.42	0.40	17.5
5	10	0.35	17.4	0.33	0.38	19.1
5	5	0.45	14.9	0.26	0.28	20.6

R_o=initial radius, ℓ=length, v_{max}=maximum velocity of liner inner surface, τ_{impl}=implosion time, ε_{kin}=(maximum liner kinetic energy)/W_{CO}, ε_{load}=(maximum energy in plasma load)/W_{CO}, I_{max}=maximum driving current. W_{CO}=initial capacitor bank energy=1.46 MJ.

A parameter study has been made of the performance of the cylindrical liner imploded by a Z-pinch current. The plasma load is modeled as a simple adiabatic fluid. The impulse-momentum theorem first employed by Shearer and Condit [8] and later extended by Gerwin and Malone [9] to include cylindrical convergence is used to treat liner compressibility. It leads to an equation to be solved at each time-step for the liner thickness as a function of the liner inside radius and of the circuit current. Thus, a zero-dimensional model of the process results, with two coupled equations in time, one for the liner inner radius R_i and one for the current. Two of the eight nondimensional parameters required to describe the dynamics prove to be very important for the energy transfer chain. They are an inductance ratio, $p_\ell = \mu_o \ell / 2\pi L_{ex}$, and a ratio of the external circuit time to a natural time of the liner, $p_t = (CV_i/R_i)\sqrt{L_{ex}/\rho_i 2\pi R_i \Delta_i \ell}$. For each value of p_ℓ, there is found to be a best value of p_t in the sense that there is negligible energy left in the bank at peak compression and a maximum in the energy transfer efficiency to the plasma. Transfer efficiencies approaching 50% are calculated with proper adjustment of p_ℓ and p_t. The functional relation between p_ℓ and the best p_t is found to be almost independent of the other parameter values.

The complete specification of Q, the gain, requires three physical parameters in addition to the nondimensional parameters mentioned above. These are the circuit time, the initial plasma temperature, and the initial liner bulk modulus. Q can be maximized by adjustment of the initial pressure and temperature. The former strikes a balance between too much compressive energy in liner material and too stiff a plasma load. The latter regulates the final temperature, T_f, and hence can pick out the peak of the $(\langle \sigma v \rangle / T_f^2)$ curve. A scaling for Q in terms of the bank capacity C exists, with $Q \sim C^{\frac{1}{2}}$ at fixed voltage and fixed initial plasma conditions. Here initial radius, thickness, and wall spacing are all to be varied as $C^{\frac{1}{2}}$.

Separate numerical simulations have been done of liner implosions using one-fifth of the Scyllac capacitor bank. These simulations are based on a model for the liner system which includes one-dimensional magnetohydrodynamics, nonlinear magnetic field diffusion and ohmic heating, and multi-phase descriptions of the liner equation of state and electrical resistivity. The assumed circuit parameters are: bank energy and voltage, 1.46 MJ and 50 kV; circuit resistance and inductance, ~550 μΩ and 4 nH. All liners are aluminum, initially 1 mm thick, and compress a lossless plasma with an initial pressure of

3.2×10^8 dyne/cm^2. The results are summarized in Table I. We find that a 3-cm liner will achieve reasonable high velocity with good transfer efficiencies both to kinetic energy and finally to the load, while maintaining a sizable initial liner volume. The peak in ϵ_{kin} occurs because smaller liners implode too fast leaving energy in the bank, while the high currents associated with larger liners cause excessive losses in the external resistance. The latter effect also causes the decreased efficiency of the ℓ=5 cm liner. All of the liners melt from ohmic heating, but none have time to drop significantly below normal density before the plasma "load" begins to be felt.

A second simulation stresses plasma effects and treats the liner approximately. The liner is described approximately using a simple equation of state. Field diffusion and thermal conduction in the plasma are computed implicitly. A simple analytic model approximates axial thermal conduction to the end plugs. Bremsstrahlung is computed including an approximation of the radiation absorbed by the low temperature plasma near the liner. Numerical modeling of the FLX and a conceptual liner reactor is used to investigate liner scaling and optimize the fusion energy release. With plasma losses, Q scaling differs only slightly from the lossless model; for example, the optimum Q scales approximately as the square root of the liner energy per unit length. The model demonstrates formation of a low temperature, high density, high field plasma sheath near the liner. It is also observed that the initial field and plasma pressures at the plasma surface must be approximately equal for adequate magnetic insulation. For reactor-like parameters Q's of at least 10 can be obtained.

ACKNOWLEDGMENT

This work was supported by the U. S. Office of Naval Research and the U. S. Department of Energy.

REFERENCES

[1] BOOK, D. L., et al., Plasma Physics and Controlled Nuclear Fusion Research (Proc. Conf. Berchtesgaden 1976) Vol. III IAEA, Vienna (1977) 507.

[2] BARCILON, A., BOOK, D. L. and COOPER, A. L., Phys. Fluids 17 (1976) 1707.

[3] BARCILON, A., et al., Plasma Physics and Controlled Nuclear Fusion Research (Proc. Conf. Tokyo 1974) Vol. II IAEA, Vienna (1975) 567.

[4] COOPER, A. L., BOOK, D. L., J. Fluid Mech. (to be published).

[5] ROBERSON, C. W., et al. (Paper IAEA-CN-37/S-5, this conf.).

[6] KRALL, N. A., et al. (Paper IAEA-CN-37/S-3, this conf.).

[7] ABRAHAMSON, G. R., GOODIER, J. N., "Dynamic plastic flow buckling of a cylindrical shell from uniform radial impulse", Fourth U.S. National Congress of Applied Mechanics, Berkeley, CA, June 18, 1962, 939-950.

[8] SHEARER, J. W., CONDIT, W. C., Energy Storage, Compression and Switching, Ed. W. H. Bostick, V. Nardi and O. S. F. Zucker, Plenum Press, New York (1976) 109.

[9] GERWIN, R. A., MALONE, R. C., Phys. Fluids (to be published).

Session U

HIGH BETA II

Chairman

R. TOSCHI
Italy
Papers U-3-1 to U-3-5 were presented
by C. Maisonnier as Rapporteur

EXPERIMENTAL AND THEORETICAL STUDIES OF HIGH-BETA TOKAMAKS*

A. AYDEMIR, C.K. CHU§, G. GEORGIOU, R.A. GROSS,
H.C. LUI, J. MARSEN, T.C. MARSHALL, Z. MUCHA,
G.A. NAVRATIL, P.G. WEBER
Plasma Physics Laboratory, Columbia University,
New York, N.Y.

J. BUSNARDO-NETO**, Y.G. CHEN†, C. CHIN-FATT,
Y.P. CHONG, A.W. DeSILVA††, G.C. GOLDENBAUM,
H.R. GRIEM, R.A. HESS, P.C. LIEWER, R.L. MERLINO,
D.P. MURPHY, A.G. SGRO+
University of Maryland,
College Park, Maryland

R.N. BYRNE,
Science Applications Inc.,
Laboratory for Applied Plasma Studies,
La Jolla, California,
United States of America

Abstract

EXPERIMENTAL AND THEORETICAL STUDIES OF HIGH-BETA TOKAMAKS.

Recent experimental and theoretical results on high-beta pinch tokamaks in the USA are summarized. Heating, confinement and plasma dynamics are reported for Columbia Torus I, Torus II and Maryland Thor. Related theoretical and 2D transport and radiation calculations are presented.

This paper summarizes experimental and theoretical results on: (1) Torus I and Torus II pinch tokamaks at Columbia University, (2) Thor toroidal theta pinch implosion heating and confinement at the University of Maryland, and (3) transport and radiation calculations of high-beta tokamaks performed at Science Applications, Inc.

---

* Research supported by Office of Magnetic Fusion Energy, US Department of Energy.

§ And Science Applications Inc., Lab. for Applied Plasma Studies, La Jolla, California.

** Permanent address: Instituto de Física, UNICAMP, Campinas, S.P., Brazil.

† Present address: Physics International Co., San Leandro, California, USA.

†† On leave at Ecole Polytechnique Fédérale, Lausanne, Switzerland.

+ Los Alamos Scientific Laboratory, Los Alamos, New Mexico, USA.

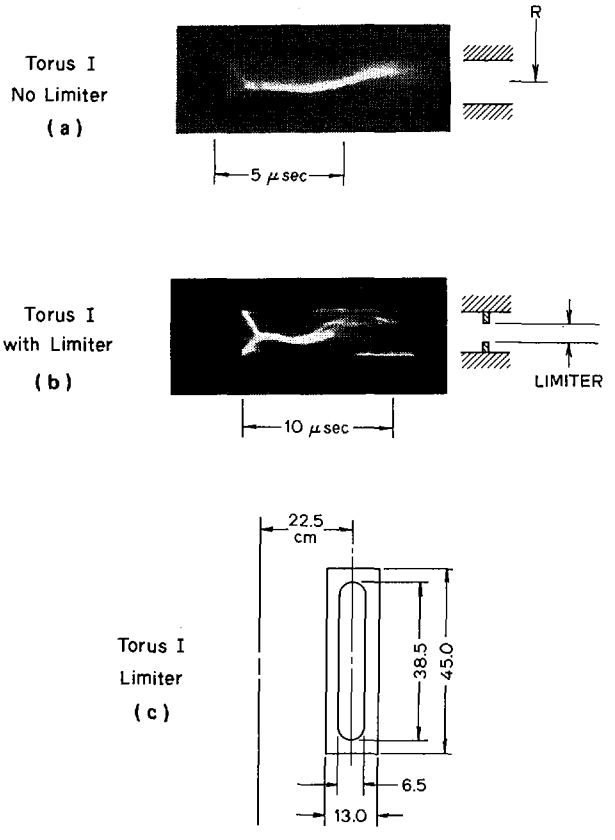


FIG.1. Radial streak photographs of Torus I: (a) without a limiter; (b) with a limiter. (c) Dimensions of Torus I limiter (in cm).

Columbia Torus I and Torus II

Torus I is a glass-wall, rectangular cross-section (b/a = 3) device with major radius R = 22.5 cm, aspect ratio R/a = 3, which operates with toroidal field $B_\varphi \sim 1$ T, and plasma current $I_\varphi \sim 110$ kA. Its description and early performance were previously presented [1]. The hydrogen plasma has a peak density $n(o) \sim 10^{22}$ m^{-3}, a temperature $T_e \sim 10$ eV, a safety factor $q(a) \sim 3$, and a volume averaged beta $\langle\beta\rangle \sim 10\%$.

We have operated Torus I with a Pyrex glass limiter and compared the resulting plasma dynamics with that observed when no limiter was installed. Data have been obtained using radial and vertical streak photographs, a local Rogowski probe, magnetic field mapping probes, and Thomson scattering. The maximum toroidal current density is about 350 A/cm^2. The presence of the limiter has very little effect upon plasma pinch dynamics. The plasma implodes at $\sim$ 3 cm/μsec, becomes well centered, then slowly loses

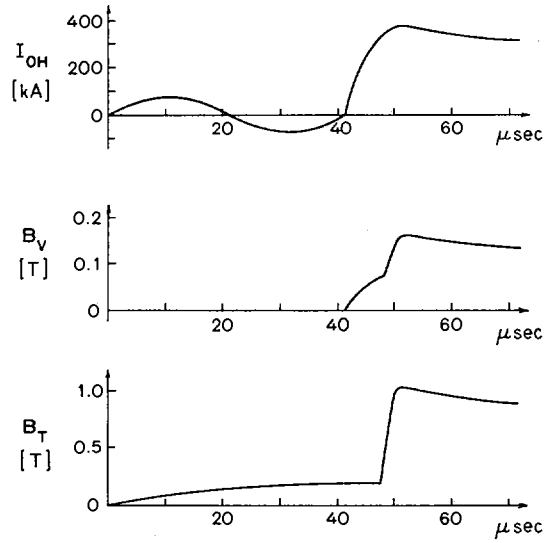


FIG.2. Programmed current and magnetic fields for Torus II. Preionization takes place in the first 40.5 μs, followed by a toroidal Z-pinch (to 44 μs), then fast heating (for 1.7 μs), followed by current crowbar.
I_{OH} = Ohmic heating current in coils; B_V = vacuum vertical field.
B_T = vacuum toroidal field.

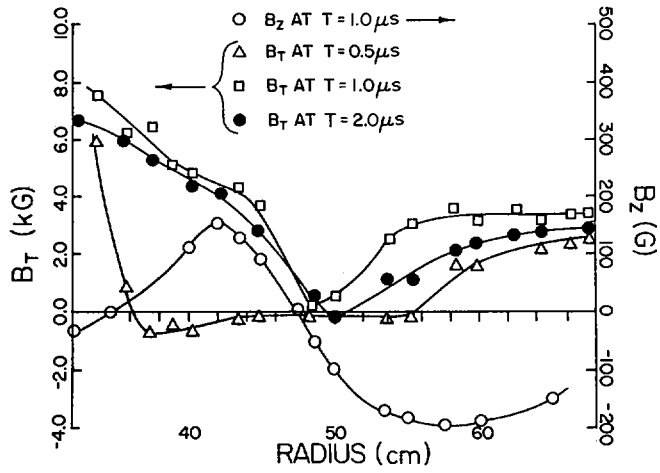


FIG.3. Measured poloidal (B_Z) and toroidal (B_T) fields as a function of major radius in Thor.

equilibrium, and drifts toward the inner wall. At about 8 μsec, depending upon initial conditions [2], the plasma column is observed to form filaments, which we suspect result from a resistive tearing mode instability. Radial streak photographs of Torus I operating with and without a limiter are shown in Figure 1.

Torus II is a new high-beta tokamak, completed in November 1977. It is similar in size and shape (rectangular minor cross-section with b/a = 2) to Torus I, but it has a much higher power heating capacitor bank (5×10^{10} watts) and separate control for all external fields and currents. The purpose of Torus II is to explore the stability of higher-beta hot-plasma tokamak configurations. The glass torus system has a base pressure of 2×10^{-7} Torr. A 9-MHz oscillator is used to provide preliminary ionization. A 16-μf, 30 kV capacitor bank is employed to preionize the gas more completely by inducing a 20-kA current in 10 mTorr of He. An initial toroidal bias field of 0.1T is simultaneously applied, after which an aircore transformer induces a toroidal plasma current. The resulting toroidal Z-pinch is followed by a fast rise-time heating and compression poloidal current pulse which is crowbarred at its peak value of 1.5 MA. The current schedules and magnetic fields are shown in Figure 2. The plasma temperature is expected to be $T > 100$ eV at a density $n(o) \sim 10^{21} m^{-3}$. After heating, the magnetic configuration is a high-beta tokamak [3], with $I_\varphi \sim 80$kA, $B_\varphi \sim 1$T.

Exploratory experiments have been performed at several different powers of the fast heating bank. For parallel operation (i.e. the toroidal field produced by the heating bank is in the same direction as the initial toroidal bias field) at 80 kV on the heating bank, we observe for ~20 μsec what appear to be MHD stable plasmas. At about 20 μsec some filamentary structure is seen. For antiparallel operation at 60 kV on the heating bank, the resulting high-beta tokamak configuration had a low value of $q \sim 1$, and poor stability was observed. Higher power antiparallel configurations, where q may be larger, have not yet been tested. Plasma equilibrium and stability are sensitive to small variations in the heating and vertical field currents. When there is too large a variance between currents of the four heating bank modules, toroidal oscillations of the plasma are observed, which result in loss of equilibrium. At low heating power, magnetic field probe measurements were made and they indicate that the heating pulse does indeed penetrate to the center of the plasma in about 2 μsec.

Theory and computation have been carried out in the following topics: (1) Initial-value, two-dimensional implosion calculations, which are similar in nature to those described in [1], except that improved numerical treatment permits the calculation all the way to equilibrium. (2) Linear initial-value stability calculations were made for diffuse profiles, excluding and including force-free currents. In qualitative agreement with results on sharp boundary profiles [4], force-free currents outside diffuse profiles stabilize external kink modes but, additionally, they stabilize the internal kink modes. In particular, for the first three toroidal modes (n = 1 to 3), force-free current can stabilize an unstable vacuum-boundary plasma, up to volume-averaged toroidal betas ~10%, provided the force-free current density is sufficiently high, i.e. comparable in magnitude to that in the main plasma [5]. (3) anaylsis of induction of force-free currents shows that these currents are changed by the radial motion of the main plasma column. Force-free currents may increase or decay as the main plasma boundary moves, depending on their initial spatial distributions [6].

Maryland Thor

Thor is a high-power [7] ($\lesssim 10^{12}$W), pulsed ($\sim$1 μsec rise time), high-voltage (< 600 kV) toroidal θ-pinch (20 cm minor radius, 50 cm major radius). To achieve an equilibrium, a toroidal current and vertical field are also provided. The main pinch and toroidal currents decay from their peak values with an L/R time of $\sim$30 μsec. The Thor experiment serves two purposes: the investigation of microinstability and other implosion heating mechanisms in the absence of rapid energy losses along open field lines, and the exploration of the compatibility of fast pinch heating with toroidal confinement in the high-beta tokamak regime. Similar experiments have been performed for the belt pinch configuration [8].

Numerical studies of the implosion were made using the cylindrical, 1-D hybrid code (particle ions and fluid electrons) of Sgro and Nielson [9] modified to include anomalous resistivity due to Buneman two-stream, ion acoustic, and lower-hybrid microinstabilities. The code also includes ionization, neutron production and charge exchange. Simulations have also been made using the hybrid code of Hamasaki [10].

All measurements reported here were made using a quartz discharge vessel with fill pressures of $\sim$2 mTorr of D_2. Previously reported measurements [11] were made in an acrylic tube. The main bank voltages were $\sim$ 50%, 65% and 80% of peak design voltage. According to interferometric measurements, the preheating results in an initial electron density of $\sim 2 \times 10^{14}$cm^{-3}, i.e. ionization is virtually complete. After implosion, peak densities approach or exceed 1×10^{15}cm^{-3}, falling by less than a factor of 2 in the first 2 μsec after crowbar. However, the density maximum moves radially outward at $\sim$ 3 cm/μsec to be compared with implosion velocities of $\sim$20 cm/μsec (at half voltage). A quasi-equilibrium is therefore attained, a conclusion which is consistent with the measured toroidal and poloidal fields. These fields are shown in Fig. 3 as functions of probe position along a diameter in the equatorial plane. They agree well with calculated high β equilibria.

Ion temperatures were estimated from neutron yields. They reach $\sim$1, 1.5 and 2 keV at the three discharge voltages. The total number of neutrons produced is about 10^6 per shot. Ion temperatures predicted from the hybrid simulations were 1.5, 2.0, 3.0 keV for maximum magnetic fields of 6, 8 and 9.3 kG with initial densities of about $n \approx 10^{14}$/cc and 0.5, 0.9 and 1.5 keV for the same fields with an initial density of $n \approx 3 \times 10^{14}$/cc. The number of neutrons calculated from the simulation ranges from 0.2×10^6 to 40×10^6, the highest yield being for the low-density, high-field case.

Electron temperatures during the implosion were measured from x-ray emission, using absorber-foil scintillator combinations and Thomson scattering of ruby laser radiation. Spatially resolved x-ray emission measurements show the most energetic x-rays and highest electron energies (8 keV) occur in the sheath region (see Fig. 4) as they also do in the simulations, suggesting the dominant role of Joule heating due to microinstabilities. Absolute x-ray intensity measurements as well as the Thomson scattering suggest the high-temperature sheath electrons diffuse throughout the plasma, resulting in a bi-Maxwellian distribution in the center with the bulk of the electrons at a temperature of about 200 eV, which is consistent with the simulations. Figure 5 shows typical profiles of the simulation runs (here B_T = 8 kG and $n = 1 \times 10^{14}$cm^{-3}) at 1.0 μs. The sheath is narrower in the simulation and there is more compression of the initial magnetic bias field, which may indicate that the experiment is more resistive.

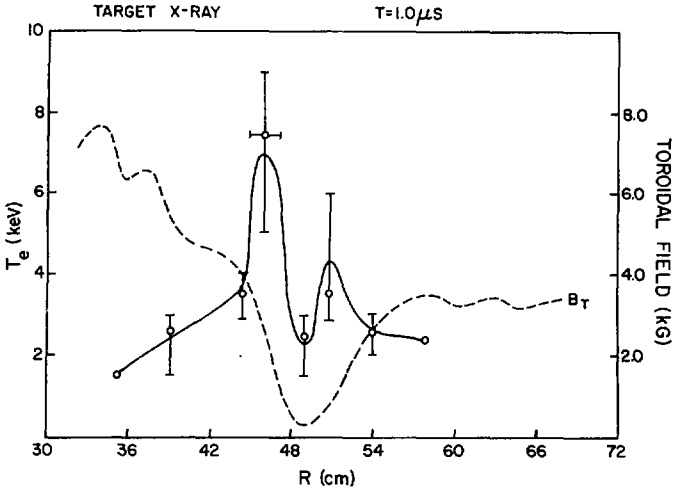


FIG.4. Electron temperature as a function of radius as determined by X-ray emission from a target probe, along with the toroidal field, at 1 μs, in Thor.

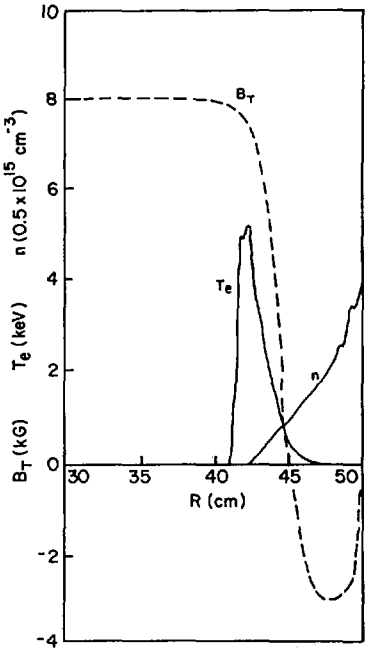
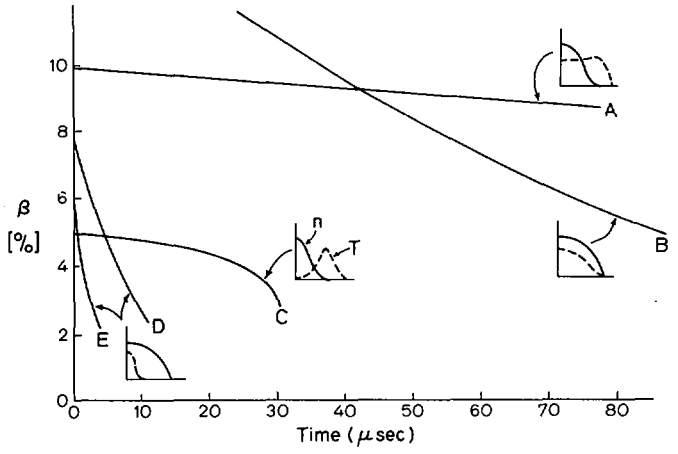


FIG.5. Magnetic field, electron temperature and density profiles from a straight cylindrical hybrid simulation with parameters chosen to match the inner half of the toroidal experiment, Thor.



A: T = 100eV, n = 5×10^{15}, 2% O, FFC,

B: T = 100eV, n = 5×10^{15}, 2% O, parabolic,

C: T = 50eV, n = 5×10^{15}, 2% O, FFC,

D: T = 50eV, n = 5×10^{15}, 2% O, parabolic,

E: T = 20eV, n = 1×10^{16}, $\frac{1}{2}$% O, parabolic,

FIG.6. Summary of the decay of beta with time for different plasma temperatures, impurity concentrations and radial profiles. Initial temperature and density profiles are indicated below the figure. Their evolved shapes are shown in the figure.

Transport and Radiation Studies

Relatively little work has appeared on transport and radiation studies for high-beta tokamaks, with the exception of the work of Becker and Düchs [12] who made a one-dimensional (radial) study of the very slender Garching BP II and BP IIA belt pinches, using measured post-implosion initial profiles and 50eV initial temperature.

We perform similar studies for 2:1 ratio ellipses, using the two-dimensional diffusion code G2M [13]. Torus I and Torus II were used as models, the former representing the general class of cold pinch-tokamaks (∿10 eV), the latter, the class of hot pinch-tokamaks (∿100 eV). There is a qualitative difference between these two classes, due to oxygen impurity radiation which has a large peak power at 20 eV.

We studied profiles in which temperature and density vary parabolically from center to edge, and 'force-free current' profiles, in which the density is peaked near the center while the temperature remains almost flat. For the cold regime, small amounts of oxygen (0.5-2%) cause a nearly uniform drop of temperature throughout the profiles. Typically, a few microseconds (2-10) mark the thermal life of the plasma Power balance shows radiated energy to be the dominant loss mechanism, with ohmic heating, heat conduction and convection smallin comparison. An interesting phenomenon is the paramagnetic distribution of the toroidal field. In previous studies excluding radiation, this phenomenon has never been calculated, although it has been observed [14]. The explanation is quite simple. When energy is convected or conducted from the plasma, the magnetic fluxes are transported analogously. Hence, the plasma remains diamagnetic if initally so. However, when energy is radiated away, the fluxes remain unchanged, and the subsequent compression of the plasma to maintain pressure balance compresses the fields to higher values and hence a paramagnetic distribution appears.

For the hot regime, withtemperatures at 100 eV, the profiles cool slowly and almost uniformly without dramatic effects, at leastto 100 microseconds, for oxygen impurities up to 5%. Power balance shows convected and conducted energies comparable to radiation. For 50 eV, the parabolic profiles show radiation is dominant in the outer regions. The core cools slowly, while the outer regions cool rapidly and "eat into' the core, until the core collapses thermally. For force-free current profiles the outer regions, now at lower density, remain hot, while the center cools by radiation, until thermal collapse occurs. However, the force-free current profiles give much slower rates of decay of β than the parabolic profiles. We summarize in Fig. 6 the decay of beta for plasma temperatures of 20, 50 and 100 eV and for the different profiles sketched.

REFERENCES

[1] CHU, C.K., et al., "Experimental and theoretical studies of belt pinches and high-beta tokamaks", Plasma Physics and Controlled Nuclear Fusion Research 1976 (Proc. 6th Int. Conf. Berchtesgaden, 1976) Vol.1, IAEA, Vienna (1977) 511.
[2] WEBER, P.G., Bull. Am. Phys. Soc. 22 (1977) 13.
[3] MARSHALL, T.C., LUI, H.C., Phys. Fluids 19 (1976) 1417.
[4] D'IPPOLITO, D.A., FREIDBERG, J.P., GOEDBLOED, J.P., REM, J., "Maximizing β in a tokamak with force-free currents", Plasma Physics and Controlled Nuclear Fusion Research 1976 (Proc. 6th Int. Conf. Berchtesgaden, 1976) Vol.1, IAEA, Vienna (1977) 523.
[5] LUI, H.C., Nucl. Fusion 18 (1978) 1365.
[6] LUI, H.C., Nucl. Fusion **19** (1979) 179.
[7] MARKINS, D., et al., in Proc. IEEE Int. Pulsed Power Conf., Lubbock, 1976 (KRISTIANSEN, M., Ed.), IEEE, New York (1977).
[8] SOLDNER, F., Phys. Fluids 21 (1978) 1036.
[9] SGRO, A.G., NIELSON, C.W., Phys. Fluids 19 (1976) 126.
[10] HAMASAKI, S., et al., Phys. Fluids 20 (1977) 65.
[11] CHEN, Y.G., et al., Phys. Rev. Lett 38 (1977) 1400.
[12] BECKER, G., DÜCHS, D.F., Nucl. Fusion 16 (1976) 763.
[13] BYRNE, R.N., KLEIN, H.H., J. Comput. Phys. 26 (1978) 352.
[14] ALLEN, A.W., et al., Phys. Rev. Lett 39 (1977) 404.

DISCUSSION

G. BECKER: What oxygen impurity profile was assumed in the calculations of radiation losses?

R.A. GROSS: The initial percentage of oxygen impurity was taken as constant, independent of radius.

CLASSICAL TRANSPORT IN BELT-PINCH IIa

G. BECKER, O. GRUBER, H. KRAUSE, F. MAST,
R. WILHELM
Max-Planck-Institut für Plasmaphysik,
EURATOM Association,
Garching,
Federal Republic of Germany

Abstract

CLASSICAL TRANSPORT IN BELT-PINCH IIa.

In the Garching Belt-Pinch IIa toroidal high-β plasmas with strongly non-circular plasma cross-sections are produced. These plasmas lose their energy mainly through impurity line radiation in about 65 μs. Simulations of these discharges with the Garching high-beta transport code show that the calculated density profile and the toroidal magnetic field strength on axis in later phases of the discharge depend sensitively on the cross-field electrical resistivity used. By comparing calculated and measured density profiles, deviations from the classical coefficients by more than a factor of 5 can be excluded. In a similar manner it is demonstrated that ion heat conduction cannot be more than 10 times classical whereas electron heat conduction is less than 200 times classical. It is concluded that particle, field and energy transport is roughly classical in Belt-Pinch IIa.

1.) Introduction

In recent years attention in tokamak physics has focused on plasma confinement and its dependence on different parameters. Among these parameters the beta value of the plasma is of considerable interest in view of the possible reactor applications of the tokamak concept. In particular, recent theoretical results indicate that MHD modes will be driven unstable already at small ß-values thus probably causing enhanced losses or even complete destruction of the confinement.

The range of ß-values where these modes might become significant (above a few per cent) is not accessible by tokamaks, at present, due to the lack of sufficient heating power. Therefore, belt-pinches which produce toroidal high-ß plasmas can supplement valuable information on high-ß plasma confinement /1/.

In the Garching Belt-Pinch IIa effects like electron or ion heat conduction, particle and field diffusion are normally masked by the dominance of impurity line radiation losses and resulting plasma convection /1,2/. Recently, however, it was possible to reduce the impurity content of the plasma by nearly an order of magnitude, lowering thus the dominance of losses due to impurities accordingly. In addition, detailed measurements of temperature and density profiles have been carried out /3,4/ which can be compared with simulations by the Garching high-beta transport code /5/. On this basis it is possible now to draw conclusions on particle, magnetic field and energy transport. Furthermore, in this paper results of simulation experiments with artificially enhanced classical transport coefficients are presented which show the sensitivity of profiles to the various enhancement factors.

TABLE I. PLASMA PARAMETERS FOR END OF DYNAMIC PHASE

10 μs	70 μs
kT_{io} = 75 eV	kT_{io} = 13 eV
kT_{eo} = 15 eV	kT_{eo} = 12 eV
n_{eo} = $4 \cdot 10^{14}$ cm^{-3}	n_{eo} = $7 \cdot 10^{14}$ cm^{-3}
$\langle ß \rangle$ = 0.6	$\langle ß \rangle$ = 0.2
$\langle ß_p \rangle$ = 4.0	$\langle ß_p \rangle$ = 1.5
2a = 20 cm	2a = 30 cm
2b = 220 cm	2b = 176 cm
R_p = 50 cm	R_p = 50 cm
q_b = 4.9	q_b = 5.2
q_o = 2.0	q_o = 2.0

The following definitions have been used:

$$\langle \beta \rangle = 8\pi \langle p \rangle / (\overline{B_t^2} + \overline{B_p^2})$$

$$\langle \beta_p \rangle = 8\pi \langle p \rangle / \overline{B_p^2}$$

$$q = \int \frac{B_t \, dl_p}{B_p \, 2\pi R}$$

2.) Experimental Set-up and Plasma Parameters

The Belt-Pinch IIa produces high-ß plasmas by shock heating in a toroidal coil system with a strongly elongated rectangular cross-section. The device has been described previously /1/. The essential parameters are: coil height 260 cm, inner coil radius 29 cm, outer coil radius 81 cm, toroidal magnetic field at R = 50 cm 1.05 kG, and toroidal plasma current 100 - 200 kA.

In the chosen standard discharge (shock voltage 120 kV, filling density 2 mTorr deuterium) the impurity content is 0.4% oxygen and 0.6% carbon normalized to the electron density. It was determined spectroscopically by adding small amounts of impurities. Plasma parameters for the end of the dynamic phase at 10 μs and at 70 μs are given in Table I.

The averages denoted by $\langle\ \rangle$ and $\overline{\ }$ are carried out over the plasma cross-section and the poloidal circumference (L_p) at the plasma surface, respectively. p is the plasma pressure, B_t and B_p are the toroidal and poloidal magnetic fields, R_p is the radius of the plasma centre, 2a and 2b are the width and the height of the pressure profile. The ß and q-values are taken from measurements of the toroidal diamagnetic flux, of the radial magnetic field profiles and of the poloidal fields outside the discharge vessel and from calculations using a free boundary equilibrium code (see Fig. 1). Indices o and b refer to the magnetic axis and the plasma boundary, respectively.

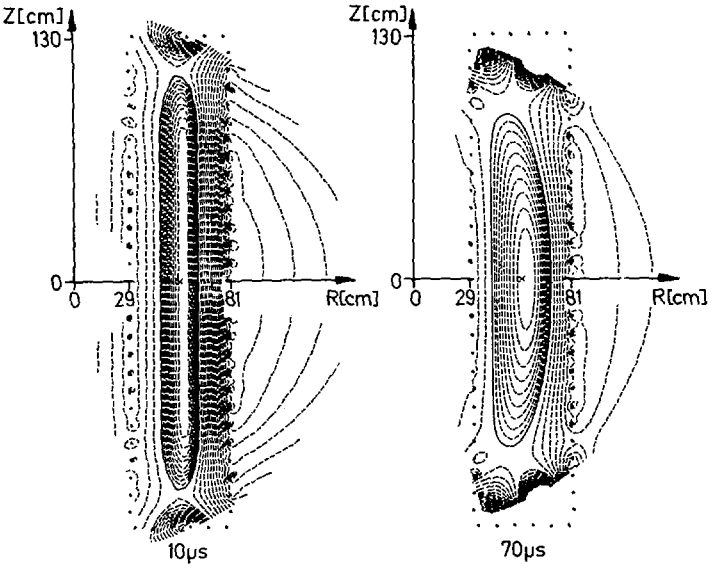


FIG.1. Flux surface plots of Belt-Pinch IIa equilibria.

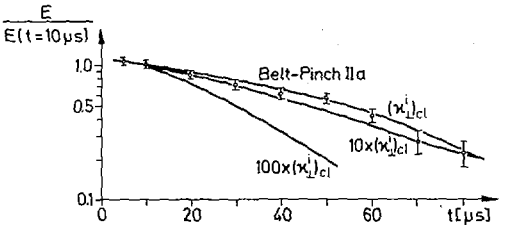


FIG.2. Time behaviour of measured and simulated total plasma energy.

The electron temperature has been measured by 90° Thomson scattering, the electron density by Thomson scattering and 3.4 μ Ashby interferometry, and the magnetic fields by internal and external probes. The ion temperature has been determined from the pressure balance. The time behaviour of the plasma energy (given in Fig. 2) was inferred from the measured diamagnetic flux taking into account the pressure contribution of the poloidal magnetic field. As a consequence of higher temperatures and reduced impurity level an evident prolongation of the energy decay time ($\tau_{1/e} = 65\mu s$) was achieved compared with BP II ($\tau_{1/e} = 20\mu s$) and the first experiments in BP IIa ($\tau_{1/e} = 35\mu s$) /2/. $\tau_{1/e}$ exceeds the energy confinement time by less than 20%.

3.) Extended Garching High-Beta Transport Code

Due to the better knowledge of the time behaviour of equilibria and profiles of densities, temperatures, magnetic fields and impurity concentrations /3,4/ it is now possible to

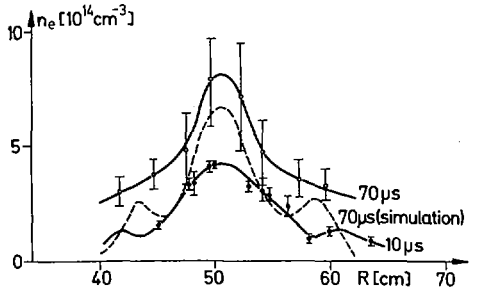


FIG.3. Time development of radial electron density profiles in the torus midplane.

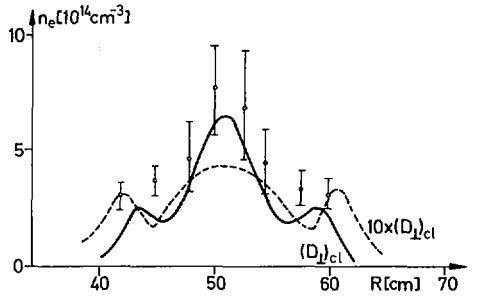


FIG.4. Comparison of measured and computed electron density profiles at 70 μs.

draw conclusions on the particle, field and energy transport in Belt-Pinch IIa. The experimental results are analyzed by an extended version of the Garching high-beta transport code /5/ and compared with predictions of simulation experiments.

The code is based on a multi-fluid model and takes into account all transport processes relevant on the diffusion time scale including high-beta effects, light impurities and neutral hydrogen. The use of classical transport coefficients is justified by the transport theory for non-circular cross-section and high-beta plasmas in the Pfirsch-Schlüter regime /6,7/. For half-axes ratios $b/a \gtrsim 5$ and $q_b \lesssim 5$ in Belt-Pinch IIa, the Pfirsch-Schlüter corrections are small, so that the experimental situation is well approximated by a transport code with classical coefficients in cylindrical slab geometry ($b/a \rightarrow \infty$).

In the extended version of the code a carbon impurity routine has been implemented in addition to the oxygen routine. As the compression of the impurity profiles $n_{imp}(r, t)$ caused by radiation losses is faster than classical diffusion in the belt-pinch, a variation of $n_{imp}(r,t)$ proportional to $n_e(r,t)$ has been included in the model. In addition to the global power balance, one can study now also radially resolved power flows. Moreover, the new program takes into account the anisotropy of the electrical conductivity and is able to simulate transport with artificially enhanced classical coefficients.

4.) Particle and Field Transport

Particle transport has been investigated by comparing computed electron density profiles and line densities with time-resolved measurements. The two side maxima on the electron density profiles at 10 μs (see Fig. 3) predicted by the simulations have been found in the experiments. Radial positions and time of occurrence in the simulations are consistent with the experimental data set. The side maxima are the consequence of a sensitive balance between plasma flow and neutral hydrogen ionization. Since we have found a sufficiently good agreement in the compression of the density near the axis (see Fig.3) and in the plasma line density, the model assumption of classical diffusion has been confirmed. There are indications that the somewhat weaker compression of the central plasma in the simulations is to be ascribed to the one-dimensionality of the model. Possible side maxima at 70 μs cannot be resolved experimentally. The measured larger density in the wings compared with the computed one at 70 μs is caused by an axial contraction in the experiment, which has not been included in the transport code and which is due to a rearrangement of the flux surface structure in the course of the discharge shown in Fig. 1 . These equilibria have been computed by fitting the measured plasma parameters and magnetic fields /3/. As can be seen, the cross-sectional area of the plasma remains unchanged, whereas there is a compression of roughly a factor of 2 in the central region, which results from strong impurity radiation losses localized there. The peripheral expansion associated with this central compression has been found in the simulation experiments, too.

At present, there exists no sufficiently developed theory which can serve as a basis for anomalous transport in high-beta plasmas, so that self-consistent calculations with anomalously enhanced transport coefficients cannot be carried out. But the sensitivity of the simulation with respect to an enhancement of a single transport coefficient, as for instance, the cross-field resistivity $\eta_\perp$ or the heat conductivities for electrons $\kappa_\perp^e$ and ions $\kappa_\perp^i$ can be studied. A homogeneous enhancement of the classical $\eta_\perp$ by a factor of ten, which corresponds to a ten times larger diffusion, results in a flat n_e -profile (see Fig. 4) and no central density compression. By varying the enhancement factor it is found that a diffusion of more than about five times the classical one can be excluded. It is concluded that there exists near classical particle confinement in Belt-Pinch IIa and that the neoclassical transport theory /6,7/ has been confirmed by the experiment.

The cross-field diffusion coefficient is proportional to $\eta_\perp$ in classical theory, which determines magnetic field diffusion. One would thus also expect only small deviations from classical field diffusion. This point was investigated by comparing simulations with the internal toroidal magnetic field of the two-dimensional equilibria. The result is that the time development of the toroidal field can be explained by the above discussed compression and by classical field diffusion. We conclude that in the electron temperature range of 10 to 30 eV of Belt-Pinch IIa $\eta_\perp$ is roughly classical.

5.) Energy Transport

In spite of the reduced impurity level the global energy balance in the present experiments is dominated by impurity ionization and radiation losses. Computed global power losses caused by conductive and convective heat transport of ions and electrons are two and three orders of magnitude smaller, respectively. Moreover, the simulations have shown that the total loss due to neutral deuterium is about 10% of the impurity losses. By comparing predictions of impurity subprograms /8/, which have been used so far in simulations of tokamak impurity losses, with measurements on the Garching belt-pinches,

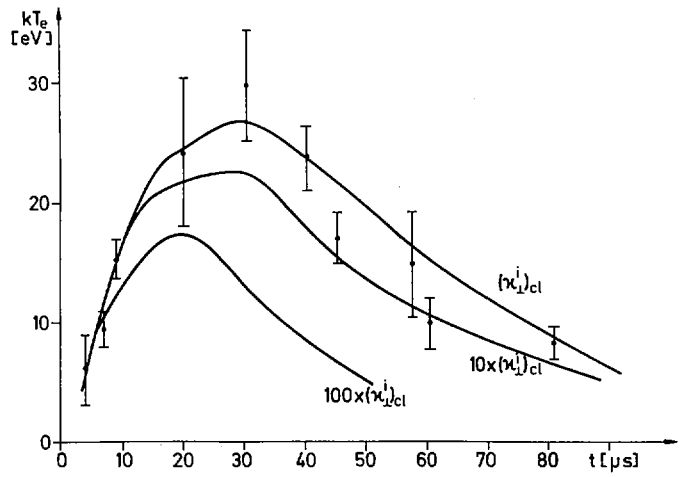


FIG. 5. Comparison of measured and calculated central electron temperatures as functions of time.

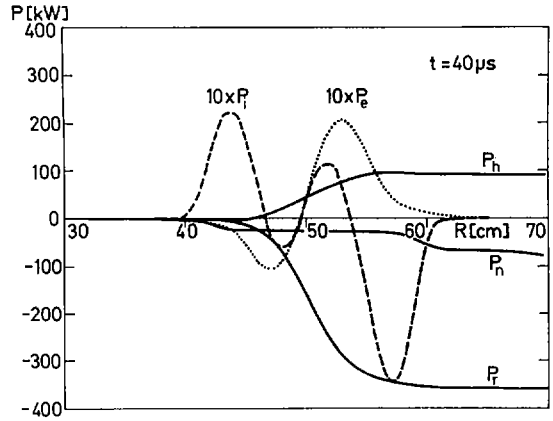


FIG. 6. Computed local power balance. P denotes integrals over power densities between the inner vessel wall and the major radius R and over 1 cm height.

it turned out that correction factors enhancing the line radiation losses must be applied. In order to obtain the measured electron temperature on axis (see Fig. 5) and the experimental energy decay (see Fig. 2), the line radiation losses in the oxygen and carbon subroutines have to be corrected by factors 4.3 ± 0.8 and 1.8 ± 0.2, respectively. These gauge factors have been evaluated by adding oxygen and carbon in the experiments and by simulating these cases. They hold for $T_e < 25$ eV and represent space and time averages over density, electron temperature and various ionization stages. In the meantime oxygen and carbon subprograms more adequate for this low temperature range have been developed on the basis of more resonant lines with more reliable oscillator strengths and effective gaunt factors /9/. These modules are able to describe the experiments without demanding for correction factors.

In Fig. 6 the radially resolved power balance for t = 40 μs is shown. The heating and loss powers given represent integrals between the radius of the inner vessel wall and the radius R and over 1 cm height. Values at R = 70 cm thus correspond to 1 cm height of the whole discharge and are called global. P_r represents the sum of losses due to ionization, recombination radiation and line radiation of oxygen and carbon and of the total bremsstrahlung. P_h is the total loss caused by neutral deuterium due to ionization, line radiation, heat conduction and convection. P_e and P_i include both thermal convection associated with the particle flow and the thermal conduction by electrons and ions, respectively. In the heating power P_h compressional heating and ohmic heating by toroidal and poloidal currents are combined. Obviously, the global energy balance is dominated by the impurity losses, which are mainly caused by line radiation, and the loss due to neutrals is roughly compensated by P_h. It can be seen that strong impurity losses occur around the plasma centre (slope of P_r-profile) and that for the present T_e-profiles the impurity loss power per cm^3 is peaked close to the magnetic axis. Hollow profiles of loss power density will occur for larger T_e-values, due to the ionization of OVI to the helium-like state. These temperatures are not accessible in these experiments.
Note that P_h shows the same radial distribution as P_r. The reason for this is that the largest contribution to P_h comes from compressional heating which increases with larger impurity losses P_r /10 /. It is interesting that the strong compression in the center is accompanied by an expansion and cooling in the outer plasma region (negative P_h near R = 43 cm and decreasing P_h near R = 59 cm). Fig. 6 also demonstrates that the main losses from neutrals occur near R = 42 and R = 59 cm, where the neutral deuterium strongly interacts with the plasma and where the side maxima of n_e occur. The changes of sign in P_e and P_i are due to the superposition of heat conduction and convection and due to the hollow T_e-profile. Although the heat flows caused by electrons and ions do not play any role at all in the global energy balance, they are both locally important.

Of course, classical heat conduction and convection is suggested by the lack of anomalities in the particle transport. Simulation experiments with various enhancement factors in front of the classical heat conduction coefficients for electrons $\kappa_\perp^e$ and ions $\kappa_\perp^i$ have been carried out. They have shown that significant deviations from the experiment occur above 10 times $(\kappa_\perp^e)_{cl}$ or above 200 times $(\kappa_\perp^e)_{cl}$. The effect of enhancing $(\kappa_\perp^i)_{cl}$ is documented in Figs. 2 and 5. Obviously, an enhancement factor of 100 yields totally incompatible results. We conclude from these arguments that classical energy confinement is present in Belt-Pinch IIa.

6.) Conclusions

Due to reduced impurity line radiation losses and measurements of profiles of plasma parameters it was possible to investigate particle and heat diffusion on Belt-Pinch IIa discharges. This was accomplished by comparing measured profiles with results from a transport code using classical or artificially enhanced transport coefficients.

The results can be summarized as follows:
The best agreement between experiment and code simulations is obtained with classical coefficients. Significant deviations between measured and computed data occur for particle and magnetic field diffusion stronger than about five times and ion heat conduction about ten times the classical value. Electron heat conduction plays a minor role in the belt-pinch so that the anomality factor can be set to less than about 200 only.

We therefore conclude that particle and energy confinement are about classical in the Belt-Pinch IIa. The transport coefficients in the Pfirsch-Schlüter regime for the strongly

elongated cross-sections of the belt-pinch are practically identical to the classical values. From these findings it follows that possible MHD instabilities and microinstabilities do not influence the confinement noticeably.

References

/1/ O. Gruber, R. Wilhelm, Nuclear Fusion 16, 243 (1976).

/2/ O. Gruber, F. Mast, H. Krause, R. Wilhelm, Proc. 6th Int.Conf. on Plasma Phys. and Contr.Nucl.Fusion Research, IAEA, Vienna (1977), Vol.I , p. 311.

/3/ G.Becker, O.Gruber, H.Krause, F.Mast, R.Wilhelm, 8th Europ.Conf.on Contr. Fusion and Plasma Phys., Prague (1977), Vol.I, p. 76 and Vol.II, p. 235.

/4/ G.Becker, O. Gruber, H.Krause, F.Mast, R.Wilhelm (to be published).

/5/ G.Becker, D.F. Düchs, Nuclear Fusion 16, 763 (1976).

/6/ E.K. Maschke, Plasma Physics 13, 905 (1971),
E.K. Maschke, Plasma Physics 14, 141 (1972).

/7/ J.B. McBride et al., Nuclear Fusion 15, 1099 (1975).

/8/ D.Düchs, H.Griem, Phys.Fluids 9, 1099 (1976).

/9/ G.Becker, O.Gruber (to be published).

/10/ G. Becker (to be published).

DISCUSSION

C.K. CHU: Is the motion of the impurities calculated self-consistently? What is the reason for the side density maxima, and are they dependent on the wall boundary conditions?

G. BECKER: The motion of impurities together with the hydrogen plasma is taken into account. Neoclassical diffusion of impurities has been neglected, since it is small compared with convection.

The side maxima of the density develop as a result of a balance between the ionization rate of neutral hydrogen and the plasma flow. They occur if the neutral-hydrogen background is sufficiently large, but they are rather insensitive to the rate of influx of neutrals at the walls.

RECENT PROGRESS IN 1-MJ PLASMA FOCUS DYNAMICS AND SCALING FOR NEUTRON PRODUCTION

C. GOURLAN, H. KROEGLER, C. MAISONNIER,
J.P. RAGER, B.V. ROBOUCH, A. GENTILINI*
Associazione Euratom-CNEN sulla Fusione,
Centro di Frascati, Rome,
Italy

Abstract

RECENT PROGRESS IN 1-MJ PLASMA FOCUS DYNAMICS AND SCALING FOR NEUTRON PRODUCTION.

Experimental observations carried out on two different types of electrode design on the breakdown phase, the rundown phase and the neutron production phase reveal the existence of several working schemes for the long time-scale phases and the possible existence of several neutron-production mechanisms. They stress the necessity of developing improved scaling laws based on more realistic physical models for the design of large-energy plasma focus devices.

1. INTRODUCTION

The scaling of a plasma focus device to high-energy level ($E_0 > 150$ kJ) has met with unexpected difficulties. They are due, to a large extent, to an improper or irrelevant physical modelling of the different phases of the experiment working scheme (commonly termed breakdown and sheath buildup, rundown, implosion and neutron production phases). The plasma focus efforts today are directed along two main lines of research:

(a) Understanding the long time-scale dynamics (from breakdown to pinch time), linked to the necessity of developing realistic scaling laws for the design of large-energy devices and evaluating their range of applicability;

(b) Understanding the short time-scale dynamics, including the intense anomalous effect accompanying neutron production and, more recently, the very late phase of the implosion.

* Guest researcher.

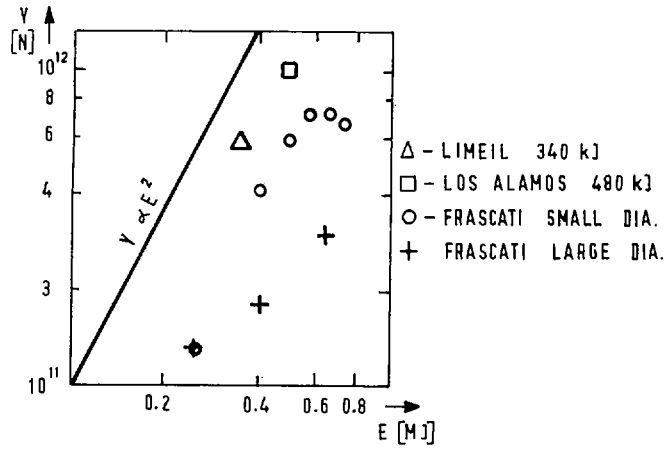


FIG.1. Scaling of neutron yield versus initial energy E_0 for a number of large-energy plasma focus devices.

The effort that aimed at maximizing the neutron yield of the Frascati 1 MJ – 40 kV (max. rating) plasma focus device, has led to two families of electrode geometries:

(i) The large-diameter system (anode dia. 370 mm) optimized at 250 kJ ($> 10^{11}$ neutrons per shot). For this geometry it has not been possible to obtain regular working regimes at higher energies.

(ii) The small-diameter system (anode dia. 160 mm) for which the range of energy within which a regular neutron yield scaling is observed is more extended (250 – 500 kJ, with respective neutron yields of 1.2 and 6 X 10^{11} neutrons per shot).

In Ref. [1] we show that in the former case there is a steady current derivation along the insulator which accounts for the limited neutron yield obtained so far. This result has since been confirmed by independent measurements (see Section 2).

Such a mechanism is not, however, the dominant cause of the discontinuation of the favourable scaling of the neutron yield (Fig.1), observed when the stored initial energy reaches values beyond 250 kJ for large diameter and 500 kJ for small diameter. This phenomenon is accompanied by characteristic changes in many properties of both long and short time-scale phases, reported in Section 3.

Systematic measurements of the neutron energy spectra using two independent methods, carried out on both geometries, show the existence of definite differences in the spectral shape and energy width, giving evidence of the existence of different neutron production mechanisms.

In the light of these results, the relevance of a number of matching rules between source and load parameters is critically discussed.

2. CURRENT SHEATH DYNAMICS AND INSULATOR PROPERTIES

The existence of a steady current loss along the insulator, documented in Refs [1] and [2], has since been confirmed by independent measurements. Figure 2 shows the current wave forms in one particular bar of the squirrel-cage type cathode of the large-diameter system at two different longitudinal positions: 75 mm (in front of the insulator) and 300 mm (total gun length is 350 mm in that case) as measured by small calibrated Rogowski coils.

Up to the time, $t = t_2$, at which the current sheath starts its radial implosion, it is demonstrated within experimental errors (less than 100 kA out of 2 MA) that, in the working regime optimized for neutron production, the current I_p flowing in the moving sheath is equal to the current flowing in the cathode at the bottom of the gun (shot-to-shot reproducibility is extremely good). Moreover, the inductance of the gun deduced from local magnetic field measurements (L_p) is equal to the value L_g deduced from the geometrical dimensions of the gun, including the skin depth in the stainless-steel electrodes.

2.1. Insulator properties

Detailed probe and Rogowski measurements are not available to analyse all possible working regimes. To determine the parametric dependence of the apparent insulator resistance R_i corresponding to the current leak we assume that:

(a) The resistance R_p of the plasma sheath is negligible up to $t = t_2$,

$$\int_0^{t_2} R_p I_p \, dt \ll L_p I_p(t_2)$$

(b) The gun inductance at $t = t_2$ is given by L_g.

Under these approximations,

$$I_p(t_2) \sim \int_0^{t_2} \frac{u_i dt}{L_g}$$

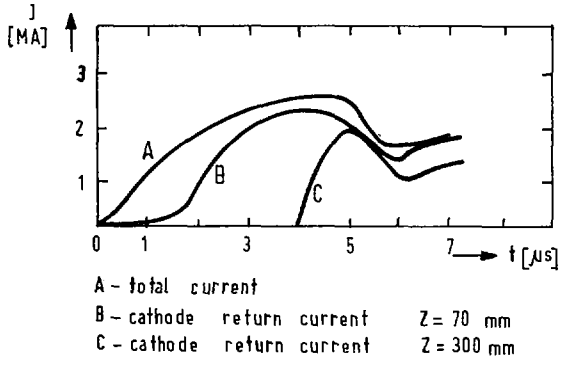


FIG.2. Total current compared with current flowing in the cathode at two different longitudinal positions (large-diameter short-length plasma focus, $V_0 = 20$ kV, $p_0 = 1.2$ torr D_2).

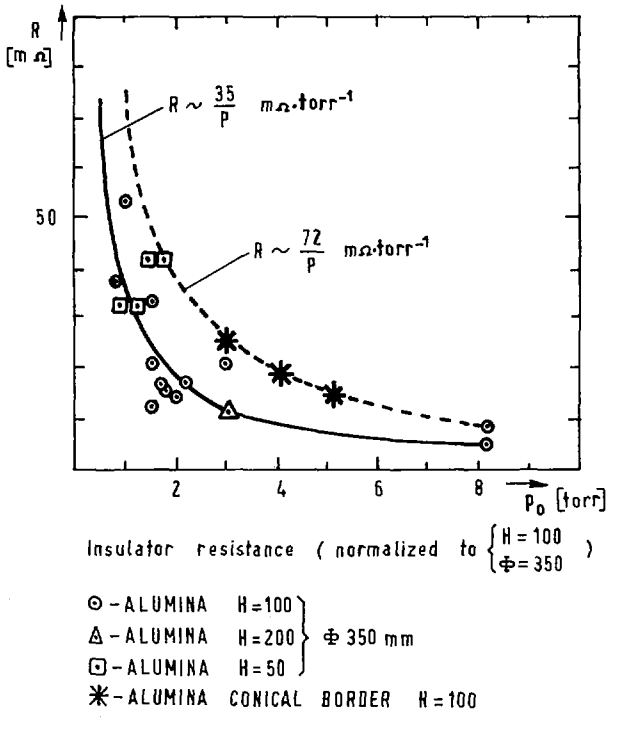


FIG.3. Insulator resistance versus filling pressure (p_0) for a 99.4% pure alumina cylinder.

where u_i is the voltage across the insulator. This allows an evaluation of an upper limit to R_i, as

$$R_i(t_2) = \frac{u_i(t_2)}{I_t(t_2) - I_p(t_2)}$$

where I_t is the total current.

It was checked, when local electrical measurements were available, that the real value of insulator resistance weakly depends upon time but remains within 10% of the mean approximate value R_i. For a 99.4% pure alumina insulator the results are (Fig.3):

(i) R_j does not depend upon the total current (and hence the local magnetic field) but only on filling pressure p_0,

$$R_i \propto p_0^{-1}$$

(ii) R_i scales linearly with insulator length (three different lengths were considered: 50, 100 and 200 mm).

Magnetic probe measurements carried out on a small-diameter plasma focus have shown that the resistivity of the current path depends on the shaping of the insulator edge near the anode, while the p_0^{-1} dependence is apparently conserved.

For a Pyrex insulator, the resistance is equal to that found with alumina at 1.5 torr D_2 and seems to be insensitive to pressure changes.

3. LIMITATIONS IN NEUTRON SCALING

It is shown in Ref. [3] that the neutron yield of plasma focus facilities scales as the fourth power of the current actually flowing in the plasma at pinch time. This scaling covers a wide range of experimental setups, from the 12-kJ Stuttgart Mini Fokus experiment to the large-energy Frascati setup working at 400 kJ. However, attempts to operate the Frascati facility at energy levels in excess of 250 kJ for the large-diameter and 500 kJ for the small-diameter electrodes system do not much increase the neutron yield (Fig.1), despite the direct observation made in some cases that a large plasma current was actually flowing in the experiment. This saturation in scaling occurs at an energy level which is specific to each experimental setup; it is accompanied by fundamental changes in many properties of the discharge which are reviewed later in this paper.

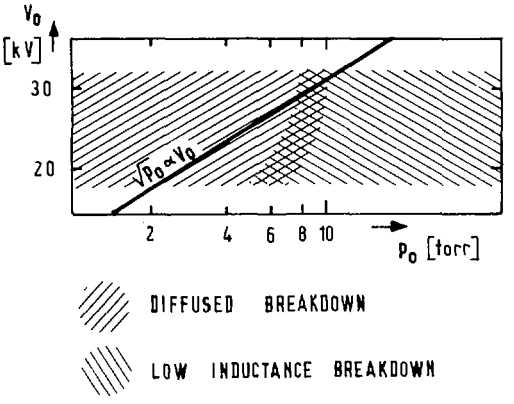


FIG.4. Delimitation in the (V_0, p_0) plane of the areas giving diffuse- and low-inductance breakdown.

3.1. Breakdown and sheath buildup

Electrical measurements carried out during the early phase of the discharge ($t \lesssim 1$ μs), have shown the existence of two different kinds of breakdown and sheath buildup. This observation holds for both kinds of electrode system and depends on the initial values V_0, p_0 of the voltage and filling pressure.

(a) Diffuse breakdown

This is characterized by a high initial value of the apparent inductance $L^+ = \int udt/I$. Magnetic probe measurements show the existence of a magnetic field everywhere in the coaxial volume facing the insulator while, correlatively, a Rogowski coil circling a bar of the cathode shows the passage of a current precursor (Fig.2). As the apparent inductance attains values larger than the inductance of the coaxial cavity facing the anode, it can be inferred that the sheath buildup is resistive and diffuse. Later on, the current distribution concentrates in a rather thick ($\sim$ 1 cm) current sheath layer along the insulator (L^+ decreases). Magnetic probe measurements show that, subsequently, only a fraction of the total current then lifts off and runs down.

(b) Low inductance breakdown

In this case, the initial L^+ value is compatible with that of the geometrical stray inductance L_0; no detectable magnetic field exists before the probe position is overtaken by the sheath. This corresponds to a localized breakdown along the insulator.

At constant initial voltage V_0, and for a given insulator type, there is a critical pressure range beyond which the breakdown is observed to change from the diffuse to the low-inductance category. Figure 4 shows such a feature for a 100-mm-high alumina insulator.

It is observed experimentally, for many plasma focus facilities which satisfy the universal neutron-yield scaling law, that $p_0 \propto V_0^2$. The intersection of this curve in the V_0, p_0 plane with the transition zone defined above is shown to determine, for the plasma focus devices studied at Frascati, the condition beyond which regular neutron scaling is no longer observed.

3.2. Existence of different rundown regimes as seen by energy balance measurements

A thorough analysis of the energy balance during rundown, based on detailed electrical measurements such as described in Refs [1] and [2], has shown the existence of two classes of rundown in which there may or may not exist a compatibility between the electrical energy actually fed into the sheath between two positions and that required for complete ionization and gas sweeping. The calculation between two definite times $t_i - t_j$ of:

(a) The kinetic energy fed into the sheath:

$$\Delta WK_i^j = \frac{1}{2} \int_{t_i}^{t_j} I_p^2 \frac{dLp}{dt} \, dt$$

(b) The resistive energy dumped in the sheath:

$$\Delta WR_{p_i^j} = \int_{t_i}^{t_j} R_p I_p^2 \, dt$$

has been carried out for the large-diameter gun at two electrode lengths (350 mm and 600 mm).

(c) Optimized regime for neutron production (20 kV, 1.5 torr). For the short gun, from time t_1 (when the sheath reaches the outer electrode radius) to time t_2 (when the sheath starts to implode), $\Delta WK_1^2 = 17.5$ kJ while $\Delta WR_{p_i^2} = 2.5$ kJ. The energy required to dissociate, ionize and fully sweep the gas contained between these two sheath positions would be 22 kJ. For the long gun, the same

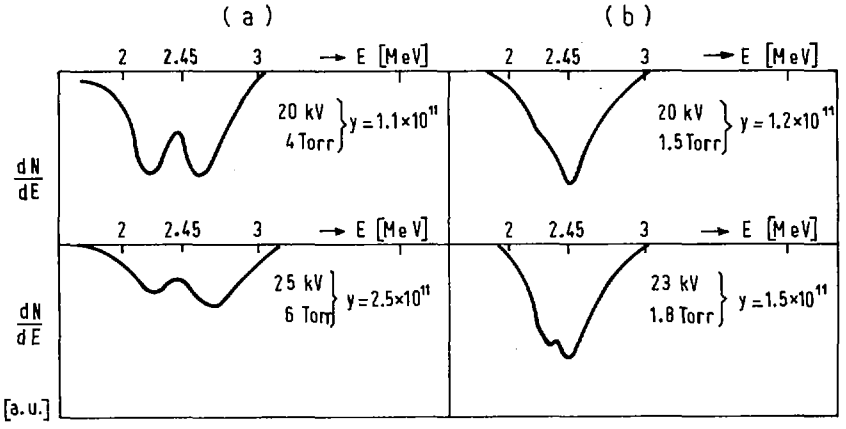


FIG.5. Time-of-flight signals detected at 113 metres:
(a) small-diameter electrode system;
(b) large-diameter electrode system.

evaluation carried out between the two sheath positions corresponding to the former $t = t_2$ position and to the start of the implosion plane ($t = t_3$) gives $\Delta WK_2^3 = 23$ kJ, while $\Delta WR_{p_2}^{3} = 6$ kJ. The complete ionization and gas sweeping would require a total of 25 kJ. The rundown is then compatible with a snowplough model in both cases.

(d) Other regimes: Increasing V_0 at constant p_0 introduces a phenomenon of current slip for which the sheath velocity increases steadily while the energy available electrically falls short of the requirement of a snowplough mechanism. Similarly, the analysis of the electrical data corresponding to a working regime at $V_0 = 33$ kV, $p_0 = 8tD_2$ (negligible neutron yield), brings the same kind of incompatibility, although the current sheath velocity slows down as the sheath approaches the anode top.

3.3. Neutronic properties

The spectral energy distribution of the neutron emission has been measured by two independent methods: the nuclear emulsion technique and the neutron time-of-flight technique (detector located in a plane perpendicular to the focus axis at 12, 34 and 113 m).

(a) Comparing the time-of-flight spectra of the neutrons emitted by the large- and small-diameter systems, respectively (Fig.5), which have the same neutron yield at the same energy level ($\gtrsim 10^{11}$ neutrons per shot at 250 kJ) it

turns out that there are obvious differences in the mechanisms for neutron production.

The spectra of the neutrons yielded by the large-diameter system is well behaved and peaked at 2.5 MeV with a FWHM of 400 keV. Practical limitations on the experimental site forbid time-of-flight measurements along the z-axis, and therefore prevent a clear answer as to whether the neutrons could be of thermal origin. The observation reported above is compatible with a thermal process corresponding to a 20–30-keV ion temperature.

The spectra of the neutrons emitted by the small-diameter system in the range of regular neutron-yield scaling presents a number of features which vary from shot to shot. In particular, a depression in the relative abundance of neutrons around 2.5 MeV is often observed. The FWHM is much larger than in the former case and reaches 650 keV, so that thermal origin for the neutrons is clearly ruled out as a unique mechanism.

(b) Comparing the neutron spectra determined on the same shot using either the nuclear plate technique or the time of flight, it turns out that the former (a true time-integrated spectrum) differs in some details from the latter (see Fig.6), in particular around 2.5 MeV.

This suggests the existence of a strongly time-dependent neutron spectrum: the neutron emission which lasts typically 150 ns at half maximum produces an apparent energy spread of 150 keV at 2.5 MeV.

Comparison of the neutron signals detected at 12, 34 and 113 metres with the X-ray signals (Fig.7) demonstrates that high-energy neutrons ($\sim$ 3 MeV) are emitted right at the start of the emission and that the relative abundance of the early high-energy neutrons is rather systematically correlated with the intensity of the hard X-ray signals (themselves synchronous with the beginning of the neutron pulse) and not with the total neutron yield.

In the case of an irregular scaling law, we notice a sharp increase in the neutron spectrum width (from 650 keV at 250 kJ to 1.1 MeV at 720 kJ), correlated to a jump in the maximum detected neutron energy, from 3 MeV to 3.7 MeV (Fig.8). This suggests either a drastic change in the neutron production mechanism or, more likely (assuming the neutron production is a mixture of several effects), the possibility that one of these mechanisms no longer scales up with energy, and therefore that the contribution of the beam effects to the total yield becomes predominant.

The important conclusion is that comparison of the neutron spectrum resulting from the use of different gun geometries, together with observation of the evolution of the spectral shape at increased energy level on a given facility, suggests the existence of different neutron-production mechanisms.

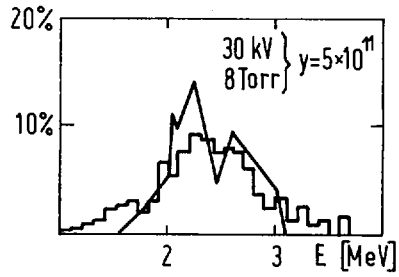


FIG. 6. Nuclear plate neutron spectrum compared with a time-of-flight neutron spectrum (same shot) $V_0 = 30$ kV, $p_0 = 8$ torr.

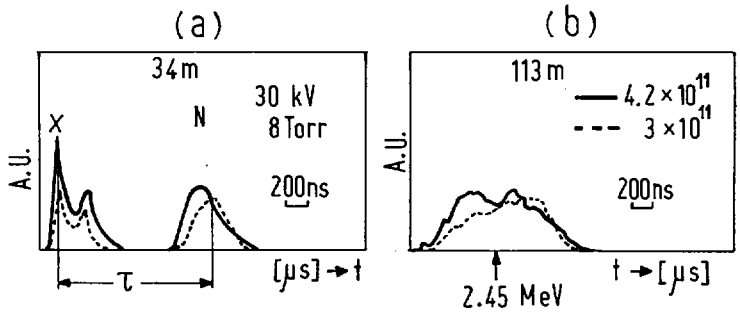


FIG. 7. (a) X-ray and neutron signals at 34 m and (b) time-of-flight signal at 113 m. τ is the time-of-flight difference between 2.45 MeV neutron and X-rays.

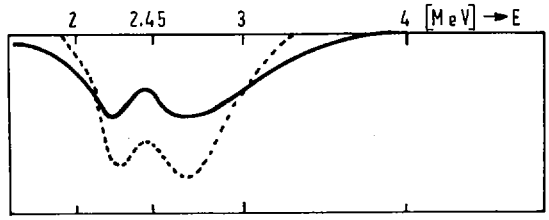


FIG. 8. Time-of-flight neutron spectra at large energy level:
----- 30 kV, 8 torr
—— 34 kV, 10 torr } *$y = 4 \times 10^{11}$ for both*

4. DISCUSSION AND GENERAL CONSIDERATIONS ON THE PLASMA FOCUS SCALING LAW

Simple scaling laws derived heuristically, assuming that the rundown phase is well described by a snowplough model, show in particular that to obtain a good compromise between the optimization of the total magnetic energy and the current at the end of the rundown phase, the gun inductance must be comparable to the stray inductance, together with the condition that about 70% of the initial electrical charge q_0 is transferred up to that time into the load circuit. For a given energy level these simple matching rules leave two undetermined parameters, usually the radius R of the anode and the voltage V_0. These scaling laws are applicable only if the condition

$$V_{sh}/V_0 \sim 15 \frac{\Delta R}{R} \sqrt{C} < 1 \qquad (1)$$

is satisfied, where V_{sh} (the resistive voltage drop along the sheath) is determined heuristically by the condition that the energy dissipated in the sheath meets the required one for total ionization (ΔR is the interelectrode radial gap; C the capacity).

It has been shown in Section 2 that the evolution of the scaling toward large-radius experiments might be limited by the appearance of low insulator resistance and consequently a large current loss. Therefore, L_g being fixed by the consideration summarized above, the only possibility left for a classical dense plasma focus (DPF) design is to decrease the length of the gun by increasing V_0.

Comparing the resistive voltage drop in the sheath predicted by Eq.(1) with the measurements carried out on both large- and small-diameter systems operated at 20 kV, 1.5 torr and 3 torr filling pressure, respectively, agreement turns out to be good ($R_p \sim 0.6$ mΩ for large diameter; $R_p \sim 2.5$ mΩ for small diameter) and the limited total current obtained on the small-diameter system is mainly to be attributed to mismatching. This limitation could be overcome by a re-arrangement of the 1-MJ condenser bank which would allow operation at 80 kV.

The discontinuation of the neutron-yield scaling properties observed beyond 500 kJ is, however, the main problem and, for the time being, seems not to be connected to a fundamental matching problem.

Many experimental observations reported in this paper imply the existence of complex physical models. In particular, the evidence that the neutron-production mechanisms in plasma focus devices are neither unique nor time-independent excludes the possibility of deriving a universal and simple modelling for all devices based on optimization of the magnetic energy or the plasma current. For instance, we do not yet know whether the nature of the turbulence responsible for neutron production is macroscopic or microscopic.

If the turbulence is macroscopic, the energy eventually converted into particle energy must be localized at the onset of instability in the plasma volume. In such a case, the tailoring of the spatial magnetic energy distribution in the gun would be of the utmost importance. Plasma focus geometries such as the large-diameter system (the limiting case being the Filippov geometry) favour a magnetic energy distribution concentrated in the pinch region. The magnetic energy contained in the short gun at the end of the rundown is a mere 13% of the energy stored in the condenser bank at the start, whereas this ratio increases to 21% in the case of the long gun. Despite this, the two facilities, which have the same magnetic energy in the pinch region, produce exactly the same neutron yield and are optimized for the same V_0, p_0 values.

If the turbulence is microscopic, the mechanism is equivalent electrically to a large resistive effect (resistance in series with the *total* gun inductance, including the stray inductance) which can absorb a large amount of magnetic energy, provided there is no finite propagation effect in the volume containing this energy (as would be the case if the magnetic field were imbedded in a low-density plasma left behind by the moving sheath). Microscopic turbulent processes are often associated with the production of high-energy particles, as observed here.

ACKNOWLEDGEMENT

We wish to thank K. Steinmetz from the Institut für Angewandte Physik II of the University of Heidelberg, who performed the nuclear plate measurements.

REFERENCES

[1] GOURLAN, C., KROEGLER, H., MAISONNIER, C., OPPENLANDER, T., RAGER, J.P., Controlled Fusion and Plasma Physics (Proc. 8th Europ. Conf. Prague, 1977) Vol. 2 (1977) 247.
[2] OPPENLANDER, T., CNEN – Centro di Frascati, Rep. 78.6 (1978).
[3] DECKER, G., et al., Paper IAEA-CN-37/U-3-2, these Proceedings.

NEUTRON EMISSION PARAMETERS IN PLASMA FOCUS DEVICES

Part A:
G. DECKER, H. HEROLD, H.J. KAEPPELER,
W. KIES, W. MAYSENHÖLDER, B. NAHRATH,
T. OPPENLÄNDER, G. PROSS, B. RÜCKLE,
A. SAUERBRUNN, P. SCHILLING, H. SCHMIDT,
M. SHAKHATRE, M. TRUNK
Institut für Plasmaforschung,
Universität Stuttgart

Part B:
K. STEINMETZ, H. BRUHNS, J. EHRHARDT,
K. HÜBNER, P. KIRCHESCH, G. MECHLER
Institut für Angewandte Physik II,
Universität Heidelberg,
Federal Republic of Germany

Abstract

NEUTRON EMISSION PARAMETERS IN PLASMA FOCUS DEVICES.

Subject of part A of this paper are results of experiments and theoretical studies aimed at improving the neutron yield from plasma focus devices and searching for correlations between neutron yield and various plasma parameters. In part B the neutron production is studied with superimposed axial magnetic field. There are typically two temporal phases of neutron emission, which are differently affected by the magnetic field, but neither the beam-target nor the moving-boiler model can explain the neutron emission alone.

Part A:

Neutron Yield Parameters in Plasma Focus Devices

(Institut für Plasmaforschung, Stuttgart)

1. Considering the plasma focus as a high quality neutron source, present focus research aims at an understanding and at an optimization of the processes leading to neutron emission. It is generally agreed that the neutron yield Y scales with the discharge current I, as $Y \sim I^n$. Thus primarily I has to be maximized. We have developed an analytical model which delivers impedance matching criteria /1/. The model shows that for a given bank energy an optimum voltage U_{opt} exists for which the maximum current I_m becomes a maximum. Generally, U_{opt} is appreciably higher than that used in present focus devices.

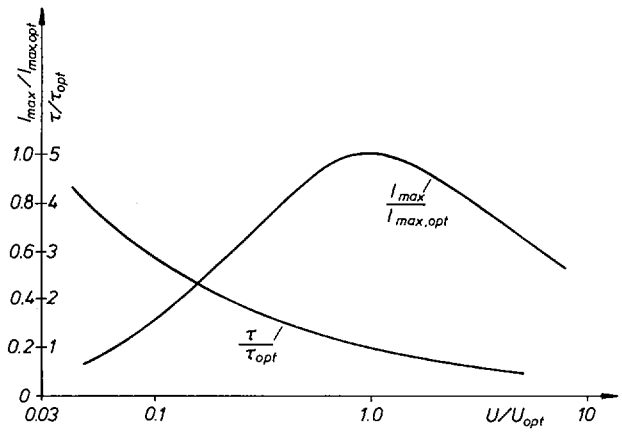


FIG.1. Universal normalized curve for discharge current and time to maximum current versus normalized bank voltage.

The circuit analyzed is an LC circuit with the time derivative of the accelerator inductance $\dot{L}$ as a constant load. Constant $\dot{L}$ means constant axial (running down) velocity, a fact verified by experimental observations. $\dot{L}$ is typically about 20 mΩ for devices with bank energies of 10 to 100 kJ. Other fixed model parameters are the bank energy W, representative for the cost of the device, and the initial current rise $\dot{I}_0$. The latter is given by the ratio of the bank voltage U and the external inductance L_0 and is representative for the state of engineering.

The optimum voltage U_{opt}, for which the maximum current has a maximum if W, $\dot{I}_0$ and L are kept constant, is given by

$$U_{opt} = 2.12\ (W\dot{I}_0\dot{L}^2)^{1/3} \tag{1}$$

With the maximum current

$$I_{m,\,opt} = 0.64\ (W\dot{I}_0/\dot{L})^{1/3} \tag{2}$$

and the current rise time

$$\tau_{opt} = 1.5\ (W/\dot{L}\dot{I}_0^2)^{1/3} \tag{3}$$

The above can be rewritten as

$$\sqrt{\frac{L_0}{C}} = 2.18\ \dot{L} \tag{4}$$

which constitutes an impedance matching condition, or, introducing U_{opt},

$$U_{opt} = 3.31\ I_{m,opt}\ \dot{L} \tag{5}$$

The above relation clearly demonstrates the necessity for selecting high voltages if large currents are to be achieved.

Fig. 1 permits an analysis of non-optimized (with respect to voltage or impedance matching) condensor banks, in terms of currents and rise-times.

Banks with voltages lower than optimum will produce high kinetic energy of axial plasma motion and relatively low magnetic energy, banks with higher voltage will show lower kinetic and higher magnetic energy. At U_{opt}, there is 17 % kinetic energy, 74 % magnetic energy, and 9 % electrical energy still stored in the bank, at the time of maximum current.

Assuming that $\dot{I}_0$ scales as $\dot{I}_0 \sim W$ with present values of 10^{12} A/s at the 100 kJ level for bank energies, Eqs. (1) to (3) lead to

$$\dot{I}_0 = 6 \cdot 10^3 \; I_m^{3/2} \; L^{1/2} \tag{6}$$

$$W = 6 \cdot 10^{-4} \; I_m^{3/2} \; L^{1/2} \tag{7}$$

The relations for the current were found to be within an error of 15 % compared to values obtained experimentally and from numerical MHD calculations.

Guided by the above considerations an appreciable current increase was achieved, increasing the voltage from 20 kV to 85 kV at fixed W of 12 kJ. The neutron yield went up by a factor 3.

A new 78 kJ, 100 kV device (DPF 78) was set up with the objective to benefit from increased energy, high $\dot{I}_0$ and the properly selected voltage in order to obtain an increased neutron yield. With $\dot{I}_0 = 2.2 \cdot 10^{12}$ A/s, $\tau = 1.5$ μs and U = 100 kV, a maximum current of $I_m = 1.3$ MA is obtained in accordance with the model results. In order to achieve maximum neutron emission, an optimization procedure (geometry and pressure variation, see paragraph 2.) was carried out. Operating at 60 kV (28 kJ), a neutron yield $Y = 1.5\ Y_{conv.}$ was found experimentally. $Y_{conv.}$ is the yield expected from W^2 scaling. From our model, $Y = 2.2\ Y_{conv.}$ was calculated. At 100 kV (78 kJ) so far $Y = 0.8\ Y_{conv.}$ is obtained, whereas $Y = 2.5\ Y_{conv.}$ is calculated. The deficiency in the latter experiment may be due to the problem of adjusting breakdown conditions, rundown phase and radial compression at the given short time scale, typical for the high current experiment. By choosing a conical (45°) tip of the center electrode, the yield could be increased by about 50 % resulting in the values cited above. Possibly pulsed gas inlet to establish appropriate gas pressures in the different parts of the device is mandatory.

2. Reproducible high neutron yield for a given condensor bank requires an adjustment of the accelerator configuration, taking into account the characteristics of the current pulse. Besides the usual variations of the filling pressure and the length of the inner electrode, it was found necessary, especially for fast machines, to optimize the inner electrode radius as well as the ratio of the electrode radii r_a/r_i /2/. For the 12 kJ high voltage focus device, adjustments from $r_i = 2.5$ cm to 1.25 cm and from $r_a = 4.2$ cm to 3.0 cm were made. Besides higher neutron output (factor 5), this also yielded a remarkable shift to higher optimum pressures (typically from 1 torr to 10 torr) and a broadening of the pressure operating range. With this latter effect, it became possible to choose such operating points which obviously reduce adverse effects like excessive current loss in the breakdown region, typically for the low pressure operating regime. Analogous experimental efforts for optimizing our high voltage device DPF 78 by means of geometry and pressure variations are up to now successful only with reduced bank energy (28 kJ, 60 kV). Here a mean neutron yield of $Y = 10^{10}$ at $r_a = 4.5$ cm, $r_i = 2.5$ cm, $l_i = 16$ cm and $p = 5$ torr is obtained. Operating at full bank energy, $Y = 2.5 \cdot 10^{10}$ is achieved at best with $r_i = 3.3$ cm, $r_a = 6.2$ cm, $l_i = 16$ cm and p = 5 to 10 torr. The r_i variation was 2.5 cm, 3.3 cm and 4.3 cm. This neutron yield does not yet reach the reference point of the energy scaling curve.

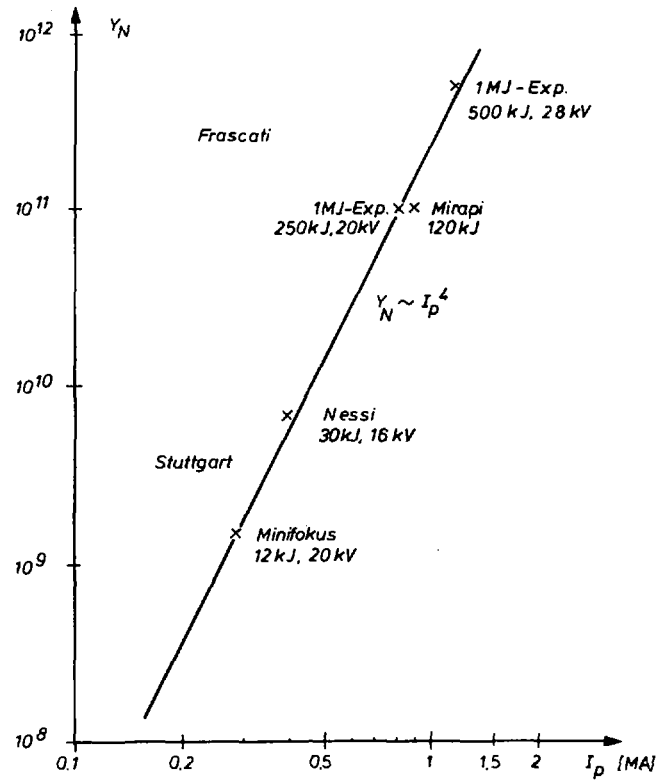


FIG.2. Neutron yield scaling with pinch current.

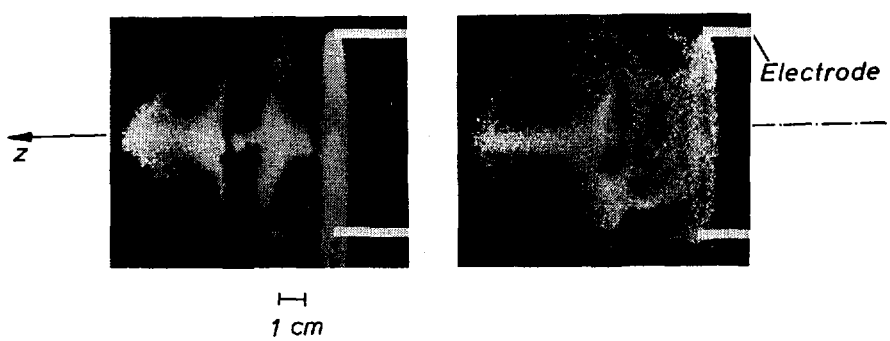


FIG.3. Soft-X-ray pinhole photographs taken during the late phase of a plasma focus with an exposure time of 3 ns, at 150 ns (left) and at 210 ns (right) after maximum plasma compression.

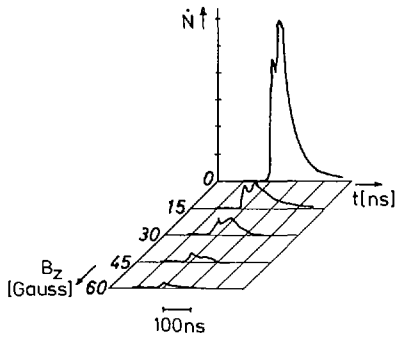


FIG.4. Time sequence of the neutron pulses with increasing axial magnetic field.

3. Various insulators consisting of different materials, such as BeO, Al_2O_3, quartz and pyrex, were tested in a focus device. The dimensions of the insulators and the geometrical and electrical parameters of the focus were kept constant. It turned out that the insulator material has strong influence on the average neutron yield and on the current sheath structure. A general feature of all insulator materials used is that a remarkable fraction of the total current (15 % to 50 %) does not participate in the pinch process and very likely remains attached to the insulator. This fraction varies with the material and is particularly low (15 to 20 %) for the BeO insulator. Measurements with magnetic probes and with visible light interferometry at the tip of the center electrode revealed that the profiles and the maximum values of the electron density and of the current density in the pinching plasma sheath depend on the insulator materials. The profile widths and the maximum values differed up to a factor of two, with BeO having the most peaked profiles in n_e and j_z. Among the materials tested, plasma sprayed Al_2O_3 was the best performer considering the neutron yield.

4. This current loss on the insulator surface obviously affects the neutron yield /3/ and the total current should no longer be used for scaling. Rather the pinch current must be used. The actual pinch current I_{pinch} was measured with magnetic probes for various focus devices. Including results from Frascati devices (Fig. 2), a neutron scaling $Y \sim I_{pinch}^4$ was found to be valid at optimum conditions.

5. In order to gain insight into the neutron production mechanism, a quest for shot to shot correlations between neutron yield and various discharge parameters (e.g. T_e, I_{pinch}, $n_{e,max}$ and various time scales of plasma dynamics) was made. No strong correlations could be found except for the amplitude of the instability signal (m = 0 instabilities) displayed by the magnetic probe. The correlation coefficient was found to be $r^2 \approx 0.7$. Obviously a fast growth of the instability is favorable for high neutron yield. Higher correlation was established when more than one of the mentioned parameters was taken into account, pointing to synergistic effects.

6. About 100 ns after the m = 0 instability, large diffuse plasma clouds with $n_e \approx 10^{17}$ cm^{-3} and $T_e \approx 300$ eV were observed by soft X-ray pictures, taken with pulsed channel plates /4/. Fig. 3 shows two photographs of this novel phenomenon, taken at 150 ns and 210 ns after the maximum pinch compression. This "late phase" of the focus during which the main part of the neutron emission occurs lasts for several 100 ns. The ion temperature in this phase is unknown. If, however, $T_i \leq 3\ T_e$ is assumed the measured neutron output cannot be explained by thermonuclear processes.

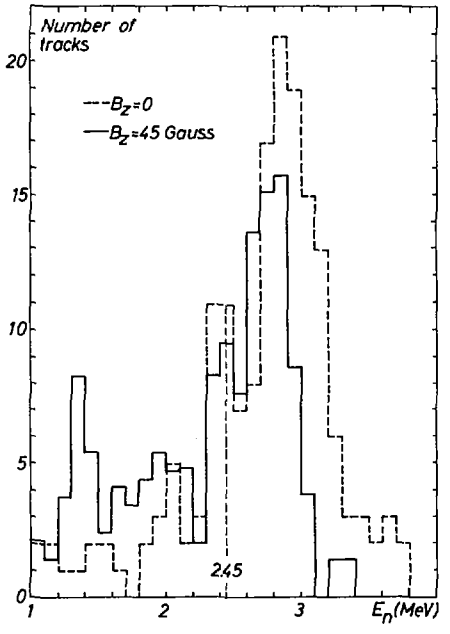


FIG.5. Neutron energy spectra from nuclear emulsion plates with and without axial magnetic field B_z, measured in axial direction.

Part B:

Neutron emission from a small plasma focus in the presence of an axial magnetic field

(Institut für Angewandte Physik II, Universität Heidelberg)

It is well known that the total neutron yield of a dense plasma focus can be reduced drastically by superimposing an axial magnetic field B on the focus. Several groups /5,6/ studied this phenomenon. However, no efforts have been made so far to find out the influence of B on the spectral behaviour and the anisotropy of the neutron emission.

We investigated the neutron emission from a 12 kJ (20 kV, 480 kA) Mather-type focus with nuclear emulsions in axial direction and by scintillators in both axial and radial direction. The scintillators were positioned in a distance of 1.2 m from the end of the inner electrode to study the temporal emission without disturbance by time-of-flight effects. The axial magnetic field was generated by a coil in the inner electrode (anode) and could be varied between 0 and 55 Gauss measured at the surface of the anode. All experiments were performed with a deuterium filling pressure of 1.0 ... 1.5 Torr giving a maximum neutron yield of 10^9N per discharge.

Without a magnetic field a typical temporal performance shows two X-ray spikes, each accompanied by a neutron emission. The first emission containes only a small part of the total neutron yield and starts 40 ns after the maximum compression which coincides with the sharp minimum of the

dI/dt-signal (I denotes the discharge current). The second follows 40 ... 60 ns delayed and yields 80 ... 90% of the total neutron output.

If an axial magnetic field is applied, the X-ray and the neutron emission changes drastically. With increasing B the time correlation of dI/dt and the first X-ray and neutron emission remains constant while the yield decreases (Fig. 4). The X-ray and the neutron emission from the second pulse become delayed and are much more reduced than the first ones; in most of the shots with B = 55 Gauss the second pulse is practically extinguished. Thus the total yield reduces to that of the first pulse.

The reproducibility of the neutron yield from shot to shot is enhanced with increasing axial magnetic field. At B = 55 Gauss the yield changes only about ± 30%, whereas it varies by a factor of 2 ... 3 from shot to shot when no axial magnetic field is present.

Nuclear emulsions show independently of B two distinct peaks at 2.5 and 2.7 ... 2.8 MeV (Fig. 5). Thus one can assume that both moving boiler and beam target mechanisms take part in the yield, however, with a beam-target contribution of 80 ... 90% (averaged over 10 shots) at B = 0 and of 70% (averaged over 70 shots) at B = 45 Gauss. So there is an evidence that the magnetic field reduces the instability-caused production more than the thermonuclear one. This is plausible if one takes into account that the growth rates of most instabilities, found to be present in the plasma focus, are more seriously affected by an axial magnetic field B than the compressional features, unless B becomes comparable to the azimuthal magnetic field of the pinch.

For a simple model of the neutron production in a plasma focus one may assume a time sequence of moving boiler and beam-target mechanisms. A theoretical estimation /7/ gives an anisotropy factor $A = Y(0^{\circ})/Y(90^{\circ}) = 1.02$ for a moving boiler plasma and A = 2.28 for a beam-target mechanism. However, time resolved measurements of the anisotropy indicate that there is no phase of neutron emission isotropic enough to be caused by a moving boiler mechanism alone. For shots with B = 0, i.e. with an almost vanishing first neutron pulse, we found A = 2 ... 2.3 (from the nuclear emulsion measurements: A = 2 ...2.2). Discharges with a high value of B (typically 55 Gauss) and an extinguished second neutron pulse show an anisotropy A = 1.5. In more than 80% of the shots with axial magnetic fields between 20 ... 45 Gauss there are two distinct neutron peaks. Usually the first pulse has a lower anisotropy (A = 1.5) and the second pulse a higher one (A = 1.7 ... 2.0). Nuclear emulsions at B = 45 Gauss give a mean value of A = 1.9.

So we can conclude also from these measurements that there is no emission phase which could be described by one model alone. It seems that the temporal emission behaviour is determined by at least two production mechanisms whose contributions vary with the superimposed axial magnetic field.

REFERENCES

/1/ Decker, G., et al., Current and Neutron Yield Scaling of Fast High Voltage Plasma Focus. Rep.IPF 77-2, Stuttgart (1977).

/2/ Chen, Y.H., et al., Enhancement of neutron yield from focus devices. 8. Eur. Conf. on Contr. Fus. and Plasma Phys., Prague, Vol. I, p. 65 (1977).

/3/ Gourlan, C., et al., Measurement of current density distribution in a megajoule plasma focus device. 8. Eur. Conf. on Contr. Fus. and Plasma Phys., Prague, Vol. II, p. 247 (1977).

/4/ Nahrath, B., Untersuchungen zur Dynamik des Fokusplasmas durch Messungen der weichen Röntgenstrahlung. Rep. IPF 78-1, Stuttgart (1978).

/5/ Bernstein, M.J., Hai, F., Neutron production in a plasma focus discharge with and without axial magnetic field. Phys. of Fluids 14, 1010 (1971).

/6/ Maisonnier, Ch., et al., Recent progress in research on plasma focus. 5. Eur. Conf. on Contr. Fus. and Plasma Phys., Grenoble, Vol. II, p. 183 (1972).

/7/ Maisonnier, Ch., et al., Structure of the dense plasma focus, Part II. 4. Conf. on Plasma Phys. and Contr. Nucl. Fus. Research, Madison, Vol. I, p. 523 (1971).

ENERGY SPECTRA OF DEUTERON AND ELECTRON BEAMS FROM FOCUSED DISCHARGES AND OPTIMIZATION CRITERIA*

V. NARDI[+§], W.H. BOSTICK[§], J. FEUGEAS[§], W. PRIOR[§+], C. CORTESE[+]

[+]Istituto Elettrotecnico Nazionale
Galileo Ferraris,
Turin, Italy

[§]Stevens Institute of Technology,
Hoboken, New Jersey,
United States of America

Abstract

ENERGY SPECTRA OF DEUTERON AND ELECTRON BEAMS FROM FOCUSED DISCHARGES AND OPTIMIZATION CRITERIA.

Deuteron beams ($\approx 10^5$ A) with a 300-keV peaked spectrum and electron beams are produced by localized sources (≈ 10 ns, ≈ 1 mm) in focused discharges. The energy spectrum of the deuteron beam ejected from a localized source in plasma focus discharges (45-75 μF at 15–18 kV; $I_{max} \sim 0.5-0.8$ MA) is derived by two independent methods: (A) ion time of flight and (B) ion-induced damage on Al plates. The ion spectrum varies from shot to shot but specific features are observed by all discharges. From method (A) the number of deuterons N(E) as a function of the ion energy E has a well defined maximum N_m 130 keV $\leqslant E \leqslant$ 320 keV. N(E) has a minimum at lower values of E and rises sharply again by further decreasing E. N(E) for $E \lesssim 50$ keV becomes substantially larger than N_m. The distribution of ion penetration range in Al yields by method (B) substantially the same spectrum as method (A). A second peak with maximum value N_M of N(E) for 15 keV $\lesssim E \leqslant 40$ keV is derived by method (B), which is most convenient for deriving the low-energy tail of the ion spectrum ($N_M \sim 9\ N_m$). The electron-beam energy (with a dominant value $\approx$ 300 keV) is determined by the length of dendrites ($\approx$ penetration range) in a lucite target inserted inside the hollow-centre electrode (anode). The higher the maximum value E_M of the observed ion energy, the higher is the total neutron yield n in a discharge. By comparing two low-voltage discharges, higher values of E_M and n are observed in the discharge which generates fewer ion (and electron) beams. In a high-voltage discharge, n has instead higher values when the discharge generates many ion/electron beams. Generalized criteria for the optimization (maximum n) of a plasma focus are derived in terms of the propagation speed of the current sheath between electrodes and of conditions for avoiding restrike behind the current sheath first formed.

* Work supported in part by Consiglio Nazionale delle Ricerche, Italy; AFOSR, Washington, DC, AES, Inc., New York, New Jersey Power & Light Co., and Jersey Central Power & Light Co., USA.

J. Feugeas is on leave from Universidad Nacional de Rosario, Argentina.

1. INTRODUCTION

Low-cost sources of high-intensity ion beams are obtained by plasma focus discharges. In our case the discharge is fed by a 45-μF capacitor bank at 15 kV with 3–5 torr deuterium fillings. Electron beams are also produced in these discharges. The typical electron energy ($\approx$ 300 keV) is assessed by the length of dendrites on a lucite disc located inside the hollow-centre electrode (anode). The ion spectrum is determined by the ion penetration range in Al targets and by the ion time of flight from a localized source. We have obtained substantially coincident spectra by these two independent methods. The time-of-flight method in a D_2 discharge is simplified by using the D-D neutron emission. The bulk of the neutron emission in a discharge, i.e. a fraction $\gtrsim 50-70\%$ of the total neutron yield (10^8-10^9/shot), is produced in the hot plasma on the discharge axis by high-energy deuteron beams with a directed kinetic energy $\gtrsim$ 10 keV–1 MeV. Ion acceleration to peak energy and peak of the neutron pulse occur within a time interval $\lesssim 1-10$ ns. The neutron source – and so the corresponding source of high-energy ions – is formed in the hot plasma by one or (in some discharges) 2–10 localized regions of high density ($\approx 10^{20}\,\mathrm{cm}^{-3}$), each with linear dimensions $<$ 1 cm. Each neutron pulse also has a tail $\approx$ 100 ns long which is produced by the part of the ion beam crossing the cold plasma. This non-localized part of the neutron source has an amplitude A_t neutrons ns^{-1} smaller by about 1/30 than the amplitude A_p of the neutron source main pulse (i.e. of the core of the neutron source). Pulse multiplicity/duration ($<5-10$ ns) of the localized neutron sources in the hot plasma axial region fits multiplicity and duration of the hard (>30 keV) X-ray pulses from the same plasma region [1]. It is consistent with collimated neutron measurements [2] and with X-ray pinhole-camera photographs [1, 3] to consider a localization in space of a neutron source (source core) even greater than the space resolution ($\approx$ 1 cm) of the neutron collimator, e.g. with the same linear dimensions[1] $\delta \approx 0.1-1$ mm of a localized X-ray source [1]. A localization of a neutron (and ion) source in space within 1 cm and in time, as we have observed in our experiments [2], makes it possible to determine the energy spectrum of the ions by a time-of-flight method. The spectrum was derived for different plasma focus discharges by a time-of-flight method and by a method based on the distribution of the observed ion-penetration range in the Al plate.

[1] Note that the symbols δ, d in Sections 1 and 2 do not indicate the same quantities as in Sections 3, 4 and 5.

2. ION ENERGY SPECTRUM

(A) Time-of-flight method

The ion spectrum is derived by the ion time of flight from the localized source (±0.5 cm from centre of anode end) to an observation region located at a distance d = 10 cm downstream along the electrode axis. A paraffin collimator (gap width 1.5 cm) for neutron-collimated measurements is pointed at the region of observation (direction 90° from the electrode axis; distance of detector from axis $\Lambda = 76$ cm [2]. The time marks are given by the hard X-ray burst ($\cong 1-2$ ns duration) which is radiated simultaneously with (at time of production of) the ion beam (specfically at the time of highest increase in ion-beam intensity at the source and of neutron emission intensity). The neutron emission from the observed region (1.5 cm wide in the axial direction) rises sharply when the bulk of the beam front reaches this region (the field of view of the collimator). To derive the ion spectrum, we used a discharge in which only one strong localized source of neutrons and of hard X-rays is formed in the plasma; both pulses in the detector signal have a sharply defined onset time. Pilot U detector systems are used for both X-rays and neutrons; time resolution is $\approx 2-3$ ns. The emission duration τ of the ion source (and of the neutron source core) is determined by the duration of the hard X-ray pulse. The onset time of both ion and X-ray source is taken as $t = 0$. The time of flight Δt of the ions from source to collimator field of view (with its centre at distance d from the source) is estimated by disentangling both instrumental broadening of the pulse and deformation due to ion velocity spread (by ion beam propagating through d) from the pulse natural width due to the duration of emission. This is accomplished by a normalization of the X-ray signal amplitude $\dot{x}(t)$ to the neutron signal $\dot{n}(t)$ so that peak amplitude of the normalized X-ray signal and of the neutron signal have the same numerical value [$\dot{x}(t) \rightarrow \dot{x}_n(t) \equiv \dot{x}\,\mathrm{Max}\,\dot{n}/\mathrm{Max}\,\dot{x}$].

We then determine the time of flight $\Delta t(E)$ of the ions via the equation:

$$\dot{x}_n(t) = \dot{n}(t + \Delta t + \Lambda/v_n - \Lambda_s/c) \qquad (1)$$

by detector outputs; $c = 30\ \mathrm{cm \cdot ns^{-1}}$; v_n is the neutron speed and Λ_s is the distance between X-ray (and ion) source and Pilot U detector ($\Lambda_s \approx \Lambda$). The number of ions $N_D \Delta E$ with an energy between E and $E + \Delta E$ is estimated by the equation:

$$N_D \approx \dot{n}/\sigma_{DD}(E) \qquad (2)$$

where σ_{DD} is the cross-section for $D(D,n)^3He$ reactions; $E = \frac{1}{2} m_D (d/\Delta t)^2$. This approximate estimate of N_D is valid when $\delta/d \ll 1$, $d/\sqrt{(2E/m_D)} \gg \tau$; otherwise

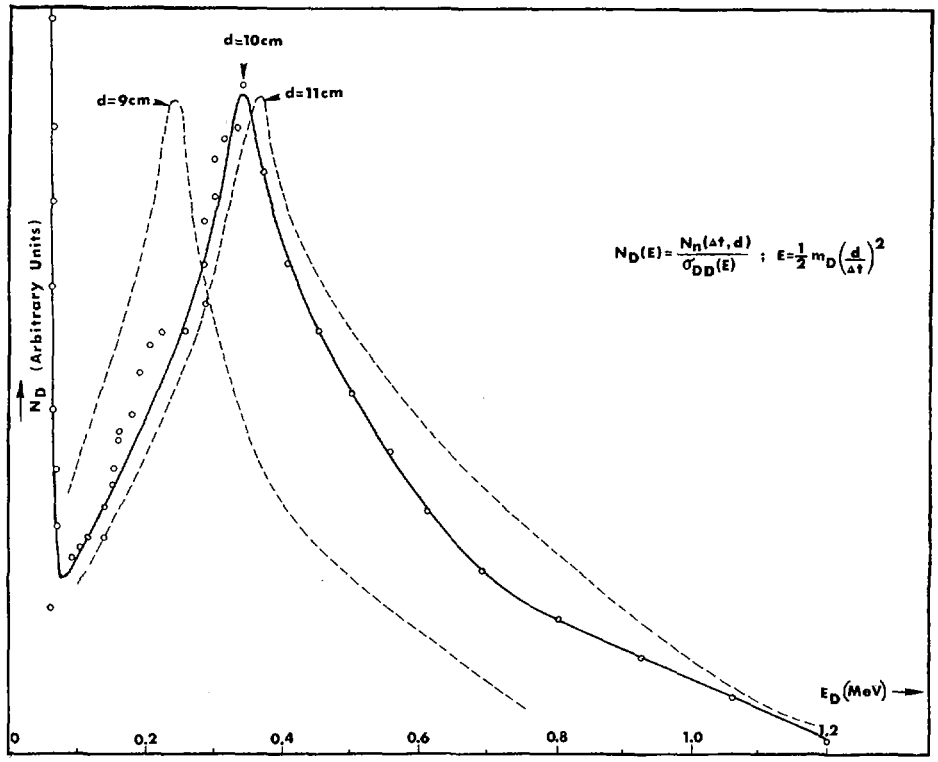


FIG.1. Ion energy spectrum by time-of-flight method.

a more complicated integral equation involving a convolution integral over τ must be used instead of Eqs (1) and (2). The spectrum in Fig.1 is derived by Eqs (1) and (2) from a discharge with a sharp neutron and X-ray pulse (FWHM of the ẋ pulse $\lesssim 3$ ns; total neutron yield $n \sim 2 \times 10^8$). An alternative arrangement was also used with one of the two neutron-detector systems very close (≈ 12 cm) to the localized source to monitor the intensity as a function of time without referring to the hard X-ray pulse. The consistency of all results has been verified. Energy losses of the ion beam in the relatively cold plasma have been considered and can be neglected for (A) energy values. The discharge chamber was filled with 3.4 torr of D_2. The assumption that the source of the ion beam is localized and coincides in space with the localized source of the first – sharply peaked – neutron and hard X-ray burst is critical in the derivation of the ion spectrum by this procedure. The dashed lines in Fig.1 give the deuteron spectrum for two different locations of the localized source of ions. A choice of values as d = 9 cm, d = 11 cm for the distance d between localized source and field of view of the collimator is still consistent with collimator-gap width.

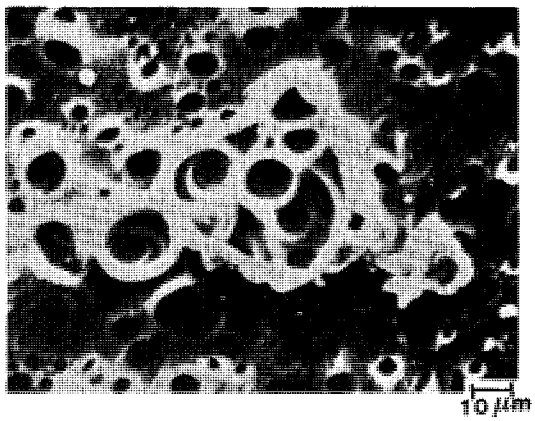


FIG.2. Scanning electron micrograph of Al plate used for deriving the spectrum in Fig.3. Exposure to a single discharge (by 5.6-torr D_2); neutron yield $\lesssim \frac{1}{2}$ yield of discharge generating spectrum of Fig.1.

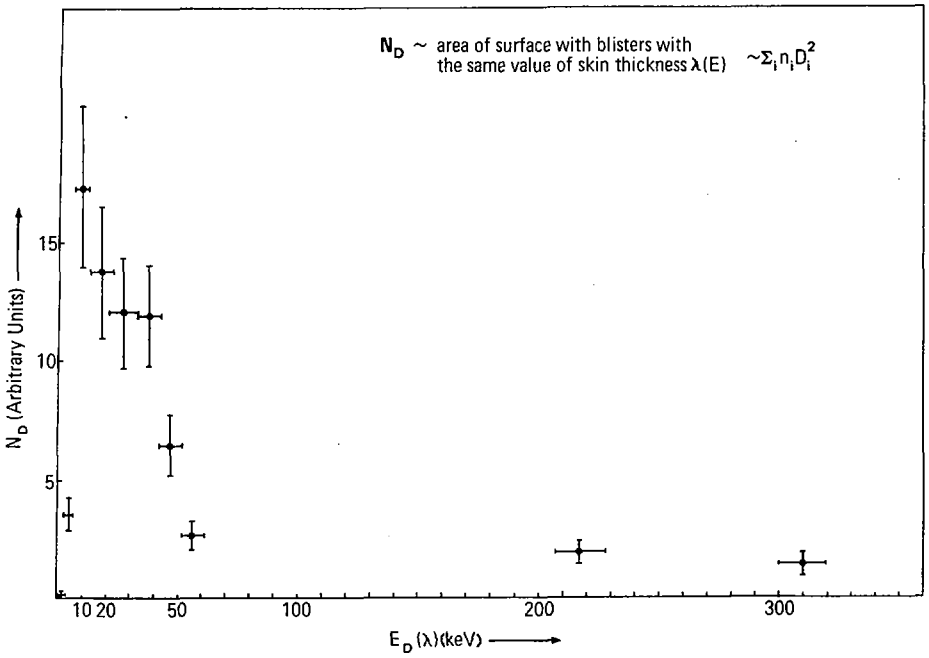


FIG.3. Ion spectrum from penetration range in Al plate [4].

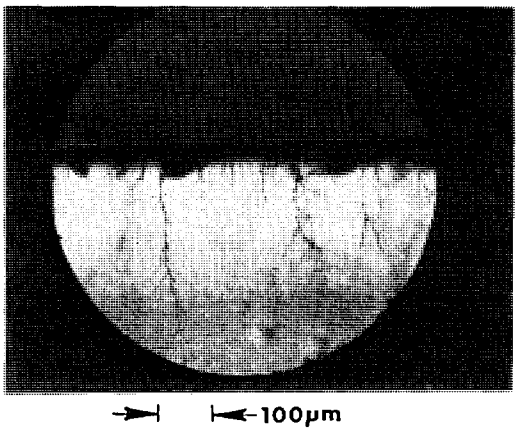


FIG.4. Dendrites due to bombardment of electron beams with a directed kinetic energy orthogonal to the lucite surface d_1-d_2. The dendrite depth is determined by the electron penetration range [5]. The best-fitting value of the electron energy is ≈ 300 keV. The lucite is inserted inside the hollow-centre electrode ~ 10 cm from anode end. The surface of the plate (orthogonal to the electrode axis during exposure to a single discharge) is orthogonal to the plane of the photograph. (Photograph by optical microscope.)

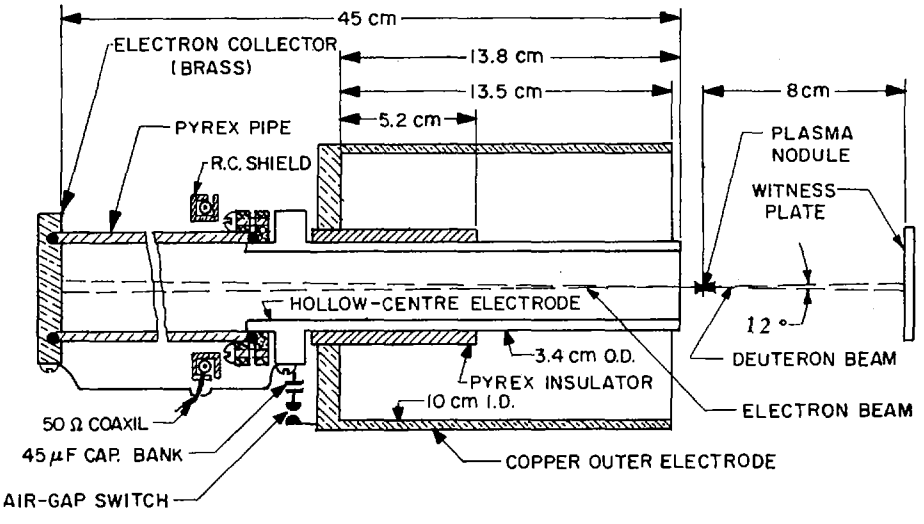


FIG.5. Schematic view of plasma focus (PF) electrodes with drift chamber for the electron beam and the Rogowski coil (RC) arrangement on the left-hand side. A metal plate (Al) for observation of the ion-induced damage was located on the axial direction. The plate was exposed to a single shot; a shield protected the plate during preliminary discharges for electrode conditioning. Targets of plastic materials were located at the end of the drift chamber (45 cm from the beam source) or closer to the source.

(B) Radiation-damage method

The surface of an Al plate orthogonal to the discharge axis is located 9 cm from the anode end. The deuteron energy E is determined by the skin thickness of the blisters which are produced by ion bombardment of the plate. The skin thickness gives the projected range $\lambda(E)$ in Al. From the observed value of λ on a blister we derive the dominant energy E of the deuterons bombarding the plate at the location of the blister. The number of deuterons with a specific value of the energy E is considered to be proportional to the area covered by blisters with the same value of $\lambda(E)$. This area is proportional to $\Sigma_i n_i(E) D_i^2(E)$, where $D_i(E)$ is a specific value of the diameter of one (or many) blister(s) with skin thickness $\lambda = \lambda(E)$, and n_i is the number of the blisters with these values $D_i(E)$, $\lambda(E)$. The spectrum peak in Fig.1 is given by ions which generate the blisters with the largest observed value of $\lambda(E)$ as in the cluster of blisters at the centre of Fig.2. Multiple readings of $D_i(E)$ and $\lambda(E)$ have been made for all the blisters ($\gtrsim 2-4 \times 10^3$) covering typical sample areas (each area $\approx 0.3 \times 0.5$ mm^2) of the Al plate. The ion spectrum is reported in Fig.3. The error bar is the standard deviation which is generated by using minimum and maximum value of D_i and of λ from the multiple readings on each blister. The ion beam propagates within a $\approx 12°$ cone on the electrode axis. The detailed internal structure of the beam is recorded by the Al plate damage (a tentative estimate of the ions with energy $\gtrsim 200$ keV gives $\gtrsim 10^{16}$; $\gtrsim 10^{12}$ ions with this energy are necessary to form one cluster of blisters as in Fig.2).

3. ENERGY AND TOTAL CHARGE OF ELECTRON BEAMS

A disc of Plexiglass (polymethylmethacrylate – PMMA) was used as a target for the electron beams which propagate along the anode axis (see Figs 4 and 5). The disc, ~5 mm thick, had the same diameter as the hollow-centre electrode (anode) and was fitted inside the anode at a distance > 10 cm from the anode end where electron beams are generated with a maximum of energy (disc surface orthogonal to the electrode axis). Dendrites are formed in the PMMA after exposure to a single plasma-focus discharge (see Fig.4) as a consequence of the fact that electrons are stopped and trapped within the PMMA and a negative space charge builds up. PMMA breakdown occurs after or during the electron bombardment. The dendrites form the discharge pattern inside the PMMA (Lichtenberg figures) and indicate that the PMMA is ruptured through the irradiated volume; the disc surface on the side of the plasma is at the positive voltage. The PMMA breakdown and the formation of the discharge pattern are easily understood by assuming that the bulk of the space charge in the PMMA is localized in a relatively thin layer parallel to the exposed – or free – surface of the disc which is

TABLE I. DATA FROM DENDRITES IN PMMA (A DISC LOCATED INSIDE CENTRE ELECTRODE-ANODE)

Q (charge of thin layer inside PMMA) = CV_{br}

V_{br} (breakdown strength of PMMA at 100°C) ~ 5 MV cm^{-1}

$C = \frac{\epsilon A}{\delta}$ capacitance of dielectric slab of thickness δ and area A

δ = observed distance between region from which dendrites originate and free surface of dielectric ($\epsilon = 2.5$ dielectric constant of PMMA)

($\delta \lesssim$ mean forward electron range in PMMA)

A = area of damaged dielectric surface ~ 0.1 cm^2 (depending on neutron yield)

Three typical values of δ have been observed (the PMMA disc is exposed to a single discharge):

$\delta(\mu m)$:	400 ± 5%	100–140	15–20
E_e(keV):	300	130–140	44–52
Q(Coulomb):	2.5×10^{-4}	$10^{-3} - 7 \times 10^{-4}$	$6.5 \times 10^{-3} - 2 \times 10^{-3}$

bombarded by the electron beam. Experiments by other laboratories provide evidence of the high concentration of the space charge in a narrow layer in PMMA samples which had been irradiated by a monochromatic electron beam [6].

The distance δ between the charge layer and the free surface of the disc is given by the depth of the sharply defined region from which the dendrites originate.

An estimate of the energy E_e of the bulk of the electrons in the beam is immediately obtained by taking the electron penetration range $\lambda_e(E_e) \cong \delta$ (E_e versus λ_e is taken from Ref.[7]). The true value of the electron energy is somewhat larger than the value of E_e as derived by this method because of the retarding field created by the charge build-up in PMMA; the relative importance of retarding field and of collision losses in slowing down the electrons has been determined experimentally by other laboratories [8]. Table I gives the three typical values of δ which have been observed in a PMMA sample after exposure to a single PF discharge. The short duration of the electron beam (~100 ns) ensures that charge-leakage effects before PMMA breakdown can be neglected.

One component of the electron beam for each observed value of δ can be defined by characterizing a beam component by the corresponding value of E_e. • The voltage due to charge accumulation in one of the three PMMA layers becomes large enough for breakdown on a time interval which cannot be expected to be the same for the three observed values of δ. Our experimental data justify the assumptions that the localized sources of the electron beams coincide in space and

time with the localized sources of the X-ray emission and that both have similar variations with time.

From the variations of the X-ray emission [3] we can consistently assume that the deposition in PMMA of the high-energy component of the beam ($E_e \gtrsim 300$ keV (see Table I)) is completed earlier and on a shorter time interval than for the other two components; the low-energy component (~ 50 keV) starts later and lasts longer than the other two components.

Under this assumption, the breakdown of the PMMA slab from free surface to $\delta \cong 400$ μm can be considered essentially independent of the breakdown processes of the two slabs with a smaller δ (these are considered to be mutually independent as well; non-interference among the three breakdown processes is also suggested by the observation that the dendrites have a tree-like pattern with few twigs and do not extend to the whole slab volume (see Fig.4)) [9]. In agreement with the previous assumption, we can estimate the electric charge Q which is deposited in each of the three thin layers inside the PMMA disc by using the formula for a planar capacitor with the dielectric breakdown strength of PMMA, i.e. $V_{br} \cong 5$ MV·cm^{-1}(an intrinsic breakdown mechanism is effective in our case) [10]. The estimated values of Q and E_e are shown in Table I.

4. ELECTRON BEAMS

A Pyrex pipe was attached at the back end of the centre electrode (Fig.5) to serve as a drift chamber for the electron beams. A shielded Rogowski coil (RC) encircling the Pyrex pipe was used to pick up the dI_e/dt signal due to electron beams. This RC was monitored simultaneously with the dI/dt signal from the total current on the electrodes. A second RC was used in many shots simultaneously with the first coil in order to obtain the integrated signal for I_e. The display of these signals from a Tektronix 7844 Oscilloscope is shown in Fig.6.

The two RCs which give the signals in Fig.6(a,b) are ≈ 20 cm away from the localized source of the electron beam (the coil location was changed in some discharges). A variety of tests were made to check the noise level and the possibility of spurious signals and to verify that the RC signal is indeed generated by the electron beam current I_e. In one type of test, (A), the shielded RC was lifted at the side of the drift tube and the display sensitivity increased several times. No signal was detected in this case. In another type of test, (B), the end of the anode near the focus was closed by a metal disc. Also, in this case the signal from the shielded RC, as in Fig.5, was absolutely flat. This and the observed damage (a circular spot with area ≈ 0.1 cm^2) on a target at the end of the drift tube after a single shot prove that the RC signal is caused by the electron beam current I_e.

The rise of I_e to peak value is very fast and in some shots is about 10 ns. The maximum observed value of I_e over about 50 shots was ≈ 5 kA. It could be

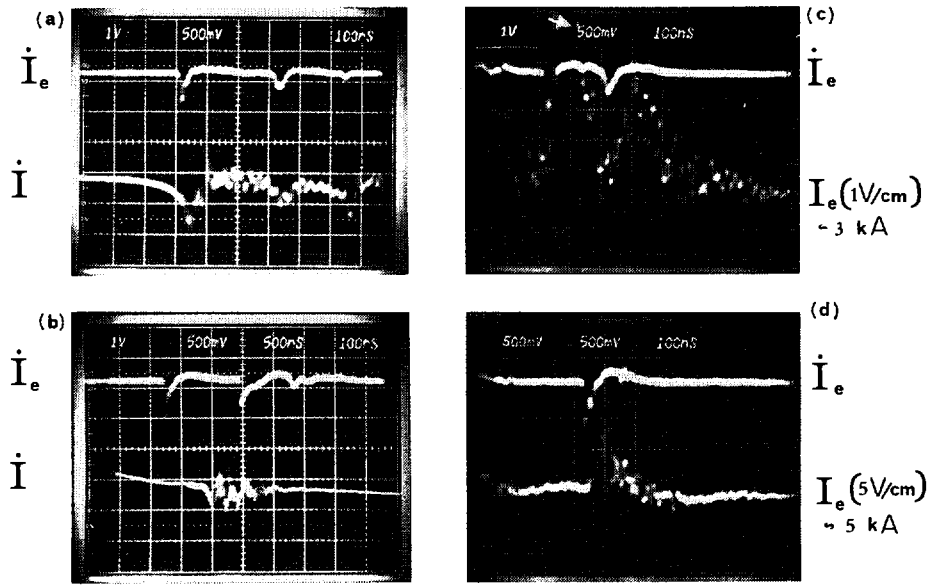


FIG.6. Rogowski coil (RC) signals for direct measurement of the electron beam current I_e. The amplitude of the upper trace in (a), (b), (c) and (d) (12.5 V·cm^{-1}, sweep speed 100 ns·cm^{-1}, time increases from left to right) gives the time derivative $\dot{I}_e$ of the beam current. This signal comes from a shielded RC located as in Fig.5 (coil length 66 mm, 23 turns with dia. of 2.2 mm). As a reference the lower trace in (a) and (b) (10 V·cm^{-1}) gives the time derivative $\dot{I}$ of the electrode current I; sweep 100 ns·cm^{-1} in (a) as in upper trace; 500 ns·cm^{-1} in (b). The lower trace in (c) and (d) gives I_e from a self-integrating RC which is located near the first coil in the same discharge. The RC for I_e (a calibrated coil of Physics Int. Co., 2.43 V·kA^{-1}) was unshielded to evaluate the noise level. A numerical integration of $\dot{I}_e$ was always made to check that the measured value of I_e was the same (within 10% or better) for both RCs. The discharge in (a) was produced with a D_2 filling at 6 torr (neutron yield $n = 2 \times 10^8 \cong \bar{n}$; in (b), (c) and (d), 7 torr of H_2). One electron beam was usually observed for each sharp $|\dot{I}|$ peak. The first peak in $\dot{I}_e$ (not recorded) was used to trigger the oscilloscope (a Tektronix 7844) in (c) and (d).

that the actual value of I_e is substantially higher, by a factor 10–40, than the RC value because of the return current which is carried by collectively accelerated ions from the gas (6 torr D_2, or H_2, as in the discharge chamber) and/or by the polarization current on the wall of the chamber. By using the value $I_e \approx 5$ kA for a beam of electrons of 300 keV with a cross-sectional area ≈ 0.1 cm^2, we estimate a power of 15 GW·cm^{-2} for this 15-J beam at the target. The hard X-ray signal from the beam-source region has a FWHM of 1–2 ns (scintillation detector signal). By taking this as the duration of the beam source, the power at the source is 0.15 TW·cm^{-2} or higher if the source diameter is smaller (this is certainly our case). A higher power value can be estimated by the energy deposition data

from the target which is consistent with a value of I_e as corrected for return current effects. Table I shows that the energy carried by a beam can be as high as $\approx$ 500 J, i.e. 10% of the energy of the capacitor bank. The power of the 300-keV component of the beam ($\approx$ 100 J) which has the shortest duration at the RC distance from the source is then ≈ 0.1 TW $\cdot$ cm^{-2}, and near the source the power is then at least 1 TW $\cdot$ cm^{-2} or higher. These values coincide with the estimated power of the ion beam in the forward direction.

5. dI/dt DATA

For each peak (or for each group of partially unresolved peaks) spanning $\sim$ 100–500 ns in the dI/dt signal (at the time of neutron emission onset) we have observed the emission of sharply collimated electron beams which propagate along the axis of the hollow anode. To find a possible correlation between total neutron yield, multiplicity of electron beams and the details of the dI/dt signal, we have analysed the dI/dt signals of $\cong$ 300 discharges with D_2 (6 torr) filling with a 75-μF capacitor bank at different voltage values (12.5 – 19.5 kV).

An external inductance was attached to this system (PF-2) in order to have for V $\cong$ 17.5 kV the same value of the peak current $I_0 \cong 7 \times 10^5$ A on the electrodes as in the 45-μF system (PF-1) at 16 kV that was used for the electron beam experiment reported in Section 4. The modified inductance of capacitor bank, transmission line and electrodes of PF-2 was $L_0 \cong 60$ nH, i.e. 1.5 times the original value of L_0 (40 nH) for usual PF-2 operation. Figure 7 shows the mean value $\bar{n}$ of the neutron yield (n = neutrons/shot) over N shots with a specific value of the voltage V on the electrodes for seven different values of V (N $\cong$ 40 shots for each value of V; the error bar in $\bar{n}$ is $\sigma/(N-1)^{\frac{1}{2}}$; σ = standard deviation).

The occurrence of restrikes on the electrodes is affected by the value of L_0. The purpose of these measurements was also to find the influence of restrikes behind the first current sheath on the axial-focus stage of this first sheath. The analysis of our data indicates that:

The correlation coefficient α_1 for n versus ν (ν = number of sharp peaks in the $|\dot{I}|$ signal from one discharge $\nu \cong 1-10$) is negative ($\alpha_1 = -0.45$) for low-voltage discharges (V $\leqslant$ 14 kV; number of discharges, about 50). The probability of non-significant random effects as a cause of this value of α_1 is < 0.1.

$\alpha_1 \cong 0$ (no correlation) for intermediate voltages (15 $\leqslant$ V $<$ 17 kV).

$\alpha_1 \cong 0.4$ (positive correlation) for a higher voltage (V $\geqslant$ 18 kV).

Similar behaviour was observed in the correlation coefficients for n versus ΣH_1, n versus ΣH_1^2, n versus $\Sigma H_i \Delta_i$, where H_i is the maximum value of the

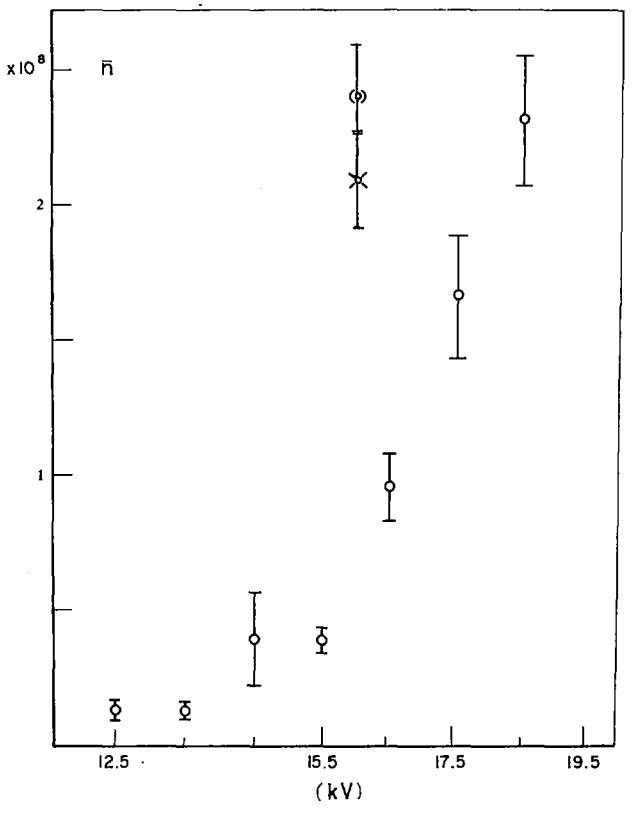


FIG. 7. The data points ○ give the mean value $\bar{n}$ of the neutron yield versus voltage for a 75-μF plasma focus with $L_0 = 60$ nH, (○) for the same system but a smaller external inductance ($L_0 = 40$ nH) and ⋉ for a smaller (45-μF) plasma focus. Electrode and insulator geometry is identical in all cases; the filling pressure, 6 torr of D_2 in all cases, is the observed optimum pressure (maximum neutron yield) for the 45-μF plasma focus at 16 kV.

i^{th} peak in $|\dot{I}|$, and Δ_i is the FWHM of this peak. For all discharges at 17.5 kV, a more detailed analysis was carried out. The steepness of the rise of the $|\dot{I}|$ signal versus time was evaluated for the first peak of $|\dot{I}|$ in a time interval from 150 ns before the $|\dot{I}|$ peak to peak time $t = 0$. $|\dot{I}|$ was fitted with $A\bar{t}^{\gamma}$; $\bar{t} \equiv (t(ns) + 150)/150$. The value of γ fitting best between 50 and 10 ns before the peak was derived for a group of high-yield discharges, $n = 3\ \bar{n}$, with a mean value $\bar{\gamma} = 4.5$, and for the group of all the other discharges ($0.1\ \bar{n} < n \leqslant 1.5\ \bar{n}$) with a mean value $\bar{\gamma} = 3.9$. This result is considered significant. The area ΔI_1 under the first $|\dot{I}|$ peak was also numerically estimated for these two groups of 17.5–kV discharges; ΔI_1 for the high-yield discharges (15% of all discharges at 17 X 5 kV) has the largest mean value; the ratio of the mean values of ΔI_1 of the two groups is = 8.5/6.5.

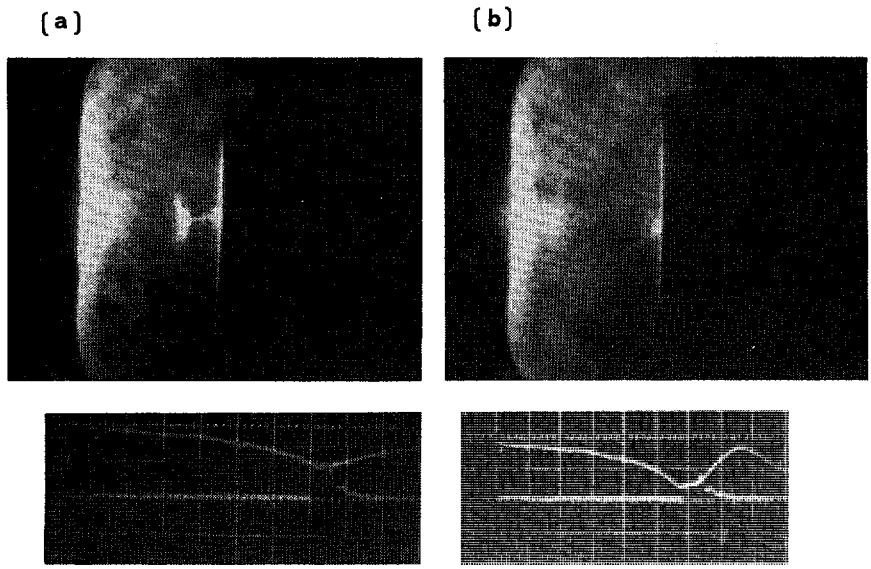


FIG.8. Image converter photograph by visible light (5 ns exposure).
Upper trace: dI/dt *(I = electrode current; sweep 100 ns·cm^{-1}).*
Lower trace indicates time at which photograph is taken (low-voltage discharge: 11 kV).
The picture (a) was taken at the time t_0 *of* |dI/dt| *peak; the picture (b) at a time* t_0+*100 ns.*

Low-yield discharges have $|\dot{I}|$ signals which frequently indicate the occurrence of restrikes at late times. A conclusion of these measurements is that in order to have a high-yield discharge at a relatively low voltage (and low speed of the current sheath) the production of a small number of electron beams corresponds to the optimization of the system. At a high voltage the reverse is true (the production of many beams seems to help avoid restrikes and to prevent the formation at a late time, ≈ 1 μs after the first discharge on the insulator, of another current sheath behind the first sheath.

Figure 8 shows images by visible light of two discharges at low voltage (45-μF system at 11 kV, 6 torr). Under these conditions the disruption of the current sheath is relatively slow, over a time interval $\geqslant$ 100 ns.

This provides a good opportunity to analyse the geometry of the axial pinch during the time of production of one electron beam. The time of production of the first electron beam coincides with the exposure time of the photograph in Fig.8(a). This indicates that the electron beam acceleration may occur in the disrupted region (dark area) of the axial column and it can be focussed in the neck of the pinch (different discharges usually have a different number of pinch neckings). The dark area can be considered as the gap of a plasma diode [11].

Figure 8(b), a different discharge, then shows that the 'electrode gap' distance (d) of this plasma diode is increasing with time.

Child's law ($\dot{J} = 2.34 \times 10^3 V^{3/2}\ d^{-2}$ ampère/cm^2) for a space-charge limited current can then be used to determine tentatively the electron current density $\dot{J}$ by knowing V, d or the beam accelerating voltage $\dot{V}$ by J, d (the length scale in Fig.8 is given by the profile of the centre electrode of diameter 3.4 cm). Any attempt to define a reliable effective parameter from this diode requires observations of a large number of discharges.

Child's law gives $V \lesssim 10$ volts for an observed value $d \approx 1$ mm (Fig.8) and an electron beam current $I_e < 10^5$ A ($Q < 10^{-3}$ Coulomb, from Table I). An observed value $V \gtrsim 300$ kV may indicate that Child's law is not valid in the electron-beam generating region and/or that the actual electron beam diameter is much smaller ($< 5-10\ \mu$m) than the electron-beam diameter estimate by time-integrated effects.

6. CONCLUSION

We estimate that at least $\approx 10^{12}$ ions are needed to produce a cluster of blisters as in Fig.2. About 10^4 of such clusters are produced in a single discharge by an ion burst with a duration ≈ 10 ns. The corresponding ion current is then $\approx 10^5$ A. The high-energy tail ($> 1-5$ MeV) of the ion spectrum can be revealed by neutron energy analysis [12] and by ^{27}Al(d,p)^{28}Al and ^{63}Cu(d,2n)^{63}Zn, ^{65}Cu(d,2n)^{65}Zn reactions [13]. The ion spectrum varies from shot to shot but specific features are observed by all discharges. From method (A) the number of deuterons N(E) as a function of the ion energy E has a well defined maximum N_m for 130 keV $\leqslant E \leqslant$ 320 keV. N(E) has a minimum at lower values of E and rises sharply again by further decreasing E. N(E) for $E \lesssim 50$ keV becomes substantially larger than N_m. N ($E \sim 1$ MeV) can still be as high as $\sim 0.1\ N_m$. The distribution of ion penetration range in Al yields by method (B) substantially the same spectrum as method (A). A second peak with maximum value N_M of N(E) for 15 keV $\lesssim E \leqslant 40$ keV is derived by method (B), which is most convenient for deriving the low-energy tail of the ion spectrum ($N_M \sim 9\ N_m$). A peak at the same energy ≈ 300 keV for both electron and ion spectra fits a particle acceleration process in which the same field accelerates both ions and electrons.

REFERENCES

[1] BOSTICK, W.H., et al., in Energy Storage, Compression, and Switching (Proc. Int. Conf. Turin, 1964),Plenum Press (1976) 261.

[2] BOSTICK, W.H., NARDI, V., PRIOR, W., Plasma Physics and Controlled Nuclear Fusion Research 1976 (Proc. 6th Int. Conf. Berchtesgaden, 1976) Vol.3, IAEA, Vienna (1977) 497.

[3] BOSTICK, W.H., NARDI, V., PRIOR, W., J. Plasma Phys. **8** (1972) 7.
[4] BOSTICK, W.H., et al., J. Nucl. Mater. **63** (1976) 356.
[5] SPENCER, L.V., Natl. Bureau of Standards, Monograph 1 (Sept. 1959); MOLEN, G.M., Aerospace Corp. Rep. (8 Apr. 1976).
[6] GROSS, B., J. Polymer Sci. **27** (1958) 138.
[7] BERGER, M.J., SELTZER, S.M., Tables of Energy Losses and Ranges of Electrons and Positrons, US Dept. of Commerce, Rep. N65-12606 (1964).
[8] LACKNER, H., KOHLBERG, I., NABLO, S.V., J. Appl. Phys. **36** (1965) 6.
[9] FUJITA, J., HIRAOKA, E., OKAMOTO, S., J. Appl. Phys. **37** (1966) 1873.
[10] O'DWYER, J.J., Theory of Dielectric Breakdown of Solids, Oxford Univ. Press (1964) p.111.
[11] NARDI, V., in Proc. 2nd Topical Conf. on Pulsed High-Beta Plasmas, Garching, 1972, p. 163;
NARDI, V., BOSTICK, W.H., PRIOR, W., Coll. Int. CNRS No.242, Physique Champs Magnétiques Intenses, Grenoble, 1974 (PAUTHENET, R., Ed.), (1975) 129.
[12] BOSTICK, W.H., NARDI, V., PRIOR, W., Plasma Physics and Controlled Nuclear Fusion Research 1974 (Proc. 5th Int. Conf. Tokyo, 1974) Vol.3, IAEA, Vienna (1975) 109.
[13] GULLICKSON, R.L., SAHLIN, H.L., J. Appl. Phys. **49** (1978) 1099, and literature quoted therein.

TURBULENCE CAUSED BY THE INTERACTION BETWEEN PLASMA AND ELECTRIC CURRENT IN THE FOCUS EXPERIMENT

A. BERNARD, J.P. GARÇONNET, A. JOLAS,
J.P. LE BRETON, J. DE MASCUREAU
Commissariat à l'énergie atomique,
Centre d'études de Limeil,
Villeneuve Saint-Georges,
France

Abstract

TURBULENCE CAUSED BY THE INTERACTION BETWEEN PLASMA AND ELECTRIC CURRENT IN THE FOCUS EXPERIMENT.

The microscopic instabilities which result from the intense electric current-plasma in the Focus experiment are studied, using laser light scattering for the purpose. The results confirm what was indicated by the magnetic-probe measurements, namely that a highly turbulent thin plasma accompanies the dense plasma layer during its implosion. It is shown that suprathermal density fluctuations occur with preferential directions of propagation. After a resistive phase the current circulates in the form of intense particle beams (electrons and ions). The electron beams are characterized by studying the X-radiation spectrum generated in two Mather-type facilities of 27 kJ and 340 kJ. In the same way, the properties of the deuteron beams in the two devices are estimated from their neutron emission. The evaluation indicates that powers in the terawatt range are attained in both the electron and the ion beams. Finally, an experiment is run in Filippov geometry and the results are compared with those obtained in Mather geometry.

1. INTRODUCTION

The importance of the Focus experiment as an intense source of particle beams has already been emphasized [1]. The electron beams give rise to X-ray emission by bombarding the anode of the discharge device and the deuteron beams create a neutron emission in the chamber gas which attains 10^{12} neutrons per shot in deuterium for the 340-kJ experiment in Mather geometry at the Limeil Research Centre. These beams are associated with the development of collective phenomena and the appearance of an anomalous resistance due to the electric current-plasma interaction. This resistance was demonstrated [2] by electrical measurements and magnetic probes. Figure 1 shows the structure of the current sheath when it reaches the axis of revolution of the chamber. A small part of the current is transported by the dense zone, but most flows into an extended zone of low density (denoted by the hatched curve in Fig.1). The electric singularity of the Focus experiment,

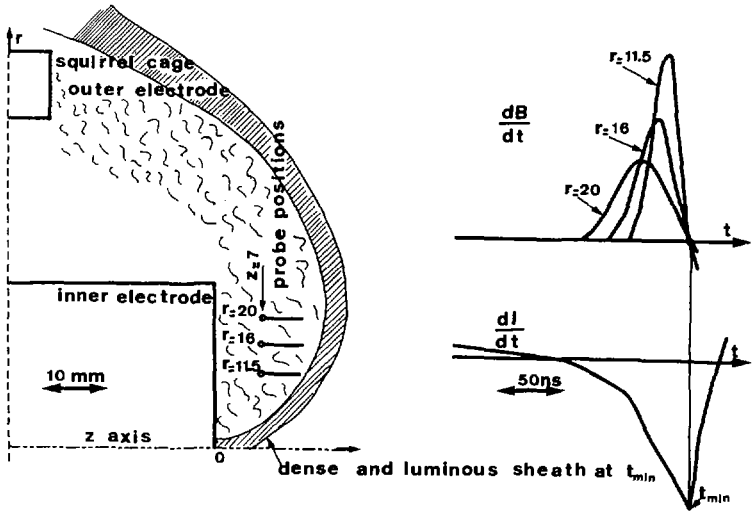


FIG.1. Structure of the current sheath determined by magnetic probes.

which reaches its maximum at the instant represented in Fig.1, is due to enhanced resistance leading to a diminution in current and an increase in the potential difference between the extremities of the plasma column. This resistance regime gives way to a different regime in which the current is transported essentially by intense beams of electrons and ions.

In the work reported here, using the Thomson-scattering diagnostic, we first study the microscopic instabilities which lead to the anomalous plasma resistivity. We then give the characteristics of the electron beam obtained with a 340-kJ bank and compare them with those of the ion beam. Finally, we present the observations made in Filippov geometry and compare them with those made in Mather-type devices.

2. STUDY OF DENSITY FLUCTUATIONS BY LASER LIGHT SCATTERING

We have already pointed out that the microscopic turbulence which develops in the final phase of a Focus discharge can be demonstrated and studied by the anomalous scattering of the light from a ruby laser [3, 4]. To characterize this turbulence, we measure the wave-number spectrum S(k) and the angular distribution $S_k(\theta)$ of the electron density fluctuations.

The measurements are performed in a 27-kJ, 40-kV Mather-type experiment (anode with flat end face, diameter 50 mm, length 250 mm, cathode in the form

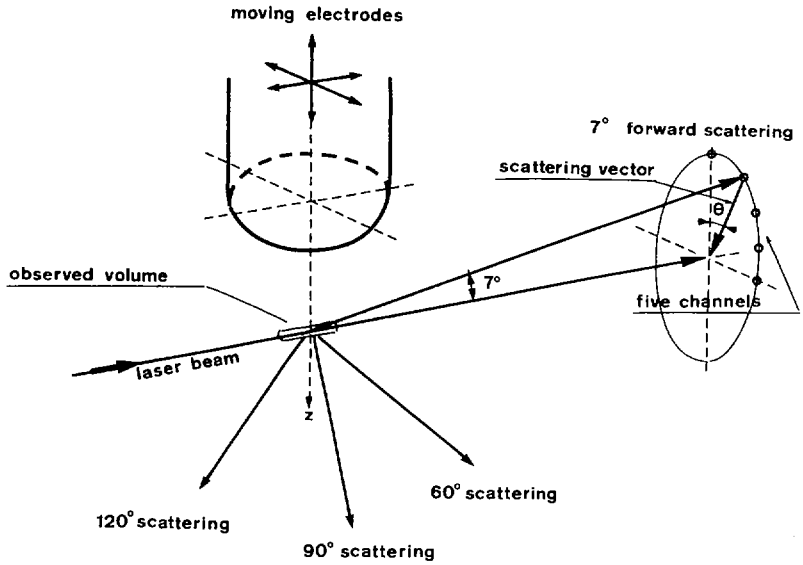


FIG.2. Schematic diagram of the experimental device for observing laser scattering.

of a squirrel cage 100 mm in diameter). The experimental device, described in detail in Ref.[3], was modified with a view to simultaneous observation of scattering at 7°, 60°, 90° and 120° to the direction of the incident laser beam, corresponding respectively to wave-numbers $k_{7°} = 1.1 \times 10^4\,cm^{-1}$, $k_{60°} = 9 \times 10^4\,cm^{-1}$, $k_{90°} = 1.3 \times 10^5\,cm^{-1}$ and $k_{120°} = 1.6 \times 10^5\,cm^{-1}$. In Ref.[4], we showed that density fluctuations were anisotropic by observing scattered light with scattering vectors parallel or perpendicular to the z-axis of the electrodes. For measurement of the angular distribution of density fluctuations at constant $|\vec{k}|$, the new assembly for 7° forward scattering is made up of five channels corresponding to different orientations of the scattering vector, its module $k = 1.1 \times 10^4\,cm^{-1}$ remaining the same. This system thus gives in a single shot the spectrum $n_e S_k(\theta)$ for a chosen plasma volume (θ is the angle between the scattering vector and the z-axis of the electrodes, and n_e is electron density). The observed region has approximately the form of a cylinder 10 mm long and 0.8 mm in diameter (Fig.2). The photoelectric detectors observe the scattered light without frequency resolution through 20-Å-wide interference filters centred on the wavelength of the ruby laser (6943 Å) and the calibration is performed in situ on the basis of Rayleigh scattering of sulphur hexafluoride. The device permits spatial study of the plasma thanks to a system of movable electrodes. The scattered signals are analysed with 2 ns time resolution carefully readjusted with photographs (1 ns exposure time), which enable the dynamics of the dense plasma to be followed,

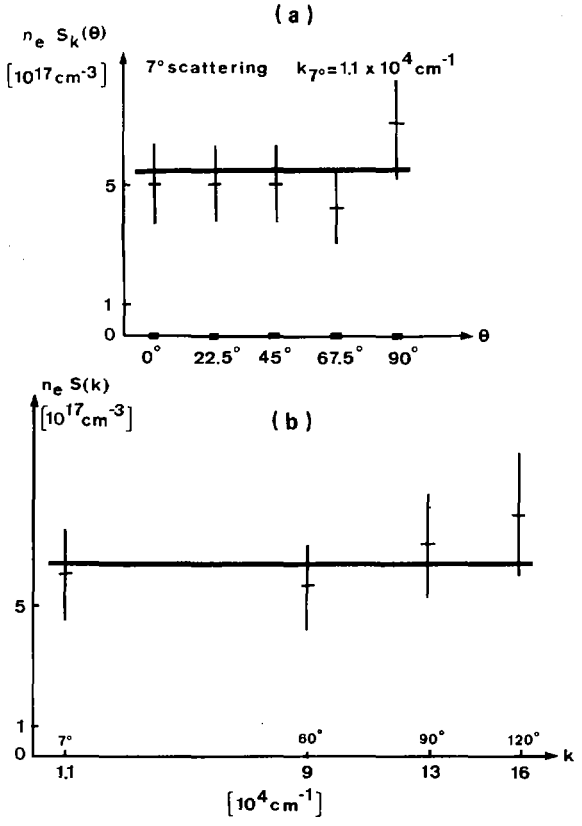


FIG.3. Scattering by the dense layer during implosion. (a) 7° scattering: spectrum $n_e S_k(\theta)$ (θ is the angle between the $\vec{z}$-axis and the vector $\vec{k}$); (b) wave-number spectrum $n_e S(k)$.

and with the electric signals V(t) and $\dot{I}(t)$, which depend on the electric impedance of the plasma.

The results presented in this paper refer to the region located at 10 mm from the anode and 12.5 mm from the axis of the electrodes (z = 10; r = 12.5), the discharge taking place in hydrogen at an initial pressure of 8 torr. We deliberately chose a relatively high pressure for this device because under these conditions the discharge dynamics are slower (implosion rate of the dense layer 1.6×10^7 cm·s^{-1}) and the scattered signals vary on a smaller amplitude scale; experimental use of the diagnostic is thereby facilitated. We obtain scattered signals when the dense and luminous layer crosses the observed region, but also before the layer reaches this region and after it has passed.

The scattered signals are different for these three situations, and we interpret the scattering obtained before and after passage of the dense layer as turbulent scattering, while the layer itself gives signals compatible with a thermalized plasma.

When the dense layer crosses the observed region at the instant of the laser pulse, we detect scattering signals which can be measured in all the observation channels. The $S_{k_7°}(\theta)$ spectrum is most often flat, although in some shots it exhibits a slight peak in the 0° or 90° direction (0° corresponds to $\vec{k}$ parallel to the z-axis and 90° to $\vec{k}$ parallel to the radial implosion rate v_r). Figure 3 gives an example of the results obtained for angular distribution $n_e S_k(\theta)$ with $k = 1.1 \times 10^4 \text{ cm}^{-1}$ and for wave-number spectrum $n_e S(k)$. It will be seen that $n_e S(k)$ is flat in the range considered, and this was verified in some twenty shots under the same conditions. The mean value obtained is $n_e S(k) = 0.7 \times 10^{18} \text{ cm}^{-3}$. Under the Salpeter theory for thermalized plasmas [5], this form of $n_e S(k)$ is possible only if the scattered signal is due to the ion component of the electron density fluctuations and if for all the directions of observation considered we have $1/k \geqslant 2\lambda_D$ (λ_D is the Debye length of the plasma). In our case, we can therefore put $1/k\lambda_D = 2$ for the 120° scattering. Let us assume equilibrium of electron and ion temperature ($T_e = T_i$); the theory will then give $S(k) = 0.5$, so that $n_e = 1.4 \times 10^{18} \text{ cm}^{-3}$. Consequently, $\lambda_D = 3.2 \times 10^{-6}$ cm and $T_e \lesssim 30$ eV. We can also consider decoupling of the electron and ion temperatures, $T_e > T_i$ or $T_e < T_i$. But under these two hypotheses we also find relatively low upper limits to the electron temperature, in accordance with the values determined earlier [3] from the frequency spectrum of the ion component and with those obtained by UV spectroscopy under vacuum.

When the dense layer is not in the field of observation at the instant of the laser pulse, we obtain scattered signals which are measurable only in the 7° channel. In the 60°, 90° and 120° channels the signals are lower than or equal to the detection threshold, which is $5 \times 10^{16} \text{ cm}^{-3}$ when the plasma's own light is taken into account. The amplitude of the signals scattered at 7° and the anisotropy as a function of orientation of $\vec{k}$ result in S(k) taking values much higher than unity, i.e. a suprathermal level of density fluctuations is established in the thin region of the plasma with predominant directions of propagation. The signals are detectable at r = 12.5 mm as soon as the dense layer attains r = 20 mm. Until the arrival of the layer the $S_k(\theta)$ spectrum retains the same bell shape of curve (Fig.4(a)), the maximum of which is found at the 45° direction. The maximum value of $n_e S(k)$ varies from 3×10^{17} to 10^{18} cm^{-3} depending on the particular shot. It will be noted that the 0° and 90° directions correspond to minima.

The signals are measurable at this point (r = 12.5, z = 10) while the layer gathers on the discharge axis, forming a filament, and even after the latter's dislocation. The shape of the $S_k(\theta)$ spectrum differs from that in the preceding cases, here exhibiting a maximum for the 0° or 22°30' direction, while the 90° direction remains the minimum (Fig.4(b)). The maximum value of $n_e S(k)$ varies between 5×10^{17} and $5 \times 10^{18} \text{ cm}^{-3}$.

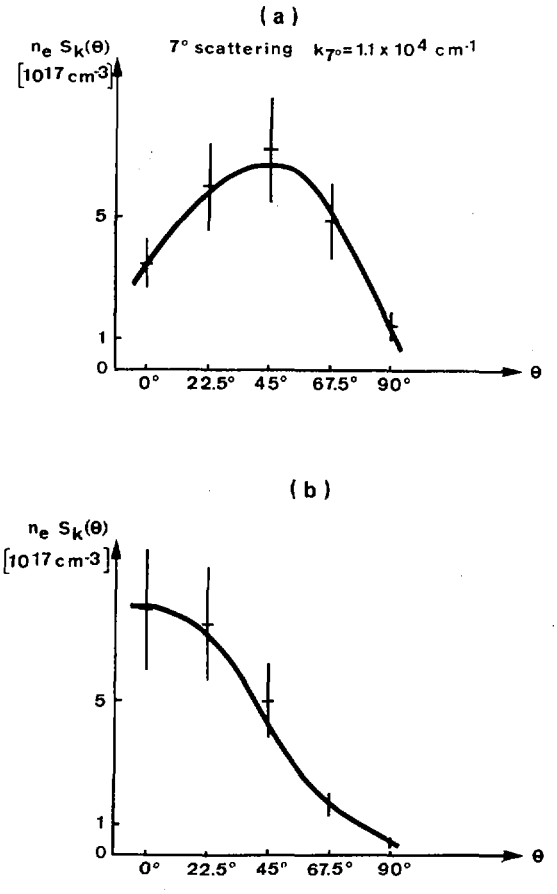


FIG.4. Angular distribution of density fluctuations $S_k(\theta)$. (a) Scattering before the dense layer; (b) scattering after the dense layer.

These results therefore confirm the magnetic probe measurements, which showed that the electric current circulated mostly outside the dense plasma layer [2]. We detect from the anomalous scattering that there is in fact a highly turbulent plasma in this zone. The angular distributions of the suprathermal density fluctuations are comparable with the angular distributions of accelerated deuterons which account for the neutron spectra [4] and the suprathermal microwave emission observed in another experiment [6].

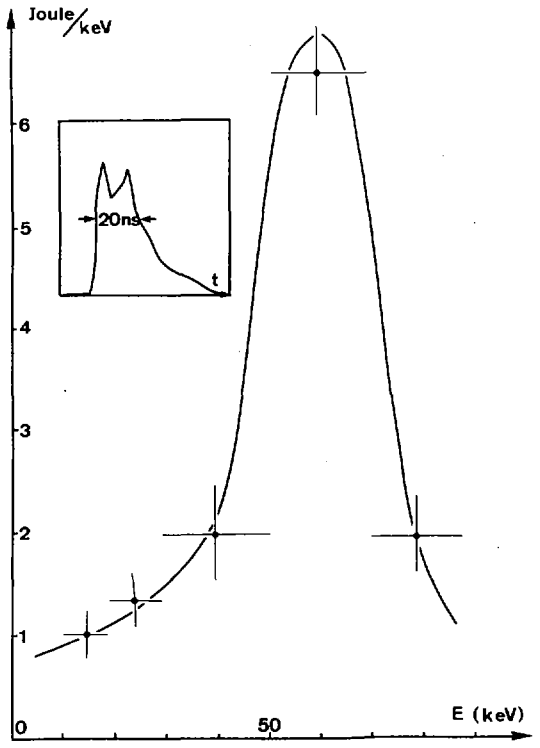


FIG.5. Spectrum of X-radiation emitted by the 340-kJ facility and evolution of the emission in time.

3. POWER OF ELECTRON AND ION BEAMS

3.1. Electron beams

When the electron beam interacts with the anode it generates a considerable amount of bremsstrahlung which can serve as a diagnostic tool for determining its power. Let us recall that the X-ray energy and spectrum were measured previously for a 27-kJ, 40-kV experiment [1]. The same study was performed with the 340-kJ, 40-kV bank. The operating conditions are quite different from those used to optimize neutron emission. The electrodes have the same diameters as before (anode ϕ 233 mm, cathode ϕ 313 mm) but are 650 mm long. The spectral and time characteristics of the X-ray emission are represented in Fig.5 for a standard discharge at an initial hydrogen pressure of 1 torr. The spectrum

TABLE I. CORRESPONDENCE BETWEEN ENERGY, V, OF ELECTRONS AND TOTAL ENERGY, W, CARRIED BY THE ELECTRON BEAM

Electron energy, V (keV)	Yield $\eta = 5.18 \times 10^{-5} V$	Facilities			
		27 kJ – 0.53 MA		340 kJ – 2.5 MA	
		Electron beam energy (kJ)	Electron beam current (MA)	Electron beam energy (kJ)	Electron beam current (MA)
50	2.59×10^{-3}	3.9	1.5	58	33
100	5.18×10^{-3}	1.9	0.4	29	8.2
200	1.04×10^{-2}	1	0.1	14.5	2
250	1.29×10^{-2}			11.6	1.3
300	1.54×10^{-2}			9.6	0.9

is determined by the Ross filter method with the use of lithium fluoride thermoluminescent detectors. The X-ray energy radiated in 4π is on average 150 J, with a duration of emission of 35 ns.

Although the interaction of an electron beam with a thick target is complex we can nevertheless make an approximate estimate of the beam energy by using the formula $\eta = 0.7 \times 10^{-6}$ ZV, where η is the ratio of radiated X-ray energy to beam energy, Z the atomic number of the target and V the energy in keV of the electrons, which are assumed to be monokinetic [7].

Table I gives the correspondence between the energy V of electrons in the beam, assumed to be monoenergetic, (first column) and the energy W, transported by the electron beam for the 27-kJ (third column) and the 340-kJ (fifth column) experiments. We can calculate power, $P = W/\tau$, because we know the mean duration of emission τ and hence the current, $I = P/V$, which is given in the fourth and sixth columns.

Although we cannot fully exclude particular phenomena which would locally generate currents higher than the discharge current, it seems more reasonable in Table I to consider only the lines leading to electron beam currents lower than the total current; this provides a lower energy limit. Moreover, analysis of the X-ray spectra by Ross filters gives the upper limit.

In the case of the 27-kJ device, we obtain for V = 100 keV: E = 1.9 kJ; I (electrons) = 0.4 MA; $P = 3.9 \times 10^{10}$ W. The current value is acceptable, while the 100-keV value is slightly high if we compare it with the experimental results of Ulrey [8], who found a maximum of the X-ray spectrum at 25 keV for V = 50 keV. But, of course, the Focus electron beam is certainly not monoenergetic. It will nevertheless be seen that by taking this approximation, we are limited to a relatively narrow range, $60 < V < 100$ keV, with a power of some 10^{10} W.

Similarly, X-ray measurements in the 340-kJ experiment lead to the choice of the following values: $200 < V < 300$ kV; $10 < E < 15$ kJ; $0.4 \times 10^{12} < P < 0.8 \times 10^{12}$ W.

3.3. Ion beams

Earlier studies [1,9] showed that more than 80% of the neutrons are emitted by a mechanism of thick-target bombardment in devices with Mather geometry. The 27-kJ facility emits 5×10^9 neutrons for a total current of 0.53 MA and the 340-kJ facility 6×10^{11} neutrons for a 2.5-MA current. In a thick target the neutron flux per incident deuteron is given by the formula

$$Y(V) = \int_0^V [\sigma(V)/\epsilon(V)]\,dV$$

where V is the energy of the deuteron, σ the total cross-section of the nuclear reaction $D(d,n)^3He$, and ϵ the stopping cross-section of the target [10]. Assuming a beam of monoenergetic ions of energy V, we can set up Table II. For each of the facilities considered, the table gives the ion beam energy and the corresponding ion current, the mean beam duration being taken as 50 ns.

Table II shows that an energy of about 60–70 keV is compatible with the current in the 27-kJ experiment. In the case of the 340-kJ facility we have to choose a much higher energy, about 200–300 keV and then find a power between 0.6 and 1 TW. These values are close to those found for the electron beams, which tends to indicate that the same phenomena accelerate both electrons and ions. Let us note, however, that the results presented correspond to two points of operation of the facility, optimized either for electron beams or for ion beams.

These results are only a first approximation because the model of deuteron slowing-down in a cold target used here is probably quite far from reality; likewise the 50-ns beam duration is merely an estimate from the results obtained in a CD_2 target [9].

TABLE II. CORRESPONDENCE BETWEEN ENERGY, V, OF IONS AND TOTAL ENERGY CARRIED BY THE ION BEAM

Ion energy V, (keV)	Yield Y(V) (neutron per deuteron)	Facilities			
		27 kJ – 0.53 MA		340 kJ – 2.5 MA	
		Ion beam energy (kJ)	Ion beam current (MA)	Ion beam energy (kJ)	Ion beam current (MA)
30	2.5×10^{-9}	5.8	3.9		
50	1.1×10^{-8}	2.2	0.8		
70	3×10^{-8}	1.1	0.3	220	62
80	4.6×10^{-8}	0.8	0.2		
100	8×10^{-8}	0.6	0.12	120	24
200	4×10^{-7}			48	4.8
300	1×10^{-6}			28	1.9

4. OPERATION IN FILIPPOV GEOMETRY

From the outset of the study it has been recognized that close similarities exist between experiments performed in Mather geometry and those in Filippov geometry. The interpretations differ, however, on the vital point of neutron emission. In the case of the Mather experiments, it has been shown by concordant results from numerous measurement methods that neutrons are emitted by the acceleration of a beam of deuterons which bombard ions and atoms of deuterium present in the chamber. In Filippov geometry, on the other hand, the neutrons are said to be emitted for the most part by a thermonuclear plasma [11,12]. We therefore thought it would be instructive to compare these two modes of operation. For that purpose, we developed an experiment with characteristics very close to those described in Ref.[11].

The anode and cathode diameters are 400 and 540 mm, respectively; the anode is 114 mm long and the anode-to-cathode distance 70 mm. It had been thought that the nature of the insulator [13] might cause a change in the plasma characteristics, and to elucidate this point the same chamber was operated first

with a Pyrex glass and then with a ceramic (99.7% purity) sleeve. The experiment uses a 164-μF condenser bank charged to 35 kV. The maximum current is 1.4 MA. The filling pressure is 1.8 torr of deuterium, which, judging by the literature, is relatively high for a Filippov device and therefore most likely to provide thermonuclear neutron emission.

The plasma was studied by several diagnostic methods: a streak camera and a 1-ns integral-image camera in visible light, an X-ray and neutron detector consisting of a scintillator coupled to a fast photomultiplier, a silver-activation neutron detector placed at 90° to the discharge axis, as well as magnetic probes. The principal results are as follows:

(a) Neutron emission attains the value of 2×10^{10} which corresponds to a Mather device operating under high pressure conditions;

(b) The photographs obtained with an integral-image camera (Fig.6(a)) and a streak camera (Fig.6(b)) show a highly indented luminous front with a speed varying from 1.6 to 2.5×10^7 cm $\cdot$ s^{-1}. After the first focussing on the axis a second compression occurs, the delay between the two being 80 ns. This operation was observed generally in the case of the Mather devices, with similar delays when the filling pressure was high.

(c) When a magnetic probe [2] is placed opposite the insulator in the interelectrode space, we find that the current sheath has a double-peak structure, as is the case with most Mather experiments. The width of this structure is about 20 mm.

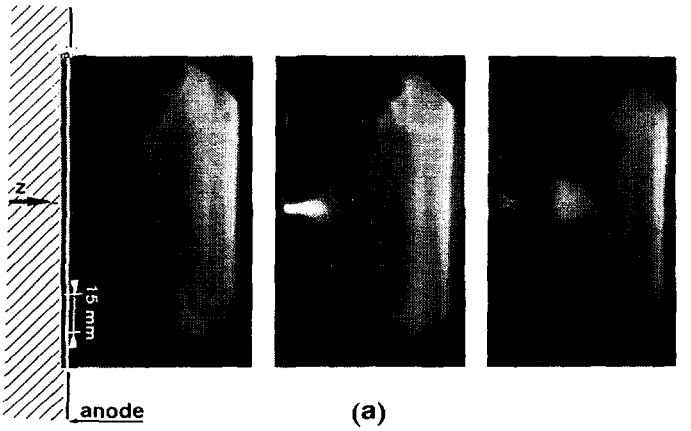
(d) The time-derivative signals of the neutron emission (Fig.6(c)) exhibit variations in shape from shot to shot, which also appear frequently in Mather geometry.

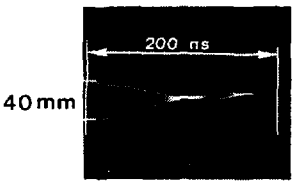
(e) There are no characteristic differences between the glass and the ceramic sleeves.

In short, no significant difference was demonstrated between the Mather and the Filippov experiments. All the results obtained with the Filippov assembly correspond to identical past observations on discharges in Mather geometry.

In view of these results it was not considered necessary to continue the study with other diagnostic methods and to repeat fully the longer and more delicate measurements performed earlier in the Mather geometry experiments.

We have found in our facilities, furthermore, that operation in Mather geometry gives better reproducibility and is more stable than operation in Filippov geometry. This can probably be attributed to the value of the ratio between total current and anode diameter. During experiments on extrapolation in Mather





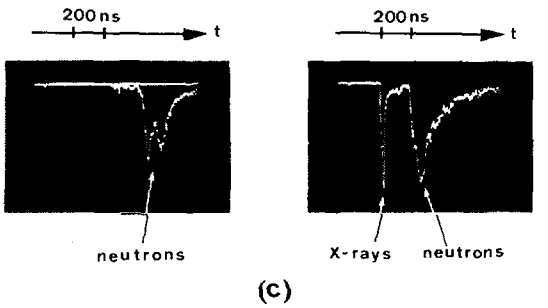


FIG.6. Filippov geometry. (a) Discharge photographs (1 ns exposure time); (b) radial implosion observed with a streak camera; (c) two examples of evolution in time of neutron emission.

geometry it was observed that if this ratio was too low operation became less satisfactory. Probably, the current density is not sufficient for a regular current sheath to form at every discharge.

5. CONCLUSION

To understand the complex phenomena involved in electric discharges of the Focus type we need to make a direct study of the microinstabilities – something which can be done effectively with the laser scattering diagnostic. Although the measurements presented here are far from final, they already show that wave excitations occur preferentially in certain directions. This point is very important in view of the fact that these directions are close to those of the deuteron beams which give rise to the neutron emission. These directions are demonstrated likewise by the plasma emission in the microwave range.

The laser scattering measurements confirm the magnetic probe results: that behind the dense front there is a lower density zone. This zone, which transports most of the current, seems to be very turbulent. Because of their very good spatial resolution the scattering measurements have also enabled us to discover another high-turbulence zone in front of the dense layer.

We have often stressed the close similarities found between all experiments where the current circulates along the axis (Z-pinch geometry), when the operating regimes allow microscopic instabilities to develop (the critical parameter connected directly with the electron-ion drift velocity is the filling pressure in the Focus experiments, the wire diameter in the exploded-wire experiments and the quantity of matter removed from the anode in vacuum sparks). Accordingly it is not surprising to find similar results in both the Mather and Filippov geometries used for the Focus discharges.

It had earlier [1] been calculated that an electric power of about 10^{12} W was available in a Mather experiment operating with a 340-kJ bank. The estimates made in this paper with the help of X-ray and neutron measurements show that the powers transferred to the electron and ion beams are quite similar. This physical phenomenon, which is observed in a wide current range, should be considered with interest for all applications where it is desired to have powers still higher than those obtainable at present. For the Focus experiments it is not necessary to store energy at a very high voltage; besides, it has been experimentally established that with an increase in current the energy transfer occurs in shorter time. One of the points which deserve to be studied in greater depth is on what target dimensions these beams can be concentrated.

REFERENCES

[1] BERNARD, A., COUDEVILLE, A., GARÇONNET, J.P., JOLAS, A., de MASCUREAU,J., NAZET, C., "Structure of current sheath and fast-particle beams in the Focus experiment", in Plasma Physics and Controlled Nuclear Fusion Research 1976 (Proc. 6th Int. Conf. Berchtesgaden, 1976) Vol.3, IAEA, Vienna (1977) 471.

[2] BERNARD, A., COUDEVILLE, A., GARÇONNET, J.P., JOLAS, A., de MASCUREAU,J., NAZET, C., in Proc. 8th Europ. Conf. Controlled Fusion and Plasma Physics, Prague, 1977, Vol.1 (1977) 64.

[3] BERNARD, A., COUDEVILLE, A., JOLAS, A., LAUNSPACH, J., de MASCUREAU, J., Phys. Fluids **18** (1975) 180.

[4] BERNARD, A., et al., "Etude de l'émission neutronique et de la turbulence dans l'expérience Focus avec une résolution temporelle de l'ordre de la nanoseconde", Plasma Physics and Controlled Nuclear Fusion Research 1974 (Proc. 5th Int. Conf. Tokyo, 1974) Vol.3, IAEA, Vienna (1975) 83.

[5] SALPETER, E.E., Phys. Rev. **120** (1960) 1528; EVANS, D.E., KATZENSTEIN, J., Rep. Prog. Phys. **32** (1969) 207.

[6] HERZIGER, G., KROMPHOLZ, H., MICHEL, L., SCHÖNBACH, K., Phys. Lett. **64** (1977) 51.

[7] EVANS, R.D., The Atomic Nucleus, McGraw-Hill (1955) 617.

[8] ULREY, C., Phys. Rev. **11** (1918) 401.

[9] BERNARD, A., COUDEVILLE, A., GARÇONNET, J.P., JOLAS, A., de MASCUREAU,J;. NAZET, C., CEA Note 1945 (1976).

[10] COON, J.H., Fast Neutron Physics, Pt.1(MARION, J.M., FOWLER, J.L., Eds), Interscience Monographs and Texts in Physics and Astronomy Vol.4 (1969) 677–720.

[11] MAISONNIER, C., PECORELLA, F., RAGER, J.P., SAMUELLI, M., Proc. 5th Europ. Conf. Controlled Fusion and Plasma Physics, Grenoble, 1972, Vol.2, p.183.

[12] GRIBKOV, V.A., KROKHIN, O.N., SLIZKOV, G.V., FILIPPOV, N.V., FILIPPOVA, T.I., JETP Lett. **18** (1973) 5.

[13] BERNARD, A., in Proc. 3rd Topical Conference on Pulsed High-Beta Plasmas, Culham, 1975, Pergamon, Oxford (1976).

RECENT PLASMA FOCUS RESEARCH

A. BAÑUELOS, H. BRUZZONE*, R. DELELLIS+,
J. GRATTON*, R. GRATTON*, H. KELLY+,
M. MILANESE+, J. POUZO+, F. RODRÍGUEZ TRELLES*
Laboratario de Física del Plasma,
Facultad de Ciencias Exactas y Naturales,
Universidad de Buenos Aires,
DIGID, Ministerio de Defensa,
Buenos Aires, Argentina

Abstract

RECENT PLASMA FOCUS RESEARCH.

It is shown that the recently reported high pressure limit for the operation of Mather-type plasma focus devices makes discrimination difficult between the scaling laws proposed for the neutron yield. On the basis of experimental results, it is suggested that this limit may explain some well-known contingencies in neutron production. Finally, problems related to the interpretation of X-ray anisotropy measurements in the plasma focus are discussed.

1. REMARKS ON SCALING LAWS PROPOSED FOR PLASMA FOCUS DEVICES

It is generally accepted that the neutron yield $\overline{N}$ of plasma focus (PF) devices scales as a power law of the current intensity $\overline{N} \sim I^{\alpha}$ $(3.3 \leqslant \alpha \leqslant 5)$ [1, 2]. On the other hand, some of us have previously pointed out [3] that a relationship $\overline{N} \sim E_p^{\beta}$ also fits the experimental results in spite of the fact that I and $E_p = \frac{1}{2} \int \dot{L} I^2 dt$ (the electromechanical work performed by the magnetic pressure on the current sheath during the coaxial stage) are, a priori, independent quantities.

The reason why present experiments cannot discriminate between these two laws lies in the existence of a high pressure limit (HPL) for PF devices [4]. This limit constrains almost all the existing devices to a range of parameters where both power laws are essentially equivalent. As we think that, for this reason, experimental discrimination between both scaling laws becomes difficult, we shall discuss this point in some detail. For this, it is very useful to use a set of analytical formulae which, at the cost of some non-essential approximations, furnishes easily manageable relationships between the electrical and mechanical parameters of Mather-type PF during the coaxial stage [5].

---

* Member of the Consejo Nacional de Investigaciones Científicas y Técnicas (CONICET), Argentina.

+ Fellow of CONICET.

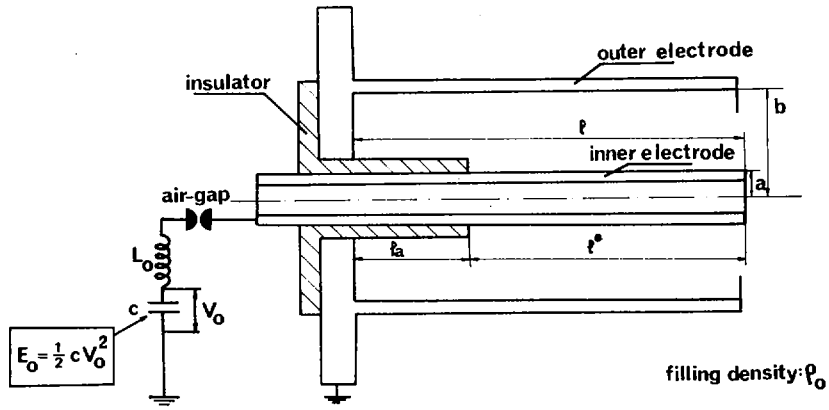


FIG.1. Definitions of parameters and symbols.

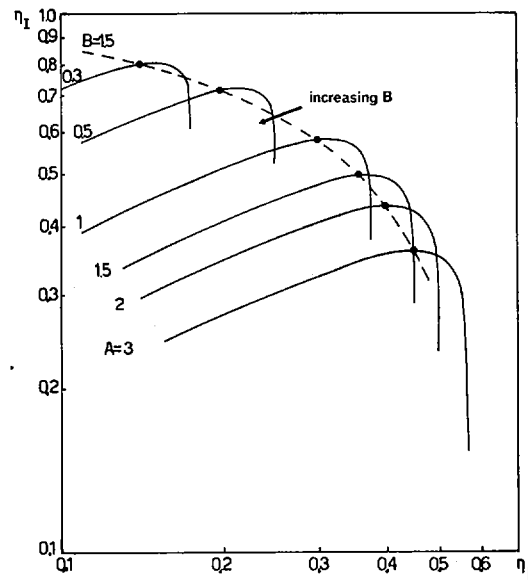


FIG.2. η_I versus η_p, with A as a parameter.

As shown in Ref. [5], it is possible to express the quantities $\eta_p = E_p/\frac{1}{2} CV_0^2$ and $\eta_I = I/I_{cc}$ (I_{cc} = short-circuit peak current), both evaluated at the end of the coaxial stage, in terms of two dimensionless parameters, A and B, which completely define the device and its operating regime. The corresponding expressions are (in MKS units):

$$A = \frac{\mu_o}{2\pi} \frac{\ell^* \ln(b/a)}{L_o + (\mu_o/2\pi)\, \ell_a \ln(b/a)}$$

$$B = \frac{\mu_o}{8\pi^2 \rho_o} \left(\frac{C\, V_o}{a\, \ell^*}\right)^2$$

$$\eta_p = \frac{A}{1+A} \frac{\sqrt{B} - 1/3}{B}$$

$$\eta_I = \frac{2}{1+A} \left[\frac{\sqrt{B}(1+A/2) - (1/2+A/3)}{2B}\right]^{1/2}$$

All symbols are defined in Fig. 1.

Since both η_I and η_p have maxima as functions of B (η_I for $B \approx 1.5$ and η_p for $B = 4/9$) we can distinguish three regimes (recall that $B \sim \rho_0^{-1}$ for a given device):

(a) Low pressure ($B > 1.5$): In this regime both quantities increase as the pressure increases.

(b) Intermediate pressure ($4/9 \leqslant B \leqslant 1.5$): In this regime η_p decreases as the pressure increases.

(c) High pressure ($B < 4/9$): Here both quantities decrease with the increasing pressure.

In Fig. 2 we give η_I versus η_p with A as a parameter. For clarity, curves of equal B are not shown, with the exception of the important case $B = 1.5$. From this figure one can see that in the regime (a) the relation $\eta_p = \eta_I^\gamma$ holds at fixed A with $\gamma \approx 2.2$.

Hence, for a given device, $E_p \sim E_0 (I/I_{cc})^\gamma = I^\gamma E_0^{1-\gamma/2}, L_0^{\gamma/2}$, so that the law $N \sim I^\alpha$ is essentially equivalent to the law $N \sim E_p^\beta$ with $\alpha = 2.2\,\beta$. On the other hand, different devices usually have similar values of A and L_0 and, since the exponent of E_0 in the above expression is very small, the relationship $E_p \sim I^\gamma$ holds approximately.

A preliminary analysis (not reported here because of space limitations) shows that practically none of the present devices can operate below $B = 1.5$ owing

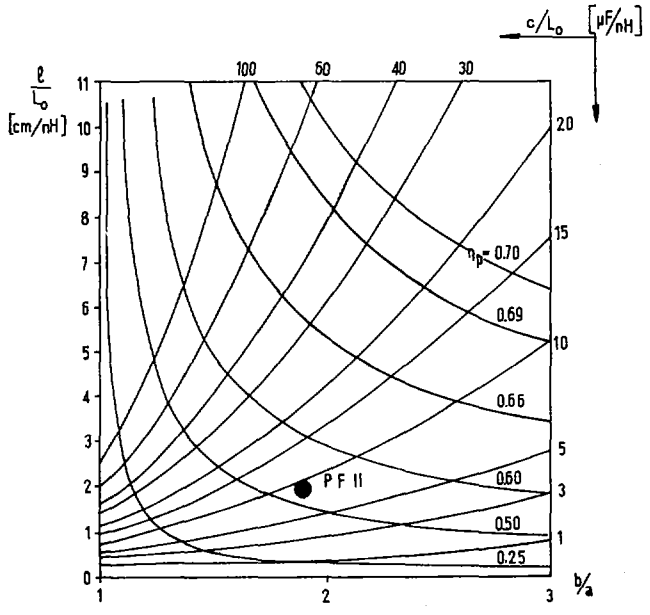


FIG.3. The parabola-like curves give the lower limit of condition (1) for B = 4/9 and different values of C/L_0 [μF/nH]. *The hyperbola-like curves correspond to* η_p *(B = 4/9) = constant.*

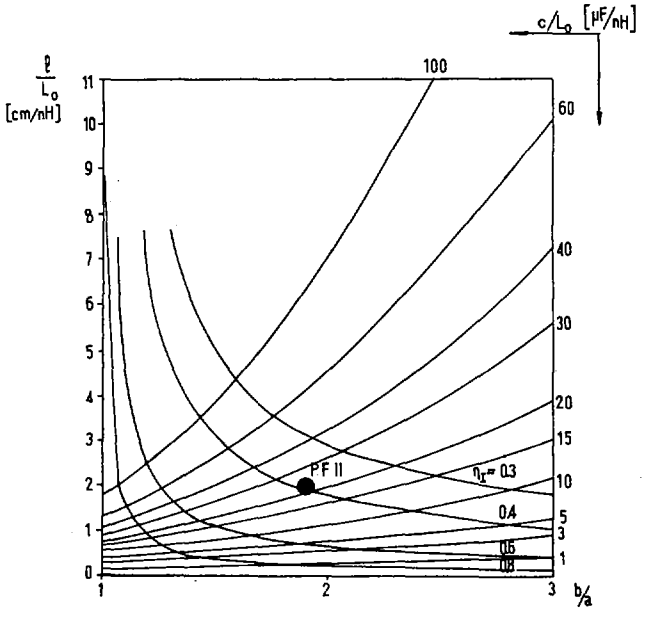


FIG.4. The parabola-like curves are similar to those of Fig. 3, but for B = 1.5. The hyperbola-like curves correspond to η_I *(B = 1.5) = constant.*

to the above HPL. For this reason, both quoted scaling laws fit the experimental results well. As another important consequence of this limitation, the maximum neutron yield is always obtained for a filling pressure p_{max} just below the HPL, because when p increases, both I and E_p increase and therefore N also increases until it drops as an effect of the HPL. This circumstance provides a possible interpretation of a result reported by Rapp [6], who suggests the constancy of the combination $E_0/(p_{max}\,\ell)$. We recall that the HPL is approximately given by [4]

$$\frac{E_p}{2M} \geq 1.5\epsilon_i \tag{1}$$

where M is the swept mass and ϵ_i the specific ionization energy of the filling gas. Hence, if p_{max} corresponds to the equality in (1), we get

$$\frac{E_p}{2M} \sim \frac{E_p}{p_{max}\,\ell} \sim \eta_p \frac{E_o}{p_{max}\,\ell} \tag{2}$$

Since η_p in Ref. [6] remains nearly constant within the working range of the apparatus, we conclude that Rapp's observations are a particular case of (2).

We now discuss the design of a PF device able to operate in the very interesting regime (b) within the limits imposed by (1).

If $\ell_a \ll \ell$ (see Fig. 1) the formulae given in Ref. [5] can be used to rewrite (1) in the form:

$$\frac{\ell}{L_o}\left[\frac{cm}{nH}\right] \geq \frac{0.01\ y\ (x^2-1)}{\sqrt{B-1/3}}\left[1+\sqrt{1+\frac{100\ (\sqrt{B-1/3})}{y\ (x^2-1)\ \ln x}}\right] \tag{3}$$

where

$$x = b/a;\quad y = C/L_o\ [\mu F/nH]$$

In Fig. 3 we plot parabola-like curves representing the lowest allowed values of ℓ/L_0 in terms of b/a (Fig. 1) with C/L_0 as a parameter and B = 4/9. In Fig. 4 similar curves for B = 1.5 are given. We can see that a higher B results in less restrictive conditions.

However, mere fulfilment of condition (1) is not sufficient; it is also necessary to design the experiment in order to achieve relatively high maximum values for both η_p and η_I. Otherwise, the resulting η_p versus p and η_I versus p curves would be very smooth with broad maxima, and hence the experiment will be useless for the desired discrimination. Unfortunately this leads to contradictory requirements, as can be seen from Figs 3

and 4, where the hyperbola-like curves correspond to η_p = const. and η_I = const., respectively. However, it is possible to reach a reasonable compromise in which η_p for B = 4/9 and η_I for B = 1.5 are both near 1/2.

As an example, we indicate in Figs 3 and 4 the point corresponding to the parameters of our PF II, a device which will start operation during the coming months. The parameters have been selected so that the apparatus will work in the pressure range of 1–10 torr (deuterium).

2. A POSSIBLE INTERPRETATION OF SOME APPARENTLY ERRATIC VARIATIONS OF THE NEUTRON YIELD IN TERMS OF THE HPL

It should be noticed that the value of ϵ_i in (1) is not always determined straightforwardly because it depends critically on the presence of even very small amounts of heavy contaminants. Consequently, ϵ_i may take values above 0.7 $MJ \cdot g^{-1}$, corresponding to pure deuterium, which is the minimum value that can reasonably be assumed in PF experiments. We suggest that some erratic variations that are usually observed in the neutron yield may be related to adsorption-desorption processes at the electrode surface, which can push the apparatus out of the region of validity of (1) in an uncontrolled way, even when the filling pressure is kept constant. These processes may produce considerable changes in ϵ_i while keeping the general features of the discharge and the dynamics of the CS practically unchanged.

In particular, we deal with observations related to some unexpected variations in the neutron yield of a small plasma focus (our PF I, E_0 = 0.87 kJ) [7].

As is well known, the average yield $\overline{N}$ for apparently fixed working conditions (specifically electrodes, insulator and filling pressure) is usually two or three times less than the yield obtained in the best shots. Another known fact, probably related to this, is that during a considerable number of shots performed after the electrodes have been exposed to the atmosphere, N is low and fluctuates strongly. During this first sequence of discharges, sometimes called conditioning,N increases on the average until a steady behaviour is attained. Data reported on these facts are scarce and usually merely qualitative; additional information would therefore be useful for improving the performance and reproducibility of PF devices.

Here we analyse the data from several hundred discharges, for electrodes made of (a) OFHC copper, (b) brass, and (c) standard copper. In every discharge we have measured N and recorded I. Side-on IC pictures were also taken. Striking differences in the behaviour of N and $\overline{N}$ were observed:

(a) With OFHC copper, after a long conditioning (some 100 discharges), a steady behaviour is reached, with the best N (2.4×10^7) at 2.4 torr (D_2); yields from individual shots fluctuate within a factor of ~ 3 around $\overline{N}$.

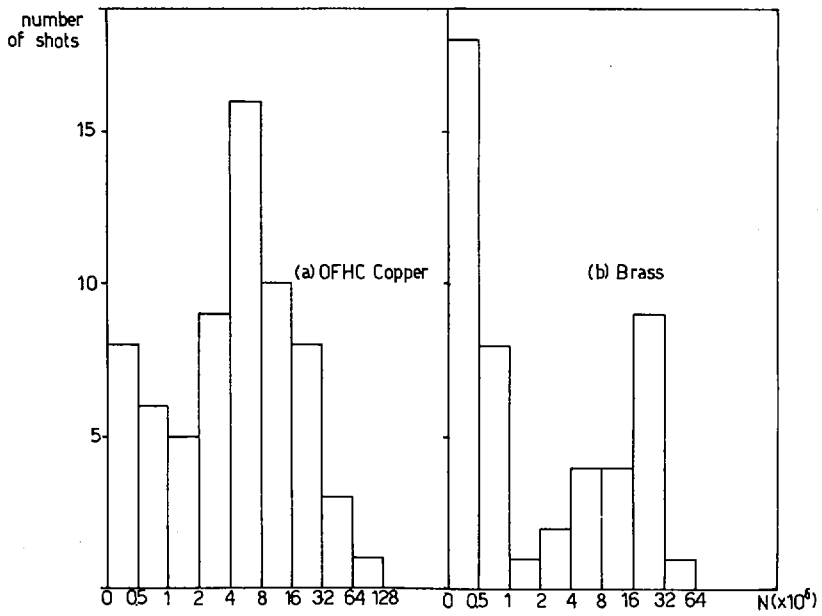


FIG.5. Histograms of the neutron yield for case (a) OFHC copper electrodes and case (b) brass electrodes.

(b) In the case of brass electrodes, a different steady behaviour is achieved after a very short conditioning (~ 5 shots). There is a marked tendency for shots with a high N to be followed by very low yield shots, and vice versa, so that a peculiar alternating behaviour results. This alternation is completely unaffected by replacement of the filling gas and flushing of the vacuum chamber. The best value of N (1.0×10^7) is obtained at approximately the same pressure as in the previous case. Figure 5 shows histograms of N for cases (a) and (b) corresponding to sequences performed after conditioning.

(c) Finally, with a gun of standard copper, we get detectable (~ 10^5) yields only after 70 shots. A subsequent series of 350 shots gave the best N (7×10^6) at 0.4 torr and very low values of N at higher pressure, with a large spread.

We pay special attention to the peculiar alternating behaviour observed with the brass electrodes. A statistical analysis shows clearly that random fluctuations should be definitively ruled out as a possible explanation. An interesting additional fact is that the $\dot{I}$ focus spike is delayed about 50 ns in the 'bad' ($N < 10^5$) shots as compared with the 'good' ($N > \bar{N}$) ones, thus suggesting that in the 'bad' shots a certain amount of relatively heavy ions, coming from the electrode surface (not from a bulk contamination of the gas, since flushing does not modify the effect)

interact with the CS. An estimate of the amount of heavy ions required to account for the delay is consistent with what should be expected from the removal of a monoatomic layer. For instance, if the heavy contaminants were oxygen ions, the observed delay could be explained by a 2.5% particle contamination, by assuming that the time of focus formation t_f depends on the mass density ρ_0 of the gas as $t_f \sim \rho_0^{1/4}$ [8]. On the other hand, the same contamination may produce an increase of ϵ_i by an appreciable factor. We explain the alternation of high-and-low-yield shots as follows: in a 'good' shot, high-energy particles impinge on the chamber walls (Pyrex) and liberate gases which are later absorbed on the electrodes. Therefore, the subsequent discharge results in a 'bad' focus, but at the same time cleans the electrodes, reproducing the conditions required for a good focus.

Of course, the remarkable alternating behaviour observed in this case may be hidden in other devices with different parameters. For instance, if the contamination induced by a single focus is not enough to make ϵ_i so large that condition (1) is reversed, a completely different behaviour may occur and the cyclic regularity may well be lost. However, our results seem to suggest that adsorption-desorption at the electrode surfaces may be partially responsible, through condition (1), for the apparently erratic variation of N in PF devices.

3. DETERMINATION OF ELECTRON BEAM ENERGIES AT THE FOCUS FROM X-RAY ANISOTROPY MEASUREMENTS

The numerous observations of the hard X-rays ($h\nu > 100$ keV) produced during the focus stage of the discharge in a Mather-type coaxial accelerator have proved the existence of high-energy electron beams directed along the electrode axis [9–11]. Analysis of the angular distribution of medium-energy X-rays ($5 < h\nu < 50$ keV) leads to the conclusion that electron beams of lower energies are also present in the focus. Here we discuss two sets of measurements performed under different conditions:

(a) Data obtained at the Stevens Institute of Technology (SIT) [12], with a hollow-anode PF (5 kJ at 15 kV) filled with 8-torr D_2. The emission at 0° and 78° from the axis was recorded by a pinhole camera ($\delta\Omega \approx 10^{-6}$ sr) with a 51-μm Be filter. Film density values (on Kodak RPR) from highly localized ($\delta r < 100$ μm) and extended sources ($\delta r \approx 1$ mm) have been measured for discharges in pure D_2.

(b) The recent results reported in Ref. [11], where the energy flux from extended sources ($\delta r \approx 3$ mm) was measured at $\phi = 0°$, 15°, 30°, 45°, 60° and 80° from the axis by TL diodes (type 400, $\delta\Omega \approx 10^{-2}$ sr) through a 2-mm-thick Al wall. The X-ray source was the NASA Langley Focus I (NASA: solid anode; 25 kJ at 20 kV) filled with pure D_2 at about 5 torr.

TABLE I. ELECTRON BEAM ENERGIES FROM X-RAY ANISOTROPY MEASUREMENTS

Reference	SIT	SIT	NASA	NASA	NASA	NASA	NASA
Typical size (mm)	0.1	1	3	3	3	3	3
Pressure (torr)	8	8	5	5	5	5	5
ϕ (°)	78±1	78±1	15±4	30±4	45±4	60±4	80±4
A_{obs} (ϕ)	2.16	1.21	1.19	1.83	2.25	2.37	2.45
U(keV)	5±5	18±8	40±10	36±9	43±11	54±13	62±15
E_o (kJ)	5	5	25	25	25	25	25
$A_{em}(\phi)$	1.55	1.52	1.04	1.13	1.26	1.35	1.51

Table I shows the observed anisotropy ratios from these experiments, which are related to the emitted intensity by

$$A_{obs}(\phi) = \frac{\int_o^U dx\ I_\phi(U,x/U)\ S(x)\ T(x)}{\int_o^U dx\ I_o(U,x/U)\ S(x)\ T(x)} \qquad (4)$$

where I_ϕ is the energy intensity emitted at an angle ϕ from the axis (as defined in Ref. [13], e.g. $x = h\nu$ is the photon energy), S(x) is the detector sensitivity and T(x) is the filter transmission [14]. We assume that the radiation originates in the bremsstrahlung from a beam of electrons, all of energy U, colliding with the ions ($n_i \gtrsim 10^{19}$ cm^{-3}) located in front of the anode.

For $8 < U < 60$ keV the values of I_ϕ can be obtained by Sommerfeld's non-relativistic formulae. A fast numerical code [15] based on a series expansion of I_ϕ [13] has been used to calculate U from the observed anisotropy ratio $A_{obs}(\phi)$. Values of this beam energy are given in Table I, where we have also evaluated the energy ratio actually emitted, defined as

$$A_{em}(\phi) = \int_0^U dx\ I_\phi\ (U, x/U) \Big/ \int_0^U dx\ I_0 (U, x/U) \qquad (5)$$

The sensitivity S(x) for NASA values has been estimated in Ref. [11] for $15 < x < 50$ keV. For the treatment of SIT values we have taken $S(x) = [x\,R(x)]^{-1}$ where R(x) is the exposure factor for RPR film defined in Ref. [16] with x^{-1} required by the definition of I_ϕ (cf. Ref. [13]).

From the results in Table I we conclude the following:

(a) Electron beams with energy $10 < U < 60$ keV exist in the focus. It is not clear whether the mean electron beam energy is correlated with the available bank energy (E_0 in Table I) or with the detector cut-off energy for each case. (Photon energy peaks at $x > 20$ keV are smoothed away by the film exposure factor in SIT measurements, and X-rays below 15 keV are shielded by 2 mm Al at NASA.) Perhaps more than one single beam exists in this energy range.

(b) Line emission (mainly from the copper K_α at 8.05 keV) can substantially affect the validity of our calculations for the extended sources at SIT, but its effects cannot be important for the high photon energies at NASA ($h\bar{\nu} > 15$ keV). The average beam energy from NASA anisotropy ratios is (47 ± 11) keV for pure D_2. This is not very different from a beam energy of (41 ± 10) keV, which can be estimated from the same ratios by assuming that 0.5% copper ions are present.

(c) Anisotropy ratios from extended sources (NASA) are the result of two contributions: softer X-rays originated in the plasma and harder X-rays from the anode surface. Although some symmetry can be ascribed to the plasma sources, the coin shape of the anode-emitting regions (cf. Fig. 1 of Ref. [11]) will result in a decrease with increasing ϕ of the solid angle subtended by the source at the detector. This geometrical effect can explain the very slow growth of A_{obs} at large observation angles and the consequently higher values of U at $\phi = 60°$ and 80°. The poor calibration available for the TL detectors [11] may also be an important source of error.

(d) The very short duration of the highly localized sources at SIT (cf. similar observations with 3 ns resolution in [17]) and the good space resolution of the observed structures justify the use of time-integrated techniques for the analysis of those minute sources. This is not rigorously valid for the extended sources, where flux contributions from other stages of the focus evolution and from the more diffuse regions near the focus cannot be neglected.

REFERENCES

[1] BERNARD, A., "Plasma focus", 3rd Top. Conf. on Pulsed High-Beta Plasmas, Culham, 1975, Pergamon, Oxford (1976).

[2] ZUCKER, O., BOSTICK, W., LONG, J., LUCE, J., SHALIN, H., Nucl. Instrum. Methods **145** (1977) 185.

[3] BRUZZONE, H., KELLY, H.J., MILANESE, M., POUZO, J., Nucl. Fusion **16** (1976) 870.

[4] GRATTON, R., KELLY, H., MILANESE, M., POUZO, J., Phys. Lett. **62A** (1977) 422.

[5] BRUZZONE, H., KELLY, H., POUZO, J., Lab. Fis. Plasma, DIGID, Buenos Aires, Rep. Inf. LFP-DIGID, P-p: 2/78, Bs.As. (1978).

[6] RAPP, H., Phys. Lett. **43A** (1973) 5.

[7] GRATTON, R., BRUZZONE, H., KELLY, H., MILANESE, M., POUZO, J., in Energy Storage, Compression and Switching (Proc. Int. Conf. Turin, 1974), Plenum, New York (1976) 255.

[8] MATHER, J.W., Methods of Experimental Physics, Vol. 9, Part B, Academic Press (1971) 202.

[9] JALUFKA, N.W., LEE, J.H., Phys. Fluids **15** (1972) 1954.

[10] JOHNSON, D.J., J. Appl. Phys. **45** (1974) 1147.

[11] HARRIES, W.L., LEE, J.H., McFARLAND, D.R., Plasma Phys. **20** (1978) 95.

[12] BOSTICK, W.H., NARDI, V., PRIOR, W.J., RODRÍGUEZ-TRELLES, F., Controlled Fusion and Plasma Physics (Proc. 5th Europ. Conf. Grenoble, 1972) Vol. 1, p. 239 and Vol. 2, p. 70.

[13] BAÑUELOS, A., RODRÍGUEZ-TRELLES, F., J. Phys. B **11** (1978) 1663.

[14] STORM, E., ISRAEL, H.J., Los Alamos Rep. LA-3753 (1967).

[15] BAÑUELOS, A., RODRÍGUEZ-TRELLES, F., Comput. Phys. Commun. **15** (1978) 125.

[16] DOZIER, C.M., GILFRICH, J.V., BIRKS, L.S., Appl. Optics **6** (1967) 2136.

[17] DECKER, G., et al., Plasma Physics and Controlled Nuclear Fusion Research 1976 (Proc. 6th Int. Conf. Berchtesgaden, 1976) Vol. 3, IAEA, Vienna (1977) 441.

DISCUSSION

ON PAPERS U-3-1 TO U-3-5

R.S. PEASE: What is the maximum enhancement of $S_k(\vartheta)$ observed, and when did it occur?

C. MAISONNIER: The measurement gives $n_e S_k(\vartheta)$. In the dense sheath both n_e and $S_k(\vartheta)$ are known, and $S_k(\vartheta) \cong 1$. In the dilute plasma located around the sheath, n_e has not been measured, so that $S_k(\vartheta)$ is unknown. All we can say is that, because $n_e S_k(\vartheta)$ is of the same order of magnitude in the dense sheath and in the dilute plasma and since n_e is, at least, 10 times smaller in the dilute plasma than in the sheath, $S_k(\vartheta)$ must be at least 10 outside the sheath. Its space and time dependence are not known.

V. NARDI: I would like to stress the fact that both the ion beam in the forward direction and the ion beam in the backward direction are highly collimated. The damage on different targets indicates that the diameter of the electron beam has practically the same value (3–5 mm) at ~ 15 cm and at 43 cm from the source. The ion beams have a collimation angle better than $\approx 6°$. The damage to the targets indicates that both electron and ion beams are formed by many clusters – or strings – of particles. Further focalization of these beams with a power of several terawatts on a small target, e.g. a pellet, will have to deal directly with clusters of particles rather than with single particles.

H. CONRADS: With reference to the two neutron spectra taken at Frascati, by the time-of-flight method and by means of nuclear-emulsion plates, I should like to know why the spectra differ in full half-width.

C. MAISONNIER: The difference is due to a variation of the neutron spectrum in time over the finite duration of neutron emission. For instance, if the energetic neutrons (energies > 3 MeV) observed with nuclear emulsion were all emitted at the end of the pulse, they would be registered as having a lower energy by the time-of-flight method.

PRINCIPLES OF PLASMA HEATING AND CONFINEMENT IN A COMPACT TOROIDAL CONFIGURATION

A.G. ES'KOV, R.Kh. KURTMULLAEV,
A.P. KRESHCHUK, Ya.N. LAUKHIN, A.I. MALYUTIN,
A.I. MARKIN, Yu.S. MARTYUSHOV,
B.N. MIRONOV, M.M. ORLOV, A.P. PROSHLETSOV,
V.N. SEMENOV, Yu.B. SOSUNOV
I.V. Kurchatov Institute of Atomic Energy,
Moscow, Union of Soviet Socialist Republics

Abstract

PRINCIPLES OF PLASMA HEATING AND CONFINEMENT IN A COMPACT TOROIDAL CONFIGURATION.

Data obtained on a so-called compact toroid – a configuration where shock compression improves the stable confinement properties – are generalized in this paper and shown to be valid in a range of B ~ 2–12 kG, plasma density n ~ 10^{14}–10^{16} cm^{-3} and chamber dimensions of 20–40 cm × 100–200 cm.

It is well known that the highest plasma heating parameters (T, β) and the maximum confinement characteristics ($n\tau$) are achieved in different physical systems: in pinches and in stationary toroidal systems, respectively.

It is, however, possible to combine, in principle, the advantages of a toroidal confinement system and the merits of pulsed heating methods in the same system such that shock compression does not worsen, but improves stable confinement conditions.

The required structure in the most interesting case of a toroid with an aspect ratio of $A \to 1$ may be created in a cylindrical chamber by sequential freezing of antiparallel magnetic fields into the plasma and their subsequent reconnection at the ends of the chamber. In the configuration obtained in this way, the tension of the poloidal field lines is not balanced by the initial plasma pressure. The longitudinal shock compression induced by this leads to abrupt heating and transverse expansion of the plasma, which undoubtedly favours stability. The achieved configuration, containing a closed magnetic field and bounded by a quasi-spherical or ellipsoidal separatrix, is called a compact toroid. A number of key problems of this programme is investigated in Refs [1,2].

Data obtained under various experimental conditions are generalized in this paper. The derived principles are general in nature in a range of magnetic fields of B ~ 2–12 kG, a plasma density of n ~ 10^{14}–10^{16} cm^{-3} and shock chamber dimensions of D = 20–40 cm and L = 100–200 cm (see Refs [1–3] for a description of the devices).

1. PULSED SHAPING OF CLOSED STRUCTURE AND METHODS OF CONTROL

It is well known that the spontaneously shaped closed structure in a 'theta-pinch-with-reverse-field' experiment is unstable. In this context, it is important to note that introduction of a stabilizing toroidal field [4] in itself does not correct the radical defects of a theta pinch with reverse field. It is natural to expect that a deeper relationship exists between the MHD-behaviour of the system and the pulsed phase of the process. These principles are investigated in the given system by a number of functional elements which permit variation of the quantitative and qualitative characteristics of the process over a wide range.

1. Pulsed injection of the working gas (hydrogen or deuterium) and induction ionization by a longitudinal variable electric field were accomplished in the experiments. The trapped flux Φ_p was created by a two-step method: by means of an initial quasi-stationary field B_0 (Fig.1) and by a magnetic field pulse of the same orientation from the shock loop. This pulse was generated by a separate bank, or the first half-period of the main shock field was used.

2. Inversion of the external magnetic field. In ordinary theta pinches (with reverse field), the plasma together with the frozen magnetic field emerges towards the wall when the external field goes through zero, which causes losses of the trapped flux and plasma, erosion of the dielectric wall and generation of impurities. One may now assume that it is this phase which is responsible, to a significant extent, for the initial perturbations of the neutral layer, which then lead to disruptions, a breakdown of the antiparallel structure, and to the development of MHD-instabilities [4–6].

A pulsed octupole barrier field (Fig.1) and a special mirror configuration at the ends were used to control the indicated processes in these experiments [2].

Owing to the elimination of plasma contact with the wall, the barrier field has a radical effect on the process with respect to all main characteristics, including the development of a tearing instability. Magnetic mirrors which form a stable magnetic structure at the ends and permit control of the loss rate through the ends and of the development of microprocesses in the neutral layer, are equally essential.

3. Reconnection of counter magnetic fields in the end zones of the shock chamber. In this phase the open magnetic field is transformed into a closed one;

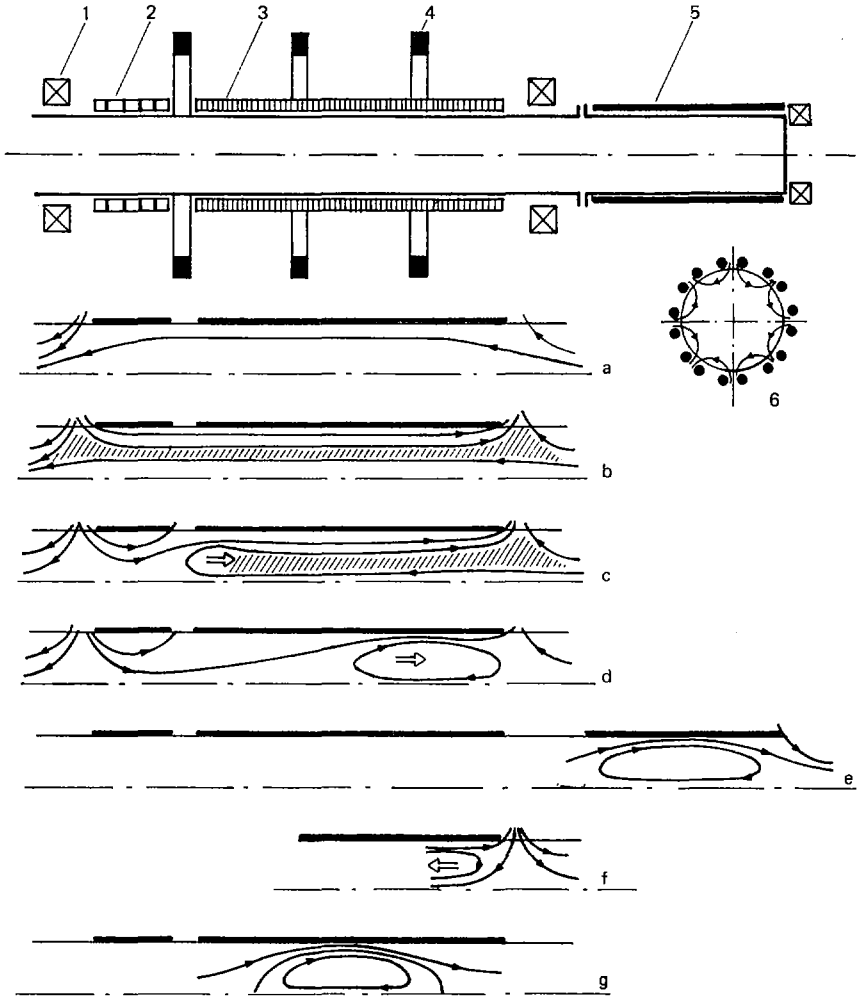


FIG.1. Experimental devices and sequence of plasma toroid heating and injection: 1) mirror coils; 2) key loop; 3) shock loop; 4) solenoid; 5) liner winding; 6) barrier field bus bars.

i.e. the magnetic field topology is changed; as a result, the heat release and loss conditions are changed; the plasma equilibrium is fundamentally destroyed, and an irreversible longitudinal compression of the plasma column is initiated.

Control of the reconnection process was achieved in this experiment by making use of the following elements (Fig.1):

a) a quasi-stationary field of antimirror configuration at the ends of the system which controls the dimensions of the reconnection zone (f);

b) a pulsed key loop which causes forced reconnection of the lines of force in the neutral field (c).

2. OPTIMIZATION OF SHOCK HEATING

The most serious difficulties of traditional theta and zeta pinches are related to the radial nature of compression and, in particular, to the rigid constraints on the field rise-time ($\tau_\sim < R/u$, u is the shock wave velocity) and the time of stability loss during strong adiabatic compression.

In our system, transition to longitudinal compression gives rise to a number of favourable physical and energetic consequences, which are determined by the factor $(L/R)^2$.

1. The temperature limit for shock heating, $T_{i,max} \sim m_i u^2/2 \sim (m_i/2)(L/\tau_\sim)^2$ increases 10–100 times if a reasonable configuration is chosen.

2. A further increase of $T_{i,max}$ is possible by using a method of sharpening the piston, unique in pinch systems, by means of controlled reconnection of fields with a time $\tau_{rc} < \tau_\sim$.

3. Shock compression (along z) leads here not to a separation of the plasma from the conducting wall but, on the contrary, to transverse expansion.

4. Since the poloidal magnetic field is localized near the current-carrying neutral layer, the energy distribution between the magnetic field and the plasma in our system is shifted considerably in favour of the plasma: $\eta = W_p/W_B \sim 0.5-1$, compared to $\eta \sim (r_p/r_W)^2 \sim 0.1$ in theta pinches.

3. TRANSPORT AND CONFINEMENT PROBLEMS

Besides the ordinary scheme of magnetic confinement (shock-field crowbar), the given system permits a unique opportunity: transport of the heated toroid from the shock chamber to an independent confinement chamber (metal cylinder) [1]. The following is achieved in this case:

1. An optimum "crowbar" mode with arbitrarily long field confinement time, $\tau \sim 4\pi\sigma R\delta/c^2$ (δ and σ are the thickness and the conductivity of the liner walls).

2. A new opportunity, for pulsed systems, of solving problems of vacuum hygiene and impurities (burn-through of liner) and thermal and radiation shielding of the shock chamber.

3. The possibility of quasi-spherical compression of the toroidal plasma by a heavy sheath with an effective field of approximately 10^6 G [3].

The results of injection into a liner with an initial magnetic field of B_L, oriented parallel to the field on the toroid surface, are presented in this paper. The magnetic elements provided in the devices (Fig.1) permitted control of the injection conditions and of the toroid dimensions in the liner.

4. STUDY OF METHODS OF MAGNETIC-STRUCTURE SHAPING

1. Figure 2 shows the main characteristics of barrier plasma confinement during the inversion phase. Without plasma the probe records a sine-wave signal;

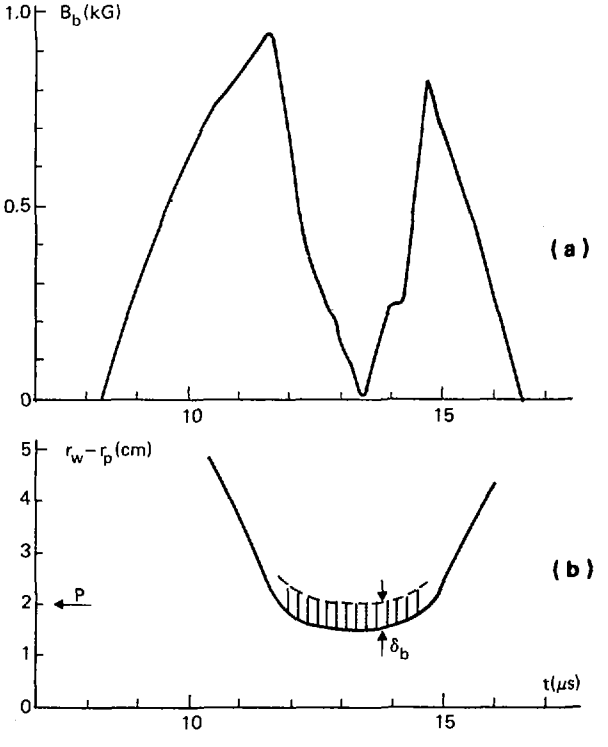


FIG.2. Deceleration of plasma by barrier field: a) oscillogram of barrier field 2 cm from wall; b) motion of plasma boundary; r_p plasma radius; δ_b thickness of barrier field skin layer; P) position of probes; $n_0 = 1.5 \times 10^{14}$ cm^{-3}; shock field in first half-period $B_\sim = 4.3$ kG, $T_\sim/2 = 13.5$ μs, $r_w = 20$ cm.

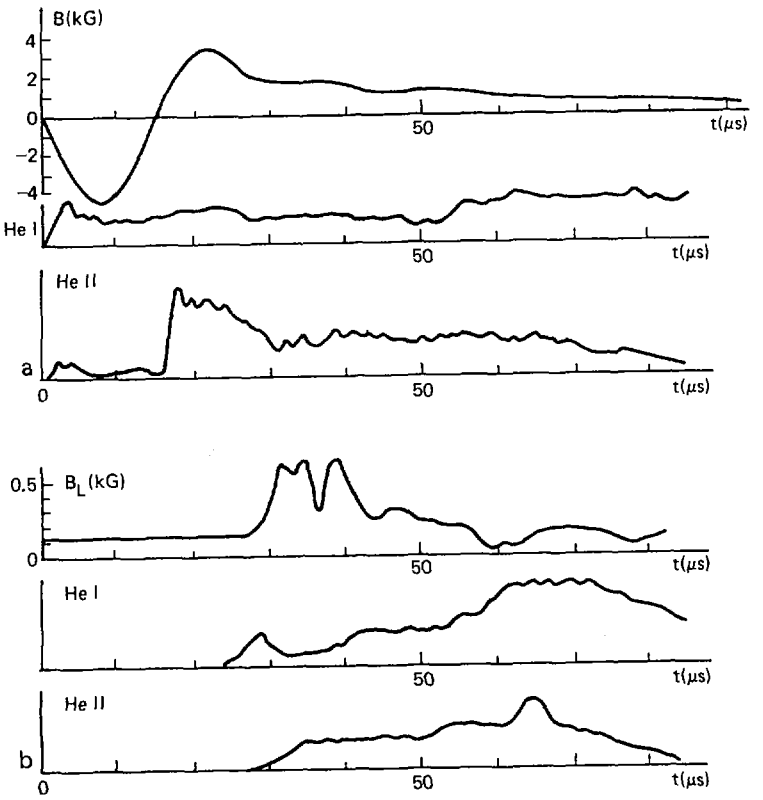


FIG.3. Intensity of He I and He II emission lines from different regions of the plasma: a) light is received parallel to the chamber axis through the transparent end wall; b) light is received through the window in the liner chamber perpendicular to the axis; B external magnetic field; B_L signal of magnetic probe placed 2 cm from liner chamber wall.

a deep gap related to the expanding plasma forcing the barrier field out occurs on the oscillogram in the operating regime. As can be seen, the probe is shielded by the plasma for approximately three μs seconds, an interval corresponding to the inversion phase. The motion of the plasma boundary during the inversion phase (Fig.2b) is reproduced when measurements of the longitudinal field inside and outside the chamber are used, by which the distance of plasma deceleration approximately 1.5 cm from the walls is determined. It follows from the oscillograms that the process is elastic reflection in nature with only a small penetration depth of the barrier field into the plasma ($\delta_B \sim 0.5$ cm). The results of measuring the He I ($\lambda = 5875.6$ Å) and He II ($\lambda = 4685.7$ Å) lines indicate

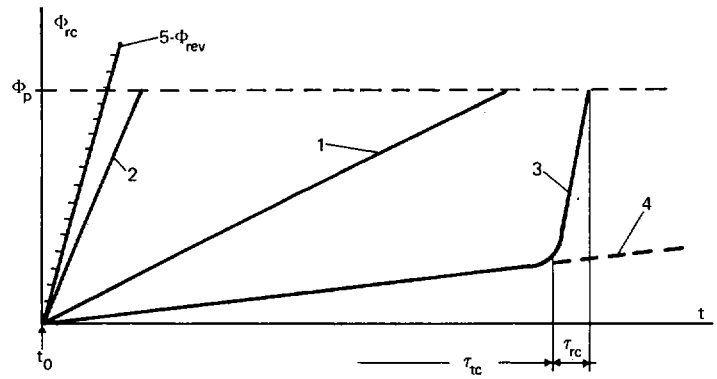


FIG.4. Different reconnection regimes: Φ_{rc} reconnected part of flux; Φ_p trapped magnetic flux; t_0 end of inversion; 1) free-end regime; 2) control of stationary antimirror; 3) sharpening by key loop; 4) deceleration by stationary mirror; 5) $\Phi_{rev}(t)$ reverse magnetic flux.

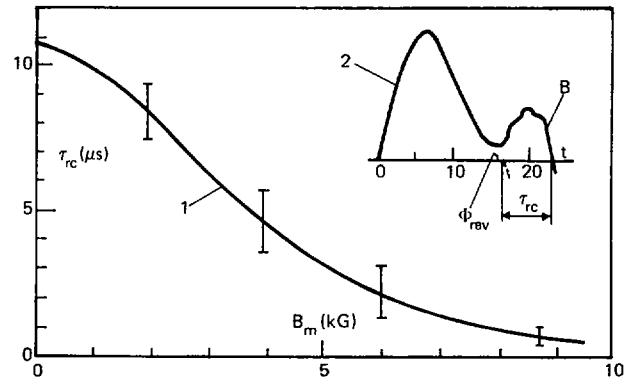


FIG.5. Reconnection time τ_{rc} as a function of stationary antimirror field B_m (1) and method of determination of τ_{rc} (2): B field on edge of shock loop on axis; Φ_{rev} reverse magnetic flux; $n_0 \sim (5-6) \times 10^{14} cm^{-3}$; shock field on first half-period $B_\sim = 4.3$ kG, $r_w = 20$ cm, hydrogen.

the absence of plasma contact with the wall (helium was introduced as a low-density additive of $n_{He} < 10$ percent of n_{H_2}). As can be seen from the oscillograms (Fig.3), there is no light flash during plasma expansion and field inversion phase which usually appears when the plasma moves towards the wall. The increase in the intensity of He II after inversion is obviously related to plasma heating in the current layer.

Three typical time scales are observed in the general case in the system in question: $\tau_{\sim} = T/4$, the rise-time of the external field (energy storage), τ_{cL}, the life-time of the stable open antiparallel magnetic structure, and τ_{rc}, the connection time (Fig.4);

a) in the simplest situation when there are no magnetic mirrors, the duration of the process is determined by diffusion through the entire plasma thickness (Fig.4(1)). Values of $\tau_{rc} \sim 10$ μs for $r_W = 20$ cm and $\tau_{rc} \sim 5$ μs for $r_W = 8.8$ cm are observed experimentally in this regime.

b) a stationary mirror field B_m of counter-orientation (Fig.1, f) leads to variation of the configuration (dimensions) of the reconnection zone. Figure 5 demonstrates the strong dependence of τ_{rc} on B; with a strong mirror of $B_m \sim 10$ kG, the connection process proceeds almost simultaneously with the rise of the reverse external field (curve 2, Fig.2).

c) the mode $\tau_{rc} < \tau_{\sim} < \tau_{cL}$ (Fig.4(3)) is optimum in all respects, which permits the use of slow ($\tau_{\sim}$) main energy storage and fast (τ_{rc}) discharge of energy into the plasma by key reconnection. The following is achieved experimentally in this regime: stable existence of an open antiparallel structure by means of a stationary mirror at the edge of the shock loop with a time of $\tau_{cL} \sim 20$–40 μs (qualitatively, curve 4, Fig.4), reduction of τ_{rc} by using the key loop by approximately an order of magntiude compared to the storage time $\tau_{\sim}$. A poloidal piston with minimum thickness (most abrupt drop of the separatrix, Fig.8) is formed in this case.

5. THE STABILITY OF THE NEUTRAL LAYER

Annihilation of the counter magnetic fluxes and the tearing instability constitute an obvious danger for retaining a regular antiparallel magnetic structure. Their development aggravates or even makes impossible longitudinal compression and shock heating of the ions. The classical resistance of the plasma may not play any significant role in the zone $n \sim 10^{14}$–10^{15} cm^{-3} and $T_e \sim 10^2$–10^3 eV; therefore anomalous turbulent resistance localized in a relatively narrow zone (in the neutral layer) where the ncessary conditions for the build-up of micro-oscillations are fulfilled (for ion sound, $v_{\alpha} > c_s$ and $T_e \gg T_i$, for a layer width of $\delta \sim c/\omega_{pi}$), is of primary importance.

The tearing instability was observed by determining radius and shape of the separatrix at different moments of time. To do this, the total magnetic flux through the chamber cross-section Φ and the external magnetic field $B_e(z)$ were measured. The radius of the separatrix was determined from these quantities:

$$r_s = r_w \left(f - \Phi/\pi r_w^2 B_e\right)^{\frac{1}{2}}$$

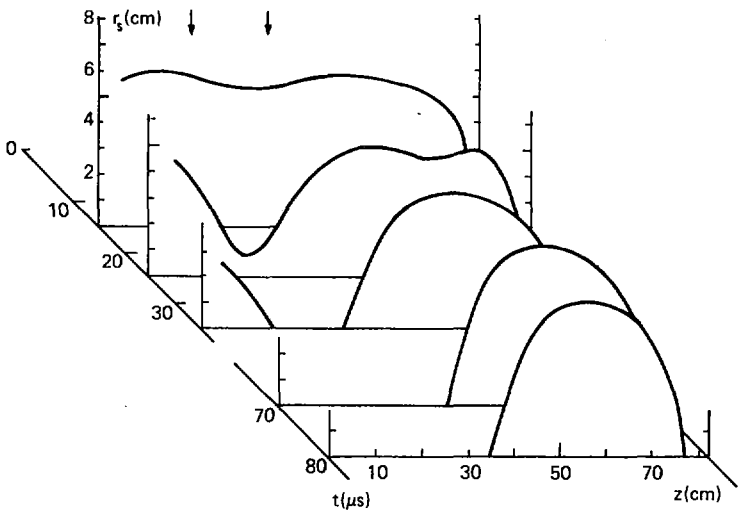


FIG.6. Evolution of separatrix during asymmetric reconnection (Right: control key loop; left: stationary mirror) and effect of external perturbation (X-ray targets 1 × 1 cm^2; position indicated by arrows); $n_0 = 2.5 \times 10^{14}\ cm^{-3}$; time counted from moment of inversion; $r_w = 8.8$ cm.

These measurements were made by a large number of external probes placed with a spacing of 10 cm along Z.

The development of the tearing instability was established experimentally as a function of the initial level of perturbations and the conditions of neutral-layer formation. A case of the crudest perturbation caused by introduction of X-ray targets into the chamber is presented in Fig.6. The development of a neutral-layer disruption is accompanied by a burst of X-rays corresponding to the appearance of non-thermal electrons with an energy of 1–2 keV.

The case of tearing instability stimulated by the proximity of the material wall during formation of the neutral layer is more common and important. The extremely strong nature of this effect, which may lead to complete breakdown of the layer at one or several points along its length, has been established experimentally. The experiment demonstrates the effective stabilization of this process by the barrier field (Fig.7).

A perturbation of the separatrix $\Delta r_s/r_s$ (related to the same time) may be completely suppressed in practice if B_b is large enough. The most important among the causes of this effect is obviously prevention or reduction of transverse losses and plasma cooling by the magnetic barrier. The ends of the system play a similar role: weakening or absence of mirrors enhance the development of a

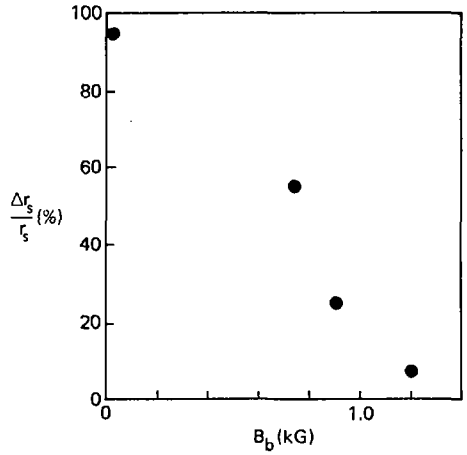


FIG. 7. Suppression of tearing mode by barrier field B_b: $\Delta r_s/r_s$ is the typical modulation depth of separatrix; $n_0 \cong 2 \times 10^{14}$ cm^{-3}; $r_w = 8.8$ cm.

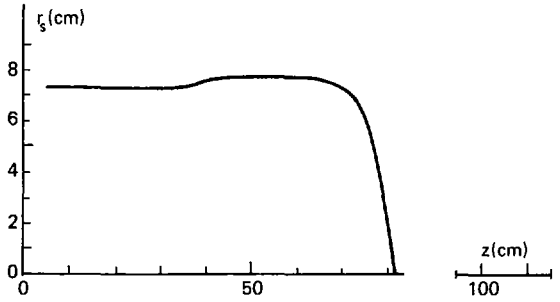


FIG. 8. Suppression of tearing instability during longitudinal compression in the system: $r_w = 8.8$ cm; $t = 8$ μs after inversion; $n_0 = 3 \times 10^{14}$ cm^{-3}.

tearing instability abruptly. A powerful stabilizing factor with respect to the tearing instability is also shock compression of the plasma. Disruption of the magnetic structure of the toroid is never observed after longitudinal compression, even in those cases when the field was closed and longitudinal compression occurred from the same end, whereas the other end, as a result of using the mirror field, remained open. This case is shown in Fig.8. Effective connection due to the key loop provided rapid closing and compression of the magnetic configuration.

It was established that longitudinal compression of the plasma not only stabilizes the neutral layer, but may also suppress perturbations that have already developed.

6. GENERATION CONDITIONS AND CHARACTERISTICS OF THE SHOCK WAVE

The data presented in this paper are mainly related to the physical aspect of the problem: 1) the dependence of the shock process on the reconnection conditions and 2) the effect of longitudinal compression on plasma stability and confinement. The optimum solution of this problem determined the choice of the experimental parameters and conditions.

A strong dependence of the effectiveness of the shock wave on the different methods of connection considered above (Fig.4) and also on the symmetry of the conditions at the opposite ends has been established.

The most complete characteristics of the process have been found by contactless external magnetic probes placed at different distances Z from the point of excitation (the typical zones of shock flow – initial state, front, piston and zero point – are clearly related to the variation of the local value of r_s and, consequently, of B_e). Besides a local probe, a diamagnetic sensor, which is a compensated pair of local and female probes with a typical difference signal of $\varphi = \pi r_w^2 B_e$ (φ is shown in Fig.9, r_w = 20 cm and z = 85 cm) was used.

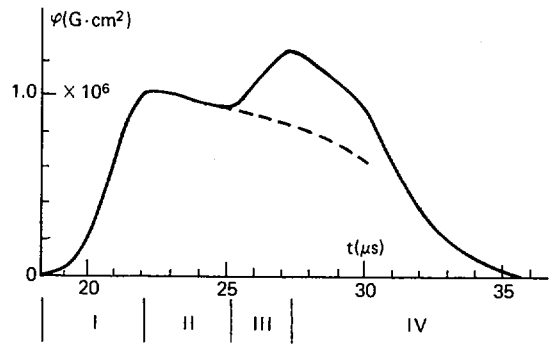


FIG.9. Diamagnetic signal with compensated pair of probes: I) inversion phase; II) state before shock wave front; III) front; IV) piston; dashed line: slow reconnection mode at free end of system; $n_0 \cong 4 \cdot 10^{14}$ cm^{-3}.

Here I is the inversion phase – the plasma is resting on the barrier field; II is the transverse compression after inversion, the state in front of the wave (reconnection and start of the wave at the end z = 0); III is the front of the longitudinal shock wave – the main diamagnetic jump; and IV is the poloidal piston zone (the approach of φ to zero due to raking of the plasma and transition to a vacuum field distribution). Figure 10 is a diagram of the wave and piston motion in this same experiment, which demonstrates the stationary

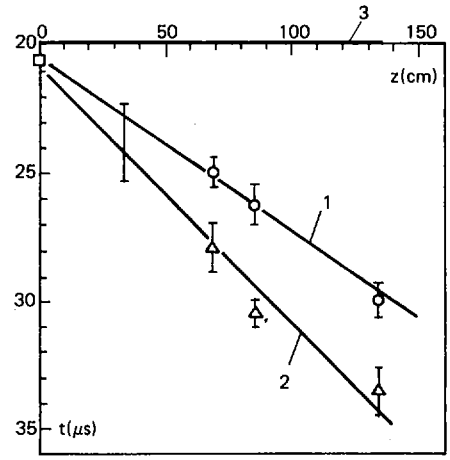


FIG.10. Propagation of longitudinal shock wave: 1) front; 2) piston; 3) position of shock loop; □ moment of reconnection; $n_0 \cong 4 \times 10^{14}$ cm^{-3}; hydrogen.

nature of the plasma shock flow. In the considered case reconnection was determined by an antimirror with time of $\tau_{rc} \sim 1-2$ μs. The shock wave is attenuated and disappears completely with an increase of τ_{rc} (because of a decrease of B_m) (Fig.9, dashed line; z = 85 cm and u = 1.5 × 10^7 cm·s^{-1} at $\tau_{rc} \sim 8$ μs, which agrees with $\tau_{rc} > z/u$).

Extreme conditions with respect to shock perturbation generation conditions are created by stationary mirrors and the key loop. In the first case there is a stable neutral layer, and the perturbations of the magnetic structure are slow and diffuse in nature and, in the second case, the formation of a maximally sharpened poloidal piston (Fig.8 considered previously) takes place.

The regulation of the reconnection at the opposite ends permits a precise re-adjustment of the process of axisymmetric two-sided compression towards a one-sided shock wave generation (as in Figs 9 and 10, where $\tau_{rc-1}/\tau_{rc-2} > 10$). We note that the asymmetric excitation mode has advantages from the viewpoint of shock wave parameters and transport of the toroid. The conducting layer in front of the shock wave (phase II, Fig.10), $r_s \leqslant 0.5 r_w$, is relatively thin ($\delta < r_s$); therefore, $\varphi = \pi r_s^2 B_e = 2\varphi_{cL}$ and its slight variation (usually approximately equal to or less than 20%) attests to the smallness of the losses.

The typical characteristics of the shock wave are: velocity u ~ (1–3) × 10^7 cm·s^{-1}, width of front $\Delta \sim r_w$, pressure behind the front $(nT)_2 = B_e^2/8\pi \sim 10^{18}$ eV·cm^{-3}, plasma density before the front $n_1 \sim (1-5) \times 10^{15}$ cm^{-3}, compression coefficient in the front $k_\parallel = n_2/n_1 \sim 2-2.5$, and total variation of plasma density

$n_2/n_0 \sim k_\parallel k_\perp$ (where $k_\perp \sim 4-5$ is the transverse compression coefficient). It follows from the given parameters that the temperature behind the front $T_e + T_i$ amounts to several hundred electron volts. Direct measurements of the ion temperature (from an analysis of the spectrum of charge-exchange neutrals) yield a typical value of $T_i \sim 100$ eV (in the range of $n_0 \sim 10^{15}$ cm^{-3}), which indicates a significant contribution of the ion component to the plasma pressure. It is important to note that the ion signal is recorded in all cases after inverstion and after the beginning of longitudinal compression, which hints at the dominant role played by shock heating.

7. INVESTIGATION OF TOROID INJECTION

The toroid is accelerated and injected in the described system in a natural manner by asymmetric reconnection at the opposite ends. In these conditions, shock compression is developed in the preferred direction – towards the liner, as a result of which shock heating of the plasma and formation of a closed magnetic structure combine organically with the acceleration of the torus as a whole.

In the conditions indicated, the toroid acquires a directional velocity approximately equal to that of the poloidal piston, $v \sim (1-2) \times 10^7$ cm·s^{-1} and is injected into the liner. The diagnostic probes located here record the dynamics, structure and parameters of the toroid.

A different-pole magnetic field near the wall ($r_w = 8.8$ cm) and at the axis of the toroid in the region of the output mirror is shown in Fig.11 in an experiment with a small-diameter chamber. The strong inhomogeneity of the mirror field along z explains the different initial ($t = 0$) levels on the two probes located in different cross-sections ($\Delta z = 13.5$ cm). Upon passing through the mirror, the field is $B = 4.5$ kG, the torus radius $r_s \sim r_w/2 = 5$ and its length is 30–40 cm; the torus expands after passing through the mirror ($r_s \sim r_w$).

The following scaling was observed in experiments with a large-diameter chamber: $r_s \sim r_w \cong 20$ cm and $\ell \sim 80$ cm. Transport is accomplished along the length of the liner, $L \cong 130$ cm.

In conditions when no means of deceleration and capture of the toroid in the liner cavity were used, it reached the dielectric end wall of the chamber and broke down within $\ell/v \sim 10$ μs. The radial magnetic-field component was recorded during this time at the end wall at a radius of $r = r_w/2$.

The motion of the injected toroid in the liner chamber is accompanied by the simultaneous appearance of a burst of plasma emission perceived in a direction perpendicular to the axis through a special window in the chamber. The intensity of the two He I (5875 Å) and He II (4686 Å) helium lines was measured in the given experiments. The later appearance and gradual increase of the relative

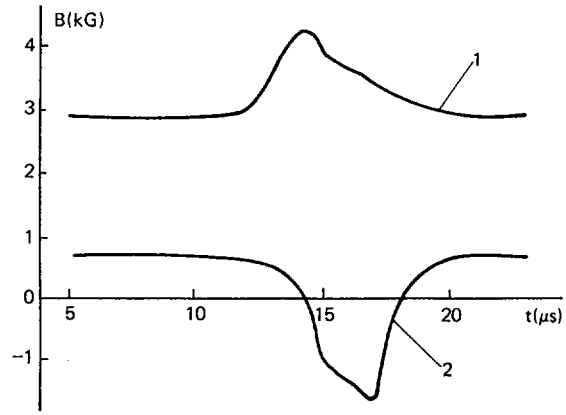


FIG.11. Injection of plasma toroid into independent chamber. Magnetic field near the wall under the output magnetic mirror (1) and at the axis 13.5 cm from it (2);deuterium.

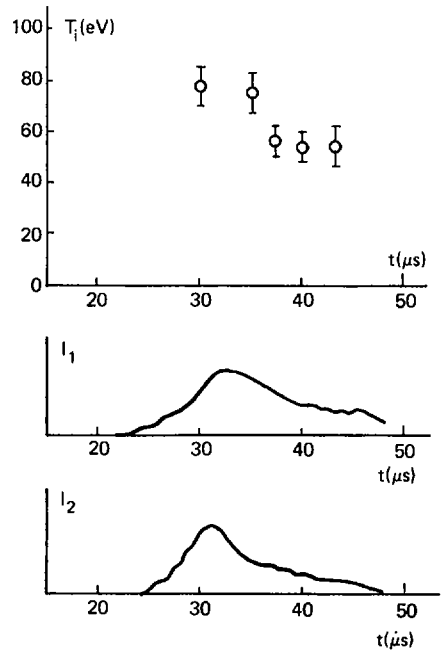


FIG.12. Ion temperature of plasma toroid injected into liner cavity: I_1 and I_2: signals from two ion analyser channels with energies of 320 and 560 eV, respectively; hydrogen.

intensity of He II (Fig.3) apparently corresponds to passage of hotter plasma regions past the window. The appearance of a new He I burst is correlated with the disappearance of the magnetic fields in the liner volume due to breakdown of the toroid upon impact against the end wall and is apparently related to subsequent expansion and recombination of the cold plasma on the walls.

The signal from the ion analyser and the course of ion temperature in the mid-section of the liner, separated from the output end of the shock loop (r_w = 20 cm) by 80 cm (the spectrum is very close to a Maxwellian one), is shown in Fig.12. It is important to emphasize that the space-time pattern of toroid motion in the liner and its main parameters are in strict agreement with the previous processes of reconnection and wave compression in the shock chamber. This is, of course, achieved with completely specified amplitude and phase adjustment of the functional elements of the system. This optimum regime will easily and reliably be reproduced. Destructions of the process of the most diverse types occur upon deviation from this regime (earlier flow of plasma with trapped magnetic fields of different orientation, multiple formations or complete cut-off of the injection channel).

8. PRINCIPLES OF COMPACT-TOROID CONFINEMENT

The pulsed processes of reconnection, shock heating and transport considered above in no way limit the possibility of introducing special stabilizing fields for prolonged plasma confinement (for example, toroidal confinement to create a tokamak-type structure) [1]. However, the physical and technological significance shown by the properties of a plasma with simplest magnetic structure formed by a purely poloidal field is obvious.

The basic principles of confinement of this configuration are manifested in the most direct form when asymmetric reconnection (by means of a key loop and stationary mirrors, Fig.1) is used and if the initial plasma density is varied. Two typical regimes differing by the value of n_0 are represented in Fig.13. Let us note the main characteristics of the process:

1. When the magnetic lines of force are closed from one end only (by the key loop, $t = t_{rc-1}$), the radius of the separatrix decreases in spite of a simultaneous decrease of B_e.

2. Reconnection at the second end ($t = t_{rc-2}$) leads to the reverse process, i.e. an expansion of the toroid. This means that at $t < t_{rc-2}$ the main energy losses of the plasma and of the closed magnetic field occur from the plasma through the open end; the loss rate is abruptly reduced after closing of the magnetic structure, and the open-flux dissipation process on the crowbar resistor becomes dominant.

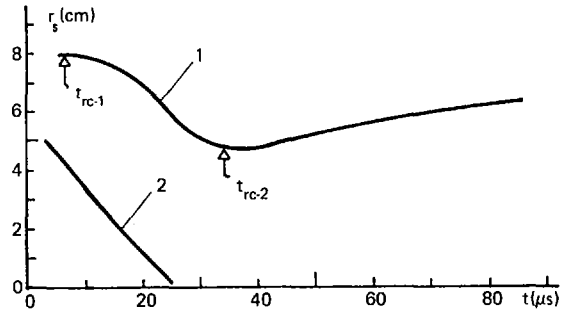


FIG.13. Time behaviour of separatrix radius: 1) $n_0 = 5 \times 10^{14}$ cm^{-3}; 2) $n_0 = 2 \times 10^{14}$ cm^{-3}; t_{rc-1}: moment of controlled reconnection of lines of force by key loop; t_{rc-2}: diffuse reconnection in mirror region. Time is counted from the moment of inversion; $r_w = 8.8$ cm; deuterium.

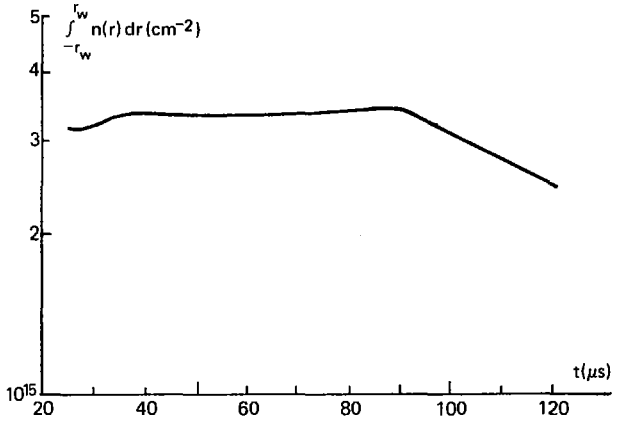


FIG.14. Probing plasma density with submillimetre interferometer in toroid confinement regime. Phase shift in the mid-section of the shock loop; $r_w = 8.8$ cm; deuterium.

3. The confinement phase is limited by the crowbar time of $\tau \sim 100$ μs. An estimate of the toroid energy during this phase reveals the approximately adiabatic nature of the process; no signs of instability of any kind are observed.

Measurements of plasma density by using a submillimetre interferometer ($\lambda = 337$ μm, Fig.14) showed a slight variation of the value of $\langle n\ell \rangle$ during the confinement phase (probing along the diameter). The plasma density starts dropping after the separatrix has moved out to the wall ($r_s \rightarrow r_w$).

4. The indicated favourable development of the process is only possible if the radius of the separatrix r_s is larger than some critical value r_c by the moment of complete closing of the magnetic structure (t_{rc-2}). In the opposite case (Fig.13(2)), the decrease of r_s continues until complete disappearance of the antiparallel magnetic configuration. We note that multiple disruptions of the neutral layer occur at $r_s < r_c$, which accelerates the dissipation process.

The quantity r_c is generally dependent on n_0 and amounts to 2.5–3.5 cm for conditions in question.

5. The radius of the separatrix at which the confinement phase begins is determined by the value of the trapped field B_p, the effectiveness of longitudinal compression and by the level of losses from the neutral layer. These dependences become most obvious when the initial density n_0 is varied. As n_0 drops, B_p decreases, and accordingly, also the radius $r_s = (1.5-2)r_w\sqrt{B_p/B_e}$. At the same time, the initial width of the neutral layer increases ($\delta \sim c/\omega_{pi}$ for ion-acoustic instability). An increase of δ/r_s reduces the effectiveness of shock heating and increases the losses. Transition from the shock compression regime to that of a strongly dissipative current layer occurs upon a combination of the effects of the indicated physical mechanisms with a decrease in n_0. The foregoing agrees with the measured value of r_c, which is of the order of c/ω_{pi}.

The data on the broadening of the He II line indicate the presence of anomalous electric-field noise in the plasma in the indicated regime. The contour of the line recorded during the longitudinal compression phase usually had an approximately Voigt central part and strongly raised wings. The relative contribution of the Doppler and dispersion broadening mechanisms in the central section of the contour amounted to $\Delta\lambda_D \cong 0.4-0.5$ Å and $\Delta\lambda_d \cong 1$ Å, respectively.

Since the given line has a strong fixed Stark component, the dispersion part of the broadening was interpreted as the effect of electric-field high-frequency oscillations. (In the conditions of experiment oscillations with frequencies ω_{pe} are high-frequency ones). The classical electronic Stark effect yields $\Delta\lambda \sim 0.1$ Å at $n \cong 10^{15}$ cm^{-3}; therefore, the observed line broadening is due to a suprathermal noise level.

An estimate of the level of electric field fluctuations, $\xi = \tilde{E}^2/8\pi nT$, during the initial shock compression phase yields $\xi = (0.5-1) \times 10^{-3}$. With regard to the strong rise of the line wings, this effect may apparently be related to the presence of a suprathermal level of low-frequency potential oscillations (for example, of the ion-acoustic type).

A number of observations, including measurements of distribution $B_z(r)$, permit us to conclude that transition into the favourable confinement regime is determined, to the greatest extent, by a transformation of the current layer. During the formation stage, its width increases from $\delta \sim c/\omega_{pi} \ll r_w$ up to $\delta \sim r_s$ after complete closing of the field and longitudinal compression. The corresponding variation of the ratio $v_d/c_s \propto 1/(\delta\sqrt{n})$ clearly agrees with the

abrupt decrease of the dissipative processes and the beginning of toroid expansion observed at this moment. The indicated diffuse nature of field distribution along the radius ($\delta \sim r_s$) is, evidently, of fundamental importance for the observed stable behaviour of the plasma without any significant MHD perturbations. An additional confirmation is the abrupt decrease of confinement time ($\tau < 10$ μs) upon transition to a considerably denser collisional plasma ($n_0 > 10^{16}$ cm^{-3}) where the neutral layer is very thin ($\delta \ll r_s$).

REFERENCES

[1] ES'KOV, A.G., et al., in Plasma Physics and Controlled Nuclear Fusion Research, (Proc. 5th Int. Conf. Tokyo, 1974) Vol.3, IAEA, Vienna (1975) 71; English translation: Nucl. Fusion Supplement 1976, 155.

[2] ES'KOV, A.G., et al., in Controlled Fusion and Plasma Physics (Proc. 7th Europ. Conf. Lausanne, 1975) Vol.1 (1975) 55.

[3] ES'KOV, A.G., et al., Third Topical Conference on Pulsed High-Beta Plasmas (3rd Top. Conf. Culham) C 37 (1975).

[4] KOLB, A.C., DIXON, R.H., DÜCHS, D., ELTON, R.C., YOUNG, M.P., in Plasma Physics and Controlled Nuclear Fusion Research (Proc. 3rd Int. Conf. Novosibirsk, 1968) Vol.2, IAEA, Vienna (1969) 567.

[5] EBERHAGEN, A.E., GROSSMANN, W., Z. Physik **248** (1973) 130–149.

[6] BODIN, H.A.B., et al., Nucl. Fusion Supplement 1962, Pt. 2 (1962) 521.

STUDY OF LINEAR THETA PINCH WITH STRONG AND FAST-RISING MAGNETIC FIELD

V.A. BURTSEV, A.B. BEREZIN, A.P. ZHUKOV,
L.A. ZELENOV, V.A. KUBASOV,
V.N. LITUNOVSKIJ, B.V. LYUBLIN,
A.G. SMIRNOV, V.G. SMIRNOV
D.V. Efremov Scientific Research Institute for Electrophysical Equipment,
Leningrad, Union of Soviet Socialist Republics

Abstract

STUDY OF LINEAR THETA PINCH WITH STRONG AND FAST-RISING MAGNETIC FIELD.

In this paper, the results of an experimental investigation into the dynamics of a fast linear theta pinch with staged heating of a dense plasma are presented. The method of inductive energy storage is used to obtain the high and fast-rising magnetic fields that are required for plasma heating. Flute instabilities are observed during the stage of fast radial collapse of the cylindrical plasma sheath. In the compression phase, the dense-plasma boundary is characterized by a proper shape. At this instant of time, the maximum electron density is $n_e = 2 \times 10^{17}$ cm^{-3}. The plasma column is surrounded by a circular zone of ~0.5 cm thickness exhibiting fast small-scale density fluctuations. In the postcompression phase, the development of large-scale plasma surges is observed, especially in the direction of the longitudinal solenoid sections. It is found that the plasma column has pronounced refractive properties because of which the interference bands are not seen in a hologram region corresponding to the dense plasma zone ($n_e \gtrsim 10^{17}$ cm^{-3}). In the plasma compression phase, an electron temperature of $T_e = 4$–6 keV is recorded at an initial deuterium pressure of $P_0 = 0.2$ torr. For increasing initial gas pressure, the electron temperature increases up to a value of 10 keV as an average over the discharges. The maximum neutron output corresponds to a pressure of $P_0 = 1$ torr. The results of a preliminary study of plasma end losses are also presented.

The fast theta pinch is, as much as ever, regarded as a feasible solution to the fusion problem. Difficulties in toroidal theta-pinch experiments aiming at the achievement of plasma pinch stability [1], have, however, increased the interest in linear pinch systems with neutral MHD-stability. Factors as the simple design of such systems and the possibility of using additional methods of plasma heating by laser radiation and high-current beams have been playing a major role, in this context [2].

The prospects of linear pinch systems as prototypes of future fusion reactors will, to a great extent, depend on whether such problems as achieving dense plasma pinches without strong radial plasma compression and the suppression of

the energy end losses will be solved successfully. As to the solution of the first problem, staged plasma heating is of considerable interest (implosive heating with subsequent adiabatic pinch compression) [3]. But its realization at high magnetic fields of tens and hundreds of kG, which are required to solve the second problem, constitutes a complex technical task. Therefore, experimental evidence is required of the fact that high efficiency of dense-plasma heating by strong fast-rising magnetic fields is an acceptable price for the ncessity of achieving high electromagnetic powers in the power supply of theta-pinch fusion systems.

In the last few years, experiments studying dense-plasma heating in a linear theta pinch with high, fast-rising magnetic field and trying to improve such field techniques have been carried out at UTRO device at the D.V. Efremov Scientific Research Institute for Electrophysical Equipment [4–6]. In these experiments, the method of inductive energy storage with pinch solenoid current switching by means of fast-acting electro-explosive foil disconnectors is used. A fast-response capacitor bank is used as the charging device for inductive energy storage and, at the same time, as a power supply for adiabatic plasma compression.

The experiments carried out in the device proved the possibility of obtaining a dense ($n_e \sim 5 \times 10^{16}$ cm^{-3}) and sufficiently hot ($T_e + T_i > 1$ keV) plasma pinch with a small radial plasma compression factor ($\eta = 2–3$) without gas pre-ionization, but with a well chosen value of the initial reversed magnetic field [5]. To obtain a plasma with such parameters in a solenoid of 50 cm length and 7 cm diameter, magnetic fields of up to $B_z = 50$ kG and with a rise-time of $\tau = 0.2–0.4$ μs were generated.

In preliminary dense-plasma heating experiments with gas pre-ionization, but without initial magnetic field, an intense X-radiation from the plasma pinch was found [6]. An estimate of the electron temperature by the absorbent-filter method gave a value of $T_e = 4–6$ keV at a maximum plasma density of $n_e = 10^{17}$ cm^{-3} ($P_0 = 0.2$ torr D_2) at the chamber axis.

Anomalous electron heating due to microinstabilities in the fast theta pinches was found and studied in Refs [7, 8] ($n_e \leqslant 10^{14}$ cm^{-3}) and [9] ($n_e \sim 10^{15}$ cm^{-3}). Further investigations are, however, necessary to clarify the mechanism governing the occurrence of a high-energy electron component in the linear theta pinch of high plasma density that was observed in the work of Ref.[6].

In our work here, results of studies which are an extension of the experiments described in Ref.[6] are presented.

Our main goal is a detailed study of the dynamics of a fast high-density theta pinch with gas pre-ionization in an expanded region of initial deuterium pressures in the discharge chamber. No initial magnetic fields were generated in this case.

The electric circuit used in the UTRO device is shown in Fig.1 (a detailed description of the device is to be found in Refs [5, 6]). Four modules of the twelve ones existing in the main capacitor bank C_1 ($W_{01} = 230$ kJ, $V_{01} = 40$ kV)

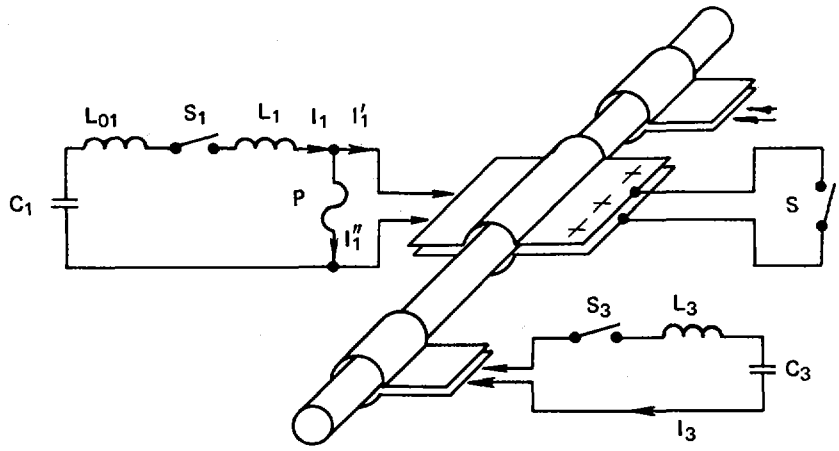


FIG.1. Electric circuitry of the device. $C_1 = 270\ \mu F$; $L_{01} = 2\ nH$; $L_1 = 50\ nH$.

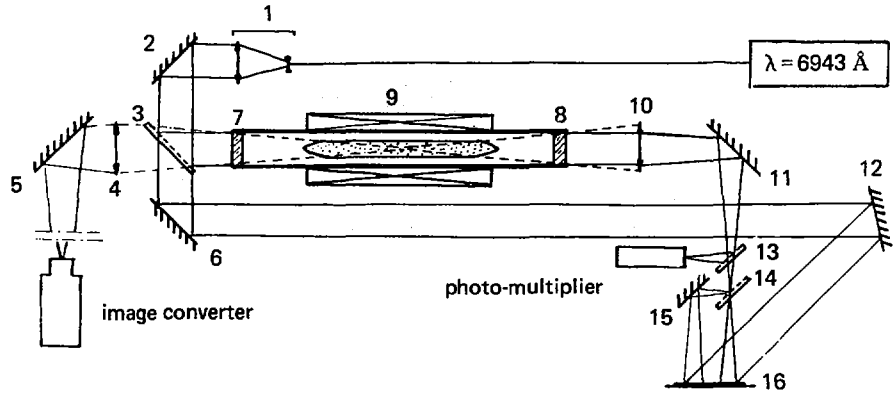


FIG.2. Optical diagram of the diagnostic installation. 1) telescope; 2,5,6,11,12) mirrors; 3,13,14) semi-transparent mirrors; 4,10) lenses, F = 50 cm; 7,8) end windows; 9) theta-pinch plasma solenoid.

were used in the experiments. Deuterium pre-ionization was carried out by two induction discharges triggered in a quartz vacuum chamber at the distance of ~10 cm from the solenoid edges, by means of capacitor bank C_3 (W_{03} = 56 kJ, V_{03} = 75 kV). The level of gas ionization in the discharge chamber inside the solenoid at the instant where the current starts flowing amounts to several per cent.

The X-radiation observed on the discharges was extracted through a 20-μm Lavsan vacuum-tight window and was studied by a three-channel detector,

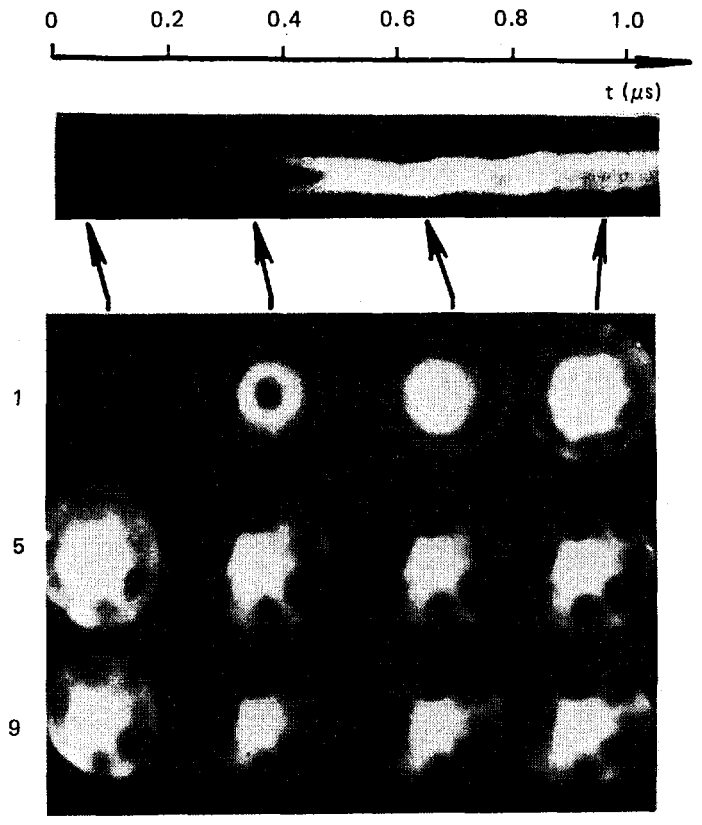


FIG.3. Plasma luminescence pictures taken in continuous-scanning and frame survey modes. $P_0 = 0.2$ *torr* D_2.

consisting of three thin scintillators covered by aluminium foils of different thickness (10–1000 μm), a fibre-optic arrangement and photo-multipliers. To obtain data on the spatial distribution of X-radiation from plasma, collimator microchannel lead glass plates (~80% Pb) were used; their thicknesses were 1.5 and 3 mm, and the hole diameter was 20 μm. In this experimental geometry, the spatial resolution of the system averaged over the cross-section of the discharge chamber was no worse than 2.5 and 1.25 cm, respectively.

The neutron radiation was recorded by an activation indium detector and scintillation recorder (the organic scintillator was terphenyl in polystyrene).

To obtain more detailed information on the spatial structure of the high-density plasma theta pinch, a diagnostic installation with a single-mode ruby laser for synchronous recording of double-and single-exposure holograms and shadow patterns was used (Fig.2). A ruby laser with good space and time

coherence was used as a light source, which allowed us to use more convenient optical circuits in carrying out the experiments (in some circuits, the difference of the object and reference beam paths reached 3 m). Transverse oscillation types were selected by diaphragms in the resonator, while longitudinal ones were selected by two glass plates separated by an air gap, which were used as a mirror of the resonance reflector. Additional elements (semi-transparent mirrors) were inserted into the optical circuit of the holographic installation; they allowed the luminescent plasma zone by means of an image converter and a photo-multiplier to be observed simultaneously.

In the experiments described, a near-shock mode was mainly investigated, when foil explosion in the storage loop and current switching into the solenoid took place at a moment close to the $T_{10}/4$-quarter period of the main capacitor bank discharge.

Image-converter observations of the plasma luminescence in the visible region of the spectrum were carried out from the ends of the discharge chamber in frame and continuous modes. Typical discharge image-converter graphs are given in Fig.3 at an initial gas pressure of $P_0 = 0.2$ torr. It is seen that during the collapse stage the discharge has good symmetry. After plasma compression towards the chamber centre, fast radial oscillations of its boundaries and full-scale surges are observed.

The dynamics of the luminescent discharge zone was studied by photometric processing of plasma luminescence time scanning. Figure 4 illustrates the evolution of the luminescent zone synchronized to the discharge current in the solenoid. Arrows show the moments of the appearance of X-(γ) and neutron-(N) radiation.

A preliminary study of the dense theta-pinch plasma dynamics by holographic interferometry showed that the plasma column formed after plasma collapse has strong refractive properties for probing radiation of the ruby laser, which led to the disappearance of interferometric band visibility in the hologram region corresponding to a dense plasma zone with a density of $n_e \gtrsim 10^{17}$ cm^{-3}. Nevertheless, information on the spatial structure of the dense plasma has been obtained by comparison of synchronously recorded double- and single-exposure holograms and shadow patterns.

A series of photos restored from holograms and shadow patterns corresponding to radial collapse, maximum compression and the after compression period are shown in Fig.5. The dense-plasma boundary (region of maximum change in the density gradient) determined by these measurements correlates well with that of plasma luminescence in the visible region.

In the phase of radial movement, flute instabilities of mode $m = 20$ developed at the outer surface of the plasma cylinder, which is well illustrated by Fig.6, which is a photo of the image restored from a hologram recorded with

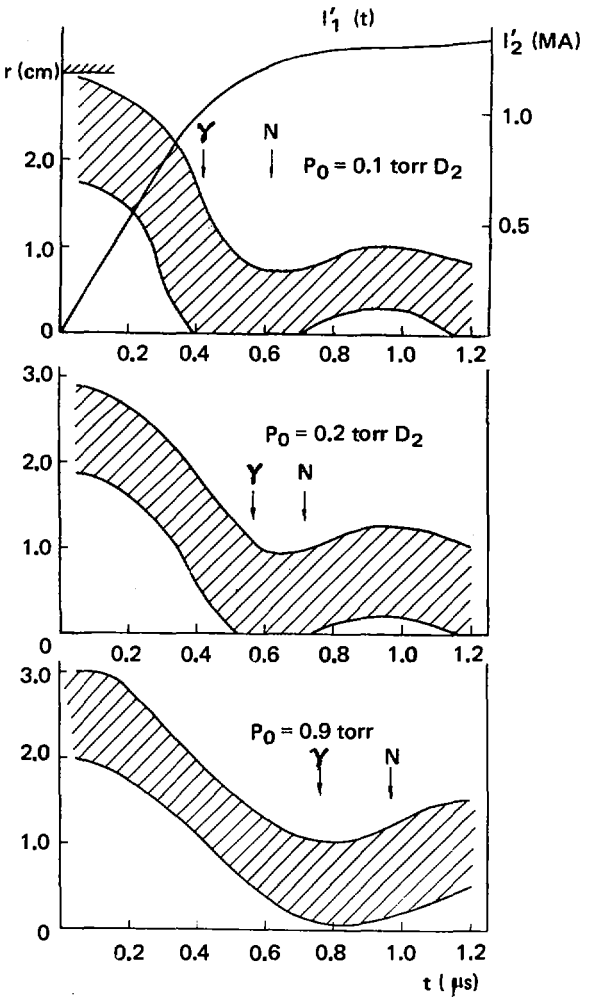


FIG.4. Plasma dynamics in luminescence zone. γ – start of X-radiation ($\hbar\nu > 10$ keV), N – start of neutron radiation.

the least number of the adjusting bands of the holographic interferometer. The growth rate, determined as $\tau = (g \cdot k)^{-1/2}$, where g is the acceleration of the plasma-magnetic-field boundary, and $k = 2\pi/\lambda = m/r$ is the wave number, is in good agreement with the observed dynamics of plasma sheath collapse (from time scanning of plasma luminescence).

In the compression phase, the dense plasma boundary has a proper configuration. The maximum plasma density for an initial gas pressure of $P_0 \sim 0.2$ torr is estimated to be 2×10^{17} cm^{-3}, by measuring the Stark broadening of the D_β line.

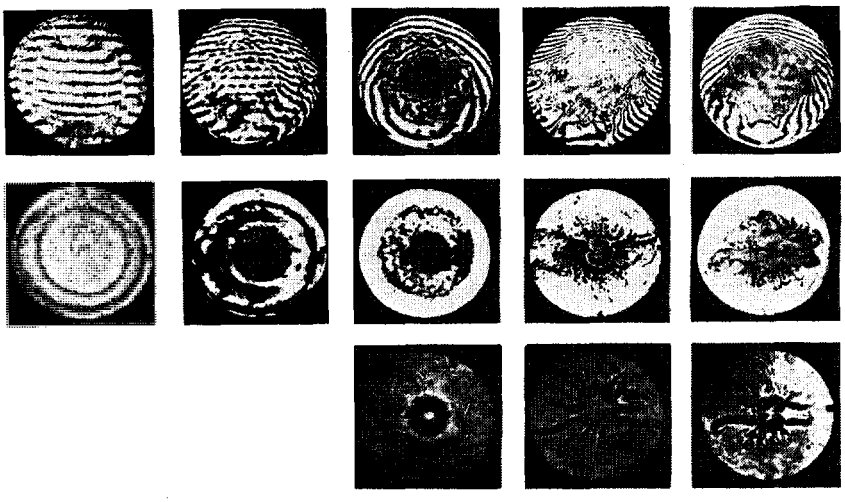


FIG.5. Synchronous double- and single-exposure holograms and shadow patterns in different phases of discharge development. $P_0 = 0.2$ torr D_2.

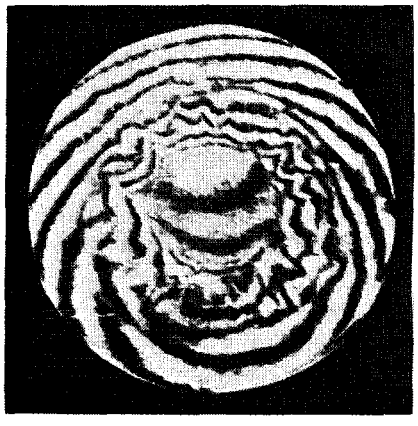


FIG.6. Photo of image restored from hologram, taken at $T = 0.35$ μs, $P_0 = 0.2$ torr D_2.

The circular zone of ~0.5 cm thickness around the dense plasma column is characterized by – compared with the hologram exposure time of ~70 ns – fast small-scale density fluctuations.

Immediately after the compression phase, large-scale surges were observed primarily in the direction of the longitudinal solenoid sections on the holograms, shadow patterns and plasma luminescence photos. Apparently, these areas of surge location are related, at least initially, with the end discharge regions. An abrupt disruption of the magnetic and gas-kinetic pressure balance after the explosion phase in the local discharge regions may be one of the possible reasons for such surges.

The central light spot on the shadow patterns in the compression phase is apparently caused by strong laser radiation refraction from substantial radial density gradients. At the same time, the corresponding area is not restored in the holograms (a dark spot is seen on the dense-plasma-pinch image background on the originals of the single-exposure holograms), which may be the result of a loss of coherence by the probing radiation due to non-linear effects during propagation in a strongly turbulent plasma.

X-radiation starting with a quantum energy of $\hbar\nu > 10$ keV from the near-axis zone corresponds to the beginning of maximum plasma compression, while its duration corresponds to that of the phase. The appearance of the integral X-radiation taken over the chamber section corresponds to the beginning of X-radiation from the near-axis zone. In Fig.7, typical oscillograms of signals from X-ray and neutron radiation monitors, together with discharge current and voltage in the solenoid, are shown. We see that the moments of maximum voltage and X-ray and neutron radiation intensities are separated in time. Measurement of electron temperature in each separate discharge by the absorbent-filter method confirmed the presence of a high-energy electron group in these discharges; this fact has been discovered earlier [6]. At the initial gas pressure of $P_0 =$ 0.2–0.4 torr, the measured values of relative X-radiation absorption give electron temperature values of $T_e = 4$–6 keV. When the initial gas pressure is increased, a tendency towards rising electron temperature is observed. In this case, the spread of experimental points is, however, increased. At $P_0 = 0.6$ torr, discharges with $T_e = 15$–22 keV are observed although most of the discharges had $T_e = 4$–10 keV.

In Fig.8 the calculated curves of the relative X-radiation absorption in filters of different thickness with plotted experimental points are presented. Sufficiently good agreement is observed between the obtained data and a calculation based on the assumption of a Maxwellian electron spectrum. It is not clear how many electrons have these energies.

Measurement of the relative neutron emission intensity has shown that, with an increase in the initial deuterium pressures, some increase in the neutron output is observed, with the maximum lying in the pressure region of 1 torr ($\sim 10^6$ per discharge). The data in question are given in Fig.9.

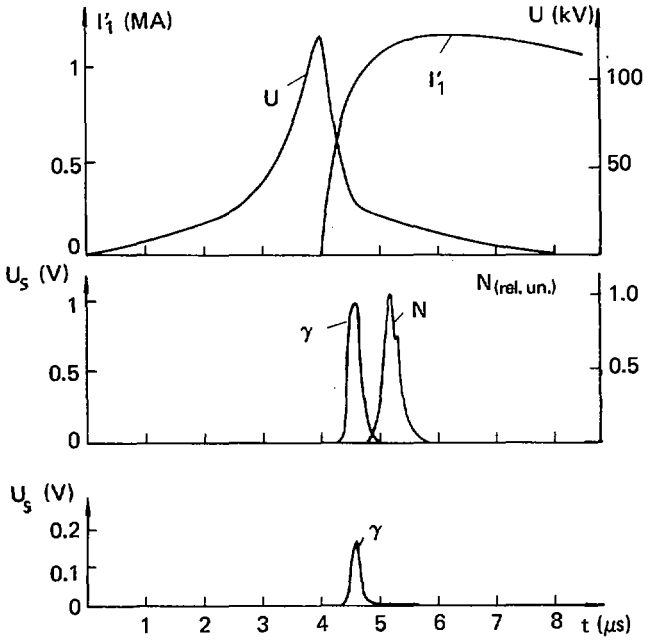


FIG.7. Typical oscillograms of X-(γ) radiation, neutron (N) radiation, current, and voltage in the solenoid, $P_0 = 0.2$ torr D_2.

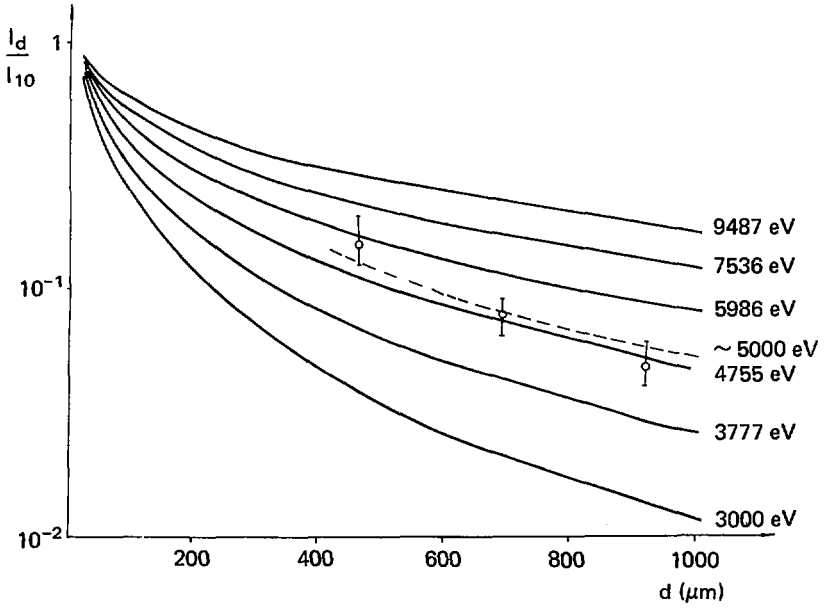


FIG.8. Calculated and experimental functions for determining the electron temperature T_e.

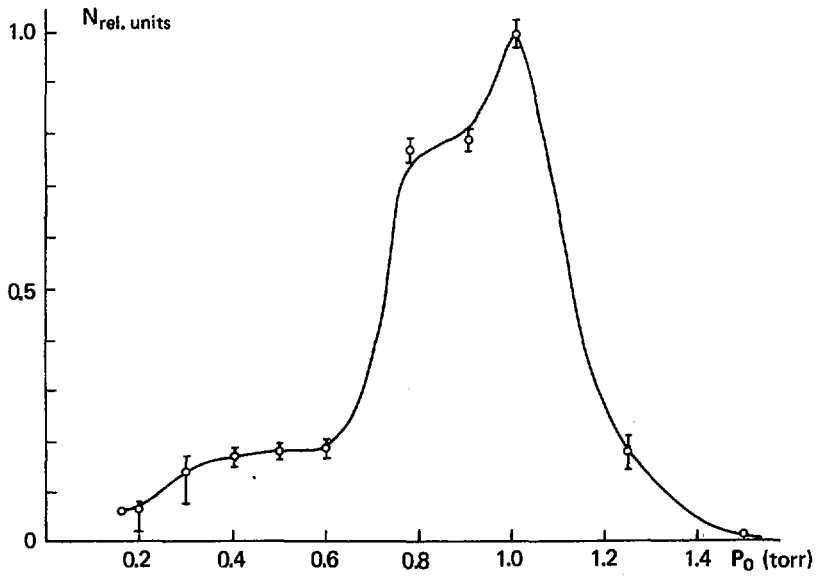


FIG.9. Dependence of relative neutron output on initial deuterium pressure in discharge chamber.

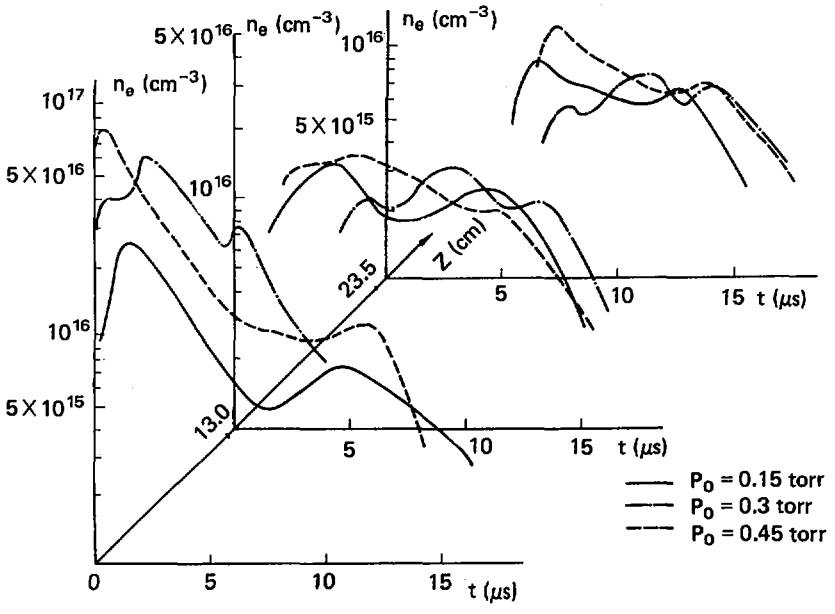


FIG.10. Time dependence of plasma density n_e at discharge chamber axis at different distances from solenoid Z.

To estimate the effect of plasma end losses on the theta-pinch balance, the plasma density has been measured at the discharge chamber axis at different distances from the ends of the solenoid. Observations were made from the side of the discharge chamber by a 'monochromator-image-converter' diagnostic system. In doing so, Stark broadening of the plasma line D_β from the near-axis zone was studied.

In Fig.10, dependence of plasma density on the chamber axis at the solenoid end and at distances of Z = 13.0 cm and 23.5 cm is presented. The leakage time of dense plasma with a density of $n_e > 10^{16}$ cm^{-3} is rather long (10–15 μs).

The maximum longitudinal velocity of plasma front motion is observed at the solenoid cut and amounts to $v_\parallel \cong 10^7$ cm·s^{-1} at $P_0 = 0.3$ torr. A further spreading takes place with a deceleration of $\dot{v}_\parallel = -10^6$ cm·s^{-2}. This phenomenon, as well as the fact that the size of the plasma clusters decreases while they propagate through the vacuum chamber, are evidently due to interaction of the plasma with the gas background in the chamber.

REFERENCES

[1] ELLIS, W.R., et al., Nucl. Fusion **14** (1974) 841.
[2] McKENNA, K.F., et al., Proc. 3rd Top. Conf., Abingdon, 1975 (1976) 375.
[3] LINFORD, R.K., et al., in Controlled Fusion and Plasma Physics (Proc. 7th Europ. Conf. Lausanne, 1975) Vol.1 (1975) 49.
[4] BURTSEV, V.A., et al., ibid., 47.
[5] BURTSEV, V.A., et al., Nucl. Fusion **17** (1977) 886.
[6] BURTSEV, V.A., et al., in Controlled Fusion and Plasma Physics (Proc. 8th Europ. Conf. Prague, 1977) Vol.1 (1977) 86.
[7] HOTTHER, K., DOWNING, J., in Controlled Fusion and Plasma Physics (Proc. 8th Europ. Conf. Prague, 1977) Vol.1 (1977) 84.
[8] COMMISSO, R.J., GRIEM, H.R., Phys. Fluids **20** (1977) 44.
[9] McKENNA, K.F., KRISTALL, R., ZIMMERMANN, E.L., Phys. Fluids **18** (1975) 1371.

END PLUGGING OF A HOT LINEAR THETA PINCH

H. AZODI, M. NARAGHI, H. TAHSIRI,
A. TORABI-FARD
Fusion Division,
Nuclear Research Centre,
Atomic Energy Organization of Iran,
Tehran,
Iran

Abstract

END PLUGGING OF A HOT LINEAR THETA PINCH.

With and without solid end plugging schemes, some plasma parameters and stability traits of a 1-m-long, 10-cm-coil-bore linear theta pinch which incorporates modular construction have been investigated. The compressed thermonuclear-like plasma, having $n_{max} \cong 10^{16}$ cm^{-3}, $T_i > 1$ keV, is stable for a short life of 5–6 μs. Numerical calculations treated in the sharp-boundary, two-fluid approximation, with the plug assumed to be held at a constant temperature and experiencing no ablation, have shown increases in n, T_e, T_i and N_N, the rate of neutron production, when the end is plugged compared to the unplugged case. Streak photography at the midplane has shown a more stable but less compressed plasma when end plugs are used. Measurements of the extent of damage incurred by the plugs have shown that a similar amount of loss of plug material occurs whether the plugs are placed at the ends of the coil or positioned 20 cm outside the coil. Further, it was determined that the plugs did not produce any unfavourable effect on the compressed plasma.

1. INTRODUCTION

The linear theta pinch has a number of advantages over toroidal configurations such as tokamaks and stellarators in its ease of plasma heating and its favorable plasma equilibrium and stability properties. Due to the simplicity of their geometry, which readily lends itself to reactor engineering, and their neutral stability, there has been a resurgence of interest in linear theta pinches. The well-known problem with these linear devices, however, remains that the plasma escapes from the open ends of the theta pinch at essentially the ion thermal velocity. The plasma pressure gradient along the magnetic field lines drives plasma out of the ends of the theta pinch in a time $\tau_{eL} \simeq \frac{L}{V_{T_i}}$ where L is the length of the device and V_{T_i} is the ion thermal speed.

Several methods [1] have been proposed to reduce end losses in theta pinches. Some of these schemes involve solid end plugs, multiple mirrors, and re-entrant end plugging [2], [3]. End plugging in the form of solid walls or a dense gas [4] presents a direct approach to the problem of stopping axial plasma flow. The increased inertia of the ablated material from the solid end plug can, in principle, prevent the particle flow. Thermal conduction as a main loss mechanism is reduced by the high-Z plasma produced by the plug material near the ends.

The object of this paper is to discuss the numerical analysis and compare some experimental work performed on solid end plugging with the ALVAND I linear theta pinch, which has produced a hot plasma of $n_{max} \simeq 10^{16} cm^{-3}$, $T_i > 1$ keV, for a period of about 5-6 μs. A description of the numerical analysis is given in Section 2. Section 3 describes the general set-up of the experiment and the end plugging used. Finally, in the last section, the discussion is summarized.

2. NUMERICAL ANALYSIS

The time behavior of the plasma parameters at the midplane of the ALVAND I theta pinch was calculated using a code developed from a computer printout of a similar code originating at LASL [5]. This code, ENLOSS, treats the theta-pinch plasma in the sharp-boundary, two-fluid approximation. The loss of particles through the open ends is accounted for by a rarefaction wave which travels from the ends to the midplane, whose velocity may be chosen as the thermal, acoustic, or Alfvén velocity. The line density at the midplane remains constant until the arrival of the rarefaction wave and decays exponentially afterwards. In view of the experimental evidence [6], the normalized loss time, η, determining the time constant of this decay is set equal to 2.6. Unlike similar codes which assume the internal flux to be constant, magnetic field is assumed to diffuse into the plasma due to finite conductivity of the plasma sheath. The electron and ion fluids are assumed to be cooled due to the decreasing crowbarred external magnetic field. Besides further cooling through particle losses and heat conduction by electrons and ions, heat exchange between the two fluids, proceeding at the classical rate, is also included.

In the case of an end-plugged theta pinch, the same code, ENLOSS, has been used, within a simplified working model, to predict the plasma behavior at the midplane. In this model we neglect the energy deposited

on the end plugs and the subsequent formation of ionized plug material regions at the ends of the plasma column. This would be as though the plugs were in contact with a heat bath at constant negligible temperature. Within this approximation the only effect of the end plugs is to hold the line density constant, which can easily be incorporated in this code.

From the established scaling law of maximum electron temperature, $(T^e_{max})^{7/2} \propto L \frac{B^2}{\tau_R}$, for the discharge characteristics of ALVAND I, B = 70 kG, and τ_R = 3 μs, a maximum electron temperature of 250 eV is expected. A 90-degree ruby-laser scattering experiment has been set up to confirm this and measure the time variation of electron temperature. The time variations of plasma parameters, for open and end-plugged cases, are presented in Figures 1, 2 and 3 for initial filling pressure of 10 mtorr, maximum density of 4 X 10^{16} cm^{-3} and maximum β of 0.9. All maxima are assumed to occur at the rise-time of the magnetic field. As may be seen from Figure 1, end-plugging the one-meter ALVAND I theta pinch is expected to increase the energy containment time by a factor of two, from 4.5 μs to about 10 μs. This improvement factor may prove to be higher in practice since the ion fluid is collisionless. In the 5-m Scylla IVP, in which the ion-ion mean free path λ_{ii} was nearly equal to L, the ion heat conduction coefficient K^i was measured to be smaller than the classical value by a factor of 20 [5]. It should be noted that the same reduction of K^i was used in calculating the above-presented results. However, in the ALVAND I device, in which $\lambda_{ii} \simeq 10$ L, ion heat conduction should contribute much less to the overall energy losses. In the absence of ion heat conduction, we expect the end-plugged energy containment time to be improved over the open-ended case by a factor of 3.5.

3. EXPERIMENTAL

A theta-pinch device (Figure 4) with the following operating parameters has been utilized: length of compression coil, 1 m; diameter (2R), 10 cm; capacitor bank energy, 400 kJ; rise-time of magnetic field, 2.7 μs; fall-time of B-field (e^{-1}), 70 μs; and maximum compression field in 10 cm diameter, 7 Tesla. In addition to the singularly fast rise-time and intense B-field characteristics of ALVAND I, a unique modular construction of the capacitor bank and power

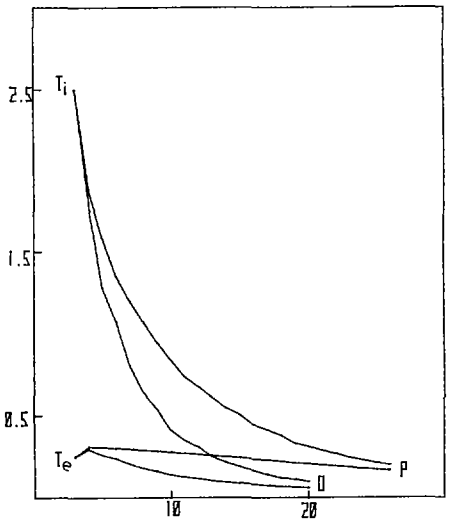


FIG. 1. Ion and electron temperatures, T_i and T_e in keV, versus time (μs), for the open (O) and end-plugged (P) ALVAND I.

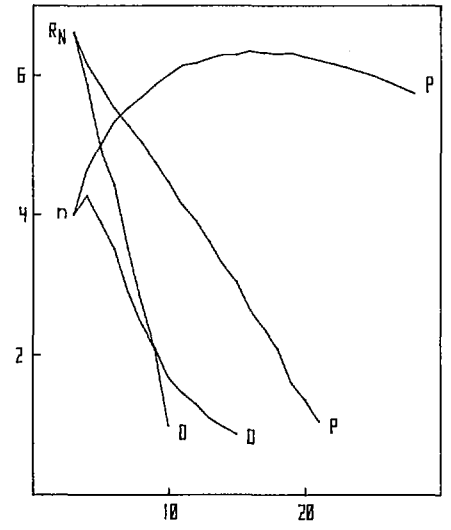


FIG. 2. Particle density, $n \times 10^{-16}$ (cm^{-3}) and rate of neutron production, $\log_{10} R_N$ ($cm^{-1} \cdot \mu s^{-1}$), versus time (μs) for the open (O) and end-plugged (P) ALVAND I.

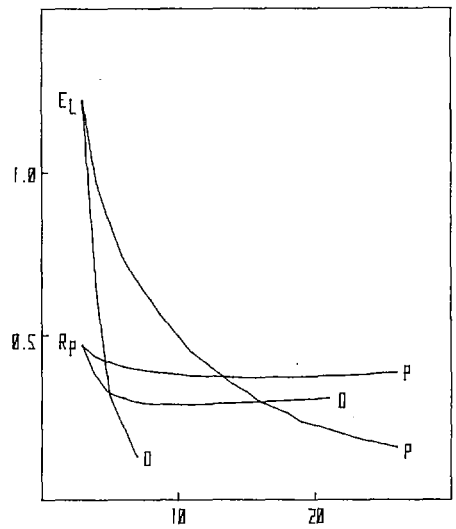


FIG. 3. Plasma radius R_p (cm) and line energy E_L ($kJ \cdot m^{-1}$) versus time (μs) for the open (O) and end-plugged (P) ALVAND I.

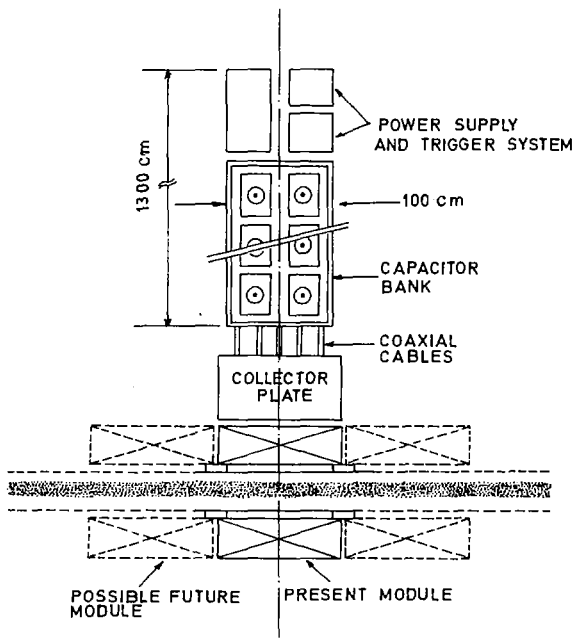


FIG. 4. General set-up of the experiment, showing modular construction of ALVAND I linear theta pinch.

supply has been adapted because it permits relatively easy tests of scaling and end-loss studies. A one-meter-wide module includes the basic components, i.e. capacitors, spark gaps, crowbar components, etc. Modules can be added as desired on either side of the compression coil to study systematically the evolution of the plasma in the linear theta pinch.

The energy storage bank for ALVAND I utilizes 78 energy storage capacitors, each rated at 2.8 μF and 60 kV. Each capacitor has its own start and crowbar switches. Both a start switch and a crowbar switch are contained in a single low-inductance enclosure mounted directly on the high-voltage bushing of each capacitor.

The electrical output from each capacitor is carried to a common collector plate by RG-17/14 low-inductance coaxial cables. The one-meter-long load compression coil is, in turn, bolted directly to the one-meter-long collector plate. Separate triggers are used for each of the 78 start and 78 crowbar switches. The start-switch trigger system uses one master trigger generator, the output of which is used to trigger eight sub-master trigger generators. Each of the sub-master trigger generators can provide ten simultaneous trigger outputs for ten start switches. An identical trigger system is used for the crowbar switches with the time delay between the start and crowbar triggers controlled by a single electronic delay generator. A high-voltage power supply is provided which can charge the full 400 kJ bank to 60 kV in less than 30 s.

Gas preionization was achieved with an axial Z-pinch discharge by providing two electrodes inside the quartz tube. The Z-pinch energy was supplied by a 6-μF capacitor charged to 30 kV. Spectroscopic measurement of the preionization gas showed that, at the time of theta-pinch discharge, more than 80% ionization of the gas occurred. The Z-pinch was fired about 50-100 μs ahead of the theta pinch. Also, no appreciable impurities were observed in the preionized gas generated by the Z-pinch discharge (Figures 5 and 6).

The diagnostic measurements currently under way use diamagnetic loop probes, Garching Instruments EL 154 image converter camera, 20-ns pulsed ruby-laser Thomson scattering, and silver-activated neutron counters. The total current, the voltage across the coil, and the axial magnetic field were measured with appropriate pick-up loops and probes.

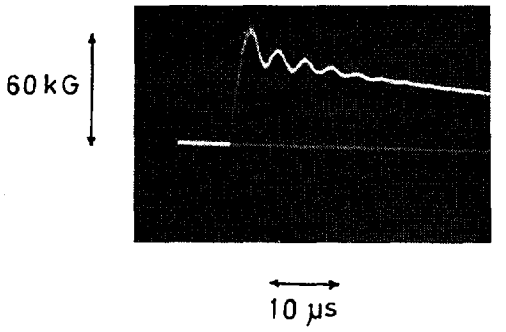


FIG. 5. Overlaid oscilloscope traces of B-field (kG) versus time (μs) in the midplane.

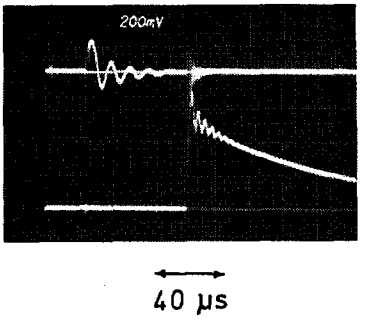


FIG. 6. Overlaid oscilloscope traces of Z-pinch preionization followed by theta pinch main current, relative intensity versus time (μs).

End plugs were used in the form of disks 5 cm in diameter and about 0.5 cm thick. The diameter chosen for the disks was a few times larger than the diameter of the plasma itself, about 1 cm. The surface of the plug was first prepared for plasma exposure by grinding it over grade-80 emery paper, then gradual progression to finer grades, and eventually finishing on a selvyt cloth fed with a suspension of 0.3-μm diamond dust. The end plug was then mounted on a stainless-steel specimen holder with its polished face towards the plasma. The specimen holder was designed to hold the end plug anywhere along the tube, enabling a comparison to be made of the radiation effects incurred by various metals and dielectrics, held at numerous points along the axis. In the case of conductive end plugs, radial slots were made in the disk to prevent the azimuthal current (Figure 7).

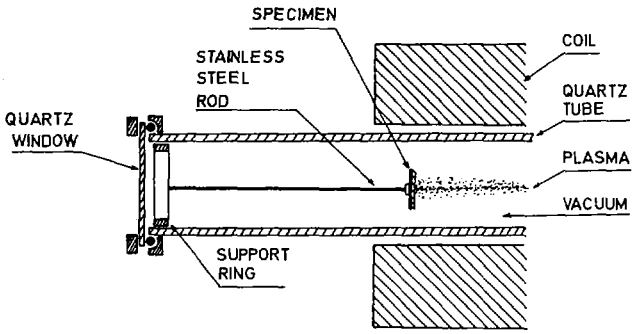


FIG. 7. Solid end plugging set-up.

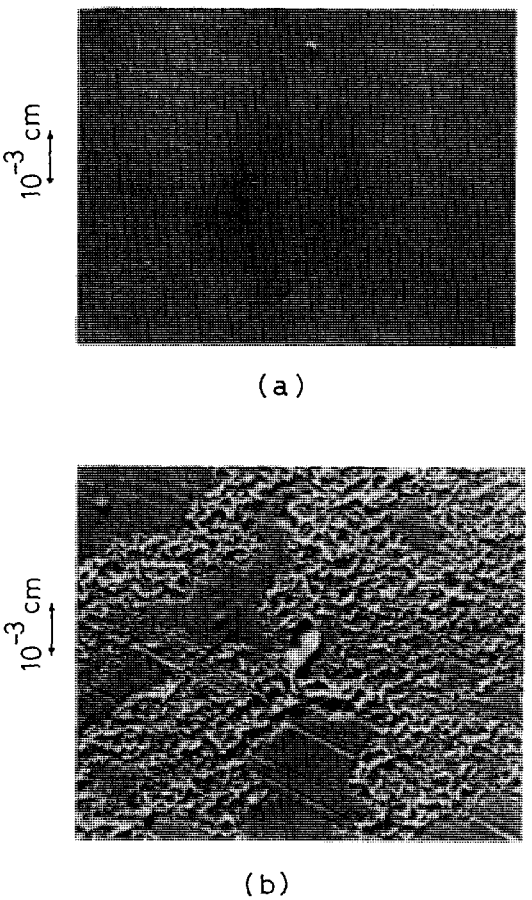


FIG. 8. Scanning electron microscope photographs taken (a) before and (b) after exposure to plasma particles. The exposure was repeated 20 times before photograph (b) was taken.

The surface of the end plug was examined and photographed both before and after plasma exposure, using optical and electron microscopes. The latter was a JEOL JSM-35 scanning electron microscope capable of attaining a resolution of 200 Å. As well as the normal secondary electron images, images relating to the topography and composition of the sample could be obtained. The sample-tilting facility incorporated into the machine made it possible to form shadows of blisters, etc., thus enabling their height to be estimated. Typical pre- and post-exposure photographs using the scanning electron microscope are shown in Figure 8.

Dielectric plugs were employed using readily available materials having various Z-values, such as boron nitride, lithium aluminum hydride, alumina, and quartz. With the dielectrics it was not possible to prepare the surfaces as meticulously as with the metals.

A base vacuum of 10^{-6} torr was provided using a turbomolecular pump. The filling pressure necessary, i.e. 3-20 mtorr, was achieved by allowing the preset pressure of gas (usually D_2) contained in a small chamber to flow into the quartz tube.

A quartz tube with an outer diameter of 10 cm and inner diameter of 9.2 cm, wall thickness 4 mm, was employed. The tube was 200 cm long, protruding 50 cm on each side of the coil to allow measurements on the plasma outside the coil. Slits were provided on the theta-pinch coil at distances of 25 cm to allow for streak photography in the middle or at other positions. A quartz window at the end flange allowed for end-view photography.

4. DISCUSSION

Streak-camera photographs, viewing from the midplane, with and without end plugs, are shown in Figure 9. Under the operating parameters used in this experiment, the examination of these streak photographs revealed that the plasma did not exhibit any wobble instability. Streak photographs from the end have shown a uniform circular compression with no sign of Raleigh-Taylor instabilities.

Also, from streak photography it was determined that the plasma lifetime, or the energy confinement time, was improved from an average of 5 μs without end plugs to about 11 μs with end plugs. The compressed plasma radius, however, was slightly larger in the second case, thus showing a less compressed plasma with the end plugs than in the open-ended case.

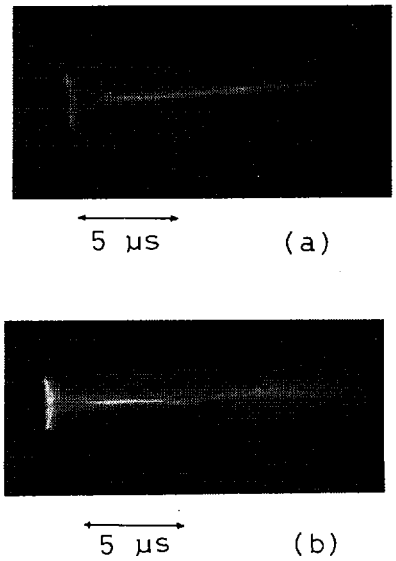


FIG. 9. Streak photographs (a) with and (b) without end plugs.

The plasma properties in the region exterior to the coil were studied by the measurement of damage incurred by the plugs. Figure 8 shows the scanning electronic microscope photographs of the end plug surface taken before and after exposure to the plasma. Examination of a series of these photographs at different axial positions has shown that the plasma properties do not change up to distances 20 cm from the ends of the coil. This result seems to confirm that the plasma flow out of the theta pinch carries the magnetic field lines, and the compressed plasma extends itself distances as much as 20 percent of the coil length.

The results from other diagnostic measurements at the time of this writing were not sufficient to make any quantitative conclusions or comparisons of empirical results with the numerical analysis presented. However, from the analysis and the experimental results which have been obtained, we may generally conclude that the solid end plugs improve the energy confinement time and energy line density, and prevent particle flow beyond the plug without having any unfavorable effect on the compressed plasma.

ACKNOWLEDGMENTS

The authors wish to acknowledge their indebtedness to Dr. A. Mohsenian for his assistance in materials testing, A. Soltanieh, A. Ghareh-Chaie, J. Goshtasbi and K. Kamali from the Neutron Physics Group for their help in neutron detection, and finally M. Farahani, A. Rashidinia, R. Rostami and B. Safaii for their aid with the experimental work.

REFERENCES

[1] UNITED STATES DEPARTMENT OF ENERGY (Division of Magnetic Fusion Energy, Applied Plasma Physics Program), Linear Magnetic Fusion, Summary of Seattle Workshop, 9–11 March 1977.
[2] MALONE, R.C., MORSE, R.L., Phys. Rev. Lett. **39** (1977) 134.
[3] COMMISSO, R.J., et al., Phys. Rev. Lett. **39** (1977) 137.
[4] HIRANO, K., WAKATANI, M., Inst. Plasma Physics, Nagoya Univ., Research Rep. IPPJ-262 (1976).
[5] SIEMON, R., LASL, private communication.
[6] McKENNA, K.F., YORK, T.H., Phys. Fluids **20** (1977) 1556.

DISCUSSION

H.A.B. BODIN: Can you say whether the experimental results confirmed the general trends predicted by the computations you described?

M. NARAGHI: The numerical analysis predicts that the end-plugged energy confinement time will be better than the open-ended time by a factor of 3.5 (Fig.3). From the streak photographs (Fig.9), it was determined that the confinement time rises from 3.5 μs to 11 μs; in other words, an improvement factor of more than 3.5 was achieved.

RECENT DEVELOPMENTS IN LINEAR THETA-PINCH AND LASER-HEATED SOLENOID RESEARCH*

K.F. McKENNA, R.R. BARTSCH, R.J. COMMISSO,
C.A. EKDAHL, K.B. FREESE, R.F. GRIBBLE,
F.C. JAHODA, G. MILLER, R.E. SIEMON,
J.U. BRACKBILL, J.P. FREIDBERG,
S.P. GARY, H.R. LEWIS,
A.G. SGRO, L. TURNER, D. WINSKE
Los Alamos Scientific Laboratory,
University of California,
Los Alamos, New Mexico

A.L. HOFFMAN, E.A. CRAWFORD,
D.D. LOWENTHAL, D.C. QUIMBY
Mathematical Sciences Northwest, Inc.,
Bellevue, Washington

G.C. VLASES, H.W. HOIDA, Z.A. PIETRZYK
University of Washington,
Seattle, Washington,
United States of America

Abstract

RECENT DEVELOPMENTS IN LINEAR THETA-PINCH AND LASER-HEATED SOLENOID RESEARCH.

Experimental and theoretical investigations of end-loss, end-stoppering, stability and heating in linear theta pinches have been conducted. Efforts of groups at the Los Alamos Scientific Laboratory (LASL), Mathematical Sciences Northwest (MSNW), and the University of Washington (UW) are reported. At LASL, the experimental results from the high-energy ($T_e + T_i = 3.3$ keV, $n_e = 1.5 \times 10^{16} cm^{-3}$) 5-m Scylla IV-P theta pinch support the following: (1) Single-mode m = 1 'wobble' instability rotation frequencies of ~ 180 kHz are associated with axial wavelengths of 400–800 cm. (2) Ion thermal conduction is an unimportant loss mechanism. (3) Evidence of rarefaction-like waves is seen. (4) The normalized end-loss time is independent of the plasma beta and collisionality regime. (5) Plasma flow from the ends remains collimated and convects magnetic fields. (6) LiD end plugs produce a three-fold increase in energy containment time over the open-ended configuration.

Theoretical work at LASL has demonstrated the following: (1) An explanation of the m = 1 'wobble' instability has been formulated. (2) A correct description of end-loss must include the magnetic curvature term in the axial momentum equation. Mirrors increase the lifetime of a collisional plasma less than guiding centre theory predicts. (3) Magnetic field

* Work performed under the auspices of the US Department of Energy.

gradient drift can reduce the growth rate of the universal drift instability. (4) Collisionless magnetoacoustic heating can be an effective heating mechanism in theta pinches. At MSNW-UW, CO_2 laser heating of low-energy ($T_e \cong T_i \cong 2$ eV; $n_e \cong 2 \times 10^{17}$ cm^{-3}) plasmas is accomplished over a 1-m column length. Maintenance of an on-axis density minimum is demonstrated.

INTRODUCTION

High energy thermonuclear plasmas can be generated in linear theta pinches. Areas of current interest in the fusion application of these devices include end-loss, stability, and heating. End losses, which present a fundamental limitation on the plasma energy containment time, result from particle loss through the theta-pinch open ends and axial thermal conduction losses along the magnetic field lines. To obtain relevant fusion reactor designs, the detailed mechanisms involved in these end-loss processes must be identified and effective end-stoppering techniques developed. In addition, an understanding of the plasma stability characteristics is required; the m=1 'wobble' is the only observed MHD instability of significance in high energy theta-pinches. The development of alternative plasma heating techniques would also enhance the theta-pinch reactor concept and reduce the technological demands presented by implosion heating.

In this paper experimental and theoretical studies of end-loss, end-stoppering, stability and heating in linear theta pinches are presented. Efforts of groups at the Los Alamos Scientific Laboratory (LASL), Mathematical Sciences Northwest (MSNW), and the University of Washington (UW) are reported. Experiments on the LASL high energy Scylla IV-P theta pinch have been directed towards the investigation of particle and thermal losses, the plasma flow and magnetic field interaction processes near the coil ends, end-loss suppression using solid material end plugs, and the plasma stability characteristics. Theoretical efforts at LASL have dealt with the driving mechanisms of the observed m=1 'wobble' instability, numerical studies of particle end-loss, instability effects on radial diffusion, and magnetoacoustic heating methods. The interaction of CO_2 laser radiation with theta-pinch like plasma columns is being studied at MSNW and UW. In these experiments the channeling of the laser light along the axis of a partially ionized plasma column, and the resultant heating, is investigated.

1. LASL SCYLLA IV-P THETA-PINCH EXPERIMENTS WITHOUT END PLUGS

1.1. Theta-Pinch Experimental Arrangement. Scylla IV-P has a maximum energy storage of 2 MJ at 60 kV primary bank voltage. Six-hundred 1.8-μF capacitors feed the 500-cm long, 11.2-cm dia. single-turn compression coil. Primary bank operation at 45 kV generates a vacuum E of 0.6 kV/cm at the inside wall of the 8.8 cm i.d. quartz discharge tube and a peak compression field, B_z, of 4.8 T is obtained 3.1 μs after discharge initiation. A crowbar system extends the magnetic field in time with an L/R decay of 110 μs. The experimental results discussed below are obtained at 45 kV primary bank voltage and with a theta-pinch fill pressure of 10 mTorr D_2. To provide access for optical and internal plasma diagnostics in the theta-pinch end regions, each end of the discharge tube is terminated, 4.5 cm beyond the coil ends, within a quartz expansion chamber. The chambers are 20 cm in dia., 45 cm long, and end-supported by 20-cm dia. metal vacuum tees.

1.2. Plasma Parameters. The plasma column total particle inventory, N_e, and axially averaged peak density, n_a, are determined from holographic ruby laser end-on interferograms. Near the time of peak magnetic field when the plasma column is highly symmetric and instability free, the plasma radius, a, is obtained from the interferometrically measured radial density profiles; a correction for refractive bending of the interferometer laser light is applied. The onset of a finite-wavelength m = 1 instability at t ≃ 5 μs distorts the radial density profiles recorded on the interferograms. The plasma radius is then determined from the relation $a = (N_e/ n_a L)^{1/2}$, where L is the coil length. It should be noted that the low-density plasma 'halo' observed to surround the central plasma column for times $t \gtrsim 15$ μs is not included in the interferogram analysis. A diamagnetic loop and probe arrangement at the coil midplane is used to measure the magnetic flux, $\Delta\phi$, excluded by the plasma. The excluded flux measurement is combined with the plasma radius data to obtain the peak plasma beta, β_a. The total plasma temperature is estimated from pressure balance, $T_e + T_i = \beta_a B_z^2/n_a k 8\pi$. The electron temperature, T_e, also measured at the coil midplane, is determined from 90° Thomson scattering. The peak magnetic field plasma parameters are: $n_a \simeq 1.5 \times 10^{16}$ cm^{-3}, $T_e + T_i \simeq 3.3$ keV, $T_e \simeq 570$ eV, $\beta_a \simeq 0.9$ and $a \simeq 1.0$ cm. At t = 6.0 μs, after the magnetic field has passed through its maximum oscillation and the crowbar has become effective, the plasma parameters are: $n_a \simeq 0.9 \times 10^{16}$, $T_e + T_i \simeq 2.3$ keV, $T_e \simeq 440$ eV, $\beta_a \simeq 0.6$ and $a \simeq 1.2$ cm.

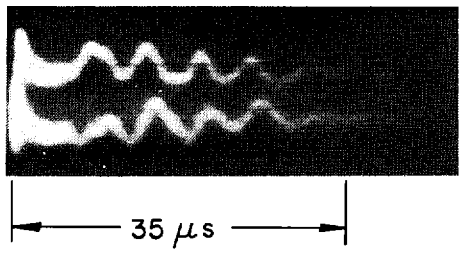


FIG.1. Stereoscopic streak photograph taken at the coil midplane.

1.3. Plasma Stability. The plasma stability characteristics are determined from side-viewing stereo streak photographs and an axial array of 18 (9 vertical and 9 horizontal viewing) optical plasma-position detectors. Figure 1 presents a typical stereo streak photograph taken near the coil midplane. The upper streak shows the plasma viewed from the top of the coil, and the lower streak shows the plasma viewed from the coil front. The slight curvature evident at early times (t < 5 μs) results from the effect of the theta-pinch magnetic field on the camera image converter tube. The MHD stable plasma column is disrupted by the onset of the m = 1 'wobble' instability at t ≃ 5 μs, which is about the time required for an Alfvén wave to propagate from the theta-pinch ends to the midplane. The following characteristics of the 'wobble' instability have been identified: (1) The column rotates in the direction expected for ion rotation. (2) When the column displays a single mode, it rotates in a plane with a node near the coil midplane. (3) Single-mode rotation frequencies of 180 ± 80 kHz are associated with wavelengths of 400 to 800 cm; however, frequencies of about twice this value have been observed in conjunction with wavelengths of 200 to 400 cm during at least part of the discharge in localized regions of the pinch. (4) The peak amplitude of the motion is about 2 cm.

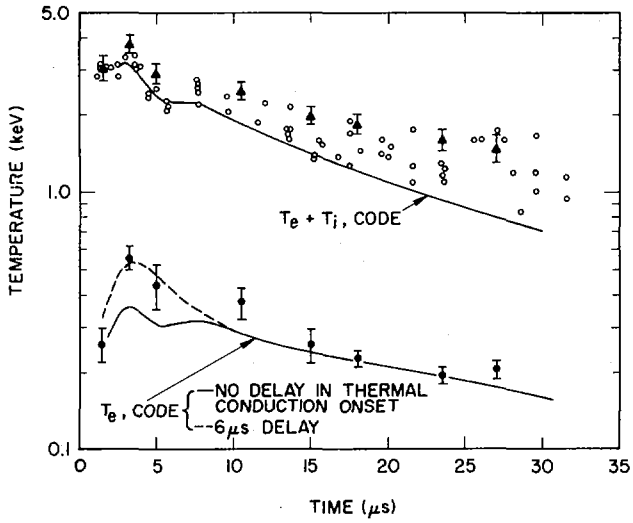


FIG.2. Time history of the electron and total plasma temperature at the coil midplane, and results from MHD code. Data points from: ● Thomson scattering; ○ pressure balance; ▲ neutron emission rate plus Thomson scattering.

Despite a substantial number of theoretical investigations of plasma rotation in theta pinches, only recently has an adequate explanation for the m = 1 'wobble' instability been provided [1]. The plasma stability is determined by solving the eigenvalue problem for the rotating plasma as described by the finite Larmor radius fluid equations including the effects of finite β and $k^2 \neq 0$, where k is the disturbance axial wavenumber. The results of these calculations indicate that the stability threshold, measured in terms of rotation, for the experimentally-observed m = 1, n = 0 mode, is the lowest of any mode (including m = 2, n = 0 and m = 1, n = 1), and in this sense it is the worst mode (m is the azimuthal mode number and n the number of radial nodes). Contrary to early intuition, the fastest m = 1, n = 0 growth rate occurs for $k^2 > 0$, while $k^2 = 0$ is neutrally stable. When both the m = 1, n = 0 and m = 2, n = 0 modes are unstable, the growth rate for the latter is greater than the m = 1, n = 0 growth rate by a factor of about 5. Good agreement with the Scylla IV-P experiment is obtained by assuming that plasma conditions are near the completely end-shorted state, and that the column has a small positive charge (as arises from ambipolar potentials). In particular, the plasma parameters appear to be in the regime where only m = 1, n = 0 is unstable, and m = 2, n = 0 is below threshold. For complete shorting and no column potential, the theory predicts neutral stability, in contradiction to the experimental observations noted above.

1.4. Energy and Particle Containment. The time histories of the total plasma temperature and electron temperature are shown in Fig. 2. The total temperature has been experimentally determined both from pressure balance and from estimates of the ion temperature obtained from the neutron emission rate (measured with plastic scintillation detectors) combined with the

electron temperature from Thomson scattering. The solid lines indicate the results of a recently developed time dependent, zero-dimensional MHD particle and heat-flow code [2], which is used here to model the plasma conditions at the coil midplane. The low values of measured T_e, relative to $T_e + T_i$, result from preferential ion heating during the implosion phase and electron heat conduction to the cold material walls at the theta-pinch ends. For $t > 10$ μs, the zero-temperature boundary condition MHD code, which utilizes classical electron thermal conduction, predicts T_e in agreement with experiment. Delaying the onset of electron thermal conduction for 3-6 μs in the code results in electron temperature predictions which are in good agreement with all the experimental data points. This suggests that a finite time is required for the plasma to flow from the theta-pinch ends, contact a cold material wall, and establish a zero-temperature boundary condition.[1] The characteristic electron thermal conduction time, approximated as $\tau_c^e \simeq (3/2)\, n_e k (L/2)^2 / K_\parallel^e$, where $K_\parallel^e$ is the parallel electron thermal conductivity, is about 1.5 μs at peak field.

The time history of $T_e + T_i$ predicted by the MHD code generally overestimates the measured total temperature decay rate. However, the code does indicate that the ion temperatures are several times greater than the electron temperatures, as observed experimentally, and are obtained by eliminating ion thermal conduction losses in the simulation. Experimentally, the ions are collisionless and thus classical ion thermal conduction, which is a diffusive process resulting from ion-ion collisional interactions, cannot be supported. The ion-ion mean free path, λ_{ii}, is ~ 700 cm at peak field and approaches L only at late times, $t > 30$ μs; $\lambda_{ee} \simeq 30$ cm at peak magnetic field. Accordingly the ions are collisionless throughout the observed plasma lifetime while the electron population remains collision-dominated. The ions lose energy via axial convection and by energy transfer to the lower energy electrons. Ion energy transfer to the collisional electron population accounts for the observed slow decay of T_e compared to τ_c^e. Based on the peak field parameters, the e-folding time constant for ion-electron energy transfer is about 40 μs.

The total plasma energy per unit length, E_ℓ, is obtained from measurements of $\Delta\phi$ and B_z. Using the pressure balance condition and approximating the peak beta as $\beta_a = 2\,\Delta\phi / B_z \pi a^2$, E_ℓ can be expressed as $E_\ell = B_z \Delta\phi / 4\pi$. Figure 3 presents the time history of E_ℓ measured at the theta-pinch midplane. The solid line gives the results of the MHD code. For $t < 5$ μs, E_ℓ is dominated by the rapid rise and fall of B_z. The quiescent period between 5 and 7 μs in which E_ℓ remains constant is terminated by the onset, at $t \simeq 7$ μs, of an abrupt decay. This observation cannot be explained by the gradual decay in B_z but rather results from the onset of convective energy losses at the coil midplane. In collisional plasmas, the onset of convective losses is initiated by the arrival of rarefaction waves from the plasma column ends at $t = L/2V$, where V is the wave speed. The results of the collisional Scylla I-C experiment suggest that the rarefaction waves propagate inward at the cusp speed U [3]. For the Scylla IV-P experiment $L/2U \simeq 7$ μs, which corresponds to the observed E_ℓ decay onset time; axial flow is initiated in the code at this time. A kinetic treatment [4] of the end-loss processes in collisionless plasmas predicts transient phenomena similar to collisional rarefaction waves. The estimated onset time of convective losses from the kinetic approach is in qualitative agreement with experiment [5]. Thus, although the detailed processes involved in the communication of the theta-pinch ends with plasma

---

[1] As pointed out by H.R. Griem, the question of energy deposition by electron thermal conduction to the relatively cold plasma flow in the expansion chambers remains unresolved.

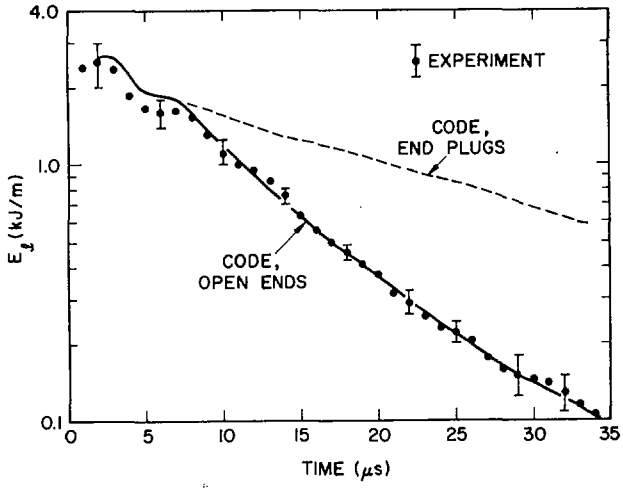


FIG.3. Time history of the energy line density measured at the coil midplane, and MHD code results for open-ended and end-plugged (no axial flow) theta-pinch configurations.

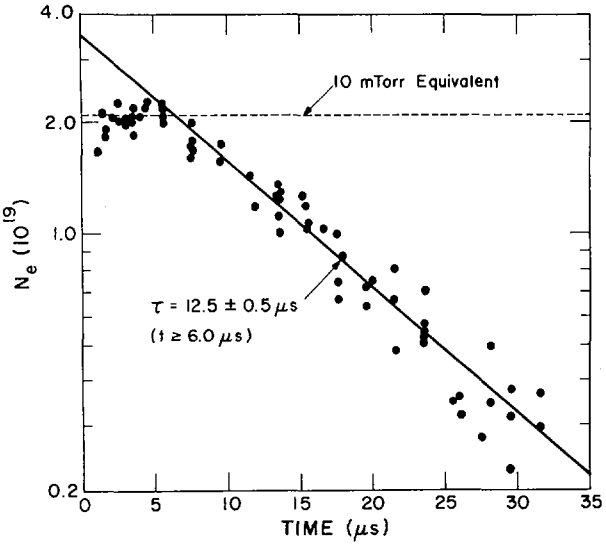


FIG.4. Time history of interferometrically determined total plasma inventory.

at the midplane are different in collisional and collisionless plasmas, the observed large-scale phenomena are similar, i.e. what would appear to be inward propagating 'waves' can be identified in both collisionality regimes.

The time evolution of the electron inventory, N_e, of the central plasma column, obtained from the end-on interferograms neglecting the 'halo' plasma, is presented in Fig. 4. The basic phenomenology of the inventory time history is identical to that observed in previous high-energy theta-pinch experiments. Specifically, N_e remains constant for an initial period of about 6 to 8 μs duration before an exponential decay is observed. The cause of this initial plateau has been identified in the present experiment and will be discussed below. A least squares fit to the data of Fig. 4, for $t \gtrsim 6$ μs, yields an e-folding end-loss time τ of 12.5 ± 0.5 μs.

1.5. Plasma Flow from the Theta-Pinch Ends. The characteristics of the plasma flow into the end expansion chambers are studied photographically, spectroscopically, with magnetic flux loops, and internally with magnetic field probes and a pressure probe sensitive to local particle momentum flux [5]. The plasma flow out of the theta-pinch ends is preceded by an axially outward propagating shock wave initiated during the implosion phase and identified photographically and from local pressure measurements. The impact pressure of the out-flow plasma following the shock wave is measured with a 2 mm dia. acoustic delay line piezoelectric pressure sensor inserted axially into an end expansion chamber. Local pressure measurements are made at various axial positions between the coil end and 26 cm downstream from the end, and extend radially over the diameter of the expansion chamber. From the pressure measurements [5,6] a highly collimated (little radial expansion) axial plasma flow is observed for the entire duration of the experimental observation time (~ 40 μs). The axially-flowing plasma is believed to expand to the walls as it enters the metal vacuum tees located ~ 50 cm from the coil ends. The collimation of the end-flow plasma results in the initial period of constant electron inventory observed interferometrically. Since the end-on interferometer responds to all the electrons within the laser beam path, and since the plasma front following the initial shock wave does not expand out of the interferometer field of view for several microseconds, no decrease in N_e will be detected during this time.

From local magnetic field probe measurements, exclusion of the magnetic field from the expansion chamber is observed until after passage of the shock wave. Near the expansion chamber axis, the magnitude of the magnetic field within the plasma following behind the shock wave exceeds the vacuum field value. These results not only indicate that the magnetic field structure external to the theta-pinch coil is distorted in the presence of plasma but also that magnetic field is 'frozen' into the plasma and convected axially with the flow.

1.6. Particle End-Loss Time. In the determination of the end-loss time τ, the data within the period of artificially constant N_e ($t < 6$ μs) was not included in the analysis. To obtain a consistent comparison, the electron inventory data from previous high-energy theta-pinch experiments have been re-analysed neglecting the period of constant N_e. For comparison with theory the measured particle end-loss time is expressed as $\tau = (L/2)[m_i/2k(T_e + T_i)]^{1/2}\,\eta$, where η is a normalizing parameter representing the ratio of measured end-loss time to thermal-transit time. In Fig. 5, η is plotted against β_a. The solid lines identify existing theories, reviewed in Ref. [7], and the X's mark the results of a recent numerical treatment [8] discussed in section 3.1. The data points (based on peak field plasma conditions) are from the collisionless Scylla IV-P,

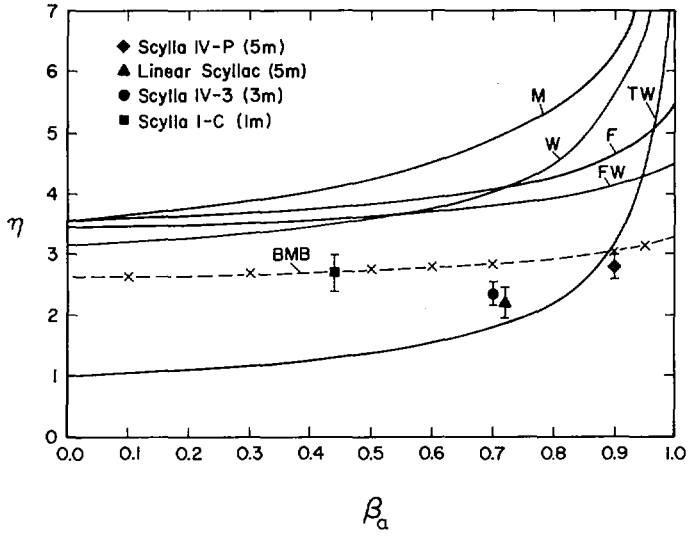


FIG.5. Theoretical and experimental results for η versus β_a.

Scylla IV-3 [9] and linear Scyllac [10] experiments and the collision-dominated Scylla I-C experiment [3]. Examination of Fig. 5 indicates the following: (1) for all experiments the measured particle end-loss times are between 2.2 and 2.8 thermal transit times; (2) the experimental values of η do not display an identifiable dependence on β_a; and (3) the experimental values of η are independent of the plasma collisionality regime.

2. LASL SCYLLA IV-P THETA-PINCH EXPERIMENTS WITH SOLID-END PLUGS

End-stoppering experiments using solid silicon dioxide (quartz), boron nitride (BN), and lithium deuteride (LiD) end plugs have been performed on Scylla IV-P. The plugs are cylindrically shaped, 5 cm in diameter and 3.8 cm thick. The front face of each plug is inserted ~5 cm inside the ends of the theta-pinch coil. Initial experiments [11] using the quartz plugs demonstrated the following: (1) the stability of the plasma column is improved compared to the open-ended case, the m = 1 instability being rapidly damped; (2) plasma does not flow past the plugs and out of the theta-pinch ends; (3) the total plasma neutron yield measured with the plugs inserted is about equal to that measured without the plugs. Ablation of the quartz plug surface amounted to less than 1 μm of plug material ablated per discharge, with about 0.1% of the plasma energy invested in the ablation process. Only a slight increase (~ 20%) in energy-confinement was measured with the quartz plugs. Particle and energy flow to the end-plug region and energy losses by atomic processes (primarily radiation) in this region dominated the energy confinement at the theta-pinch midplane. In an attempt to reduce the energy loss by atomic processes, more recent experiments have been conducted using the lower Z (Z = atomic number) BN and LiD plugs. Results (1)-(3) noted above are also observed in the BN and LiD end-plug experiments.

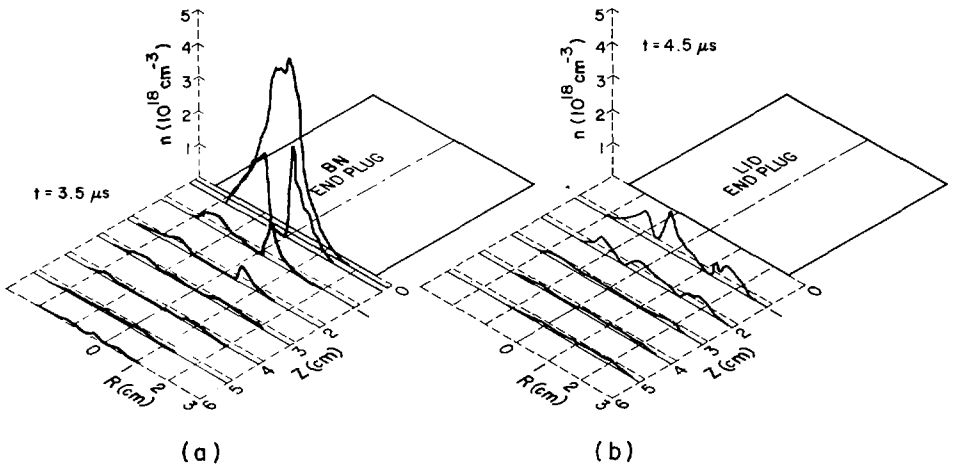


FIG.6. Ablated and ionized end-plug material radial density profiles for (a) BN and (b) LiD end plugs.

2.1. Density Measurements in the Plasma-Plug Interaction Region. Side-viewing ruby laser interferometry is used to observe the ablated plasma near the end-plug surface. Figure 6 presents radial density profiles determined from Abel inversion of the interferometer fringe shift profiles recorded at early times during the discharge for the BN and LiD end plugs. For the BN plugs (Fig. 6a) the density profile close to the plug face (z=0.1 cm) is nearly Gaussian with an e-folding radius about equal to that of the plasma column radius and with peak densities resulting from ablation and subsequent ionization in excess of 5×10^{18} cm^{-3}. At axial positions z > 0.1 cm the ablated BN plug material is concentrated at the outer edge of the column where the axial pressure is less than on the column axis, resulting in annular density profiles. The axial electron line density is determined from area integration over the BN plug radial density profiles. Analysis of the line density profiles shows that the ablation layer formation time is 1-1.5 μs and that the layer attains a thickness of about 1 cm at $t \simeq 5$ μs. After this time the line density slowly decreases, indicating an attenuation in the plug material ablation rate. With the BN end plugs the time history of E_ℓ, measured at the coil midplane, is approximately the same as that measured with the quartz plugs.

LiD is the lowest-Z solid end-plug material available at room temperature. The line radiation from this material should be burned through at an electron temperature of 100 eV. Side-on interferograms obtained with the LiD plugs indicate a higher density of ablated plug material than observed for the BN end-plugs. A sufficient quantity of plug material is ablated and ionized in the first few microseconds of the discharge such that the interferogram fringes within a centimeter of the plug face are completely obscured. Typical radial density profiles obtained with the LiD end plugs are shown in Fig. 6b. As with the BN plugs, a high electron density is observed at the outer edge of the plasma column. However, with the LiD plugs a high concentration of ablated plug material electron density is also measured along the plasma column axis; this observation agrees qualitatively with theoretical predictions [12]. From line density

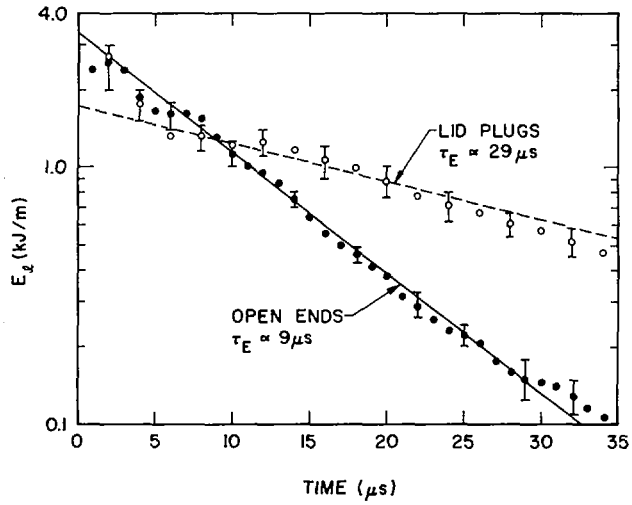


FIG. 7. Time history of the energy line density measured at the coil midplane for the open-ended and LiD end-plugged theta-pinch configuration. τ_E is obtained from a least-squares fit to the data for $t \geq 6.0$ μs.

analysis, the ablation layer formation time is about 1-2 μs. The layer attains a thickness of about 3 cm at t ≃ 5 μs. The ablation process is attenuated for t > 5 μs.

2.2. Energy Line-Density Measurements with LiD End Plugs. With the LiD plugs, E_ℓ measurements at the theta-pinch midplane show a significant increase in energy confinement time over that obtained in the open-ended geometry and with higher-Z end plugs. The time history of E_ℓ with and without the LiD plugs is presented in Fig. 7. With the LiD plugs the energy containment time, τ_E, is increased over a factor of three (from 9 to 29 μs) above that measured with open ends. This result is in agreement with the MHD code calculations shown in Fig. 3, in which the axial plasma flow is stopped and the decay of the midplane plasma energy is dominated by electron thermal conduction to non-radiating ablated plug material and the decay of the confining magnetic field. The calculated [13] line and continuum radiation losses from the LiD plugs are significantly less than that from the higher-Z plugs. In addition, a much higher density of ablated material is experimentally observed to propagate into the plasma column with LiD plugs than with the BN plugs. These results indicate that radiation losses with the LiD plugs are small enough to permit the formation of an ablation zone of sufficient pressure to impede the axial flow and associated energy losses of the deuterium plasma.

3. LASL LINEAR THETA-PINCH THEORETICAL RESEARCH

3.1. End-loss Studies. The computed η values shown in Fig. 5 by the X's are the result of a study of end-loss in which the time-dependent equations for magnetohydrodynamic flow in two dimensions are solved numerically [8]. Other qualitative results of this study are: (1) The total mass in a theta pinch decays exponentially in time due to end-loss with an

end-loss time which is proportional to length. (2) The end-loss time is insensitive to the boundary conditions at the outflow ends. That is, the end-loss time with free expansion at the end, as in the case of a long guide field, is virtually identical to the end-loss time with zero pressure, as in the case of a high-Z end plug. (3) The end-loss time, normalized to the thermal transit time, η, is significantly different from other theories (c.f. Fig. 5), especially in its lack of dependence on the plasma beta [7]. The end-loss time agrees relatively well with experimental data.

A study of the results of the numerical calculations indicates the magnetic field curvature term contributes significantly to the axial momentum equation, and may account for the difference between the results of two-dimensional and one-dimensional solutions of the time dependent equations [14]. The axial momentum equation is written as follows,

$$\rho\left(\frac{\partial w}{\partial t} + u\frac{\partial w}{\partial r} + w\frac{\partial w}{\partial z}\right) + \frac{\partial p}{\partial z} = B_r\frac{\partial B_z}{\partial r} - \frac{\partial}{\partial z}\left(\frac{B_r^2}{2}\right)$$

$$+2 \qquad 0 \qquad 4 \qquad -9 \qquad -3 \qquad 0$$

where ρ and p are the plasma density and pressure, u, B_r, w and B_z, the components of velocity and magnetic field in r and z respectively. Below each term is its typical relative value in the numerical solutions. Note that $B_r\partial B_z/\partial r$ is comparable to $\partial p/\partial z$, and therefore will have a significant effect on the axial flow. The absence of this term, among others, in the one-dimensional approximation probably accounts for the difference in the computed values of η between the one- and two-dimensional solutions. (The simplest description of end-loss may result from the long, thin approximation, $a/L \ll 1$, where a is the plasma radius and L the length of the theta pinch [15]. In this approximation, only the last term in the above equation is $O((a/L)^2)$ and may be deleted. However, no comparable solutions of the ordered equations are available.)

The results of a study of the effect of single mirrors on plasma confinement are shown in Fig. 8. There, the variation of η with mirror ratio, M, is shown for $0.25 \leq M \leq 4$, and compared with measurements made on linear Scyllac [10]. In agreement with that experiment, the mirrors reduce end-loss, but much less effectively than guiding center theory predicts.

3.2. Magnetic Gradient Effects on the Universal Instability. The density gradient driven universal instability is expected to govern radial diffusion in theta-pinch plasmas on fusion time and distance scales since, unlike other cross-field instabilities, it is unstable for arbitrarily small density gradients. However, finite plasma beta (either due to the inclusion of magnetic gradient or electromagnetic effects) tends to reduce the growth rate of the universal instability and can even stabilize it [16]. Here the linear Vlasov theory of the universal instability in a unidirectional magnetic field ($\mathbf{B} = \hat{z}B$) is considered in the slab model with the local approximation in the electrostatic limit but including the full resonant effects of a magnetic field gradient drift. Inclusion of the ∇B drift requires expression of the linear dispersion relation in terms of an integral over $v_\perp$, the perpendicular drift speed. Solutions to the dispersion relation computed without approximation demonstrate that the effect of a magnetic field gradient (expressed here in terms of the local ion beta, $\beta_i = 8\pi nkT_i/B^2$) is to reduce the maximum growth rate γ_m of the universal instability. Numerical analysis demonstrates that the ion ∇B effects are more important than the corresponding electron contributions,

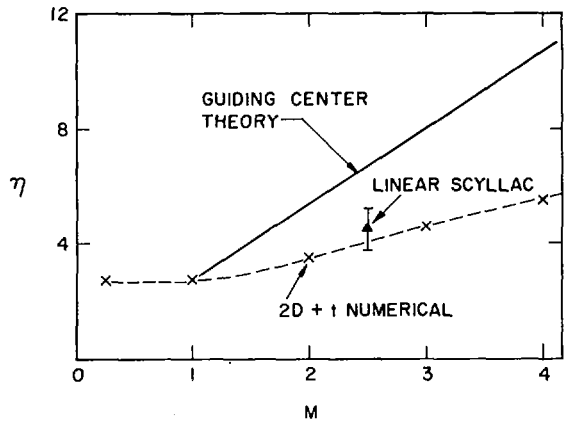


FIG.8. Comparison of the variation of η with M as computed from the two-dimensional, time-dependent equations with guiding center theory and data from linear Scyllac.

but that both act to reduce the growth rate. The increased damping is due to velocity space broadening of the electron Landau resonance driving term and a similar extension of the ion Landau damping term into the resonant ion region. The velocity broadening of the electron resonance is small compared to the width of the electron distribution, and these computations have demonstrated that expansion of the electron susceptibility to first order in the reciprocal magnetic gradient scale length (ϵ_B) yields results equivalent to those from the full integral. However, a relatively small value of β_i brings the ∇B resonance well into the ion distribution, and various approximations to the ion susceptibility fail as β_i increases. One approximation, an expansion of the ion susceptibility to first order in ϵ_B, yields a maximum growth rate that agrees with the exact result to within a few percent for only rather low values of β_i, $\beta_i < 0.02$, and is roughly 60% larger at modest β_i, $\beta_i = 0.2$, for typical parameters ($T_i = T_e$, $m_i = 3674\ m_e$, ratio of electron-ion relative drift speed to ion thermal speed = 0.05). A second approximation, which involves replacing the v_I^2 factor in the Fried-Conte function with $2\ T_i/m_i$, is somewhat better. The maximum growth rate computed with this approximation agrees with the exact result to within 2% for $\beta_i < 0.08$ and is only 20% larger at $\beta_i = 0.2$.

3.3. Magnetoacoustic Heating. Magnetoacoustic heating is an attractive method for preferentially heating plasma ions when an appropriate dissipative mechanism exists at a convenient magnetoacoustic resonant frequency. The observations of collisionless damping of magnetoacoustic waves in a high-beta plasma [17] are experimental evidence for the existence of a dissipative mechanism in a collisionless plasma. For a linear theta pinch, magnetoacoustic heating would not impose a limitation on end-stoppering schemes. With a judicious choice of parameters, magnetoacoustic heating may allow the use of lower values of induced RF electric fields than are required when implosion heating is the sole method of heating.

We have studied theoretically the physics relevant to magnetoacoustic heating of a screw pinch (equivalent to a theta pinch when $B_\theta = 0$) in a collisionless plasma regime by two approaches and we are applying the results to cases of experimental interest. Heating times and associated induced RF electric fields have been computed. Both approaches are based on the Vlasov-fluid model [18] in which collisionless ions and massless, fluid electrons are treated under the assumptions of quasi charge neutrality and negligible displacement current. The two approaches differ with respect to their ordering of small parameters and with respect to their treatment of the boundary between the plasma and a surrounding vacuum. In the first treatment [19], the techniques of earlier analyses [20] have been combined with an ordering scheme adapted to the study of magnetoacoustic waves. The basic smallness parameter is the ratio (ion gyroradius)/(plasma radius); in terms of that parameter, the quantities local plasma beta, (plasma radius)/(any scale length of the wave) and (phase velocity along the magnetic field)/(ion thermal velocity) are assumed to be of order unity. This ordering scheme applied to the Vlasov-fluid model provides a physical description of the plasma which contains kinetic effects along the magnetic field lines but retains only fluid-like effects transverse to the field lines; finite-ion-gyroradius effects do not contribute in leading order. A basic result of applying this description to a pinch configuration is the identification of ion Landau damping as a viable dissipative mechanism for converting magnetoacoustic wave energy into ion thermal energy [19]. The Landau damping causes a phase shift in the response of the plasma relative to the phase of an imposed oscillation of the confining magnetic field; this shift is responsible for the dissipation. At a magnetoacoustic resonance the amplitude of the plasma response and the associated rate of dissipation peak. The total rate of energy dissipation is obtained by calculating the Poynting vector external to the plasma column. That the energy dissipated is converted completely into ion thermal energy is proved by use of a thermal transport equation derived from the ion Vlasov equation. In order to obtain the shortest doubling time, τ_d, for the plasma energy with the least induced RF electric field, E, it appears desirable to operate at a ratio of (phase velocity along the magnetic field)/(ion thermal velocity) roughly equal to 0.7. For theta-pinch parameters, we have obtained τ_d's on the order of 10^{-4} s with fields E on the order of 80V/cm.

In the second approach, the effect of finite ion gyroradius on magnetoacoustic heating of a sharp-boundary screw pinch is being studied. In order to take proper account of the sharp boundary, the starting equations are those derived previously for applying the Vlasov-fluid model to a sharp-boundary screw pinch [21]. Within the pinch the collisionless Boltzmann equation for the Vlasov-fluid model has been solved analytically for small values compared to unity of kr_L and ω/ω_{ci}, where k is the largest relevant wavenumber, r_L is the ion gyroradius, ω is the frequency, and ω_{ci} is the ion cyclotron frequency. Finite-ion-gyroradius effects were kept to zeroth and first order and the solution is valid up the sharp boundary. Because this approach uses a more general ordering, it also should be possible to determine whether dissipative mechanisms other than Landau damping are operative for magnetoacoustic heating in a collisionless plasma. A differential equation for $\underset{\sim}{u}$ ($\underset{\sim}{A}^{(1)} = \underset{\sim}{u}\underset{\sim}{XB}^{(0)}$ where $\underset{\sim}{A}^{(1)}$ = perturbation vector potential and $B^{(0)}$ = equilibrium magnetic field) containing finite gyroradius effects was derived by substituting the solution of the collisionless Boltzmann equation into the transverse force-balance equation (the component perpendicular to $\underset{\sim}{B}$ of the Maxwell $\underset{\sim}{A}\underset{\sim}{XB}$ equation). An analytical solution of the equation for $\underset{\sim}{\xi}$ was used to calculate the heating of the pinch in the presence of an oscillatory driving electric field on a cylindrical surface in the vacuum region surrounding the pinch [22]. Numerical studies have been made to examine the primary m=0 magnetoacoustic

resonance in sharp-boundary pinches whose equilibrium parameters were chosen to model the staged theta pinch experiment at LASL [23]. The dependence of the heating rate upon r_L/r_o and kr_o was investigated, where r_o is the pinch radius. The numerical results, which are quite similar for both experiments, can be summarized as follows: 1) For large axial wavelengths ($kr_o < 0.01$), the resonance is extremely narrow and is little affected by changes in r_L/r_o. Because of the narrowness of the resonance, absorption of such long-wavelength waves is uninteresting as a practical heating mechanism. 2) For axial wavelengths such that $kr_o \simeq 2$, the resonance is quite different. For example, with $r_L/r_o = 0.01$, the full width at half maximum is in the range of a few to several percent, and maximum values of Q (the heating rate normalized to the plasma kinetic energy) in the range of $0.0005\ \omega_{ci}$ to $0.02\ \omega_{ci}$ have been computed for a driving electric field of 50 volts/cm. The rate of collisionless absorption for these short axial wavelengths can be very large and may provide a useful heating mechanism for fusion experiments. The plasma response and the heating rate $\underline{j}\cdot\underline{E}$ exhibit radial structure whose scale length is of the order of r_L.

4. MSNW-UW CO_2 LASER-HEATED SOLENOID RESEARCH

The laser heated solenoid fusion concept was formulated to take advantage of the fortuitous match between the absorption length for CO_2 laser radiation at 10.6 μm of reactor grade plasmas and the length needed to achieve net energy output from open-ended linear reactors. The principal requirement of this approach is the necessity of channeling the laser radiation along the centerline of a solenoidal magnet over long column lengths through the formation and maintenance of an on-axis electron density minimum in the plasma. This minimum can be created either by laser breakdown of a neutral gas in a steady magnetic field or by a combination of laser heating and theta-pinch implosion in a rising magnetic field. The latter method, by which the plasma is removed from the wall, is the subject of the present experiments. In this case, the density minimum must be maintained against diffusive erosion from the vacuum boundary.

Beam propagation and heating has been investigated in two separate experiments, one at MSNW employing several kJ's of CO_2 laser radiation in a 2-μs pulse to heat plasma columns contained in a 1-meter long, 3.8 cm bore solenoid producing a magnetic field rising to 6 T in 4.7 μs. Experiments at the UW utilize a 1 kJ laser and a 22-cm long, 3.3 cm bore solenoid producing a magnetic field rising to 14 T in 4.2 μs.

4.1. One-Meter Experiment (MSNW). The MSNW experiment is described in detail in Ref. [24]. A 35-cm diameter annular laser beam is focused to a 2-mm spot size by a 5-meter focal length mirror. Diamagnetic loops measure the excluded flux at either end and in the center of the solenoid. Cross-tube time-dependent interferometry, radial streak photography, and time-dependent spectroscopy are performed through slots at the magnet center. The entire vacuum chamber is statically filled with hydrogen or deuterium at pressures between 0.25 and 2.0 mTorr. The heating results at low and high pressures are remarkably different, reflecting the ability to maintain the on-axis density minimum necessary for beam trapping.

The gas in the magnet is preionized by a fast 12-kA Z-discharge lasting about 1.5 μs, and the main field capacitor bank is switched on 2.5 μs later. Laser heating is initiated during the 300 ns implosion phase. The basic theta pinch produces a plasma compressed by a factor of 2 (at higher pressures) to 3 (at lower pressures) in diameter with a measured temperature

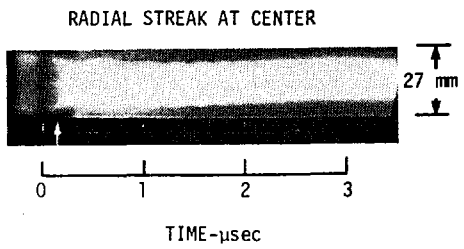


FIG.9. Radial streak photograph of laser-heated 1.5 mtorr D_2 theta-pinch plasma.

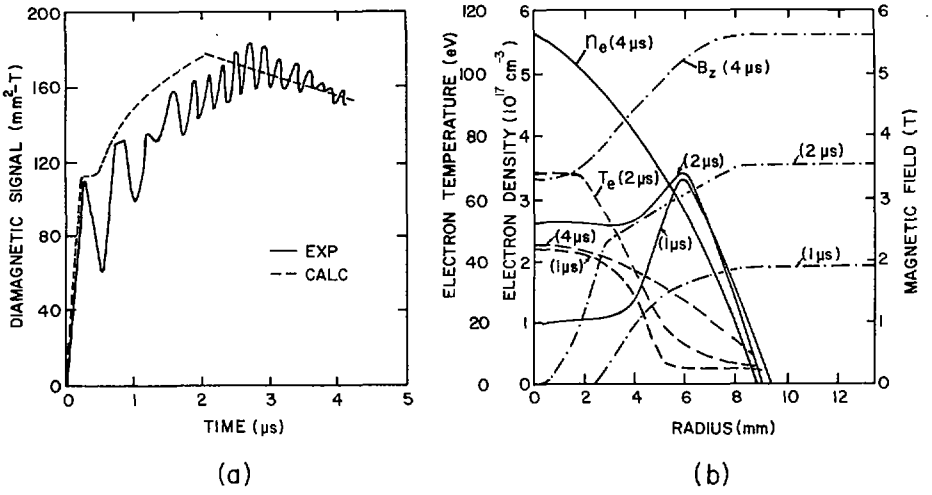


FIG.10. Laser-heated 1.5 mtorr D_2 theta-pinch plasma:
(a) Comparison of experimental and calculated diamagnetic signals; (b) calculated plasma profiles.

of at most 2 eV. At the lower pressures (p_0 < 1 mTorr), laser heating raises the plasma to line energies of about 3 J/cm and peak temperatures of about 40 eV. This heating is nearly uniform along the column length, but decreases rapidly in effectiveness after about 1 μs into the laser pulse. Interferometric measurements indicate a loss of the required density minimum at this time, and lack of continued heating can be attributed to unfavorable beam refraction.

By contrast, laser heating is continuous throughout the 2-μs laser pulse for the higher fill pressures. There is a slight propagation delay in heating from one end of the column to the other, but the column is still heated nearly uniformly. Figure 9 shows a typical radial streak of the heated plasma at 1.5 mTorr D_2 fill pressure. The hydrodynamic bouncing is typical for high β. The diamagnetic signal in the center is compared in

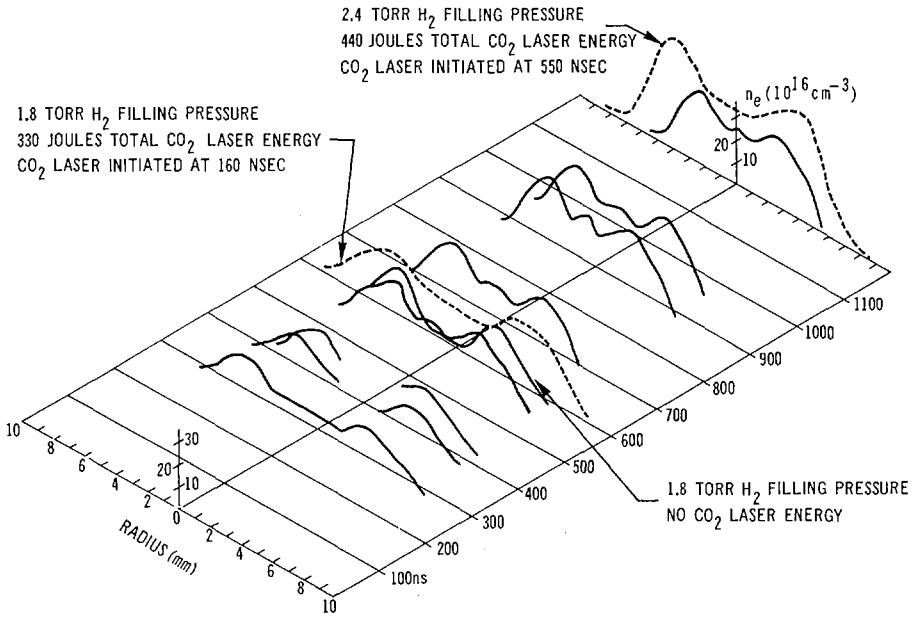


FIG.11. Interferometrically measured radial density profiles for various times in the 22-cm solenoid. Solid curves: unheated columns; dashed curves: laser-heated columns.

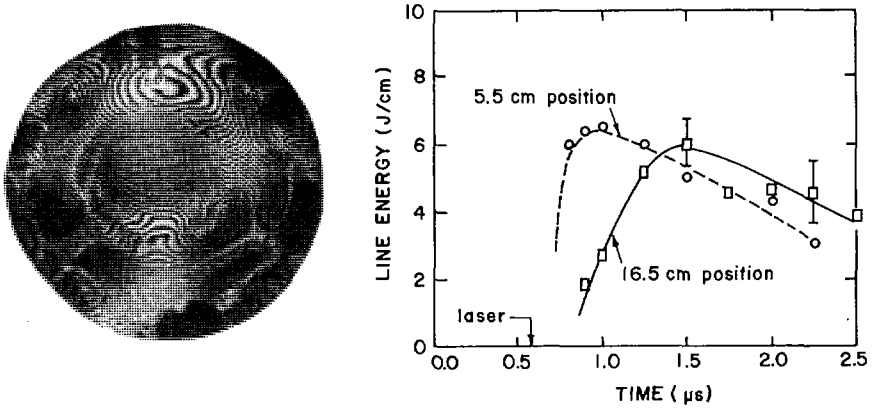


FIG.12. (a) Interferogram of laser-heated plasma in 22-cm solenoid. p_0 = 1.8 mtorr; laser energy 360 J initiated at 220 ns. Picture at 640 ns.

(b) Line energy densities versus time for 22-cm laser-heated solenoid, measured with diamagnetic loops.

Fig. 10a with a one-dimensional, quasi-steady pressure balance model. This model cannot reproduce the hydrodynamic bouncing, but the agreement with the average measured diamagnetism is excellent, even though the calculated absorption length decreases to less than 1 m by the end of the 2-μs laser pulse. In contrast with the lower pressure results, the diamagnetic signal increases throughout the laser pulse, indicating very efficient beam trapping. The plasma energy inferred from the diamagnetic loop measurements increases after the laser pulse to a peak value of 8.5 J/cm.

Figure 10b shows the calculated plasma profiles as a function of time for this experiment. They show a density well persisting throughout the 2-μs laser pulse. Experiments carried out on a shorter solenoid in the UW experiment, where axial interferometry is possible, confirm this density minimum for high fill pressures. The appearance of the 3434 A^{o} C_{VI} line in spectrographic measurements confirms the peak calculated temperatures. Due to the high density, the electron and ion temperatures are nearly equal and the decay in peak temperature after the laser pulse is due to thermal conduction and radial equilibration. While the laser pulse is on, a strong thermoelectric effect produces a $\beta \approx 1$ condition in the center of the plasma, which is reduced due to diffusion to $\beta = 0.65$ at 4 μs. These experiments clearly indicate efficient beam trapping, maintenance of a density minimum, heating and subsequent adiabatic compression of the plasma. Based on this success, the magnet length is being extended to 3 m, the peak field to 15 T with a 8-μs rise time, and the laser energy increased to about 8 kJ in a 3-4 μs pulse length.

4.2. 22-cm Experiment (UW). Emphasis has been placed on axial interferometry in the UW experiments in order to accurately measure the radial electron density profile. Diamagnetic loops have been located at 5.5 cm and 16.5 cm in order to correlate the plasma line energy with the laser-heated profiles. The evolution of density profiles produced by the theta pinch alone, for a fill pressure p_0 of 1.8 mTorr, is shown by the solid curves on Fig. 11. The plasma is only partially ionized, and an on-axis density minimum can be seen to be present during the 300-ns implosion, and after 500 ns. Strong laser heating was measured by both diamagnetic loops when laser heating was initiated before 300 ns or after 500 ns. Figure 12a shows a typical interferogram for the late time laser heating, and Fig. 12b shows the plasma line energies inferred from the diamagnetic loop signals. Heated plasma electron density profiles are also shown by a dashed line on Fig. 11 for comparison with the unheated profiles. The electron density minimum is deepened, the total line density increases due to laser-induced ionization, and the column expands significantly due to the increased energy content. Correlation of diamagnetic and interferometric data 1 μs into the laser pulse yields a centerline temperature, assuming a Gaussian temperature profile, of 60 eV, $\beta \simeq 1$, with $n_e = 3 \times 10^{17}$.

Details of these experiments are reported elsewhere [25]. Some further conclusions are: (1) timing of the laser pulse relative to the main field rise for efficient column heating is quite sensitive in small-bore plasma tubes but should be less so in reactor size tubes; (2) peak temperatures in the UW experiments are governed by free streaming end losses; (3) laser energy addition reduces the tendency of the column to form flutes; (4) alignment of the laser beam is more critical at higher f numbers; (5) there is preliminary evidence that material end plugs substantially increase the plasma lifetime in accordance with predictions; and (6) wall light-up occurs on some shots and is believed to be due to refraction of the outer portions of the beam to the tube wall.

REFERENCES

[1] FREIDBERG, J. P., and PEARLSTEIN, L. D., Phys. Fluids 20 7 (1978) 1207.
[2] STOVER, E. K., KLEVANS, E. H., and YORK, T. M., Phys. Fluids 21 (1978) 2090.
[3] McKENNA, K. F., and YORK, T. M., Phys. Fluids 20 9 (1977) 1556.
[4] DRIECER, H., presented at the Third International Symposium on Plasma Heating on Toroidal Devices, Varenna, Italy (1976). Also available as Los Alamos Scientific Laboratory report LA-UR-76-2010 (1976).
[5] McKENNA, K. F., BARTSCH, R. R., COMMISSO, R. J., EKDAHL, C. A., and SIEMON, R. E. (to be published). Also available as Los Alamos Scientific Laboratory report LA-UR-78-1909 (1978).
[6] McKENNA, K. F., COMMISSO, R. J., EKDAHL, C. A., FREESE, K. B., KRISTAL, R., JONES, I. R., QUINN, W. E., and SIEMON, R. E., Eighth European Conference on Controlled Fusion and Plasma Physics, Prague, Czechoslovakia (1977), Vol. I, p. 85.
[7] FREIDBERG, J. P., and WEITZNER, H., Nucl. Fusion 15 2 (1975) 217.
[8] BRACKBILL, J. U., MENZEL, M. T., and BARNES, D. C., Third Topical Conference on Pulsed High-Beta Plasma, Culham, England (Pergamon, New York, 1976), p. 375.
[9] GRIBBLE, R. F., QUINN, W. E., and SIEMON, R. E., Phys. Fluids 14 9 (1971) 2042.
[10] THOMAS, K. S., HARRIS, H. W., JAHODA, F. C., SAWYER, G. A., and SIEMON, R. E., Phys. Fluids 17 6 (1975) 1314.
[11] COMMISSO, R. J., EKDAHL, C. A., FREESE, K. B., McKENNA, K. F., and QUINN, W. E., Phys. Rev. Lett. 39 3 (1977) 137.
[12] MALONE, R. C., and MORSE, R. L., Phys. Rev. Lett. 39 3 (1977) 134.
[13] McKENTY, P., MORSE, R. L., and SOWERS, G. W., to be published.
[14] WESSON, J. A., in Plasma Physics and Controlled Nuclear Fusion Research (Proc. 2nd Int. Conf. Culham, 1965) 1, IAEA, Vienna (1966) 223.
[15] WEITZNER, H., Phys. Fluids 20 3 (1977) 384.
[16] MIKHAILOVSKAYA, L. V., and MIKHAILOVSKII, A. B., Sov. Phys.-JETP 18 (1964) 1077.
[17] GROSSMANN, W., KAUFMANN, M. and NEUHAUSER, J., Nucl. Fusion 13 3 (1973) 462.
[18] FREIDBERG, J. P., Phys. Fluids 15 6 (1972) 1102.
[19] TURNER, L., submitted to the Physics of Fluids ; also available as Los Alamos Scientific Laboratory report LA-UR-78-1782.
[20] TURNER, L., Phys. Fluids 20 4 (1977) 654 and Phys. Fluids 20 4 (1977) 662.
[21] LEWIS, H. R., and TURNER, L., Nucl. Fusion 16 6 (1976) 993.
[22] LEWIS, H. R., Proceedings of the Annual Controlled Fusion Theory Conference (May 4-6, 1977, San Diego, California) paper H8.
[23] JACOBSON, A. R., BUCHENAUER, C. J., DOWNING, J. N., and THOMAS, K. S., Phys. Rev. Lett. 37 14 (1976) 897.
[24] HOFFMAN, A. L., CRAWFORD, E. A., and LOWENTHAL, D. D., Appl. Phys. Lett. 33 4 (1978) 282.
[25] HOIDA, Hiroshi, Ph.D. Thesis, University of Washington (1978).

DISCUSSION

H.J. HOPMAN: You say that when BoN plugs are used plasma energy is radiated away, whereas with LiD plugs this is not the case. Is the energy content of the plasma large enough to strip the ablated Bo and N gas completely? This would result in reduced radiation.

K.F. McKENNA: If the end-plug ablation products are to be stripped completely, the plasma electron temperature must be several times larger than the hydrogen-like (single-electron) ionization potential of the ablated material. The hydrogen-like ionization potentials for boron and nitrogen are 340 eV and 666 eV, respectively, whereas the potential for lithium is 122 eV. Since the maximum electron temperature in Scylla IV-P is 570 eV, only the ablated lithium deuteride plug material would be expected to be fully stripped.

H.A.B. BODIN: The ϑ-pinch and the laser-heated solenoid provide similar confinement systems after the initial heating and formation phase. Is there any difference between the two with respect to electron heat conduction, and has the wobble instability been observed in the laser-heated solenoid?

K.F. McKENNA: Although detailed measurements of electron heat conduction have not been carried out in either the theta pinch or the laser-heated solenoid, electron thermal conduction effects would be expected to be identical in both devices.

The m = 1 "wobble" instability has not been observed in the high-density ($\sim 10^{17}$ cm^{-3}) low-temperature (50–100 eV) plasmas generated in present laser-heated solenoid experiments; however, the m = 2 instability is observed. This instability (m = 2) has also been identified in theta pinches operating in the same plasma regime.

H.L. BERK: Has the m = 1 instability any effect on confinement time?

K.F. McKENNA: If the m = 1 instability carried the plasma column to the discharge tube wall, a significant loss in radial confinement could be expected. However, the instability saturates at a low level, with a maximum radial displacement of about one plasma diameter. No effect on axial confinement time has been observed in the presence of the m = 1 instability.

H.L. BERK: Is damping of the m = 1 instability correlated with theory?

K.F. McKENNA: Damping of the m = 1 instability has not been treated theoretically.

K.N. SATO: Have you measured diffraction and transmittance of the CO_2 laser beam in the plasma, and, if so, by what method?

K.F. McKENNA: A crude measure of the CO_2 laser beam transmittance is obtained with a time-integrating bolometer. No direct measurement of the diffracted laser beam energy has been made.

K.N. SATO: How great is the optimum energy absorption?

K.F. McKENNA: In the optimum solenoid fill pressure conditions, essentially all the incident CO_2 laser beam energy is absorbed by the plasma.

Session H

NON-AXISYMMETRIC SYSTEMS I

Chairman

D. PALUMBO
CEC

HEATING, CONFINEMENT AND FLUCTUATIONS IN THE CLEO STELLARATOR

D.W. ATKINSON, J.E. BRADLEY, A.N. DELLIS,
P.C. JOHNSON, D.J. LEES, P.J. LOMAS, W. MILLAR,
A.C. SELDEN, L.E. SHARP*, P.A. SHATFORD, P.R. THOMAS
Culham Laboratory,
(Euratom/UKAEA Fusion Association),
Abingdon, Oxon.,
United Kingdom

Abstract

HEATING, CONFINEMENT AND FLUCTUATIONS IN THE CLEO STELLARATOR.

The confinement of an Ohmically heated plasma has been investigated in the CLEO stellarator. The electron energy replacement time is found to decrease as the drift parameter, characterized by the ratio of electron drift velocity to electron thermal velocity, is increased. Density fluctuations have been seen but do not appear to explain the observed loss as being due to a drift instability. A beam of neutrals has been injected into a plasma produced by Ohmic heating: ion heating has been observed. The results have been compared with theoretical models. It is shown that increased power input will be necessary to sustain a currentless plasma of the same parameters as those produced by Ohmic heating.

1. INTRODUCTION

CLEO is a conventional stellarator, having 7 field periods of $\ell = 3$ windings on a torus of mean major radius 90 cm and bore 28 cm. When the lobes of the outermost closed magnetic surface are defined by 13 cm radius tungsten limiters, the resulting plasma boundary has a mean radius of approximately 10 cm. The maximum toroidal field is $B_T = 20$ kG. The apparatus and initial results have been described in earlier papers [1-3]. This paper presents some results on scaling of confinement, and the possible effects of fluctuations. There is also a section dealing with experiments to heat a plasma, produced by ohmic heating, by injecting an energetic beam of neutrals.

Principal diagnostics used on the experiment include:- a single channel 2 mm microwave interferometer with direct reading density display; photon scattering using a 5 J ruby laser for profiles of T_e and n_e measured at R = 90 cm along a vertical radius above the horizontal median plane; soft X-ray emission from minor radii between r = ±7 cm(vertically) using uncooled Si detectors and foil absorbers; energy spectra of neutral particles emitted both radially and tangentially; Fourier transform spectroscopy of electromagnetic emission from 30 to 300 GHz (including electron cyclotron radiation and its lower harmonics) viewed in a horizontal plane; a cooled Si-Li detector X-ray spectrometer which can scan across the plasma in a vertical plane; absolute intensity of Hα emission from plasma regions both close to and remote from a limiter and a low-noise multi-channel 2 mm interferometer used to study density fluctuations in the outer plasma regions.

---

* Now at the Australian National University, Canberra, Australia.

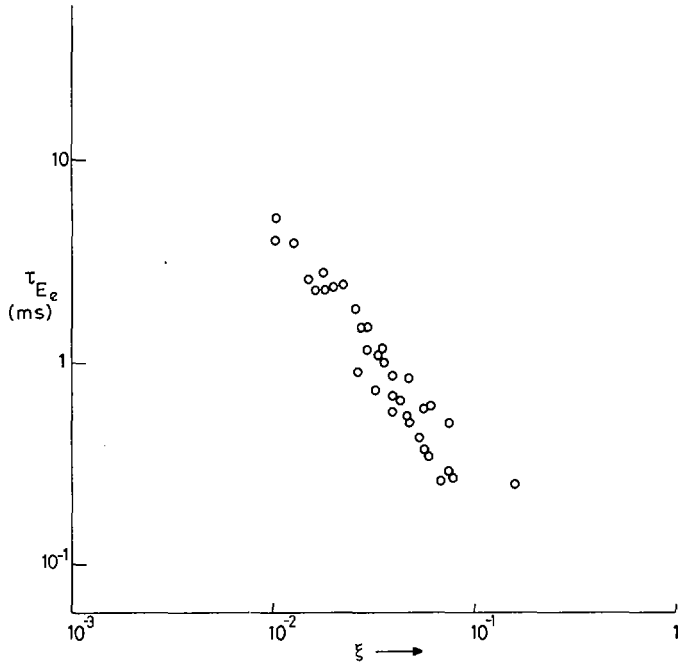


FIG. 1. Variation of electron energy replacement time with mean drift parameter $\xi = v_d/\overline{v}_e$.

2. CONFINEMENT OF OHMICALLY HEATED PLASMA

We use a simple electron energy replacement time τ_{Ee} defined as follows:

$$\frac{d}{dt}(W_e) + \frac{W_e}{\tau_{Ee}} = I_g\left(V - L_g\frac{dI_g}{dt}\right)$$

where $W_e = 6\pi^2 R_o \int_o^a rn(r)T_e(r)dr = A\,\bar{n}_e\hat{T}_e$

is the total electron energy, n(r) and $T_e(r)$ have profiles given by photon scattering and $\bar{n}_e$ and $\hat{T}_e$ are respectively the mean electron density (from interferometry) and central temperature (laser). A is a profile factor which may vary for different plasma conditions. Note that, as defined, τ_{Ee} excludes ion energy and includes inelastic collisions and radiative power losses in the power input term.

It is generally found that τ_{Ee} increases as current decreases and density increases. Gas puffing is used, and thus density and gas current can be varied independently. The overall effect of different densities, currents and electron temperatures on τ_{Ee} can be seen by plotting its value against the drift parameter

$$\xi = \frac{v_d}{v_e} \propto \frac{I_g}{n_e T_e^{\frac{1}{2}}}.$$ This is shown in Fig.(1).

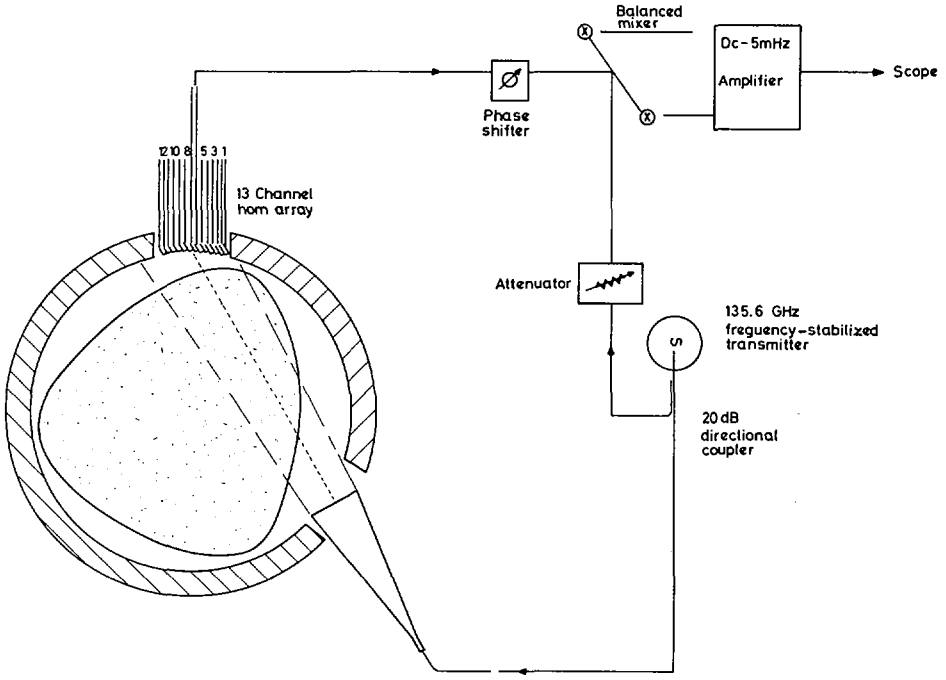


FIG. 2. Schematic arrangement of the apparatus for measuring density fluctuations.

This result indicates clearly a trend towards poorer confinement at large drift parameters. There is evidence, at drift parameters ~ 0.01, of a B_T^2 dependence of τ_{Ee} [3]. At larger values of ξ this dependence is lost.

3. DENSITY FLUCTUATION MEASUREMENT

In order to assess the contribution to energy loss due to density fluctuations in the outer regions of the plasma the apparatus shown in Fig.(2) has been constructed. A 2 mm wavelength microwave beam about 7 cm wide traverses the plasma, emerging with phase and amplitude variations across the beam caused by the fluctuations. The signal is recorded in a frequency range of $1\ \text{kHz} \leq f \leq 35\ \text{MHz}$ at up to 8 positions across the beam by a system of 13 receiving antennae. Scale lengths and frequency spectra of the density fluctuations are related to the appropriate time and position correlations of the received signals.

Fluctuations are seen in the frequency range of $1\ \text{kHz} \leq f \leq 50\ \text{kHz}$ with a phase change which would correspond to a maximum of $\frac{\delta n}{n}$ of $\sim 10\%$ rms. These fluctuations correlate over several adjacent channels and also with the fluctuations of poloidal magnetic field seen at the edge of the plasma. There also appears to be some correlation with the sawtooth modulation of the soft X-ray intensity corresponding to the $q = 2$ surface. Thus the density fluctuations are interpreted as being of MHD origin although the mode numbers are not yet known.

Fluctuations have also been looked for in the frequency range 50 kHz ≤ f ≤ 500 kHz, for $0 < k_\perp < 3$ cm^{-1}. There appears to be no signal visible above the noise level of the apparatus. The measurement puts a limit in this frequency region of $\frac{\delta n}{n} \leq 0.2\%$ rms. Following the method used by Hamberger et al.[4] we can express this fluctuation level as a particle containment time. It gives $\tau_p \sim 0.2$ sec, and this is thus too long to explain the observed loss.

Under some circumstances e.g. very low density, there is some activity seen in the region 5 MHz ≤ f ≤ 35 MHz. At this time there is a large intensity of hard X-rays, so the phenomenon may be correlated with a runaway condition.

Thus the only fluctuations of importance which have been observed so far with this technique seem to be well correlated and could be of MHD origin. Higher frequency fluctuations having the character of drift waves, such as were seen using the same technique in the TORSO torsatron[4] have not yet been observed. Thus unlike the TORSO result, drift waves cannot be clearly identified as a source of plasma loss.

4. NEUTRAL INJECTION THEORY AND EXPERIMENTS

The results described in section 2 indicate a significant improvement in confinement at low ohmic current. Neutral injection has already proved successful for heating tokamak plasmas. The neutral beam is converted into fast ions by charge exchange and ionization (deposition); some of these fast ions are on confined orbits (trapping) and the resulting circulating ion beam gives energy to thermal plasma (slowing down). Deposition, trapping and slowing down of the injected particles agree broadly with theory. This experience suggests that the technique might successfully be applied to a stellarator where alternative heating methods are of great interest and importance.

CLEO gives almost tangential access limited by the helical windings to a clear passage of 8 x 6 cm of elliptical cross section. An 8 cm diameter ion source [5] operated at 24 keV delivers ∿ 50 kW of neutrals to the torus with equal fluxes of H^+, H_2^+ and H_3^+. The effects of stray machine fields on the source and beam blocking reduce the power delivered to the plasma boundary to 35 - 40 kW. This power, if efficiently transferred to the plasma, would be useful in comparison with the 20 - 80 kW of ohmic heating power.

(a) Theoretical model

The guiding centre orbits of fast ions in real stellarator fields have been discussed previously [6] and it has been shown that the orbits are well described, for low pitch angles at least, by a poloidal field given by an average transform

$$\iota(r) = \iota(a) \left(\frac{r}{a}\right)^{2\ell-4}$$

where $\iota(a)$ is the transform at the plasma edge, a. Some calculations have been carried out by computing fast ion trajectories in real stellarator fields. The results show that the orbits can be well represented by a guiding centre model using the averaged rotational transform.

We then use the conserved quantities magnetic moment and canonical angular momentum, and an expression for the vector potential of combined equivalent

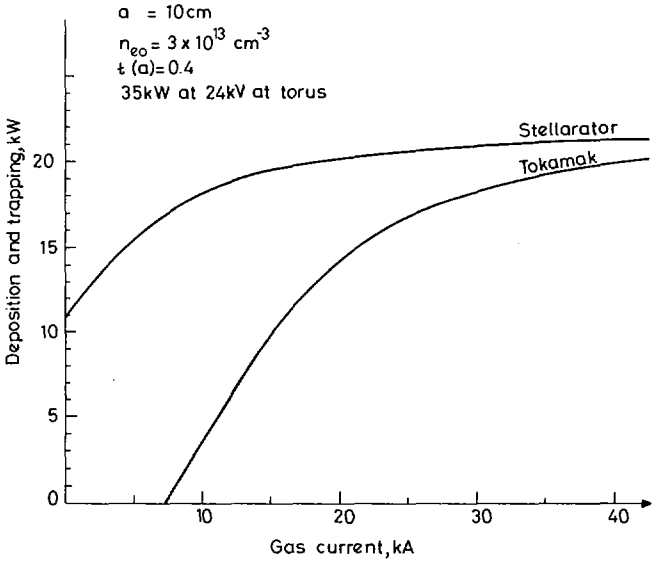


FIG.3. Variation of neutral power deposited in the plasma with gas current for tokamak and stellarator modes. It is assumed that the power at the plasma boundary is 35 kW.

stellarator field and tokamak like field, (assuming a parabolic current density distribution), and obtain an expression for the maximum energy injected proton born at the minor radius r in the equatorial plane which is trapped:-

$$\frac{E^{\frac{1}{2}}}{\cos\beta} = \frac{\left(\frac{e}{2m}\right)^{\frac{1}{2}}}{1 \mp \frac{r}{a}} \left\{ B_T R(a)\, a \left[1 - \left(\frac{r}{a}\right)^4\right] + \frac{\mu_o I R_o}{2\pi a}\left[3 - 4\left(\frac{r}{a}\right)^2 + \left(\frac{r}{a}\right)^4\right]\right\} \qquad (1)$$

in MKS units. Here B_T is the toroidal field in Tesla, I the gas current in amps, and R_o the plasma major radius in metres. The signs - and + refer to co and counter injection w.r.t. the plasma current, β is the ion pitch angle and E its energy in eV. For a parabolic plasma density profile, we divide the neutral beam into beamlets with equal fluxes of the three energy components, calculate the deposition as a function of position along the beamlet and use equation (1) to calculate the trapping. Thus we obtain the power transfer into circulating fast ions. The model is optimistic in that the loss orbit is assumed to be one which ventures outside the mean separatrix radius r = 10 cm, and no account is taken of the non-axisymmetric nature of the separatrix, but its usefulness lies in its ability to deal with vacuum transform and gas current simultaneously. The model agrees with the Oak Ridge deposition and trapping code [7] for zero vacuum transform. Slowing down of the circulating ions and energy partition between ions, electrons and charge exchange loss are calculated using the Fokker Planck code of reference [8].

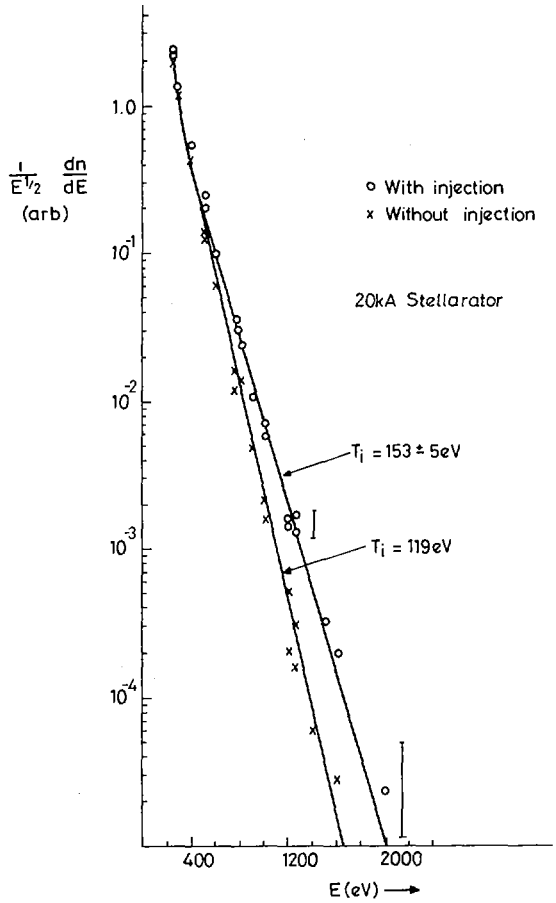


FIG.4. Thermal ion energy spectra with and without neutral injection into a 20-kA plasma current in stellarator mode. The centre of the plasma is pushed 4 cm inwards with vertical field. Mean density ~1.5 X 10¹³ cm⁻³, T_e ~ 600 eV.

Fig.3 shows the calculated dependence of deposition and trapping on gas current for both stellarator and tokamak modes in CLEO. A 35 kW beam and a mean plasma density 1.5 x 10^{13}cm^{-3} are assumed. It can be seen that for the stellarator the power input to trapped circulating fast ions can be significant even at low ohmic current. Slowing down calculations indicate that, for neutral densities between 10^{9} and 10^{10}cm^{-3} the fraction of power transferred to the plasma varies from 90% to 10% .

(b) Experimental results

A range of injection experiments is listed in Table I. The ohmically-heated stellarator plasmas injected have covered the range I_g = 5 - 20 kA, $\bar{n}_e$ = 0.5 - 2.0 x 10^{13}cm^{-3} with vacuum transform ι(a) ≃ 0.6. In addition two

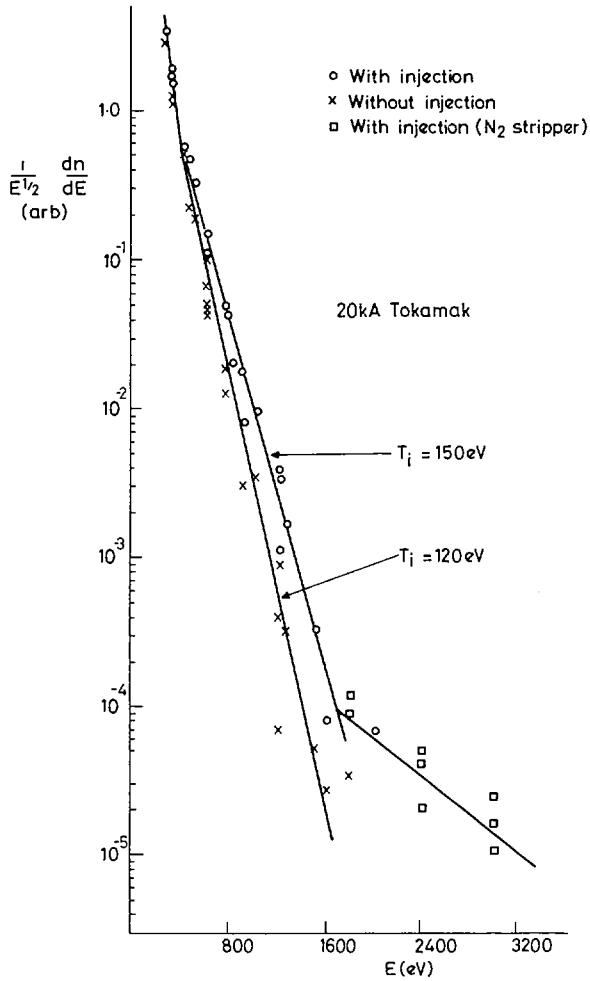


FIG. 5. Thermal ion energy spectra with and without neutral injection into a 20-kA plasma current in tokamak mode. Mean density $\sim 2 \times 10^{13}$ *cm*$^{-3}$, $T_e \sim 500$ *eV.*

afterglow injection experiments with $I_g \to 0$, and two tokamak experiments have been performed. The calculated values of deposited power, trapped power and power transferred to each of plasma ions and electrons for the appropriate plasma parameters are also included in the table.

When a small vertical field is used to displace the current channel of the 20 kA stellarator inwards by 4 cm from its equilibrium position without vertical field, then the ion temperature rise upon injection increases from a marginal 10% to the unequivocal 25% shown by the thermal neutral energy spectrum of Fig. 4. This temperature rise is consistent with calculations which predict 2 - 9 kW of injected power transferred to plasma providing up to 32%

TABLE I. EXPERIMENTAL AND THEORETICAL PARAMETERS

	Experiment								Theory				
	$\bar{n}_e$ $10^{18}cm^{-3}$	I_g kA	B_T kG	$\iota(a)$	R cm	T_e eV	T_i eV	ΔT_i eV	Ohmic Power kW	Deposited Power kW	Trapped Power kW	Power to electrons kW	Power to ions kW
Ohmically Heated Stellarator	2.0	20	18.7	0.6	92	550	140	10±10	60				
	* 1.5	20	18.7	0.6	88	-	119	30±10	60	22	20	3-9	2-9
	1.0	20	18.8	0.6	90	600	130	0±6	50		17	1-5	1-6
	1.8	10	15.5	0.6	89	135	63	0±6	58		19	< 8	<1.3
	1.5	10	15.7	0.6	87	230	81	7±5	50	22	15	7-11	2-5
	1.0	10	18.8	0.6	89	-	116	11±7	30				
	0.5	5	18.8	0.6	-	160	60	-	~10	11	8		
Afterglow	0.5	0	18.8	0.6	90	LOW	⩽50	-	0	11	6	1-3	<0.3
	* 1.0	0		0.6	-	⩽25	⩽50	-	0	11	6	?	?
Tokamak	* 2.0	20	17.6	0	90	500	130	30±10	50		16	6	8
	1.5	10	17.5	0	91	320	120	10±10	24	20	3		

* Results referred to in §4(b). For 20 kA stellarator case, inwards displacement of current channel with resulting reduction of neutral density produced a significant temperature rise. All results represent the average behaviour over at least 20 shots with and without injection at the same conditions.

of the electron to ion collisional power transfer on axis. The effect of the major radius displacement is to improve deposition and trapping since the neutral beam is tangent to the torus at R = 81 cm, well inside the equilibrium major radius. There is also a reduction in background neutral density so that charge exchange losses are smaller.

Fig. 5 shows that similar heating can be obtained with a well centred tokamak discharge with plasma current I_g = 20 kA, as is to be expected from Fig. 3.

The similarity between tokamak and stellarator injection indicates that effects due to trapping in the mirrors in the helical field may not be important with tangential injection.

The ion temperature rises in the lower gas current discharges of Table I are small, $\sim$ 10%, and not much in excess of statistical errors and shot to shot reproducibility.

This is to be expected because of the poor deposition at the low density in these discharges. We can draw some conclusions from the slowing down spectra measured by the tangential neutral particle energy analyser. Fig. 6 shows the fast ion spectra for the 20 kA tokamak and stellarator discharges already discussed. These show the usual 3 peaks corresponding to the acceleration of molecular species in the ion source. The shape of the spectrum near the 24 keV injection energy can be used as a diagnostic for Z_{eff} and neutral density (9). In CLEO the bremsstrahlung anomaly factor as measured by the soft X-ray spectrometer shows that Z_{eff} is very close to unity, so that fast spectrum can be used to estimate the neutral density averaged over the fast ion orbits to a factor $\sim$2. Fig. 6 indicates $n_o \sim 5 \times 10^9 cm^{-3}$ for the stellarator case and $\sim 10^9 cm^{-3}$ for the tokamak case. These figures are to be compared with central values of $n_o \sim 2 \times 10^9 cm^{-3}$ and $2.5 \times 10^8 cm^{-3}$ for the 20 kA stellarator and tokamak respectively, each with $\bar{n}_e \sim 10^{13} cm^{-3}$, obtained from a radial scan of Hα emission.

We can then estimate the total circulating ion beam density n_{bex} close to the injection energy from the absolute value of the 24 keV neutral flux. The theoretical ion beam density per unit production of circulating ions n_{bth} can be calculated at the injection energy, knowing n_e, T_e, T_i and n_o, using reference (8). Since deposition is roughly linear with plasma density for $\bar{n}_e \lesssim 1.5 \times 10^{13} cm^{-3}$, $n_{bth}\,\bar{n}_e$ is proportional to the total theoretical ion beam density. A figure of merit for fast ion orbit confinement (trapping) is then given by $\eta = \dfrac{n_{bex}}{n_{bth}\,\bar{n}_e}$ which is normalised to unity for the 20 kA tokamak discharge.

Values of η obtained for the discharges in Table I are plotted against gas current for the 24 keV component in Fig. 7. Trapping calculations, as described earlier are also shown, again normalised to the 20 kA tokamak case, since these are not very density sensitive. The stellarator experiments are in rough agreement with the calculations, showing that useful orbit confinement can still be achieved in low or zero gas current plasmas. Note that the 10 kA tokamak result is much better than calculations suggest, but this is probably due to a much sharper current density profile in this discharge than is assumed in the calculation.

An injection experiment has been performed on a currentless afterglow plasma obtained by firing a capacitor bank into a second primary winding on

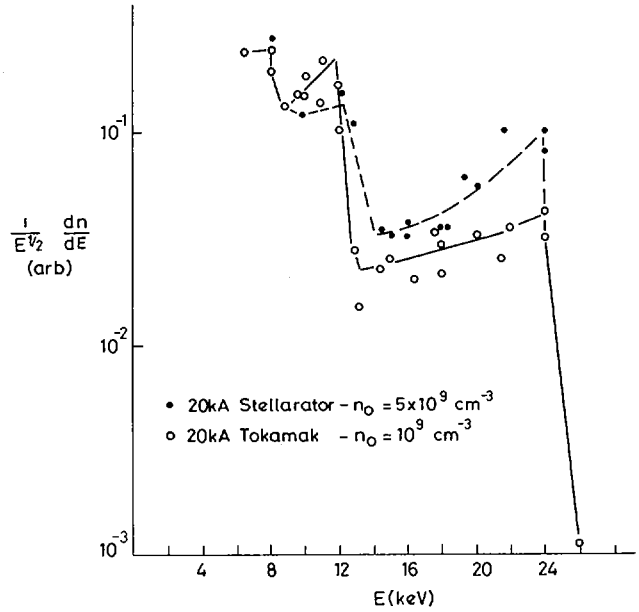


FIG. 6. Fast-ion spectra (tangential viewing) for 20-kA stellarator and tokamak. Values of neutral density calculated from the slope of the curve are indicated.

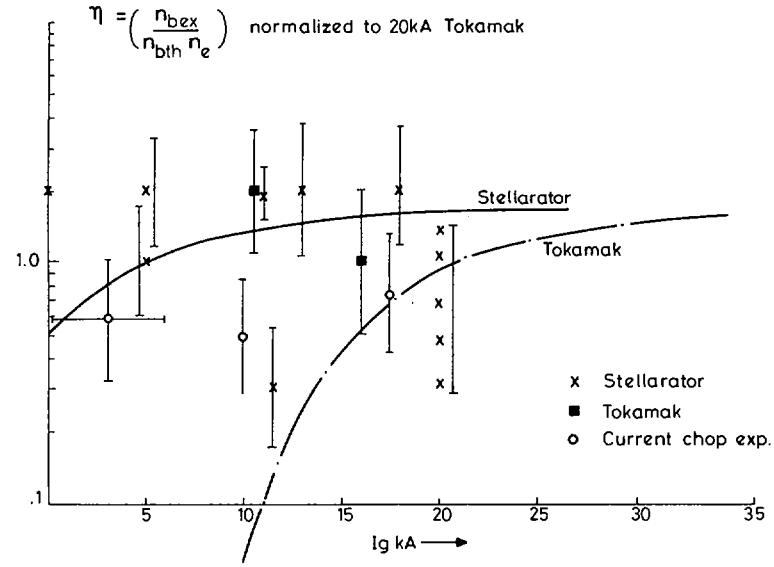


FIG. 7. Variation of ion trapping efficiency (normalized to 20-kA tokamak) with plasma current for stellarator and tokamak modes. The full curves are theoretical dependence evaluated for a plasma radius of 10 cm.

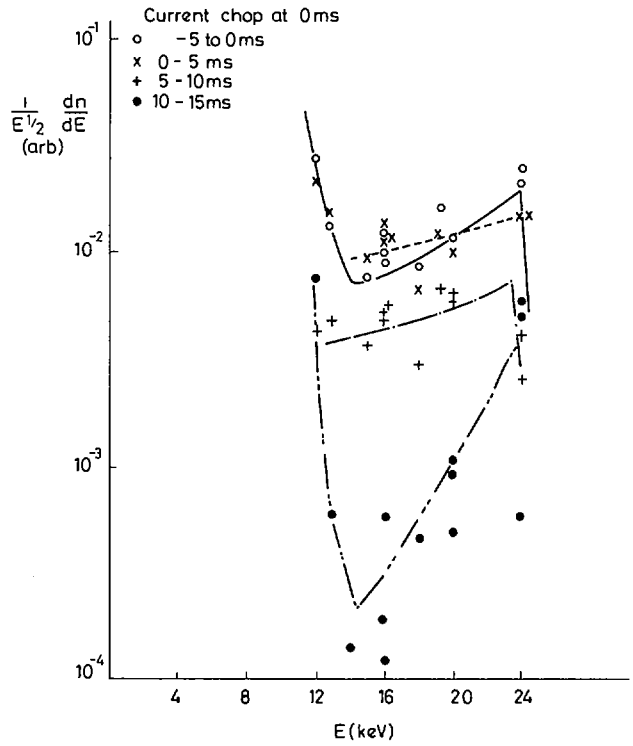


FIG.8. Fast-ion spectra for a sequence of time slices centred around a current chop.

the ohmic heating transformer so as to reduce a plasma current of 17.5 kA to zero in 8 ms. The 30 ms neutral injection pulse was turned on before the reverse bank and continued after current zero into the afterglow. The plasma showed increased MHD turbulence during current decay but dense afterglows $\bar{n}_e \sim 10^{13}cm^{-3}$ were achieved. Slowing down spectra are shown in Fig. 8 for different time slices, time zero being the reverse bank firing time. At times 5 - 10 ms there is evidence for continued trapping and slowing down after current zero, but later at 10 - 15 ms slowing down is characteristic of a high neutral density and charge exchange loss.

(c) Summary of neutral injection results

1. A simple theoretical model for the deposition and trapping of injected ions has been developed, which represents the vacuum transform in an averaged way and adds on the gas current transform. This is justified by calculation of fast ion orbits in real stellarator fields. For low vacuum transform, tokamak calculations have been carried out using now widely used codes.

2. Unequivocal ion heating of up to 25% has been observed for tokamak and stellarator mode with ohmic heating currents of 20 kA, as expected theoretically.

3. Heating has not been observed at low ohmic heating current because low plasma density and high neutral density make power transfer inefficient.

4. Experimental measurement of fast ion confinement suggests that orbit losses are not a serious problem at low gas current for the stellarator.

5. Calculations show that provided high plasma density, $\bar{n}_e \simeq 1 - 2\times10^{13}\text{cm}^{-3}$, low neutral density $n_o \lesssim 10^9\text{cm}^{-3}$, currentless plasmas can be achieved, 140-200 kW of neutral power to the torus will be sufficient to sustain pure stellarator plasmas of similar parameters to those obtainable by ohmic heating. If these conditions cannot be met neutral powers $\sim$ 500 kW will be required.

5. CONCLUSIONS

1. Experiments on the confinement of ohmically heated plasmas in the stellarator have shown that the energy replacement time depends mainly on the drift parameter ξ. The value of τ_{Ee} decreases smoothly as ξ is increased.

2. These results suggest that the best stellarator confinement will occur with currentless plasmas.

3. In order to achieve such plasmas we have studied the injection of a beam of fast neutrals into the plasma produced by ohmic heating.

4. The results show that overall power transfer efficiency is limited by low plasma density and high neutral density with consequent charge exchange losses.

5. Taking trapping of fast ions into account, in order to sustain a completely currentless plasma with the same energy input as is presently produced by ohmic heating, a beam power at least 3 times that at present available at the torus will be required.

6. In order to evaluate a possible mechanism of energy loss from the ohmically heated plasma we have studied density fluctuations by a microwave scintillation method. It is not yet possible to say that there is any relation between fluctuation levels and the energy loss mechanism.

6. ACKNOWLEDGEMENTS

We are grateful to Dr R J Bickerton for his continued interest in this work and also to Dr J Lister for his work on fast ion orbits and preliminary power transfer calculations. The authors would also like to acknowledge the continued support given by the rest of the CLEO team.

7. REFERENCES

(1) ATKINSON, D. W. et al., Plasma Physics and Controlled Nuclear Fusion Research, Vol. II (Vienna 1976) 71.

(2) ATKINSON, D. W. et al., Phys.Rev.Lett. 37 (1976) 1616.

(3) ATKINSON, D. W. et al., Proc. 8th Int, Conf. on Controlled Fusion and Plasma Physics, Prague, (1977) Vol. II, 93.

(4) HAMBERGER, S. M. et al., Phys.Rev.Lett. 37 (1976) 1345.

(5) ALDCROFT, D., et al., Nuclear Fusion 13 (1973) 393.

(6) GIBSON, A. and TAYLOR, J. B. Physics of Fluids, 10 (1967) 2653.

(7) ROME, J. A., CALLEN, J. D., CLARKE, J. F. Nuclear Fusion 14 2 (1976) 141.

(8) CONNOR, J. W. and CORDEY, J. G. Physics of Fluids 17 (1974) 1626.

(9) GOLDSTON, R. J., MAZZUCATO, E., SLUSHER, R. E. and SURKO, C. M. Plasma Physics and Controlled Nuclear Fusion Research, (Vienna 1976) Vol. I, 371.

DISCUSSION

J.D. CALLEN: Have you in fact shown that the electron energy containment time τ_{E_e} depends on the drift parameter ξ? That is, have the variations of τ_{E_e} with the separate factors in ξ (density, current density, electron temperature) been investigated to show that ξ represents the appropriate and/or only relevant combination of plasma parameters? For example, could the scaling be explained by $\tau_{E_e} \sim \eta$ nearly as well as in tokamaks?

D.J. LEES: We have taken all our experimental results with $n_e = 5 \times 10^{12} - 10^{14}$ cm^{-3}, $T_e = 50$–1000 eV, $I_g = 5$–25 kA and plotted them versus many parameters. The only scaling which appears to emerge is the drift parameter one. It was to see whether this empirical law had any physical significance that we performed the density fluctuation measurements. It is, therefore, disappointing that the results have so far been negative.

J.P. FREIDBERG: How does the energy confinement time vary with and without the stellarator fields? In particular, at fixed $\xi = V_d/V_e$, what are the corresponding confinement times?

D.J. LEES: The concept of $\tau_{E_e} \propto a^2/\xi$ seems to apply equally to tokamak and stellarator plasmas with Ohmic heating. In our case the tokamak plasma radius is narrower than that of the stellarator by a factor of ~ 2. Thus, generally, ξ is larger in the tokamak. For the same value of ξ, tokamak τ_{E_e} is perhaps 2–4 times smaller than τ_{E_e} in the stellarator.

C.M. SURKO: The maximum growth for drift waves is expected to be in the range of wave vectors such that $k_\rho \cong 0.5$, where ρ is the gyroradius with the electron temperature and ion mass. It would, therefore, be at wave vectors larger than those reported in your paper. Does this not stand in the way of your conclusion that drift waves are not responsible for the variation of τ_E with plasma parameters?

D.J. LEES: Firstly, there is some evidence in toroidal systems that $k_\perp \rho_i \sim 1$ is not necessarily the fastest growing mode, but possibly smaller $k_\perp$. Secondly, it is true that we would like to work over a range of $k_\perp$ greater than that given by the scintillation experiment. To this end we are going to study microwave scattering.

S. YOSHIKAWA: When you use neutral beam heating with gas current $I_g = 0$, what is the energy confinement time of the ions and electrons?

D.J. LEES: Turbulence, possibly produced by skin currents, seems to cause T_e to decrease rapidly; thus conditions when the current has decayed, in the current interruption experiment, do not remain the same as in the presence of current. The energy confinement time for electrons increases as the current is decreased by a factor of two, but then decreases again as the temperature falls. Ion energy confinement is roughly similar.

J.D. CALLEN:. You have shown charge-exchange spectra with and without neutral-beam injection for both tokamak and stellarator configurations. In the tokamak case the fast-ion slowing-down tail on the thermal background was evident, but in the stellarator case no such tail was to be seen. Have you looked for a fast-ion tail in the stellarator case?

D.J. LEES: We have not yet looked properly in the stellarator case. The high-energy tail was seen only when nitrogen was used in the stripping cell of the analyser instead of hydrogen. The count rate in the stellarator case was much lower than for a tokamak, and so far the high-energy tail has been buried in the detector noise.

ENERGY AND PARTICLE CONFINEMENT IN THE OHMICALLY HEATED W VII-A STELLARATOR

W VII-A TEAM:

B. CANNICI, G. CATTANEI, A. CAVALLO, D. DORST, A. ELSNER, G. GRIEGER, H. HACKER, J. HOW, H. JÄCKEL, R. JAENICKE, P. JAVEL, J. JUNKER, M. KICK, F. LEUTERER, C. MAHN, S. MARLIER, G. MÜLLER, W. OHLENDORF, F. RAU, H. RENNER, H. RINGLER, J. SAFFERT, J. SAPPER, P. SMEULDERS, M. TUTTER, O. VOLLMER, A. WELLER, E. WÜRSCHING, H. WOBIG
Max-Planck-Institut für Plasmaphysik,
Association Euratom-IPP,
Garching,
Federal Republic of Germany

Abstract

ENERGY AND PARTICLE CONFINEMENT IN THE OHMICALLY HEATED W VII-A STELLARATOR.

The density regime in the Wendelstein stellerator has been extended to $\bar{n}_e = 10^{20}$ m^{-3} by gas puffing in helium discharges. The density seems to be limited already by small amounts of impurities (i.e. $\leqslant 1\%$ of oxygen). These radiate at the plasma edge, constrict the discharge, and finally terminate it when the losses exceed the available Ohmic heating power. The energy confinement time τ_E increases with electron density but reaches a maximum followed by a rapid decrease connected with strong radiation losses. The particle confinement time shows a similar behaviour. Maximum densities were obtained for stationary helium discharges with $B_0 = 3.5$ T, $I_p = 35$ kA, and the external rotational transform $\iota_0 = 0.14$. For smaller values of the rotational transform the density increase is limited by disruptive instabilities. The ion temperature agrees with neoclassical scaling.

INTRODUCTION

The Wendelstein VII-A stellarator has l=2, m=5 helical windings which, at a main field $B_0 = 3.5$ T, produce an almost shearless external rotational transform $0.055 \leq \iota_0 \leq 0.23$. The major radius is $R_0 = 2.0$ m and the minor radius is defined by the 0.13 m radius of the molybdenum limiter which, because of the elliptical cross-section of the magnetic surfaces, is equivalent to an average plasma radius of ~0.1 m. Results from

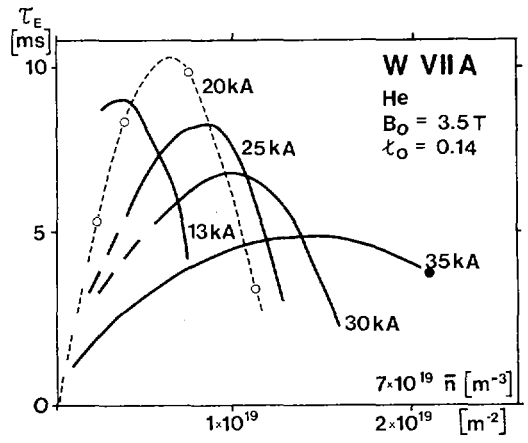


FIG.1. Diamagnetic measurements of the energy confinement time τ_E for helium discharges with various plasma currents I_p. Averaged density $\bar{n} = \int ndA/\int dA$.

ohmically heated plasmas at moderate densities have already been reported at the Berchtesgaden [1] and Prague [2] conferences. Now the investigations have been extended to the high-density regime since high densities are required for sufficient absorption with the nearly perpendicular injection experiment planned for W VII-A. Access to this regime became possible by technical improvements of the OH-circuit, leading to an increase of the control range of the loop voltage from 5 to 10 volts and of the ohmic heating power to 400 kW. Helium was used instead of hydrogen in order to take advantage of the following effects:

For the same temperature the resistivity and thus the available power density rises as Z_{eff} goes from one to two.

Chemical processes leading to a release of oxygen from the wall via the production of water with the impinging atomic hydrogen [3] should disappear in helium discharges. Therefore, the radiation losses should be reduced and the reproducibility improved.

The recycling coefficient ρ is close to one for helium instead of 0.7 for hydrogen [2] so that there is no need for an additional gas feed to maintain stationary conditions.

The main effect found in W VII-A is that even if disruptive instabilities are suppressed, τ_E does not continuously grow with n but goes through a maximum and then steeply decreases. At even higher densities the discharge can no longer be maintained with the available ohmic heating power.

CONFINEMENT AT HIGH DENSITIES

In order to find the optimum confinement conditions for high densities and the physical reason for the density limitation, the external transform, ι_o, and the plasma current, I_p, were varied for B_o = 3.5 T. In Fig. 1 the gross energy confinement time $\tau_E = \frac{W}{P_{OH}}$ is plotted versus n for different currents and ι_o = 0.14, where W is the total plasma energy, and P_{OH} the ohmic input power. All data are taken from quasistationary discharges with pulse lengths >100 ms, where the density was changed by gas puffing during current build-up.

W is calculated from diamagnetic measurements. In hydrogen experiments the values obtained from electron temperature and density profiles measured by Thomson scattering and ion temperatures deduced from charge-exchanged neutrals agreed well with the diamagnetic measurements,but in helium discharges they show a systematic deviation of about -25 %. At lower densities τ_E follows the well-known scaling $\tau_E \sim n$. Also, reduction of τ_E with increasing I_p is observed. Therefore, in this regime τ_E roughly scales with ξ^{-1} where ξ is the drift parameter, $\bar{\xi} \sim \frac{I}{\bar{n}\sqrt{k\bar{T}_e}}$. At higher densities a saturation and a subsequent steep decrease of τ_E is observed. These phenomena are shifted to higher densities if the plasma current is increased. Measurements of the 5015 Å He-I line in three different planes (including that of the limiter) have shown a similar behaviour also for the particle confinement time.

The highest density, $\bar{n} = 10^{20} m^{-3}$ or $\int n dl = 2.2 \times 10^{19} m^{-2}$, was obtained for I_p = 35 kA with $\iota(a) \approx 0.5$ ($q \approx 2$). The input power was 350 kW and $kT_e(o)$ = 200 eV. Fig. 2 gives profiles of n_e and T_e for this discharge. They are flat inside the q=1 surface [1,2], indicating that the transport coefficients are high in this region. The confinement takes place within the rather thin sheath between the q=1 surface and the plasma edge. Rather steep gradients can obviously be balanced there.

Any further increase in n would require an increase of the input power, i.e. of the current density. This could be achieved by lowering the external transform or by increasing B_o. These effects have been observed indeed but, as already stated, a too low external transform ($\iota_o < 0.14$) leads to disruptive instabilities, well known from tokamaks, which prohibit the access to higher densities when approaching q(a) = 2.

In order to illustrate the situation, the ratio of maximum density to maximum current density versus $\iota_p \approx I_p/B$ is plotted for different values of ι_o in Fig. 3. This procedure is similar to [4] but modified for the inclusion of the stellarator effect. One observes that for larger ι_o, where disruptions are suppressed, the density limit is proportional to the plasma current and to $(1-\iota_o)$. The dependence on B could not be verified since for these experiments B was always between 3 and 3.5 T. Below ι_o = 0.14 the density limit is increasingly determined by disruptions and progressively shifted to lower values. Finally, for

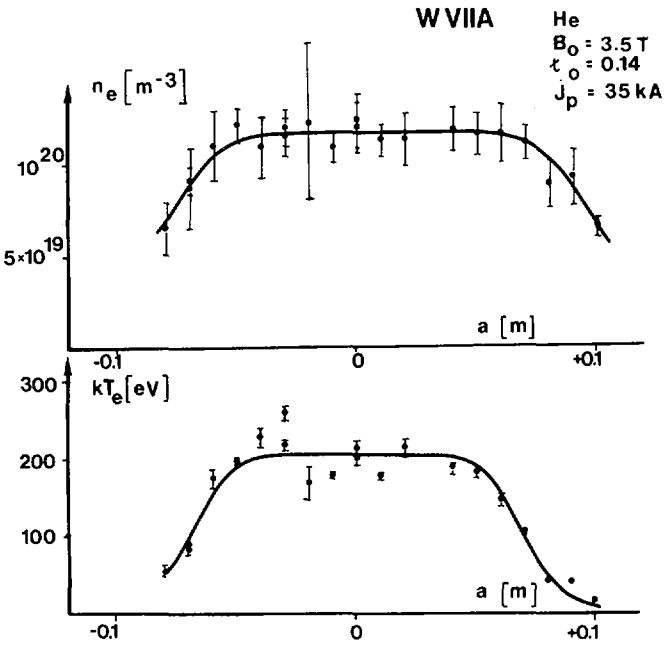


FIG. 2. Measured density and electron temperature profiles at line density 2.2 $\times 10^{19}$ m^{-2} (indicated by ● in Fig. 1).

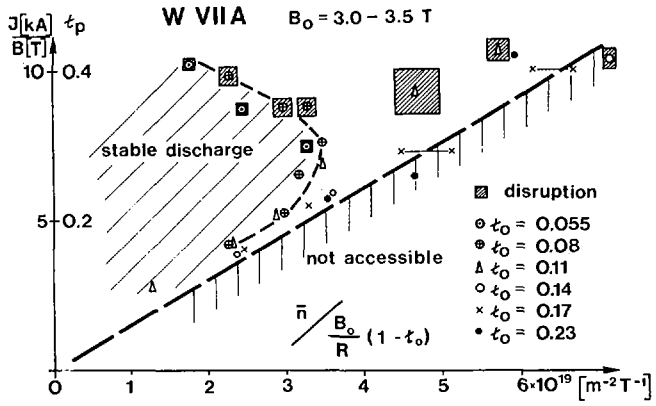


FIG. 3. Density limitations for various I_p and external transforms, ι_0. The average maximum densities divided by the central current densities ($\bar{n}/j(0)$) are plotted versus the internal transform ι_p. The conditions when disruptions determine the discharge are indicated.

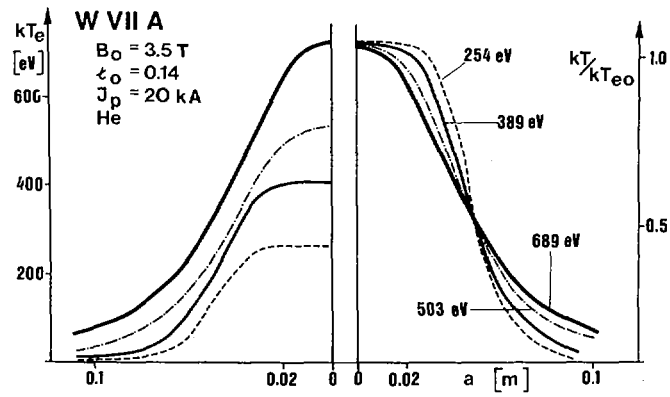


FIG.4. Temperature distributions for the four different discharges marked by ○ in Fig.1. The central temperatures are given for the normalized profiles.

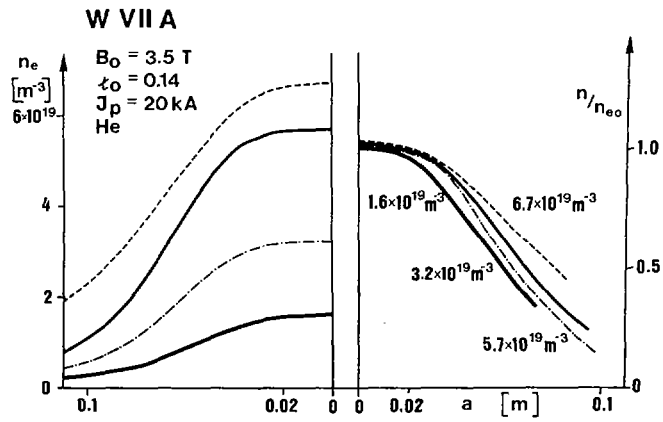


FIG.5. Density profiles corresponding to Fig.4. The central density is given for the normalized profiles.

ι_o = 0.055 the 'disruptive branch' typical for tokamaks is reached. If the density then approaches the critical value for disruptions, a significant change of the MHD modes is observed [5]. At higher external transform, the stronger equilibrium in the helical field may be responsible for maintaining the discharge at higher densities, in spite of the occurrence of phenomena, such as mode coupling and locking to the limiter [5].

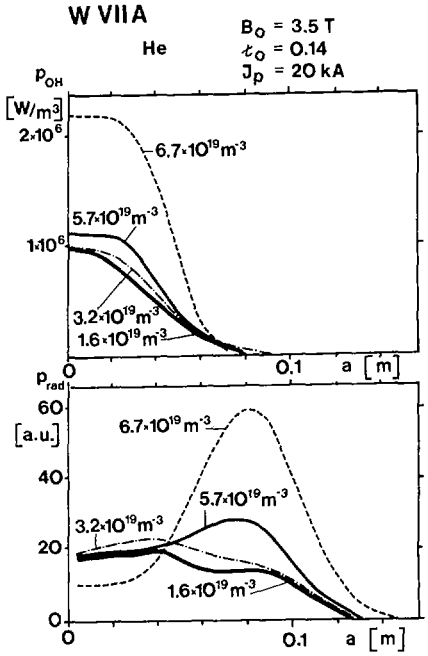


FIG. 6. P_{OH}, *heating power density, and relative* P_{rad}, *radiation power density, obtained by Abel inversion from bolometer measurements for the four selected discharges of Figs 4 and 5.* P_{rad} *is given in arbitrary units (a.u.). 100 a.u. are approximately equivalent to* 10^6 $W \cdot m^{-3}$. *The central densities are indicated.*

The dependence of τ_E on n was studied in detail for 20 kA discharges. For a set of density values, Figs 4 and 5 show radial profiles of temperature and density. In addition, the normalized curves were plotted. With increasing n_e the T_e profiles show a strong reduction of T_e in the outer regions as well as a decrease of temperature in the centre. Since the current is kept constant, these effects lead to a concentration of the current towards the centre and, consequently, to an expansion of the q=1 surface since within q=1 the current density is limited to $j \sim \frac{B}{R}(1-\iota_o)$. In this way the region of high transport is expanded and the confinement region reduced by both effects, the expansion of the q=1 surface and the decrease of T_e in the outer regions.

Radially resolved bolometric measurements lead us to believe that the shrinkage of the profiles is caused by radiation cooling of the plasma edge. Fig. 6 shows bolometric measurements for the four discharges of Figs 4 and 5 along with the local ohmic input. At low densities a density increase produces little change in the radial distribution of the radiated power and the ohmic power input as well, indicating that the reduction in

temperature is balanced by a reduction of Z_{eff}. Again one has to keep in mind that I_p is kept constant. The density increase from 3.2 x $10^{19}m^{-3}$ to 5.7 x $10^{19}m^{-3}$ and further to 6.7 x $10^{19}m^{-3}$ does show a definite increase in radiated power at the plasma edge along with an increase of ohmic power in the centre, to account for the additional losses. Since Z_{eff} is around 2 and since the temperature is still more reduced (see Fig. 4), the loop voltage increases to keep up the current.

This radiated power is attributed to impurity radiation. It is responsible for the shrinkage of the T_e profiles and the reduction of the central temperature. It is interesting to note that there is also an indication of radiation from the plasma centre, which seems to decrease for higher densities or decreasing central temperature.

Although the bolometer used has not yet been calibrated with radiation standards, the sensitivity was estimated from its calorimetric properties and the variation of its output signal with the variation of the plasma radiation. This leads to the conclusion that, at least at higher densities, the wall receives about 80 % of the ohmic power input. Another 10 - 20 % of the ohmic power is typically found on the limiter.

RADIATION LOSSES AND IMPURITY CONTENT

In order to look for impurities and their concentration, radial profiles of spectral lines of several species have been taken shot by shot in the UV and VUV region and compared with the bolometer measurements. The spectroscopic measurements give maximum oxygen concentrations of 1 % and Fe concentrations of 0.1 % at n(o) = 5.7 x $10^{19}m^{-3}$. These impurities together with the helium radiation may explain the strong radiation losses from the plasma edge (20 - 70 eV) because, as seen from Fig. 5, the electron density at the plasma edge shows a stronger increase than in the centre (for a given temperature, $P_{rad} \sim n_{imp} \times n_e$).

At present there is not a clear picture as far as the comparison with the bolometric measurements is concerned and, in particular, the origin of the radiation from the plasma centre for temperatures above 350 eV is unknown. Photographic recordings, however, with a grazing incidence spectrograph do show many unresolved lines between 60 and 80 Å radiating from the plasma centre. Their identification is not yet clear. If it were Fe, the radiation should extend down to 40 Å and if it were Mo other Mo lines should also occur which were not detected.

To prove that small amounts of impurities radiating from the plasma edge can severely influence the profiles and the confinement, small amounts of Ne were added to the discharges. Neon was selected since, for the conditions of these discharges, it greatly resembles oxygen [6] without showing its intense wall affinity.

Fig. 7 shows τ_E as a function of line density for helium discharges and helium discharges where 10^{17} and 2 x 10^{17} atoms of

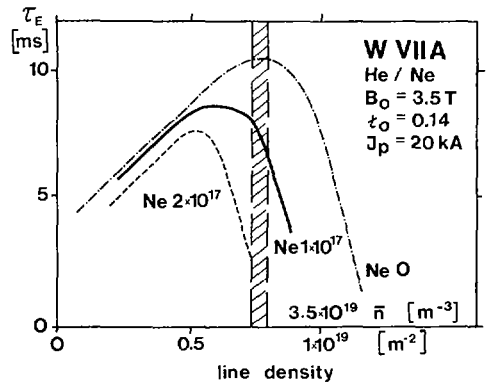


FIG. 7. Energy confinement τ_E versus the density for various neon contents at I_p = 20 kA. At line density 8 × 10^{18} m^{-2} (dashed region), 10^{17} particles correspond to a concentration of 1%.

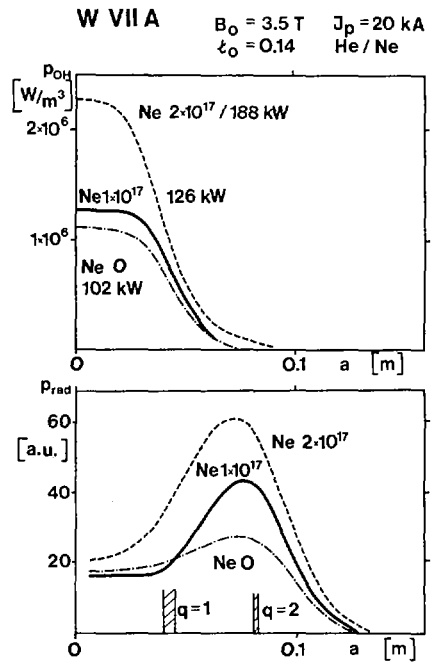


FIG. 8. P_{OH} heating power density and P_{rad} radiation power density for the three cases of Fig. 7 at line density 8 × 10^{18} m^{-2}, central density 5 × 10^{19} m^{-3}.
(P_{rad}: 100 a.u. are approximately equivalent to 10^6 W·m^{-3}.)

Ne had been added. At 8 x 10^{18} m^{-2} line density, this corresponds to 1 % and 2 % impurity content. Again there is little effect at small electron densities, but a drastic change at higher densities. The maximum available density is strongly reduced by this amount of impurity content.

In Fig. 8, radial profiles of radiated power from bolometer measurements along with profiles for the ohmic power input have been plotted. They clearly show the increase of radiated power from the plasma edge. Temperature profiles also shrink for these cases.

So, either by adding small amounts of impurities or by increasing the electron density, one can reach the point where radiative losses influence the temperature profiles and deteriorate the confinement [7] .

Alternatively, the radiation from the plasma centre was increased by adding 3 x 10^{16} atoms of krypton to the discharge. Krypton is expected to radiate from the centre of the discharge, between 200 and 500 eV [6] and the corresponding radiated power was detected by the bolometer. In essence, this leads to a reduction of the effective ohmic heating and thus to a lower central electron temperature. In addition, with increasing helium density the oxygen in the discharge again provides edge cooling and thus a further decrease of the central temperature until the density limit is reached. This confirms the conclusion that edge cooling is responsible for the existence of the density limit rather than radiation losses directly from the plasma centre.

ION HEAT CONDUCTION

An assessment of the contribution of the ion heat conduction to the total energy balance requires the knowledge of the ion temperature and its radial distribution. However, in helium discharges the low charge-exchange rate and the low stripping efficiency do not yield large enough signals to determine the ion temperature by charge-exchange analysis. This problem was circumvented by adding a hydrogen gas puff to the helium discharges and determining the helium ion temperature by measuring the hydrogen ion temperature via charge-exchange analysis. When scanning off the centre, the charge-exchange flux detected by each channel of the energy analyser (0.4 to 2 keV) revealed a strong decrease. In the outer regions, however, the temperature deduced from these signals significantly exceeded the electron temperature. This is not compatible with the electron ion heat-exchange rate, according to which the ion temperature can hardly exceed the electron temperature. For the energy balance it is assumed therefore that the T_e and T_i profiles are proportional to each other.

In Fig. 9 the central values of kT_e and kT_i versus the line density are plotted for the same conditions as in Fig. 7. Theoretical curves for the ion temperature are shown for comparison. They are based on neoclassical ion heat conductivity

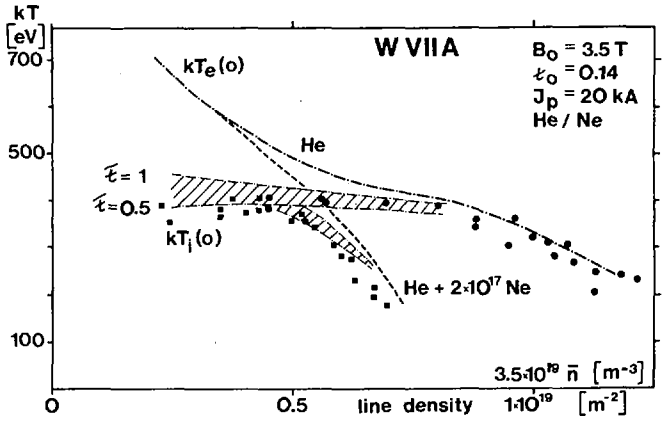


FIG. 9. The variation of the central electron and ion temperatures with density is shown for two different cases; to one of them neon was added. Theoretical curves of the ion temperatures based on the neoclassical heat conductivity for $\bar{\iota}$ = 0.5 and $\bar{\iota}$ = 1.0 are given for comparison (dashed regions).

and on classical heat exchange between electrons and ions. The agreement is quite good. Small deviations between measured and calculated temperatures are probably caused by additional charge exchange losses at low densities and by a transition to the collision-dominated regime at low ion temperatures. In all cases, the power transferred to the ions is only a small fraction of the ohmic power.

SUMMARY

For helium the density range of the Wendelstein VII-A stellarator was extended to $\bar{n}_e = 10^{20}$ m^{-3}.

Low concentrations of impurities, e.g. oxygen less than 1 % at higher densities $\bar{n}_e > 5 \times 10^{19}$ m^{-3}, dominate the confinement by radiation losses at the plasma edge and reduce the temperature. It is interesting to note that this boundary layer may resemble the cold plasma blanket concept. The maximum density is determined by the available ohmic power.

Helium discharges with 1 to 2 % neon added show that the accessible density range is reduced with increasing impurity concentrations since for a given temperature the radiative power increases according to $P_{rad} \sim n_e \times n_{imp}$.

For $\iota_0 < 0.14$ the discharge becomes sensitive to disruptive instabilities. The density limit caused by these instabilities coincides with the optimum values obtained in tokamaks related to the restricted current density $j \sim B/R(1-\iota_0)$ within q=1.

Measurements of ion temperature agree with neoclassical expectations. Therefore, the electron - ion heat transfer seems not to be responsible for the reduction of the electron temperature at higher densities.

ACKNOWLEDGEMENTS

This paper would not have been possible without the continuous endeavours of the technical crew.

REFERENCES

[1] W VII-A TEAM, in Plasma Physics and Controlled Nuclear Fusion Research (Proc.6th Int.Conf. Berchtesgaden, 1976) 2, IAEA Vienna (1977) 81.

[2] W VII-A TEAM, in Controlled Fusion and Plasma Physics (Proc.8th Europ.Conf. Prague 1977) 2 (1977) 73.

[3] F. WAELBROECK, H.J. DIETZ, P. WIENHOLD, Rep.Jül.-1448 (1977).

[4] J.W.M. PAUL et al., in Controlled Fusion and Plasma Physics (Proc.8th Europ.Conf. Prague 1977) 2 (1977) 49.

[5] W VII-A TEAM, paper IAEA-CN-37/H-3, these Proceedings

[6] D.E. POST et al., Atomic Data and Nuclear Tables 20 (1977) 397-439.

[7] P.H. REBUT, B.J. GREEN, in Plasma Physics and Controlled Nuclear Fusion Research (Proc. 6th Int.Conf. Berchtesgaden, 1976) 2, IAEA Vienna (1977) 3.

DISCUSSION

R.W. CONN: It has been suggested that τ_e scaling in stellarators is similar to that found in tokamaks and that, given comparable machines, similar confinement is obtained. However, both your paper and the one presented by D.J. Lees (paper H-1) indicate that $\tau_E \propto n$ scaling is not found in stellarators, but that τ_E varies as the drift parameter. What is your opinion on this question at present?

H. RENNER: At low currents the external transform obviously improves the confinement. For high currents (with q = 1 reached in the centre) there is practically no difference between tokamak and stellarator scaling. The increase of external transform changes the profiles and reduces the central temperature. The drift scaling, which includes temperature and density, accordingly fits better over a large parameter range. Introduction of the external transform improves the stability and allows an extension of the parameter range to higher densities, for example where radiation dominates the discharge.

J.D. CALLEN: In tokamaks such as ISX-B the energy confinement time τ_E goes through a maximum as the density is increased. There, the effects of ion heat conduction at the finite plasma current are found to be responsible for the saturation of τ_E with density over the central, confinement region of the plasma. Could such an effect be responsible for the maximum of τ_E with density you have shown?

H. RENNER: No, we exclude the possibility that ion heat losses make any major contribution to the electron energy balance. The W-VII machine would be expected to have a much smaller ion heat conductivity coefficient than ISX owing to the higher toroidal field (3.5 T). Accordingly, in W-VII energy transfer to the ions is reduced, as the difference between ion and electron temperature is smaller at approximately the critical density where τ_E passes through its maximum. It seems that the region with high radiation losses is inaccessible in tokamaks because disruptions restrict the density.

INVESTIGATION OF THE m=2 MODE AT q-VALUES AROUND 2 IN THE W VII-A STELLARATOR

W VII-A TEAM:

B. CANNICI, G. CATTANEI, A. CAVALLO, D. DORST,
A. ELSNER, G. GRIEGER, H. HACKER, J. HOW,
H. JÄCKEL, R. JAENICKE, P. JAVEL, J. JUNKER,
M. KICK, F. LEUTERER, C. MAHN, S. MARLIER,
G. MÜLLER, W. OHLENDORF, F. RAU, H. RENNER,
H. RINGLER, J. SAFFERT, J. SAPPER, P. SMEULDERS,
M. TUTTER, O. VOLLMER, A. WELLER, E. WÜRSCHING,
H. WOBIG, M. ZIPPE
Max-Planck-Institut für Plasmaphysik,
Association Euratom-IPP,
Garching,
Federal Republic of Germany

Abstract

INVESTIGATION OF THE m=2 MODE AT q-VALUES AROUND 2 IN THE W VII-A STELLARATOR.

In the W VII-A stellarator with Ohmic heating, radial profiles of q(r) are similar to those in tokamaks. The m=2, n=1 tearing mode is observed over a wide range of plasma parameters extending to regions where current disruptions usually occur in comparable tokamaks. Typical frequencies are 1–20 kHz; the relative amplitude can reach 2.5% without disruptions. The amplitude of the m=2 mode decreases with increasing helical field or external rotational transform. Simultaneously with the onset of a coupling between the m=1 and m=2 mode, a steep increase of the m=2 amplitude is observed, which is caused either by an increase of the plasma current, by the electron density, or by the content of low-Z impurities. The occurrence of disruptions in tokamaks may be connected with the locking of the m=2 mode at the limiter as observed in W VII-A under these conditions.

INTRODUCTION

The Garching Stellarator WENDELSTEIN VII-A provides an external rotational transform $\iota_o \leq 0.23$ with low shear [1]. For ohmically heated plasmas, radial profiles of $j(r)$ and $q(r)$ derived from measured temperature profiles are similar to those in Tokamaks, but usually the flat internal region within $r(q=1)$ is broader.

Low-frequency fluctuations are observed with mode structures proportional to $\exp i(\omega t - m\theta + n\varphi)$, where θ and φ are the poloidal and toroidal angles, respectively, ω is the angular frequency in the laboratory frame, and m and n are integers.

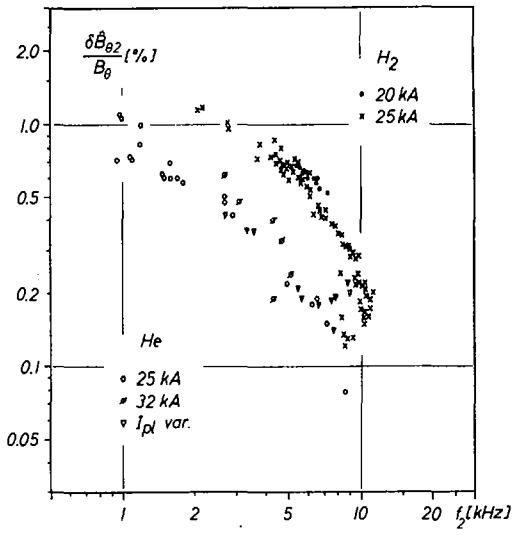


FIG. 1. Relative amplitude as a function of the frequency of the m=2, n=1 mode for H_2 and He and various plasma currents at $B_0 = 3.5$ T and $\iota_0 = 0.11$. I_{pl} var. means that the plasma current has been varied from 8 to 30 kA (cf. Fig.4).

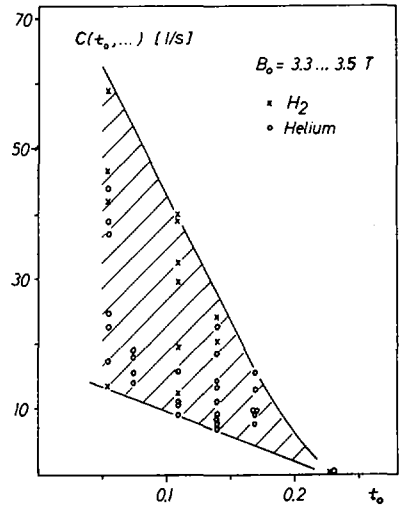


FIG. 2. C versus the external rotational transform ι_0 for discharges in H_2 and He. C describes the dependence of the relative amplitude of the m=2, n=1 mode on ι_0. The spread of the points reflects that C is also dependent on other discharge parameters.

The mode structure is analysed by means of 3x4 poloidal magnetic field probes and 12 soft X-ray diodes. The modes can be attributed to rational magnetic surfaces with a rotational transform $\iota = 1/q = n/m$.

The dependence of the m=2, n=1 mode on various parameters like ι_o, n_e, I_{pl} and its influence on other discharge parameters is discussed in this paper.

DEPENDENCE ON EXTERNAL ROTATIONAL TRANSFORM

At small external rotational transform, $\iota_o \leq 0.11$, the m=2, n=1 mode is the dominant one, similar to the tearing modes in Tokamaks [2,3]. In W VII-A, however, the relative amplitude, $\delta\hat{B}_{\theta 2}/B_\theta$, of the m=2 mode is decreasing with increasing ι_o (B_θ is the poloidal field of the plasma current alone). This indicates that the mode stability is markedly improved by the external helical fields. Figs 1 and 2 will be used to demonstrate this behaviour by separating the dependence of the m=2 amplitude on parameters other than ι_o as far as possible.

In Fig. 1 for a fixed value of $\iota_o = 0.11$ the range of amplitudes and frequencies, f_2, of the m=2 mode is shown for discharges in H_2 and He at various plasma currents, I_{pl}. This figure is obtained by varying the electron density, n_e, and demonstrates that the product

$$\frac{\delta\hat{B}_{\theta 2}}{B_\theta} \cdot f_2 = C$$

is only weakly dependent on f_2, n_e and I_{pl}. Further, it was observed that f_2 is close to the electron diamagnetic drift frequency, $f_{diam.el.}$, which is not explicitly depending on ι_o. Hence, it follows from

$$\frac{\delta\hat{B}_{\theta 2}}{B_\theta} \approx \frac{C}{f_{diam.el.}} = C(\iota_o,\ r(q=2),\ldots?)\cdot B_o \cdot \frac{n_e}{\nabla p_e}\Bigg|_{r(q=2)}$$

that the dependence of the amplitude on ι_o is contained only in the factor C which is shown in Fig. 2. The decrease of the m=2 amplitude with increasing ι_o can clearly be seen, and at $\iota_o = 0.23$ the m=2, n=1 tearing mode has no longer been observed.

DEPENDENCE ON n_e, I_{pl} AND IMPURITIES

Close to Tokamak operation, at $\iota_o = 0.055$, curve a) of Fig. 3 shows the typical behaviour of the m=2 mode amplitude with increasing n_e at constant plasma current. The steep increase of the amplitude in the range between $n_{eo} = 3$ and 4×10^{13} cm^{-3} occurs together with the onset of a coupling between the m=1 and m=2 mode as seen from the soft X-ray signals [2,3,4]. Simultaneously, the sawtooth amplitude decreases [3,4]. Hydrogen and helium discharges show a similar behaviour, but in helium the mode amplitude usually has its increase at somewhat higher densities.

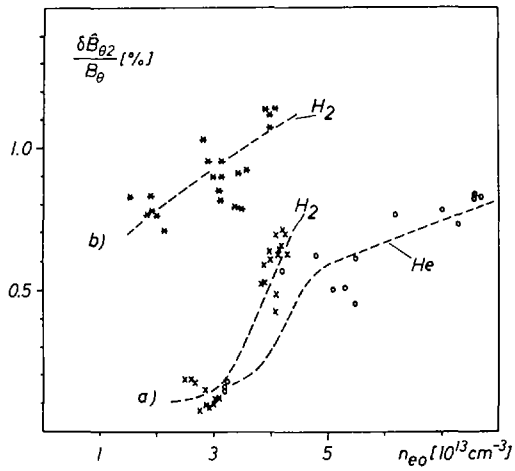


FIG. 3. Relative amplitude of the m=2, n=1 mode versus the central electron density n_{e0} for $B_0 = 3.5$ T, $\iota_0 = 0.055$ and for two different plasma currents: (a) $I_{pl} = 25$ kA; $q(a) \approx 3.7$; (b) $I_{pl} = 34$ kA; $q(a) \approx 2.9$. Measurements were taken as a function of microwave line density. For convenience, this was converted into n_{e0} by assuming a parabolic profile.

At higher plasma currents of 34 kA the amplitude of the m=2 mode is considerably larger at low densities (Fig. 3, curve b)). Predisruptions [4] are now seen on the soft X-ray signals close to the q=2 surface which trigger sawteeth at q=1. This may be the cause of the amplitude and frequencies of the m=2 mode being modulated up to $\pm$ 40 % in correlation with the sawteeth. No strong coupling between the m=1 and m=2 mode can be observed in this case. The predisruption phenomenon disappears at higher values of ι_0.

For ι_0 = 0.11 - 0.14 the dependence of the amplitudes and frequencies of different modes on I_{pl} and n_{e0} is shown in Figs 4 and 5. Fig. 4 shows the dependence of the m=2 mode on I_{pl} for nearly constant n_{e0}, and Fig. 5 its dependence on n_{e0} for fixed I_{pl}. In both cases the amplitude of the m=2 mode increases steeply with I_{pl} or with n_e, simultaneously with the onset of a coupling between the m=1 and the m=2 mode.

Progressively with increasing amplitude, the rotation of the m=2 islands is impeded by an interaction with the limiter [3]. The separatrix of the islands seems to be locked to the limiter for an increasingly longer period and therefore the frequency finally goes to zero. For an intermediate situation typical oscilloscope traces are shown in Fig. 6. The phases of the limiter signals shown correspond to the m=2 structure. The distance between the calculated q=2 surface and the effective plasma radius is 1.5 cm. Therefore, if the m=2 islands extend to the plasma edge, their full width would have to be about 3 cm. Similar statements were made by the TFR Group [3].

After having reached a maximum amplitude, either for $q(a) \approx 2.5$ or for $n_{eo} \approx 8 \times 10^{13}$ cm^{-3}, the m=2, n=1 mode is no longer visible. Then a m=3, n=2 mode usually remains, being sometimes coupled with a mode which appears to be m=2, n=2.

Injecting a fixed small quantity of neon into helium discharges of various densities, the maximum of the m=2 amplitude is shifted to lower densities.

Summarizing, to generate the steep increase of the amplitude of the m=2 mode, it is equivalent to increase

(i) the plasma current,
(ii) the electron density, or
(iii) the content of low-Z impurities.

m=2 MODE AND DISRUPTIONS

Fig. 5 shows that for $n_{eo} \approx 7 \times 10^{13}$ cm^{-3} the behaviour of the amplitude and the frequency of the m=2 mode with increasing density is very similar to the time evolution of the m=2 mode in Tokamaks immediately before a disruption [2,3]. In the Stellarator W VII-A these phenomena, which are highly transient in a disrupting Tokamak discharge, can be studied under stationary conditions by varying the density from shot to shot. It is interesting to note that a drastic reduction of the energy confinement time τ_E coincides with the steep increase of the amplitude of the m=2 mode (Fig. 5, upper part)[5]. Since many other plasma parameters like T_e, Z_{eff} or the impurity radiation vary simultaneously, it is difficult to decide whether the m=2 mode is responsible for the decreasing confinement, or whether the change of other parameters diminishes the confinement [6] and causes the m=2 mode to grow at the same time. In a Tokamak the corresponding rapid loss of thermal energy [2] results in an inward shift of the plasma as observed during a disruption, whereas in W VII-A the helical fields provide an equilibrium position for the plasma which helps to avoid disruptions; they are absent if the external rotational transform $\iota_o \geq 0.14$.

Although the circumstances usually leading to disruptions in Tokamaks have been studied in detail in W VII-A, the disruption phenomenon itself has rarely been investigated systematically. The following has been observed: (i) For $\iota_o = 0.055$ and high electron densities it is possible to obtain disruptions with a behaviour of the m=2 mode similar to that in Tokamaks. (ii) At $\iota_o = 0.11$, $q(a) \approx 2$ and high electron densities ($n_{eo} = 1.4 \times 10^{14}$ cm^{-3}), disruptions have also been observed in cases where no m=2 mode was visible, but a small m=3, n=2 mode was dominant. (iii) Under similar conditions, but reducing n_e to 1/10 of the above value, an amplitude of the m=2 mode up to 2.5 % has been measured without occurrence of disruptions.

FURTHER EFFECTS RELATED TO m=2 MODES

Strong m=2 modes modulate the signals also of various other diagnostics in W VII-A, e.g. the total plasma current

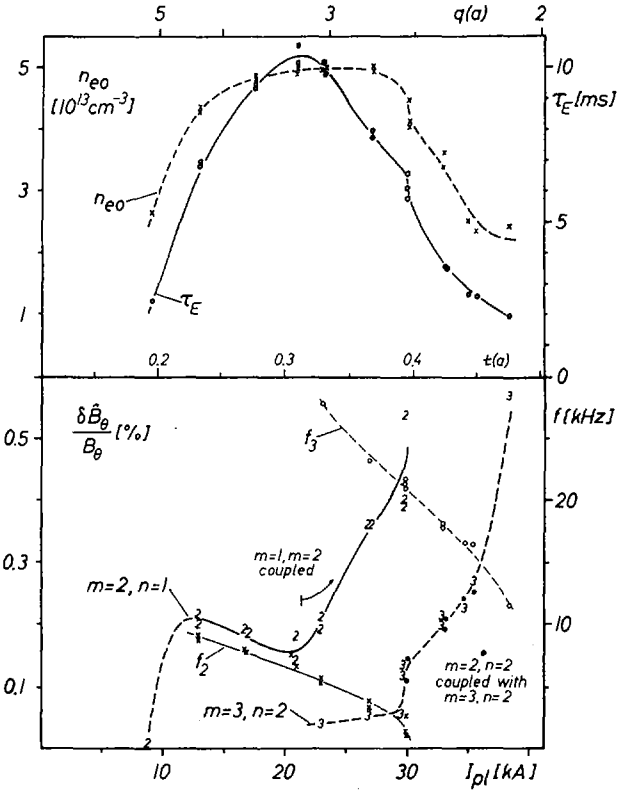


FIG. 4. Variation of the relative amplitude and the frequency of the different modes observed with increasing plasma current for helium discharges at $B_0 = 3.5$ T and $\iota_0 = 0.11$. In the upper half the simultaneous variation of the central density n_{e0} and the energy confinement time τ_E derived from the diamagnetic signal is shown. The discharges are performed with identical amounts of He introduced during current build-up.

($\delta I_{pl}/I_{pl} \lesssim 0.1$ %), the microwave density ($\delta n_e/n_e \lesssim 5$ %), the limiter potentials ($\Delta U \lesssim 5$ V), and the H_α or He I emission seen in the limiter plane ($\delta I/I \lesssim 2$ %). Comparing the phases of the m=2 oscillations on the magnetic probes with those of the microwave density and the soft X-ray diodes indicates that the fluctuations of the current density and of the electron temperature are in phase and out of phase to those of the electron density. This seems to be consistent with the model for tearing modes, since for kink modes all three of them should be in phase.

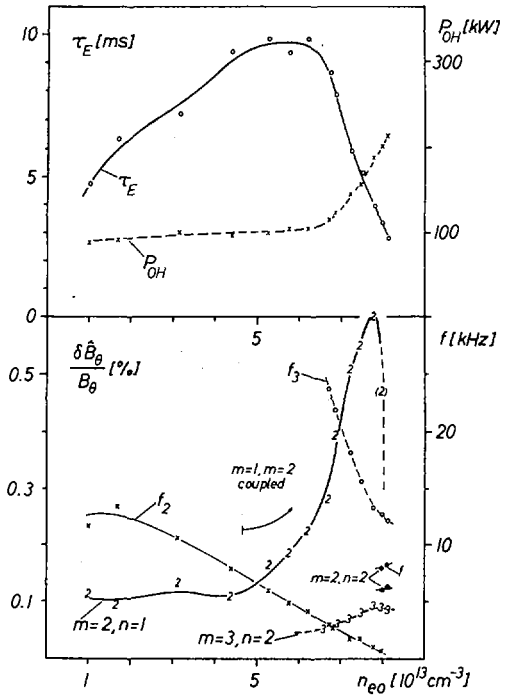


FIG.5. Variation of the relative amplitude and the frequency of the different modes observed with increasing central density for helium discharges with constant plasma current I_{pl} = 20 kA ($q(a) \approx 2.9$) at B_0 = 3.5 T and ι_0 = 0.14. In the upper half the simultaneous variation of the energy confinement time τ_E and the Ohmic heating power P_{OH} is shown.

m=2 MODE AT q < 2

In correlation with sawteeth, a m=2, n=1 mode can still be observed at q(a) < 2. An example is given in Fig. 7 where the m=2 mode grows already during the risetime of the sawteeth. Usually, only one to two cycles with large amplitude can be seen immediately after the sawtooth disruptions. Presumably, the sawteeth give rise to changes in the profiles, thus creating a m=2 mode for a short time. Since the rational q=2 surface is now beyond the limiter, this could be a m=2, n=1 external kink mode.

SUMMARY

The relative amplitude of the m=2 tearing mode decreases with increasing ι_0, and for ι_0 = 0.23 this mode has no longer been observed.

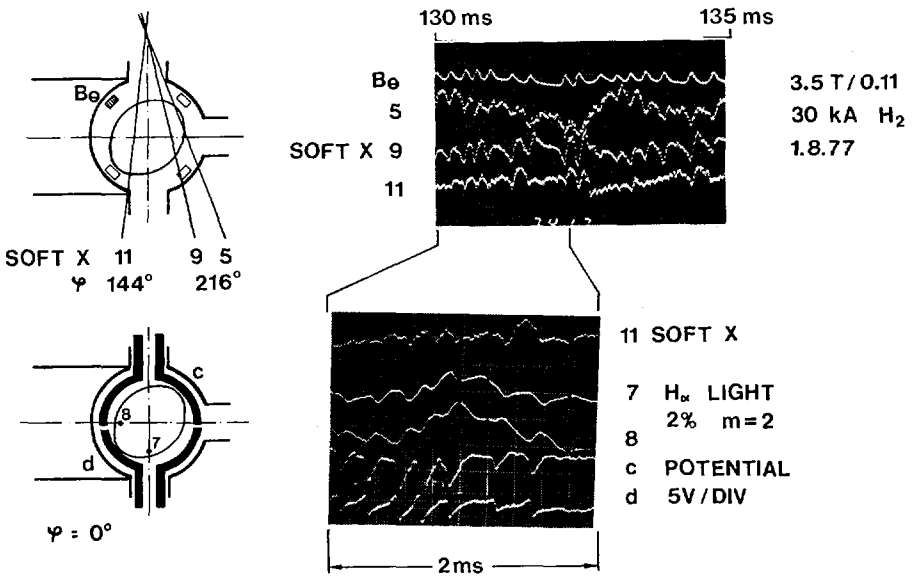


FIG. 6. m=2 mode locked to the limiter for irregular intervals. The upper half shows traces of one B_ϑ coil and of 3 soft X diodes, viewing along different plasma chords (see top insert). In the lower half the corresponding fluctuations of two H_α light signals and two limiter potentials are recorded at an increased sweep. The image points 7 and 8 and the two limiter segments c and d are identified in the lower insert.

A steep increase of the mode amplitude always occurs simultaneously with the onset of a coupling between the m=1 and m=2 modes.

This increase can be generated by increasing I_{pl}, n_e or the content of low-Z impurities.

At large m=2 amplitudes locking of the m=2 islands to the limiter is observed. In comparable Tokamaks this effect usually leads to current disruptions which do not occur in W VII-A if ι_0 is large enough.

As far as the dependence of the energy confinement on the m=2 amplitude is concerned, no definite answer can be given yet, since several competitive and perhaps even counteracting effects are active at the same time.

ACKNOWLEDGEMENTS

This paper would not have been possible without the continuous endeavours of the technical crew.

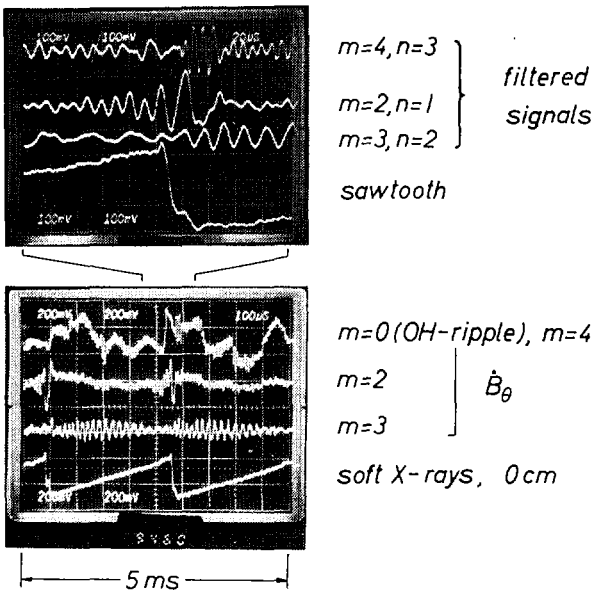


FIG. 7. Time behaviour of different modes and their correlation to sawteeth signals on the central soft X diode for a H_2 discharge at $B_0 = 3$ T, $\iota_0 = 0.23$ and $q(a) \approx 1.65$. By using series connections of B_θ coils, the individual modes have been separated according to their m numbers.

REFERENCES

[1] W VII-A Team, in Plasma Physics and Controlled Nuclear Fusion Research (Proc. 6th Int. Conf. Berchtesgaden, 1976) 2, IAEA, Vienna (1977) 81.

[2] KARGER F., et al., in Plasma Physics and Controlled Nuclear Fusion Research (Proc.6th Int.Conf. Berchtesgaden, 1976) 1, IAEA, Vienna (1977) 267.

[3] EQUIPE TFR, Nucl. Fusion 17 (1977) 1283.

[4] W VII-A Team, in Controlled Fusion and Plasma Physics (Proc. 8th Europ. Conf. Prague 1977) 1 (1977) 127 and 2 (1977) 236;

W VII-A Team, in Controlled Fusion and Plasma Physics (Proc.8th Europ. Conf. Prague 1977) 2 (1977) 73.

[5] Berry, L.A., et al., in Plasma Physics and Controlled Nuclear Fusion Research (Proc.6th Int.Conf. Berchtesgaden, 1976) 1, IAEA, Vienna (1977) 49.

[6] W VII-A Team, paper IAEA-CN-37/H-2, these Proceedings.

DISCUSSION

N. SAUTHOFF: One interpretation of the "locking" of the (2,1) and (1,1) modes and the (3,2) and (2,2) modes is that toroidal – i.e. (1,0) – effects induce mode components of (m ± 1,n). Does this toroidal eigenmode phenomenon correspond to your observations?

R. JAENICKE: There is strong evidence that all the observed modes are different modes, belonging,for example,to different rational surfaces given by $\iota = n/m$.

J.P. FREIDBERG: In a tokamak, increasing the current eventually leads to disruptions. Is there, in a stellarator with fixed Ohmic heating current, any analogous instability anticipated as the amplitude of the stellarator field is increased?

R. JAENICKE: No, but the confinement will eventually be lost, since the current density is limited to $q \geqslant 1$. Therefore, the radius of the $q = 1$ surface approaches the plasma radius, and inside the $q = 1$ surface the transport coefficients can be considered to be infinite.

CURRENT EQUILIBRIUM AND EFFECTIVE ION CHARGE IN L-2 STELLARATOR PLASMA

D.K. AKULINA, Eh.D. ANDRYUKHINA, G.S. VORONOV,
M.S. BEREZHETSKIJ, S.E. GREBENSHCHIKOV,
I.S. DANILKIN, B.I. KORNEV, O.I. FEDYANIN,
I.S. SBITNIKOVA, Yu.V. KHOL'NOV, I.S. SHPIGEL'
P.N. Lebedev Institute of Physics of the
USSR Academy of Sciences, Moscow,
Union of Soviet Socialist Republics

Abstract

CURRENT EQUILIBRIUM AND EFFECTIVE ION CHARGE IN L-2 STELLARATOR PLASMA.

This paper presents data on the equilibrium of a current in a stellarator magnetic field. It is shown that the equilibrium of a plasma column is only determined by the vacuum rotational transform angle at constant longitudinal and external transverse fields. The transverse field of the current is identical with the external transverse field. An investigation of the plasma radiation at a frequency of 2 ω_{Be} was carried out. It is shown that at a plasma density of $n > 7 \times 10^{12}$ cm^{-3} the electron temperature obtained from the intensity of the cyclotron radiation is in a good agreement with the results of X-ray measurements and the radial temperature distribution is near to parabolic. Measurement of the effective ion charge in the plasma shows a discrepancy between the values obtained from plasma conductivity and those obtained from radiation in the soft-X-ray and visible regions of the spectrum. $Z_{eff} \sim 2$ at the centre of the column. The usual plasma parameters are $n \sim 1.5 \times 10^{13}$ cm^{-3}, $T_e = 700$ eV, $T_i \sim 150$ eV.

1. INTRODUCTION

First experiments on second-generation stellarators (L-2, CLEO, W-VII) have demonstrated the possibility of obtaining a dense plasma of high temperature and rather high values of particle and energy confinement times. Thus the stellarator programme attains a new stage of development. The results have established a very close relationship between research on tokamaks and that on stellarators and raise the question of what promise stellarators show as a possible model of a thermonuclear reactor.

All experiments were performed with Ohmic heating, but it must be noted that many problems posed by this method remain unsolved. The main function of the current in stellarators is plasma production and heating. However, the longitudinal current may affect plasma confinement both positively (because of

the increase of the confining poloidal field) and negatively. The latter effect may be due to perturbations of the field structure in the stellarator and also to the development of instabilities.

In the L-2 stellarator, the existence of a certain critical value of the current where the total rotational transform angle near the axis reaches a value of $t = 1$ was observed [1]. In the present paper, we shall not be concerned with the problem of plasma stability but we shall dwell on issues of plasma current equilibrium and equilibrium state characteristics in a current region below the critical current.

Table I presents some stellarator parameters.

Most of the experiments were done with $\dot{t}(0) = 0.185$ where the separatrix is located inside the vacuum chamber and no limiter was used. The discharge was produced in hydrogen at initial pressures of $p = (0.4 - 2.0) \times 10^{-4}$ torr. The duration of the quasi-stationary plasma current was $25 - 30$ ms, as a rule. The mean plasma density $n_e \sim 1.5 \times 10^{13}$ cm^{-3}, and the electron temperature in the region near the axis reached 700 eV. The ion temperature was up to 150 eV. The energy life-time of the plasma was $T_E = 8 - 10$ ms and depended on the magnitude of the toroidal field [2].

TABLE I. SOME STELLARATOR PARAMETERS

Major torus radius	R = 100 cm
Minor vacuum chamber radius	r = 17.5 cm
Longitudinal field strength	B = 16 kG
Multipole order of helical winding	l = 2
Mean radius of last closed surface	a = 11.5 cm
Total angle of rotational transform on axis	$\dot{t}(0) = 0.185$
Rotational transform angle on boundary surface	$\dot{t}(0) = 0.7 - 0.8$

2. PLASMA COLUMN EQUILIBRIUM IN THE STELLARATOR

Equilibrium in stellarators is provided by multipole-magnetic-field components produced by helical windings. The transverse field $B_\perp$ (external or current field) leads to a displacement of the magnetic axis by an amount of $|\Delta r| = (R/t(0))\ |B_\perp|/B_0$.

Previous experiments on Ohmic heating carried out with the L-2 stellarator at $\dot{t}(0) = 0.185$ confirmed that the external transverse field does not have an important effect on the plasma parameters.

The experimental results of studies into the dependence of current column location (or, more precisely, the centre of the current) on the magnitudes of the plasma current I and the external transverse field at two values of the rotational transform angle are presented.

A theoretical analysis shows that the additional rotational transform angle $\iota_I(r) = R/5r^2\ B_0$ produced by the plasma current does not affect the displacement of the magnetic surfaces. Therefore, the displacement of the magnetic surfaces depends on the value of $\iota_{st}(r)$ but not on the total rotational transform angle, $\iota_I(r) + \iota_{st}(r)$. Under the operating conditions of the L-2 stellarator, the rotational transform angle on the magnetic axis $\iota(0)$ is four times smaller than on the boundary surface.

A pair of measuring loops located along the length of the torus was used to measure the displacement of the current centre along the radius. The flux $\Phi_\perp$ passed through the surface between these loops which were connected with one another.

This flux may, in principle, be calculated for a circular plasma current with allowance for toroidality at a constant value of the current density distribution, $j = j(r)\ (1 - (r/R)\cos\varphi)$, where φ is the angle along the minor circumference of the torus.

Figure 1a shows the dependence of the current centre location on plasma current and external transverse field strength for $\iota(0) = 0.185$. The magnitude of current displacement with respect to the magnetic axis of the vacuum stellarator field is plotted on the ordinate. This figure shows that, at constant transverse field, the current displacement is proportional to the current and, at I = const, to the external transverse field. Similar results were obtained for a four times smaller magnitude of the helical field $\iota(0) = 0.05$ (Fig.1b). In this case, the value of the displacement is higher because of the smaller rotational transform angle, as $\Delta r \sim 1/\iota(0)$.

The linear dependence of current centre displacement on current and external transverse field strength shows that the distribution remained unchanged all over the range of the variable.

From Fig.1, we can determine current values leading to the same displacement of the current centre at different values of the external transverse fields and, hence, calculate the effective value of the transverse field produced by the current under realistic experimental conditions. The transverse field values found by this method appear to be almost 30% smaller than corresponding values calculated for the current ring in free space. Apparently, this discrepancy is due to the presence of an iron core inside the plasma ring which decreases the transverse current field. In other words, equilibrium is, in our case, to one third due to the transformer iron and to two thirds due to the stellarator field.

We see that the displacement, at a given helical stellarator field, is a linear function of the total transverse field, and the transverse current field is equivalent

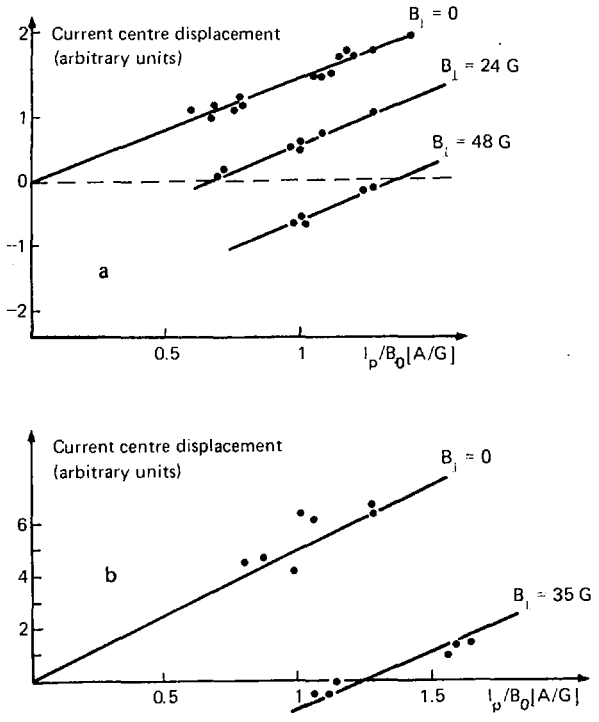


FIG.1. Displacement of current centre (in relative units) versus I_p/B_0 at different transverse field strengths. a) $\epsilon = 0.228$, $\iota(0) = 0.185$, $B_0 = 12$ kG; the dotted line represents the magnetic axis; b) $\epsilon = 0.114$, $\iota(0) = 0.05$, $B_0 = 14$ kG.

to the external transverse field (Fig.2). The equilibrium of a plasma ring at given values of longitudinal and external transverse fields is determined by the vacuum rotational transform angle, $\iota(0)$, only. Hence, the magnetic stellarator field may provide plasma equilibrium.

The results of the current centre displacement as given here did not take into account the effect of finite plasma pressure. This assumption proves to be justified at the plasma densities and temperatures observed in the experiments. The estimates show that the effect of β on the displacement of the magnetic surfaces must be taken into account when nT increases 3–4 times.

3. ELECTRON CYCLOTRON PLASMA RADIATION AND MEASUREMENT OF ELECTRON TEMPERATURE

We have studied electron cyclotron plasma radiation in order to obtain electron temperature profiles in the L-2 stellarator. The measurements were carried out at the second-harmonic cyclotron frequency [3].

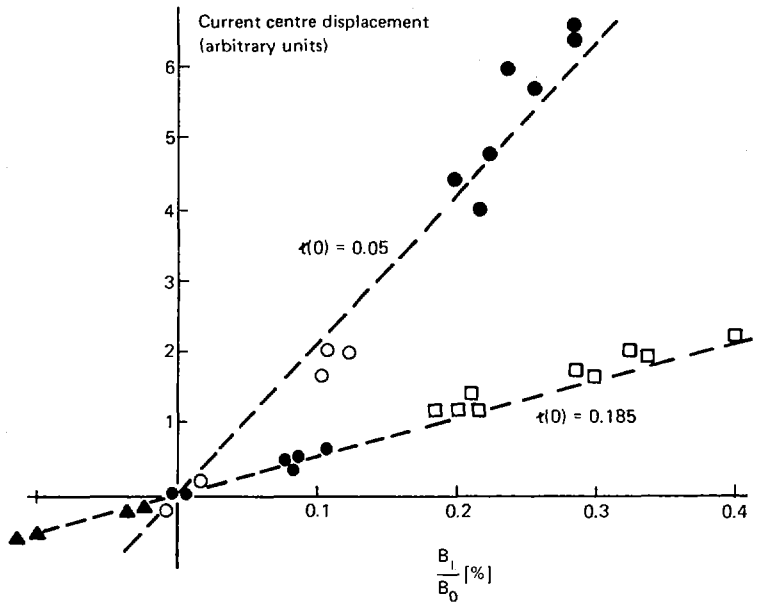


FIG.2. Displacement of current centre (in relative units) versus total transverse field, $t(0) = 0.05$: ● – $B_\perp = 0$, ○ – $B_\perp = 35$ G; $t(0) = 0.185$: ▲ – $B_\perp = 48$ G, ● – $B_\perp = 24$ G, □ – $B_\perp = 0$.

In the case of $\tau \gg 1$, where τ is the coefficient characterizing the optical thickness of the radiating layer, the plasma appears to be optically thick ("black body") and the radiation at the given harmonic cyclotron frequency is proportional to the plasma temperature T_e.

Measurements of cyclotron plasma radiation were performed through the outer horizontal port along the major torus radius. A horn, 50 cm in length, and with an aperture of 8 cm, was employed as a receiver. A teflon lens with a focal distance of 20 cm permits a narrow diagram of the receiver directivity to be obtained. The angular width of the receiver diagram in the plasma region is 6° and the spot at the centre of plasma is about 1.5 cm. A superheterodyne receiver operating in the 4-mm region with 15% frequency deviation was used for radiation detection.

The calculation of the τ coefficient for second-harmonic cyclotron radiation in the case of typical L-2 stellarator parameters gives a value of $\tau \geqslant 5$. The presence of a metal vacuum chamber leads to an increase in the factor τ, owing to multiple reflections.

From the measurements, we conclude that radiation is of a resonance nature. These measurements were carried out in the region near 2 ω_{Be}, with a variable stellarator magnetic field and constant receiver frequency as well as for variable

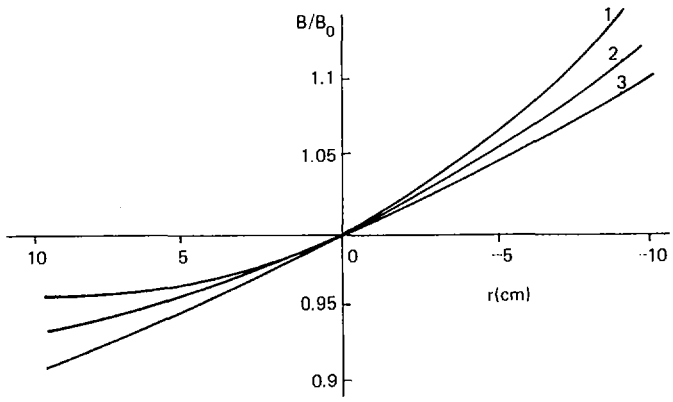


FIG.3. Variation of field modulus along direction of measurement.

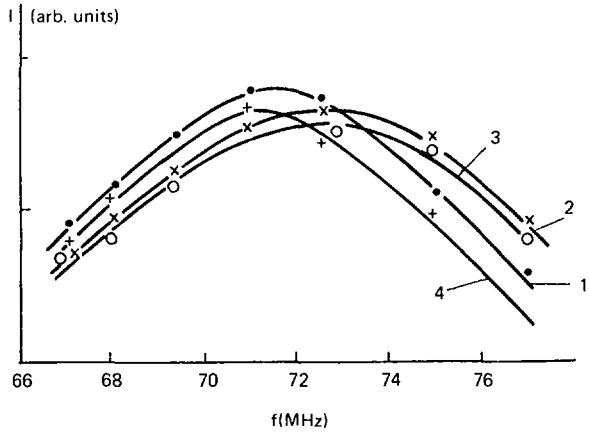


FIG.4. Radiation power versus frequency for different moments of time. Curve 1: 10 ms, 2: 15 ms, 3: 20 ms, 4: 25 ms.

receiver frequency and B = const. Figure 4 shows radiation power versus frequency for different moments with respect to the initial discharge stage. The resonance width is determined by the inhomogeneity of magnetic field and radial distribution of electron temperature. The displacement of the curves is due to the variation of the magnetic field strength with time. The electron temperature as calculated from the absolute radiation intensity within the experimental accuracy coincides with the temperature obtained from the soft-X-ray radiation and is determined by the method of laser scattering.

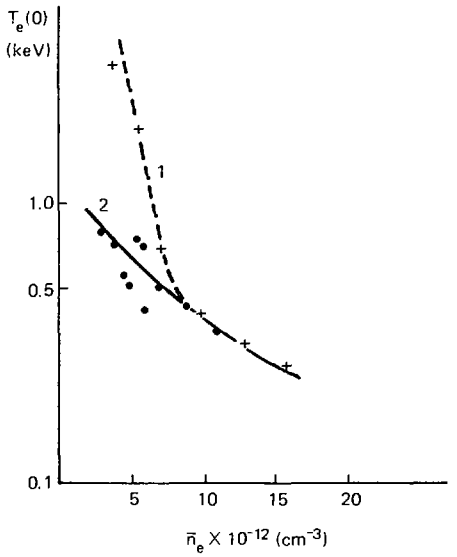


FIG.5. Radiation temperature versus mean electron density (curve 1) and electron temperature as determined from the soft-X-ray energy spectrum (curve 2), $\epsilon = 0.228$.

The nature of radiation changes abruptly during the transition to the low plasma densities ($n_e \leqslant 5 \times 10^{12}$ cm^{-3}). In this case, the intensity of high-frequency radiation at the initial stage of the discharge increases with time and then decreases with a large time constant, and radiation exists even when the plasma current is turned off. The radiation plasma temperature reaches 5 keV under these conditions. In addition, a substantial broadening of the radiation spectrum occurs. This effect is apparently due to the presence of an appreciable number of runaway electrons in plasma [4]. Figure 5 shows the relationship between radiation plasma temperature and plasma density (see the crosses in Fig.5 and the curve 1 corresponding to them). Curve 2 and the black dots correspond to the temperature from the soft-X-radiation spectrum. We see that these two methods are in good agreement for plasma densities $n_e \geqslant 7 \times 10^{12}$ cm^{-3}. For lower densities, the radiation plasma temperature is substantially higher than the electron plasma temperature.

We can see from the data presented here that measurements of plasma radiation at the second-harmonic cyclotron frequency for plasma densities of $n_e \approx 10^{13}$ cm^{-3} make it possible to determine the electron temperature and also its radial distribution, owing to the inhomogeneity of the magnetic field strength over the cross-section. Since the surfaces with B = const in the L-2 stellarator do not coincide with the magnetic surfaces, in the limits of the diagram of the

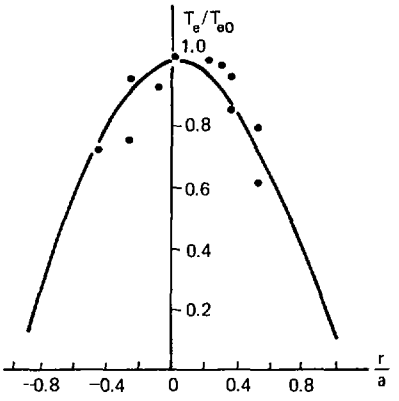


FIG. 6. Radial electron temperature distribution. The solid curve is a calculated parabola, • denotes experimental values.

receiving horn directivity, the contribution to the radiation at the resonance frequency is made by the points of plasma volume on the different radii and with different electron temperatures.

Figure 3 shows the change in modulus of B along the direction of measurement. Curve 2 represents the change in the magnetic field along the axis of the receiver diagram while curves 1 and 3 correspond to the change in the magnetic field along the lines displaced left and right of the torus axis by a distance of 2 cm. We can also see that the measurement accuracy becomes worse from the centre of plasma towards the outside. Figure 6 shows the measured electron temperature distribution in the horizontal direction. The solid curve represents the calculated distribution corresponding to the law $T_e(r) = T_0(1 - r^2/a^2)$. It may be postulated that, within experimental accuracy, the radial distribution of the electron temperature is close to a quadratic parabola.

The superposition of a transverse field shifts the location of the electron temperature maximum. The measured displacement coincides with the calculated displacement of the plasma column magnetic axis.

4. INVESTIGATION OF EFFECTIVE PLASMA ION CHARGE

An important characteristic of hydrogen plasma confined in a trap is the amount of impurities and the corresponding effective plasma ion charge. The usual method of determining the mean value of Z_{eff} is based on measuring the plasma column resistance.

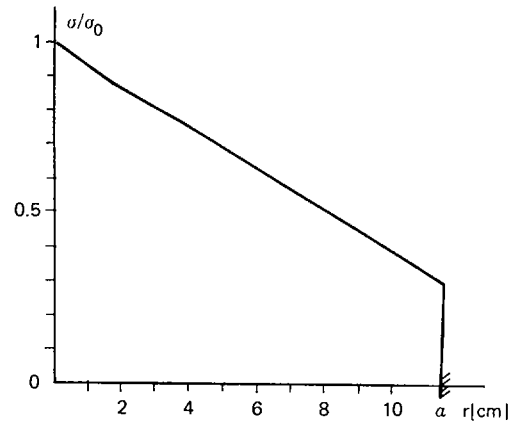


FIG. 7. Conductivity due to stellarator-type trapped particles versus plasma radius. For the calculation, $T_e(r)$ = const was assumed.

The specific resistance of a fully ionized plasma is determined by the following expression [5]:

$$\rho_0 = 5.2 \times 10^{-3} \frac{\ln \Lambda}{T_e^{3/2}} Z\gamma(z)$$

where

$$\gamma = \frac{1.51 + 0.57\,Z}{1.08 + Z}$$

In toroidal devices, the effect of trapped particles on the plasma conductivity leading to an increase in plasma column resistance must be taken into account. In the case of a stellarator, it is necessary to take into account the effect of particles on the helical field non-uniformity. The effect of these trapped particles on plasma conductivity was calculated by Kovrizhnykh. If we write the specific plasma resistance as $\rho = \rho_0/f(r)$ then

$$f(r) = 1 - 1.95\,\epsilon_\perp^{1/2} + 0.74\,\epsilon_\perp$$

where $\epsilon_\perp = \ell\epsilon I_\ell(\ell dn)$, $I_\ell(\ell dn)$ is a modified Bessel function, ℓ is the multipole order of a helical field, ϵ the amplitude of the helical harmonic, and $d = N/R$ is the wave number of a helical winding with N pitches. The expression holds true in a range of the collision frequencies $\nu_0 < \ell\alpha\, v_{T_e}\, \epsilon_\perp^{3/2}$ and is satisfied for the plasma

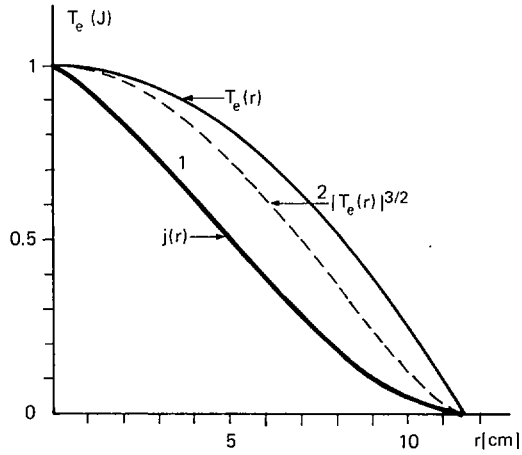


FIG.8. Current density distribution for parabolic $T_e(r)$ distribution, with allowance for stellarator-type trapped-particle effect on the conductivity.

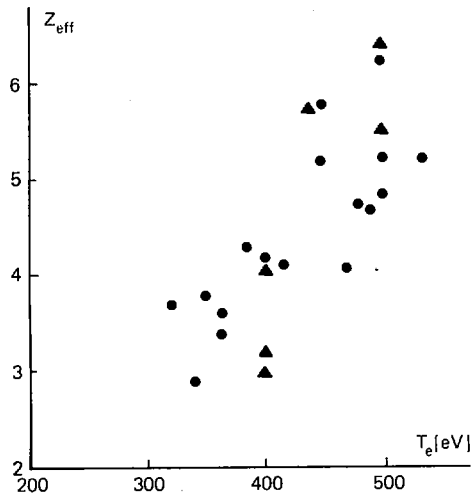


FIG.9. Z_{eff} versus electron temperature. $I_p = 12 - 18$ kA, $\overline{n_e} = (0.8 - 1.2) \times 10^{13}$ cm^{-3}, ● – $B_0 = 12$ kG, ▲ – $B_0 = 16$ kG.

parameters of the L-2 stellarator. Figure 7 shows the influence of the trapped-particle effect on the plasma conductivity for $\iota(0) = 0.185$ in the L-2. The normalized dependence of the plasma column conductivity due to the particles trapped is also shown. The calculation was based on the assumption that $T_e(r) = \text{const}$. We see from this figure that the plasma conductivity on the boundary of the plasma column deteriorates 3 times due to the stellarator-type trapped particles.

In calculating the plasma column resistance and, accordingly, the magnitude of Z_{eff} we took the electron temperature radial distribution as $T_e(r) = T_{e0}(1 - r^2/a^2)$.

Figure 8 shows the calculated current density distribution in a stellarator taking account of the trapped-particle effect. We also see the difference between current density distributions calculated taking stellarator-type trapped particles into account (curve 1) and those calculated without allowing for them (curve 2). The total effect leads to a 1.6-times increase in the total resistance of the plasma column.

Figure 9 shows measurements of Z_{eff} from conductivity. The circles correspond to measurements made in different shots during one year on our device. They differ by vacuum conditions, initial hydrogen pressures and magnitudes of plasma current. As can be seen from the figure, the effective plasma charge varies, on the average, from 3 to 6 in the given temperature range. The electron plasma temperature decreases, as a rule, with increasing plasma density in a single series of experiments. But measurements made at different shots show that the value of the electron temperature is not determined unambiguously by the plasma density and depends on a number of uncontrolled conditions such as the state of the vacuum chamber walls. This is well illustrated by Fig.9 which shows the variation of the electron temperature in the range of 300–500 eV at practically constant plasma density. It is also difficult to establish an unambiguous relationship between the temperature and the magnitude of the Ohmic heating current from the data obtained from different measurements. One observes a certain tendency for increase in the effective plasma charge with increasing electron temperature, in spite of some point scatter.

The other method of estimating an effective plasma charge is based on the soft-X-ray measurements. From the absolute measurements of X-ray plasma intensity in an energy range of 1.5–4 keV we determine the enhancement factor which shows how many times the plasma radiation observed in the experiment is more intense than the calculated bremsstrahlung radiation for pure hydrogen plasma. The impurity concentration and the effective plasma charge may be calculated from the enhancement factor provided that one kind of impurity is dominant.

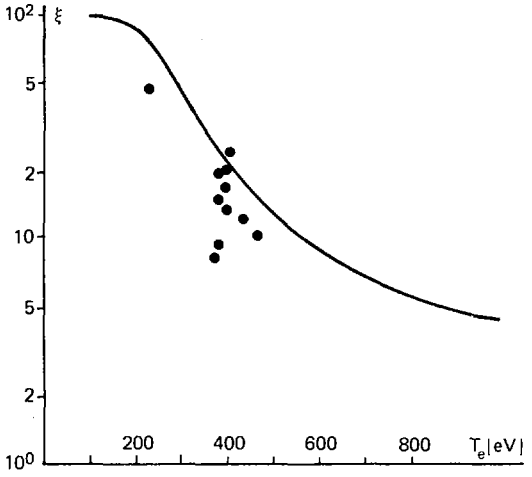


FIG.10. Enhancement factor ξ versus electron temperature. The solid curve represents the calculation for the case where oxygen appears to be the dominant impurity (1%). The points correspond to the experiment.

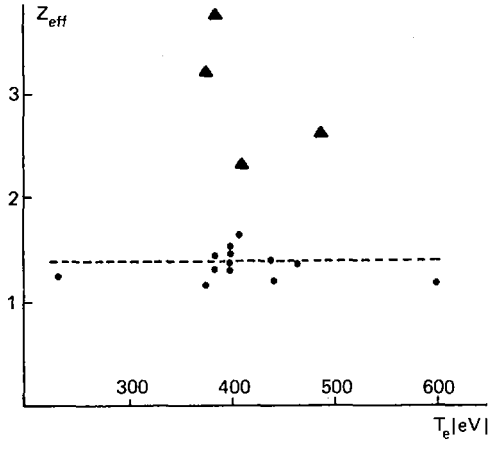


FIG.11. Z_{eff} versus electron temperature as measured from soft-X-ray spectrum (●) and from spectroscopic measurements (▲).

In the framework of this assumption,

$$Z_{eff} = 1 + \frac{(\xi-1)\, Z\, (Z_0-1)}{Z_0^2\, \gamma}$$

Where Z_0 practically coincides with the charge of an impurity nucleon and γ shows how many times the summary radiation of that type of ions with account for recombination is stronger than bremsstrahlung radiation.

As X-ray radiation is mostly determined by the central and hot test region of the plasma, estimates of impurity ion concentration and effective plasma charge only refer to the centre of the plasma column.

Figure 10 shows the results of measuring the enhancement factor for different plasma temperatures. Circles designate results of experimental measurements. The solid curve corresponds to the theoretical dependence of the enhancement factor for the case of 1% oxygen ions in the coronal model. So, if we assume oxygen to be the dominant impurity, its concentration at the centre of the plasma column must be ~ 1%. Generally speaking, the assumption of oxygen as the dominant impurity does not contradict the results of spectral measurements in the visible spectral region. Measurement of the intensity of both O II (λ = 4415 Å) and C III (λ = 4647 Å) lines carried out simultaneously with X-ray measurements showed that the oxygen ion concentration near the boundary of the plasma column is 1.5 – 2 times higher than the carbon ion concentration.

Figure 11 shows the values of Z_{eff} as obtained from X-ray measurements. We see from this figure that $Z_{eff} \sim 1.5$ in the temperature range under investigation. That is appreciably lower than the corresponding values obtained from plasma conductivity.

The calculation of Z_{eff} was carried out within the framework of the corona equilibrium. The fact that the real experiments do not correspond to the coronal model may be due to two factors. Firstly, the plasma has not had the time to obtain an equilibrium distribution over the charge states of the impurity ions and, secondly, the finite ion life-time in a trap must be taken into account, which has an appreciable effect on the equilibrium distribution over the charge states. Exactly taking into account both factors is rather complex and requires the knowledge of transport processes of highly ionized impurities across the plasma column. An approximate calculation of the hydrogen ion ionization in a plasma with account for the finite life-time at $n\tau \sim 10^{11}$ cm^{-3}·s, corresponding to the confinement conditions of the L-2 stellarator, shows that, by 15–20 ms after the start of the discharge, $\bar{\gamma}$ attains a value which is half that of γ, corresponding to the coronal model. These estimates almost coincide with the results of Ref. [6] in which the effect of the finite ion life-time in a trap was also estimated. The twofold decrease of the factor $\bar{\gamma}$ – compared to the corona equilibrium calculations – leads to a corresponding increase in Z_{eff} from 1.5 to 2 at the plasma centre.

The same difficulties due to the fact that there are no data on impurity dynamics across the plasma column and due to finite life-time also arose when the results of spectral measurements in the visible spectral region were treated.

In Fig.11 the triangles show the results of estimating Z_{eff} from the light intensity of both O II and C III lines on the plasma periphery. We see that the values of Z_{eff} obtained by this method are lower than the corresponding values calculated from plasma conductivity.

5. CONCLUSIONS

Experiments carried out in 1977–78 showed that the stellarator field provides equilibrium of a current-carrying plasma column.

Investigations of the electron temperature distribution from the intensity of the magnetic bremsstrahlung radiation at 2 ω_{Be} showed that the $T_e(r)$ profile is, within the accuracy of measurements, close to the parabola

$$T_e(r) = T_e(0)\left(1 - \frac{r^2}{a^2}\right)$$

It follows from soft-X-ray radiation analysis that the effective ion charge Z_{eff} is about 2 in the region near the axis of the plasma column, and the average value over the column cross-section value of Z_{eff} obtained from conductivity is 3–6. It may be postulated that there is a disagreement between the mean value of the effective charge calculated from plasma conductivity, on the one hand, and Z_{eff} at the centre of the plasma column as determined from the absolute intensity of the soft-X-ray spectrum, on the other hand. Disagreement is observed not only in the absolute values of Z_{eff} but also in the dependence of these values on the plasma temperature when $\bar{n}_e$ = const. At present, there is no evidence for a mechanism explaining this discrepancy.

In the near future, experiments on pulsed gas puffing aiming at an increase of the plasma density are going to be carried out on the L-2 stellarator.

Experiments on ion cyclotron frequency heating will be started in 1979.

ACKNOWLEDGEMENTS

The authors would like to express their gratitude to M.S. Rabinovich and L.M. Kovrizhnykh for their interest in this work and useful discussions,to S.N. Popov and M.A. Blokh for discussions and experimental assistance, to N.M. Zverev and the technical assistants for providing the perfect operation of the entire L-2 stellarator.

REFERENCES

[1] AKULINA, D.K., et al., in Plasma Physics and Controlled Nuclear Fusion Research (Proc. 6th Int. Conf. Berchtesgaden, 1976) Vol. 2, IAEA, Vienna (1977) 115; SHPIGEL', I.S., in Controlled Fusion and Plasma Physics (Proc. 8th Europ. Conf. Prague, 1977) Vol. 2 (1977) 109.
[2] AKULINA, D.K., et al., ibid., Vol. 1, 129.
[3] ENGELMANN, F., CURATOLO, M., Nucl. Fusion **13** (1973) 497.
[4] ROZHDESTVENSKIJ, V.V., et al., Plasma Phys. **4** (1978) 61.
[5] SPITZER, L., Physics of Fully Ionized Gases, New York - London (1962).
[6] VON GOELER, S., et al., Nucl. Fusion **15** (1975) 301.

INJECTION OF A SOLID HYDROGEN PELLET INTO THE L-2 STELLARATOR

N.P. DONSKAYA, M.S. RABINOVICH, G.S. VORONOV
P.N. Lebedev Institute of Physics of the
USSR Academy of Sciences,
Moscow,
Union of Soviet Socialist Republics

Presented by Eh.D. Andryukhina

Abstract

INJECTION OF A SOLID HYDROGEN PELLET INTO THE L-2 STELLARATOR.

Experiments on the injection of solid hydrogen pellets into the L-2 stellarator are discussed in the paper. Pellets and laser parameters are given. The pellet life-time in the plasma is discussed. Account of plasma cooling during the plasma-pellet interaction substantially increases the pellet life-time.

The idea of using laser plasma for injection was put forward soon after the invention of the laser [1].

Successful experiments on laser injection of plasma into the stellarator were conducted with the Protocleo [2] and Tor-I [3] devices. The programme of the L-2 stellarator includes further development of these studies. In contrast to the other experiments [3, 4] where massive metallic Be and Li targets were used in the experiments with L-2 stellarator, solid hydrogen pellets will be employed.

For the production of pellets, a cryostat was constructed in the Physical Technical Institute of Low Temperatures, Ukrainian Academy of Sciences. This cryostat make it possible to obtain cylindrical pellets 0.4–0.8 mm in diameter and 0.2–2 mm in length.

Solid hydrogen is frozen from the gas phase on a needle cooled by liquid helium. This needle is placed in a capillary with an appropriate diameter. Before a pellet is thrown down the needle is pushed out of the capillary up to the liquired length. Pellet injection is provided by throwing down hydrogen during needle heating [4]. The mean deviation of a pellet from the vertical during a fall from a height of 20 cm is about 0.5 cm and about 50% of the pellets touch the laser focus 0.5 mm in diameter. A full description of this cryostat will be given elsewhere.

The laser pulse duration must be long enough to provide full evaporation and ionization of a pellet.

For the experiments described here a neodymium laser with an output energy of up to 300 J was prepared. Prolongation of a pulse is provided by inserting a non-linear absorber plate made of cadmium selenide into the resonator. The pulse duration may vary from 30 up to 300 ns.

Depending on pellet and focus size and the effectiveness of plasma trapping by the magnetic field of a target, we expect that an initial plasma of a density of $n_e \sim 10^{13}$ cm^{-3} and an ion temperature of up to 200 eV may be obtained. The electron temperature appears to be very low (about 1 eV) owing to the practically adiabatic volume enlargement during the injection. We may increase the electron temperature with the help of auxiliary heating e.g. Ohmic heating. Such a plasma may be of interest for the study of transport processes in stellarators at different ratios of electron and ion temperatures.

Solid-hydrogen pellet injection may be also used to raise the density of a plasma produced by other methods. Consequently, experiments on a solid-hydrogen pellet injection into a plasma obtained by Ohmic heating are planned.

First experiments in this direction are proposed to be carried out at the Ohmic discharge initiation at the moment when a pellet crosses the centre of the magnetic surfaces. Recently, similar experiments were carried out at the Pulsator tokamak. But the interaction of plasma with a pellet in a stellarator at the initial stage of the discharge may differ from the pellet-plasma interaction in a tokamak as in the L-2 stellarator the rotational transform angle near the magnetic axis is not equal to zero when there is no plasma current. The runaway electrons which are very important for the intensity of pellet evaporation are quite different in both cases.

For future experiments, it is proposed to inject pellets into the plasma only when the discharge has fully developed. Calculation of the life-time of a pellet 0.8 mm in diameter in a plasma with parameters characteristic for the Ohmic heating regime in the L-2 stellarator ($n_e \sim 10^{13}$ cm^{-3}, $T_e \sim 500$ eV) gives $\tau_p \sim 400$ μs. The plasma radius a = 11 cm. So the velocity which a pellet injected into the plasma must have in order to reach the centre is not less than $V_p \sim 3 \times 10^4$ cm$\cdot$s^{-1}.

In Ref. [6], however, the plasma parameters are treated as constant. The energy content of plasma is, as a matter of fact, comparable to the heat deposition needed for evaporation, ionization, and heating of a pellet, hence the plasma parameters cannot remain constant during pellet evaporation. Taking into account plasma cooling due to the interaction with a pellet increases the pellet life-time up to milliseconds and, accordingly, decreases the necessary value of the pellet velocity down to $3 \times 10^3 - 10^4$ cm$\cdot$s^{-1}.

Another important field in which pellet injection is applied is the creation of dense plasma targets for various heating methods requiring high densities such as, e.g. neutral beams.

The cloud of hydrogen from a pellet can, fortunately, only be increased up to several centimetres before full ionization. This fact may be explained by the coincidence of two facts: the dissociation cross-section of hydrogen molecules by moderate-energy electrons is 250 times smaller than the ionization cross-sections [7], and the cross-section of charge exchange of protons and molecular hydrogen at energies of 100 eV is small. As a result of pellet evaporation and ionization, a plasma region of about 1 cm^3 with a density of $n_e \sim 10^{15}$ cm^{-3} is produced and appears to be a sufficiently effective target for transverse neutral injection.

REFERENCES

[1] ASKAR'YAN, G.A., DELONE, N.B., RABINOVICH, M.S., Zh. Ehksp. Teor. Fiz. **46** (1964).
[2] BOLTON, R.A.E., et al., in Plasma Physics and Controlled Nuclear Fusion Research, (Proc. 4th Int. Conf. Madison, 1971) Vol. 3, IAEA, Vienna (1971) 79.
[3] ANDRUKHINA, Eh.D., et al., Pis'ma Zh. Ehksp. Teor. Fiz. **14** (1971) 317.
[4] TANIMOTO, M., KITSUNEZAKI, A., SEKIGUCHI, T., J. Phys., E (London) Scient. Instr. **5** (1972) 27.
[5] Jahresbericht des Max-Planck-Instituts für Plasmaphysik (1977) 2.1.6.
[6] PARKS, P.B., TURNBULL, R., FOSTER, C., Nucl. Fusion **17** (1977) 539.
[7] MESSI, G., BARKHOP, E., Electron and Ion Collisions, Moscow (1958) in Russian.

DISCUSSION

ON PAPERS H-4(A) AND H-4(B)

K. UO: You said that the magnetic axis undergoes a shift due to the vertical field produced by the Ohmic heating current, and that this shift is larger with a lower transform. What about the shift of the separatrix due to this same vertical field?

Eh.D. ANDRYUKHINA: The shift of the separatrix with the same Ohmic heating current is $\iota(a)/\iota(0)$ times smaller than the shift of the magnetic axis ($\iota(a)$ is the rotational transform on the separatrix).

H.P. FURTH: I have a comment that relates to all of the last four papers. These papers all demonstrate that various improvements can be made in tokamak performance by adding helical windings. The advantage gained, however, is offset by the reduction in plasma size and field strength which results because the helical windings occupy some of the most valuable space inside the toroidal field coils. My suggestion is that for the improvement of tokamaks it may be most effective to place helical windings only on the large-major-radius half of the tokamak chamber, thus raising the rotational transform on the outer half of the magnetic surfaces. In this way a real net improvement over simple tokamaks may be achieved.

J.L. SHOHET: I should like to point out that it is possible to make a stellarator configuration with no toroidal field coils, namely a torsatron. No "real estate" can then be lost inside the toroidal field coils, because there are none.

M.S. RABINOVICH: I would just like to point out that a stellarator with large shear, such as the L-2 device, and with current is very different from a tokamak or a stellarator without shear and with current, like the Wendelstein VII A. In the L-2 stellarator the $q = 1$ point is located on the edge of the plasma where the temperature is low, and $q = 2$ is within the plasma. In this case there are no sawtooth oscillations or internal disruptions. As has been shown at Princeton, this magnetic surface configuration is, in fact, the most stable, and at the same time a magnetic limiter is created.

ANALYTICAL INVESTIGATIONS OF EQUILIBRIUM AND STABILITY IN THREE-DIMENSIONAL MHD CONFIGURATIONS

D. LORTZ, J. NÜHRENBERG
Max-Planck-Institut für Plasmaphysik,
Euratom-IPP Association,
Garching,
Federal Republic of Germany

Abstract

ANALYTICAL INVESTIGATIONS OF EQUILIBRIUM AND STABILITY IN THREE-DIMENSIONAL MHD CONFIGURATIONS.

Expansion of an MHD equilibrium around its magnetic axis yields the following results for three-dimensional toroidal configurations without Ohmic heating current: the limits for the critical β-values according to a necessary and a sufficient criterion are raised to 0.2 and 0.05, respectively. The configuration achieving these values has 20 periods and may be described as a special toroidal equilibrium near a helical equilibrium. High-β stellarator equilibria (i.e. equilibria without longitudinal current) are investigated with an asymptotic expansion around the unidirectional field. The new feature of this expansion is the use of different length scales for the periodicity length L_p over which the rotational transform is of the order one and the length scale L of the stabilizing corrugations, $L \ll L_p$. The first-order fields are determined from two coupled elliptical equations which have to be solved with non-periodic boundary conditions in a domain of length L.

1. INTRODUCTION

The search for acceptable stable toroidal MHD equilibria without ohmic heating current proceeds along three main lines. Apart from the numerical approach, which attempts to solve the three-dimensional problem directly, and which is not considered here, there are the methods of expansion of a toroidal configuration around its magnetic axis and of global (asymptotic) equilibrium expansion by means of small parameters. This paper presents results obtained by these methods.

The expansion around the magnetic axis (see, for example, [1-3]) is adequate to obtain a first assessment of the equilibrium and stability properties of a three-dimensional configuration in a relatively easy way and therefore allows a systematic search in the space of configurations and elimination of many configurations which have too low ß-values to be acceptable, e.g. the classical $\ell = 2$ stellarator. We have written a numerical program which evaluates equilibrium ß-values and the stability properties according to necessary and sufficient stability criteria for general three-dimensional configurations and present several case studies: toroidal equilibria which

are approximately helical; equilibria whose magnetic surfaces are purely elliptical and centered with respect to the magnetic axis as starting point for stable equilibria; $\ell = 2$ stellarator equilibria with $\ell = \pm 1$ corrugations; and equilibria with different length scales for the stabilizing corrugations and the periodicity length. The last study showed that stable, $\beta \approx 1$ equilibria near the unidirectional finite-β field may exist and prompted the global expansion discussed in this paper. The essential point is that no satisfactory expansion around the unidirectional finite-β field with smooth pressure profile has yet been found if the rotational transform per period is small (see, for example, [4-7]). The reason appears to be that there is then no mechanism other than profile dependent shaping of flux surfaces to satisfy the equilibrium condition that $\int d\ell/B$ be constant on magnetic surfaces [8]. A possible way out is to keep the rotational transform per period finite. Hitherto this has been investigated by allowing a longitudinal current which leads to screw-pinch-type equilibria [7]. Employing different length scales for the length over which the rotational transform is of the order one and the three-dimensional corrugations, we show that it is possible to obtain an equilibrium expansion around the unidirectional finite-β field without longitudinal current, i.e. of the stellarator type.

2. EXPANSION AROUND THE MAGNETIC AXIS

Parameters and functions of the arc length along the magnetic axis occurring in such a study are: $\dot{p}$ (derivative of pressure with respect to volume), $\varkappa$ (curvature of magnetic axis), τ (torsion of magnetic axis), c_o (field on the magnetic axis), e (ellipticity of cross-section), α (turning angle of ellipses), S_a^*, S_b^* (shifts of magnetic surfaces with respect to magnetic axis), δ^*, Δ^* (triangularities of surfaces), V_s (separatrix volume obtained by third-order separatrix), $\beta_e \approx \dot{p} V_s / c_o^2$ (equilibrium β-value), β_n, β_s (critical β-values obtained from the stability limit according to the necessary criterion [1] and the sufficient criterion for configurations without longitudinal current [2], respectively). For details of the theory see, for example [3].

2.1. Approximately helical equilibria

We consider toroidal equilibria which are near helical equilibria in the sense that a helical equilibrium is approached with increasing number of periods on the torus. The β-values which can be achieved in a helical equilibrium according to the necessary and the sufficient stability criterion are characterized by the following facts. The maximum values are achieved in the scaling:

$$\left.\begin{aligned} &\varkappa = \varepsilon \varkappa_1 , \quad \tau = 1 + \varepsilon^2 \tau_2 , \quad L = 2\pi \\ &c_o = 1 , \quad e = 1 + \varepsilon e_1 \\ &-4 S_a^* + \delta^* = 0(\varepsilon) \end{aligned}\right\} \varepsilon \to 0$$

which describes a helical equilibrium with finite $\ell = 3$ fields and small $\ell = 1$ and $\ell = 2$ components. To $O(\varepsilon^2)$ the necessary and the sufficient criterion are, respectively (for $\dot{p} < 0$),

$$-2\varkappa_1^2 - 2e_1^2 + 3e_1\varkappa_1\delta^* > 0$$

$$-2\varkappa_1^2 - 2e_1^2 + 3e_1\varkappa_1\delta^* + 8\pi^2\dot{p}\varkappa_1^2 > 0$$

The volume inside the separatrix is given by

$$V_s = \frac{8}{27}\,\frac{4\pi^2}{\delta^{*2}}$$

Thus, β_n is unlimited for $\delta^* > \frac{4}{3}$ in the framework of this scaling, while

$$\beta_s \leq \frac{1}{6}\,\frac{\left(\frac{e_1}{\varkappa_1}\right)^2}{1+\left(\frac{e_1}{\varkappa_1}\right)^2}\,, \qquad \delta^* = \frac{4}{3}\,\frac{1+\left(\frac{e_1}{\varkappa_1}\right)^2}{\frac{e_1}{\varkappa_1}}$$

Defining the aspect ratio by

$$A = \left(\frac{L^3}{4\pi V_s}\right)^{\frac{1}{2}}$$

we obtain as aspect ratio of a torus with M periods in the limit of large M

$$A = \sqrt{3}\,M\,\frac{1+\left(\frac{e_1}{\varkappa_1}\right)^2}{\frac{e_1}{\varkappa_1}}$$

Numerical calculations [8] show that the optimum ß values for finite values of $\varkappa$ are close to the above limits for $\varkappa \approx 0.1$. Choosing $e_1 = \varkappa_1$, we obtain for $\tau = 0.9$ (i.e. $\varkappa = 0.436$, $e = 1.436$) as optimum values $\beta_n = 0.23$ (for $4\pi^2\dot{p} = -4$, $\delta^* = 1.26$), $A \sim 3$, and $\beta_s = 0.058$ (for $4\pi^2\dot{p} = -1.1$, $\delta^* = 1.91$), $A \sim 3$.

We now turn to toroidal equilibria near the helical equilibria described above. Toroidally closed curves may be found which can be described to first approximation in $O(M^{-1})$ by

$$\varkappa = \varkappa_0 + \varkappa_1 \cos\ell$$

$$\tau = \tau_0 + \tau_1 \cos\ell$$

where $\varkappa_0$, τ_0 are curvature and torsion of the helical magnetic axis and $2\pi M$ is the total length of the toroidal magnetic axis. Keeping the other parameters of the equilibrium (e, c_0, $\dot{p}$) fixed and obtaining β_n by adjusting δ^*, one finds that β_n drops drastically to about 0.01 for M = 20. One is thus

forced to look for an analytical guideline to keep the unfavourable toroidal effects for a fixed number of periods smaller. Here, we choose the following recipe: the perturbation of the helical equilibrium is adjusted in such a way that the parallel current density $j \cdot B/B^2$ associated with the pressure gradient [9, 10-12] is not perturbed in leading order. With

$$e = e_0 + e_1 \cos \ell$$

$$c_0 = 1 + c_1 \cos \ell$$

this leads to the condition:

$$\frac{\varkappa_1}{\varkappa_0} - \frac{\tau_1}{\tau_0} - \frac{3}{2} c_1 + e_1 \frac{e_0 (e_0^2 - 3)}{2 (e_0^2 + 1)} = 0 \qquad (1)$$

The following optimum results are then achieved for M = 20:

(i) $\beta_n = 0.19$ with $\varkappa_0 = 0.44$, $\varkappa_1 = 0.14$, $\tau_0 = 0.91$, $\tau_1 = 0.06$, $e_0 = 1.44$, $e_1 = -0.08$, $c_1 = 0.18$, $4\pi^2 \dot{p} = -4.4$, $\delta^* = 1{,}46$, $A = 70$;

(ii) $\beta_n = 0.047$ with $4\pi^2 \dot{p} = -1.1$, $\delta^* = 1.9$; the other parameters as in (i).

For lower values of M (M = 10 has been tested) the achievable critical ß-values drop substantially without lowering of the aspect ratio if eq. (1) is used.

2.2. Elliptical centered equilibria

There are equilibria whose magnetic surfaces are purely elliptical and centered with respect to the magnetic axis, i.e. the magnetic surfaces exhibit neither triangularity nor shifts with respect to the magnetic axis, $S_a^* = S_b^* = \delta^* = \Delta^* = 0$ [13].

The conventional β_e estimate is unbounded for these configurations. Here, we studied the β_n value which can be obtained by imposing a stabilizing triangular corrugation. Starting from an equilibrium of this type with 13 periods and

$$\varkappa = 0.43 + 0.17 \cos\ell - 0.02 \cos 2\ell + \ldots$$

$$\tau = 0.90 + 0.01 \cos\ell - 0.12 \cos 2\ell + 0.06 \cos 3\ell + \ldots$$

$$e = 1.65 - 0.14 \cos\ell + 0.38 \cos 2\ell - 0.25 \cos 3\ell + \ldots$$

$$\alpha = -\frac{\ell}{2} + 0.29 \sin\ell + 0.24 \sin 2\ell - 0.18 \sin 3\ell + \ldots$$

$$4\pi^2 \dot{p} = -1.1$$

(only some Fourier coefficients of the exact solution are given), the addition of $\delta^* = \delta_0 \cos \frac{\ell}{2}$ was studied to determine a representative value of β_n. The result, $\beta_n = 0.026$,

$A \sim 60$, $\delta_0 = 3.5$, shows that a large equilibrium ß-value as starting point in search of stable equilibria is a poor selection criterion.

2.3. The $\ell = 2$ stellerator with variable curvature

As starting points for a study of a stellarator with plane magnetic axis with variable curvature we use two representative cases of the simple $\ell = 2$ stellarator with circular magnetic axis [14]:

(a) $n = 5$, $\varkappa = \frac{1}{5}$, $\tau = 0$, $\alpha = \frac{\ell}{2}$, $e = 2$, $4\pi^2\dot{p} = -0.22$, $\delta^* = \delta_1 \cos\alpha$, $\delta_1 = 1.41$, $\Delta^* = \Delta_1 \sin\alpha$, $\Delta_1 = 1.88$, $ß_e = 0.018$, $A \sim 12$ as representative case for the achievable $ß_e$. We note that the adjustment of δ^* and Δ^* is important. With $\delta_1 = \Delta_1 = 0$ and the other parameters unchanged the result is $ß_e = 0.0033$, $A \sim 29$.

(b) $n = 5$, $\varkappa = \frac{1}{5}$, $\tau = 0$, $\alpha = \frac{\ell}{2}$, $e = 2$, $4\pi^2\dot{p} = -0.034$, $\delta_1 = 0.22$, $\Delta_1 = 0.27$, $ß_n = 0.0042$, $A \sim 10$ as representative case for the achievable $ß_n$. For $\delta_1 = \Delta_1 = 0$, $ß_e = 0.01$, $A \sim 6$.

We now study the modification of these equilibria with

$$\varkappa = \varkappa_0 + \varkappa_1 \cos\ell$$

Starting from case (a) with $\delta_1 = \Delta_1 = 0$, $ß_e$ is maximized with respect to $\varkappa_1$: $ß_e = 0.056$ for $A \sim 7$ and $\varkappa_1 = 0.85$. Associated with this large increase in $ß_e$ is a large drop of the parallel current density associated with the pressure gradient. The configuration may also be described as nearly elliptical and centered, since the local aspect ratio

$$A_{loc} = \left(\frac{L\pi}{V_S} \; \frac{1}{\varkappa_{max}^2} \right)^{\frac{1}{2}}$$

drops from 29 to 1.3.

Starting from case (b) with $\delta_1 = \Delta_1 = 0$, the analogous result is: $\varkappa_1 = 0.325$, $ß_e = 0.078$, $A \sim 2.3$, $A_{loc} \sim 0.9$, which shows that the interpretation as elliptical centered equilibrium is the more appropriate one since the reduction in parallel current density is only moderate for this case.

The stability of both types of configurations was investigated with

$$\delta^* = \delta_1 \cos\frac{\ell}{2} + \delta_3 \cos\frac{3\ell}{2}$$

$$\Delta^* = \Delta_1 \cos\frac{\ell}{2} + \Delta_3 \cos\frac{3\ell}{2}$$

The result is that β_n stays of the order of a few tenths of a per cent, so that the same conclusion as at the end of 2.2 can be drawn.

2.4. Equilibria with different length scales

Considering the results concerning β_s for $\iota = 0$ equilibria [3, 15] and helical equilibria (see 2.1), one is led to the question whether or not it is possible in the framework of the present theory to obtain equilibria for which β_s is unbounded. If one excludes equilibria with straight magnetic axis and large variation of c_0 and e [16] and stable elliptical centered equilibria [13] from consideration, the expression for the magnetic well (see, for example, [2]) shows that unboundedness of β_s can only occur for $|\varkappa|_{max}$, $|\tau + \alpha'|_{max} \to 0$, if $e \neq 1$, which is necessary for the possibility of stabilization by triangular deformation [1]. Furthermore, non-vanishing rotational transform is necessary. The configuration thus cannot be periodic over one full turn of the normal of the magnetic axis. Introducing $\tau_0 = 1$ and $\varkappa, \tau + \alpha' \sim O(\varepsilon)$, we see that the period of the configuration is of the order $2\pi/\varepsilon$. The simplest equilibrium of this kind is given as follows:

$$\varkappa = \varepsilon \quad , \quad \tau = 1 + O(\varepsilon^2)$$

(representing a helical magnetic axis with period 2π),

$$\alpha' = -1 + \varepsilon \quad , \quad L_p = 2\pi/\varepsilon$$

(representing one full turn of the elliptical cross-section in space),

$$e = e_0 \neq 1$$

$$\dot{p} L_p \sim O(1)$$

(representing a finite pressure gradient for the helical period as reference length),

$$\delta^* = \delta_1 \cos\alpha \sim 0 \tag{1}$$

(representing a deformation of $O(\varepsilon)$ over a lateral extension comparable to the helical period),

$$\beta_e \sim \dot{p} L_p^3 / \delta^{*2} \sim O(\varepsilon^{-2})$$

(achieved if a lateral dimension comparable to L_p is admitted). Two sets of numerical results are:

(i) $\varepsilon = 0.1$, $\tau = (1-\varepsilon^2)^{1/2}$, $\dot{p} L_p^2 = -2$, $\delta_1 = 10.6$, $\beta_s = 0.039$, $A \sim 16$,

(ii) $\varepsilon = 0.02$, $\tau = (1-\varepsilon^2)^{1/2}$, $\dot{p} L_p^2 = -10$, $\delta_1 = 11.6$, $\beta_s = 0.80$, $A \sim 18$.

3. EXPANSION AROUND THE FINITE-β UNIDIRECTIONAL FIELD FOR EQUILIBRIA WITHOUT LONGITUDINAL CURRENT

Inspection of the scaling introduced in Sec. 2.4 shows that it describes a perturbation of the unidirectional field if a lateral extension comparable with the helical period is considered. We thus see that long periodicity length (L_p) equilibria with finite rotational transform over this period may be chosen nearly unidirectional on a segment whose length L is of the order of the lateral dimension ($L \ll L_p$). The equilibrium becomes expandable by applying non-periodic boundary conditions at the ends of the segment considered.

We shall introduce the toroidal curvature later and start by using a Cartesian coordinate system x, y, z and the equilibrium equations in the form

$$\begin{aligned} P_{,i} - B_k B_{i,k} &= 0 \\ B_{i,i} &= 0 \end{aligned} \tag{2}$$

where $P = p + \frac{1}{2} B^2$ and the summation convention is used. We solve the equations in the following domain: for $0 \leq z \leq L$ the boundary of the domain is given by (φ is the usual polar coordinate)

$$M := \{ x = X(\varphi, z) \ , \ y = Y(\varphi, z) \} \tag{3}$$

with the additional condition that

$$\begin{aligned} X(\varphi - \delta, L) &= X(\varphi, 0) \cos\delta + Y(\varphi, 0) \sin\delta \\ Y(\varphi - \delta, L) &= -X(\varphi, 0) \sin\delta + Y(\varphi, 0) \cos\delta \end{aligned} \tag{4}$$

which means that the boundary at z = L is obtained from that at z = 0 by rotation by the angle δ . The boundary conditions are $\vec{n} \cdot \vec{B} = 0$ on M, i.e.

$$B_x Y_{,\varphi} - B_y X_{,\varphi} + B_z (X_{,\varphi} Y_{,z} - X_{,z} Y_{,\varphi}) = 0 \tag{5}$$

and

$$\begin{aligned} &B_x(\xi, \eta, L) - B_x(x, y, 0) \cos\delta - B_y(x, y, 0) \sin\delta = 0 \\ &B_y(\xi, \eta, L) + B_x(x, y, 0) \sin\delta - B_y(x, y, 0) \cos\delta = 0 \\ &B_z(\xi, \eta, L) - B_z(x, y, 0) = 0 \\ &\xi = x \cos\delta + y \sin\delta \\ &\eta = -x \sin\delta + y \cos\delta \end{aligned}$$

expressing that the fields at z = L are obtained from those at z = 0 by rotation by δ. Thus, a periodic configuration is obtained with period $L_p = Ln$ if $\delta = 2\pi m/n$.

Introducing $\delta = \varepsilon \delta_1$ and $d = \frac{\delta_1}{L}$, expanding equations and boundary condition with respect to ε and choosing

$$\overset{\circ}{M} := \{ x = \overset{\circ}{X}(\varphi),\ y = \overset{\circ}{Y}(\varphi) \}$$

the zeroth-order solution is given by the finite-ß unidirectional field

$$P = p + \frac{1}{2} b^2 = \text{const}$$

where $b(x,y) = \overset{\circ}{B}_z(x,y)$ and is arbitrary except for $b(\overset{\circ}{X},\overset{\circ}{Y}) = \text{const}$. The first-order equations and solutions are

$$\begin{aligned}
&\hat{P}_{,x} - b\hat{B}_{x,z} = 0\\
&\hat{P}_{,y} - b\hat{B}_{y,z} = 0\\
&\hat{P}_{,z} - b\hat{B}_{z,z} - b_{,x}\hat{B}_x - b_{,y}\hat{B}_y = 0\\
&\hat{B}_{x,x} + \hat{B}_{y,y} + \hat{B}_{z,z} = 0\\
&\hat{B}_x = \frac{1}{b}\hat{Q}_{,xz} - \hat{F}_{,y} + \alpha y b\\
&\hat{B}_y = \frac{1}{b}\hat{Q}_{,yz} + \hat{F}_{,x} - \alpha x b\\
&\hat{B}_z = \frac{1}{b}\hat{Q}_{,zz} - \frac{1}{b^2}(b_{,x}\hat{Q}_{,x} + b_{,y}\hat{Q}_{,y}) - \alpha z D b + \hat{T}\\
&\hat{P} = \hat{Q}_{,zz}
\end{aligned}$$

where $\hat{Q}(x,y,z)$ is the first-order periodic corrugation, $\hat{F} = \hat{F}(b)$, $\hat{T}(x,y)$ is arbitrary in this order, and $D = y\partial_x - x\partial_y$. The equation for $\hat{Q}$ is obtained from the condition that the divergence vanish:

$$b\Delta\hat{Q} - 2(b_{,x}\hat{Q}_{,x} + b_{,y}\hat{Q}_{,y}) = 0 \qquad (7)$$

The first-order boundary conditions are

$$\hat{B}_x \overset{\circ}{Y}_{,\varphi} - \hat{B}_y \overset{\circ}{X}_{,\varphi} + b(\overset{\circ}{X}_{,\varphi}\hat{Y}_{,z} - \hat{X}_{,z}\overset{\circ}{Y}_{,\varphi}) = 0$$

on M and

$$\hat{B}_x(x,y,L) - \hat{B}_x(x,y,0) = 0$$

$$\hat{B}_y(x,y,L) - \hat{B}_y(x,y,0) = 0$$

$$\hat{B}_z(x,y,L) - \hat{B}_z(x,y,0) + \delta_1 Db = 0$$

Here, $\hat{X}(y,z)$, $\hat{Y}(y,z)$ are the first-order perturbation of the cylindrical boundary. With

$$\hat{X} = dz(\mathring{X}_{,y} + \mathring{Y}) + \tilde{\hat{X}}$$

$$\hat{Y} = dz(\mathring{Y}_{,y} - \mathring{X}) + \tilde{\hat{Y}}$$

the condition (4) is satisfied with periodic $\tilde{\hat{X}}$, $\tilde{\hat{Y}}$. Furthermore, we may assume without loss of generality that

$$\langle \tilde{\hat{X}} \rangle = \langle \tilde{\hat{Y}} \rangle = 0$$

where $\langle\ \rangle = \int \ldots dz/L$. The boundary condition on M then reduces to

$$\hat{Q}_{,x}\mathring{Y}_{,y} - \hat{Q}_{,y}\mathring{X}_{,y} + b^2(\mathring{X}_{,y}\tilde{\hat{Y}} - \mathring{Y}_{,y}\tilde{\hat{X}}) = 0 \qquad (8)$$

so that eqs. (7), (8) are a Neumann problem for Q with respect to M with periodic boundary conditions with respect to z:

$$\hat{Q}(x,y,L) = \hat{Q}(x,y,0)$$

$$\hat{Q}_{,z}(x,y,L) = \hat{Q}_{,z}(x,y,0)$$

and the solution has the property $\langle \hat{Q} \rangle = 0$.

The second-order equations are

$$\begin{aligned}
&\hat{\hat{P}}_{,x} - b\hat{\hat{B}}_{x,z} + A_x = 0, \qquad A_x = -\hat{B}_\kappa \hat{B}_{x,\kappa} \\
&\hat{\hat{P}}_{,y} - b\hat{\hat{B}}_{y,z} + A_y = 0, \qquad A_y = -\hat{B}_\kappa \hat{B}_{y,\kappa} \\
&\hat{\hat{P}}_{,z} - b\hat{\hat{B}}_{z,z} - b_{,x}\hat{\hat{B}}_x - b_{,y}\hat{\hat{B}}_y + A_z = 0, \qquad A_z = -\hat{B}_\kappa \hat{B}_{z,\kappa} \\
&\hat{\hat{B}}_{\kappa,\kappa} = 0
\end{aligned} \qquad (9)$$

The solutions are

$$\hat{\hat{B}}_x = \frac{1}{b}\hat{\hat{Q}}_{,xz} - \hat{\hat{F}}_{,y} - H_{,y} + dy\hat{T} + dz\,\partial_y D\hat{F} - d^2 yz\,Db$$

$$-\frac{d}{b}z(\partial_x D\hat{Q}_{,z} - \frac{1}{b}\hat{Q}_{,xz}Db) + \frac{d}{b}(\partial_x D\hat{Q} - \frac{1}{b}\hat{Q}_{,x}Db) + \frac{1}{b}\tilde{A}_x$$

similar expressions for $\overset{2}{B}_y$, $\overset{2}{B}_z$, and

$$\overset{2}{P} = \overset{2}{Q}_{,zz} - d z D \overset{1}{Q}_{,zz} + \tfrac{1}{2}(\nabla \overset{1}{F})^2 + \frac{1}{2b^2}\langle(\nabla \overset{1}{Q}_{,z})^2\rangle$$

$$- \tfrac{1}{2} d^2(x^2+y^2) b^2 + 2d \int b \, d\overset{1}{F} + \int h \, d\overset{1}{F}$$

Here, $\overset{2}{F} = \overset{2}{F}(b)$, $H = -b^{-3} \langle \overset{1}{Q}_{,x} \overset{1}{Q}_{,yz} \rangle$, $\tilde{A}$ is periodic with $\langle \tilde{A} \rangle = 0$, and $\overset{2}{Q}$ solves an inhomogeneous equation analogous to eq. (7). The solubility condition for the second-order equations is obtained by introducing

$$A = \bar{A} + \tilde{A}_{,z}$$

Note that $\bar{A}$ is not a constant with respect to z) and considering the cross-derivative of the first two equations of eqs (9). The result is (' = d/dF)

$$\Delta \overset{1}{F} - b^{-3} \dot{b} \langle (\nabla \overset{1}{Q}_{,z})^2 \rangle - d^2 b \dot{b}(x^2+y^2) + h(\overset{1}{F}) = 0 \qquad (10)$$

and may be verified directly by inserting $\overset{2}{B}_x$ and $\overset{2}{P}$ in eq. (9a). Except for the new term proportional to d^2, eq. (10) is identical to the result in [7].
Equation (10) completes the first-order calculation. Non-vanishing d enables us to solve eq. (10) for vanishing longitudinal current, as is seen from the relation

$$\oint_{\overset{1}{F}_o} \vec{n} \cdot \nabla \overset{1}{F} \, d\ell + \overset{1}{J}(\overset{1}{F}_o) + d\left[2 \int_0^{\overset{1}{F}_o} b \dot{V} \, d\overset{1}{F} + \int_0^{\overset{1}{F}_o} \dot{b} \left(\oint |\nabla \overset{1}{F}|^{-1} \vec{r} \cdot \nabla \overset{1}{F} \, d\ell \right) d\overset{1}{F}\right] = 0$$

where $\oint \cdots d\ell$ is the contour integral along $\overset{1}{F}$ = const, $V = \oint |\nabla F|^{-1} d\ell$, $\overset{1}{J}$ is the first-order longitudinal current. This relation is obtained from eq. (10) by eliminating $h(\overset{1}{F})$ in favour of $\overset{1}{J}(\overset{1}{F})$.

A second-order toroidal curvature can readily be included by using

$$d\ell^2 = dx^2 + dy^2 + \vec{r}_{,\varphi}^{\,2} d\varphi^2, \quad |\vec{r}_{,\varphi}| = \sqrt{g} = 1 - \varepsilon^2 \overset{2}{\varkappa} x, \quad \overset{2}{\varkappa} = \text{const}$$

instead of Cartesian coordinates. The result is an additional term in eq. (10), namely $2 \overset{2}{\varkappa} x \dot{b} b$.

4. CONCLUSION

The case studies using expansion of an equilibrium around its magnetic axis presented in this paper show that within the framework of this theory:

(i) β_e values may be increased considerably by the concepts of lowering the parallel current density associated with the pressure gradient and of searching for elliptical centered equilibria;

(ii) $\beta_n \approx 0.2$ and $\beta_s \approx 0.05$ for genuine toroidal configurations. This is a large increase compared with the result for the $\ell = 2$ stellarator. Automatic search in configurational space may lead to a further increase of these values;

(iii) β_s is formally not bounded.

The asymptotic expansion around the unidirectional finite-ß field is, to our knowledge, the first satisfactory high-ß stellarator expansion.

Both theoretical approaches have developed to the degree that interaction with 3-D numerical codes may become useful. Another urgent point which has to be taken into account is the susceptibility of configurations without longitudinal current to ballooning-type instabilities (see, for example, [17]).

REFERENCES

[1] MERCIER, C., Nucl. Fusion **4** (1964) 213.
[2] LORTZ, D., NÜHRENBERG, J., Z. Naturforsch. **31a** (1976) 1277.
[3] LORTZ, D., NÜHRENBERG, J., "Stable MHD equilibria", Theoretical and Computational Plasma Physics (Proc. 3rd Int. 'Kiev' Conf. Trieste, 1977), IAEA, Vienna (1978) 305.
[4] HERRNEGGER, F., NÜHRENBERG, J., Proc. 2nd Top. Conf. on Pulsed High-Beta Plasmas, Garching, 1972, IPP/I/127 (1972) 49.
[5] NÜHRENBERG, J., in Theoretical Aspects of Controlled Thermonuclear Research (Proc. Sherwood Mtg. Arlington, 1975) p. 75.
[6] BARNES, D.C., et al., Plasma Physics and Controlled Nuclear Fusion Research 1976 (Proc. 6th Int. Conf. Berchtestaden, 1976) Vol.2, IAEA, Vienna (1977) 203.
[7] SPIES, G.O., Nucl. Fusion **18** (1978) 1671.
[8] CORREA, D., Garching Rep. IPP 1/149 (1974).
[9] LORTZ, D., NÜHRENBERG, J., Nucl. Fusion **18** (1978) 807.
[10] PFIRSCH, D., SCHLÜTER, A., Max-Planck Inst., Munich, Rep. MPI/PN 7/62 (1962).
[11] NÜHRENBERG, J., Nucl. Fusion **12** (1972) 383.
[12] LORTZ, D., NÜHRENBERG, J., Proc. 8th Europ. Conf. on Controlled Fusion and Plasma Physics, Prague, 1977, Vol.1 (1977) 91.
[13] LORTZ, D., NÜHRENBERG, J., to be published in Z. Naturforsch.
[14] LORTZ, D., NÜHRENBERG, J., Nucl. Fusion **17** (1977) 125.
[15] HERRNEGGER, F., et al., Plasma Physics and Controlled Nuclear Fusion Research 1976 (Proc. 6th Int. Conf. Berchtesgaden, 1976) Vol.2, IAEA, Vienna (1977) 183.
[16] FURTH, H.P., ROSENBLUTH, M.N., Phys. Fluids **7** (1964) 764.
[17] CORREA-RESTREPO, D., Z. Naturforsch. **33a** (1978) 789.

DISCUSSION

H. WOBIG: In ideal theory the pressure profile p (ψ) is arbitrary. What profile was used in your theory, and how sensitive are the results to this choice?

J. NÜHRENBERG: In the first part of the paper, where we present results obtained with the expansion around the magnetic axis, the profile p(V) enters as the parameter $\dot{p}(0)$, i.e. the derivative with respect to volume evaluated on the magnetic axis. The dependence on this parameter is quantitatively discussed in Section 2.3: the two sets of results are obtained for values of $\dot{p}(0)$ differing by a factor of about 6.

The expansion around the unidirectional field, presented in the second part of the paper, is valid for arbitrary p(V), here represented by $b(\hat{F})$. The non-linear coupling of Eqs (7) and (10) is due to $db/d\hat{F}$.

Session L

NON-AXISYMMETRIC SYSTEMS II

Chairman

R. WIENECKE
FRG
Papers L-3-1 and L-3-2 were presented
by J.P. Freidberg as Rapporteur

RF HEATING EXPERIMENTS ON HELIOTRON DEVICES AND ANALYSIS OF EQUILIBRIUM AND STABILITY OF STRAIGHT HELICAL HELIOTRON PLASMA

K. UO, A. IIYOSHI, H. AKIMUNE, T. OBIKI,
S. MORIMOTO, M. WAKATANI, A. SASAKI,
K. KONDO, O. MOTOJIMA, M. SATO, T. MUTOH,
I. OHTAKE, M. NAKASUGA, T. MIZUUCHI,
S. KINOSHITA, K. HANATANI
Plasma Physics Laboratory,
Kyoto University,
Gokasho, Uji

T. AMANO
Plasma Physics Laboratory,
Faculty of Engineering,
Osaka University, Osaka

S. HAMADA
Department of Physics and
Atomic Energy Research Institute,
College of Science and Engineering,
Nihon University, Tokyo,
Japan

Abstract

RF HEATING EXPERIMENTS ON HELIOTRON DEVICES AND ANALYSIS OF EQUILIBRIUM AND STABILITY OF STRAIGHT HELICAL HELIOTRON PLASMA.

Heating experiments in the Heliotron D device with use of the shear Alfvén wave have continued. It is found that for high initial electron temperature plasmas the electrons of the central region are heated effectively, but for low initial electron temperature plasmas the electron heating is localized at the spatial resonance region ($\omega = k_{\parallel} v_A(r_0)$). In the Heliotron DM device, a plasma of higher energy density of the order of $n_e T_e \sim 10^{16}\ cm^{-3} \cdot eV$ ($n_e = 5 \times 10^{13}\ cm^{-3}$; $T_e = 160$ eV) has been obtained by means of higher current density ($\overline{J_{OH}} \sim 150\ A \cdot cm^{-2}$). The MHD equilibrium of a straight helical heliotron with separatrix configuration is calculated for a parabolic pressure profile and a uniform plasma current. MHD stability against low-m internal mode is examined. The pressure-driven internal mode becomes unstable when a resonant surface exists in the plasma column.

1. SHEAR ALFVÉN WAVE HEATING EXPERIMENTS IN HELIOTRON D

Plasma heating experiments in an Alfvén wave frequency range have been performed continuously [1–4] in Heliotron D. The results of effective electron heating have already been reported. Here, the measurement of the radial electron temperature profile of the plasmas is described. The wave magnetic field in the plasma is measured in order to investigate wave properties and to compare them with the theory.

The details of the Heliotron D device have already been described [3, 4]. An antenna structure to be used in the heating experiment was placed inside the vacuum chamber and outside the helical coil. The measurement of the RF antenna and the diagnostic apparatus is shown schematically in Fig.1. The azimuthal mode number, m, of the antenna is ±2. The dimensions of the antenna were chosen so as not to excite the compressional Alfvén wave. The RF power was fed into the antenna through a coaxial cable and a matching circuit from a power generator with maximum output power 1 MW and fixed frequency 405 kHz.

A radial profile of the electron temperature was measured by laser scattering (one result is shown in Fig.2). At the centre the electron temperature is about 80 eV without the RF pulse and it increases up to about 130 eV with the RF pulse. It is clearly shown that the plasma body is mainly heated and there is no local heating. In this electron temperature regime, the thermal velocity of the electrons is much higher than the phase velocity of the wave. Then the kinetic Alfvén wave [5] can be excited and damping length is sufficiently long. The plasma body can then be heated.

The RF heating pulse is also applied to low-temperature plasma. A typical profile of the electron temperature is shown in Fig.3. The temperature of the base plasma is roughly 5 eV and increases up to 18 eV when the RF power is applied. In this case, the RF pulse length is about 0.25 ms. The temperature profile has two peaks around the points r = 8 cm and 5 cm. Figure 4 shows the radial profile of the wave magnetic field. The azimuthal component, $\tilde{B}_\theta$, has the minimum, and the radial component, $\tilde{B}_r$, has the maximum at the spatial resonant point where the local Alfvén speed coincides with the phase velocity of the wave, i.e. $\omega/k_\parallel = v_A(r)$, where v_A is Alfvén speed. This qualitatively agrees with the theoretical prediction [5]. As shown in Figs 3 and 4, the electron temperature becomes maximum at the resonance points. This indicates that in the low electron temperature plasma the kinetic Alfvén wave can be strongly damped and can hardly be excited, so the wave seems to have MHD behaviour.

The effect of Ohmic currents on the plasma confinement is also examined for the RF-heated plasma with the use of a diamagnetic loop. The plasma energy decreases with time after the RF pulse is turned off. The energy lifetime can be estimated from the decay of the diamagnetic signal. As a preliminary result,

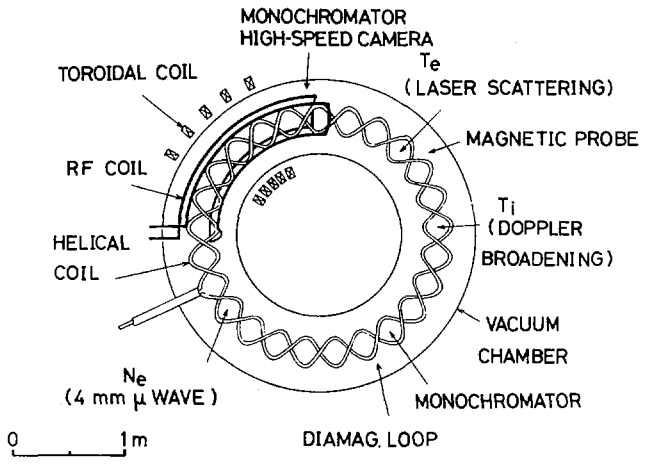


FIG.1. Schematic diagram of experimental set-up.

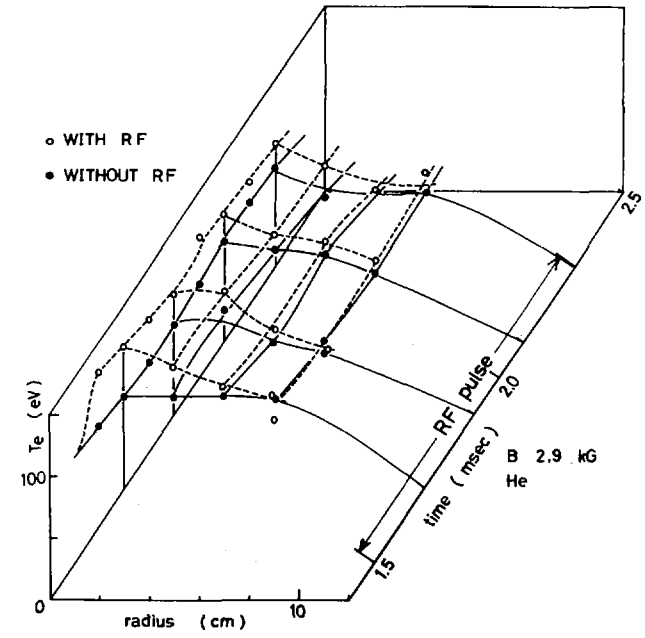


FIG.2. Space-time dependence of electron temperature.

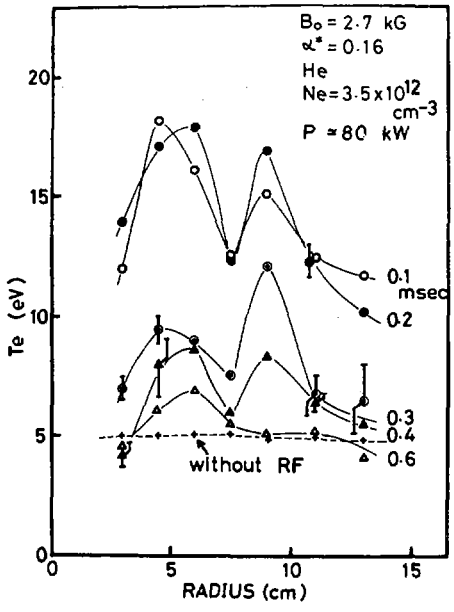


FIG.3. Radial distribution of electron temperature (RF pulse 0–0.24 ms).

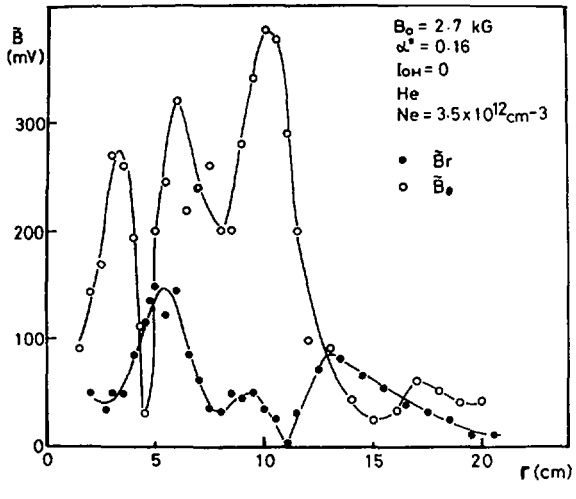


FIG.4. Radial profile of wave magnetic field (1 G·100 mV^{-1}).

we found that the energy lifetime is about twice as long in the currentless plasma as that of Ohmically heated plasma. This may indicate that confinement is better for the currentless plasma in the heliotron field.

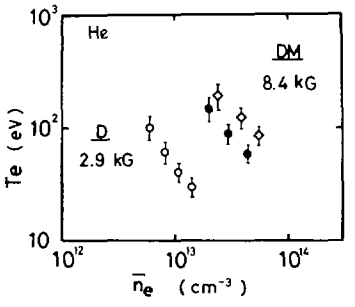


FIG.5. Mean electron density $\bar{n}_e$ versus peak electron temperature T_{e0}. ○: $\bar{J}_{OH} = 24\ A \cdot cm^{-2}$; ●: $\bar{J}_{OH} = 80\ A \cdot cm^{-2}$; ◇: $\bar{J}_{OH} = 112\ A \cdot cm^{-2}$.

2. CONFINEMENT OF HIGH CURRENT DENSITY PLASMA IN HELIOTRON DM

One research objective of Heliotron DM [3] (R = 45 cm; $\bar{r}_p \cong 4$ cm; B = 10 kG) is to extend the plasma parameters of Heliotron D (R = 108.5 cm; $\bar{r}_p \cong 10$ cm; B = 3 kG) into the higher energy density regime by increasing the Ohmic current density up to 150 $A \cdot cm^{-2}$ (~30 $A \cdot cm^{-2}$ in Heliotron D). Figure 5 shows peak electron temperature T_{e0} as a function of the mean electron density $\bar{n}_e$. Since the plasma current is disrupted in the lower density region ($\bar{n}_e < 1 \times 10^{13}/cm^3$), the density of normal operation is rather high. The density up to $10^{14}/cm^3$ has been obtained without accompanying current disruption. The energy replacement time of the electron is around 100 μs. As described below, the power loss due to the line radiation of the impurities is relatively small compared to the Ohmic power. Internal structure of the plasma column has been investigated by various diagnostic instruments (Langmuir probes, Thomson scattering of a laser light, vacuum ultra violet (VUV) monochromator) placed at different positions around the torus. These measurements show that a magnetic island of m = n = 1 exists around the magnetic surface of $\iota = 1$. The most probable origin of the error field which causes the island is the helical coil feeder. By using a more compact feeder and applying a correcting field, the conductivity of the plasma is increased by 40% at present. Further improvement of the confinement properties is expected by using more suitable correcting coil systems.

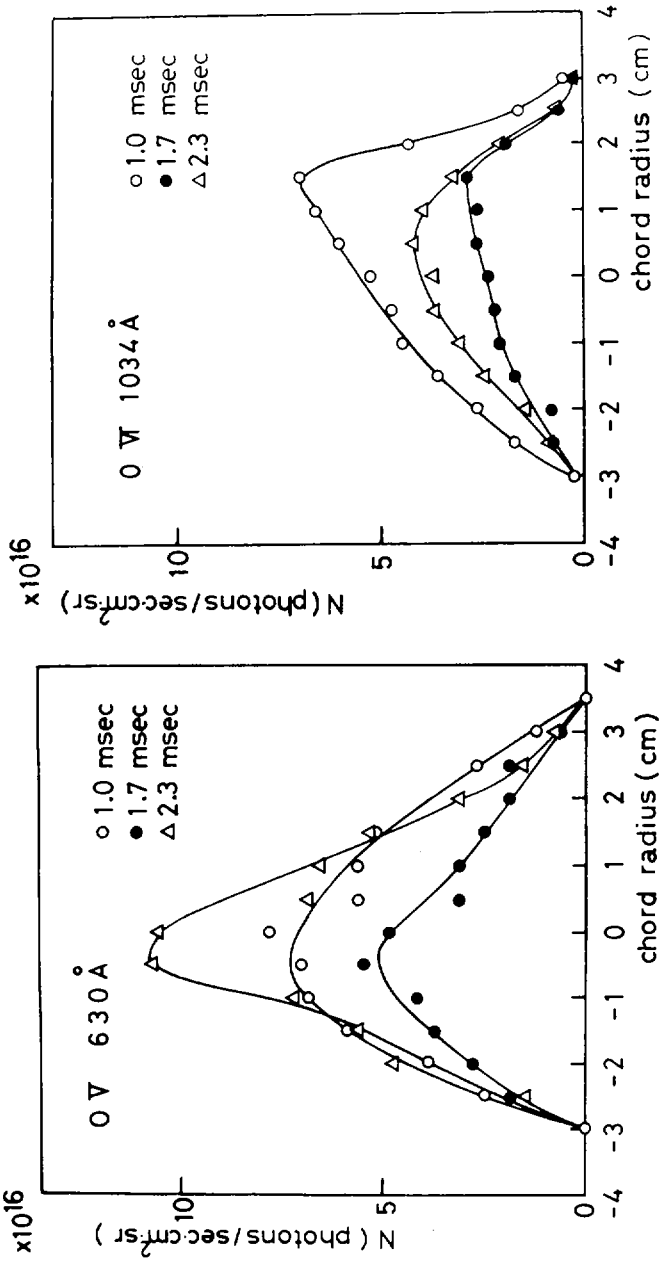


FIG. 6. Emission profiles in OV 630 Å and OVI 1034 Å light. 'Chord radius' refers to height of the line of sight above or below the torus midplane.

Spatial distributions of VUV emissions are measured using a 0.5-m normal incidence monochromator (500–1600 Å), which is calibrated by the atomic branching ratio method. Up-down scans of emission from light impurity ions are performed with a set of movable concave and plane mirrors inserted between the plasma and the monochromator. The field view at the centre of the plasma is typically a 1 cm (vertical) × 4 cm (horizontal) rectangle.

Strong emission lines from light impurity ions are observed: OIII (508 Å), OIV (555 Å), OV (630 Å, 760 Å), OVI (1034 Å); CII (904 Å), CIII (977 Å), CIV (1549 Å). Figure 6 shows vertical scans of the OV (630 Å) and OVI (1034 Å) emissions at the plateau of the discharge. The marked asymmetry of the OVI line is observed. This may be understood qualitatively by the asymmetric electron temperature profile caused by the island structure. When symmetry is observed, we performed Abel transformation and obtained volume emissivity to estimate radiated power. The radiation is mainly from OV (630 Å) and amounts to 600 $mW \cdot cm^{-3}$ at the centre of the plasma column. The mean Ohmic power is about 9 $W \cdot cm^{-3}$. The O^{+4}, O^{+5} ion concentrations are about 2.5×10^{11} cm^3 and 1×10^{11} cm^3, respectively.

3. EQUILIBRIUM AND STABILITY OF STRAIGHT HELICAL HELIOTRON

3.1. Equilibrium

For conventional stellarators, MHD equilibrium is analysed by assuming a small expansion parameter $\rho = 2\pi r/L$, where L is the pitch length of the helical winding and r is the minor radius. This approximation is not applicable for the helical heliotron equilibrium, because ρ is the order of unity in the vicinity of the last magnetic surface [6]. A new analysis has been carried out to study the equilibrium of a straight helical heliotron involving the region $\rho \sim 1$ where the rotational transform $\iota = \iota_F + \iota_{OH}$ exceeds unity. Here ι_F and ι_{OH} denote a rotational transform due to the helical winding and the plasma current, respectively.

The magnetic flux function ψ in helically symmetric equilibrium is given as

$$\frac{1}{h^2 r}\frac{\partial}{\partial r}\left\{h^2 r \frac{\partial \psi}{\partial r}\right\} + \frac{1}{h^2 r}\frac{\partial^2 \psi}{\partial u^2} + (B_z(0) - J)\frac{d}{d\psi}(B_z(0) - J) + \frac{1}{h^2}\frac{dp}{d\psi} = 0 \qquad (1)$$

where $u = \theta - \kappa z$; $\kappa = 2\pi/L$; $h^2 = 1/(1 + \rho^2)$; and $B_z(0)$ is the magnetic field on the axis. Here we assume J and p are the linear functions of ψ. Solutions of Eq.(1) given by Correa and Lortz are used for the plasma region [7], and

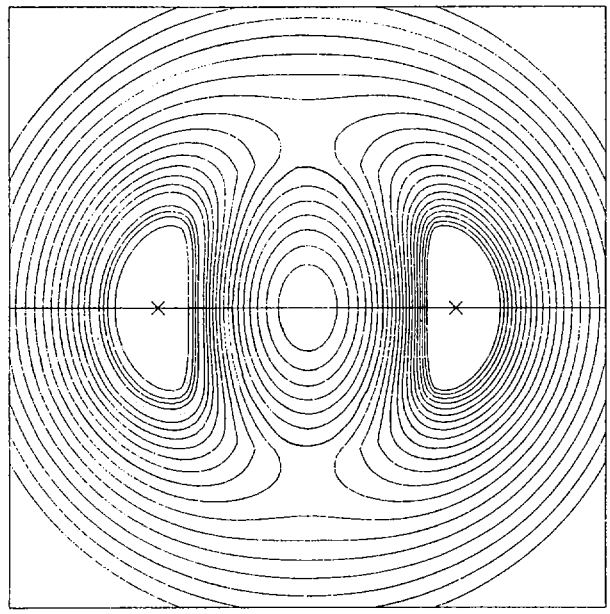


FIG. 7. Equilibrium of Heliotron E for $\iota_{OH} = -0.305$ and $\iota_F(a) \cong 2.3$. β at the magnetic axis is 10%. $\iota_F(a)$ is rotational transform at the outermost magnetic surface.

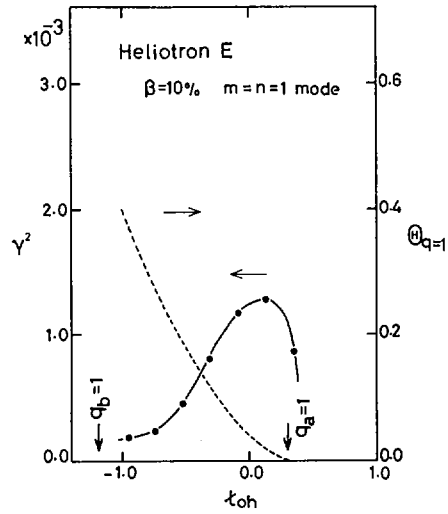


FIG. 8. Growth rates of the m = 1 internal mode as a function of ι_{OH}. The equilibrium with $\iota_{OH} = -0.305$ corresponds to Fig. 7. The growth rate is normalized by the Alfvén transit time across the length $L/2\pi$. The Alfvén velocity is calculated at the magnetic axis. The shear at $\iota = 1$ (or $q = 1$) is also shown.

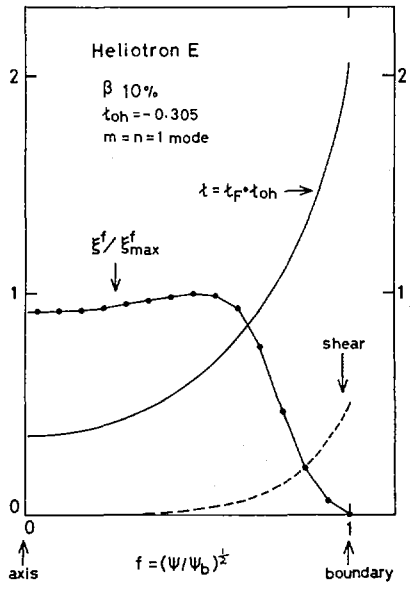


FIG.9. The eigenfunction ξ^f (normal displacement to the magnetic surface) of the m = 1 mode for $\iota_{OH} = -0.305$ and the profiles of rotational transform and shear are shown.

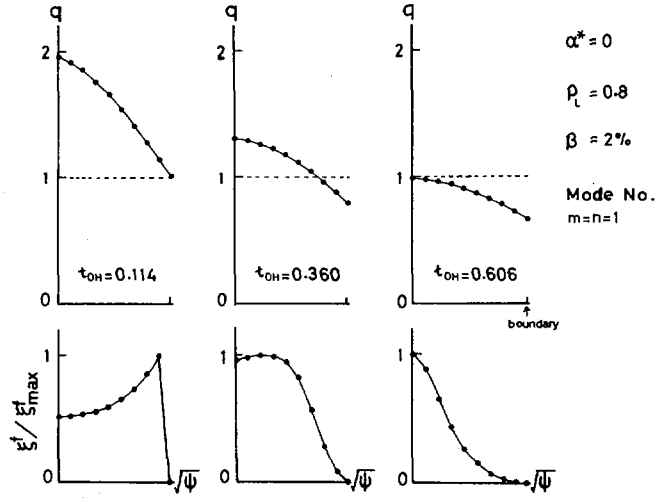


FIG.10. The eigenfunctions ξ^f of the m = 1 mode are shown for $\iota_F(a) \cong 0.8$ and $\beta = 2\%$.

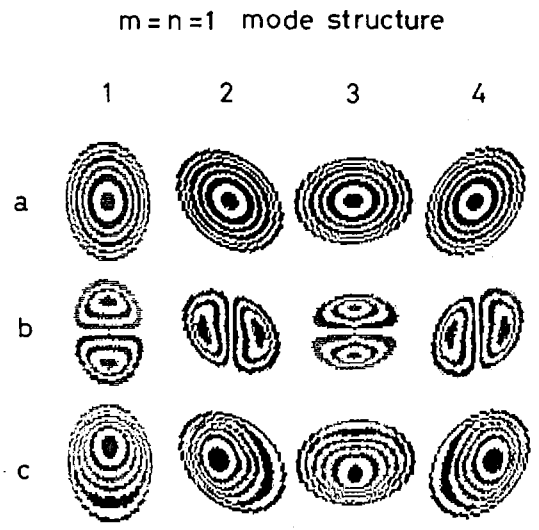


FIG. 11. Columns (1), (2), (3) and (4) show contour plots of the pressure distribution at four cross-sections separated by a quarter of the system length. (a) Equilibrium pressure distributions. (b) Perturbed pressure distributions. (c) The $m = n = 1$ deformation is found by superposing (a) and (b).

solutions in the vacuum region are expressed by Bessel functions. The initial shape of the plasma surface is given by the outermost vacuum magnetic surface. Matching the boundary conditions at the plasma-vacuum interface by changing the plasma shape iteratively, we obtain free-boundary equilibria for the helical heliotron. Figure 7 shows the Heliotron E equilibrium. The rotational transform ι is approximately equal to the sum of ι_F and ι_{OH}. The influence of the plasma pressure (for $\beta \lesssim 10\%$) and the plasma current ($-1 \lesssim \iota_{OH} \lesssim 1$) on the shape of the magnetic surface is small in the straight heliotron system.

3.2. Stability

The stability property of the low-m internal modes in the straight heliotron is examined by solving the linearized ideal MHD equations as an initial boundary value problem. An explicit finite-difference approximation method (essentially the same as Ref. [8]) is applied to a non-orthogonal curvilinear co-ordinate system (f, u, ζ) which is convenient to treat helically symmetric configurations. f, u and ζ are defined as follows:

$$
\begin{aligned}
f &= \sqrt{\psi/\psi_b} \\
x^* &= \kappa r\cos\theta = \rho(f, u)\cos(u + \zeta) \\
y^* &= \kappa r\sin\theta = \rho(f, u)\sin(u + \zeta) \\
z^* &= \kappa z = \zeta
\end{aligned}
\qquad (2)
$$

where ψ_b is the value of ψ at the boundary. Fourier analysis along the cyclic coordinate ζ reduces the problem to two dimensions. The growth rate of the dominant mode and the associated eigenfunction are obtained by the exponential growth of the perturbation under the fixed-boundary condition. The conducting shell is set on the outermost magnetic surface, which is almost elliptical.

The following results have been obtained:

(a) When a resonant surface satisfying $\iota = \iota_F + \iota_{OH} = n/m$ exists in the plasma column, the internal modes with (m = 1; n = 1), (m = 1; n = 2), (m = 2; n = 1) and (m = 2; n = 2) become unstable. The growth rate of the m = 1, n = 1 internal mode and the shear at $\iota = 1$ are shown in Fig.8. It seems that a large shear at the resonant surface reduces the growth rate.

(b) The eigenfunction, the rotational transform and the shear profile are shown in Fig.9. The eigenfunctions for $\iota_F(a) \sim 0.8$ are shown in Fig.10. These figures show that the perturbation of the m = 1 internal mode is almost restricted inside the resonant surface. Contour plots of the perturbed pressure distribution are shown in Fig.11. The mode is similar to that predicted for the m = 1 internal kink mode in tokamaks [9], although the radial dependence of $q = 1/\iota$ is different from that of a tokamak.

(c) The internal modes examined here are unstable even for $\iota_{OH} = 0$ (see Fig.8). It is estimated that the instability is driven by the pressure gradient. The straight heliotron equilibrium with $\beta > 5\%$ does not satisfy Mercier's stability criterion for localized modes except in the peripheral high shear region.

(d) Higher modes with $m \geqslant 3$ cannot be pursued by the restriction of mesh numbers used in the code 16 X 17 to solve the upper half plane.

REFERENCES

[1] IIYOSHI, A., OBIKI, T., SATO, M., SASAKI, A., MUTOH, T., ADACHI, S., UO, K., in Proc. 3rd Int. Meeting on Theoretical and Experimental Aspects of Heating of Toroidal Plasmas, Euratom, Grenoble, 1976, Vol.2, p. 305.

[2] GOLOVATO, S.N., SHOHET, J.L., TATARONIS, J.A., Phys. Rev. Lett. 37 (1976) 1272.

[3] UO, K., IIYOSHI, A., OBIKI, T., et al., Plasma Physics and Controlled Nuclear Fusion Research 1976 (Proc. 6th Int. Conf. Berchtesgaden, 1976), Vol.2, IAEA, Vienna (1977) 103.

[4] OBIKI, T., MUTOH, T., ADACHI, S., SASAKI, A., IIYOSHI, A., UO, K., Phys. Rev. Lett. 39 (1977) 812.
[5] HASEGAWA, A., CHEN, L., Phys. Rev. Lett. 35 (1975) 370.
[6] UO, K., Nucl. Fusion 13 (1973) 661.
[7] CORREA, D., LORTZ, D., Nucl. Fusion 13 (1973) 129.
[8] KURITA, G., AMANO, T., Jpn. Atomic Energy Res. Inst. Tokyo Rep. JAERI-M 6774 (1976).
[9] SHAFRANOV, V.D., Sov. Phys.-Tech. Phys. 15 (1970) 175.

DISCUSSION

J.L. SHOHET: I would like to point out that, given the non-axisymmetric and toroidal nature of your experiment, the relation $\omega = k_{||} V_A$ does not hold, because V_A varies considerably over a wavelength. In fact, if you plot the surfaces V_A = const for your experiment, they will be hyperbolas that extend nearly over the entire cross-section of the plasma, and even local heating would then result in bulk heating. However, until you solve the eigenvalue problem, which consists of a system of partial differential equations rather than algebraic relations as you have assumed, it will be unclear just where in the plasma the resonance exists; and no conclusion can be drawn regarding the nature of the heating mechanism until this resonance location is known.

K. UO: I cannot agree that the relation $\omega = k_{||} V_A$ does not hold in a non-axisymmetric toroidal plasma. As we have shown in Fig.4, the magnetic probe signals from the wave provide experimental support for the existence of this resonance surface.

H. WOBIG: Is the plasma-vacuum boundary fixed during the iteration process for the helical equilibrium or is it determined by the iteration?

K. UO: Each iteration gives new ψ_I and ψ_{II}, and these determine the new plasma boundary. Thus the plasma-vacuum interface is determined by the iteration in each case.

A THREE-DIMENSIONAL MHD CODE

R. CHODURA, A. SCHLÜTER, M. KAUFMANN, W. LOTZ
Max-Planck-Institut für Plasmaphysik,
Association Euratom-IPP,
Garching, Federal Republic of Germany

Abstract

A THREE-DIMENSIONAL MHD CODE.

The equation for the residual force is solved by a three-dimensional code producing approximate solutions iteratively. Applications are given for stellarator-type equilibria with various values of beta; the stability of these equilibria is checked.

INTRODUCTION

A threedimensional MHD code has been developed which produces in an iterative procedure approximate solutions to:

$$(1) \quad \underset{\sim}{F} := \underset{\sim}{j} \times \underset{\sim}{B} - \operatorname{grad} p = 0$$

which are (approximately) stable. It was applied, in particular, to find stellarator-type equilibria of various values of β and to check their stability.

PROCEDURE

A stable magnetohydrostatic equilibrium can be found as the magnetic field $\underset{\sim}{B}(\underset{\sim}{x})$ which together with a pressure distribution $p(\underset{\sim}{x})$ minimizes the energy

$$(2) \quad W = \int \left(\frac{B^2}{2} + \frac{p}{\gamma - 1} \right) dV, \qquad p = \rho^{\gamma}$$

under the constraints (which correspond to infinite conductivity and mass conservation)

$$(3) \quad \delta\rho = - \nabla \cdot (\rho \underset{\sim}{\xi}), \qquad \delta \underset{\sim}{B} = \nabla \times (\underset{\sim}{\xi} \times \underset{\sim}{B})$$

and the boundary condition $\underset{\sim}{\xi} = 0$ at the fixed boundary.

A computer code which uses this principle was described in Ref.[1] and [2]. W is there discretized in a co-moving coordinate system defined by the magnetic field. The code used here, of which earlier versions were described in Ref.[3] and [4], employs an Eulerian space-fixed system of either Cartesian or cylindrical coordinates. Though this renders the fulfillment

of the constraints (3) more tedious, it simplifies the numerical expressions all together considerably and makes it thereby possible to approach an equilibrium extremely closely (compare e.g. the reduction of the mean square of the residual force $\underset{\sim}{F}$ in fig.2). A further advantage of an Eulerian system lies in the greater adaptability of the boundary conditions. The boundary need not coincide with a magnetic surface; thus, e.g. external uniform fields can easily be applied with varying strength.

The procedure starts from an initial magnetic field described by its vector potential and an initial pressure distribution. Two different algorithms are implemented and used consecutively to generate the iteration:

a) Modified steepest descent (or modified conjugate gradient);
b) Numerical solution of the corresponding parabolic differential equation, by a modified Chebychev scheme.

Both algorithms start at each "time" by evaluating the residual force $\underset{\sim}{F}$ at all grid points. In a) the displacement is set proportional to $\underset{\sim}{F}$:

$$(4) \quad \underset{\sim}{\xi} = \alpha \underset{\sim}{F}; \qquad \alpha > 0$$

A value $\bar{\alpha}$ is calculated which, given $\underset{\sim}{F}$, would decrease W by the largest amount. It has been found that a choice of $\alpha = (0.8 \ldots 0.9)\,\bar{\alpha}$ gives in the long run the best convergence. This can be further improved if the maximization of the decrease of W is performed in the "plane" spanned by the instantaneous $\underset{\sim}{F}$ and the $\underset{\sim}{\xi}$ of the previous iteration step ("method of conjugate gradients"). Here again it is decisive that the "ideal" procedure is modified by decreasing the displacement ξ slightly, so that at each iteration the maximal decrease of W is not quite attained.

In algorithm b) the parabolic d.e. is solved by an explicit integration scheme in which the "time" step varies in cycles of length N (N = 30 ... 300) according to

$$\Delta t_\nu = \Delta t_0/(1 + \varepsilon + \cos(2\nu-1)\pi/2N); \quad \nu = 1, \ldots, N, \ \varepsilon > 0$$

where Δt_0 will (indepent of N) be chosen as large as is compatible with numerical stability. The average time step $\sum \Delta t_\nu / N$ will (for $\varepsilon \to 0$) increase like N and a speed of convergence similar to that of algorithm a) can be achieved. For the numerical success it is essential that a small but finite ε be chosen and that the Δt_ν should not be used in their natural monotonic order.

The spatial dependence is discretized by using a finite cell approximation to the energy integral of eq.(2), and corresponding finite forms of mass and flux conservation in place of eq.(3). From the variation of the energy W with respect to arbitrary displacements $\underset{\sim}{\xi}$, a discretized expression for $\underset{\sim}{F}$ can be derived which together with eq.(4) guarantees the monotonic decrease of W. As long as $\langle F^2 \rangle$ also decreases, the successive iteration steps describe the approach to an equilibrium. This

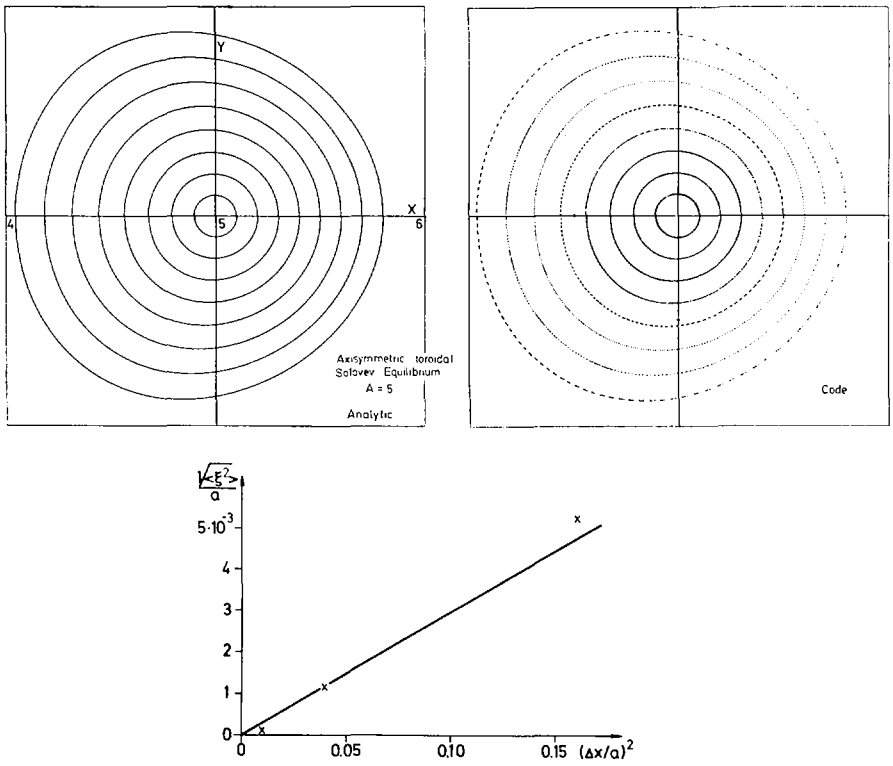


FIG.1a. Comparison of an axisymmetric toroidal equilibrium as determined analytically and by the code. R.m.s. deviation of the numerical result from true value for different mesh sizes Δx is shown.

approach may be quite close, even for an unstable equilibrium if the unstable modes are not, or very little, excited. The development of an instability shows up by an increase of $<F^2>$ in time. In any case, using method b), from the asymptotic time dependence of $<F^2>$ in the vicinity of an equilibrium, the eigenvalue of the least damped or fastest growing dominant mode can be derived.

TESTS

In Fig.1a we have used an analytical axisymmetric toroidal equilibrium, namely the "Solovev" equilibrium [5] as the initial condition for the code. The code then determines a final state which already with a coarse grid of 10 × 10 × 10 differs from the exact solution only very little. The r.m.s. displacement $\sqrt{<\xi^2>}$ at all grid points decreases with the square of the mesh size Δx.

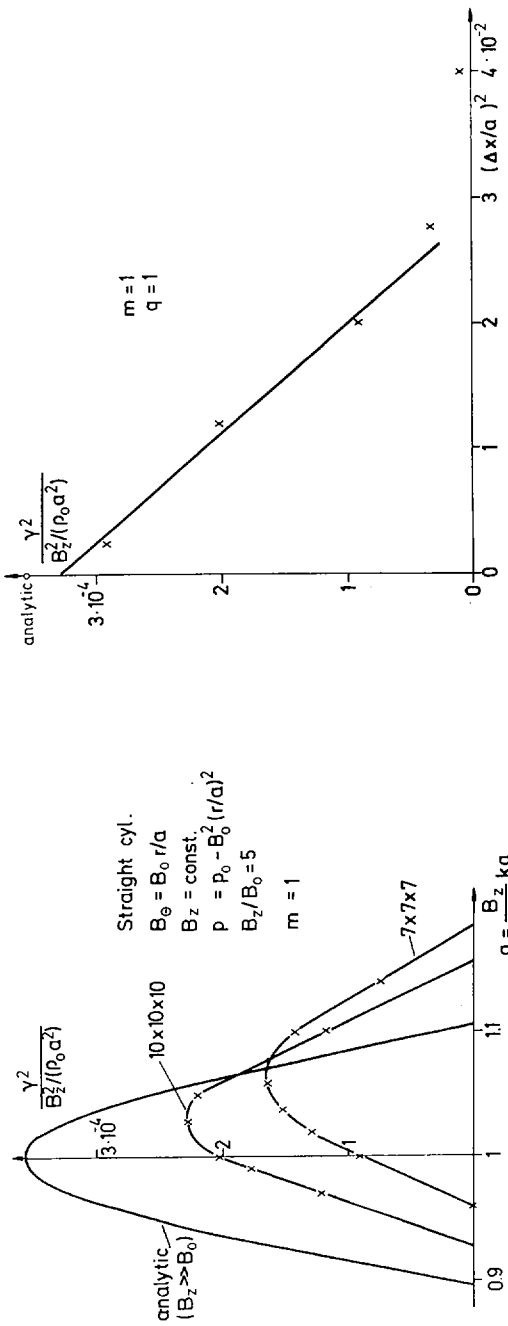


FIG. 1b. Normalized growth rates of a straight cylindrical plasma with uniform current density for m = 1 eigenmodes with different k calculated analytically and by the code for different numbers of grid points. Convergence of the value for m = 1, q = 1 with decreasing mesh size Δx is achieved.

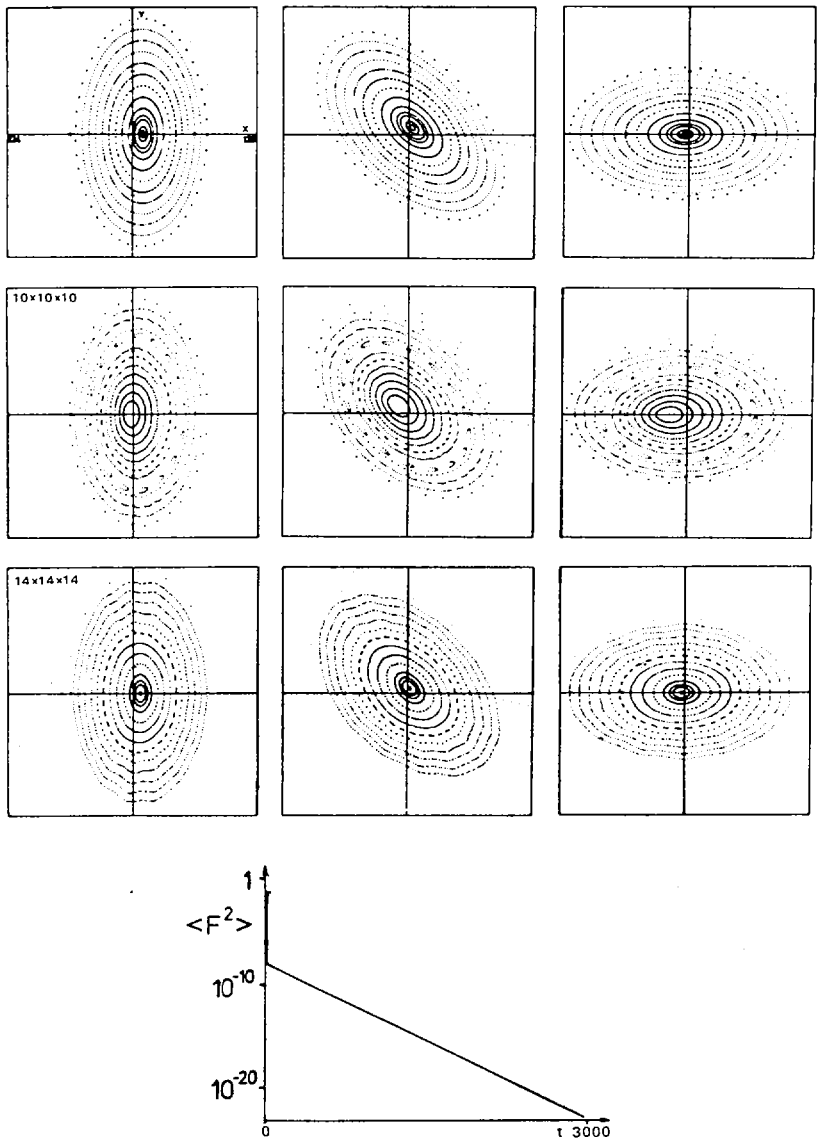


FIG.2. Helical toroidal ℓ = 1, ℓ = 2 equilibrium with vertical field, β = 1/8, aspect ratio A = 125, N = 100 periods and t = 6.9 . . . 6.4 in a 10 X 10 X 10 and 14 X 14 X 14 grid. First line: initial state, second line: final state in a 10^3 -grid, third line: final state in a 14^3 -grid, fourth line: decrease of the mean square residual force $\langle F^2 \rangle$ with time t.

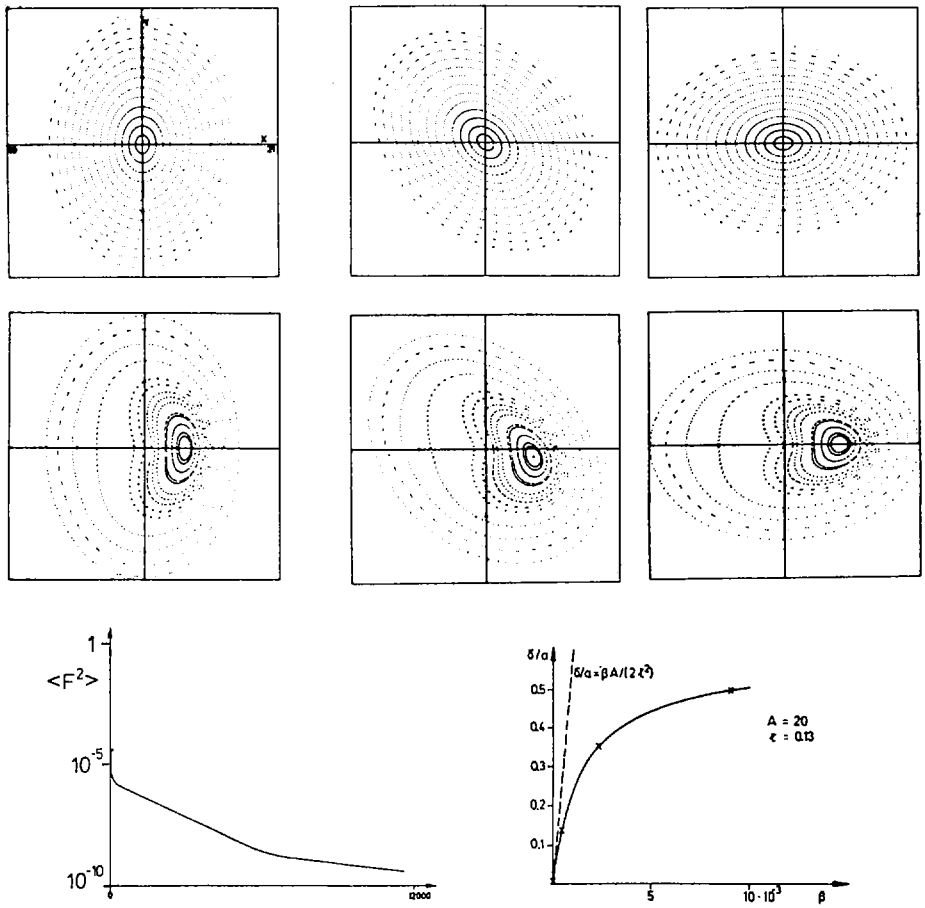


FIG.3. Pure ℓ = 2 helical toroidal equilibrium with β = 0.002, A = 20, N = 5, ε = 0.13 in a 10 × 10 × 10 grid. First line: initial state, second line: final state, third line: residual force; shift of the magnetic axis δ with β.

In Fig.1b a straight cylindrical equilibrium with constant current profile was disturbed by m = 1 disturbances with different wave numbers k in axial direction. The MHD growth rate γ^2 has been determined for different grid sizes from the "time" behaviour of the solution after the most unstable mode became dominant. Again, the deviation from the true eigenvalue [6] decreases with the square of the mesh size.

RESULTS

Fig.2 shows a stellarator-type equilibrium with maximum $\beta = 1/8$ and aspect ratio A = 125. We start from the vacuum field shown in the first line by flux contours in different poloidal planes. It is a combination of $\ell = 1$ and $\ell = 2$ helical fields, both having 100 periods along the circumference centered by a uniform "vertical" field. The initial pressure distribution is axisymmetric. The final equilibrium is given in the second line for a 10 × 10 × 10 and in the third line for a 14 × 14 × 14 grid. The flux surfaces are found by integrating numerically the lines of force and plotting the intersection points with the respective poloidal planes. As can be seen, the existence of a system of nested surfaces is preserved during the computation. The magnetic axis in the 10^3-grid is shifted slightly inward as compared to the finer 14^3-grid. The reduction of the forces in the grid points in the course of iterations is shown by the $\langle F^2 \rangle$-curve for the 10^3-grid.

A pure $\ell = 2$ helical toroidal $\beta = 2 \cdot 10^{-3}$ equilibrium with much smaller aspect ratio (A = 20) and only 5 periods along the circumference is shown in Fig.3. Since no "vertical" field was applied the magnetic axis is shifted outward. This shift increases with increasing β as shown in the last curve. It is compared to an analytic calculation [7] which is applicable for small δ only and does not take into account flux compression in the presence of a conducting wall.

In Fig.4 we investigate the stability properties of two straight helical $\ell = 2$ and $\ell = 3$ equilibria, respectively. The first and third lines show flux contours of the equilibria in poloidal planes half a period apart. The consecutive lines show the displacement vectors of unstable eigenmodes in these planes. The time history of our procedure is given below: We first approximate an equilibrium fairly accurately. Instead of waiting for a disturbance growing up from stochastic noise level, we excite a disturbance with a prescribed symmetry m = 1, n = 0. This disturbance, after being partly damped, evolves in a pure unstable eigenmode which stays constant in space for several growth times and is shown here. These modes are aligned to the helicity of the equilibrium. Their growth rates in Alfvén transit times at the axis is by a factor of 2 smaller than that calculated from a sharp boundary model.

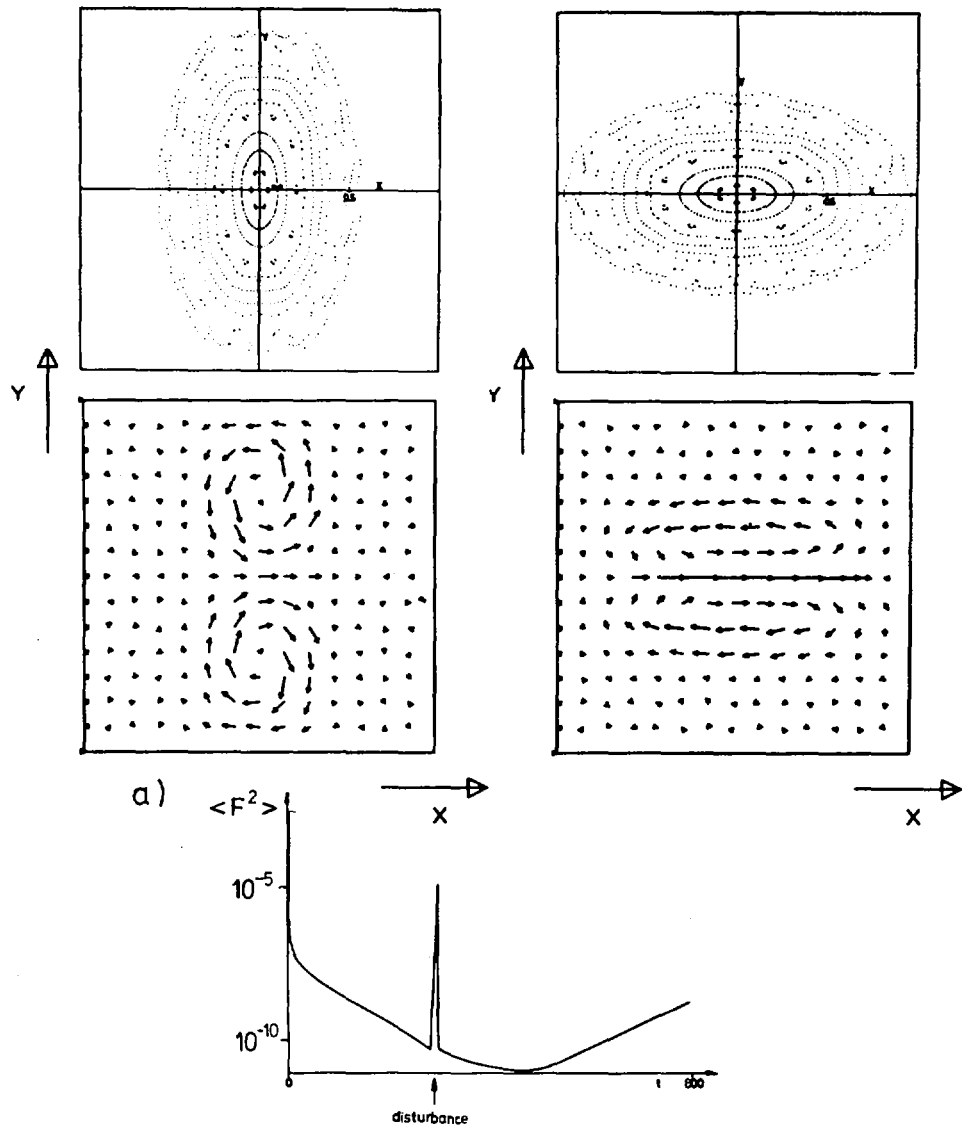
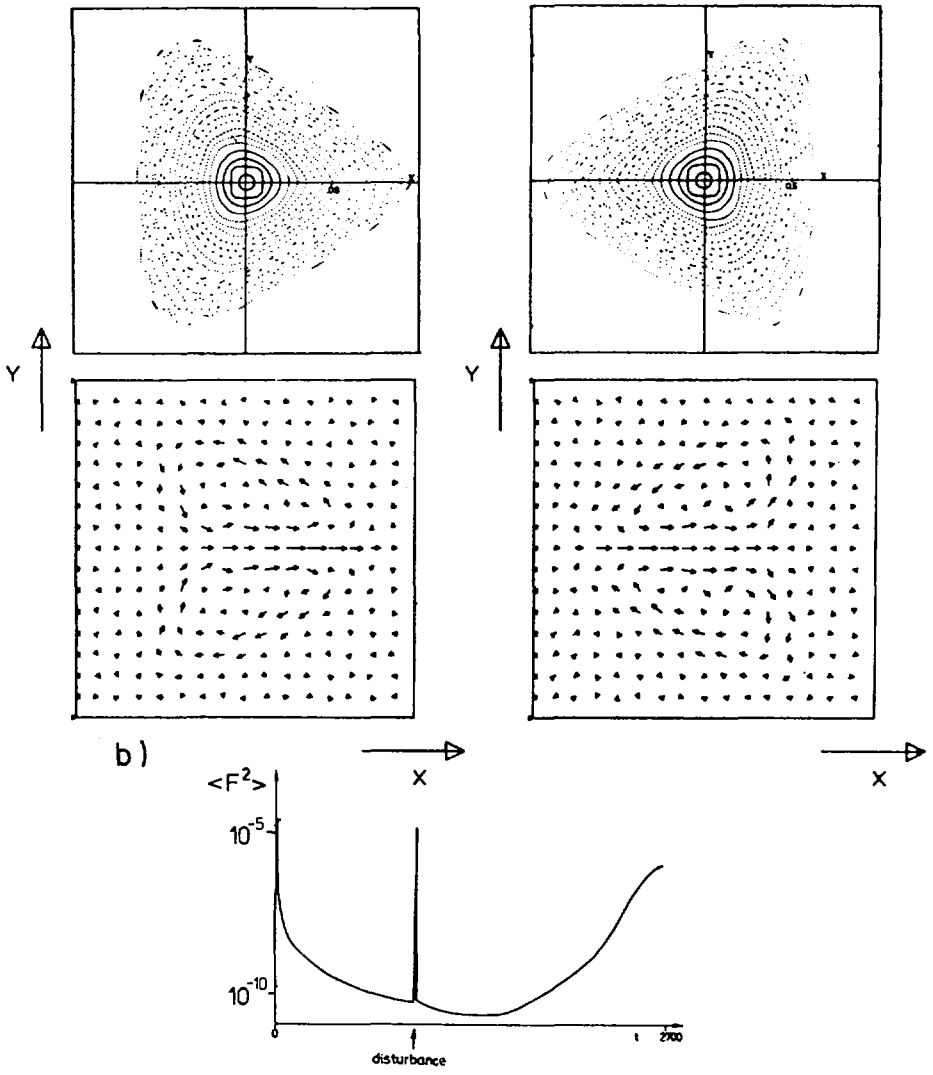


FIG.4. m = 1, n = 0 eigenmodes (line 2) of straight helical a) ℓ = 2 and b) ℓ = 3 equilibria (line 1) with β = 1/2 in two poloidal planes one half-period apart. The eigenmodes are launched by exciting an m = 1, n =0 Fourier disturbance (line 3).


Y
Y
X
X
b)
<F²>
10⁻⁵
10⁻¹⁰
0
t
2900
disturbance

REFERENCES

[1] BETANCOURT, O., GARABEDIAN, P., Proc.Nat.Acad.Sci.USA 73 (1976) 984.

[2] HERRNEGGER, F., BETANCOURT, O., GARABEDIAN, P., Proc.7th Int.Conf.on Plasma Phys.and Contr.Nucl.Fusion Res., Paper No.L-3-2 (1978)

[3] SCHLÜTER, A., CHODURA, R., Proc.3rd Top.Conf.on Pulsed High Beta Plasmas Culham (1975) (EVANS, E.D., ed.) Perg. Press, p.187

[4] CHODURA, R., SCHLÜTER, A., Proc.2nd Europ.Conf.on Computat. Physics, Garching (1976), (BISKAMP, D., ed.) Rep.IPP 6/147

[5] SOLOVEV, L.S., ZhETF 53 (1967) 626; Sov.Phys.JETP 26 (1968) 400

[6] GOEDBLOED, J.P., HAGEBEUK, H.J.L., Phys.Fluids 15 (1972) 1090

[7] SHAFRANOV, V.D., YURCHENKO, E.I., Nucl.Fusion 8 (1968) 329

DISCUSSION

F. HERRNEGGER: Have you investigated the development of magnetic islands in detail? It strikes me that this might be an important application of your Eulerian code.

A. SCHLÜTER: A fair representation of magnetic islands in the code would require a very fine mesh and hence rather long computing time. For this reason we have postponed the treatment of such configurations.

F. HERRNEGGER: What are the essential advantages of the Lagrangian code you are developing as compared with the Eulerian code?

A. SCHLÜTER: Dr. Schwenn and I have been developing a code where the grid points follow the motion of the plasma. Unlike the code developed by Garabedian and Betancourt, which you have used, ours holds also for the motion on the magnetic surfaces. One advantage of these Lagrangian codes is the absence of any discretization error of local flux conservation.

NEW RESULTS IN HIGH-BETA MHD THEORY*

D.C. BARNES, J.U. BRACKBILL, T.E. CAYTON,
R.Y. DAGAZIAN, J.P. FREIDBERG, W. SCHNEIDER
Los Alamos Scientific Laboratory,
Los Alamos, New Mexico

L.S. HALL
Lawrence Livermore Laboratory,
Livermore, California

H. GRAD, W. GROSSMANN, D.C. STEVENS,
E. TURKEL, S. WOLLMAN
Courant Institute of Mathematical Sciences,
New York University,
New York, N.Y.,
United States of America

Abstract

NEW RESULTS IN HIGH-BETA MHD THEORY.

New results are described in the following three areas of high MHD theory: (1) equilibrium and stability of diffuse high-β stellarators; (2) MHD equilibrium and stability of minimum-B mirror traps; and (3) simulation of simple and reversed-field mirror machines.

I. High-Beta Stellarator Studies (LASL)

Both analytic and numerical studies have been performed which demonstrate the existence of high-β stellarator equilibria and make a practical connection with experiments.

A. Analytic Studies

An analytic formulation has been derived for calculating equilibria in a diffuse high-β stellarator configuration. Although analytic sharp boundary equilibria have been known for some time [1-4], the extension to diffuse profiles is non-trivial. The reason for this is associated with the misleading intuition from sharp boundary theory which suggests that diffuse high-β stellarator equilibria could be obtained by expansion about a straight cylindrically symmetric θ-pinch field, $B(r)\underset{\sim}{e}_z$. Expansions of this type turn out to be incompatible with toroidal periodicity constraints and no such equilibria exist.

* Work performed under the auspices of the US Department of Energy.

The expansion described here overcomes this difficulty by considering the basic θ-pinch field to be of the form $B(r,\theta)\underset{\sim}{e}_z$; that is, one must consider the leading order system to consist of noncircular flux surfaces with finite toroidal shifts. Under this assumption diffuse high-β stellarator equilibria can be found.

The leading order field is the θ-pinch field just described. The first order fields are a combination of helical fields, each one characterized by $\ell\theta + hz$. In principle there can be an arbitrary number of induced and applied helical fields with different ℓ values, but all with the same pitch number h. In practice, for well confined equilibria, two and only two helical fields (ℓ and $\ell+1$) can be applied. Also, no purely transverse fields are allowed in first order. The helical fields are determined from a potential function ϕ, which satisfies a second order partial differential equation with $B(r,\theta)$ appearing in the coefficients. Toroidal effects are first assumed to enter in second order. To calculate the second order fields, a periodicity condition (resulting from z-independent terms) must be satisfied. This condition imposes a second constraint between ϕ and B. Thus, the problem of finding high-β stellarator equilibria can be cast in the form of two nonlinear, coupled partial differential equations for the unknowns ϕ and B.

These equations are given by

$$\nabla_\perp\cdot\left(\frac{\nabla_\perp\phi}{1-\beta}\right) - \frac{h^2\phi}{1-\beta} = 0 \tag{1}$$

$$|\nabla_\perp\phi|^2 + h^2|\phi|^2 = G(\beta) - \frac{B_a^4}{R}(1-\beta)^2\, r\cos\theta \tag{2}$$

where B_a is the applied θ-pinch field; $\beta = 1 - B^2(r,\theta)/B_a^2$; R is the major radius of the torus; $G(\beta)$ is an arbitrary free function; and the helical field is determined by $\underset{\sim}{B}_\perp = \nabla_\perp\phi/B(r,\theta)$. At $r = 0$, ϕ and β must be regular. At the outer boundary, $r = b[1+\sum_\ell \Delta_\ell \cos(\ell\theta+hz)]$, there is a shaped conducting shell on which $\underset{\sim}{n}\cdot\underset{\sim}{B} = 0$.

Equations (1) and (2) have been solved analytically in the small hr limit for two cases: (1) small but finite β and $\Delta_o \sim \Delta_1 \sim \Delta_2$ and (2) finite β and Δ_o, $\Delta_2 \ll \Delta_1$. The result is a diffuse analog of the well known sharp boundary equilibrium relationship corresponding to zero toroidal shift. The consequences of these analytic calculations are discussed in conjunction with the numerical studies in Sec. IB.

Finally, a comparison has been made with the low-β stellarator. In both cases, helical fields are required to provide closed flux surfaces. However, in a high-β stellarator the toroidal drift force is balanced by the interaction of two helical fields; ℓ, $\ell+1$. In a low-β stellarator a single helical field suffices. Here, the toroidal drift force is balanced not by the helical fields but by the interaction of a small vertical field with the small induced toroidal dipole current.

B. Numerical Studies

Numerical solutions of the diffuse, high-β stellarator equilibrium problem are also presented, which are obtained by solving finite difference

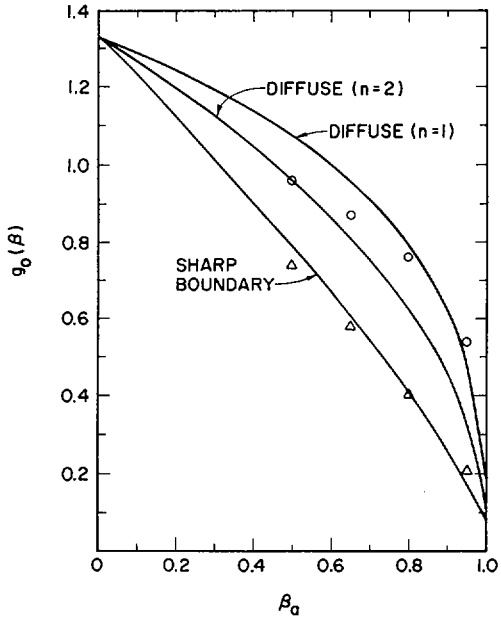


FIG.1. The results of numerical equilibrium calculations compared with analytic theory. The triangles and circles denote numerical equilibria with sharp boundary and Gaussian-like plasma profiles respectively.

approximations to the nonlinear, time-dependent equations describing ideal, magnetohydrodynamic flow in three dimensions as described in [5,6]. Such solutions have provided answers to practical design questions associated with existing experiments which arise because, in contrast with tokamaks or even low-β stellarators, equilibria exist only for numerically correct helical field amplitudes.

Equilibria have been computed for diffuse profile plasmas with parameters corresponding to existing experiments. Similarly to the sharp boundary theory, the numerical calculations and the asymptotic theory described in Sec. IA give a diffuse equilibrium relation for $\ell=1,0$ which scales as $hRB_{\ell=0}B_{\ell=1}/B_a^2 = g_o(\beta)$, and for $\ell=1,2$ as $RB_{\ell=1}B_{\ell=2}/aB_a^2 = g_1(\beta)$, where $\Delta_o = B_o/2B_a$, and $\Delta_{\ell\neq 0} = (B_{\ell\neq 0}/B_a)\,(b/a)^{\ell-1}$, and the B_ℓ are evaluated at the plasma radius, a. For $B_\ell/B_a << 1$, the numerical results with $\ell=1,0$ are compared in Fig. 1 with analytic theory. The numerical results were computed for a Gaussian-like profile and the analytic theory for the profiles $\beta = \beta_a/[1+(r/a)^4]^n$, n = 1,2. Both the analytic and numerical results show significant differences from the sharp boundary theory, indicating that the equilibrium is sensitive to the profile.

The numerical calculations of diffuse equilibria for ha and B_ℓ/B_a finite, as in the Scyllac and Isar experiments, give similar scaling, and have been compared with experimental results [7,8]. For example, when adjustments to the equilibrium fields of the Scyllac feedback sector were made to compensate for the diffuse profile effects predicted by theory, an increase in confinement time from 25 μs to 45 μs was observed [7].

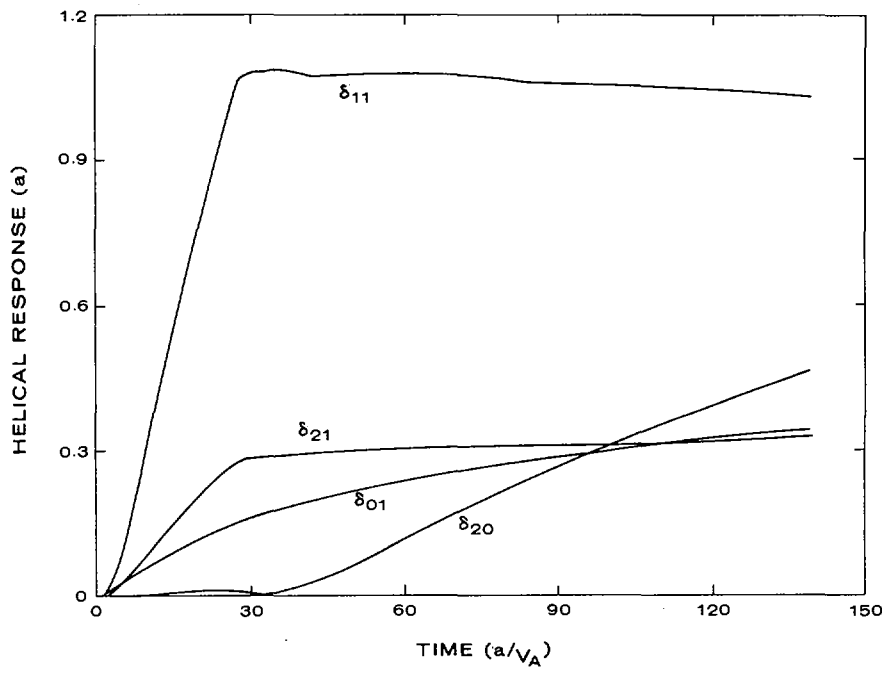


FIG.2. The amplitude of the plasma responses $\delta_{\ell n}$, where n is the wave number in units h, to the simultaneous application of $\ell = 0$, $\ell = 1$, and $\ell = 2$ fields with $n = 1$. Note that δ_{20}, the elliptical deformation of the column in response to F_{02}, is larger than δ_{21}, the response to the applied $\ell = 2$ field, and still growing. Continued growth will bring the plasma into contact with the wall.

An Isar-like configuration[9] with $\ell = 0, 1, 2$ fields has also been studied, because of the potential for reducing the dependence of the equilibrium fields on β by using three helical fields. As a result of appropriately combining them, the different dependence on β of the stellarator force, $\underset{\sim}{F}_{10}$, (produced by the interaction of $\ell = 0$ and $\ell = 1$ fields) and that of $\underset{\sim}{F}_{12}$, (produced by the $\ell = 1$ and $\ell = 2$ fields) cancels the net β dependence without cancelling the total $\underset{\sim}{F}_{10} + \underset{\sim}{F}_{12}$ force. However, the interaction of $\ell = 0$ and $\ell = 2$ fields also produces a force, $\underset{\sim}{F}_{02}$, with $\ell = 2$ symmetry and no axial dependence. Numerical calculations for a straight system with parameters such that $\underset{\sim}{F}_{10} + \underset{\sim}{F}_{12} = 0$ indicate that F_{02} results in large, unbounded, and therefore unacceptable deformations of the plasma as shown in Fig. 2. This deformation can be suppressed by applying a relatively large [$\sim (\Delta_0\Delta_2)^{1/2}$] vertical field.

Finally, wall-stabilized equilibria have been calculated with plasma-to-wall ratio, $b/a = 3$. All diagnostics indicate an approach to stationary equilibrium in contrast to the unstable motion typically observed in cases with $b/a > 4$.

In summary, we now have obtained analytic and numerical high-β stellarator equilibria whose properties and scaling can be related to experiments and earlier theory.

II. MHD Equilibrium and Stability of Minimum-B Mirror Traps (LLL)

In a general high-beta guiding-center MHD equilibrium of an anisotropic minimum-B mirror-trapped plasma, stability is determined by the sign of the Kruskal-Oberman[10] energy variation. For near-marginally-stable flux-localized perturbations, and within a positive factor, the energy variation is[11]

$$\Delta W = \int d\ell \, \{(h/2\pi B^2)(\nabla\psi+\mu\nabla\alpha)^2(\underset{\sim}{b}\cdot\nabla\phi)^2$$

$$+ \left[(\mu T/B)\underset{\sim}{\kappa}\cdot\underset{\sim}{b} \times (\nabla\psi+\mu\nabla\alpha) + \Theta\right]\phi^2\} \qquad (3)$$

where $\phi(\ell)$ is the amplitude of the perturbation whose principal displacements are along $\underset{\sim}{b} \times (\nabla\psi+\mu\nabla\alpha)$, μ is an arbitrary constant, and (ψ,α) are flux coordinates. The trap is supposed omnigenous [12], allowing the pressures to be taken to depend only upon B and the principal flux coordinate ψ. For a well-designed and well-injected mirror trap, the quantities $h(\psi,B)$, $\partial h/\partial\psi$, and $T(\psi,B)$ are all positive, where $h = B+4\pi B^{-1}(p_\perp-p_\parallel)$, $T = (-4\pi/B)\left[(\partial p_\parallel/\partial\psi) + (h/B)(\partial h/\partial B)^{-1}(\partial p_\perp/\partial\psi)\right]$. Likewise, $F > 0$, where $F = B^{-2}\left[h^2(\partial h/\partial B)^{-1} + 12\pi p_\parallel - (B^2 + 8\pi p_\perp)^{-1}(B^2-4\pi p_\parallel)^2\right]$, and $0 \leq \Theta \leq (F/2\pi B)\left[\underset{\sim}{\kappa}\cdot\underset{\sim}{b}\times(\nabla\psi + \mu\nabla\alpha)\right]^2$, where $\underset{\sim}{b} = B^{-1}\underset{\sim}{B}$ and $\underset{\sim}{\kappa} = \underset{\sim}{b}\cdot\nabla\underset{\sim}{b}$. Hence necessary and sufficient conditions for the stability of flux-localized perturbations are given by the nonexistence of solutions of the Euler-Lagrange equations along a line of force which are obtained by use of the limiting forms of Θ in ΔW. Nevertheless, Eq. (3) may still be difficult to apply.

Under circumstances of considerable interest to the mirror program, it is frequently assumed that the principal radial density gradients can be relegated to a small boundary layer, $(1-\varepsilon)\Psi < \psi < (1+\varepsilon)\Psi$, near the surface of the plasma. When ε is very small, the angular flux coordinate α can exhibit rapid variation from flux surface to flux surface, $\nabla\alpha\cdot\nabla\psi = O(\varepsilon^{-1})$, causing considerable difficulty with the numerical analysis. Thus new analytic procedures have been derived for the solution of equilibrium in terms better suited to the examination of stability when ε is small. Stringent stability boundaries are found.

In small-curvature straight-axis mirror traps, conversion of the usual cylindrical coordinates (r,θ,z) into a mixed coordinate set (ψ,θ,z) permits the introduction of a single function $P(\psi,\theta,z)$, the coordinate potential, which fully defines the finite beta geometry. Thus, if partial derivatives in (ψ,θ,z) coordinates are denoted by subscripts, then

$$B^2 + 8\pi p_\perp = B_v^2 \, , \; \frac{1}{2} r^2 = P_\theta \, , \; \alpha = 2\pi B P_\psi \qquad (4)$$

where $B_v(z)$ is the known induction of the vacuum configuration on axis. If $\zeta = (h/B)\underset{\sim}{b}\cdot\nabla\underset{\sim}{b} = (4\pi h/cB^2)\underset{\sim}{j}\cdot\underset{\sim}{b}$, then the equilibrium equation[12] $B\zeta' = -T\underset{\sim}{\kappa}\cdot\underset{\sim}{b}\times\nabla\psi$ may be rewritten

$$(h/\alpha_\theta)\left[R_\theta(R'/2R)_\psi - R_\psi(R'/2R)_\theta - (2R\alpha_z/\alpha_\theta)_\psi\right]$$

$$= -\int_{-\infty}^{z} d\ell(T/\alpha_\theta)\left\{R_\theta(R'/2R)_z - R_z(R'/2R)_\theta - (2R\alpha_z/\alpha_\theta)_z\right.$$

$$\left. + \left[R(\alpha_z/\alpha_\theta)^2 + (R')^2/4R\right]\right\} \tag{5}$$

where $R' = \underset{\sim}{b}\cdot\nabla R = R_z - (\alpha_z/\alpha_\theta)R_\theta$, and we have used the boundary condition that $\zeta \to 0$ as $z \to -\infty$. The scalar function $c(z)$ measures the quadrupole induction in the interior of the plasma (where the pressures are independent of ψ), $\underset{\sim}{B} = B\underset{\sim}{e}_z - (r/2)(dB/dz)\underset{\sim}{e}_\theta + (r/2)B(dc/dz)(\underset{\sim}{e}_r\cos 2\theta - \underset{\sim}{e}_\theta \sin 2\theta)$. Likewise, $\tilde{P} = (\psi/2\pi B)\arctan(e^c \tan\theta)$ in the interior. When $\beta = 8\pi p_\perp/B_v^2$ is small, or at arbitrary β but near the inner boundary layer surface, Eq. (5) admits an analytic solution,

$$a_\psi = \left(\frac{1}{4}\right)\sin 2\alpha \int_0^z dz_1 \left\{(\cosh c - \sinh c \cos 2\alpha)^{-1}\right.$$

$$\left.\int_{z_1}^{\infty} dz_2 (T/B)(X \sinh c - 2Y \cosh c)\right\} \tag{6}$$

where $X = (dc/dz)^2 + B^{-2}(dB/dz)^2 - 2(d/dz)(B^{-1}dB/dz)$ and $Y = B^{-1}(dB/dz)(dc/dz) - d^2c/dz^2$, with X and Y both evaluated on axis.

For large-aspect-ratio (small curvature) configurations, the most unstable perturbations satisfy $\underset{\sim}{\xi} = \underset{\sim}{b} \times \nabla\phi$ [13], and the energy variation becomes[11]

$$\Delta W = (8\pi)^{-1} \int d\psi d\alpha d\ell \left\{(h/2\pi B^2)\left[(BD\phi/D\psi + \alpha_\psi BD\phi/D\alpha)'\nabla\psi + \alpha_\theta(BD\phi/D\alpha)'\nabla\theta\right]^2\right.$$

$$\left. + M(BD\phi/D\alpha)^2 - 2\tilde{\zeta}(BD\phi/D\alpha)(BD\phi/D\psi + \alpha_\psi BD\phi/D\alpha)'\right\} \tag{7}$$

where $\nabla\phi = (D\phi/D\psi)\nabla\psi + (D\phi/D\alpha)\nabla\alpha + \phi'\underset{\sim}{b}$. The function $\tilde{\zeta}$ vanishes at low β or near the inner boundary layer surface, and in this same regime

$$M = (T\alpha_\theta/B)\left[(\alpha_z/\alpha_\theta)^2 + (R'/2R)_z + (R'/2R)^2 + (BR'/2\alpha_\theta)(\alpha_\theta/BR)'\right]$$

$$- \left[(h/B)(R_\theta/2R)\alpha_\psi'\right]' - \pi T\,(R_z R_\theta/R\alpha_\theta)\alpha_\psi' \tag{8}$$

The system is flute unstable if $\int M\, d\ell < 0$, unless line tied. In any event, ballooning is also possible for perturbations $|BD\phi/D\psi + \alpha_\psi BD\phi/D\alpha| << |BD\phi/D\alpha|$, provided solutions exist to the Euler-Lagrange equation

$$\left[(h\alpha_\theta^2/4\pi B^2 R)u'\right]' - Mu = 0 \qquad (9)$$

where $u = -BD\phi/D\alpha$. Thus, the nonexistence of solutions of Eq. (9) is necessary for stability. It is also sufficient, as can be shown by the reduction of an earlier condition due to Newcomb [13].

When β/ε is large, the last term of Eq. (8), which is $O(\beta^2/\varepsilon^2)$, dominates the other terms, which are $O(\beta/\varepsilon)$. Hence, in wells of baseball symmetry, instability occurs away from the symmetry planes when β/ε exceeds a number of order unity. Thus, unless stabilized by finite orbit effects (which might permit the existence of a boundary layer of thickness comparable to a typical cyclotron orbit diameter), it appears that flat-topped pressure profiles are inconsistent with the achievement of high beta. Instability is associated with the presence of geodesic curvature, $\underset{\sim}{\kappa}\cdot\underset{\sim}{b} \times \nabla\psi \neq 0$. In turn, $\underset{\sim}{j}\cdot\underset{\sim}{b}$ does not vanish everywhere. Drift currents accumulate charge at one point on a line of force which must then flow off at another point.

III. Simulation of Simple and Reversed-Field Mirror Machine (NYU)

The problem considered is the buildup of a mirror confined plasma including a transition with field reversal. A strong theoretical indication has been given that field reversal will occur 'naturally' in a plasma without injection[14] if the mirror coils are properly programmed. To confirm this requires simulation with a transport code which includes the capability of following changes in topology. We have constructed an axially symmetric, macroscopic code which is a modification of earlier, very efficient, transport codes for the Doublet[15] and Divertor[16]. Numerical results in the adiabatic limit (zero resistivity and heat conductivity) are presented here. Results with full transport and energy and mass sources will be presented elsewhere.

The model includes 'classical' plasma diffusion and heat flow. We recall[17] that in a symmetric mirror machine there is no skin effect. The Grad-Hogan formulation [18,19] is followed in order to eliminate the convection velocity and in this way rigorously separate out 1-D transport from 2-D geometry evolution. Proper choice of independent and dependent variables [19], [20] allows the 1-D transport to take the form of a standard diffusion system with second derivatives explicitly shown, allowing numerical stability and accuracy to be determined.

The independent (1-D) variable is taken to be the mass, $M = \int \rho dV$. We write ϕ for $\partial\phi/\partial M$ and $d\phi/dt$ holding M fixed ($\phi' = \partial\phi/\partial V$). Conservation of mass, flux and energy (with V as independent variable),

$$\rho_t + (\rho U)' = 0 \quad , \quad U = \oint u\cdot dS = \frac{dV}{dt}$$

$$\psi_t + U\psi' = \eta\langle r^2\rangle F \quad , \quad F = (K\psi')' \, , \; K = \langle|\nabla V|^2/r^2\rangle \qquad (10)$$

$$p_t + Up' + 2pU' = (\lambda_* T')' + \eta\langle r^2\rangle F^2 \quad , \quad \lambda_* = \lambda(T)/\omega^2\tau^2$$

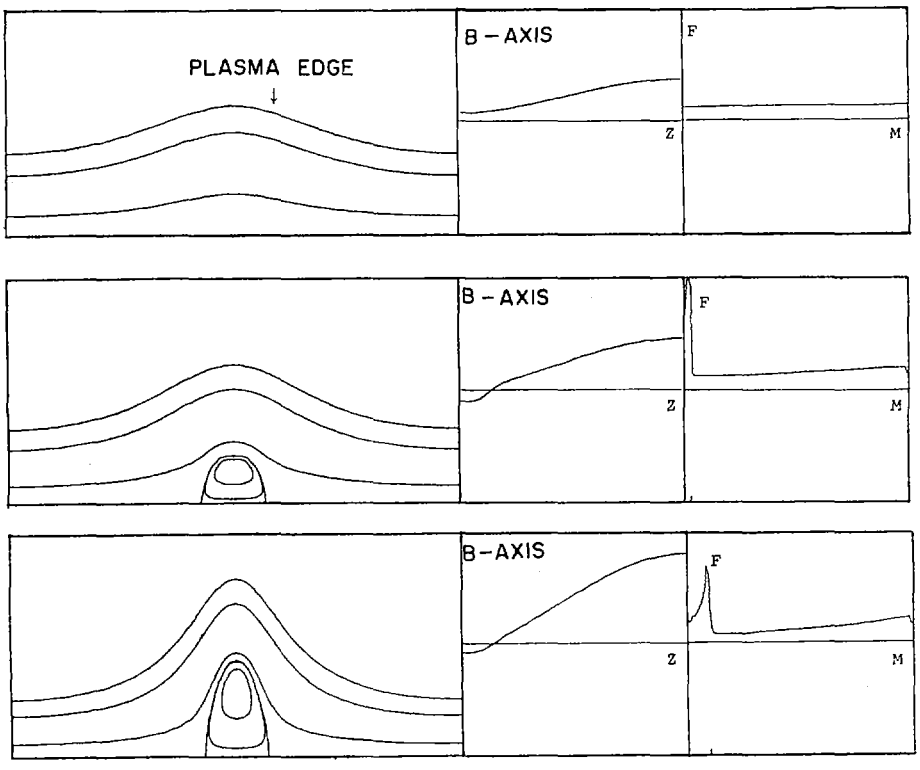


FIG.3. Adiabatic compression sequence – island formation.

are rewritten in terms of M,

$$\sigma(M) = \dot{\psi} = \psi'/\rho \quad , \quad \mu(M) = p/\rho^2$$

$$\frac{d\sigma}{dt} = (\eta\langle r^2\rangle F)' \quad , \quad F = \rho(K\rho\sigma)' \tag{11}$$

$$\frac{d\mu}{dt} = \frac{1}{\rho}\,[\lambda_* \rho(\mu\rho)']' + \eta\langle r^2\rangle F^2/\rho^2$$

where the auxiliary variable ρ is obtained from the pressure balance $(K\psi')' = -dp/d\psi$,

$$\dot{\rho}[K\sigma^2 + 2\mu] + \rho[\sigma(K\sigma)' + \dot{\mu}] = 0$$

$$\rho = \frac{a}{[K\sigma^2+2\mu]^{1/2}} \exp\left\{-\frac{1}{2}\int \frac{\sigma^2 dK}{K\sigma^2+2\mu}\right\}$$

The second derivatives, $\ddot{\rho}$, in (11) are eliminated explicitly in terms of $\ddot{\sigma}$ and $\ddot{\mu}$. The quantities σ and μ diffuse; ρ, etc., are carried along. The eigenvalues of the 2×2 matrix of second derivatives (diffusion coefficients, dimensionally $M^2(t)$) are

$$\lambda = \frac{1}{2}(\lambda_o + \rho\lambda_*) \pm \frac{1}{2}[\lambda_o^2 + \rho^2\lambda_*^2 - 2\beta\rho\lambda_*\lambda_o]^{1/2}$$

where

$$\beta = \frac{2\mu}{2\mu+K\sigma^2} = \frac{p}{p + \frac{1}{2}\langle B^2\rangle}, \qquad 0 < \beta < 1$$

$$\lambda_o = \eta K\langle r^2\rangle\rho^2\beta$$

If the energy equation is replaced by a simple source (as in a 'Flux Conserving Tokamak'), $d\mu/dt = Q$, the single classical diffusion coefficient, $\lambda = \lambda_o$ is obtained. To be precise, no skin effect is present with a plasma-vacuum interface. But a limiter, scraping off plasma, will give a very slowly diffusing skin at the classical diffusion rate λ_o rather than at the normal skin rate λ_o/β.

Figure 3 shows condensed information of an adiabatic run in which the mirror ratio is increased in steps. The current profiles (precisely, $F = \langle J/r\rangle$), originally flat, are deformed as shown. As in a Doublet [15], there is a current peak at the separatrix. The magnetic field profiles on axis are also shown.

REFERENCES

[1] BLANK, A.A., GRAD, H., WEITZNER, H., Plasma Physics and Controlled Nuclear Fusion Research (Proc. 3rd Int. Conf. Novosibirsk, 1968) Vol. 2, IAEA, Vienna (1969) 607.

[2] RIBE, F.L., Free-Boundary Solutions for High-Beta Stellarators of Large Aspect Ratio, Los Alamos Sci. Lab. Rep. LA-4098·(1969).

[3] ROSENBLUTH, M.N., JOHNSON, J.L., GREENE, J.M., WEIMER, K.E., Phys. Fluids **12** (1969) 726.

[4] MILLER, G., Phys. Fluids **20** (1977) 928.

[5] BRACKBILL, J.U., Methods Comput. Phys. **16** (1976) 1.

[6] BARNES, D.C., BRACKBILL, J.U., Nucl. Sci. Eng. **64** (1977) 18.

[7] BARTSCH, R.R., CANTRELL, E.L., GRIBBLE, R.F., et al., Nucl. Fusion **18** (1978) 1027.

[8] BARTSCH, R.R., et al., "$\ell = 1, 2$ high-beta stellarator", submitted to Phys. Fluids.

[9] FÜNFER, E., KAUFMANN, M., LOTZ, W., et al., Nucl. Fusion **15** (1975) 133.

[10] KRUSKAL, M.D., OBERMAN, C., Phys. Fluids **1** (1958) 275.
[11] HALL, L.S., Lawrence Livermore Lab. Rep. UCRL-80260, in preparation.
[12] HALL, L.S., McNAMARA, B., Phys. Fluids **18** (1975) 552.
[13] NEWCOMB, W.A., Lawrence Livermore Lab. Rep. UCID-17182 (1976).
[14] GRAD, H., "The fat mirror machine", Sherwood Annual Theory Meeting, Berkeley, 3–5 April 1974.
[15] GRAD, H., HU, P.N., STEVENS, D.C., TURKEL, E., "Classical plasma diffusion", Plasma Physics and Controlled Nuclear Fusion Research 1976 (Proc. 6th Int. Conf. Berchtesgaden, 1976) Vol. 2, IAEA, Vienna (1977) 355.
[16] TURKEL, E., STEVENS, D.C., GRAD, H., "Numerical diffusion in a divertor configuration", Am. Phys. Soc. Annual Mtg. Div. Plasma Physics, Atlanta, 1977; Bull. Am. Phys. Soc. **22** (1977) 1095.
[17] GRAD, H., "Classical plasma diffusion", Conf. on Plasma Physics, Kiev, 1970. English publication, Advances in Plasma Physics **5** (1974) 103.
[18] GRAD, H., HOGAN, J., Phys. Rev. Letters **24** (1970) 1337.
[19] GRAD, H., HU, P.N., "Classical diffusion: equations and numerical algorithms", Sherwood Annual Theory Meeting, Madison, 7–9 April 1976.
[20] GRAD, H., HU, P.N., "Classical diffusion: theory and simulation codes", to appear in Proc. Workshop on High-Beta Plasmas, Varenna, September 1977.

STABILIZING EFFECTS OF $\ell = 2,3$ HELICAL FIELDS ON HIGH-BETA STELLARATOR CONFIGURATIONS*

F. HERRNEGGER
Max-Planck-Institut für Plasmaphysik,
Euratom-IPP Association,
Garching, Federal Republic of Germany

O. BETANCOURT, P. GARABEDIAN
Courant Mathematics and Computing Laboratory,
New York University, New York,
United States of America

Abstract

STABILIZING EFFECTS OF $\ell = 2,3$ HELICAL FIELDS ON HIGH-BETA STELLARATOR CONFIGURATIONS.

A computer code is used to investigate equilibrium and stability of high-β stellarator configurations. Both a diffuse pressure profile and a free surface between the plasma and the vacuum regions are included. The code takes into account the important flux constraint of prescribing the rotational transform μ. Toroidal $\ell = 0,1,2$ equilibrium solutions are given which agree very well with the ISAR T1-B experiment. The dependence of the rate of change λ for $m = 1$, $k = 0$ modes on helically symmetric $\ell = 1,2,3$ fields is given, showing the dominant stabilizing effect due to the $\ell = 3$ field. A convergence study is made for the dependence of the rate of change of $m = 1$, $k = 0$ and $m = 2$, $k = 0$ modes on the mesh size in a straight $\ell = 1,3$ configuration.

1. INTRODUCTION

The calculation of toroidal magnetohydrostatic equilibrium solutions obeying no symmetry condition and allowing for arbitrary pressure profiles and β-values has been attacked recently by various methods [1-4]. In the present paper a computer code described elsewhere [1,2] is applied to investigate MHD equilibrium and stability of straight and toroidal high-β stellarator configurations including a vacuum region outside. In the code the MHD energy principle is applied to search for stationary states of the potential energy using a Lagrangian description. The code is a useful tool for the design of experiments such as the $\ell = 1,2,3$ high-β INTEREX experiment now

* Work supported by the US Department of Energy under Contract No.EY-76-C-02-3077 with New York University.

under construction at Garching and for investigating the stabilizing effects of helically symmetric $\ell \geq 2$ fields on the m = 1, k = 0 mode (m and k are the mode numbers in the poloidal and longitudinal directions, respectively). The convergence behavior of the growth rate with mesh size similar to Ref. [5] is discussed for m = 1, k = 0 and m = 2, k = 0 modes. Toroidal ℓ = 0,1,2 high-β equilibrium solutions are given. A convergence study of the restoring forces for various mesh sizes shows that for a finite mesh size the restoring forces are overestimated. The extrapolation of the restoring forces with mesh size gives excellent agreement with the ISAR T1-B high-β stellarator experiment. The stabilizing effect of helically symmetric ℓ = 2,3 fields on the m = 1, k = 0 mode is discussed. It turns out that the flux constraint of prescribing the rotational transform μ is very important for the stabilization mechanism; the effect of the μ-constraint is significant in cases where μ is small at the magnetic axis as in the high-β stellarator configurations.

2. MODEL AND METHOD

2.1. Variational principle

The computer code [1,2] used here describes magnetohydrostatic equilibrium solutions and their stability in a toroidal geometry with a nonplanar magnetic axis and arbitrary β values. Typical applications are toroidal high-β stellarator configurations. The code can also be used to describe nonlinear three-dimensional effects in other finite-β configurations. The plasma is surrounded by a vacuum region; the free surface in between is a magnetic surface where a surface current can be present. The vacuum region is bounded by an electric conducting wall with arbitrary shape.

The method consists of a numerical search for stationary states of the potential energy

$$E = \iiint \left\{ \frac{B^2}{2} + \frac{p}{\gamma - 1} \right\} dx_1 \, dx_2 \, dx_3$$

subject to appropriate constraints. Here p is the kinetic pressure, B is the magnetic field, x_i denote cartesian coordinates, $\gamma = 5/3$ is the adiabatic coefficient. The relation between p and the plasma density ρ is given by $p = \rho^{\gamma}$. If E has stationary states, then these are considered to be magnetohydrostatic equilibria. If the stationary states represent local minima of the potential energy, these equilibrium solutions are stable. It is assumed that the toroidal magnetic surfaces are nested. The magnetic surfaces are used as coordinate surfaces labeled by the coordinate s where s = 0 is the magnetic axis; u is the poloidal angle around the magnetic axis; v is the toroidal angle ($0 \leq u \leq 1$, $0 \leq v \leq 1$). The advantage of using a Lagrangian method is that arbitrary boundary shapes and the free surface between plasma and vacuum can be described easily.

The potential energy E is minimized subject to the five constraints:

(a) B is divergence-free everywhere: $\nabla \cdot B = 0$;

(b) the poloidal and toroidal magnetic fluxes, F_P , F_T , within each magnetic surface in the plasma region are fixed:

$$\int_{\substack{u=\text{const.} \\ s \leq s_0}} B \cdot dS_P = F_P(s_0) \ , \qquad \int_{\substack{v=\text{const.} \\ s \leq s_0}} B \cdot dS_T = F_T(s_0)$$

where dS_P is a surface element on a ribbonlike surface u=const. bounded by the magnetic axis and the magnetic surface s_0 ; dS_T is the surface element on v = const. surfaces;

(c) the mass within each magnetic surface is fixed:

$$\iiint_{s \leq s_0} \rho \, dx_1 \, dx_2 \, dx_3 = M(s_0)$$

(d) the total poloidal and toroidal magnetic fluxes, F_P^V, F_T^V, in the vacuum region are fixed;

(e) the normal components of the magnetic field on the free surface and on the wall vanish.

The Euler equations for this variational principle are the magnetohydrostatic equations:

$$-\nabla p + J \times B = 0 \qquad J = \nabla \times B \quad \text{in the plasma}$$

$$\nabla \times B = 0 \quad \text{in the vacuum}$$

$$[p + B^2/2] = 0 \quad \text{at the free surface}$$

here J is the current density and [ ] denotes the jump of the total pressure at the free surface. The most general solution for a divergence-free B is

$$B = \nabla s \times \nabla \psi$$

where s is a single-valued function, ψ is periodic in u and v. Since B must be single-valued, the general expression for ψ in terms of the poloidal and toroidal fluxes is given by [1,2]:

$$\psi = - F_T'(s) \, u + F_P'(s) \, v + f(s,u,v)$$

where ' = d/ds and f is a periodic function in u and v; $\mu = dF_P/dF_T$ is the rotational transform. Modified cylindrical coordinates (r,θ,z) are introduced by

$$x_1 = (R_T + r) \cos \theta, \quad x_2 = (R_T + r) \sin \theta, \quad x_3 = z$$

where R_T is the large radius of the torus in units of the mean radius of the wall cross section; $EP = 1/R_T$ is the inverse aspect ratio. The toroidal angle v is specified by $\theta = 2\pi v$. All lengths are measured in units of the mean wall radius. The

physical coordinates r,z in the plasma region ($0 \leq s \leq 1$) are considered to be dependent variables given by

$$r = r_0(v) + R(s,u,v)\ [r_1(u,v) - r_0(v)]$$

$$z = z_0(v) + R(s,u,v)\ [z_1(u,v) - z_0(v)]$$

where R is a dimensionless radius periodic in u,v obeying the boundary conditions $R(s=0,u,v) = 0$ at the origin and $R(s=1,u,v) = 1$ at the free surface; $r_0(v)$, $z_0(v)$ are the equations for the magnetic axis; $r_1(u,v)$, $z_1(u,v)$ are the equations for the free surface; the mean radius of the free surface cross section is denoted by R_A. A similar coordinate transformation is applied for the vacuum region where the equations $r_2(u,v)$, $z_2(u,v)$ for the outer wall appear. These are given for the present study by

$$r_2 + iz_2 = r_b \exp(iU) + \Delta_1 \exp(iV) - \Delta_2 \exp[-i(U-V)] \tag{1}$$

$$r_b = 1 - \Delta_0 \cos V + \Delta_{22} \cos 2(U-V) + \Delta_{33} \cos 3(U-V)$$

where $U = 2\pi u$, $V = 2\pi v$; the helically symmetric distortions of the wall are denoted by Δ_1, Δ_{22}, Δ_{33}; Δ_0 is the $\ell = 0$ distortion; Δ_2 is the nonhelically symmetric $\ell = 2$ distortion; L is the length of the period of the $\ell = 1$ field. One has to solve [2] the equations for ψ, r_0, z_0, R, and one equation for the free surface. A conjugate gradient method is applied introducing an artificial time t.

2.2. Computation of growth rates; convergence with mesh size

The rate of change λ of a stable or unstable mode is determined from the time behavior of the Fourier mode with wave numbers m, k. Initially the mode is excited by a rigid displacement of the plasma column or a distortion of the magnetic surfaces. Unstable modes are exponentially growing and stable modes are exponentially decaying functions of the form $Q = a \exp(\lambda t) + b$, where a+b is the initial amplitude and b is the asymptotic value of the Fourier coefficient for stable modes as t goes to infinity. There are several reasons to include the constant b. In case of toroidal high-β stellarator equilibria, the magnetic axis and the magnetic surfaces can be shifted off the geometric center of the outer wall. Therefore, if the mode is stable for any reason then the asymptotic values of the $m = 1$, $k = 0$ Fourier coefficients can be different from zero. In case of stable $m = 1$, $k = 0$ modes in helically symmetric $\ell = 1,3$ configurations ($\Delta_{33} \neq 0$) we found that b was negligibly small by using 12 q ($q = 1,2,\ldots$) intervals to represent the three periods of the Δ_{33}-distortion. When q was a noninteger number (e.g. $q = 5/4$), then b was not negligible depending on the actual grid size and it converged to zero with decreasing mesh size.

The rate of change λ is computed from

$$\lambda = \frac{\partial}{\partial t} \ln Q \quad \text{for } b = 0 \quad \text{or} \quad \lambda = \frac{\partial}{\partial t} \left(\ln \frac{\partial Q}{\partial t}\right) \quad \text{for } b \neq 0$$

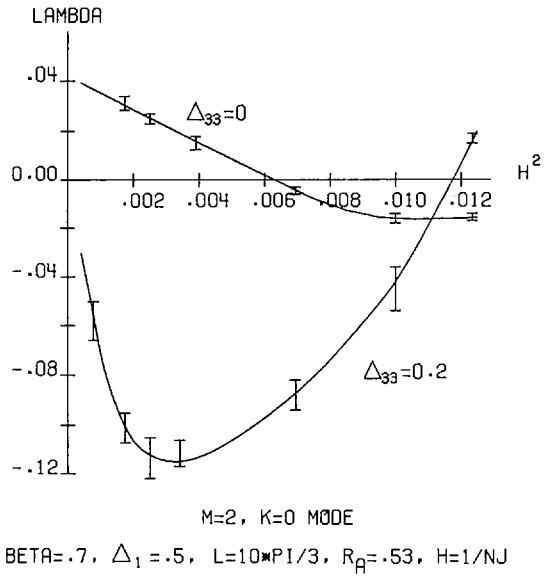


FIG.1. Rate of change of λ *versus* H^2 *in a helically symmetric* $\ell = 1$, $\ell = 3$ *configuration.*

by making a least squares fit over intervals of different lengths at various time steps. This number is roughly constant in time after the mode with a sizable amplitude has been developed and if no other mode of sizable amplitude is present. We have shown for m = 1, k = 0 and m = 2, k = 0 modes, that λ does not depend on the amplitude of the perturbation as long as it is not too large. In that regime the code describes the linearized behavior of a mode and the rate of change λ represents a measure for the eigenvalue of the linearized magnetohydrodynamic operator. In the case of systematic convergence studies we changed the time step Δt according to $\Delta t \sim H$ as the grid size H was changed (H = 1/NJ, NJ is the number of intervals in the u-direction); the ratios of the mesh sizes in the s-, u-, v- directions were kept constant. We have investigated the convergence behavior of λ_1 depending on the mesh size H for m = 1, k = 0 modes in straight helically symmetric ℓ = 1,3 configurations. These configurations are described by the parameters: β = 0.7, Δ_1 = 0.5, $\Delta_{33} \leq 0.2$, R_A variable, L = $10\pi/3$, EP = 0, μ = 0, wall radius/plasma radius = 3.6; these parameters are relevant to the INTEREX experiment. The rate of change λ_1 converges like H^2: $\lambda_1 = \bar{\lambda}_1 + \Lambda_1 H^2$, where $\bar{\lambda}_1$ and Λ_1 are:

Δ_{33}	$\bar{\lambda}_1$	Λ_1	R_A
0.0	0.006	4.98	0.67
0.1	-0.014	5.38	0.67
0.2	-0.092	8.26	0.67
0.0	0.016	5.28	0.53

In the case of global free surface m = 2, k = 0 modes, the convergence study of λ_2 with mesh size and the results are shown in Figure 1 for the same configuration.

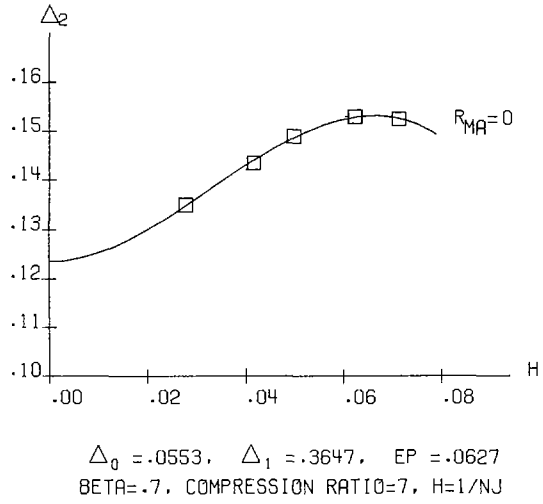


FIG.2. Convergence of Δ_2 as a function of H.

3. APPLICATIONS AND RESULTS

3.1. Toroidal ℓ = 0,1,2 equilibria; comparison with the ISAR T1-B experiment

It was shown by the ISAR T1-B [6] and Scyllac [7] experiments, that by superimposing additional fields, toroidal ℓ = 1, high-β equilibria can be achieved. The experiments in Garching and Los Alamos differ in that the toroidal drift force is compensated for by different helical fields. As shown in the following, the present code can simulate these high-β stellarator experiments. The wall simulating the ISAR T1-B experiment is given by Eq. (1); the parameters are: $\Delta_0 = 0.0553$, $\Delta_1 = 0.3647$, $\Delta_{22} = \Delta_{33} = 0$, Δ_2 variable, EP = 0.0627, wall radius/plasma radius = 7, $\beta = 0.7$, $\mu = 0$, 16 periods around the torus, $R_A = 0.5$. If Δ_2 is smaller than the equilibrium value, the plasma drifts in a toroidal outward direction roughly like a parabola. The equilibrium value for Δ_2 was determined from the drift motion. For this Δ_2 the plasma showed almost no motion for a long period of time compared with the simple toroidal drift time ($\Delta_0 = \Delta_2 = 0$), although the unstable m = 1, k = 0 motion is observed. Alternatively the equilibrium value for Δ_2 is determined by fixing the mean position R_{MA} of the magnetic axis with respect to the geometric center of the wall. The Δ_2-value giving the minimum residual force on the magnetic axis is the approximate equilibrium value. Within a small error both methods give the same value for Δ_2 using 14×24×24 intervals in the (s,u,v) directions. In the case of $R_{MA} = 0$, Figure 2 shows the equilibrium distortion Δ_2 of the wall as a function of the mesh size. The solid curve is a least squares polynomial of third degree assuming that for small H an H^2-convergence is recovered. From this convergence

study we obtained an extrapolated equilibrium value of Δ_2=0.124. This result agrees very well with the ISAR T1-B [6] experiment where a value of about $\Delta_2 = 0.12$ was determined.

3.2. Effect of D-shaped plasma cross sections on m=1, k=0 modes

By applying helically symmetric $\ell = 2,3$ fields, a D-shaped wall cross section is produced. The dependence of λ_1 on helically symmetric Δ_1, Δ_{22}, Δ_{33} distortions of the wall is investigated for the $m = 1, k = 0$ modes in straight helical configurations. The parameters are: $\beta = 0.7$, EP = 0, $R_A = 0.67$, $\mu = 0$, wall radius / plasma ardius = 3.6, $L = 10\pi/3$, $\Delta_0 = 0$, $\Delta_2 = 0$. If the helical distortions are small we can make a Taylor series expansion around the θ-pinch. In the Taylor series for λ_1 all terms up to fourth order are kept:

$$\lambda_1 = \overset{\circ}{\lambda}_1 + \sum_{i,j,k=1}^{3} (b_i \Delta_{ii} + b_{ij} \Delta_{ii} \Delta_{jj} + b_{ijk} \Delta_{ii} \Delta_{jj} \Delta_{kk}) + O(\Delta_{ii} \Delta_{jj} \Delta_{kk} \Delta_{\ell\ell})$$

Here $\Delta_{11} = \Delta_1$; $\overset{\circ}{\lambda}_1$ is the rate of change in the θ-pinch configuration different from zero in the discretized model. From simple geometrical symmetry considerations it follows that only 7 coefficients are different from zero. Suppose there is only one helical distortion present. Then these configurations are invariant to the transformations $\Delta_{ii} \to -\Delta_{ii}$. Therefore λ_1 is an even function of Δ_{ii} and hence $b_i = b_{iii} = 0$, i = 1,2,3. Because of similar symmetry considerations it follows that $b_{23} = b_{223} = 0$, $b_{12} = b_{122} = 0$, $b_{113}\Delta_1^2\Delta_{33} + b_{133}\Delta_1\Delta_{33}^2 = 0$. We have determined the remaining coefficients and obtained for H = 1/24:

$$\lambda_1 = 0.014 + 0.076\Delta_1^2 + 0.12\Delta_{22}^2 - 4.15\Delta_{33}^2 + 2.08\Delta_{22}\Delta_{33}^2$$
$$-1.35\Delta_1\Delta_{22}\Delta_{33} + 0.01\Delta_1\Delta_{33} + 0.71\,\Delta_1^2\Delta_{22}$$

There is a dominant stabilizing Δ_{33}^2-term.

4. CONCLUSION

The convergence study for the rate of change λ shows that the stabilizing effect due to the $\ell = 3$ field is significantly larger than the truncation error of the method. The rate of change for unstable and stable modes can be computed by the code. Toroidal $\ell = 0,1,2$ high-β stellarator equilibria with diffuse pressure profiles and vacuum field outside are found by a numerical search for stationary states of the potential energy. Performing an extrapolation with mesh size for the restoring forces, the code can be used to design experiments. The code works well for high, medium and low β-values.

REFERENCES

[1] BETANCOURT, O., GARABEDIAN, P., Proc. Nat. Acad. Sci. U.S.A. 73 (1976) 984.

[2] BAUER, F., BETANCOURT, O., GARABEDIAN, P., "A Computational Method in Plasma Physics," Springer-Verlag, New York, 1978.

[3] BARNES, D. C., BRACKBILL, J. U., Nucl. Sci. and Engineering 64 (1977) 18.
[4] CHODURA, R., SCHLÜTER, A., in 2nd European Conf. on Comput. Physics (D. Biskamp, Ed.), p. C2 (Garching, 1976 1PP 6/147).
[5] HERRNEGGER, F., SCHNEIDER, W., Nucl. Fusion 16 (1976) 925.
[6] FÜNFER, E., KAUFMANN, M., NEUHAUSER, J., SCHRAMM, G., 7th European Conf. Contr. Fusion and Plasma Physics, Vol. 2, p. 151 (Lausanne 1975).
[7] BARTSCH, R. R., CANTRELL, E. L., GRIBBLE, R. G., KLARE, K. A., KUTAC, K. J., MILLER, G., QUINN, W. E., Nucl. Fusion 18 (1978) (to be published).

DISCUSSION

ON PAPERS L-3-1 AND L-3-2

H.H. FLEISCHMANN: I am interested in the generation of field-reversed configurations in mirrors simply by changes in the external field. Have you any results indicating how the size of the field-reversed configuration relates to other plasma parameters such as plasma size, Larmor orbits, and so on?

J.P. FREIDBERG: The NYU group is at present beginning a parameter study to determine what initial β-values, mirror ratios and volume ratios are required to obtain reversals, and the results should be forthcoming in the near future.

H.L. BERK: Is the reversed-field equilibrium obtained by the NYU group (paper L-3-1) without resistivity?

J.P. FREIDBERG: The NYU field reversal simulations were computed with the adiabatic code in which electrical resistivity and thermal conductivity are set to zero. However, the NYU group is at present developing a code with η and k not zero to investigate the difficulty of maintaining self-reversal.

H.L. BERK: Do they apply a reversal to the external field in order to obtain the reversed-field equilibrium?

J.P. FREIDBERG: No, field reversal is obtained without reversing the externally applied field.

H.L. BERK: Did you say that the $\ell = 3$ equilibrium was a rotational transform? If so, is it truly an equilibrium?

J.P. FREIDBERG: In the MPIP-NYU equilibrium calculations and stability calculations the rotational transform is set to zero. There appears to be no problem in finding toroidal equilibrium even with zero rotational transform.

H.A.B. BODIN: What was the assumption made about β in the last part of your talk, concerning the $\ell = 3$ controversy? Was it arbitrarily high?

J.P. FREIDBERG: In the cases you are referring to, β was assumed to be finite, $\beta \sim 1$. In specific numerical calculations β was typically 0.7.

F.L. RIBE: The '$\ell = 3$ controversy' arose from a discrepancy between the Garabedian-Betancourt and Brackbill numerical calculations of Scyllac diffuse equilibria at NYU and Los Alamos – calculations of, basically, $\ell = 1,0$ and $\ell = 1,2$ equilibria. NYU found stable equilibria and LASL did not. Now we see that the transformless $\ell = 3$ contribution in straight geometry is indeed stabilizing. Would you expect this $\ell = 3$ stabilization to carry over to the large-aspect-ratio toroidal case?

J.P. FREIDBERG: If the $\ell = 3$ stabilization predicted by the MPIP-NYU computation persists after the controversy is resolved, it would probably carry over to the fully toroidal system. However, the stability controversy is still unresolved and I would like to refrain from predicting which way it will go.

EXPERIMENTAL AND THEORETICAL STUDIES OF THE ELMO BUMPY TORUS (EBT)*

R.A. DANDL, F.W. BAITY, Jr., K.H. CARPENTER,
J.A. COBBLE, H.O. EASON, J.C. GLOWIENKA,
G.R. HASTE, M.E. HESSE,+ S. HIROE, N.H. LAZAR,
B.H. QUON, T. UCKAN, T.L. WHITE,
HEAVY ION BEAM GROUP,++
UV SPECTROSCOPY GROUP,§
C.L. HEDRICK, D.B. BATCHELOR, L. DELEANO,
R.C. GOLDFINGER, E.F. JAEGER, L.W. OWEN,
D.A. SPONG, J.S. TOLLIVER
Oak Ridge National Laboratory,
Oak Ridge, Tennessee

J.B. McBRIDE, N.A. KRALL, A.L. SULTON, Jr.
Science Applications, Inc.,
La Jolla, California,
United States of America

Abstract

EXPERIMENTAL AND THEORETICAL STUDIES OF THE ELMO BUMPY TORUS (EBT).

The confinement of plasma produced by electron cyclotron heating in the ELMO Bumpy Torus (EBT) has been studied in the regime stabilized by the diamagnetism of annular, energetic electrons. The electron density ($n_e = 1-2 \times 10^{12}$ cm^{-3}) and temperature ($150 \leqslant T_e \leqslant 600$ eV) and ion temperature ($30 \leqslant T_i \leqslant 150$ eV) have been measured over a range of operating conditions. Measurement of the direction of the electric field (inward-pointing) inside the toroidally confined plasma has led to improved neoclassical theoretical models of plasma transport which describe reasonably well the observed parameter dependences over a wider range of collisionality than reported previously.

---

* Research performed under Union Carbide Corporation Contract W-7405-eng-26 with the Office of Fusion Energy (ETM), US Department of Energy.

+ On leave from Centre d'études nucléaires de Grenoble, Grenoble, France.

++ F.M. Bieniosek, F.J. Bresnock, P.L. Colestock, K.A. Connor, R.L. Hickok, and S.S. Kuo, Rensselaer Polytechnic Institute, Troy, New York, USA.

§ H.W. Moos, J.M. Tyson, and E.S. Warden, The Johns Hopkins University, Baltimore, Maryland, USA.

I. EXPERIMENTAL STUDIES

The plasma in the ELMO Bumpy Torus (EBT) [1] is confined in steady state in a 'bumpy' magnetic field produced by joining 24 magnetic mirror cells into a large aspect ratio torus. Heating power is provided by cw microwaves resonant at electron cyclotron frequencies at both 18 GHz (up to 60 kW) and 10.6 GHz (up to 30 kW); the latter is used primarily to sustain the energetic electron population and form the diamagnetic annuli.

The toroidal plasma in EBT has been shown to be macroscopically stabilized by the field modification resulting from the diamagnetic electron annuli [1]. The plasma properties have been measured over a sufficient range of operating parameters – in this stabilized magnetic configuration, using a broad spectrum of diagnostic techniques – that general correlations with neoclassical theoretical models can now be made. This close interplay between experiment and theory has led to improvements in the models and better understanding of the plasma which has intensified the incentive to raise the applied microwave frequency, heating power and toroidal magnetic field.

In the macrostable regime, free-free bremsstrahlung measurements have been obtained to determine the toroidally confined electron temperature and density. The temperatures are observed to rise with decreasing ambient pressure or increased power and lie in the range $150 \leq T_e \leq 600$ eV. The observed densities follow, in general, a similar behavior and increase by about a factor of three to a maximum of $n_e \sim 2 \times 10^{12}$ cm^{-3} in this operating range. These data may be combined with applied power to evaluate the energy lifetime of the toroidal plasma component. Assuming that the fraction of applied power deposited in the toroidal component (compared to the power to sustain the energetic annulus and the surface plasma) is constant, in Fig. 1 we present the energy lifetime (normalized by multiplying by electron temperature) plotted against the electron collisionality $\nu/\Omega = 2.7 \times 10^{-7}\, n/T_e^{5/2}\, [1 + (0.7)e\phi/T_e]^{-1}$. Also shown are curves calculated from neoclassical transport rates which take into account the ambipolar electric field. In this same range, the charge-exchange neutral energy distribution has been measured using both nitrogen and cesium charge-exchange cells with $30 \leq T_i \leq 150$ eV. The radial distribution of the ion temperature has also been determined from an array of four spatial channels. The energetic plasma ions lie within the diamagnetic annuli, r = 15 cm. An energetic Rb^+ beam has been injected through the plasma and the plasma potential determined from measurements of the change in beam energy of multiply charged rubidium ions which results from ionization in the bulk electron population [2]. Spatial mapping of the points of ionization confirms the plasma size described above and provides a direct measurement of the ambipolar electric field. The potential at the center of the plasma lies in the range -100 to +100 V and is negative relative to the potential maximum found at the position of the annulus. The relatively good agreement in shape of the points in Fig. 1 with the curve for $e\phi/T_e = 1$ is especially significant since the measured potentials are consistent with this value.

Optimization of the plasma parameters occurs when magnetic error fields are globally canceled by superimposed, weak, quadrupole magnetic fields. With this optimization, toroidal plasma currents (normally ~100 A), which are driven by the component of the ambipolar electric field along the magnetic field lines, are nulled, fluctuation levels are minimized, and almost complete symmetry of the radial electric field is measured. An example of these data is shown in Fig. 2 as a function of the imposed horizontal error field produced by one pair of the quadrupole winding.

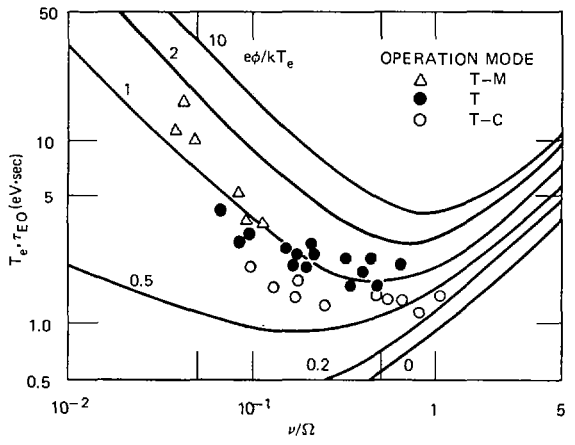


FIG.1. Product of electron temperature, T_e, and energy confinement time, $\tau_E = \int nT_e dV/P$, as a function of electron collisionality. Data points were obtained from bremsstrahlung measurements over a wide range of operating power and ambient neutral density.

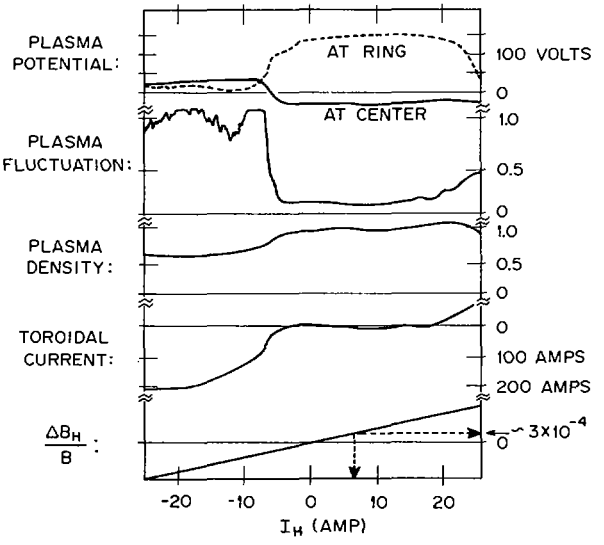


FIG.2. Influence of horizontal component of imposed error field on various plasma parameters: plasma potential well (potential difference between potential maximum and minimum), plasma density fluctuations seen on 70-GHz interferometer, plasma density ($n_e \ell$), and toroidal current measured with pickup loop.

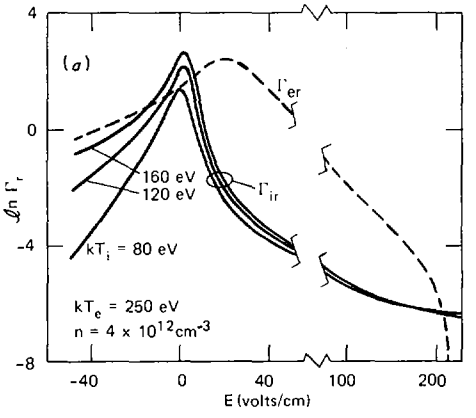


FIG.3. Electron and ion particle flux versus ambipolar electric field.

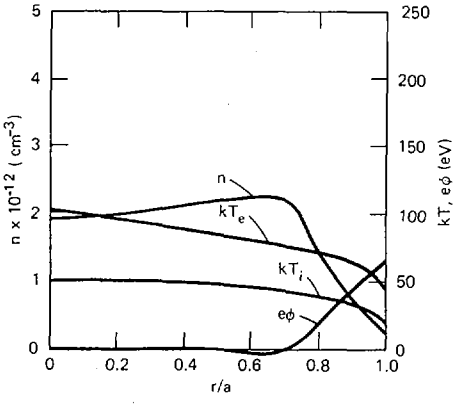


FIG.4. Steady-state radial profiles of plasma density, n, *ambipolar potential,* ϕ, *electron temperature,* kT_e, *and ion temperature,* kT_i.

Spatially resolved spectroscopic impurity measurements have been carried out using stereoscopic observation of the emitted u.v. and visible characteristic line radiation. The impurities (primarily carbon and sputtered aluminum) are found predominantly in the space outside the region of closed drift surfaces filled by the hot, bulk plasma. In the toroidal plasma region, $\frac{n\ (carbon)}{n_e} = 6 \times 10^{-5}$, whereas in the surface plasma outside this region, $\frac{n\ (carbon)}{n_e} \sim 10^{-2}$. Aluminum densities are the same order of magnitude.

In order to permit observations over an expanded plasma parameter range, a 28-GHz, 200-kW, cw, gyrotron [3] is under development for EBT use by Varian Associates. Theoretical results indicate increased densities and temperatures

can be expected from the higher-power, shorter-wavelength heating sources. Experiments are presently under way at these higher magnetic fields, and initial results will be described.

II. EBT THEORETICAL STUDIES FOCUSING ON TRANSPORT

Here we discuss the latest neoclassical transport description of EBT losses which has been sufficiently refined to self-consistently include the ambipolar electric field. Other theoretical topics are discussed by N. A. Uckan et al. [4].

Transport rates in EBT depend sensitively on the radial ambipolar electric field in contrast to other devices, such as tokamaks [5-7]. In the absence of such a field, electrons and ions of the same energy and pitch angle have coincident orbits and step sizes; electron particle fluxes would thus greatly exceed those of ions due to their higher collision frequency. The resulting ambipolar electric field equalizes the electron and ion particle fluxes and greatly influences plasma confinement.

There are two simply conceptualized ways of producing equality of the two fluxes. First, a radially outward-pointing field can electrostatically confine electrons, reducing their flux to that of the ions. Alternatively, a radially inward-pointing electric field (for normal magnetic gradient regions) will enhance ion diffusion by a cancellation of the $\vec{E} \times \vec{B}$ poloidal drift with the magnetic poloidal drifts. The latter mechanism is apparently relevant to the stable T-mode of EBT-I. Indeed, the experimentally observed sign of the electric field changes sign near the minor radius at which the gradient in B is reversed by the hot electron annuli — as required for partial cancellation of the ion magnetic and $\vec{E} \times \vec{B}$ drift to produce banana-shaped orbits.

The ORNL one-dimensional radial transport model, which has been developed to simulate the T-mode of operation self-consistently, calculates the ambipolar potential and temperature profiles [7]. Figures 3 and 4 show typical results of these calculations. From Fig. 3 it is apparent that there are three roots to the particle flux condition $\Gamma_i = \Gamma_e$. The positive root corresponds to the electrostatic mechanism mentioned earlier. The two roots near the peak in Γ_i correspond to the mechanism which involves partial cancellation of $\vec{E} \times \vec{B}$ and magnetic drift motion. As described in Ref. [7], only the most negative electric field value of $\Gamma_i = \Gamma_e$ in Fig. 3 provides thermally stable solutions. The stability of this type of solution is relatively insensitive to boundary conditions. For example, the neutral edge density may be treated as a constant, or reflux boundary conditions may be used.

The results obtained using this model give lower temperatures or higher collisionality than experimental observations indicate. In fact, calculations of Ref. [7] are based on transport coefficients whose validity is limited to high collisionality. At lower collisionality, the details of particle orbits (e.g. banana-shaped orbits) become more important. Recently, we have developed a formalism for calculating EBT neoclassical transport coefficients which allows inclusion of such orbit details. While the preliminary results are extremely encouraging, the full import of these newer transport coefficients remains to be assessed.

III. SPACE-AVERAGED EBT MODELING

Although multidimensional models, as discussed in the previous section, contain a wealth of detail, space-averaged ('point') models are also useful,

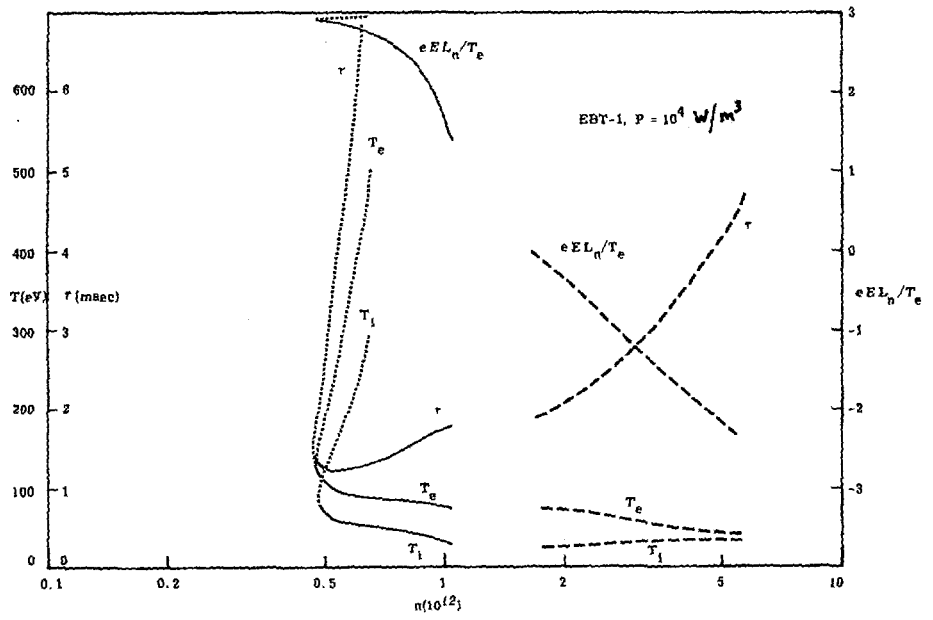


FIG.5. Operating characteristics for EBT-I.

both in obtaining scans of parameter space for scaling studies and in identifying equilibria which can be the starting point for 1-D studies. In this section, we present such a model and demonstrate its ability to produce results comparable to the 1-D treatment. The model equations assume neoclassical losses as in the previous section, replacing gradient scale lengths by the plasma minor radius. The model equations are those given in Refs [6,8], except that we now distinguish the neoclassical particle confinement time τ_p from the electron and ion energy confinement times τ_{Ee} and τ_{Ei} [5]:

$$\tau_{p\alpha}^{-1} = \frac{4}{3}\left(\frac{R_c}{R_T}\right)^2 \nu_\alpha \frac{\left(1 + 2\eta_\alpha + q_\alpha L_n E/T_\alpha\right)}{\left(1 + q_\alpha E R_c/T_\alpha\right)^2 + \nu_\alpha^2/\Omega_{o\alpha}^2}$$

$$\frac{\tau_p}{\tau_{E\alpha}} = \frac{7}{2} \frac{\left(1 + 101/7\ \eta_\alpha + q_\alpha L_n E/T_\alpha\right)}{\left(1 + 2\eta_\alpha + q_\alpha L_n E/T_\alpha\right)}$$

Ambipolarity constrains $\tau_{pe} = \tau_{pi} = \tau_p$ and thus determines the self-consistent radial electric field. η_e and η_i are the ratios of density gradient scale length to the electron and ion temperature gradient scale lengths, typically chosen to be unity. The neutral density is related to the plasma density by $n_o + \varepsilon n$ = constant. The model is flexible in that the total particle density, plasma plus neutrals, can be held fixed by choosing $\varepsilon = 1$, while the neutral density is fixed if we choose $\varepsilon = 0$. The form of this relation has no effect on the operating equilibria but influences the stability.

Figure 5 shows typical power balance curves for EBT-I, illustrating the scaling trends predicted by the point model. We chose the input parameters to characterize EBT-I, assuming that the microwave power absorbed is $P_\mu = 10^4$ W/m^3. Note the existence of negative electric field solutions at the higher densities, where the electrons and ions are apparently well coupled thermally. As the density decreases, the negative electric field branch gives way to a positive electric field branch along which the temperature rises and the plasma becomes highly collisionless. The negative electric field branch is characterized by collisional scaling and the confinement is controlled by the ions $\tau \sim \tau_{Ei}$. When the field changes sign at lower density and lower collisionality, the confinement becomes controlled by the electrons $\tau \sim \tau_{Ee}$. The positive electric field branch exhibits both stable and unstable operating points regardless of the neutral model. The highly collisionless (dotted) portion is always unstable, while the lower temperature (solid) portion is always stable. The stability of the negative electric field branch (dashed) is much more sensitive to the neutral model. The model used here predicts stable operation along the negative field branch, as in the experiment, for $\varepsilon \geq 10 n_0/n \geq 10^{-2} - 10^{-1}$. Thus, the stability of the negative roots is sensitive to the feedback stabilizing influence of the neutral particles. The scaling trends, sign of the ambipolar fields, and stability properties of the various branches in Fig. 5 are consistent with the 1-D code calculations.

As in 1-D, we find that higher power tends to shift the operating characteristics to higher density and somewhat higher temperature while not substantially altering the shape of the curves. In all cases, however, temperatures were somewhat lower on the negative field branch (perhaps a factor of 2-4) than the highest temperatures reported by the experimenters.

We conclude that neoclassical operation on the collisional negative electric field branch is roughly consistent with the lower temperature regimes measured in EBT, but not with the higher temperature collisionless regimes also observed experimentally (which correspond to negative ambipolar electric fields). Additional physics input to the model is thus required if in fact a neoclassical description of plasma loss is adequate for the collisionless regime.

REFERENCES

[1] DANDL, R.A., EASON, H.O., EDMONDS, P.H., ENGLAND, A.C., GUEST, G.E., HEDRICK, C.L., HOGAN, J.T., SPROTT, J.C., in Plasma Physics and Controlled Nuclear Fusion Research (Proc. Conf. Madison, WI, 1971), Vol. II, IAEA, Vienna (1971) 607; DANDL, R.A., EASON, H.O., GUEST, G.E., HEDRICK, C.L., IKEGAMI, H., NELSON, D.B., in Plasma Physics and Controlled Nuclear Fusion Research (Proc. Conf. Tokyo, Japan, 1974), Vol. II, IAEA, Vienna (1975) 141.

[2] COLESTOCK, P.L., CONNOR, K.A., HICKOK, R.L., and DANDL, R.A., Phys Rev. Lett. 40 (1978) 1717.

[3] ZAYTSEV, N.I., PANKRATOVA, T.B., PETELIN, M.I., FLYAGIN, V.A., "Millimeter- and Submillimeter-Wave Gyrotrons," Radiotekh. Electron. [Radio Eng. Electron. Phys.] 19 (1974) 1056-60.

[4] UCKAN, N.A., et al., "The ELMO Bumpy Torus (EBT) Reactor," Paper I-3, this meeting.

[5] KOVRIZHNYKH, L.M., Sov. Phys. – JETP 29 (1969) 475.

[6] HEDRICK, C.L., et al., Nucl. Fusion 17 (1977) 1237.
[7] JAEGER, E.F., et al., Phys. Rev. Lett. 40 (1978) 866.
[8] McBRIDE, J.B., and SULTON, A.L., Jr., Nucl. Fusion 18 (1978) 285.

DISCUSSION

F.L. RIBE: I was interested to hear about the new data on EBT obtained with the gyrotron microwave source. Would you say a few words about the plasma parameters obtained?

R.A. DANDL: Given the same magnetic field configuration (scaled to the 28 GHz frequency) and applying about 50% more power than in the comparable 18 GHz case, we obtained electron temperatures in about the same range (i.e. 200–300 eV) and densities increased by approximately 50%. The maximum 28 GHz power used in these experiments was 45 kW-cw.

H. DREICER: As you have given us information about the temperature of the bulk electrons in the EBT plasma, I wonder whether you could describe the mechanism by which the bulk electrons are heated. In particular, how much of their energy derives from the high-energy ring electrons rather than directly from ECRH, and what is the nature of the bulk electron velocity distribution? If it is Maxwellian or near-Maxwellian, is it characterized by anisotropy in temperature, i.e. is $T_{\perp_e} \gg T_{\parallel_e}$?

R.A. DANDL: The bulk electrons are heated rather slowly by ECRH on the Mod "B" resonant surfaces that intersect the mirror axis of the torus. More rapid heating and consequent formation of the high B ring electrons occur on the off-axis Mod "B" resonant surfaces that are tangent to flux lines. This heating takes place by second-harmonic coupling with respect to the 18-GHz bulk heating frequency and by fundamental frequency coupling to the 10.6-GHz profile heating. The toroidal electron distributions are Maxwellian within the limits of our soft-X-ray measurement system.

PLASMA STABILITY CONTROL IN A TOROIDAL SYSTEM BY FEEDBACK AND HF FIELDS

R.A. DEMIRKHANOV, A.G. KIROV,
V.P. SIDOROV, L.F. RUCHKO, S.N. LOZOVSKIJ,
A.V. SUKACHOV, A.V. NYUSHKOV
Sukhumi Physico-Technical Institute
of the USSR State Committee for Utilization
of Atomic Energy,
Sukhumi,
Union of Soviet Socialist Republics

Presented by K.N. Stepanov

Abstract

PLASMA STABILITY CONTROL IN A TOROIDAL SYSTEM BY FEEDBACK AND HF FIELDS.

The paper deals with theoretical and experimental aspects of controlling MHD plasma stability in toroidal systems by feedback systems and HF fields. Results are presented of theoretical studies on resonant excitation of helical MHD oscillations in a current-carrying plasma column (stable Shafranov modes) by the mutipole helical HF field ($\Omega \lesssim \omega_{HF}$). The effect of such an oscillation build-up on the evolution of unstable helical modes is discussed. The conditions for exciting helical oscillations (depending on the direction of the HF field rotation, as well) and the main criteria for stabilization are given. – Results of experimental studies on kink instability stabilization by a feedback system with M = 1, 2, 3; N = 1 for various values of q ($q = 2\pi/\iota_\Sigma$, where ι_Σ is the total angle of rotational transform) in the R-0 stellarator are presented. On stabilizing the main unstable mode for a given range of values of q, the discharge parameters are improved. A stabilizing effect is only provided by introducing a certain phase shift into the feedback circuit and by choosing the amplifier gains. Stabilization improves the plasma thermal insulation and increases its energy content.

1. INTRODUCTION

The main goal of investigating plasma stability control in toroidal systems by feedback and HF fields is the stabilization of the most dangerous modes of MHD current instabilities and the attainment of a safety factor q close to unity in tokamak-type devices. Obtaining a stable plasma with small values of q is stimulated by the opportunity of optimizing the thermonuclear tokamak and developing a compact reactor with high specific plasma energies. It has been

theoretically [1] and experimentally [2] shown that MHD instabilities can be stabilized dynamically for small values of q by using a skinning multipole HF field. It was experimentally demonstrated [3] that under conditions of helical resonance to be discussed later the HF currents in the circuit needed for stabilization are substantially lower.

In the second part of the present paper, a theoretical analysis of helical resonance is given. These results allow a theoretical analysis of the experimental results on resonant HF heating of ions to be made [4]. This section also gives the main criteria for stabilization in helical resonance conditions when the unstable helical modes are most efficiently suppressed by the excitation of stable natural plasma oscillations (stable Shafranov modes).

Another way of attaining small values of q is the method of feedback stabilization [5, 6] which is more favourable in terms of energy. Particular attention is drawn to the exploration of selective measures to stabilize various modes of kink instabilities ($m = 1, 2, 3$; $n = 1$) and to the effect of stabilizing these instabilities on the macroscopic plasma parameters. It is shown that feedback stabilization results in a considerable growth of the plasma energy parameters and improves its confinement.

2. EXCITATION AND STABILITY OF HF HELICAL SHAFRANOV MODES

2.1. Helical HF fields excited in a plasma

Let us consider the problem of exciting HF fields in a cylindrical plasma column placed in a stationary magnetic field. The problem reduces to the determination of the HF field generated in the plasma by HF currents flowing through the helical circuit of radius b. The exciting currents in the circuit are given by $\tilde{I}_{\varphi,z} = \tilde{I}_{0\varphi,z} \exp i(\Omega t - M\varphi - k_z z)$, the amplitudes $\tilde{I}_{0\varphi}$, $\tilde{I}_{0z}$ being related through $\tilde{I}_{0\varphi} + \tilde{I}_{0z} k_z b/M = 0$. The problem is solved for $\beta = 8\pi n_0 T/H_0^2 \ll 1$, $\tilde{\beta} = 16\pi n_0 T/\tilde{H}^2 \gg 1$.

With $I_z = 0$ ($H_\varphi = 0$), accurate analytical expressions for generating fields can be obtained; the expressions are, however, too cumbersome in the general case. They become much simpler if the following additional assumptions are made which are satisfied with sufficient accuracy under real experimental conditions [4, 7]:

$$\text{(a)}\ \nu, \Omega \ll \sqrt{|\omega_{He}|\omega_{Hi}},\quad \text{(b)}\ \frac{m_e \Omega \sqrt{\nu^2 + \Omega^2}}{m_i |\omega_{Hi}^2 - \Omega^2|} \ll 1,\quad \text{(c)}\ \frac{\Omega}{c} \ll k_z \ll \frac{1}{a}$$

where ν is the effective collision frequency. In the general case, we assume $\nu \sim \Omega \sim \omega_{Hi}$ and inequality (b) can be replaced by the condition

$|\omega_{Hi}-\Omega|/\omega_{Hi} \gg m_e/m_i$, which is practically always fulfilled in the domain of validity of the MHD model, $|\omega_{Hi}-\Omega| \gg k_z v_{Ti}$.

On these assumptions, the plasma is described by a dielectric tensor ϵ_{ik} with the components $\epsilon_1 = \epsilon_{xx} = \epsilon_{yy} \cong \omega_{pi}^2/(\omega_{Hi}^2 - \Omega^2)$, $\epsilon_2 = i\epsilon_{xy} = -i\epsilon_{yx} \cong (\Omega/\omega_{Hi})\epsilon_1$, $\epsilon_3 = \epsilon_{zz} \cong -\omega_{pe}^2/(\Omega(\Omega - i\nu))$.

With conditions (a), (b) and (c) satisfied, as a result of solving Maxwell's equations for plasma and vacuum and meeting the boundary conditions (for circuit and plasma boundary), the following expressions are obtained for the HF magnetic field in the plasma:

$$\tilde{H}_r = -\frac{4\pi i\sigma}{c}\tilde{I}_{0z}\left(\frac{a}{b}\right)^{|M|-1}\frac{1}{\mathcal{F}}\left\{(\epsilon_1-\sigma\epsilon_2)f_M(r) - N_\parallel^2\left(\frac{r}{a}\right)^{|M|-1}\right\}\exp i(\Omega t - M\varphi - k_z z)$$

$$\tilde{H}_\varphi = -\frac{4\pi}{c}\tilde{J}_{0z}\left(\frac{a}{b}\right)^{|M|-1}\frac{1}{\mathcal{F}}\left\{(\epsilon_1-\sigma\epsilon_2)\varphi_M(r) - N_\parallel^2\left(\frac{r}{a}\right)^{|M|-1}\right\}\exp i(\Omega t - M\varphi - k_z z) \qquad (1)$$

where

$$f_M(r) = \frac{M}{k_1 r}\,\frac{J_M(k_1 r)}{J'_M(k_1 a) - \frac{M}{k_1 a}\frac{\epsilon_2}{\epsilon_1}J_M(k_1 a)}$$

$$\varphi_M(r) = \frac{J'_M(k_1 r)}{J'_M(k_1 a) - \frac{M}{k_1 a}\frac{\epsilon_2}{\epsilon_1}J_M(k_1 a)}$$

$$k_1^2 = \frac{\Omega^2}{c^2}N_1^2 = \frac{\Omega^2}{c^2}\frac{\epsilon_3}{\epsilon_1}(\epsilon_1 - N_\parallel^2),\quad \mathcal{F} = 2N_\parallel^2 - (\epsilon_1-\sigma\epsilon_2)(f_M(a) - \varphi_M(a))$$

$$N_\parallel^2 = \frac{ck_z}{\Omega},\quad \sigma = \operatorname{sign} M \equiv \frac{M}{|M|}$$

These expressions can be simplified for $|k_1|a \gg 1$, which is valid (excluding the region where $\epsilon_1 \cong N_\parallel^2$) in a dense plasma with $\delta_0 \ll a$ (here, δ_0 is the 'classical" skin layer depth). This condition is always satisfied in real experiments. When $|k_1|a \gg 1$, it is sufficient to assume in Eq.(1) that $f_M(r) \to 0$, $\varphi_M(r) = \exp((r-a)/\delta_s)$, where $\delta_s = 1/ik_1 = \sqrt{(1-i\nu/\Omega)}/\sqrt{(1-N_\parallel^2/\epsilon_1)}$.

The fields in the plasma are a superposition of two types of waves, a fast magneto-acoustic wave and an Alfvén-type wave corresponding to an ordinary Alfvén wave only for $\epsilon_1 \cong N_\parallel^2$, and damped strongly over the remaining range of parameter values, vanishing at distances of the order of $|\delta_s|$.

Expressions (1) show that there are two types of resonance effects: one defined by the condition $|J'_M(k_1a) - (M/k_1a)(\Omega/\omega_{Hi})\, J_M(k_1a)| = \min$ at $\epsilon_1 \cong N_\parallel^2$ and $|k_1|a \sim 1$ (Alfvén wave resonance), and the other by the condition $\gamma \cong 0$ ('helical resonance' [4, 7, 8]). The Alfvén resonance can only be sufficiently well defined in a collisionless plasma (though even in this case it can be seen from Eq.(1) that the HF field amplitude does not become infinite, and, for $\nu \gtrsim \Omega$, as follows from the expression for k_1, damping causes considerable broadening of the resonance curve. In the case of helical resonance, the resonance condition (at $|\delta_s| \ll a$):

$$2N_\parallel^2 - \epsilon_1 + \sigma\epsilon_2 = 0 \tag{2}$$

is virtually independent of ν and there is no collision-induced resonance broadening within the framework of the linear approximation. Thus, only in this case there are favourable conditions for efficient pumping of HF field energy into the plasma. Solving Eq.(2) with respect to Ω/ω_{Hi} we find:

$$\left(\frac{\Omega}{\omega_{Hi}}\right)_{res} = A(\sqrt{A^2+2} + \sigma A), \quad A = \frac{k_z c}{\omega_{pi}} \tag{3}$$

We see that, for a given plasma density, there are two values of the resonance frequency Ω_{res} (or of the resonance field H_{res} at fixed frequency) which differ considerably for $A \gtrsim 1$ and correspond to various directions of HF field rotation. This conclusion is in agreement with the experimentally [7] observed highly asymmetric type of resonance excitation with respect to the direction of wave rotation. For $M > 0$, the wave rotates in the direction of the cyclotron rotation of electrons (diamagnetic rotation), and for $M < 0$, in the direction of the cyclotron rotation of ions (paramagnetic rotation).

At small values of the parameter A, we obtain the previous result [4, 8]: $\Omega_{res} = \sqrt{2}\, A\omega_{Hi}$ or $(1/\sqrt{2})\sqrt{4\pi n_0 m_i}\ \Omega/k_z$.

For $\Omega \cong \omega_{Hi}$, helical resonance for the case of paramagnetic wave rotation ($\sigma = -1$) is only found for $A \to \infty$ (i.e. for $k_z \to \infty$ or $n_0 \to 0$). Thus, a coincidence of helical and cyclotron resonances appears to be impossible. However, a possible decay of the pump wave (for $\Omega \cong \omega_{Hi}$, $\sigma = +1$, $A = \frac{1}{2}$) is not excluded when cyclotron modes make a contribution to it; this possibility would substantially raise the efficiency of plasma heating.

The absolute value of H_{res} as calculated from Eq.(3) differs from the experimental value by nearly a factor of two. The reason for this discrepancy is not yet clear. It is possible that, for $\epsilon_1 \cong N_\parallel^2$, the initial wave decays, exciting the same type of wave with $\Omega' \cong \Omega$ and $k_z' = 2k_z$.

2.2. Shafranov mode stabilization in the helical resonance regime

The evolution of helical Shafranov modes has been investigated in the nonlinear approximation [9], in toroidal [10] and elliptical geometries [11], including finite plasma resistance which results in reconnection of the field lines, and the formation of magnetic islands and disruptive instabilities [12]. The ideal of controlling the stability of helical Shafranov modes by using an externally excited helical multipole wave [1] seems to be interesting and promising in practice. The stability of helical plasma oscillations is discussed below in a simple model with uniformly distributed density ρ and current I_z against the helical pump wave $\vec{\tilde{H}} \sim \exp i(\Omega t - M\varphi - k_z z)$. The perturbation of the stationary values for this case is of the following type:

$$\vec{f}_s = \sum_{s=-\infty}^{+\infty} \vec{f}_s \exp i(\omega_s t + m_s \varphi + k_s z), \quad \omega_s = \omega + s\Omega, \quad m_s = m + sM, \quad k_s = k_z + sK_z$$

and represents an infinite series of oscillators. For the sake of simplicity, we shall assume that the oscillators within the plasma are not coupled and interaction between them is due to boundary conditions only at the plasma boundary. The conditions at the free boundary consisting in the normal field component vanishing and the continuity of the pulse flux density tensor result in an infinite system of interlinked algebraic equations. The determinant of this system of equations is put equal to zero and gives the dispersion relation describing the average development of a helical m,n Shafranov mode (in the zero Mathieu zone) and the process of helical-wave decay (in the first Mathieu zone).

The system of equations obtained in the single-fluid hydrodynamic approximation (for $\Omega \ll \omega_{Hi}$) and describing helical-oscillation development against a helical pump wave takes the following form:

$$\left\{L_s(m_s, n_s q, \omega_s^2) + \frac{\langle I_k^2(a)\rangle}{L_0^2(M,Nq,\Omega^2)}\left[L_{s+1}(m_{s+1}, n_{s+1}q)\right.\right.$$

$$\left.\left. + L_{s-1}(m_{s-1}, n_{s-1}q)\right]\right\}\Psi_s + \frac{\langle I_k(a)\rangle}{L_0(M,Nq,\Omega^2)}\left[\frac{(m_s - n_s q)(m_s - n_s\tilde{q})}{2|m_s|}\right.$$

$$+ \frac{(m_{s-1} - n_{s-1}q)(m_{s-1} - n_{s-1}\tilde{q})}{2|m_{s-1}|} + \frac{\tilde{H}_{\varphi i}}{\tilde{H}_{\varphi e}} - 1\Big]\Psi_{s-1}$$

$$+ \frac{\langle I_k(a)\rangle}{L_0(M,Nq,\Omega^2)}\left[\frac{(m_s - n_s q)(m_s - n_s\tilde{q})}{2|m_s|}\right.$$

$$\left. + \frac{(m_{s+1} - n_{s+1}q)(m_{s+1} - n_{s+1}\tilde{q})}{2|m_{s+1}|} + \frac{\tilde{H}_{\varphi i}}{\tilde{H}_{\varphi e}} - 1\right]\Psi_{s+1} \tag{4}$$

Here $L_s(m_s, n_s q, \omega_s^2) = \Omega_s^2 a^2/c_{A\varphi}^2 - \omega_s^2 a^2/c_{A\varphi}^2 \equiv \hat{\Omega}_s^2 - \hat{\omega}_s^2$
$\Omega_s^2 = \alpha^2 - 1 + 2(m_s - n_s q)^2 - 2\alpha(m_s - n_s q)$ is the eigenfrequency and α is the skinning parameter. The second term in curly brackets is a non-linear shift of the eigenfrequency. Without casing and for long-wavelength oscillations, $k_s a \ll 1$, the frequency shift of the eigenoscillations is given by

$$\Delta\hat{\Omega}_s^2 = \langle h_{\varphi e}^2\rangle |m_s| \left\{\frac{(m_{s+1} - n_{s+1}\tilde{q})^2}{2|m_{s+1}|} + \frac{(m_{s-1} - n_{s-1}\tilde{q})^2}{2|m_{s-1}|} + \frac{\tilde{H}_{\varphi i}^2}{\tilde{H}_{\varphi e}^2} - 1\right\} \tag{5}$$

where $\tilde{q} = a\tilde{H}_z/R\tilde{H}_\varphi$ is the safety factor calculated for an alternating pump field. $\langle h_{\varphi e}\rangle = \langle \tilde{H}_{\varphi e}\rangle/\overline{H}_\varphi$ is the average value of the dimensionless pump field. The expression for $\langle h_{\varphi e}\rangle$ can be expressed in the form:

$$\langle h_{\varphi e}\rangle = \frac{\langle \tilde{I}_k(a)\rangle}{\hat{\Omega}^2 - \hat{\Omega}_{res}^2} \tag{6}$$

where

$$\langle \tilde{I}_k(a)\rangle = \frac{\langle \tilde{J}_z(b)\rangle}{I_z} \left(\frac{a}{b}\right)^{|M|}\left\{\Omega^2 - (M - Nq)(M - Nq - 2\sigma)\right. \tag{7}$$

is the dimensionless circuit current $\hat{\Omega}^2_{res}(M, Nq) = 2(M-Nq)(M-Nq-\sigma)$. Average stability ($s = 0$) for the simplest case $\alpha = 1$ is obtained from the condition $L_s(m_s, n_s q, \omega_s^2) + \Delta\hat{\Omega}_s^2 = 0$, i.e.

$$\hat{\omega}^2 = 2(m-nq)(m-nq-\text{sign } m) + \Delta\hat{\Omega}_s^2 \qquad (8)$$

The above expression and Eq.(6) indicate that, in the helical resonance regime $\hat{\Omega}^2 \cong \hat{\Omega}^2_{res}$, the helical mode is stabilized with arbitrarily small currents in the circuit, $\langle\tilde{I}_k\rangle$. In other words, the helical instability of mode m appears to be forbidden if the HF current in the circuit exceeds some critical value $\tilde{I}_{cr}$, i.e.

$$\langle\tilde{I}_k^2(a)\rangle \geqslant \tilde{I}_{cr}^2 = \frac{(\hat{\Omega}^2 - \hat{\Omega}^2_{res})^2}{2|m|\{\max(m,M) + \tilde{H}^2_{\varphi i}/\tilde{H}^2_{\varphi e} - 1}$$

Stability is here due to the non-linear frequency shift (increase). It is important to note that the frequency shift is proportional to the instability wave number m and also to the multipolarity of the pump wave (for $M > m$).

3. STABILIZATION OF LOWER MODE KINK INSTABILITIES BY FEEDBACK SYSTEMS IN THE R-0 DEVICE

3.1. Introduction

Numerous experimental and theoretical studies on feedback stabilization of unstable plasmas have been published [5, 6, 13–16]. The stabilization of the hot-plasma instabilities in toroidal systems requires contactless methods for the plasma column to be affected. This problem can be solved by placing a system of appropriately wound coils [15] along the plasma column periphery and connecting these to control amplifiers. In this case, by varying the amplitude-phase frequency characteristics (APFC) of the amplifiers, various boundary conditions can be realized at the surface where the conductors are placed. Experiments with such a feedback system performed on the R-0 device [5] showed that, with a correct choice of APFC, the discharge characteristics can be improved and one can work at lower values of q. If the hot region is surrounded by plasma with relatively low conductivity, tearing instabilities may arise. To stabilize these, amplifiers with narrower bandwidth may be used. Experiments on the T0-1 demonstrated stabilization of an instability that was, in all probability, a tearing mode [6].

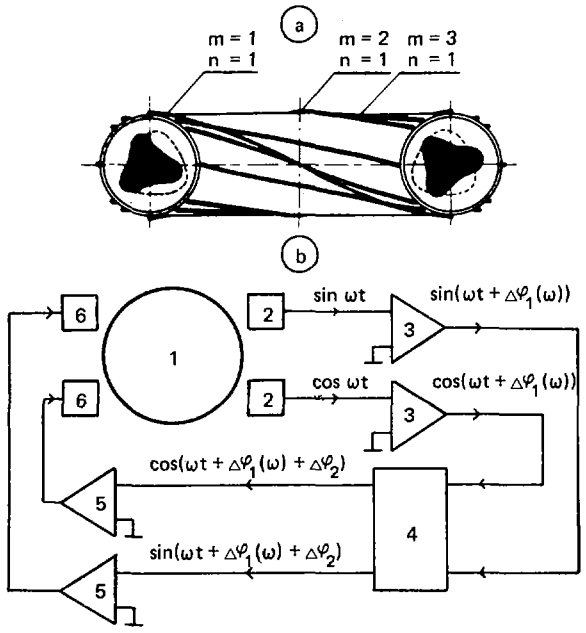


FIG.1. (a) Arrangement of feedback windings on vacuum chamber; (b) block diagram of feedback system: 1) plasma; 2) 'sine' and 'cosine' probe windings; 3) pre-amplifiers; 4) summator; 5) power amplifiers; 6) control windings.

3.2. Experimental device

The experiments were performed in the toroidal R-0 device [5]. The feedback stabilization system includes three pairs of helical windings with M = 1, 2, 3; N = 1 and six electronic amplifiers with a range of operating frequencies from 0.1 to 1.5 MHz and a maximum loading current of I_{max} = 15 A. Each pair of windings consists of 'sine' and 'cosine' windings shifted by an angle of $\pi/2$ relative to each other along the torus major azimuth. Figure 1a shows the winding locations on the chamber (only "sine" windings are shown), and Fig.1b shows the functional circuit diagram of the feedback system for a single mode.

Besides the frequency-dependent phase shift $\Delta\varphi_1(\omega)$ introduced individually into each amplifier, the feedback amplifiers have facilities for introducing a frequency-independent phase shift $\Delta\varphi_2$ which is realized by summing the signals of the sine and cosine windings.

3.3. Investigation of kink instability regions

To elucidate the behaviour of the kink instability in stellarators in greater detail, the discharge behaviour was studied within a wide range of rotational transform angles. On the whole, the regions of development of instabilities of various modes are of a type that is predicted by the theory for a parabolic current distribution in the plasma. As in previous experiments [17], together with the development of the helical instability with a given wave number m, intense helical oscillations with $m \pm 1$ were observed simultaneously.

To determine the characteristic frequencies of the instability development, active diagnostic techniques were applied in the plasma: currents of various frequencies were passed through the helical windings, and amplitude and phase of the plasma-reflected signals were recorded. These experiments showed that on approaching the threshold for instability development, an abrupt change occurred on the plasma-reflected-signal phase. For $m = 2$ and our parameters, the phase shift peak occurred within the frequency range of 600–800 kHz, which corresponds approximately to the values of $\Omega_{\varphi A}$ for the experimental conditions.

3.4. Stabilization of $m = 3$, $n = 1$ mode; $2 < q < 3$

The stabilization experiments study the effect of the feedback system on the kink instability with varying safety factor q, i.e. in various regions of the stability diagram. It was found that in the region of $m = 3$ instability development a stabilizing effect was observed when the feedback amplifiers with the $m = 3$ windings were switched on, while for amplifiers with other windings this effect was not observed (Fig.2). In this case, the instability development threshold is shifted towards lower values of q. Here, the gain of the feedback amplifiers K_0 defined as the ratio of the control magnetic field at the plasma column boundary to the magnetic field of the plasma current perturbation was equal to 0.75–1.0.

Figure 3 shows the traces characterizing the variation in the discharge behaviour on changing the frequency-independent phase shift $\Delta\varphi_2$ in the feedback circuit. For non-optimal phase shift, the instability development restricts the plasma current (Fig.3a), and $m = 3$ helical modes appear (Fig.3b). For optimal phase shift, a growth in current is observed in the plasma (Fig.3c), the oscillations being of decaying type (Fig.3d).

3.5. Stabilization of $m = 2$, $n = 1$ mode; $1 < q < 2$

When the safety factor q decreases, it is necessary to switch on feedback amplifiers with $M = 2$ windings. After stabilization, the plasma parameters improve considerably, magnitude and duration of the plasma current increase, and the

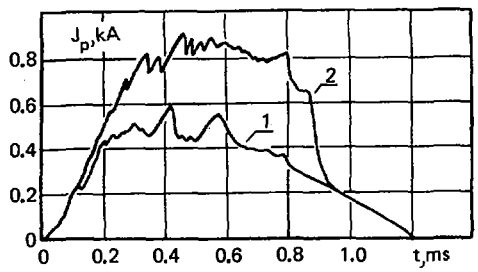


FIG.2. Plasma current. Stabilization of $m=3$, $n=1$ kink instability; $\iota_0 \cong 0.43\,\pi$, $B_0 = 5.5$ kG, $p \cong 5 \times 10^{-4}$ mmHg: 1) feedback off; 2) feedback on.

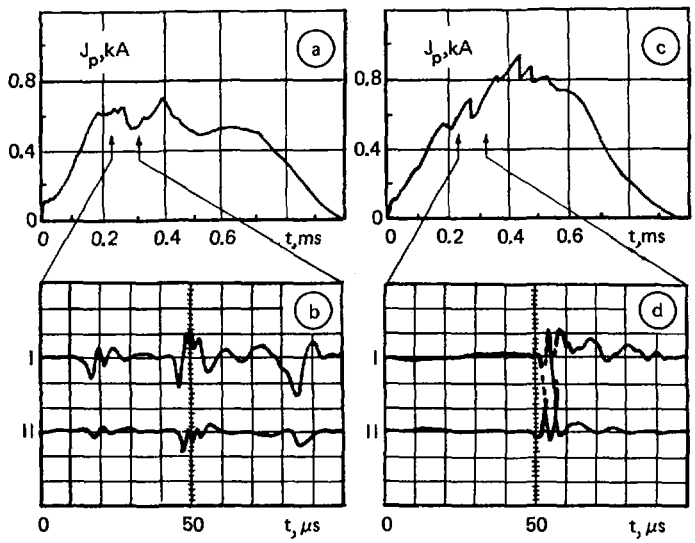


FIG.3. Stabilization of $m=3$, $n=1$ kink instability; $\iota_0 \cong 0.43\,\pi$, $B_0 = 5.5$ kG, $p \cong 5 \times 10^{-4}$ mmHg. Feedback on.

a) Plasma current (unstabilized case);

b) I – $m=3$, $n=1$ perturbation (arb. units),
II – $M=3$, $N=1$ control winding current (arb. units);

c) Plasma current (stabilized case);

d) I – $m=3$, $n=1$ perturbation (arb. units),
II – $M=3$, $N=1$ control winding current (arb. units).

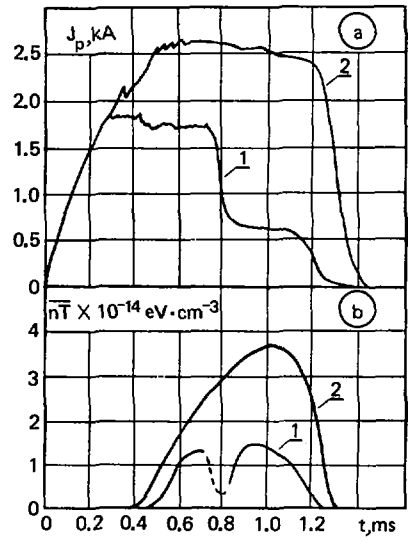


FIG.4. Stabilization of $m=2$, $n=1$ kink instability; $\iota_0 \cong 1.1\ \pi$, $B_0 = 6.6$ kG, $p \cong 5 \times 10^{-4}$ mmHg:
a) Plasma current;
b) Plasma diamagnetism;
1 – feedback off;
2 – feedback on.

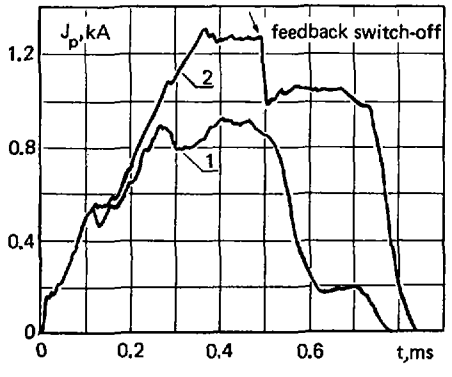


FIG.5. Plasma current. Stabilization of $m=2$, $n=1$ kink instability; $\iota_0 \cong 0.9\ \pi$, $B_0 = 4.7$ kG, $p \cong 5 \times 10^{-4}$ mmHg:
1 – feedback off;
2 – feedback on at discharge start.

plasma diamagnetism increases, indicating an improvement of plasma confinement. Figure 4 gives current traces and values of ⟨nT⟩, for unstabilized (curves 1) and stabilized (curves 2) regimes. A stabilizing effect was observed at an amplifier gain of $K_0 = 1.0$

An experiment was carried out where the stabilizing system was switched off after the peak current value had been reached (the moment of switch-off is indicated by an arrow in Fig.5). As a result, the plasma current drops to the unstabilized value. Thus, the stabilization system not only ensures passage of the instability development threshold, but also confines the plasma current in a new stable state, thus avoiding the development of dangerous instabilities.

A characteristic feature of all stabilization experiments was the fact that the stabilizing effect was only established on introducing a certain phase shift, $\Delta\varphi_\Sigma = \Delta\varphi_1(\omega) + \Delta\varphi_2$, into the feedback circuit, with the amplifier gains chosen correctly.

3.6. Stabilization of m = 1, n = 1 mode; $q \cong 1$

By further increase of the current, i.e. reduction of the safety factor q, the plasma current attained the maximum value for the given magnetic fields.

In this region of q, the experiments with the M = 1 feedback system have been carried out, showing that the M = 1 feedback system does not affect the discharge parameters in the parameter range where the m = 1 mode has to start. This situation may be due to a 'non-observable' m = 1, n = 1 mode at $q \cong 1$. It is not excluded either that we are dealing here with an internal mode and another principle of constructing the feedback stabilization system should be employed.

3.7. Plasma parameters in the stabilized regime

The experiments with feedback systems showed that plasma confinement was improved in the stabilized regime. The traces in Fig.4b show that in the stabilized regime a substantial growth of the plasma column energy content takes place; it increases with time up to the value where $\beta \cong 4 \times 10^{-4}$ is attained, which is close to the limiting equilibrium β for the R-0 device. Later on, the plasma column equilibrium is apparently violated, and, as a result, the current drops in the plasma and ⟨nT⟩ decreases.

The plasma density measured by using a microwave interferometer shows that the plasma density varies slightly during the discharge, amounting to a value of 1.0×10^{13} cm^{-3}.

The electron temperature in the plasma determined from the conductivity at $Z \cong 1.5$ is $T_e \cong 100$ eV, which is close to the temperature found from diamagnetic measurements on the assumption that the plasma temperature and density are distributed parabolically along the radius.

The improvement of plasma confinement is indicated by the rise of the plasma energy life-time up to 50 μs in the stabilized regime. For comparison, we note that this time must be 70 μs, according to the accepted scaling law for tokamaks.

3.8. Conclusions

Thus, experiments carried out to stabilize various m = 1, 2, 3; n = 1 kink instability modes, showed that the discharge parameters were improved on stabilizing the unstable mode dominant in the region given. Stabilization improves the plasma confinement and, thus, its energy content. Further experiments are required to study the possibility of stabilizing the m = 1 mode.

ACKNOWLEDGEMENTS

The authors wish to thank A.M. Abzyanidze for his assistance in carrying out the experiments and L.Ya. Malykh for measurements of the plasma density.

REFERENCES

[1] SIDOROV, V.P., SOLDATENKOV, T.R., Nucl. Fusion **12** (1972) 73.
[2] DEMIRKHANOV, R.A., KIROV, A.G., ZHARIKOV, V.N., MALYKH, N.I., RUCHKO, L.F., ZHDANOV, V.A., Pis'ma Zh. Ehksp. Teor. Fiz. **17** (1973) 397.
[3] DEMIRKHANOV, R.A., KIROV, A.G., IL'INSKIJ, S.E., MALYKH, N.I., ONISHCHENKO, V.V., in Controlled Fusion and Plasma Physics (Proc. 8th Europ. Conf. Prague, 1977) Vol. 1, Prague (1977) 156.
[4] DEMIRKHANOV, R.A., KIROV, A.G., LOZOVSKIJ, S.N., NEKRASOV, F.M., ELFIMOV, A.G., IL'INSKIJ, S.E., ONISHCHENKO, V.V., in Plasma Physics and Controlled Nuclear Fusion Research (Proc. 6th Int. Conf. Berchtesgaden, 1976) Vol.3, IAEA, Vienna (1977) 31.
[5] DEMIRKHANOV, R.A., KIROV, A.G., RUCHKO, L.F., SUKACHEV, A.V., MAJBUROV, V.B., NYUSHKOV, A.V., Pis'ma Zh. Ehksp. Teor. Fiz. **26** (1977) 89.
[6] ARTEMENKOV, L.I., IVANOV, N.V., KAKURIN, A.M., MUKHIN, P.A., POPKOV, L.N., CHUDNOVSKIJ, A.N., SHVINDT, N.N., GVOZDKOV, Yu.V., CHERKASHIN, M.Yu., Pis'ma Zh. Ehksp. Teor. Fiz. **27** (1978) 108.
[7] DEMIRKHANOV, R.A., KIROV, A.G., IL'INSKIJ, S.E., MAJBUROV, V.B., ONISHCHENKO, V.V., TARASEVICH, A.I., KADYSH, I.Ya., MALYKH, L.Ya., Preprint SFT1–3, Sukhumi (1976).
[8] ELFIMOV, A.G., NEKRASOV, F.M., LOZOVSKIJ, S.N., DOROKHOV, V.V., Preprint SFT1–2, Sukhumi (1976).
[9] KADOMTSEV, B.B., POGUTSE, O.P., Zh. Ehksp. Teor. Fiz. **65** (1973) 575.
[10] POGUTSE, O.P., YURCHENKO, F.P., Preprint ORNL/tr-4410, Oak Ridge (1977).
[11] CHANCE, M., GREENE, J.M., GRIMM, R.C., JOHNSON, J.L., Nucl. Fusion, **17** (1977) 65.

[12] KADOMTSEV, B.B., Fiz. Plazmy **1** (1975) 710.
[13] LADIKOV, Yu.P., SAMOILENKO, Yu.I., Zh. Tekh. Fiz. **42** (1972) 2062.
[14] MOROZOV, A.I., SOLOV'EV, L.S., Zh. Tekh. Fiz. **34** (1964) 1956.
[15] ARSENIN, V.V., At. Ehnerg. **33** (1972) 691.
[16] BOL, K., et al., in Plasma Physics and Controlled Nuclear Fusion Research (Pro. 5th Int. Conf. Tokyo, 1974) Vol. 1, IAEA, Vienna (1975) 83.
[17] DEMIRKHANOV, R.A., KIROV, A.G., RUCHKO, L.F., SUKACHEV, A.V., Preprint SFT1–4, Sukhumi (1976).

DISCUSSION

K. BOL: You showed us a figure indicating that when the feedback is turned off the plasma current drops in $\sim 5\ \mu s$. That implies very high plasma resistivity and I wonder whether, in such a situation, the theory for the helical modes which you described has any relevance.

K.N. STEPANOV: No special measurements were made in the course of this work to determine the nature of the instability that was being suppressed. Some of the observed oscillations, with frequencies around 500 kHz, were of the order of the MHD surface mode frequency, viz. $f \sim (1/2\pi a)\, CA_\varphi/\sqrt{4\pi\rho}$, so that one might expect the excitation of a non-resistive mode. It may be that the increase in plasma resistivity which accompanies the loss of stability will change our ideas on this subject.

Session J

OPEN SYSTEMS I

Chairman

F. ENGELMANN
Netherlands

2XIIB PLASMA CONFINEMENT EXPERIMENTS*

T.C. SIMONEN, J.F. CLAUSER, F.H. COENSGEN,
D.L. CORRELL, W.F. CUMMINS, R.P. DRAKE**,
J.H. FOOTE, A.H. FUTCH, R.K. GOODMAN,
D.P. GRUBB, A.L. HUNT, G. MELIN***,
A.W. MOLVIK, W.E. NEXSEN, B.W. STALLARD,
W.C. TURNER
Lawrence Livermore Laboratory, University of California,
Livermore, California,
United States of America

Abstract

2XIIB PLASMA CONFINEMENT EXPERIMENTS.

This paper discusses results of plasma confinement experiments in the 2XIIB magnetic mirror device. Experiments attempting to achieve field-reversal using neutral-beam injection in which the central magnetic field is reduced by 90% but field lines are not closed are reported. Experiments with different neutral-beam aiming show that at constant beta both electron temperature and the energy-confinement parameter ($n\tau$) increase at larger radius. Finally, recent improvements in electron temperature and microinstability measurements are discussed.

INTRODUCTION

At the previous International Atomic Energy Agency meeting we[1] reported results from the 2XIIB magnetic-mirror confinement experiment, which demonstrated that the drift-cyclotron loss-cone (DCLC) mode could be maintained in a quasilinear stable state, that plasma confinement improved with increasing mean ion energy, and that peak beta greater than unity could be achieved on axis. In the last two years we have conducted further experiments, improved plasma parameters, and made additional comparisons with theory. Our new work included field-reversal experiments, large-diameter plasma experiments, and investigations of DCLC stabilization and electron temperature associated with the field-reversed mirror[2] and the tandem mirror[3] configurations being developed as magnetic mirror reactor concepts.

The 2XIIB minimum-B yin-yang magnet set is normally operated at 0.67-T central field with a 2:1 mirror ratio. A schematic of 2XIIB is shown in Fig. 1. Up to 7 MW (500 A equivalent atom current) of neutral deuterium or 4 MW (380 A) of neutral hydrogen are injected by 12 Lawrence

* This work was performed under the auspices of the US Department of Energy under Contract No. W-7405-ENG-48.

** Johns Hopkins University.

*** On leave from Association Euratom-CEA, Grenoble, France.

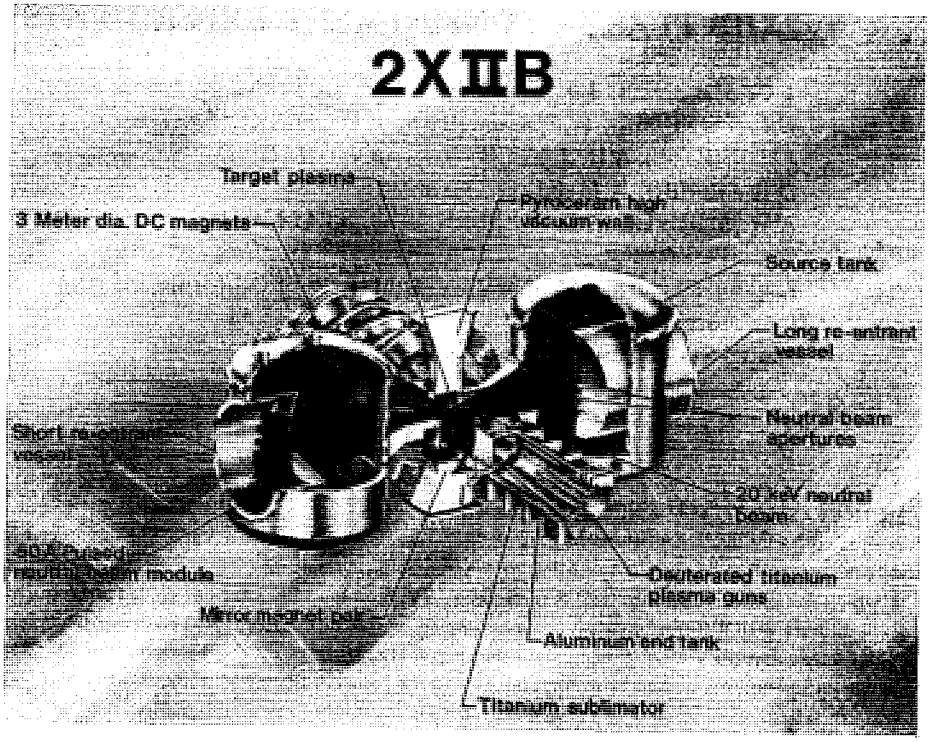


FIG. 1. The 2XIIB device used for plasma-confinement experiments at Lawrence Livermore Laboratory.

Berkeley Laboratory (LBL) 20-kV neutral-beam modules.[4] The plasma is stabilized by streaming plasma supplied either by deuterium (or hydrogen) plasma guns or by neutral gas injected near the mirror throat. The duration of the beams, streams and magnetic field is 10 ms.

FIELD REVERSAL EXPERIMENTS

Closure of magnetic field lines by plasma diamagnetic currents offers the possibility of substantial improvement in plasma confinement relative to open-ended magnetic mirrors. Such magnetic configurations have been created using relativistic electron beams,[5,6] reversed-field theta pinches,[7] and plasma guns.[8]

Our present field-reversal experiments were motivated by the unprecedented high betas achieved in earlier experiments. The largest reduction of vacuum magnetic-field strength was obtained using tangential neutral-beam aiming (Fig. 2a), which enhances the axis-encircling component of the ion diamagnetic current. We inferred a 90% depression of the on-axis magnetic field (field-reversal factor, $\Delta B/B = 0.9$) by approximately 100 kA of circulating ion current. In general beta increases with beam current. We expect further reduction in the magnetic field will result from

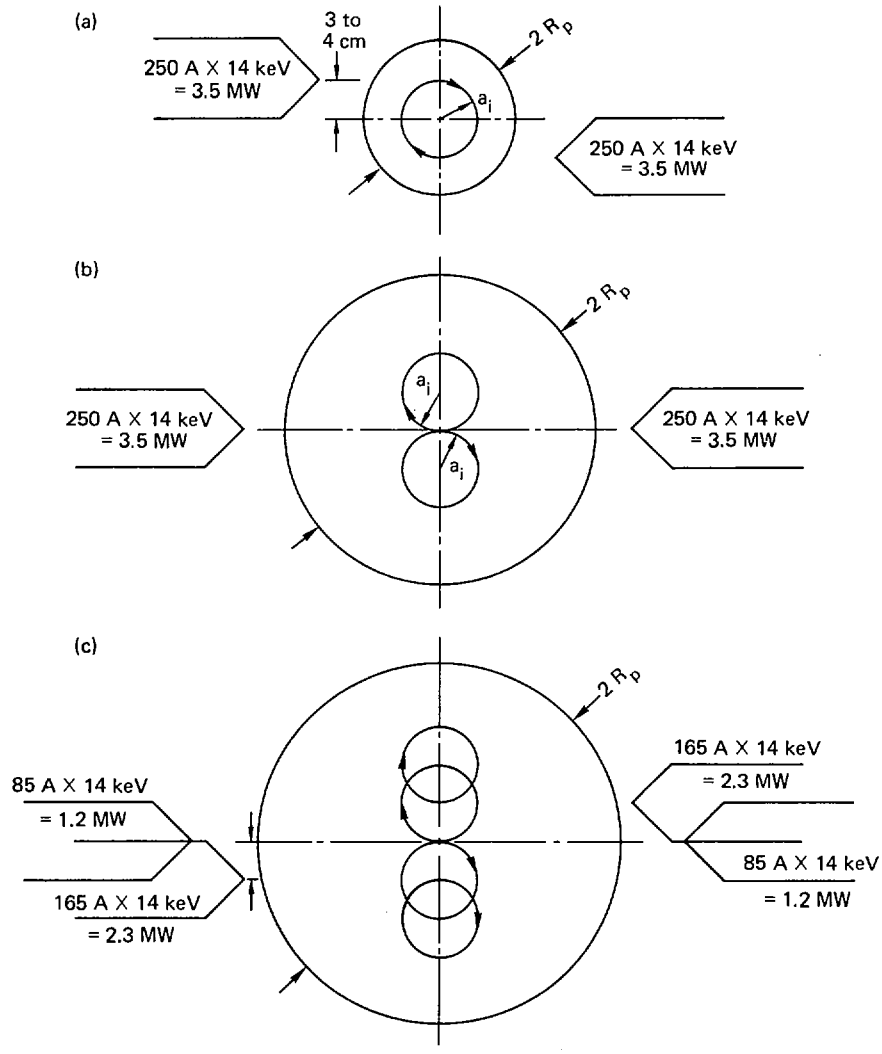


FIG. 2. Beam-aiming configurations shown to scale for (a) field-reversal experiments, (b) head-on injection experiments, and (c) large-diameter plasma experiments.

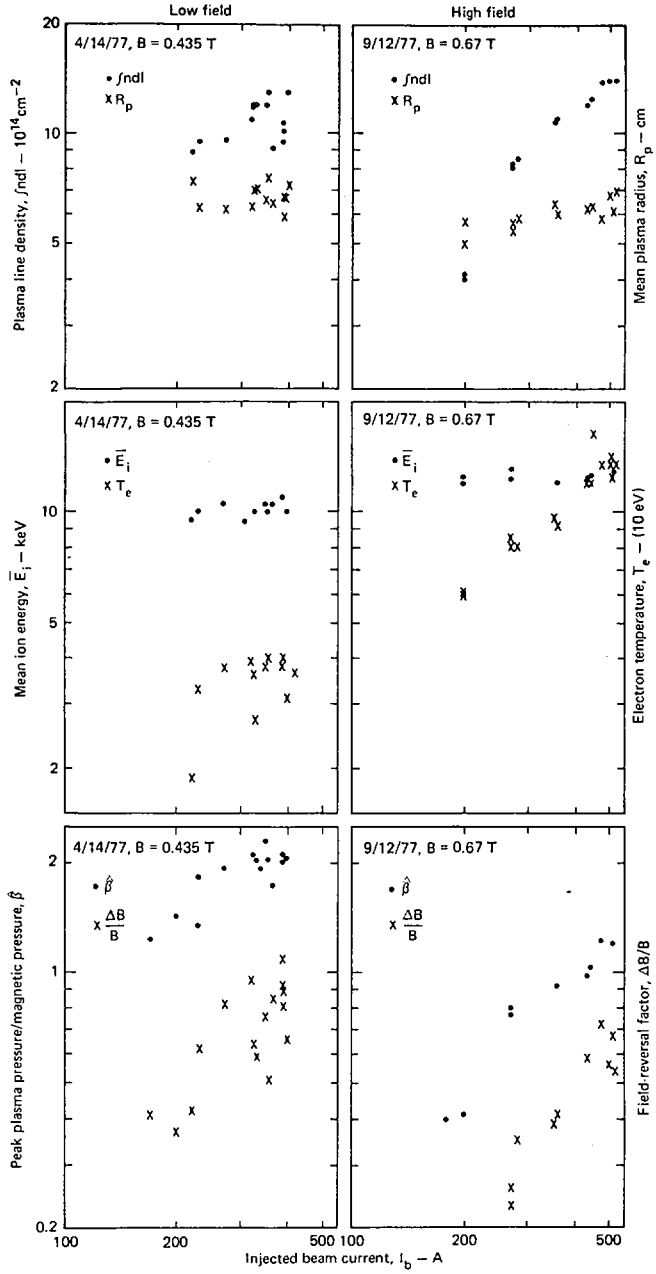


FIG. 3. Plasma parameters for field-reversal experiments for low- and high-magnetic field strengths as a function of incident neutral-beam current: (a) Line density and plasma radius; (b) mean ion energy and electron temperature; (c) peak beta and field-reversal factor, $\Delta B/B$.

more intense beam injection or better stabilization. Since electron currents tend to cancel the ion diamagnetic currents, we anticipate that a factor of three increase in neutral-beam current or ion lifetime is required to achieve a substantial volume of closed field lines.[9]

Field-reversal experiments were done at two values of vacuum field strength, B = 0.67 T (mirror ratio, R = 2.0) and B = 0.435T (R = 1.8), with the tangential beam-aiming arrangement in Fig. 2a. There were a number of differences in machine conditions between the low-and high-field experiments. Scaling of the measured plasma parameters as functions of injected neutral-beam current, I_b is shown in Figs. 3a and 3b for the two values of vacuum-field strength. Plasma line density increased with injected beam current. The mean plasma radius R_p and axial length L_p, defined as the 1/e point of the line-density profiles, was nearly independent of beam current (R_p = 6.5 cm and L_p = 16 cm). We obtained these measurements with a multichannel array of neutral-beam attenuation probes.

Electron temperature, T_e, measured by Thomson scattering, increased linearly to 140 eV with beam current for the high-field data (see Fig. 3b). The scatter of these T_e measurements for the low-field data was believed to be associated with the changing vacuum environment of the plasma. We obtained the mean ion-energy measurements in Fig. 3b with a 15-channel charge-exchange analyzer. For both experiments the mean ion energy was independent of beam current. The mean injected-atom energy for these experiments was estimated from the full-, half-, and third-energy fractions measured by the LBL group[4] and from the acceleration voltages, giving E_b = 14.1 keV (low field) and E_b = 13.3 keV (high field).

Figure 3c shows the plasma beta on axis, $\hat{\beta} = 8\pi \hat{n}_i \bar{W}_i / B_{vac}^2$, and the field-reversal parameter, defined to be the field change on axis, divided by the vacuum field

$$\frac{\Delta B}{B_{vac}} = \frac{1}{B_{vac}} \frac{\mu_o}{2\pi} \frac{M}{R_p^2 \left(R_p^2 + L_p^2\right)^{1/2}} \qquad (1)$$

The parameter M is the bulk plasma diamagnetic moment measured by a plasma-encircling loop. The relationship between the field change on axis and externally measured dipole moment is derived for a cylindrical current sheet with radius R_p and half-length L_p and is a good approximation to a rigid rotor with Gaussian current-profile $j_\phi = en(o)\Omega r \cdot \exp(-r^2/R_p^2 - z^2/L_p^2)$. The scale lengths R_p and L_p, taken from the line-density profiles, were cross-checked for the low-field data with an array of small magnetic-loop probes that are close to the plasma surface and that measure the shape of the plasma-current distribution.

Fig. 3c shows that $\hat{\beta}$ increases with I_b reaching $\hat{\beta} = 2.3$ for the low field and $\beta = 1.2$ for the high field. Since the plasma length is comparable to the diameter, $\hat{\beta} > 1$ does not imply field reversal. The effect of finite length and the resulting magnetic-field line curvature is included in Eq. 1. For the data at B_{vac} = 0.435 T, $\Delta B/B_{vac}$ increases approximately linearly with beam current, reaching an average value $\Delta B/B_{vac} = 0.9 \pm 0.2$ at I_b = 400 A. The data at B_{vac} = 0.67T increases with beam current, but reaches a lower value $\Delta B/B_{vac} = 0.6 \pm 0.1$ at I_b = 500 A.

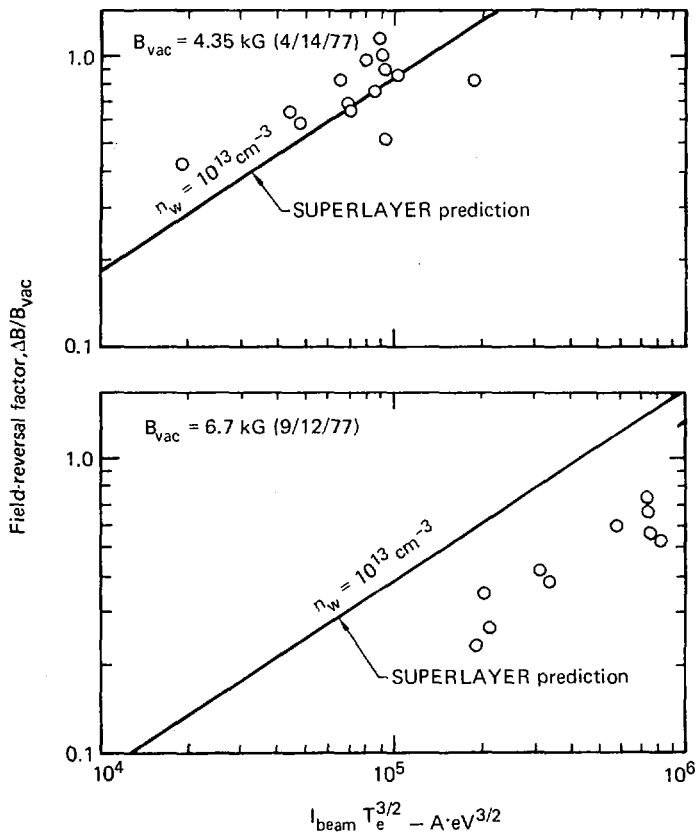


FIG. 4. Comparison of experimental data with SUPERLAYER particle-stimulation code.

Figure 4 compares experimental results with the "SUPERLAYER" particle-simulation code[9] for background stream density of 10^{13} cm^{-3}. The experimental data for B_{vac} = 0.435T are in reasonable agreement with the code predictions, since these experiments were more strongly dominated by electron drag, which is properly treated in the SUPERLAYER calculations. The high-field data is below the code predictions presumably because these experiments are more strongly dominated by DCLC - mode wave diffusion; which is included in SUPERLAYER as a time independent parameter which was adjusted to match the calculated mean ion energy to measured values.

In Fig. 5a we plot the ion-energy confinement parameter, $\hat{n}\tau_E$. The mean ion-energy lifetime, τ_E, is defined as the stored energy divided by the trapped neutral-beam power. According to quasilinear theory, $\hat{n}\tau_E$ should initially increase as $T_e^{3/2}$ since electron-drag losses decrease and saturates at a limit imposed by the increasing DCLC losses. To support this interpretation, we found that ion-cyclotron fluctuations increased above $T_e \approx 80$ eV where $\hat{n}\,\tau_E$ flattens. Further increases in $\hat{n}\tau_E$ require better stabilization, higher ion energy, or larger plasma radius.

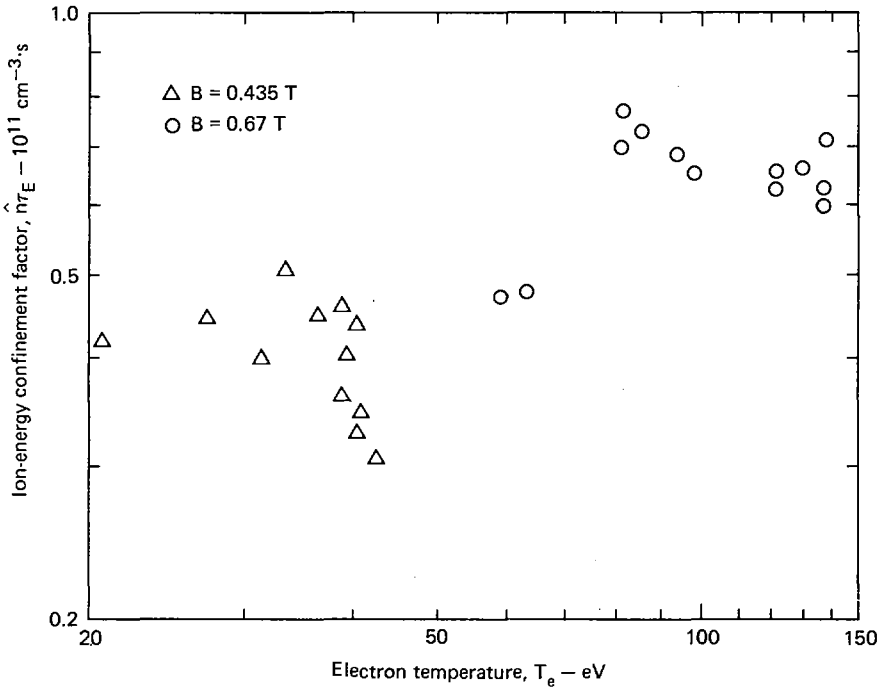


FIG. 5. Comparison of $\hat{n}\tau_E$ with electron temperature.

LARGE-RADIUS EXPERIMENTS

To maintain marginal stability of the DCLC mode in 2XIIB, it is necessary to supply a warm streaming plasma. Energy exchange with the electrons of this unconfined stabilizing plasma will reduce T_e and hence the energy-containment time of the mirror-trapped ions. The minimum warm-plasma density, n_w, that must be supplied is shown in Fig. 6. These calculations[10] are for $\beta = 0.5$; a hot-plasma energy $W_i = 1/2\ M_i v_H^2 = 15$ keV; a hole size $v_h/v_H = 0.1$; and a warm-stream energy of $v_w/v_H = 0.05$. Simply put, the larger the plasma size, R_p, compared with the ion Larmor radius, a_i, the smaller the fraction of warm to hot plasma necessary for DCLC stability.

To test the scaling of plasma parameters such as T_e and $\hat{n}\tau_E$ with R_p/a_i, we ran the 2XIIB experiment with the neutral-beam aiming configurations shown in Fig. 2. This resulted in changes of R_p/a_i from 2 to 6. The plasma size was determined by the measurements shown in Fig. 7.

When comparing results at various values of R_p/a_i, we restricted the data to those with Gaussian-shaped radial profiles with approximately the same beta (0.4). We introduced no beta or density corrections. Figure 8 shows that both T_e (averaged over several shots) and $\hat{n}\tau_E$ increase with larger values of R_p/a_i. The higher values of T_e and $\hat{n}\tau_E$,

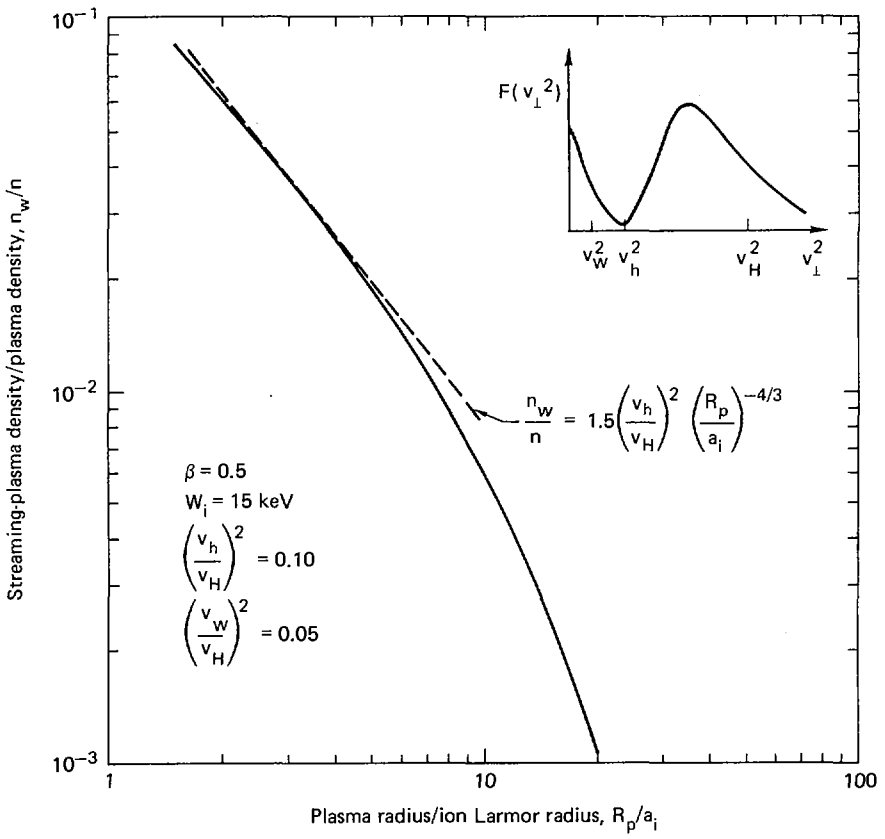


FIG. 6. Theoretical minimum-required stream density normalized to hot-ion density versus plasma radius for 2XIIB plasma parameters.

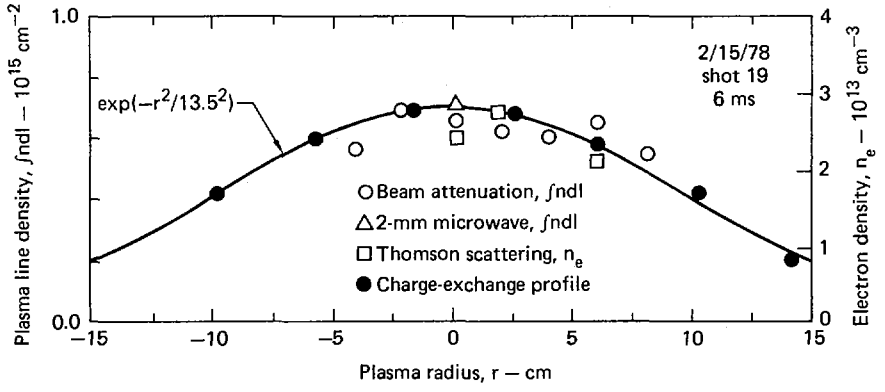


FIG. 7. Radial density-profile measurements of large-diameter 2XIIB plasma.

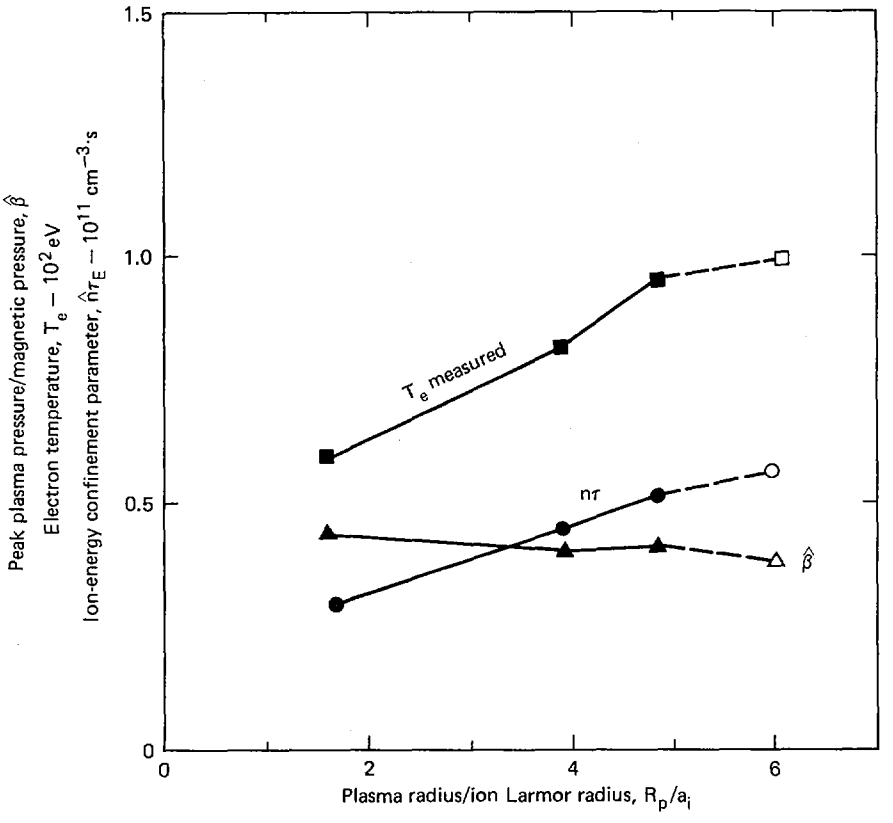


FIG.8. Electron temperature and $\hat{n}\tau_E$ scaling with R_p/a_i for constant beta. Solid data points depict deuterium; open points depict hydrogen.

discussed in the field-reversal section, were obtained at higher values of beta. These values were unattainable at the larger radii since the beam power had to fill a larger volume.

To compare the experimental results of Fig. 8 with the DCLC quasi-linear theory, we note that the experimental points lie in the domain of Fig. 6 where $n_w/n \propto (R_p/a_i)^{-4/3}$. The electron temperature has been calculated by equating the heating from ion-electron collisions to the electron power loss (which is assumed to be proportional to stream current times T_e). In this case $T_e \propto (R_p/a_i)^{1/3}$ and $\hat{n}\tau_E \propto T_e^{3/2} \propto (R_p/a_i)^{1/2}$. The measured electron temperatures have such an R_p/a_i dependence but are about 30% below the optimum theoretical value of T_e. One source of this difference is thought to be the poor energy-distribution match between the actual and optimum streaming plasma being supplied to the hot plasma.

DISCUSSION

In addition to the field-reversal and large-radius experiments discussed in previous sections we made a number of fundamental mirror physics measurements relating to DCLC-mode stabilization, DCLC-mode properties, and electron temperature.

Stabilization of the DCLC mode is studied by measuring the stream current with a gridded electrostatic analyzer. The stream current transmitted through the plasma varies during a shot to as low as the minimum value calculated[11] to stabilize the DCLC mode and follows the theoretical scaling with plasma density, ion energy, and electron temperature.

Frequency and azimuthal wavelength measurements of ion-cyclotron oscillations were found to have the characteristics of the DCLC mode[12] Radial rf profile mesurements were made with a multi-tip rf probe outside the mirror cell. This measurement revealed that the DCLC mode had a large radial extent and a single, narrow frequency peak that was the same at all radial positions. The frequency is near the beta-corrected ion-cyclotron frequency at the center.

We increased electron temperature to 140 eV by (a) relocation of streaming-plasma guns and gas-box baffles, (b) increased neutral-beam power, and (c) improvements in vacuum-wall surface conditions. These temperatures were well above those possible if classical thermal conduction is a dominant process. Langmuir-probe measurements external to the mirrors indicated a lower electron-temperature in the ends compared to the center and a rather complex axial temperature profile. A Monte Carlo electron code[13] was used to show that such profiles could be calculated.

In summary, field-reversal experiments reached field-reversal factors up to $\Delta B/B = 0.9$. The large-radius experiments demonstrated improved mirror confinement by size scaling.

Further progress on 2XIIB will rely on improving stabilization techniques that simultaneously increase electron temperature and reduce fluctuation losses. An electron-heating technique demonstrated by Ioffe[14] and at MIT[15] is being investigated on the more energetic 2XIIB plasma. The Tandem Mirror Experiment (TMX),[16] which will begin operation later this year, has provisions for additional and higher energy neutral-beams. TMX is expected to be better stabilized and to have higher electron temperature, since it is stabilized from the solenoid.

References

1 COENSGEN, F. H., et al., Plasma Physics and Controlled Nuclear Fusion Research (Proc. 6th Int. Conf. Berchtesgaden, Germany, 1976) 3, 135.

2 CARLSON, G. A., et al., IAEA Conf. and Workshop on Fusion Reactor Design, University of Wisconsin, 1977.

3 LOGAN, B. G., et al., "Tandem Mirror Reactors," IAEA-CN-37/R3, these proceedings.

4 BAKER, W. R., et al., Plasma Physics and Controlled Nuclear Fusion Research (Proc. 4th Int. Conf. Tokyo, 1974) 1, 329.

5 FLEISCHMAN, H. H., et al., "Recent results and work on field-reversing E and P Layers." Paper IAEA-CN-37/S4, these Proceedings.

6 ROBERSON, C.W., et al.,"Reversed Magnetic Fields Induced by a Rotating E-beam" Paper IAEA-CN-37/S4, these Proceedings.

7 LINFORD, R. K., et al.,"Field Reversal Experiments" Paper IAEA-CN-37/S1-1, these Proceedings.

8 ALFVEN, H., et al., J. Nucl. Energy, Part C, Plasma Phys. 1 (1960) 116,.

9 ANDERSON, D. V., et al., "Field Reversal in Mirror Machines," Paper IAEA-CN-37/S1-2, these Proceedings. The SUPERLAYER calculations in Fig. 4 are by R. P. Freis and W. C. Condit.

10 PEARLSTEIN, L.D., Lawrence Livermore Laboratory, private communication (1978).

11 BERK, H. L., et al., Plasma Physics and Controlled Nuclear Fusion Research (6th Int. Conf. Berchtesgaden, Germany, 1976) 3, 147.

12 TURNER, W. C., et al., Phys. Rev. Lett. 39 (1977) 1089.

13. ROGNLIEN, T. D., Lawrence Livermore Laboratory, private communication (1978).

14 IOFFE, M. S., et al., Zh. Ehsp. Tecr. Fiz. 67 (1974) 2145; also Sov. Phys. JETP 40 (1975) 1064.

15 KLINKOWSTEIN, R. E., SMULLIN, L. D., Phys. Rev. Lett. 40 (1978) 771.

16 BALDWIN, D. E., et al., "Studies of Tandem Mirror Confinement," IAEA-CN-37/J4, these Proceedings.

DISCUSSION

T. KAWABE: Have you made any direct measurement of potential in the mirror as a function of the electron temperature?

T.C. SIMONEN: No, but we have made measurements which indicate that the stream current transmitted through 2XIIB decreases as the electron temperature increases.

D.D. RYUTOV: Did you observe any high-frequency plasma activity in the large-radius experiment? And what is the amplitude of the ion-cyclotron oscillations?

T.C. SIMONEN: We have observed ion-cyclotron fluctuations; their amplitude is in the 50-V range.

RF PLUGGING OF LASER-PRODUCED PLASMA IN A CUSP FIELD

T. SATO, R. KUMAZAWA, K.N. SATO,
T. WATARI, S. OKAMURA, M. ICHIMURA,
S. HIDEKUMA, T. FUKAGAWA, T. AOKI,
T. KAWAMOTO, K. ADATI, S. HIROE,
H. OBAYASHI, T. HATORI, T. WATANABE,
K. TAKAYAMA
Institute of Plasma Physics,
Nagoya University,
Nagoya

S. OKADA, R. YOSHINO, H. SAITO,
S. SUDO, T. SEKIGUCHI
University of Tokyo,
Tokyo,
Japan

Abstract

RF PLUGGING OF LASER-PRODUCED PLASMA IN A CUSP FIELD.

The RF plugging scheme is applied to confine a laser-produced plasma from a polyethylene target in a spindle cusp field (TPD-III). All the cusp ends are plugged by RF fields, electrostatic mode at line cusp and electromagnetic mode at point cusps. Dependence of the plugging effect on the RF voltages (0–3 kV) and the frequencies (around the local ion cyclotron frequencies) is systematically investigated. Particle confinement time is directly obtained from the density decay at the centre of the confinement region. The RF plugs can evidently increase the particle confinement time by a factor of 5 (from 19 μs without RF to 95 μs with RF), for a plasma in the regime of density $6–3 \times 10^{13}$ cm^{-3} and ion temperature 35–15 eV. The application of RF fields results in a fourfold increase in ion temperature. Energy confinement time is also measured and a sizeable improvement is found for the RF plugged plasma.

1. INTRODUCTION

A series of experiments on radio-frequency plugging of plasma in a cusp or a mirror field has been carried out at IPP, Nagoya. Ion loss flux from the line cusp was remarkably reduced by an application of rf electric field in the line cusp region and a scaling relation for line cusp plugging was obtained in the plasma density range from 10^8 to 3×10^{12} cm^{-3} [1]. For

a mirror plugging, decrease of loss flux was observed when an rf electromagnetic field was applied to plasma at the mirror throat by type-III coil [2]. It was effective in the plasma density up to 10^{14} cm^{-3}. Since the plasma at the mirror throat has similar features to that at the point cusp, type-III coil is expected to be suitable for point cusp plugging as well.

In the previous experiment, plasma was injected into the confinement region along the magnetic field. The effectiveness of rf plugging has been evaluated by the relative ion loss flux which is defined as the ion loss flux with rf plug normalized by that without rf plug.

In this experiment, we confirm that the reduction of loss flux is equivalent to the improvement of the particle confinement time. The confinement time is measured directly. The plasma is produced instantaneously at the center of the cusp field by laser irradiation. All the cusp ends are plugged, in contrast to the previous experiments.

2. EXPERIMENTAL SETUP

This experiment is carried out on TPD-III (Fig.1). The cusp magnetic field is adopted. The distances between the null point of the cusp field and the positions of maximum magnetic field are 25 cm for the line cusp and 37 cm for the point cusp, and the magnetic field strengths for them are 3.2 kG and 7.7 kG, respectively. The base pressure in the confinement region is less than 3×10^{-6} torr.

The plasma is produced at the null point of the cusp field by glass laser irradiation (50-70 J, 20 ns, focus spot size of 500 μm) of a fixed polyethylene target, 50 μm in diameter. The target is sustained by a glass stem. The plasma loss to the stem is experimentally confirmed to be negligible by measuring the decay time with an additional stem. Plasma parameters are obtained by a 70-GHz microwave interferometer, double probes, diamagnetic loops, a monochromator and multi-grid energy analysers,

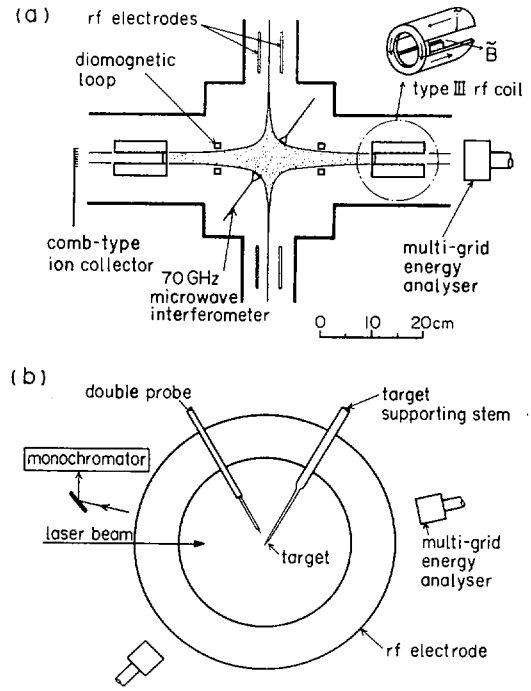


FIG.1. Schematic drawings of TPD-III and diagnostic tools.
(a) Side view. A type-III RF coil is set at each point cusp and RF electrodes are set up at the line cusp. (b) Front view.

installed as shown in Fig.1. Plasma diameter is measured by an 8-channel comb-type ion collector placed just outside the point cusp. Plasma loss fluxes from the line and the point cusps are observed by the multi-grid energy analysers.

The rf electrodes, a pair of parallel plates which have outer diameter 50 cm and inner diameter 34 cm, are set at the line cusp with a separation of 4 cm. A type-Ⅲ coil which has inner diameter of 5 cm and length of 10 cm is placed for each point cusp.

The rf oscillator for the line cusp plug has an output power of 100 kW with 2 ms duration. The frequency can be varied from 4.7 MHz to 7.5 MHz and is higher than the local ion cyclotron frequency of hydrogen, ω_c^L,

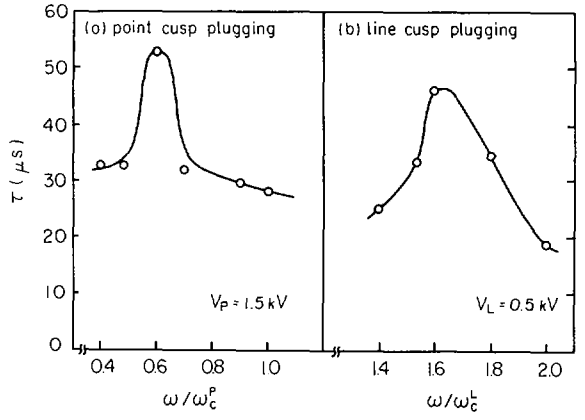


FIG.2. Frequency dependences of particle confinement time: (a) for point cusp plugging of $V_P = 1.5$ kV and $V_L = 0$; (b) for line cusp plugging of $V_L = 0.5$ kV and $V_P = 0$.

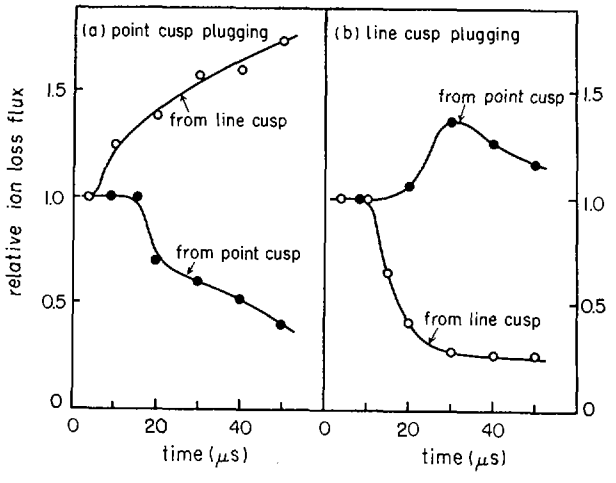


FIG.3. Time variations of relative ion loss flux to line and point cusps: (a) for point cusp plugging of $V_P = 2.2$ kV and $V_L = 0$; (b) for line cusp plugging of $V_L = 1.4$ kV and $V_P = 0$.

under the electrodes. The rf power for two type-III coils is fed from a 500-kW rf oscillator, the frequency of which is fixed at 6.25 MHz and is lower than the local ion cyclotron frequency of hydrogen, ω_c^P. Since a polyethylene target is used, the plasma is composed of hydrogen and carbon ions. We tune rf frequency to near the ion cyclotron frequency of hydrogen. The interaction between rf field and carbon ions is probably small [3].

3. EXPERIMENTAL RESULTS

After laser irradiation, the plasma expands, fills up the cusp field within a microsecond and escapes gradually through the cusp ends. Attention is paid to this escaping stage. The typical plasma parameters from 5 μs to 20 μs after the laser irradiation with no rf field are: the electron density n_o = (6-3) × 10^{13} cm^{-3}, the ion temperature T_{io} = 35-15 eV, the electron temperature T_{eo} = 15-6 eV, the particle confinement time τ_o = 20 μs and the energy confinement time τ_{Eo} = 2.5-13 μs. Particle confinement time is determined by the density decay measured at the confinement region and energy confinement time by the variation of the diamagnetic signal.

For the point cusp plugging, particle confinement time, τ, is measured as a function of the magnetic field strength with a fixed frequency, $\omega/2\pi$ = 6.25 MHz, with no application of line cusp plugging. The optimum value of ω/ω_c^P is determined to be 0.6 when the applied rf voltage to type-III coils, V_p, is 1.5 kV as shown in Fig.2(a). For the line cusp plugging, τ is measured for various rf frequencies with a fixed magnetic field strength. As shown in Fig.2(b), the optimum frequency is 1.6 ω_c^L under the condition of constant rf voltage (V_L = 0.5 kV). These features agree with the previous experimental results [1,2].

Figure 3(a) shows the loss fluxes through the line and the point cusp when the rf field is applied only to the point cusp. The decrease in the point cusp loss and the increase in the line cusp loss are observed, reproducing the results obtained previously [1,2]. Similarly Fig.3(b) shows the loss fluxes when the rf field is applied only to the line cusp. The decrease in the line cusp loss and the increase in the point cusp loss are observed. Based on these results, we now apply the rf fields to all the cusp ends with their optimum frequencies given in Fig.2(a) and (b). The time variations of the plasma density with and without rf field are

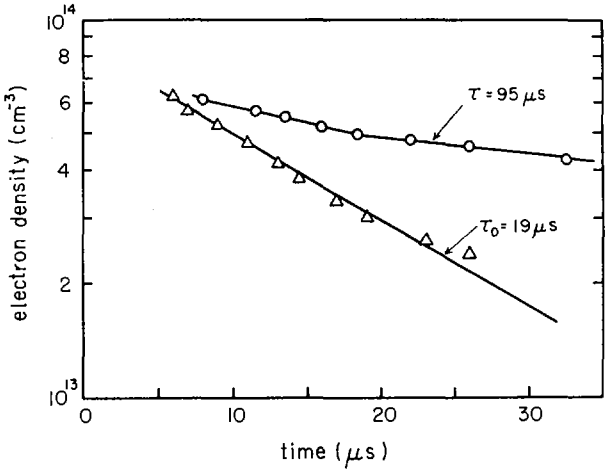


FIG.4. Time variations of the electron density in the case of $V_P = V_L = 3$ kV (○) and without RF plugging (△).

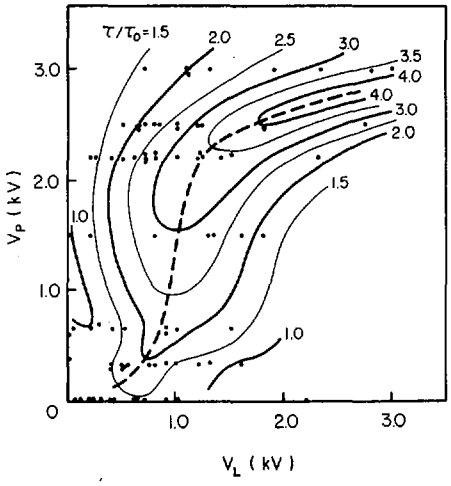


FIG.5. Contour map of τ/τ_0 in V_P-V_L plane: the broken line indicates that the ridge and dots are the measuring points.

shown in Fig.4. The particle confinement time, τ, is 95 μs with rf field, while it is 19 μs without rf field. This improvement in particle confinement is brought about with rf field tuned for hydrogen ions. Considering that carbon ions are left free from rf field, the plugging of hydrogen ions is possibly more effective.

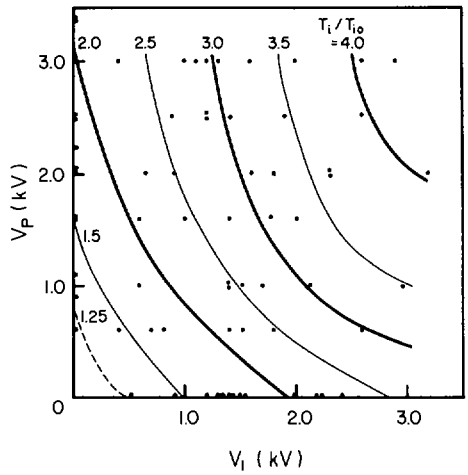


FIG.6. Contour map of T_i/T_{i0} in V_P-V_L plane: dots are the measuring points.

The confinement time is a function of V_P and V_L. The contour lines of τ/τ_o in V_P-V_L plane are shown in Fig.5. It can be read from this figure that, increasing V_P and V_L along the broken line, we will have a higher value of τ/τ_o. If V_L is increased with constant V_P, the value τ/τ_o passes its peak and decreases, and if V_P is increased with constant V_L, the same situation occurs. The decrease of τ/τ_o by unbalanced increases of V_P or V_L is due to ion heating by rf field; it is known that rf plugging is accompanied by ion heating [1,2]. The ion temperature is actually observed and found to be a monotonic increasing function of V_P and V_L. Figure 6 shows the contour map of T_i/T_{io} in V_P-V_L plane. When V_P = 3 kV and V_L = 3 kV, the ion temperature is found to be four times higher than that without rf field.

Figure 7(a) shows the decay curves of the signal of the diamagnetic loop with and without rf field. The slow decay when the rf field is applied represents partly the improvement of energy confinement and partly

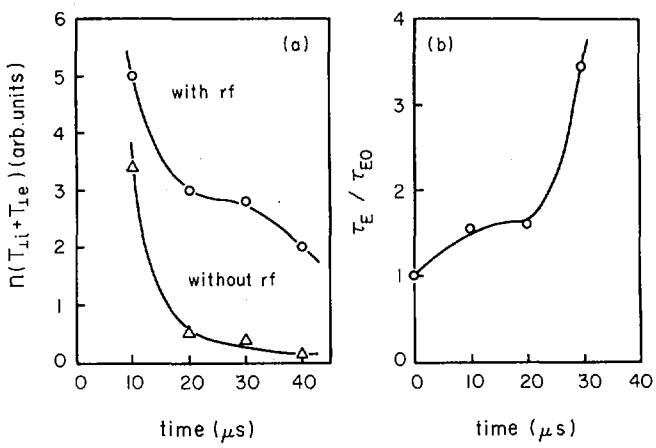


FIG.7. (a) Decay curves of the diamagnetic signal with (○) and without (△) RF plugging. (b) Time variation of the energy confinement time with RF plugging normalized by that without RF plugging.

the heating of the plasma. We separate these effects and estimate the energy confinement time τ_E by following equations:

$$\tau_E = \frac{\varepsilon}{Q - d\varepsilon/dt} \tag{1}$$

with

$$\varepsilon = \int n(T_e + T_i)dV \tag{2}$$

where ε is the total energy of the plasma confined in the cusp field and Q is the rf power fed into the plasma. We calculate Eq.(2) from the data of the diamagnetic loop and the density profile measured with the double probe. We measure Q with a directional coupler, subtracting the reflected power from the incident power. Substituting these values into Eq.(1), we get the energy confinement time at each moment [see Fig.7(b)]. We conclude from this figure the energy confinement time is improved, as well as the particle confinement time, by the application of the rf field.

4. DISCUSSION AND CONCLUSION

It is verified that the reduction of loss flux through the cusp ends gives an increase of confinement time in a plasma produced at the null point of the cusp by laser irradiation. By application of rf field to all the cusp ends, τ/τ_o becomes five for a plasma whose density is 5×10^{13} cm^{-3}. The rf plugging is accompanied by ion heating: ion temperature of 15 eV is raised up to 60 eV by rf fields of 3 kV. The particle confinement time in a cusp field is inversely proportional to the ion temperature. If this effect is taken into account, the present result may be equivalent to an increase in τ/τ_o by a factor of twenty. The energy confinement time of the rf plugged plasma is measured and it is found also to be improved by rf plugging. The directly measured value of τ/τ_o agrees with that derived from the measured loss flux reduction. Longer confinement time is obtained by increasing the rf field, where the rf field strength at the line and the point cusp must have a certain relation in order to keep a balance between the plugging effect and the heating effect.

The RFC-XX device, which is three times as large as the present TPD-III in linear dimension and equipped with line cusp field of 20 kG and 1 MW rf oscillators, has been constructed. It is expected to give much longer confinement time and to make clear the relation between rf plugging and rf heating.

ACKNOWLEDGEMENT

The authors wish to thank S. Fujiwaka for the design of the target supporting system.

REFERENCES

[1] HIROE, S., et al., Plasma Physics and Controlled Nuclear Fusion Research 1976 (Proc. 6th Int. Conf. Berchtesgaden, 1976) Vol.3, IAEA, Vienna (1977) 427.

[2] WATARI, T., et al., Controlled Fusion and Plasma Physics (Proc. 8th Europ. Conf. Prague, 1977) Vol.1 (1977) 103.

[3] HIDEKUMA, S., et al., Phys. Rev. Lett. 33 (1974) 1537.

DISCUSSION

D.E. BALDWIN: You quoted densities of 5×10^{13} cm^{-3}. Did these occur at the field null or under the cusps? And how great was the density decrease from the centre to the cusp region?

T. SATO: We measured the electron density in the field null region. In the cusp region the density decreases to 10% of that at the field null point.

B.C. GREGORY: I have three questions concerning the power flow from the RF power supplies to the plasma. First, how much power is absorbed by the plasma?

T. SATO: The RF power input to the plasma is 5 to 10 kW.

B.C. GREGORY: And does it all couple into ion heating?

T. SATO: Yes, virtually all the RF power is absorbed by the ions.

B.C. GREGORY: The RF voltages are high, so I wonder whether you have noticed local arcs or discharges in the RF electrode region. Or is the magnetic field insulation adequate for the voltages you apply?

T. SATO: There is no local arc in the RF plug region. We have occasionally observed an RF discharge which produces little increase in density. However, there are no serious problems in the application of the RF fields.

TRANSVERSE PARTICLE LOSSES IN AXIALLY ASYMMETRICAL OPEN TRAPS

M.E. KISHINEVSKIJ, P.B. LYSYANSKIJ, D.D. RYUTOV,
G.V. STUPAKOV, B.M. FOMEL', B.V. CHIRIKOV,
G.I. SHUL'ZHENKO
Institute of Nuclear Physics,
Novosibirsk, Union of Soviet Socialist Republics

Abstract

TRANSVERSE PARTICLE LOSSES IN AXIALLY ASYMMETRICAL OPEN TRAPS.

The effect of axial asymmetry of the magnetic field on transverse plasma losses from traps with improved longitudinal confinement is discussed in this paper. The role of these losses is characterized by the angle of rotation $\Delta\psi$ of the guiding centre of the particle around the magnetic axis during motion of the particle from mirror to mirror. The transport regimes are classified as a function of the angle $\Delta\psi$. Corresponding analytical estimates of the transport coefficients are presented. – A stochastic instability leading to collisionless diffusion due to field perturbation as a result of slight misalignments in the magnetic system was studied experimentally in terms of a specially constructed electron model in which the electrons moved in longitudinal magnetic and radial electric fields. – Resonance and stochastic diffusion were also investigated numerically in terms of a special model. The numerical results are in satisfactory agreement with simple analytical estimates for the instability boundary and diffusion rate under the joint effects of resonances and multiple scattering.

1. INTRODUCTION

The recently proposed multi-mirror [1] and ambipolar [2] traps as well as traps with reverse magnetic field [3] permit a reduction of particle losses along the magnetic field and a significant increase in the plasma life-time compared to the ion scattering time. Consideration of transverse plasma losses from the trap may be significant in this case. The possible effect of an axial magnetic-field asymmetry on these losses is discussed in the paper (it is proposed that an asymmetrical field be used to provide MHD-stability in some variants of the devices mentioned above (see Fig. 1).

We shall assume that the electric and magnetic fields are static and vary smoothly in space, which allows us to regard the total energy $\mathcal{E}$ and the magnetic moment μ of the particle as conserved quantities.

As was noted in Ref. [4], an important parameter characterizing the particle motion in the devices in question is the torsion angle $\Delta\psi$ of the particle around the magnetic axis of the system during motion from mirror to mirror, $\Delta\psi = \pi\Omega/\Omega_{\parallel}$,

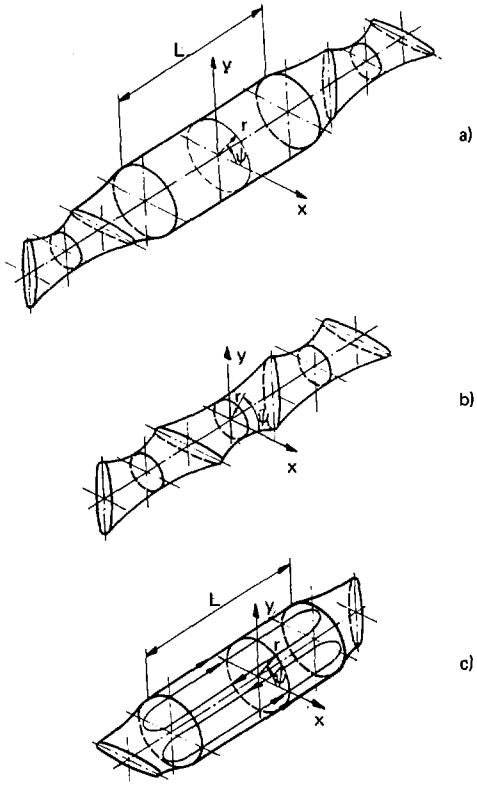


FIG. 1. Magnetic-field configuration in devices with improved longitudinal confinement: a) ambipolar trap; the characteristic feature of this system is in the presence of a long axially symmetric section in the central mirror system; b) fragment of multi-mirror trap with axially asymmetric field improving MHD plasma stability; c) trap with reversed field; since the region with closed magnetic surfaces is "submerged" in the axially asymmetric field, the magnetic field in this region has no axial symmetry either, in general.

where Ω and $\Omega_{\parallel}$ are the azimuthal drift and the longitudinal oscillation frequencies, respectively.

The longitudinal invariant I is also conserved for $\Delta\psi \ll 1$, in addition to $\mathcal{E}$ and μ. If $\mathcal{E}$ and μ and the initial position of the particle are given, the condition I = const determines the drift envelope described by the particle trajectory.

The drift envelope may be characterized unambiguously by the shape of its cross-section in the equatorial plane of the trap (Fig. 1). Introducing a polar co-ordinate system r, ψ in this plane, we may write $I = I(\mathcal{E}, \mu, r, \psi)$.

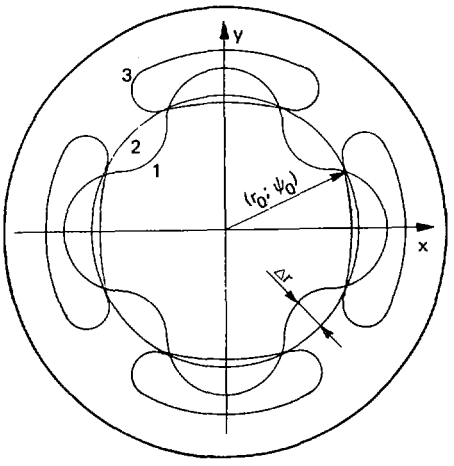


FIG.2. Cross-section of drift surfaces in equatorial plane of trap for particles starting at point r_0, ψ_0 with different values of & and μ. Trajectories 1 and 2 correspond to transient particles and trajectory 3 to a trapped particle.

It is essential that the drift envelopes are, in general, different (Fig. 2) for particles with different values of & and μ, starting at the same point (r_0, ψ_0). This peculiarity, which is typical for axially asymmetrical systems, may be a source of increased transverse plasma losses from the trap. In fact, since the parameters & and μ vary owing to particle collisions, the particle may jump from one drift envelope to another and finally impinge on the chamber wall. Since the divergence Δr of the drift envelopes (Fig. 2) may be much greater than the Larmor radius, these losses may be much greater than classical. The situation is similar here to that prevailing in neoclassical transport mechanisms in toroidal systems [5]. However, unlike the latter, the absence of an additional additive integral of motion makes diffusion possible owing to collisions of particles of the same kind. In this case, electron diffusion is faster than ion diffusion in view of the higher collision frequency in most practically interesting cases. From the condition of quasi-neutrality, this means that plasma losses are actually determined by the slower ion diffusion. Therefore, we shall be talking particularly about ions throughout the paper. A summary of the results of the theory for the case when $\Delta\psi \ll 1$ is presented in Section 2.

Let us now turn to the situation with $\Delta\psi \gtrsim 1$, typical for long traps. In this case, I is no longer an integral of motion, but diffusion is mainly determined by "resonance" particles for which $\Delta\psi/\pi = \Omega/\Omega_\parallel = \ell/k$, where ℓ and k are natural numbers. These particles undergo the greatest radial displacements. Diffusion

of resonance particles along the radius occurs as a result of collisions in this case (similar to neoclassical diffusion discussed above). The corresponding calculations are presented in Section 3. A simple homogeneous model of resonance diffusion is described in Section 4, and the results of numerical experiments with this model are presented.

An overlap of resonances and a stochastic instability of motion leading to radial diffusion even with total absence of collisions (see, e.g. Ref. [6]), occur at still higher values of $\Delta\psi$ when the amplitude of radial displacements of the resonance particle exceeds the distance between adjacent resonances. Finally, experiments on transverse diffusion in this mode, conducted on the electron model, are described in Section 5.

Let us point out in concluding this section what values of $\Delta\psi$ are typical for different traps. In ordinary short traps and in the case of a multi-mirror trap, $\Delta\psi \ll 1$. In long traps with reverse field and in the central mirror system of an ambipolar trap, $\Delta\psi \gtrsim 1$ for ions, $\Delta\psi \ll 1$ for electrons, and $\Delta\psi \gg 1$ for alpha-particles.

2. NEOCLASSICAL DIFFUSION

In this section, a qualitative classification of different diffusion regimes for $\Delta\psi \ll 1$ is presented. Detailed calculations may be found in [7].

Let us introduce

$$I_0(\mathcal{E}, \mu, r) = (1/2\pi) \int_0^{2\pi} I(\mathcal{E}, \mu, r, \psi)\, d\psi \equiv \langle I \rangle \tag{1}$$

and let us assume that $I = I_0 + \delta I$, where, obviously, $\langle \delta I \rangle = 0$. The quality of the trap with respect to the effect indicated above is determined by the parameter $\alpha \equiv \delta I / I_0$. In traps with improved longitudinal confinement, there should obviously be $\alpha \ll 1$ (otherwise, there would be $\Delta r \sim R$, and the plasma life-time could not exceed the ion scattering time τ_i).

The condition of conservation of I permits us to find the shape of the drift surface cross-section in the equatorial plane of the trap, $r(\psi, \mathcal{E}, \mu)$ (the particle trajectory in the r, ψ plane). By using the smallness of δI, it is easy to find

$$r(\psi, \mathcal{E}, \mu) = r_* - \frac{\delta I}{(\partial I_0/\partial r)|_{r=r_*}}, \quad r_* \equiv \langle r \rangle \tag{2}$$

The typical trajectories described by this equation are shown in Fig. 2 (curves 1 and 2); they are closed, bypassing the magnetic axis of the system (the particles moving along these trajectories will be called transient particles below). The order of magnitude of the 'range' occupied by the drift surface, $\delta r = r_{max} - r_{min}$, is equal to αR.

Formula (1) becomes invalid when the derivative $\partial I_0/\partial r$ vanishes. For these particles, finding the shape of the trajectories in the r, ψ plane requires expansion of I_0 in the deviation $r - \langle r \rangle$, with an accuracy of up to second-order terms of smallness. As it turns out, banana-shaped trajectories localized on one side of the system axis appear in this case (the corresponding particles are called trapped below). The typical 'range' of the banana trajectories is $\delta r_{ban} \sim \alpha^{1/2} R$. If the period of transient-particle motion is denoted by τ_d (the drift time around the axis of the system), the period of motion along the trajectory for trapped particles is $\tau_{ban} \sim \alpha^{-1/2} \tau_d$.

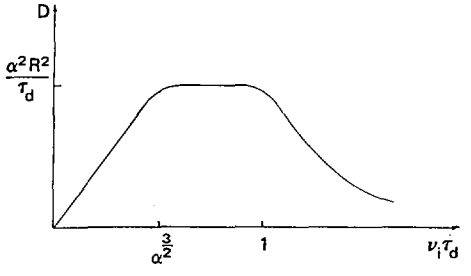


FIG.3. Dependence of diffusion coefficient D on ion collision frequency in neoclassical regime.

Although the fraction of trapped particles is small (of the order of $\alpha^{1/2}$) it is these particles that determine the rate of transport under certain conditions. The situation here is similar to that described by the neoclassical theory of transport processes in toroidal systems [5][1] Specifically, if the effective frequency of collisions, $\nu_i \alpha^{-1}$, which transform trapped particles into transient ones, is small compared to τ_{ban}^{-1}, the analogue of a 'banana' regime with a diffusion coefficient D proportional to the collision frequency (Fig.3) appears. At higher values of ν_i, the diffusion coefficient is independent of ν_i (plateau regime) and, finally, at $\nu_i > \tau_d^{-1}$, a regime is realized in which trapped particles are irrelevant. The diffusion coefficient drops as ν_i^{-1}, in this case. Also possible is a case where $\partial I_0/\partial r$ does not vanish anywhere and there are no trapped particles in the trap.

[1] Similar effects were discussed in Ref. [8] for a system of toroidally connected mirrors.

Then, at $\nu_i < \tau_d^{-1}$, a regime is established in which diffusion is determined by the transient particles. This regime is called that of rotational diffusion in Ref.[7].

3. RESONANCE DIFFUSION

In the case of $\Delta\psi \gtrsim 1$, the particle motion in the trap may be investigated by considering the passage of the particle through the equatorial plane of the trap. The law of motion is then given by the transformation relating the polar co-ordinates $\bar{r}$, $\bar{\psi}$ to their values r, ψ in the preceding step. The radial displacement of the particle, $\Delta = \bar{r} - r$, is determined by drifts in the asymmetrical mirror and is a function of the co-ordinates r, ψ and the parameters $\mathcal{E}$, μ. It turns out that the expression $\Delta = a(r, \mathcal{E}, \mu)\cos 2\tilde{\psi}$, where $\tilde{\psi}$ denotes the azimuthal angle of flight into the mirror, calculated from its plane of symmetry, is valid for Δ near the axis of the trap. Taking into account that opposite mirrors are rotated by 90°, we can easily write down the desired transformations relating $\bar{r}$, $\bar{\psi}$ and r, ψ [9]. It is convenient, in this case, to fix each second particle transit through the equatorial plane:

$$F = r + a\cos 2\left(\psi + \frac{1}{2}\Delta\psi\right) - a\cos 2\left(\psi + \frac{3}{2}\Delta\psi\right), \quad \bar{\psi} = \psi + 2\Delta\psi \tag{3}$$

For the bulk of the particles, the magnitude of the radial displacements described by transformations (3) is, by order of magnitude, equal to a. An exception are those particles for which the value of $\Delta\psi(r, \mathcal{E}, \mu)$ is close to $k\pi/2$, where k assumes odd values, $k = 1, 3, 5 \ldots$ On the assumption that $|\Delta\psi - k\pi/2| \ll 1$, double use of transformation (3) leads both to small variations in r and to small variations in ψ (with an accuracy of up to the insignificant term $2k\pi$). Therefore, we may turn from discrete transformations to differential equations for velocities $\dot{r}$, $\dot{\psi}$:

$$\dot{r} = \frac{a(r_k, \mathcal{E}, \mu)}{t_\parallel}(-1)^{\frac{k+1}{2}} \sin 2\psi, \quad \dot{\psi} = \frac{r - r_k}{t_\parallel}\psi'(r_k, \mathcal{E}, \mu) \tag{4}$$

where $t_\parallel$ is the time of flight of the particle through the trap, $r_k = r_k(\mathcal{E}, \mu)$ is the resonance radius determined from the equation $\Delta\psi(r_k, \mathcal{E}, \mu) = k\pi/2$ and $\psi' \equiv \partial\Delta\psi/\partial r$. Equations (4) can be integrated elementarily and yield the shape of particle trajectories in the r, ψ plane. Specifically, banana-shaped trajectories and trajectories bypassing the magnetic axis of the system are again found here. The characteristic magnitude of the radial displacements of the resonance particles is equal to $|a/\psi'|^{1/2}$.

The well known law of motion of the resonance particles allows us to write down a kinetic equation describing the evolution of their distribution function. Solving it, we can calculate the transport coefficients in the resonance regime [9]. The qualitative dependence of the diffusion coefficient on ν_i is presented in Fig. 4. Here, we can again distinguish a resonance banana regime with linear dependence of D on ν_i and a plateau regime.

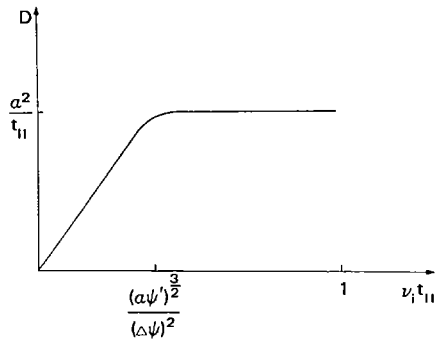


FIG. 4. Dependence of diffusion coefficient D on ion collision frequency in resonance regime.

As can be seen from Fig. 4, the maximum diffusion coefficient is reached in the plateau region in the resonance regime. We present an expression for it here, obtained under some simplifying assumptions, i.e. it was assumed in the derivation that the azimuthal drift is only caused by the electric field; a collision term for scattering from fixed Coulomb centres was used and the particle distribution function was taken to be proportional to $\delta(v - v_0)$:

$$D = \frac{\pi}{4L^2 \Omega v_0} \sum_k a^2 \left(\frac{2L\Omega}{k\pi}\right)^3 \qquad (5)$$

Here v_0 is the particle velocity, $\Omega = cE/Br$ is the angular drift velocity, the resonance value of μ is determined from the condition $\mu = (mv_0^2/2B) \times [1 - (2L\Omega/k\pi v_0)^2]$, and the value of displacement a is calculated for a particle with a resonance value of μ. The summation is carried out over odd values of k higher than $2L\Omega/\pi v_0$.

4. THE HOMOGENEOUS MODE OF RESONANCE DIFFUSION

Let us consider another method of estimating the transverse diffusion coefficient in a trap, in which the particle motion may approximately be described

by a transformation of type (3). Let us first note that it may be re-written in the form:

$$\bar{r} = r + a\cos 2\tilde{\psi};\ \bar{\tilde{\psi}} = \tilde{\psi} + \Delta\psi + \frac{\pi}{2} \tag{6}$$

where the azimuthal angle of flight into the mirror, $\tilde{\psi}$, is calculated from the plane of symmetry of each of the mirrors rotated with respect to each other through an angle $\pi/2$ (see Section 3). We shall now linearize this transformation in r in the neighbourhood of the resonance value of $r = r_k$ and take into account, also in the linear approximation, the random variations in $\Delta\psi$ and also in $\tilde{\psi}$ due to multiple scattering. As a result, we find the transformation:

$$\bar{q} = q + \frac{\xi}{\sqrt{\tau}};\ \bar{p} = p + K\cos\phi;\ \bar{\phi} = \phi + \bar{p} + \bar{q} \tag{7}$$

where $\phi = 2\tilde{\psi}$; $p = 2(r - r_k)(\partial\Delta\psi/\partial r)$; ξ is a random variable with $\langle\xi\rangle = 0$; $\langle\xi^2\rangle = 1$; τ is the number of flights during which the mean square variation of the phase ϕ due to scattering is equal to one, and $K = 2a(\partial\Delta\psi/\partial r)$ is a resonance overlap parameter [6, 10].

The homogeneous model (7) describes the diffusion process locally in a small neighbourhood, $\Delta r \ll r$; $\Delta v \ll v$; and $\Delta\theta \ll 1$. The average (over p) resonance diffusion coefficient of the system (7) satisfies the scale relation $\langle D\rangle/K^2 = f(s)$ for $K \ll 1$ and $\tau \gg 1$ and is described by the expression

$$\langle D\rangle \equiv \frac{\langle(\Delta p)^2\rangle}{N} = \frac{K^2/2}{1 + \pi^2 S^2/8};\ S = K^{3/4}\sqrt{\tau} \tag{8}$$

where N is the number of iterations (time of motion). $\langle D\rangle$ may be calculated analytically in both limits ($S \gg 1$ and $S \ll 1$). For $S \gg 1$, the resonance particles (inside the resonance separatrix) diffuse together with the resonance: $p_k = 2\pi k - q$ (see relations (7)) (banana diffusion regime). For $S \ll 1$, the diffusion rate reaches a maximum value of $D_{pl} = K^2/2$, corresponding to random and independent values of the phase ϕ (plateau regime). The correlations between successive values of ϕ are destroyed upon averaging over p. In the intermediate range of $S \sim 1$, expression (8) is the simplest interpolation between both limits. It is convenient in that the inverse diffusion rates, and also the particle life-times, are additive:

$$\frac{1}{\langle D\rangle} = \frac{1}{D_{pl}} + \frac{1}{D_{ban}};\ T = T_{pl} + T_{ban} \tag{9}$$

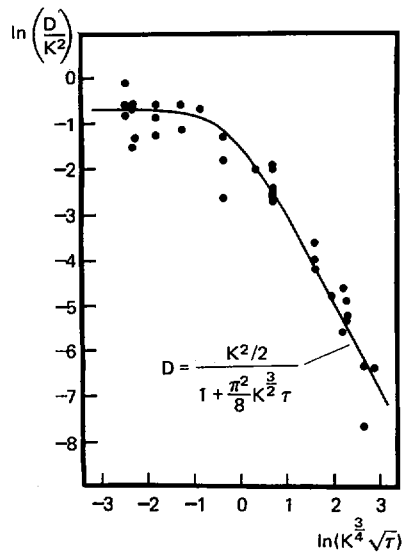


FIG.5. Diffusion rate D for homogeneous model (Section 4): Dots: result of numerical calculation of transformation (7); curve: theoretical function (8); K: resonance overlap parameter; τ: phase "drift" time (number of transits) due to multiple scattering.

For $K \gg 1$, the diffusion rate has a maximum value D_{pl} independent of τ, because of resonance overlapping (see, e.g. Refs [6, 10]). With due account of scattering, the range of maximum diffusion may be significantly larger ($S \lesssim 1$).

The results of a numerical calculation of the diffusion rate in the homogeneous model are presented in Fig. 5. The diffusive nature of the process was checked by comparing the values of D for four time segments on each trajectory of system (7). The following values of the parameters were used in the calculation: $K = 0.001 - 0.25$; $\tau = 0.36 - 16\,600$; and $N = 4000 - 80\,000$. Each value of D was found in Fig. 5 by averaging over several (10 – 100) trajectories with different initial conditions (p_0, ϕ_0). The mean ratio of the numerical values of D to the theoretical values (8) is equal to 1.05 for all points in Fig. 5.

The value of the radial diffusion coefficient D(r) for the initial transformation (3) or (6) may be found by averaging expression (8) over θ and v, on which the parameters a and $\Delta\psi$ (6) and also the parameters K and τ(7) a depend.

5. THE ELECTRON MODEL

5.1. Experiment

A SEM (stochastic electron model) device was designed for experimental study of the transverse losses in long traps with radial electric field. The device

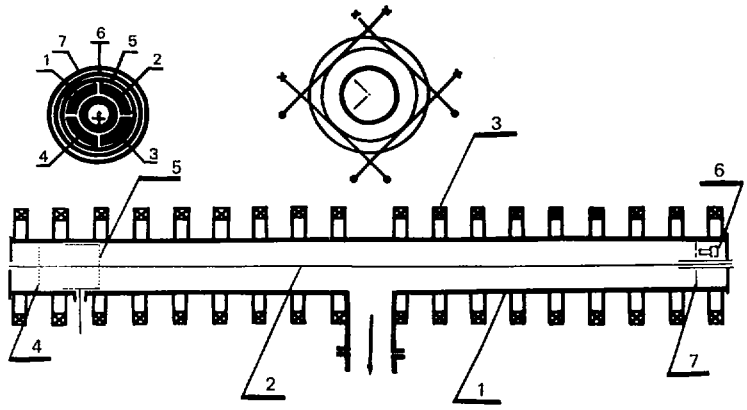


FIG. 6. SEM experimental device: 1) metal vacuum chamber; 2) filament; 3) solenoid coil; 4) sectional collector; 5) electrostatic mirror with grid; 6) electron gun cathode; 7) electron gun anode (also trapping blocking electrode). Numbering and arrangement of collector sections shown in upper part of figure (left).

is shown in Fig. 6. Electrons with energies of 50–100 eV are injected parallel to the axis of the trap at a radius of $r_0 = 15$ mm and are trapped by two electrostatic mirrors located at a distance of $\ell = 180$ cm from one another. The electrons are dumped onto a sectional collector (Fig. 6) within a certain time after injection (confinement time). The number of electrons in different zones of the trap is proportional at this moment to the current to the corresponding sections of the collector. The radial electric field was created by a thin filament stretched along the axis of the trap. The voltage on the filament V_b varied within a range of ± 500 V. The magnetic field was $B_0 \approx 170$ G. The electron flight time between the mirrors was $t_{\|} \sim 0.3$ μs. The residual-gas pressure was approximately 6×10^{-8} torr.

It was initially proposed to install an asymmetrical magnetic mirror on one end of the trap. However, the first experiments conducted without a magnetic trap, i.e. in a seemingly axially symmetrical system, showed that strong diffusion leading to a decrease of the electron life-time by more than one order of magnitude occurred at a torsion angle of $|\Delta\psi| \gtrsim 1$. This result, unexpected at first glance, drew our attention to the problem of estimating the required accuracy of producing the magnetic field of long open traps. Therefore, we subsequently decided to concentrate on a study of this problem.

The main results of the experiments are presented in Figs 7 and 8 and in Tables I and II. A typical example of the dependence of the total current I (to all sections of the collector) on the confinement time measured in the number

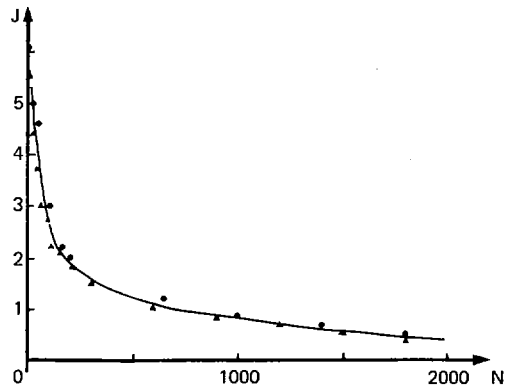


FIG.7. Current to collector (all section joined together) versus confinement time. Current is expressed in relative units and confinement time in number of electron transits: $\Delta\psi(r_0 = 2.03$ (first minimum of current in Fig. 8); ▲ ... $\mathcal{E}_0 = 100$ eV; ● ... $\mathcal{E}_0 = 50$ eV.

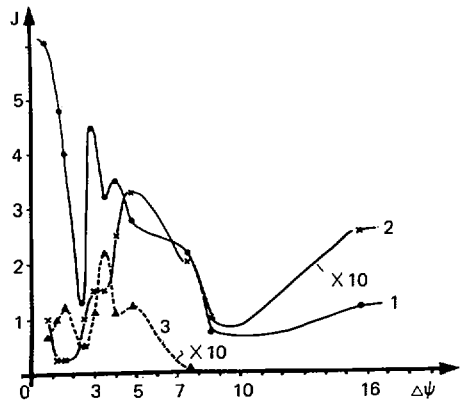


FIG.8. Current (in relative units) to different sections of collector versus torsion angle $\Delta\psi$ for $\mathcal{E}_0 = 100$ eV and electron confinement time of 100 μs: curve 1) sections 1–5 joined together; curve 2) sections 6–7 joined together (signal amplified tenfold is shown); curve 3) internal section (signal also amplified tenfold).

of flights (N) for two values of nominal (at $V_b = 0$) electron energy ($\mathcal{E}_0$) and torsion angle on the gun radius of $\Delta\psi(r_0) = 2.05$ is shown in Fig. 7. The characteristic feature of this dependence is the existence of two components: a short-lived component with half-life of $N_1 = 60$ flights and a long-lived component with $N_2 \approx 1500$. The latter is comparable (although appreciably less than) to the electron life-time in the trap due to scattering from the residual gas (see Table I). In the considered case the fraction of the long-lived component is $s = 0.20$.

TABLE I. DEPENDENCE OF ELECTRON LIFE-TIME IN THE TRAP ON THE TORSION ANGLE

$\Delta\psi$	s	N_1	N_2	$\Delta\psi$	s	N_1	N_2
−1.32	1.0	–	3900	1.60	1.0	–	4200
−1.73	0.45	61	1800	1.90	0.53	96	2400
−2.03	0.20	60	1500	2.07	0	45	–
				2.21	0	12	–
−2.62	0.38	87	2460	2.63	0.50	192	2900
−3.03	0.67	227	2300	3.06	1.03	–	2950
−3.33	0.38	195	2100	3.77	0.27	490	2860
−4.74	0	155	–	4.50	0	191	–
−6.03	0	111	–	5.28	0	177	–
				6.64	0	332	–
−12.2	0	113	–				
−14.2	0	131	–				
$V_b < 0$; $\mathcal{E}_0 = 100$ eV				$V_b > 0$; $\mathcal{E}_0 = 100$ eV			

The dependence of the life-times N_1 and N_2 and of the fraction s on $\Delta\psi(r_0)$ is presented in Table I for $\mathcal{E}_0 = 100$ eV and for both signs of $V_b(\Delta\psi)$. The first line of the table corresponds to the boundary of the instability ($\Delta\psi_{cr} = -1.32$ for $V_b < 0$ and $\Delta\psi_{cr} = 1.60$ for $V_b > 0$). For lower values of $|\Delta\psi|$, the electron life-time is independent of $\Delta\psi$ and is determined by the scattering from the residual gas.

The complex nature of the electron motion in the transient region with respect to $\Delta\psi$ near the instability boundary can be seen from the data of Table I. The life-time remains approximately constant and s = 0 for large torsion angles ($|\Delta\psi| \gg 1$).

The structure of electron diffusion is more clearly seen in Fig. 8, where the currents to different sections of the collector are presented as a function of $\Delta\psi$ for $\mathcal{E}_0 = 100$ eV and a confinement time of 100 μs (N ~ 300). The instability boundary, two minimum values of current (and, accordingly, of the life-time) and one maximum are clearly visible. Despite the seeming complexity and confusion of the observed processes, the experimental data are explained

TABLE II. PERTURBATION AMPLITUDES d (mm) FOR TYPICAL VALUES OF $\Delta\psi(r_0)$ (in parentheses, see Fig. 8)

Nominal electron energy ($\Delta\psi = 0$)	100 eV ($\Delta\psi > 0$)	100 eV ($\Delta\psi < 0$)	50 eV ($\Delta\psi < 0$)
Stability boundary on gun radius $K(r_0) = 1$	1.17 (1.60)	1.43 (−1.32)	2.09 (−0.90)
Stability boundary on aperture radius, $K(r_a) = 1$	–	2.63 (−6.10)	3.47 (−4.77)
Outer edge of first resonance on gun radius r_0, first minimum of N_1	0.95 (2.10)	1.10 (−2.22)	0.95 (−2.11)
Outer edge of first resonance on aperture radius r_a, second minimum of N_1	–	3.17 (−7.27)	2.96 (−6.25)
Centre of first resonance on gun radius r_0, maximum of N_1	(3.05)	(3.05)	(2.89)
Average life-time of N_1 for $\lvert\Delta\psi\rvert \gg 1$	0.99	1.32	–

comparatively simply and naturally by the stochastic-instability theory for the case of overlapping of non-linear resonances, to which we shall now turn our attention.

5.2. Theory

Let us proceed from the following approximate equations of electron motion in a magnetic trap with a radial electric field:

$$\dot{r} = \sum_n A_n \sin\left(\psi - \frac{\pi n z}{\ell} + \alpha_n\right)$$

$$\dot{z} \approx v_\parallel \approx v; \quad \dot{\psi} = \Omega(r) \tag{10}$$

Here z is the co-ordinate along the trap axis; ψ is the azimuthal angle; ℓ is the distance between mirrors equal to the spatial half-period of the perturbation; and A_n and α_n are the amplitudes and phases of the spiral perturbation harmonics.

The system of first-approximation resonances is shown in Fig. 9, where it is assumed, for simplicity, that all $\alpha_n = 0$ ($A_n > 0$). The condition of resonance on the n-th perturbation harmonic has the form: $\Omega(r) = \pi nv/l$ or: $\Delta\psi(r) = \Omega t_{\parallel} = \pi n$. Since $\Omega \sim 1/r^2$ in the electric field of a thin filament, the resonance radii r_n decrease as $n(r_n = r_1/\sqrt{n})$ increases, while the resonance density increases for $r \to 0$. Therefore, there is always a stochastic zone near the filament (the resonance overlap zone) which is propagated over greater radii as $|\Delta\psi|$ increases.

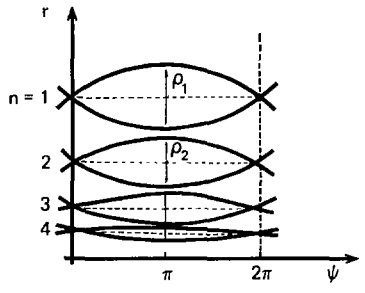


FIG. 9. Resonance arrangement for electron model (Section 5): n . . . number of perturbation harmonic (10); ρ . . . resonance width (its separatrix); resonance values of radius shown by the dashed line.

The width of a separate non-linear resonance ρ_n (Fig. 9) is given by

$$\frac{\rho_n}{r_n} \approx \sqrt{\frac{s8d_n}{r_n \Delta\psi(r_n)}} \tag{11}$$

where $d_n = A_n t_{\parallel}$ is the new amplitude of the perturbation harmonic, equal to the maximum radial electron displacement in the resonance during a single flight. The resonance overlap parameter is

$$K(r) \approx 2.5 \left(\frac{\rho}{\Delta r}\right)^2 \approx 8|\Delta\psi(r)|\frac{d}{r} \approx 1 \tag{12}$$

where Δr is the distance between adjacent resonances and the factor 2.5 takes into account the effect of higher-approximation resonances [10, 11]. The last equality in expression (12) determines the stability boundary [6, 7].

For $K \gg 1$, the diffusion rate is maximum (see Section 4): $D(r) \approx d_n^2/t_{\parallel}$ while the life-time of the short-lived component may be estimated as

$$N_1 \approx \frac{r_0^2}{t_{\parallel} D(r_0)} \approx \left(\frac{r_0}{d_n}\right)^2 \tag{13}$$

The appearance of the long-lived component is explained by the fact that the centre of the first resonance remains intact near the stability boundary ($K(r_0) \gtrsim 1$) [10], i.e. the stochastic component does not penetrate this zone. The maximum fraction of the long-lived (stable) component, therefore, corresponds to $|\Delta\psi(r_0)| = \pi$ when the centre of the first resonance is located precisely on the gun radius r_0 (see Table II).

The minimum of the life-time N_1 (the first in Fig. 8) corresponds to a somewhat lesser value of $|\Delta\psi(r_0)|$ when the outer edge of the first resonance (its separatrix) is located on the gun radius. In this case, the electrons are quickly transported along the separatrix or, rather, along the stochastic layer around the separatrix [10, 11] to the small radius ($\rho_1/r_1 \approx 0.4$), and disappear rapidly.

In a similar fashion, the second minimum of N_1 corresponds to that value of $|\Delta\psi|$ where the outer edge of the first resonance reaches the chamber aperture of $r_a = 27.5$ mm ($\rho_1/r_1 \approx 0.6$).

The emergence of the stability boundary to the radius of the outer aperture (r_a) leads to an outward diffusion flow abruptly reducing the life-time of N_1 in the zone after the maximum (Fig. 8).

All the characteristic features of the function $N_1(\Delta\psi)$ enumerated above could be calculated if the perturbation amplitudes d_n were known. Since they are unknown in the case considered, one may proceed differently: the unknown amplitudes are estimated by the measured characteristics of the function $N_1(\Delta\psi)$, assuming that all of them are of the same order, $d_n \sim d$. The results of the estimates are shown in Table II. It is obvious that the values of d as calculated by different methods agree with each other in order of magnitude, thus confirming the validity of the diffusion mechanism assumed.

The main source of perturbations in the electron model is misalignment of the magnetic lines with respect to the equipotential lines of the electric field or, otherwise, the non-equipotentiality of the magnetic lines. The mean square angle of this misalignment is of the order of 5×10^{-3} rad according to the data of Table II, which corresponds to a radial magnetic field of approximately 1 G.

It should be noted that this perturbation will be suppressed to a significant degree in the plasma, because of equalization of the electric potential along the magnetic lines. Therefore, the main perturbation in the plasma will apparently be related to radial particle drift due to azimuthal variation of the magnetic field. An analysis of the effect of this perturbation may be carried out in a similar manner on the basis of Eqs (10).

ACKNOWLEDGEMENTS

In conclusion we should like to take the opportunity to express our deep gratitude to G.I. Dimov and I.N. Meshkov for useful discussions.

REFERENCES

[1] BUDKER, G.I., MIRNOV, V.V., RYUTOV, D.D., Pis'ma Zh. Ehksp. Teor. Fiz. **14** (1971) 320; LOGAN, G.B., BROWN, I.G., LIEBERMAN, M.A., LICHTENBERG, A.J., Phys. Rev. Lett. **29** (1972) 1435.
[2] DIMOV, G.I. ZAKAJDAKOV, V.V., KISHINEVSKJ, M.E., Fiz. Plazmy **2** (1976) 597; FOWLER, T.K., LOGAN, B.G., Comments Plasma Phys. Contr. Fusion **11** (1977) 167.
[3] McNAMARA, B., ANDERSON, D.V., BOYD, J.K., BYERS, J.A., COHEN, R., CUTLER, T.A., HALL, L.S., POST, R.F., RENSINK, M.E., Plasma Physics and Controlled Nuclear Fusion Research (Proc. 6th. Int. Conf. Berchtesgaden, 1976) Vol. 3, IAEA, Vienna (1977) 161.
[4] RYUTOV, D.D., STUPAKOV, G.V., Pis'ma Zh. Ehksp. Teor. Fiz. **26** (1977) 182.
[5] GALEEV, A.A., SAGDEEV, R.Z., in Voprosy teorii plazmy (Problems of Plasma Theory) **7**, Moscow, Atomizdat (1973) 205.
[6] ZASLAVSKIJ, G.M., CHIRIKOV, B.V., Usp. Fiz. Nauk. **105** (1971) 3.
[7] RYUTOV, D.D., STUPAKOV, G.V., Fiz. Plazmy **4** (1978) 501.
[8] CORDEY, Y.G., WATSON, C.J.H., in Plasma Physics and Controlled Nuclear Fusion Research (Proc. 5th Int. Conf. Tokyo, 1974) Vol. 2, IAEA, Vienna (1975) 643.
[9] RYUTOV, D.D., STUPAKOV, G.G., Dokl. Akad. Nauk. SSSR **240** 5 (1978).
[10] CHIRIKOV, B.V., Fiz. Plazmy **4** (1978) 521.
[11] CHIRIKOV, B.V., Universal Instability of Multi-dimensional Oscillator Systems, Phys. Rep. (to appear).

DISCUSSION

D.R. SWEETMAN: In a practical mirror system one would expect radial electric fields to be present. Do you have self-consistent calculations of the orbits which include these fields, or do you have any idea how they would affect your conclusions?

D.D. RYUTOV: Under typical conditions, it appears that the electron diffusion coefficient D_e is much larger than D_i. This means that the electrons acquire Boltzmann equilibrium not only along the magnetic field lines, but also across the field; that is, $n_e = \text{const.} \exp(e\varphi/T_e)$. Thus the quasineutrality condition $n_e = n_i$ just defines the electric potential distribution, $\varphi = \varphi(\vec{r})$. The large value of D_e has also other implications: strong radial electron diffusion can, on the one hand, stabilize certain oscillation modes; on the other hand, it can have a negative effect, resulting in large electron thermal losses across $\vec{B}$ if the vacuum conditions are imperfect and a cold ambient plasma is present.

F.R. SCHWIRZKE: In an experiment with electrostatic mirrors confining a plasma with a radial electron temperature gradient, there is an electric field in the outward radial direction, too. How does this influence the electron diffusion experiments?

D.D. RYUTOV: Since D_e and χ_e are large, the electron temperature gradient must die out very rapidly, so T_e will become homogeneous.

STUDIES OF TANDEM MIRROR CONFINEMENT*

D.E. BALDWIN, R.H. COHEN, J.H. FOOTE, L.S. HALL,
T.B. KAISER, B.G. LOGAN, L.D. PEARLSTEIN,
T.D. ROGNLIEN
Lawrence Livermore Laboratory, University of California,
Livermore, California

J. KESNER
Department of Nuclear Engineering, University of Wisconsin,
Madison, Wisconsin,
United States of America

Abstract

STUDIES OF TANDEM MIRROR CONFINEMENT.

The paper describes a number of physics studies relevant to tandem mirror confinement. The basic axial confinement laws are given and it is shown that T_e depends critically upon end loss. Sufficient central-cell end loss can stabilize the drift-cyclotron loss-cone mode in the plugs, although the resultant T_e scaling is too slow for reactors. Minimum-B plugs stabilize flute MHD- and rotation-driven modes; local ballooning sets limits on $\beta \gtrsim 0.5$. Proper magnetic symmetry is important for good drift confinement. For small increases in the total injected power, supplementary ion-cyclotron RF heating can halve the neutral-beam energy required to maintain plug densities.

I INTRODUCTION

A tandem mirror (TM) system [1,2] has three collinear mirror plasmas: two small, magnetically confined, hot end-cells (plugs) of average energy E_p and density n_p; and a large-volume, less hot central cell of temperature T_c and density $n_c < n_p$. Electrons of temperature T_e are confined in the overall ambipolar potential. Central-cell ions with $T_c < \Phi_c$ are confined by the potential barrier

$$e\Phi_c = T_e \ln(n_p/n_c) \qquad (1)$$

Important physics questions addressed in the first generation of TM experiments will include microstability of the plugs, MHD curvature- and rotation-driven flute and ballooning stability, ion-drift confinement, and ion-electron confinement and energetics under neutral-beam and ion-cyclotron heating and direct electron heating. We discuss topics relevant to these for conditions typical of experiments under construction, e.g., the Tandem Mirror Experiment (TMX) at the Lawrence Livermore Laboratory [3], and conceptual reactors [4].

---

* This work was performed under the auspices of the US Department of Energy by the Lawrence Livermore Laboratory under contract number W-7405-ENG-48 and the University of Wisconsin under contract number ET-78-C-024710.

II MICROSTABILITY OF THE PLUGS

TM plugs are susceptible to loss-cone modes such as the drift-cyclotron loss-cone (DCLC) mode [5] thought to dominate all current high-density ($\omega_{pi}/\omega_{ci} >> 1$) mirror machines. The conditions for plug stability can constrain system parameters; therefore, they must be granted primary consideration in a TM system design. Because of the small plug length in units of gyroradii, instabilities such as the high frequency convective mode [5] and the Alfvén ion-cyclotron mode are calculated not to be significant [6].

Several means for stabilizing the DCLC modes have proven successful in low energy mirror machines [7,8], and others have been proposed [9,10,11]. In energetic neutral-beam-powered mirror plasmas, only stabilization by a low-energy stream has proved routinely successful to date [12], although there is evidence [13] for the predicted reduction in the stream required with increasing radial scale length [14]. Both theoretically [14] and experimentally [12], the flux of ions found necessary to stabilize 2XIIB (radius ~ 2 to 3 ion gyroradii) is given by

$$j_{stab} = \frac{3.2\cdot 10^{7}\lambda T_e^{3/2}(\mathrm{keV})n_p(\mathrm{cm}^{-3})}{(R_p - 1)A_p^{1/2}E_p(\mathrm{keV})L_p(\mathrm{cm})} \quad \mathrm{cm}^{-3}\cdot\mathrm{cm}\cdot\mathrm{s} \qquad (2)$$

where L_p, and R_p, and A_p are the plug length, β-enhanced mirror ratio, and ion atomic number, respectively, and λ is a coefficient, theoretically about unity, which is to be determined from experiment. A value of $\lambda \approx 0.5$ is inferred from measured fluxes [15].

The minimum flux cited above was calculated from the requirement of a minimum density of low-energy ions needed to partially fill the loss cone, coupled with the fact that these ions are confined only for an axial transit time. We calculate this minimum density and consider other effects of low-density, low-energy plasma in combination with the hot loss-cone plasma by numerically integrating a differential equation described earlier [16]. This equation along $\underset{\sim}{B}$ allows finite β and variation of B and density. In particular, we have modeled a Maxwellian central-cell plasma that is blocked by the ambipolar potential of a mirror plasma. For $\beta >> m_e/m_i$, we do not find that the combination of two adjacent plasmas is stable by virtue of a flute average [17]. Instead, unless the axial extent of the hot plasma is $\lesssim c/\omega_{pi}$, we find that warm plasma is required at the midplane. Because in the TM application such warm plasma must be considered lost from the central cell, its lifetime in the plug is only a transit time; and we recover Eq. (2) as the required flux through the plug.

As a result of these considerations, TMX has been designed so that in its minimum operating mode the flux of the central-cell loss flowing through the plugs equals j_{stab} in Eq. (2). This condition is used to determine the operating parameters given in the next section. Should alternate plug stabilization techniques prove successful in reducing the required central-cell loss flux, those operating parameters will improve accordingly.

We note that because this high end loss lowers T_e, TM reactors must rely upon some other means for DCLC stability, except possibly for a

fusion-fission hybrid [4]. It is important, therefore, to demonstrate the effectiveness of one of the means in Refs. [7-11] in a hot, neutral-beam-sustained mirror machine.

III PARTICLE AND ENERGY AXIAL CONFINEMENT

Because both electrons and thermalized central-cell ions are magnetically and potentially confined, the procedure for calculating their loss rates is that of Pastukhov [18]. His results have been generalized to (multiple) ion species and bounce-averaged electron motion in the three-cell system [19]. Here, we assume a single hydrogenic ion species and neglect electron scattering in the plugs relative to that in the (large volume) central cell. For the species label a = e or c (c for central-cell ions), temperature T_a, 90°-scattering rate

$$\tau_a^{-1} = \frac{\pi}{\sqrt{2}} e^4 n_c \lambda_a m_a^{-1/2} T_a^{-3/2} \tag{3}$$

(where λ_a is the Coulomb logarithm), confining potential Φ_a for each species defined as positive, and mirror ratio R_c, we write the Pastukhov formulae for $e\Phi_a/T_a \gtrsim 2$ as

$$\left.\frac{dn_a}{dt}\right|_{loss} = -\frac{n_c \varepsilon_a}{\tau_a g(\varepsilon_a R_c)} \left(\frac{T_a}{e\Phi_a}\right) \exp\left(-\frac{T_a}{e\Phi_a}\right) \tag{4}$$

$$\frac{3}{2} \left.\frac{d(n_a T_a)}{dt}\right|_{loss} = (T_a + e\Phi_a) \left.\frac{dn_a}{dt}\right|_{loss} \tag{5}$$

where $\varepsilon_e = 2$, $\varepsilon_c = 1$, $e > 0$, and

$$g(x) = \frac{\sqrt{\pi}}{2} (1 + x^{-1})^{1/2} \ln\left[\frac{(1 + x^{-1})^{1/2} + 1}{(1 + x^{-1})^{1/2} - 1}\right] \tag{6}$$

We define the particle flux per unit volume into the central cell and each plug, j_c, j_p, and the respective volumes per unit area L_c/B_c, L_p/B_p, with lengths $L_{c,p}$ and magnetic field strengths $B_{c,p}$. Although for a reactor $j_c L_c/B_c \approx 2 j_p L_p/B_p$, we assume here that $j_c L_c/B_c \gg 2 j_p L_p/B_p$ as it is for TMX operation due to the requirement of DCLC stability (see Sec. II). The ratio $e\Phi_e/T_e$ is determined by equality of loss rates from Eq. (4),

$$\left.\frac{dn_c}{dt}\right|_{loss} = \left.\frac{dn_e}{dt}\right|_{loss} = j_c \tag{7}$$

for typical TMX confinement $e\Phi_e/T_c \approx 5.5$; for a reactor, ≈ 6.5. Because gas-fed ions are lost from the central cell by heating, we must consider energy balance in conjunction with confinement. Electrons are heated by the plug ions and cooled by the central-cell ions and electron loss; again for $j_c L_c/B_c \gg 2 j_p L_p/B_p$ this gives

$$\frac{3}{2} \frac{d}{dt}(n_c T_e) = 2 \frac{L_p B_c n_p^2 E_p}{L_c B_p (n\tau)_{eq}} + P_{e\text{-}aux} - \frac{3}{2} \frac{n_c^2 (T_e - T_c)}{(n\tau)_{eq}} - (e\Phi_e + T_e) j_c \tag{8}$$

where $(n\tau)_{eq} = 1.4 \cdot 10^{12}\, T_e^{3/2}(\text{keV})$ (for D^+) is the electron-ion equipartition time. $P_{e\text{-aux}}$ represents any auxiliary power into the electrons, e.g., that fraction deposited either by neutral injection into the central cell or by direct electron heating. The central-cell ion power flow is similar, except that by charge exchange a gas-feed source introduces a power loss but no particle loss. For a ratio of charge-exchange to ionization cross sections σ_x/σ_i, the ion power balance becomes

$$\frac{3}{2}\frac{d}{dt}(n_c T_c) = \frac{3}{2}\frac{n_c^2(T_e - T_c)}{(n\tau)_{eq}} + P_{c\text{-aux}} - \left[e\Phi_c + T_c\left(1 + \frac{3}{2}\frac{\sigma_x}{\sigma_i}\right)\right] j_c \tag{9}$$

If Eqs. (8) and (9) are added, we obtain

$$\frac{3}{2}\frac{d}{dt}\, n_c(T_e + T_c) = 2\,\frac{L_p B_c}{L_c B_p}\,\frac{n_p^2 E_p}{(n\tau)_{eq}} + P_{e\text{-aux}} + P_{c\text{-aux}} - \eta T_e j_c \tag{10}$$

where we introduce

$$\eta = T_e^{-1}\left[e\Phi_e + T_e + e\Phi_c + T_c\left(1 + \frac{3}{2}\frac{\sigma_x}{\sigma_i}\right)\right] \tag{11}$$

as the energy, in units of T_e, carried off by each injected electron and its associated ion; η is a slowly varying parameter, dominated by $e\Phi_e/T_e$, having a value about 8.

For fixed plug parameters n_p, E_p, these rate equations describe classical TM confinement for arbitrary j_c. Their solutions have been compared with solutions of the full Fokker-Planck equation [19], giving ± 20% agreement for $R_c \gtrsim 3$ and $e\Phi_c/T_c \gtrsim 2$.

As discussed in Sec. II, the TMX plugs will be stabilized to DCLC by adjusting sources for the central cell according to Eq. (2). With volume weighting, stability requires

$$j_c \gtrsim 2.3 \cdot 10^7\, \frac{\lambda B_c}{B_p(R_p - 1)}\, \frac{T_e^{3/2}(\text{keV})\, n_p(\text{cm}^{-3})}{E_p(\text{keV})\, L_c(\text{cm})} \tag{12}$$

in which case for no auxiliary power Eqs. (10) and (12) give

$$T_e(\text{keV}) = 0.11\left[\frac{\beta_p B_p^2(T)\, E_p(\text{keV})(R_p - 1) L_p(\text{cm})}{\eta\lambda}\right]^{1/4} \tag{13}$$

where β_p is the plug beta. As in 2XIIB, the loss flux required to stabilize the plugs lowers T_e well below its classical value. As long as T_e is held to this scaling, improvement with plug parameters is slow.

Based on these equations, we have developed a rate code to study transient behavior [20] such as startup in TMX. To model the TMX plugs subject to DCLC, we set

$$\frac{dn_p}{dt} = \max\left\{\frac{n}{\tau_p};\ j_{stab} - j_c\,\frac{L_c B_p}{L_p B_c}\right\} \tag{14}$$

where $\tau_p \approx \tau_{eq}$, which approximates very well the full quasi-linear code [14]. We find that reaching a steady state in TMX within the 25-ms beam pulse requires a programmed central-cell gas feed, with a short, initial pulse 5 times the steady state. We have also studied transient reactor problems, such as purging of thermalized plug alphas, replacing Eq. (14) with an improved model for classical plug confinement [20].

IV LOW-FREQUENCY STABILITY

Both rotation and local bad curvature in the transitions between the central cell and the plugs can drive low-frequency modes in a TM system. The plugs are generally rigid due to their high pressure and minimum-B, with line-bending displacements accordingly excluded from them.

We investigate the stability to both flute and ballooning interchange modes using a differential-eigenvalue equation along $\underset{\sim}{B}$, which is localized by an eikonal approximation normal to $\underset{\sim}{B}$. With $\underset{\sim}{B} = B\underset{\sim}{b} = \nabla\psi \times \nabla\theta$, $d\ell = \underset{\sim}{b}\cdot d\underset{\sim}{r}$, $\underset{\sim}{E}_\perp = -B\nabla_\perp U$, and $U(\psi,\theta,\ell) = \tilde{U}(\ell)\exp S(\psi,\theta)$, we use an equation obtained by Newcomb [21]:

$$\frac{d}{d\ell}\left\{\frac{|\nabla S|^2}{B}\left[1 + \frac{4\pi}{B^2}(p_\perp - p_{\parallel})\right]\frac{d\tilde{U}}{d\ell}\right\} + \frac{4\pi}{B}\left\{\omega^2|\nabla S|^2\frac{M}{B^2} + \frac{\partial}{\partial\psi}(p_\perp + p_{\parallel})\frac{\partial S}{\partial\theta}\left[\frac{\partial S}{\partial\theta}K_\psi - \frac{\partial S}{\partial\psi}K_\theta\right]\right\}\tilde{U} = 0 \tag{15}$$

where the curvature has been written $\underset{\sim}{K} = \underset{\sim}{b}\cdot\nabla\underset{\sim}{b} = K_\psi\nabla\psi + K_\theta\nabla\theta$, and M is the mass density. Except for the allowance for anisotropic pressure, this is the equation used to study ballooning modes in tokamaks [22].

In solving Eq. (15), we have used quasi-analytic models for the vacuum field and the pressures in finite-β equilibria. In the paraxial approximation, the flux coordinates are

$$\psi = \frac{1}{2}\hat{B}(z)\left\{x^2\exp\left[-2C(z)\right] + y^2\exp\left[2C(z)\right]\right\}$$
$$\theta = \tan^{-1}\left\{\frac{y}{x}\exp\left[2C(z)\right]\right\} \tag{16}$$

where $\hat{B}_{vac}(z)$ and $C(z)$ are chosen to fit numerical vacuum field calculations. As a model, we use the finite pressure depression of $\hat{B}$

$$\hat{B}^2 + 8\pi p_\perp(\hat{B},\psi) = \hat{B}^2_{vac}(z) \tag{17}$$

both in the plugs and in the central cell including electron pressure, but we assume that $C(z)$ is unaltered. In the plugs, we have used the ion pressure profiles

$$p_{\parallel}(B,\psi) = h(\psi)B(B_1 - B)^{\nu} \text{ and } p_\perp(B,\psi) = h(\psi)\nu B^2(B_1 - B)^{\nu-1} \tag{18}$$

where B_1 and ν are parameters chosen to fit the injected profiles, and we have verified the mirror and firehose stability criteria,

$$\frac{\partial}{\partial B}\left[B^2 + 8\pi p_\perp\right] > 0 \qquad \text{and} \qquad B^2 + 4\pi(p_\perp - p_{\parallel}) > 0 \tag{19}$$

for the chosen parameters. In the central cell, the ions are isotropic, as are the electrons are everywhere. These models, together with the parameter $\xi = 2\psi(\partial S/\partial\psi)/(\partial S/\partial\theta)$, fix the coefficients in Eq. (15). Alternate field or pressure models can also be used.

Equation (15) is solved subject to either of two boundary conditions, $dU/d\ell\big|_{\pm L/2} = 0$ (free) or $\tilde{U}(\pm L/2) = 0$ (line tied), where for most purposes L is the overall length. To solve, ω^2 is approximated by a Rayliegh-Ritz method as a first guess for a shooting technique. For fixed plug parameters and vacuum field, the parameter space (ψ,θ,ξ) is searched for the maximum central cell $\beta_c = [8\pi n_c(T_c + T_e)/B^2_{vac}]_{\ell=0}$ for which $\omega^2 > 0$ everywhere.

There are no flute solutions of Eq. (15) provided the line integral of the $\partial(p_\perp + p_{\parallel})/\partial\psi$ -term is positive. This depends upon the ratio $p_\perp/p_{\parallel}$, occurs for a sufficiently large ratio of plug to central-cell pressure, and results from a pressure-weighted flux-tube volume that decreases with ψ. If we assume this to be the case, as in TMX, the β_c-limit estimated from equality of the MHD growth time with the Alfvén time through the bad-curvature region is of order unity. Numerically, we find β_c-limits in the range 0.5 to 0.6 for the TMX magnet set.

Rotation-driven modes of a straight column having low azimuthal and radial mode numbers (m and n, respectively) have been described by Freidberg and Pearlstein (F-P) [23] in the context of finite Larmor radius fluid equations. For rigid-rotor equilibria, they find two classes of modes. The first, having $m \geq 2$, $n \geq 0$, is most unstable for $k_z = 0$; the second, having $m = 1$, $n = 0$, requires $k_z \neq 0$. The former has the larger growth rates, particularly $m = 2$, $n = 0$; however, the latter has the lower threshold for rotation, arbitrarily small in the ion diamagnetic direction.

We first apply their results to ballooning in the central cell. Assuming that the radial electric field is given by Boltzmann-distributed electrons [24], $e\Phi_c(r) \approx$ constant + $T_e \ln n_c(r)$, the F-P result for the growth rate of the $m = 2$, $n = 0$, mode when $T_e > T_c$ is given by

$$\gamma_{rot} \approx \Omega^* \left[\frac{T_e}{T_c}\left(\frac{T_e}{T_c} + 1\right)\right]^{1/2} \quad \text{where } \Omega^* = \Omega_c \frac{2\rho_c^2}{r_c^2}\left(1 + (1 - \beta_c)^{1/2}\right)^{-1} \tag{20}$$

ρ_c, Ω_c are the vacuum ion gyroradius and frequency, and β_c is the on-axis beta. This mode is stabilized for $k_z V_a \gtrsim \tfrac{1}{2}\gamma_{rot}$, where V_a is the Alfvén speed. We take $k_z = \pi/L_c$ to obtain the condition

$$\frac{\beta_c}{\left[1 + (1 - \beta_c)^{1/2}\right]^2} < \pi^2 \frac{T_c}{T_e}\left(\frac{r_c^2}{L_c \rho_c}\right)^2 \tag{21}$$

For both TMX and reactors, the ratio of lengths is nearly unity; so that this condition is easily satisfied. For our assumed electric field model and $T_e > T_c$, $m = 2$, $n = 0$ requires the largest k_z for stability; so Eq. (22) is a sufficient condition for ballooning stability of all the F-P rotation modes.

Satisfaction of Eq. (21) does not ensure stability to a rotation-driven flute having no finite-k_z stabilization. The F-P modes were derived for a cylindrical plasma. For flute stability in a TM, the minimum-B plugs must stabilize the rotating central cell; therefore this question must be addressed allowing for both the nonaxisymmetry and the

axial variation. As a tool for including axial variation, Eq. (15) assumed large m and is local in angle. It is therefore unsuitable, especially for the F-P m = 2,n = 0 mode having the largest $k_z = 0$ growth rate. A flute-averaged r,θ description of this mode will be developed in the future; here we estimate its effect.

The rotational drive is potentially dangerous because it acts over the entire central-cell length L_c, whereas curvature is limited to the two transitions, each of length L_{tr}. To compare the two, we compare the weighted growth rates, given by Eq. (20) and $\gamma^2_{MHD} = \sqrt{R_c}\, r_c^4 \Omega^{*2}/\rho_c^2 L_{tr}^2$, where R_c is the central-cell mirror ratio. For rotation not to dominate curvature requires $L_c \gamma^2_{rot} \lesssim 2L_{tr} \gamma^2_{MHD}$, or

$$\frac{T_e}{T_c}\left(\frac{T_e}{T_c} + 1\right) \lesssim 2\sqrt{R_c}\, \frac{r_c^4}{\rho_c^2 L_{tr} L_c} \tag{22}$$

For both TMX and one set of reactor parameters [4], this inequality is barely satisfied, showing that rotation is an important consideration for flute stability but that it will not severely alter results that neglect it.

V VACUUM DRIFT SURFACES

The minimum dependence of drift surface on pitch angle, called omnigenity, relies on the symmetry about the central cell midpoint $z \to -z$, $\theta \to \pi/2 - \theta$. Particles of constant ε, μ drift on surfaces of

$$J = \sqrt{2} \oint d\ell \sqrt{\varepsilon - \mu B - \frac{q}{m}\Phi} = \text{constant} \tag{23}$$

In the paraxial expansion [see Eq. (16)], $d\ell = dz$ and

$$B(\psi,\theta,z) = \hat{B}(z) + \psi[G_1(z) + G_2(z) \cos 2\theta] + O(\psi^2) \tag{24}$$

where

$$\begin{Bmatrix} G_1 \\ G_2 \end{Bmatrix} = \left[(C')^2 - \frac{1}{\sqrt{\hat{B}}}(\sqrt{\hat{B}})''\right] \begin{Bmatrix} \cosh 2C \\ \sinh 2C \end{Bmatrix} + C'' \begin{Bmatrix} \sinh 2C \\ \cosh 2C \end{Bmatrix} \tag{25}$$

and a similar expansion holds for Φ. For the above symmetry, G_1 is even in z and G_2 is odd, so that

$$J = J_0(\varepsilon,\mu,\psi) + \psi^2 \cos 4\theta\, J_1(\varepsilon,\mu) + O(\psi^4) \tag{26}$$

with θ-dependence appearing only in order ψ^2. Drift orbits follow

$$\frac{d\psi}{d\theta} = 4\psi^2 \frac{J_1}{\partial J_0/\partial\psi} \sin 4\theta \tag{27}$$

For vacuum fields, $\partial J_0/\partial\psi \approx$ constant, and Eq. (27) is in excellent agreement with numerically calculated fields and orbits. Violation of the above symmetry gives $\Delta\psi/\psi = O(1)$ [25] and much enhanced radial mixing. For finite β and $\Phi \neq 0$, Eq. (27) can lead to banana orbits due to $\partial J_0/\partial\psi$ vanishing locally, which has numerous implications for transport [24].

The splitting of drift surfaces of particles with positive and negative parallel velocity results from $G_2(z) \neq 0$ in Eq. (24). As shown in Ref. [24], this leads to an enhanced transport when the axial bounce and rotational frequencies of the particles are comparable. This splitting can be reduced to higher order in ψ provided G_2 can be made to vanish. If the vacuum field is designed to satisfy this condition, the actual field and Φ will also satisfy it.

VI ION-CYCLOTRON HEATING OF PLUGS

We have begun investigation of ion-cyclotron resonance heating (ICRH) in TM plugs as a means for reducing required neutral-beam energies or currents. Although many topics bear on a final evaluation, we have focused initially on the effects of velocity space transport induced by ICRH in the diffusive approximation, modifying an existing Fokker-Planck code [26]. We consider second-harmonic and fundamental heating, in which is included parallel cooling when $\omega < \omega_{ci}$ (local) and $k_{\parallel} \neq 0$ [27]. The two frequencies behave qualitatively alike, although the harmonic generates a more energetic tail.

In considering ICRH as a method for supplementing reduced energy neutral beams, we find similar confinement for the same total net power, provided neutrals are injected with energies at least twice the ambipolar cutoff $e\Phi/(R - 1)$. For example, under reactor conditions, a constant density can be maintained with halved injection energy, doubled current, and 25% ICRH-power. For laboratory plasmas, we also find that confinement improves with ICRH; however, due to the increased ion energy, there can be an important power loss through charge exchange [28]. These studies will continue and will be reported at a later date.

Finally, we are studying the feasibility of using ICRH to trap end-lost central-cell ions in the plugs [28]. If successful, this would avoid use of many or all neutral beams, but the possible deleterious effects on confinement in the central cell must be carefully assessed.

REFERENCES

[1] DIMOV, G. I., et al., Fiz. Plasmy 2 (1976) 597.
[2] FOWLER, T. K., LOGAN, B. G., Comm. on Plasma Phys. and Cont. Fus. Res. 2 (1977) 167.
[3] COENSGEN, F. H., Lawrence Livermore Laboratory, Rep. Prop-148 (1977)
[4] LOGAN, B. G., et al., Paper CN-37/R-3, these Proceedings.
[5] POST, R. F., and ROSENBLUTH, M. N., Phys. Fluids 9 (1966) 730.
[6] WATSON, D. C., et al., Lawrence Livermore Laboratory, UCID-17486 (1977).
[7] IOFFE, M. S., et al., Zh. Eksp. Teor. Fiz. 67 (1974) 2145 [Sov. Phys.-JETP 40 (1975) 1064].
[8] KLINKOWSTEIN, R. E., SMULLIN, L.D., Phys. Rev. Lett. 40 (1978) 771.
[9] BERK, H. L., et al., Plasma Phys. and Cont. Nucl. Fus. Res. (Proc. 3rd Int. Conf. Novosibirsk, 1968) 2, IAEA, Vienna (1969) 151.
[10] TANG, W. M., PEARLSTEIN, L. D., BERK, H. L., Phys. Fluids 15 (1972) 1153.
[11] ARSENIN, V. V., PASTUKHOV, V. P., Fiz. Plasmy 3 (1977) 306 [Sov. J. Plasma Phys. 3 (1977) 172].
[12] COENSGEN, F. H., et al., Plasma Phys. and Cont. Nucl. Fus. Res. (Proc. 6th Int. Conf. Berchtesgaden, 1976) 2, IAEA, Vienna, (1977) 135.
[13] SIMONEN, T. C., et al., Paper CN-37/J-1, these Proceedings.

[14] BALDWIN, D. E., BERK, H. L., PEARLSTEIN, L. D., Phys. Rev. Lett. 36 (1976) 1051; BERK, H. L., et al., Plasma Phys. and Cont. Nucl. Fus. Res. (Proc. 6th Int. Conf. Berchtesgaden, 1976) 3 IAEA, Vienna (1977) 147.
[15] MOLVIK, A. W., Bull. Am. Phys. Soc. 22 (1977) 1144.
[16] BALDWIN, D. E., et al., Plasma Phys. and Cont. Nucl. Fus. Res. (Proc. 4th Int. Conf. Madison, 1971) 2, IAEA, Vienna (1971) 735.
[17] IVANOV, A. A., ROSLYAKOV, G. V. Cont. Fus. and Plasma Phys. (Proc. 8th European Conf. Prague, 1977) 1, (1977) 98.
[18] PASTUKHOV, V. P., Nucl. Fusion 14 (1974) 3.
[19] COHEN, R. H., et al., to be published in Nucl. Fusion.
[20] COHEN, R. H., to be published.
[21] NEWCOMB, W. A., Lawrence Livermore Laboratory Rep. UCID-17182 (1976).
[22] CONNER, J. W., et al., Paper CN-37/P-1, these Proceedings.
[23] FREIDBERG, J. P., PEARLSTEIN, L. D., to be published in Phys. Fluids.
[24] KISHINEVSKII, M. E., et al., Paper CN-37/J-3, these Proceedings.
[25] LAO, L. L., CONN, R. W., KESNER, J., submitted to Nucl. Fusion.
[26] MIRIN, A. A., Lawrence Livermore Laboratory Rep. UCRL-51615 (1975).
[27] BUSNARDO-NETO, J., et al., Phys Rev. Lett. 36 (1976) 28.
[28] KESNER, J., to be published in Nucl. Fusion.

DISCUSSION

D.D. RYUTOV: My question relates to the problem of stabilizing the DCLC mode by means of a cold plasma stream. Have you considered the possibility of stabilizing this mode by applying a radially inhomogeneous plasma stream concentrated mostly at the plasma periphery?

D.F. BALDWIN: Yes, we have; and we plan to attempt this in MFTF. If your conjecture concerning good radial mixing of electrons in tandem mirrors is correct, this technique would result in low T_e in those machines.

T. KAWABE: What effect do cold electrons or trapped cold ions on the axial periphery have on stabilization of the DCLC mode?

D.F. BALDWIN: At high β, the axial localization of the mode is of the order of c/ω_{pi}. Except for corresponding short plasmas, the mode can localize away from the cold plasma.

PLASMA CONFINEMENT IN GAMMA 6 (TANDEM MIRROR)

S. MIYOSHI, K. YATSU, T. KAWABE, K. ISHII,
A. ITAKURA, H. ISHIZUKA, S. HAGIWARA
University of Tsukuba,
Ibaraki-ken,
Japan

Abstract

PLASMA CONFINEMENT IN GAMMA 6 (TANDEM MIRROR).

Several results from the GAMMA 6 (tandem mirror) confinement experiments are reported. The target plasma with 5×10^{13} cm^{-3} density is produced by hydrogen-loaded titanium washer guns, and is stable macroscopically in the tandem mirror magnetic field configuration. The neutral beam (7 keV, 1.5 A) injection into the target plasma at both side plug mirrors raises each plasma potential. The tandem-type plug potential is then confirmed experimentally in GAMMA 6. Some formation of plug potential by heating plasma electrons with a relativistic electron beam (360 keV, 50 kA, 50 ns) is also observed. An application of an RF plug on the end-sheet plasma in the tandem mirror considerably increases the confinement time of the plasma produced by ECR microwave in GAMMA 6. This RF plug includes the adiabatic effect. These experimental results show the improvement of mirror-type plasma confinement and suggest the increase of Q value in the tandem mirror.

1. INTRODUCTION

Experiments in the tandem mirror type device (GAMMA 6) have achieved good plasma confinement. The tandem mirror [1–3] is designed to improve plasma confinement, and a few of them are now under construction in the United States of America. GAMMA 6 has two distinct features: one is an application of the RF plug [4–6] on the end-sheet plasma of the tandem mirror, and the other is electron heating by a relativistic electron beam (REB) to enhance the plug potential. In this paper the investigation of plasma behaviour, the establishment of tandem-type potential by neutral beam injection, the effect of an RF plug and production of plug potential with an REB in GAMMA 6 are reported.

Figure 1 is a schematic diagram of the GAMMA 6 plasma. The GAMMA 6 magnets are two minimum-B, Yin-Yang sets with 1 T mirror field, 2.4:1 mirror ratio, and 78 cm mirror distance, central solenoid coils 158 cm long, and a central field of 0.16 T. The characteristics of the neutral beam injector are 10 kV, 3.5 A maximum into a 10 cm × 12 cm area. In this experiment, 7 keV, 1.5 A neutral beams are injected into the target plasma at both plug mirrors from one side of

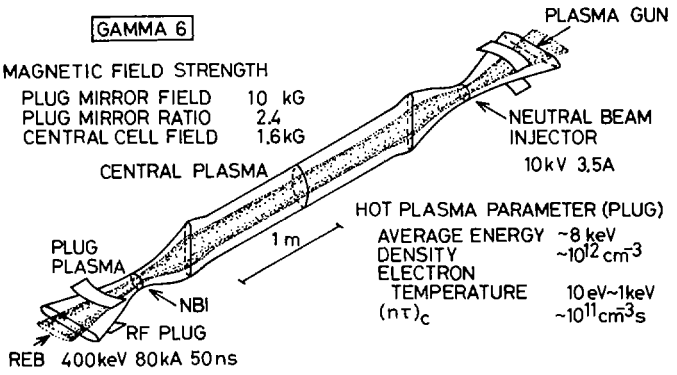


FIG.1. Schematic diagram of GAMMA 6 plasma.

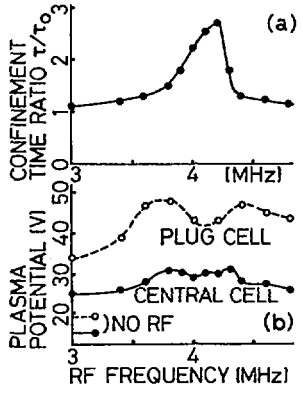


FIG.2. Frequency of the RF field versus (a) ratio of confinement time (τ_0 indicates confinement time without RF), (b) plasma potential.

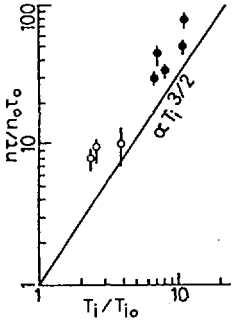


FIG.3. Ion temperature versus increase of confinement time by the RF plug in a single mirror field. The suffix zero indicates no RF. $T_{i0} = 1$ eV; $n_0 = 3 \times 10^9$ cm^{-3}.

the plasma. The target plasma made by the hydrogen-loaded titanium washer guns is of several times 10^{13} cm^{-3} density (as shown by Fig.4(b)). The hot plasma parameters shown in the figure are the expected values. An RF (several MHz) electric field (70 $V \cdot cm^{-1}$) is applied between the plate electrodes at both ends of the plasma for the RF plug. The REB,with a value of 360 keV, 50 kA, 50 ns, is used for electron heating and enhancement of plug potential.

2. RF PLUG

The RF plug experiment is carried out by using a microwave (2.45 GHz, 800 W cw) produced plasma in hydrogen gas of 4×10^{-5} torr. The plasma density is 3×10^{9} cm^{-3} in the two regions and 2×10^{8} cm^{-3} in the central cell. The electron temperature is about 7 eV and the ion temperature 1 eV. The plasma loss flux to the end is kept constant. The increase of the plasma confinement time depends on the frequency of the RF field, as shown in Fig.2(a). The confinement time in the end cells also increases as in the central cell. The measured confinement time τ_0 without RF plug is about 1 ms in GAMMA 6. By classical calculation, the confinement time of single minimum-B mirror plasma is about 100 μs. The plasma potential is increased by the RF field and has some dip at the frequency with the density maximum as shown in Fig.2(b). This phenomenon has not yet been explained.

The scaling law of the RF plug in the tandem mirror is rather complicated to find. The RF plug is also tested in a single minimum-B region of GAMMA 6. An increase in confinement time as well as ion heating is observed (Fig.3). The classical $n\tau$ value in the mirror field is proportional to 3/2 power of the ion temperature, as shown by the solid line in Fig.3. The increase of the $n\tau$ value is partially explained by ion heating. However, all results have a higher value than the solid line in Fig.3, which suggests that the RF plug has an adiabatic confinement effect and improves the mirror confinement.

3. POTENTIAL FORMATION BY NEUTRAL BEAM INJECTION

In the neutral beam injection experiment, the vacuum chamber is evacuated to less than 5×10^{-7} torr in order to minimize the loss of hot ions by charge exchange. A hydrogen neutral beam of 7 keV, 1.5 A is injected into the target plasma in one end cell. The pulse length of the beam is 3 ms, which is much longer than the duration of the plasma gun. The plasma potential is measured by a probe located at r = 6 cm from the axis. An eight-channel electrostatic energy analyser is used to detect high-energy neutral atoms escaping from the plasma by charge exchange ($\bar{E}_i$ = 7 keV).

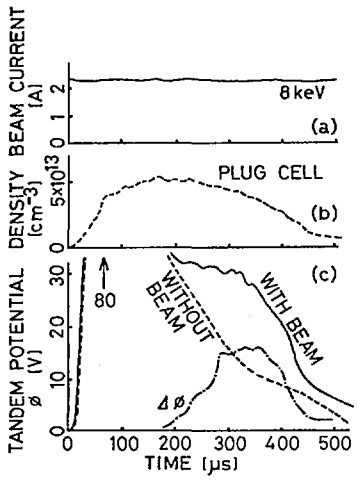


FIG.4. Time behaviour of: (a) neutral beam equivalent current; (b) target plasma density at the plug cell centre; (c) floating potential in the plug cell at r = 0 cm with and without the neutral beam (potential difference between plug and central cell centre).

The neutral beam injection increases the plasma potential by several volts, and high-energy neutral atoms are observed by the energy analyser. The time behaviour of the plasma potential with and without the beam is shown in Fig.4(c). The plasma potential increases with the neutral beam current (Fig.5). In the central cell, however, no change in the plasma potential is observed. This result shows the formation of the plug potential by the neutral beam injection.

4. REB INJECTION

Heating the plasma and trapping the electron beam injected into the plasma in the tandem mirror configuration has been investigated theoretically [7], and the effect of the potential plug seems to be enhanced. To study these phenomena experimentally, an REB source is attached at the south end of GAMMA 6.

The REB source consists of a Marx generator, a water-filled pulse line, and a diode section. The Marx generator can be charged up to 1 MV with an energy of 5.5 kJ. The water line consists of a pulse form line and a transmission line with 5 Ω impedance. In the diode section there are a circular cathode (8 cm in diameter) and an anode which is 10 mm away from the surface of the cathode. For the anode, 10 μm and 20 μm titanium foil or mesh made of stainless steel are used. Round the diode, additional coils are set to produce an axial magnetic field with strength up to the same value as that of the mirror field. In the present experiment, the charging voltage for the Marx generator changed from 500 kV to 800 kV to form an electron beam with energy up to 360 keV.

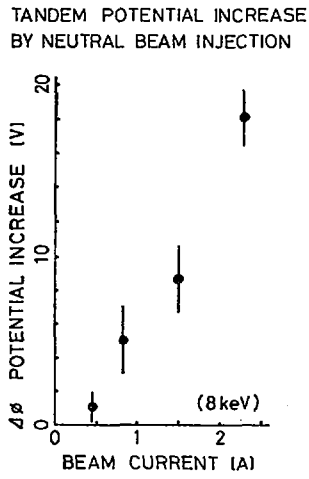


FIG.5. Dependence of potential increase on the neutral beam equivalent current.

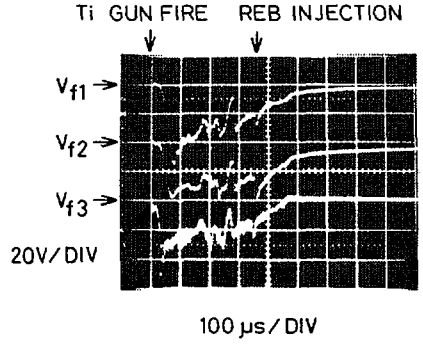


FIG.6. Temporal variations of floating potential of REB-side plug (V_{f1}), of central cell (V_{f2}), and of gun-side plug (V_{f3}).

A plasma is produced and injected by a titanium washer gun located at the other end of the machine. The axial density and its profiles are measured by three spherical probes which are inserted to the centre of each plug and the central cell. The axial density profile changes in time in the following way: up to 450 μs after the gun is fired, the density of the plasma in the gun-side plug is about 10^{13} cm^{-3}, while that in the central cell and the REB-side plug are about 10^{12} cm^{-3}. After 500 μs, the density in the gun-side plug becomes of the order of 10^{12} cm^{-3}, and the axial profile of the density becomes rather flat. The axial profile of the floating potential varies in time. Up to 100 μs, the potential in the gun-side plug is rather lower than those of the other side and the central cell, while after 250 μs the profile becomes flat.

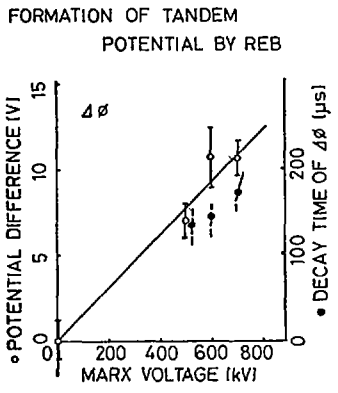


FIG. 7. Dependence of well depth of the floating potential on Marx voltage of the REB source.

The changes of the floating potential of the three probes are shown in Fig.6. When the REB is fired at about 350 μs after the gun is fired, the floating potentials of the REB injection side plug (V_{f1}), the central cell (V_{f2}), and the gun-side plug (V_{f3}) drop abruptly by about 100 V or more, and they tend to recover within 5–10 μs. V_{f1} and V_{f3} come back to the value expected if the REB were not injected; however, V_{f2} recovers to a certain degree and then changes with a slower time constant, and eventually a potential well is formed. The depth of the well is about 20 V and it decays within 200 μs.

The well depth is plotted against the Marx voltage in Fig.7. The values are taken at about 450 μs (100 μs after the REB is fired) when the abrupt change of potential disappears. From Fig.7 it is seen that by increasing the beam power the well becomes deeper.

Theoretical analysis of the relation of the floating potential to the plasma potential indicates that the existence of hot electrons in the plasma increases the potential difference, and the potential difference is a function of the density ratio of the hot and warm components and the temperatures. Taking this analysis into account, it can be said that when the axial profile of the floating potential shows the shape of a well by REB injection along the field, either a 'real' potential well is formed or the hot electron component in the central cell is produced more than in the plugs.

5. SUMMARY

The principal results of the GAMMA 6 experiments are:

(a) Production of plug potential by neutral beam injection;
(b) Effect of REB on plug potential;

(c) Effect of RF plug on tandem mirror plasma confinement; and
(d) Macroscopic stability of target plasma in the tandem mirror.

These experimental results show an improvement of plasma confinement and suggest an increase of Q value.

REFERENCES

[1] KELLEY, G.G., Plasma Phys. **9** (1967) 503.
[2] DIMOV, G.I., ZAKAIDAKOV, V.V., KISHINEVSKIJ, M.E., Sov. J. Plasma Phys. **2** (1976) 326.
[3] FOWLER, T.K., LOGAN, B.G., Comments Plasma Phys. Controlled Fusion **2** (1977) 167.
[4] WATARI, T., HIROE, S., SATO, T., ICHIMARU, S., Phys. Fluids **17** (1974) 2107.
[5] HIROE, S., et al., Phys. Fluids **21** (1978) 676.
[6] YATSU, K., SADAMOTO, Y., MIYOSHI, S., J. Phys. Soc. Jpn. **43** (1977) 1467.
[7] KAWABE, T., et al., Kakuyugo Kenkyu **39** (1978) 130.

DISCUSSION

B.G. LOGAN: Does the potential difference between the plug and centre cell agree with a Boltzmann factor – that is, $T_e \ln$ (n plug/n solenoid)?

S. MIYOSHI: Yes, it does.

F.R. SCHWIRZKE: REB injection, neutral-beam heating and RF plugging – all these heating mechanisms increase the electron temperature. The measured change in the floating potential depends on this temperature increase as well as on a change of plasma potential. Did you take this into account in interpreting the experimental results?

S. MIYOSHI: Yes. The electron temperature at the plug is higher than in the central region (within a factor of two). If one takes this into account the tandem potential emerges a little larger than the experimental values.

D.E. BALDWIN: You showed a linear relationship between $\Delta\Phi$ and beam current. Does this correspond to a change in T_e or in the density ratio?

S. MIYOSHI: The density ratio is constant, so it corresponds mainly to an increase in T_e. I would assume that the $\Delta\Phi$ increase is a function of neutral-beam power.

T.C. SIMONEN: Did the RF heating also increase the solenoid ion energy, and, if so, did the central $n\tau$ increase?

S. MIYOSHI: Yes; however, the increase with ion temperature is rather small compared with what is found in a single min-B mirror. The $n\tau$ value of the overall tandem mirror plasma was increased by a factor of nine.

Session S

OPEN SYSTEMS II

Chairman

V.O. JENSEN
Denmark
Papers S-1-1 and S-1-2 were presented
by L.D. Pearlstein as Rapporteur

FIELD REVERSAL EXPERIMENTS (FRX)*

R.K. LINFORD, W.T. ARMSTRONG, D.A. PLATTS,
E.G. SHERWOOD
University of California,
Los Alamos Scientific Laboratory,
Los Alamos, New Mexico,
United States of America

Abstract

FIELD REVERSAL EXPERIMENTS (FRX).

The equilibrium, confinement, and stability properties of the reversed-field configuration (RFC) are being studied in two theta-pinch facilities. The RFC is an elongated toroidal plasma confined in a purely poloidal field geometry. The open field lines of the linear theta pinch support the closed-field RFC much like the vertical field centres the toroidal plasma in a tokamak. Depending on stability and confinement properties, the RFC might be used to greatly reduce the axial losses in linear fusion devices such as mirrors, theta pinches, and liners. The FRX systems produce RFCs with a major radius R = 2–6 cm, a minor radius a ~ 2 cm, and a total length $\ell \sim 35$ cm. The observed temperatures are $T_e \sim 100$ eV and $T_i = 150–350$ eV with a peak density $n \sim 2 \times 10^{15}$ cm^{-3}. After the plasma has reached equilibrium, the RFC remains stable for up to 30 μs, followed by the rapid growth of the rotational m = 2 instability, which terminates the confinement. During the stable equilibrium, the particle and energy confinement times are more than 10 times longer than in an open-field system. The behaviour of the m = 2 mode agrees qualitatively with the theoretically predicted instability for rotational velocities exceeding some critical value.

I. INTRODUCTION

The reversed-field configuration (RFC) shown in Fig. 1 is topologically similar to the astron configuration, except that the toroidal current in the RFC is carried by thermalized plasma particles with $v_{drift} < v_{thermal}$. RFC's have been produced in numerous theta pinch experiments [1-8] and recently by relativistic electron beams where the beam does not remain in the plasma [9-10].

The early experiments, prior to the mid-60's, exhibited destruction of the RFC in less than 3μs. The annihilation of the reversed field was not associated with any macroscopic distortion of the plasma shape, except for the disappearance of the central hole [2]. Observations included tearing-mode-induced rings that normally coalesced before the annihilation [3], and the m=2 rotational instability that appeared afterwards [1,2]; however, the cause of the RFC destruction is not known.

* Work performed under the auspices of the US Department of Energy.

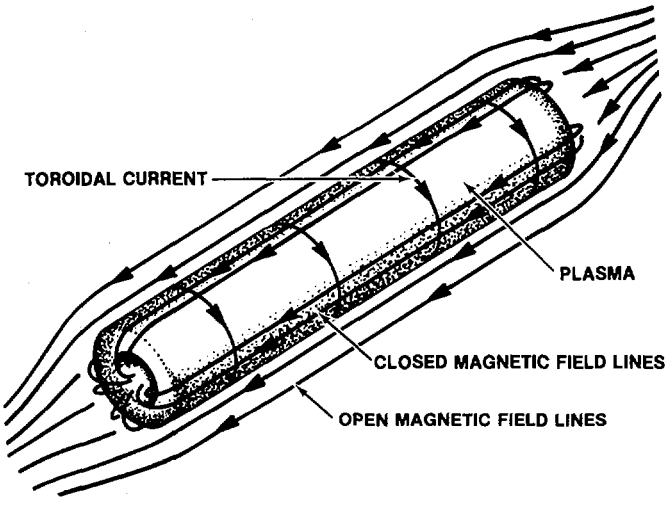


FIG. 1. Reversed-field configuration.

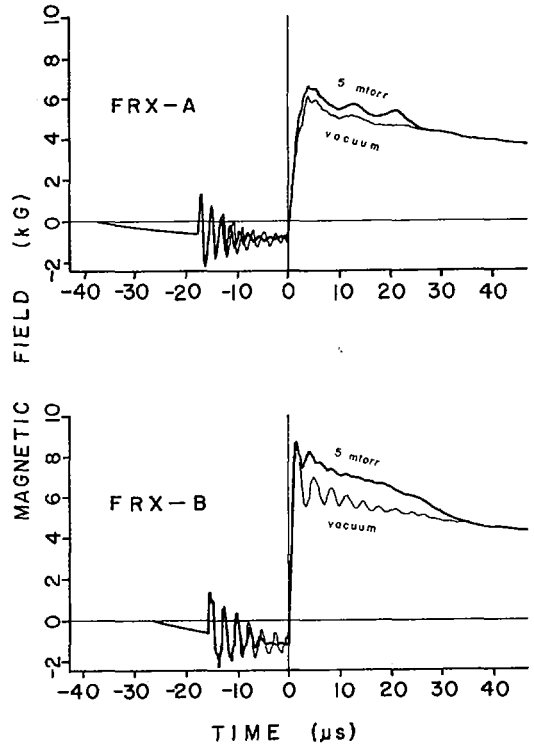


FIG. 2. Comparison of external B field measured in FRX-A and FRX-B between quartz tube and coil at axial midplane. Traces are shown for both vacuum and static 5-mtorr D_2 fill pressure.

More recent results have extended the lifetime of the RFC up to 25μs [7] and then to 50μs [8]. The absence of the expected MHD (kink) and tearing instabilities has stimulated the hope that the RFC might be used to reduce end losses in linear systems. The RFC equilibrium and stability is being studied in two linear-theta-pinch facilities, FRX-A and FRX-B, in conjunction with several theoretical efforts.

II. EXPERIMENTAL SYSTEMS

Both FRX-A and FRX-B produce the RFC in a 20-cm i.d. quartz tube inserted in a 25-cm i.d., one-turn, theta-pinch coil about 1 m long. A 10% mirror field is produced by shaping the end of the coil. The majority of the detailed diagnostics have been done on FRX-A, which has a 7-kG peak-field capability with a 3.2μs rise time. Similar studies have been initiated on the more energetic FRX-B (12 kG and 1.8μs rise time).

The temporal behavior of the external B-field shown in Fig. 2 is produced by conventional crowbarred theta-pinch circuits operating in the "reversed bias" mode. The sequence begins with the slowly rising negative bias field, followed by the ringing theta-pinch preionization (PI), and then at t=0, the main field rises rapidly and is crowbarred with a 150-200μs decay time. Comparison of the vacuum shot with the static 5 mTorr D_2 fill shows the increased damping of the ringing PI as the plasma is formed. The bias field and PI plasma are allowed to diffuse before the main field reverses the external field and implodes the plasma. The oppositely directed bias and main fields reconnect near the ends of the system [3,7] forming the RFC (see Fig. 1). The RFC excludes the open field lines from a substantial volume of the coil. This excluded flux effect results in a lower coil inductance and a higher coil current and external field shown in Fig. 2. When the RFC is destroyed (in this case, by the rotating m=2 mode), the field rapidly returns to the vacuum value. This effect has proved to be a reliable measure of the RFC lifetime. Fig. 2 represents typical data, but not the longest lifetimes observed in the two machines.

Other diagnostics are shown in Fig. 3. The spectrometer is used to estimate the electron temperature profiles by observing the OV 2781Å, CIII 2297Å, and CV 2271Å lines. The ion temperature and rotational velocity is inferred from the polychromator measurement of the Doppler broadening and shift of the CV 2271Å line. In addition to the end-on interferometer shown in Fig. 3, a feedback stabilized interferometer was used to measure the line density through the plasma diameter at various axial positions. A pressure probe [11] has also been used to measure the spatial and temporal behavior of the plasma escaping out of the end of the system.

III. EXPERIMENTAL RESULTS

The macroscopic behavior of the plasma is indicated by the side-on streak and end-on framing pictures in Fig. 4. Five phases of the plasma behavior can be seen during the usual "clean" mode of operation (Fig. 4(b)): (1) PI (t<0), (2) implosion, field reconnection, and axial contraction (0<t<5μs), (3) equilibrium (5<t<15μs), (4) onset and growth of the rotational m=2 instability (15<t<19μs), and (5) the disruption of the RFC and loss of confinement (19<t<23μs). This behavior is very similar to that observed by Eberhagen and Grossmann [7].

An abrupt switch from clean to "dirty" mode operation (Fig. 4(a)) is produced by increasing the fill pressure, lowering the plasma purity, or lowering the power input to the plasma. This behavior suggests that the

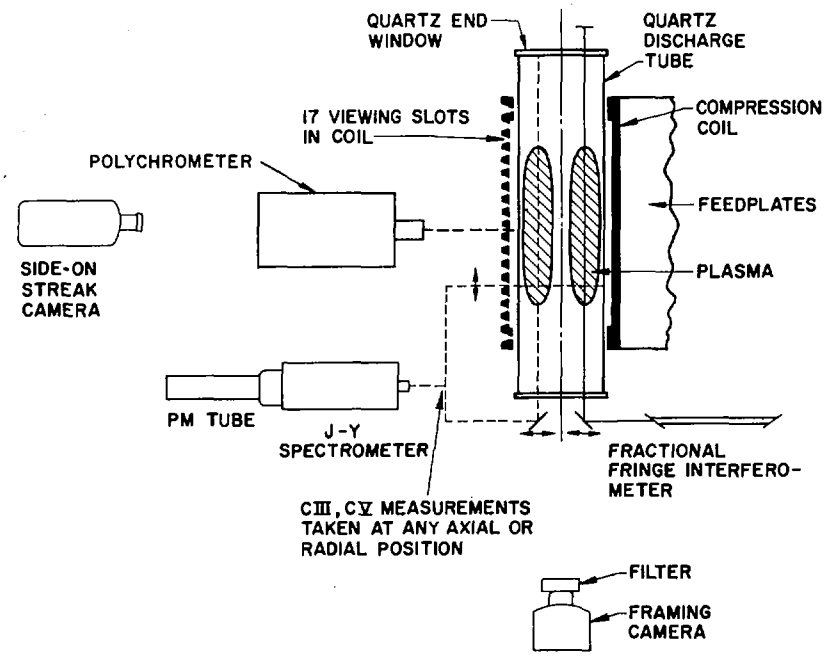


FIG. 3. Schematic arrangement for some of the diagnostics on FRX-A.

dirty mode is caused by failure to burn through a radiation barrier. The sudden destruction of the RFC before the onset of the rotational instability (Fig. 4(a)) characterizes the dirty mode and was observed in the behavior of the early experiments; however, the mechanism of the early RFC destruction is not understood. The dirty mode plasma contains CIII throughout the plasma life, indicating an electron temperature $T_e \lesssim 20$ eV. During the clean mode, OV burns through during the implosion and CV exists during equilibrium and instability phases, indicating that $T_e \sim 100$ eV (see Fig. 5). The remainder of the paper considers only clean mode behavior.

The axial profiles of transverse line density shown in Fig. 6 confirm the plasma length of about 35 cm indicated by the streak photographs during the equilibrium phase. The axial profiles are also confirmed by CV radiation measurements. The hollow radial profile indicated by the framing pictures is also confirmed by CV radiation and end-on interferometry. However, accurate measurements of the radial density profile are hindered by cold plasma outside the region of the implosion coil.

Ion temperatures are inferred from the Doppler broadening of the CV 2271Å line, which does not suffer from signicant Stark effects in the density range of interest. Depending on the strength of the implosion field, T_i varies between 150 and 350 eV. For the densities of interest, the equilibration time between the CV and deuterium is less than 5μs. The ion temperature is independent of radius and appears to decrease by about 20% during the 14μs of the equilibrium and instability phases. Although this

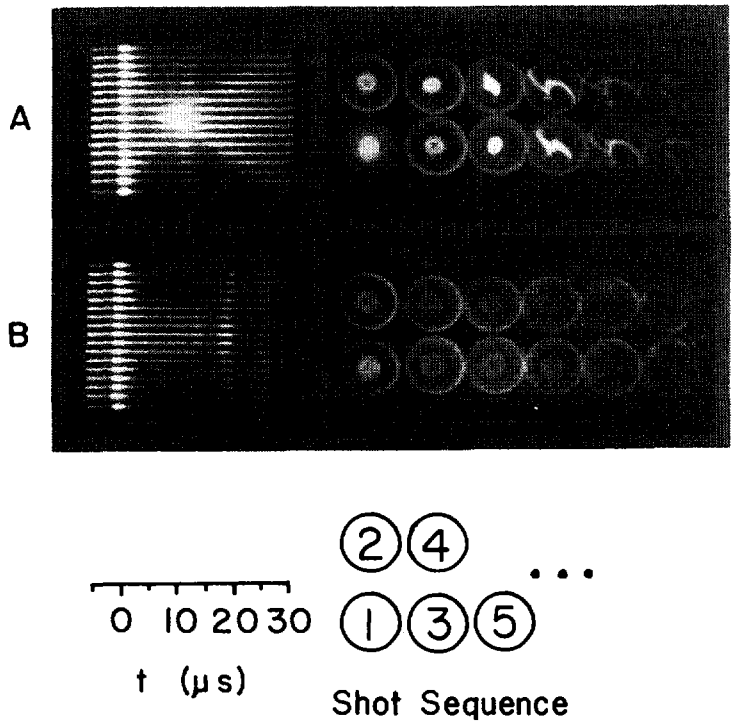


FIG.4. Side-on streak and end-on framing pictures for the (A) dirty mode and (B) clean mode of operation. The framing rate is 1.7 μs/frame, with the first frame at t = 3 μs. The thin, outer luminous ring in the framing pictures corresponds to the 20-cm diameter quartz tube.

decrease is about the same as the uncertainty of the measurement, it is also the amount that is consistent with classical equilibration between electrons and ions, assuming T_e is fixed.

During the equilibrium and instability phases, the temporal behavior of the plasma size, density (Fig. 6), electron temperature (Fig. 5), and ion temperature indicate energy and particle confinement times that exceed 40 μs, which is more than 10 times the expected confinement in an open-field system. Furthermore when the RFC is disrupted, the observed particle loss rates are consistent with the expected 3 to 4 μs, and the drop in CV (Fig. 5) is consistent with the slightly faster electron thermal losses expected [12,13] along open-field lines.

These results indicate that the enhanced confinement is due to closed-field lines, but the reversed field has also been measured directly. A magnetic field probe was inserted along the axis of the system that measured reversed fields of the order of 85% of the external fields. However, this internal probe shortened the lifetime of the RFC and was removed.

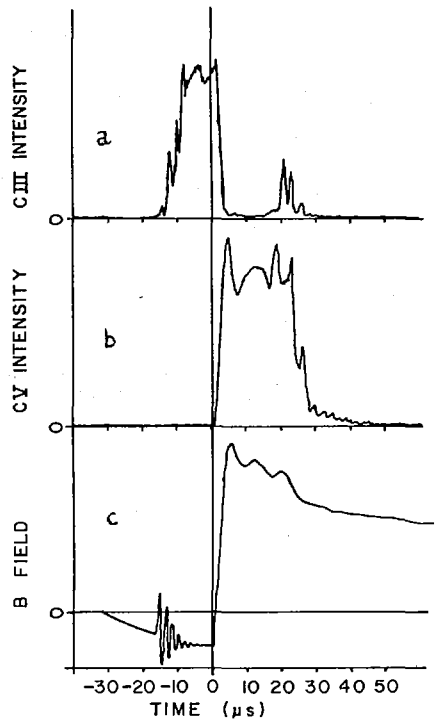


FIG. 5. Oscilloscope traces comparing the temporal behaviour of the (a) C III 2297 Å radiation, (b) C V 2271 Å radiation, and (c) the external magnetic field for clean-mode operation. The intensities of the two carbon lines are plotted on the same scale.

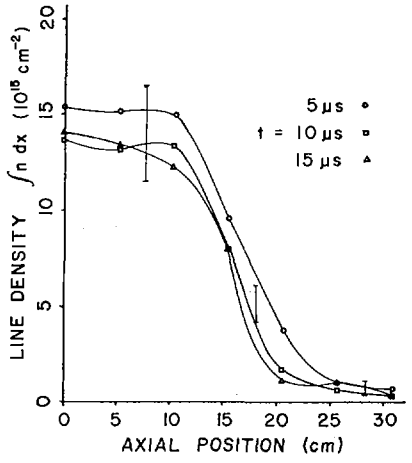


FIG. 6. Line density through RFC diameter as a function of axial position for three times during equilibrium phase. Connecting lines are added for visual clarity.

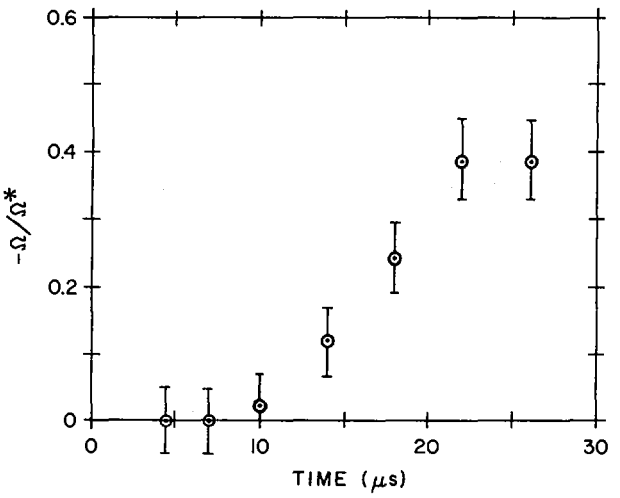


FIG. 7. Temporal history of C V rotational velocity normalized to deuterium diamagnetic drift velocity.

Pressure probe measurements of the plasma escaping from the end of the coil region confirmed and clarified several other measurements. A short, small burst of pressure was measured at all radii, which apparently corresponds to plasma lost at the time of implosion before the field line closure. All subsequent plasma loss occurred in a circular jet of plasma along the system axis less than 4 cm in diameter at the mirror peak and expanding along a vacuum flux tube. Time of flight measurements of this jet indicate that the majority of plasma loss occurs in two equally energetic bursts of similar mass that originate during (1) the axial contraction and (2) just following the RFC disruption. Between these two bursts (during the equilibrium and instability phases) the pressure from the escaping plasma corresponds to a characteristic loss time of 50 to 80 μs. The first pressure burst corresponds to the loss of 1/2 the initial fill during the axial contraction. This measurement is consistent with the measured inventory after the axial contraction. The magnitude of the two pressure peaks also agrees with a plasma pressure equal to the confining field pressure (β=1). In addition, assuming an appropriate rigid rotor density profile, the measured density, temperatures, and B field are consistent with pressure balance. The cause of the loss of plasma during the contraction phase is not yet understood.

Ion rotational velocity is determined by the Doppler shift of the CV 2271Å line along a variety of chords through the plasma. The temporal behavior of the observed rigid-rotor rotation is shown in Fig. 7. The onset of the rotational instability always occurs at the same normalized value of rotation.

Several minor modifications of the system have been made in an attempt to limit the rotation or generally to extend the life of the plasma. Since Kurtmullaev and co-workers [7] did not see the m=2 mode, hexapole fields

were added and both first- and second-half-cycle operation were used in an effort to duplicate their results. No significant change in the maximum attainable lifetimes was observed.

Quartz end plugs were inserted in an effort to control the radial electric field and the associated rotation [14]. The effects were generally detrimental, but the results were clouded by possible interference of the plugs with the PI process. Experimentally, the plasma stability is very sensitive to the PI conditions.

The passive mirrors were removed from the end of the main coil in FRX-A and separately powered mirror coils were added. With a 1 μs quarter period risetime and a mirror ratio ~2, the uncrowbarred mirrors resulted in RFC lifetimes up to 45 μs. The plasma parameters under these conditions are being measured. The mirror power supply will soon be crowbarred to provide additional axial implosion energy, similar to the Kurtmullaev experiment. A possible explanation for the improved lifetime is that more rapid closure of the field lines confines a larger fraction of the plasma, and hence, greater inertia opposes the accelerating torque.

The higher energy FRX-B can produce up to 40 μs RFC lifetimes with the original passive mirrors.

IV. DISCUSSION

The radial equilibrium profile of the observed RFC is probably similar to an infinitely long system because the length ~35 cm is long compared to its radial dimensions ≲6 cm. Viscosity will cause the radial equilibrium to approach a rigid-rotor profile. Although existing measurements such as ion rotation are all compatible with the rigid-rotor model, accurate radial density and B-field profiles are needed to determine the actual radial equilibrium. The axial equilibrium behavior of the plasma is similar to the results of belt-pinch equilibrium calculations [15,16]. The plasma in both FRX systems contracts to about 1/3 of the coil length and oscillates slightly with the crowbarred field modulation (Fig. 2) with very little change in radial dimensions. Several attempts are being made [17] to calculate the equilibrium shape with appropriate FRX boundary conditions.

The observed confinement time during the equilibrium phase of about 40 to 80 μs is longer than predicted for Bohm diffusion, but is substantially shorter than the 300 μs classical time, assuming the estimate of T_e=100 eV is accurate. These shorter confinement times might be caused by micro-instability-enhanced diffusion [18,19] or by ion-ion diffusion. This like-particle diffusion can dominate electron-ion diffusion for small values of a/ρ_i where a is the minor radius of the plasma and ρ_i is the ion gyro radius in the external field [20]. For the observed values of $2<a/\rho_i<3$, both sources of anomalous diffusion are viable. The diagnostic studies of the recently observed longer-lived plasmas should increase the accuracy of the measured particle and energy confinement time.

The study of the stability properties of the FRX-produced plasmas is dominated by the rotational m=2 mode. The rotational modes for a standard theta pinch have been theoretically determined by Freidberg and Pearlstein [21]. The theory predicts a stable range of normalized rotation $0<-\Omega/\Omega^*<1$ for a rigid-rotor profile. Freidberg modified the model to handle the rigid-rotor RFC. He made a simple, but not unique, analytic continuation in the vicinity of the singular point at B=0. The result predicted

the critical rotation of $-\Omega/\Omega^* \sim 1.6$ for the m=2 mode. Because the finite Larmor radius (FLR) expansion used in the code breaks down near B=0, the validity of the result was suspect. However, the results were verified ($-\Omega/\Omega^* \sim 1.5$) by using a Vlasov fluid code [22] that correctly calculates the orbits near B=0.

The experimental and theoretical results qualitatively agree that a stable range of rotation does exist. However, the theoretically predicted value of the critical rotation is four times higher than experimentally observed. The error bars in Fig. 7 do not include the uncertainty in determining Ω^* from measured quantities, but it is certainly accurate to within a factor of 2. Other possibilities exist to explain the error, such as that the RFC may not have the assumed rigid-rotor equilibrium, or the CV ions may not be rotating at the same velocity as the deuterium, even though calculations indicate they should.

The apparent lowering of the rotational threshold for instability may arise from a coupling between the rotational mode and the MHD kink mode. Because of the geometry, the fastest growing kink mode probably results in the same m=2 distortion. Even though geometry and FLR effects may reduce the growth rate of the kink so that it is not observed in a non-rotational form during the plasma lifetime, the free energy in the field that drives the kink may lower the threshold of the rotational mode. Since both rotational models are one dimensional, they do not contain this possible driving force. Freidberg is examining the possibility of adding a gravitational term to simulate this effect. In addition, a 3-dimensional MHD code [23] is being used to study the effects of geometry and rotation on the kink mode [24].

The macroscopic tearing of the plasma into distinct rings has never been observed in the FRX systems. In spite of recent advances in the understanding of tearing modes [25,26], a two-dimensional model may have to be developed to accurately determine the stability of finite length layers as produced in the FRX systems. But even if long layers tend to tear into distinct rings, the result may not be detrimental to fusion concepts [27].

The continuing focus of research is to understand and control the m=2 rotational instability. Detailed experimental studies of the dependence of this mode on temperature, geometry, and RFC formation process are being pursued. Advanced theoretical models including geometry and kinetic affects are under development.

ACKNOWLEDGEMENT

The assistance of Dr. C. J. Buchenauer in the development of the UV polychromator is gratefully acknowledged. In addition, the expert technical services of G. L. Stelzer and G. M. Sandoval are greatly appreciated.

REFERENCES

[1] ROSTOKER, N., KOLB, A. C., Phys. Rev. 124 (1961) 965.
[2] BODIN, H. A. B., NEWTON, A. A., Phys. Fluids 6 (1963) 1338.
[3] BODIN, H. A. B., Nucl. Fusion 3 (1963) 215.
[4] LITTLE, E. M., QUINN, W. E., Phys. Fluids 6 (1963) 875.
[5] ALIDIERES, M., AYMAR, R., JOURDAN, P., KOCCHLIN, F., SAMAIN, A., Plasma Phys. 10 (1968) 841.

[6] KALEK, A., KONEN, L., NOLL, P., SIGUTA, K., WAELBROEK, F., WATANABE, K., WITULSKI, H., "Limitation of the Confinement of Plasma in a Liner Theta Pinch with Trapped Reverse Magnetic Field," Conf. Plams Phys. and Contr. Nucl. Fusion, Novosibirsk, Vol. II (1968) 581.
[7] EBERHAGEN, A., GROSSMANN, W., Z. Phys. 248 (1971) 130.
[8] ES'KOV, A. G., et al. "Plasma Confinement in a Pulsed System With a Compact Toroidal Configuration." (Proc. Seventh European Conf. Controlled Fusion and Plasma Physics 1975) 1 Lausanne (1975) 55.
[9] HAMMAR, D. A., ROBSON, A. E., GERBER, K. A., SETHIAN, J. D., Physical Lett. 60A (1977) 31.
[10] ROBERSON, C. W., Bull. Am. Phys. Soc. 22 (1977) 1168.
[11] YORK, T. M., Rev. Sci. Instrum. 41 (1970) 519.
[12] CHU, T. K., JOHNSON, L. C., Phys. Fluids 20 (1977) 1684.
[13] GARY, S. P., SGRO, A. G., DESILVA, A. W., submitted to Phys. Fluids.
[14] COMMISSO, R. J., EKDAHL, C. A., FREESE, K. B., MCKENNA, K. F., QUINN, W. E., Phys. Rev. Lett. 39 (1977) 137.
[15] KADISH, A., STEVENS, D. C., Nucl. Fusion 14 (1974) 821.
[16] BAKER, D. A., MANN, L. W., "Toroidal Belt Pinch Equilibria," Los Alamos Scientific Laboratory internal report LA-UR-73-104 (1973).
[17] MANN, L. W. (LASL), ANDERSON, D. V. (LLL), GROSSMANN (NYU), personal communication.
[18] DAVIDSON, R. C., KRALL, N. A., Nucl. Fusion 17 (1977) 1313.
[19] HAMASAKI, S., KRALL, N. A., Bull. Am. Phys. Soc. 22 (1972) 1136.
[20] TUSZEWSKI, M., LICHTENBERG, A. J., Phys. Fluids 20 (1977) 1263.
[21] FREIDBERG, J. P., PEARLSTEIN, L. D., to be published in Phys. Fluids.
[22] SEYLER, C. E., to be published.
[23] BRACKBILL, J. U., Meth. Comp. Phys., 16 (1976) 1.
[24] ANDERSON, D. V., personal communication.
[25] FINN, J. M., KAW, P. K., Phys. Fluids 20 (1977) 72.
[26] DRAKE, J. F., LEE, Y. C., Phys. Fluids 20 (1977) 1341.
[27] GROSSMANN, W., SEYLER, C. E., STEINHAUER, L., Bull. Am. Phys. Soc. 22 (1977) 1189.

FIELD REVERSAL IN MIRROR MACHINES*

L.D. PEARLSTEIN, D.V. ANDERSON,
D.E. BALDWIN, J.A. BYERS, B.I. COHEN,
R.H. COHEN, W.C. CONDIT, T.K. FOWLER,
R.P. FREIS, T.B. KAISER, R.F. POST,
M.E. RENSINK, G.R. SMITH
Lawrence Livermore Laboratory,
University of California,
Livermore, California

A.H. BOOZER
Plasma Physics Laboratory,
Princeton University,
Princeton, New Jersey,
United States of America

Abstract

FIELD REVERSAL IN MIRROR MACHINES.

Some of the physics issues anticipated in field-reversed mirrors are discussed. The effect of current cancellation due to electrons is described. An estimate is made of the required impurity level to maintain a field-reversed configuration. The SUPERLAYER code is used to simulate the high-β 2XIIB results, and favourable comparisons require inclusion of quasi-linear RF turbulence. Impact of a quadrupole field on field-line closure and resonant transport is discussed. A simple self-consistent model of ion currents is presented. Conditions for stability of field-reversed configurations to E X B-driven rotations is determined.

INTRODUCTION

The principal advantage of a field-reversed-mirror (FRM) configuration is that there is no external toroidal field. Consequently β is high, and the configuration can be made small and simple, particularly if it can be sustained by neutral beams. The problems are numerous. Can the configuration be generated with ion current; that is, do self-generated electron currents cancel? How is the equilibrium sustained, and is it pulsed? Finally, conventional wisdom suggests that in the absence of any toroidal field [1] the system is unstable if the layer is too long (tearing), if the aspect ratio is too small (MHD), or if the Larmor orbit

* Work performed under the auspices of the US Department of Energy by the Lawrence Livermore Laboratory under contract number W-7405-ENG-48 and Princeton University under contract number EY-76-C-02-3073.

is too small (MHD). In the face of these is a stable configuration feasible? It is the purpose of this paper to examine these questions and to indicate our level of understanding at this time.

In Sec. 1, we describe the equations governing equilibrium, emphasizing the role played by electrons. The consequences of constraints imposed by current cancellation are discussed. Next, a comparison is made between 2XIIB and the two-dimensional code called SUPERLAYER. One defect of the code is the restriction to axisymmetry. We next assess the role quadrupole fields play upon injection (the effective stretching of the source), equilibrium (the opening of field lines), and transport (the degrading of confinement through single-particle resonances). This section concludes with an analytic model of an ion layer. Finally, in Sec. II, we address stability, where we consider the influence of finite Larmor radius (FLR) and large aspect ratio on rotation-driven instabilities.

1. EQUILIBRIUM AND TRANSPORT

1.1. Electron Physics

In an FRM configuration generated and sustained by neutral beams, the first point to resolve is the extent to which electrons cancel the ion current. At a field null, electrons by resistive drag will speed up to the ion velocity unless there is some other competitive viscous force allowing a net current, such as generated by slower moving, higher Z impurities (Ohkawa current [2]). Away from a null, electron current must be due to E x B drifts, and so it is bounded by the potentials sustained across flux surfaces. For substantial current cancellation, the E x B velocity must be of the order of ion speed, requiring a potential ($e\phi$) drop of the order of the ion temperature (T_i). Consequently, on the open field lines where $T_e << T_i$ and $e\phi \sim T_e$, electron currents are negligible. On the other hand, on closed field lines there is no such limitation, and we must solve explicitly for the self-consistent potential. In both of these cases the external viscous force that is required to maintain this differential rotation comes from the interaction of the electrons on the open field lines with the walls.

To study these effects due to electrons [3], we consider an axisymmetric hybrid model wherein the ion dynamics are determined from a two-space, three-velocity particle code (SUPERLAYER)[4]. The magnetic and electric fields are given by

$$\underset{\sim}{B} = \frac{1}{r} \nabla\psi \times \hat{\theta}, \quad \underset{\sim}{E} = -\underset{\sim}{\nabla}\phi - \frac{1}{rc}\frac{\partial\psi}{\partial t}\hat{\theta} \tag{1}$$

and the self-generated toroidal field can be made negligible. The electrons are treated as an E x B fluid given by

$$n_e = n_i Z_i \text{ , quasi-neutral} \tag{2}$$

and

$$\underset{\sim}{E} + \frac{\underset{\sim}{v}_e}{c} \times \underset{\sim}{B} = \frac{m_e \nu_{ei}}{n_e e}\sum n_i Z_i^2 (\underset{\sim}{v}_i - \underset{\sim}{v}_e) = \eta(\underset{\sim}{j} - e\sum n_i \underset{\sim}{v}_i Z_i (1 - \frac{Z_i}{Z_{eff}}))$$

$$= \eta(j - j^{OHKAWA}) \tag{3}$$

with

$$\nu_{ei} = \frac{4}{3}\sqrt{\frac{2\pi}{m_e}}\,\frac{n_e e^4 \ln\Lambda}{T_e^{3/2}} \tag{4}$$

Consequently, with Ampère's law, neglecting displacement currents, we obtain

$$\frac{\partial\psi}{\partial t} + \underset{\sim}{v}_e \cdot \underset{\sim}{\nabla}\psi - \frac{r^2 c^2}{4\pi}\eta\underset{\sim}{\nabla}\cdot\frac{1}{r^2}\underset{\sim}{\nabla}\psi = \eta c r j^{\text{OHKAWA}} = \alpha r c \eta j \tag{5}$$

where the second equality holds when there is only one species having a non-zero velocity. Note the bootstrap current [5] $\underset{\sim}{v}_e\cdot\underset{\sim}{\nabla}\psi\ /\ \eta r c$. There are several simple points that can be obtained from Eq. (5). First, at the null (O-point), if the electron velocity is finite, steady state is not possible in the absence of the seed current. It should be emphasized that <u>any</u> process that breaks the relation $P_{ei}/n_e = \eta j$ leads to a seed current. Further, if field reversal is achieved, it can only be lost in a resistive diffusion time.

We estimate the seed current necessary for reversal by examining the steady-state solution of Eq. (5) in the paraxial limit ($B_r << B_z$). For an ion source localized near the position of the null r_0, write the ion source $nv_r = (r - r_0)S$ and then integrate over the plasma volume to obtain

$$1 = \frac{\alpha}{a_i}\int_{r_0}^{r_1} dx\, \exp\left(\frac{S\tau_{skin}}{2nr_0^2}\left((r - r_0)^2 - (x - r_0)^2\right)\right) \tag{6}$$

where for $\beta \sim 1$ we use $nm_i v_\theta^2 = B_0^2/4\pi$,

$$\tau_{skin} = \frac{4\pi r_0^2}{\eta c^2} = \left(\frac{r_0}{a_i}\right)^2 \tau_{drag}\ , \quad a_i = v_\theta/\omega_{ci}$$

where ω_{ci} is the gyrofrequency at the vacuum field, v_θ is the ion thermal velocity, and r_1 is the last closed flux radius where B is assumed to have its vacuum value. The term multiplying the integral is just the ratio of the self field, due to the Ohkawa current, to the vacuum field.

To apply this result to the slow buildup in the present 2XIIB experiments, we argue as follows. The injection current must be sufficient to drive the field close to zero while the field lines are open and T_e is low; in this regime, $S\tau_{Drag} \approx n$ or for the trapped current

$$\frac{I_{trap}\,\tau_{drag}}{L} \propto \frac{r_0^2}{a_i^2} \tag{7}$$

We now compare this with the condition that a well developed field-reversed steady state exists for the same T_e, noting that this should be pessimistic because T_e should climb on closed lines. For fixed α , Eq. (6) may be thought of as giving $S\tau_{skin}/\ n \propto I_{trap}\,\tau_{drag}/L$ as a function of r_0/a_i. The combination of this result and Eq. (7) forms a minimum in the required trapped current; for $\alpha = 0.2$ this lies at $r \approx 2r_0 \approx 4a_i$. Thus, the required radius is about twice that of 2XIIB,

which is roughly four times the volume. Folding in the increased trapping efficiency, we conclude that to achieve field reversal in the experimental regime, a threefold increase in injection current, or an equivalent increase in the energy containment on the open lines, is required. This increase in lifetime to $\tau_E \approx \tau_{drag}$ would require better suppression of rf turbulance at high β. These basic electron physics equations, Eqs (1-5), coupled with the constraint

$$\int \frac{dl}{B} \nabla \cdot \underset{\sim}{j} = 0$$

are being coupled with the ion pusher, SUPERLAYER, in a new hybrid simulation code.

1.2. SUPERLAYER Simulation

In addition to the electron physics, which is presently being worked into SUPERLAYER, we have developed a Monte Carlo package to model the drift-cyclotron loss-cone (DCLC) rf activity on open lines and charge exchange off the beams. The former generates transport (i.e. diffusion coefficients) in agreement with the quasilinear model of DCLC. Since the electron physics package is not complete, only energy transfer to electrons has been considered; thus, at present we are only able to simulate the approach to B = 0. Typical runs contain between 10 000 and 60 000 superparticles. We select the electron temperature (and the rf level, which determines the ion energy) to agree with the experiment, and then determine the remaining equilibrium quantities as a function of injection current. The DCLC turbulence not only modifies the energy distribution; it also causes appreciable radial diffusion. In addition results are sensitive to the stream current imposed. At present, this current is an external parameter. Agreement between simulation and experiment [6] is reasonably good at two field strengths for peak densities, $\Delta B/B$ and radii. However, the plasma length is too short in the simulation by a factor ~ 2. This discrepancy is believed to be due to the neglect of a quadrupole field in the simulation, which now brings us the question of what we neglect by assuming axisymmetry.

1.3. Quadrupole Fields

An obvious effect of the quadrupole field is the tipping of the field lines away from the axis, effectively lengthening the source. To evaluate this effect, we have superimposed an external quadrupole field in SUPERLAYER and have observed stretching of ion-ring equilibria by the right magnitude. However, the introduction of the quadrupole field raises more subtle issues. First is the question of whether field lines can then close if the field is reversed. The second issue is how badly do single-particle resonances for axis-encircling particles degrade confinement.

First consider the question of the opening of field lines [7]. To show the scaling, we superimpose externally applied toroidal and quadrupole fields on the field-reversed configuration. As a model, we again assume that $B_z >> B_r$ almost everywhere and use the paraxial approximation (except over a small region where field lines turn). In this case, the field-reversed configuration can be written:

$$r^2 - r_0^2 = \pm r_0^2 \frac{\eta}{\eta_0} \tag{8a}$$

$$B_z^2 = B_v^2 \tanh^2 \eta \,, \quad \eta \geq 0 \tag{8b}$$

$$\underset{\sim}{B}_T = \hat{\theta}\, \frac{r}{R}\, B_T \tag{8c}$$

and

$$\underset{\sim}{B}_q = B_q\, \frac{r}{R}\, (\hat{r} \cos 2\theta - \hat{\theta} \sin 2\theta) \tag{8d}$$

Note that η_0 is the value of η on the last closed-field line and is related to the vacuum flux by $\exp(\psi/\psi_0) = \cosh^2\eta$. Also, Eq. (8a) is the equation of a field line (η constant) in the absence of B_q and B_T that we now treat as a perturbation. Now the equations of motion of a field line due to this perturbation can be written:

$$d\psi \,/\, \oint \frac{dl}{B}\, \underset{\sim}{B}_q \cdot \nabla\psi = \; d\theta \,/\, \oint \frac{dl}{B}\, (\underset{\sim}{B}_q + \underset{\sim}{B}_T) \cdot \nabla\theta \tag{9}$$

Thus

$$\eta = \eta(z = 0)\, \frac{\sin 2\theta(z = 0) - \dfrac{B_T}{B_q}}{\sin 2\theta - \dfrac{B_T}{B_q}} \tag{10}$$

Consequently, field lines are confined if $|B_T/B_q| > 1$. This analysis ignores diamagnetic effects on the quadrupole field. To ascertain whether plasma currents can shield out the quadrupole field is an unanswered question and awaits the development of a self-consistent three-dimensional equilibrium code.

Another aspect of asymmetry is how it affects radial transport. Specifically, axis-encircling particles can satisfy resonance conditions, in which case perturbations due to quadrupole fields can enhance particle losses. Luckhardt and Fleishmann[8]have suggested that such is the cause of the enhanced electron losses in the RECE-BERTA ring experiment. An important observation is that the sudden losses occur at fixed values at $\delta = \Delta B/B$ (independent of B_q) and that the losses between these fixed values are proportional to the collision frequency but enhanced by a factor proportional to B_q. These features suggest that, near the fixed values of δ, a sizable fraction of the plasma intercepts the loss region, whereas at other values there is 'neoclassical'-like transport with an effective banana width $\propto B_q^{1/2}$.

Assume that particles in this general three-dimensional system possess three good invariants; then the resonance condition associated with these invariants is

$$m\Omega_z + n\Omega_r + L\Omega_\theta = 0 \tag{11}$$

If particles could maintain this resonance relation, they would simply drift out of the confined region under the influence of a symmetry-breaking field. The fact that the Hamiltonian of the system is a nonlinear function of the invariants (actions) bounds the regions of resonance. The quadrupole field couples degrees of freedom if L = 2 and m is odd. Then the invariants oscillate about resonant values slowly, compared with their associated frequencies. The amplitudes ΔI and island frequency $\Omega_I \propto B_q^{1/2}$. If this swing intercepts a radial limiter, plasma loss results.

To evaluate these effects, we expand about circular orbits and write the Hamiltonian in action-angle variables, viz

$$H_0 = \Omega_r (I_\theta) I_r + \Omega_z (I_\theta) I_z + \omega_{ci}^2 (I_\theta) R^2 (I_\theta) \frac{m_i}{2} \tag{12}$$

The procedure then is to cast the perturbed Hamiltonian due to B_q in action angle variables, which have a nearly constant phase when Eq. (11) is satisfied. Then, following Chirikov [9], we make a further canonical transformation to obtain a new Hamiltonian dependent on this slow phase and action and hence deduce the oscillation amplitudes of the original actions:

$$\begin{bmatrix} \Delta I_r \\ \Delta I_\theta \\ \Delta I_z \end{bmatrix} = \begin{bmatrix} -n \\ 2 \\ -m \end{bmatrix} \times B_q^{1/2} M \tag{13}$$

where M is a completely determined but complicated decreasing function of m and n.

To apply this calculation to RECE-BERTA, we choose the flux to satisfy

$$\psi = \frac{B_0 r^2}{2} \left[1 - \delta \exp \left(- \frac{r^2}{L_r^2} - \frac{z^2}{L_z^2} \right) \right] \tag{14}$$

with L_z = 11 cm and L_r = 16 cm, and thus the current-density peaks at r = 9 cm.

We have calculated resonance positions and widths in I_r, I_z space for 450-keV electrons at various values of δ. We identify a 'well populated' region corresponding to particles that do not hit the limiter and turn axially at Z_t < 10 cm. We find that, as δ is varied, resonances move slowly in the axial tail (Z_t > 11 cm) but rapidly in the well populated region; e.g. the m = 3, n = 0 resonance sweeps through the latter region as δ changes from 0.62 to 0.56, corresponding to a time short compared with the ring decay time (10^{-5} s) but slow compared with the island frequency (10^{7} s^{-1}) for B_q(r = 10 cm)/B = 0.02. Hence, particles lying in I-space within ΔI of the radial limiter are lost during a sweep, while the increase in diffusion coefficient for the remaining particles is neoclassical (banana regime):

$$D \sim (\Delta I)^2 \nu \sim B_q^{1/2} \nu \tag{15}$$

In this model, the most notable resonances were δ = 0.73 (m = n = 1), δ = 0.55 (m = 3, n = 0) and δ = 0.14 (m = 3, n = 1). In RECE-BERTA, only two resonances have been identified, which we speculate to be the latter two. As for the first resonance, a more exact treatment might predict its onset to lie at δ > 1 and thus not in present data. There are other weaker resonances intercepting the limiter that have also not been observed. It should be emphasized that our model field is crude, assumes fixed scale lengths, and ignores mirroring in the vacuum field. The weakness in the Hamiltonian model is the inadequate treatment of particles with large excursions. It should be noted that resonances hang up in these regions.

These effects have also been investigated with the exact orbit, single-particle code ORBXYZ. To date, comparisons have been limited, but for the principal resonances studied, δ is as predicted and the excursions scale with analytic theory.

Such resonance should degrade confinement in the very high β-regime in 2XIIB. However, if the radius is doubled for significant bootstrapping as required for field reversal, the number of axis-encircling particles should be small, the frequencies should be disparate, and this resonant diffusion should disappear.

1.4. Analytical Model of a Field-Reversing Ion Layer

To help gain insight into the physics of field-reversed states, we investigated an analytically solvable case. The model is a Z-independent, axially symmetric entity in which monoenergetic ions of fixed canonical angular momentum $f \sim \delta(E - E_0)\ \delta(L - L_0)$ move in the self-consistent fields generated by their motion in the external field B_0. For the chosen ion-distribution function the ionic azimuthal current is $j_\theta = v_\theta/r$. Use of this relation, together with that required by conservation of canonical angular momentum, leads immediately to a differential equation of Bessel form for $y = v_\theta/v$, the dimensionless azimuthal velocity of the ions:

$$\frac{d^2y}{dx^2} + \frac{1}{x}\frac{dy}{dx} - \left(\frac{1}{x} + \frac{1}{x^2}\right) y = 0 \qquad (16)$$

where $x = K(r/a_i)$, a dimensionless radius, a_0 is the ion gyroradius in the (uniform) vacuum field B_0, and K is a constant (later determined) that is a measure of the dimensionless radius of the entity $K \approx a/a_i$.

The general solution to this equation is

$$y = AI_2(2x^{1/2}) + BK_2(2x^{1/2}) \qquad (17)$$

Boundary conditions to be imposed are: (1) $y = -1$ at $r = a$ and $r = s$ (inner radius of entity) and (2) $a_i = a_0$ at $r = a$ (i.e. ion gyroradius at outer boundary equals vacuum-field gyroradius). With the above, a closed solution is obtained wherein A and B are given as functions of s/a and a/a_i, from which follow self-consistent fields and orbits.

Some conclusions from the analysis:

- Field reversal is only possible for $a/a_0 > 2.0$.
- Large, thick layers produce higher field reversal:

$$\frac{B(s)}{B_0} \approx -\ (a/s)^{1/2}\ ,\quad a >> a_0\ ;\quad a >> s \qquad (18)$$

- Depending on the sign of y at $r = s$, either field reversal or field enhancement may be achieved.

2. STABILITY

To ascertain the stability of an FRM we must include FLR and a large aspect ratio. To examine these effects we relax the length constraint

and use the paraxial approximation. We also consider a rigid-rotor equilibrium so that (see Eq. (8))

$$p_\perp = \frac{B_0^2}{8\pi} \frac{1}{\cosh^2\eta} \tag{19}$$

$$\rho = \rho(0) \frac{1}{\cosh^2\eta} \tag{20}$$

and the rotation frequency

$$\omega = \omega_* + \omega_{ExB} = \frac{2V_{Alf}^2}{\omega_{ci} r_0^2} \frac{\eta_0}{1 + \frac{T_e}{T_i}} (1 + K) \tag{21}$$

where

$$V_{Alf}^2 = \frac{B_0^2}{4\pi\rho(0)} \tag{22}$$

and $K = T_e/T_i$ for electrostatically confined electrons and comes from the E x B drift. Also, the mean particle frequency is given by

$$\omega_2 = \omega_{ExB} + \langle\omega_{\nabla B}\rangle = \frac{2V_{Alf}^2}{\omega_{ci} r_0^2} \frac{\eta_0}{1 + \frac{T_e}{T_i}} \left(K - \frac{1}{2\sinh^2\eta}\right) \tag{23}$$

We assume field-line lengths scale with η. How we resolve the singularity at $\eta = 0$ will be described presently.

The perturbed equations for this configuration ($E_\parallel = 0$) have been derived previously [10] and will be applied here. For the perturbed radial displacement, we have the equation

$$\frac{1}{r} \frac{d}{dr} \eta r^3 \rho T \frac{d\xi}{dr} = (m^2 - 1)\eta\rho T\xi - r\eta \frac{d\rho}{dr} (\omega^2 + k^2 V_{Alf}^2)\xi \tag{24}$$

with

$$\rho T = \rho(\eta) (\omega - m\omega_1) (\omega - m\omega_2) - k^2 B^2/4\pi \tag{25}$$

We consider rotation-driven modes which are flute-like. Consequently, we average over a line ($k^2 = 0$) to obtain

$$\frac{d}{d\eta} \begin{Bmatrix} (\eta + \eta_0)^2 \eta_0 \\ (\eta^2 + \eta_0^2)\eta \end{Bmatrix} \rho T \frac{d\xi}{d\eta} = \frac{m^2 - 1}{4} \begin{Bmatrix} \eta_0 \\ \eta \end{Bmatrix} \xi\rho T + \omega^2\rho(\eta) \begin{Bmatrix} \eta_0(\eta + \eta_0) \\ \eta^2 \end{Bmatrix} \xi \tanh\eta \tag{26}$$

when the upper (lower) quantities pertain to the open (closed) field lines. Note that because ξ is only a function of η through the flute average, the boundary condition or regularity at $r = 0$ is lost. Now to close the problem we need a constraint at the null. Both solutions are well behaved; $E_\theta = 0$ does not determine the proper solution at the null. We then have as η approaches zero, the two solutions

$$\xi_1 = \eta^2$$

$$\xi_2 = 1 + \frac{m^2 - 1}{16\,\eta_0^2}\,\eta^2 \ln\eta^2 \tag{27}$$

The next point is to obtain the appropriate linear combination. Recalling Eq. (23), we see that breakdown in the model occurs in the ∇B drift, which diverges at $\eta = 0$, and that an appropriate particle treatment would lead to a finite term. Consequently, we model this effect by writing

$$\omega_2 = 2\,\frac{V_{Alf}^2}{\omega_{ci} r_0^2}\,\frac{\eta_0}{1 + \frac{T_e}{T_i}}\left(K - \frac{1}{2(\eta^2 + \nu^2)}\right),\quad \nu^2 = \frac{a_i}{r_0 \eta_0} \tag{28}$$

To obtain this scaling, we have made use of the linear expansion $B = 2B_0(r - r_0)\,\eta_0/r_0$. Now, near the null the differential equation, Eq. (26), takes the form

$$\frac{d}{d\eta}\,\frac{\eta}{\eta^2 + \nu^2}\,\frac{d\xi}{d\eta} = \frac{m^2 - 1}{4\,\eta_0^2}\,\frac{\eta}{\eta^2 + \nu^2}$$

solving by iteration, we generate the solution ($\eta >> \nu$)

$$\xi = 1 + \frac{m^2 - 1}{16\,\eta_0^2}\,\eta^2\,(\ln\eta^2 - 1 + \ln\nu^2) \tag{29}$$

which then determines the linear combination. Note that the other solution diverges logarithmatically and must be discarded. It must be remarked that this result is only qualitative. A rigorous treatment requires the solution of the Vlasov equation in the vicinity of the null, where the magnetic field is linear. Our results show that as $\nu^2 \to 0$ (small Larmor radius) the system is most stable ($K \approx 1.2$). Recall that in this limit the solution at the null is ξ_1. On the other hand, as $\nu^2 \to 1/\eta_0 (a_i/r_0 = 1)$ the threshold drops to $K \approx 0 (E = 0)$. In this limit the solution at the null is predominantly ξ_2. These results do not agree with the Los Alamos Scientific Laboratory experiment [11], whose stability threshold is lower yet. It should be emphasized that there is a linear combination at the null with marginal stability at zero rotation; however, the solution is inconsistent with our boundary-layer analysis.

REFERENCES

[1] MARX, K.D., Phys. Fluids 11 (1968) 357; BERNSTEIN, I., et al., Proc. Roy. Soc. A244 (1958) 17; SUDAN, R.N., ROSENBLUTH, M.N., Phys. Rev. Lett. 36 (1976) 972.

[2] OHKAWA, T., Nucl. Fusion 10 (1970) 185.

[3] BALDWIN, D., RENSINK, M., Comments Plasma Phys. and Controlled Fusion 4 (1978) 55; BALDWIN, D., FOWLER, T.K., Lawrence Livermore Laboratory Rep. UCID-17691 (1978).

[4] BYERS, J.A., Phys. Rev. Lett. 39 (1977) 1476.

[5] BICKERTON, R.J., et al., Nature (London) 229 (1971)110; KADOMTSEV, B.B., SHAFRANOV, V.D., Plasma Physics and Controlled Nuclear Fusion Research 1971 (Proc. 4th Int. Conf. Madison, 1971) Vol.2, IAEA, Vienna (1971) 479 (in Russian); English transl. Nucl. Fusion Suppl. (1972) 209.

[6] SIMONEN, T.C., et al., paper IAEA-CN-37/J-1, these Proceedings.

[7] BOOZER, A.H., Nucl. Fusion 18 (1978) 1663.

[8] LUCKHARDT, S.C., FLEISCHMANN, H.H., Phys. Rev. Lett. 39 (1977) 747.

[9] CHIRIKOV, B.V., A Universal Instability of Many-Dimensional Oscillator Systems, to be published in Phys. Reports.

[10] PEARLSTEIN, L.C., FRIEDBERG, J.P., to be published in Phys. Fluids.

[11] LINFORD, R.K., et al., paper IAEA-CN-37/S-1-1, these Proceedings.

DISCUSSION

ON PAPERS S-1-1 AND S-1-2

H.A.B. BODIN: The data presented from the Los Alamos reversed-field theta-pinch showing improved confinement over the system without reversed field imply 'better stability than expected' of the end regions with strongly unfavourable curvature. Previously, when these systems were studied, there was no proper explanation of this; qualitatively, finite Larmor radius was suggested, but there are other factors. Have we now a better understanding? In particular, is there a quantitative treatment corresponding to the experimental condition?

L.D. PEARLSTEIN: If the external field is uniform (no curvature), there can be no rigid m = 1 interchange instability. This displacement must be zero frequency even though the self-consistent field has curvature. This does not rule out higher-m modes or non-rigid displacements; for these modes FLR effects could stabilize. The lines with some good curvature are separated from the closed field configuration by a separatrix. I should think that, if the closed field region were interchange-unstable, plasma would escape through this separatrix. The elongation of the plasma reduces the kink drive, which, combined with FLR effects, could stabilize this mode. The authors of paper S-1-1 speculate that bending of the field lines (the kink drive), neglected in the theory of rotational instability, might account for the optimistic threshold condition calculated.

D.R. SWEETMAN: Could you discuss, quantitatively, the importance of the Ohkawa current in obtaining field reversal? Does the presence of reverse currents have a substantial effect on the beam current required?

L.D. PEARLSTEIN: The magnitude of Ohkawa current required to maintain field reversal depends upon the ratio of minor radius to Larmor radius, (a/ρ_0). For $a/\rho_0 \lesssim 2$ the Ohkawa current must generate almost all of the reversed flux; for $a/\rho_0 \gtrsim 2$ the current analogous to the 'bootstrap' current in tokamaks reduces the required Ohkawa current by a factor $\exp[-\frac{1}{2}(a/\rho_0)^2]$. Since the Ohkawa current is proportional to the beam current, and since the required injection current goes up with volume, we estimate that 1500 A, roughly three times the available current, was required to reverse the field in 2XII-B.

H.H. FLEISCHMANN: With regard to your calculation on the orbital resonances, I would like to ask whether you have any results concerning the influence of hexapole fields or the influence of quadrupole fields in axially extended rings?

L.D. PEARLSTEIN: There have been no calculations with hexapole fields as yet. The calculation with quadrupole fields used a model Hamiltonian which is not accurate near the axial boundary. This model is now being improved.

EXPERIMENTAL STUDIES OF LOSS MECHANISM UNDER THE INFLUENCE OF CYCLOTRON INSTABILITIES IN A RAREFIED PLASMA

V.A. ZHIL'TSOV, P.M. KOSAREV, V.Kh. LIKHTENSHTEJN,
D.A. PANOV, A.A. SKOVORODA, A.G. SHCHERBAKOV
I.V. Kurchatov Institute of Atomic Energy,
Moscow, Union of Soviet Socialist Republics

Presented by Dzh. G. Lominadze

Abstract

EXPERIMENTAL STUDIES OF LOSS MECHANISM UNDER THE INFLUENCE OF CYCLOTRON INSTABILITIES IN A RAREFIED PLASMA.

An anomalous loss mechanism of ions and electrons in a mirror machine is investigated. – The experiments were carried out at the Ogra-3 and Ogra-3B devices with low-density plasma ($10^8 - 10^{10}$ cm^{-3}). Losses of plasma are the result of its radial transport across the magnetic field under the influence of an oscillating electric field with a frequency comparable to the particle drift frequencies. The well determined character of charged-particle motion in the field of the low-frequency wave is destroyed by the changes in the particle energies. The electron energy changes through Coulomb collisions, and that of the ions as a result of cyclotron oscillations. It is shown experimentally that if the low-frequency oscillations are suppressed cyclotron oscillations do not give rise to ion losses under the conditions of the experiment.

1. INTRODUCTION

Experiments with rarefied plasmas ($\omega_{pi} \lesssim \omega_{Bi}$) accumulated in mirror machines by means of fast-atom injection showed that an ion cyclotron instability gave rise to a significant loss of ions [1–5]. Moreover, an anomalously high positive plasma potential had been observed in a number of devices [1–4], which proved the existence of non-classical electron losses.

So far, such characteristics as density or magnetic-field thresholds of instabilities, mode structures of oscillations, and their spectra have been studied comparatively well.

The channels for particle loss are, however, only insufficiently known. The only possible mechanism of ion loss associated with a change in the transverse ion energy – and, consequently, with particle diffusion in velocity space and with filling the trap volume up to the magnetic mirrors – does not agree with the experimentally observed high plasma anisotropy. Generally speaking, ion loss

under the influence of cyclotron oscillations with rather narrow frequency spectra would contradict the conservation of the superadiabatic invariant.

The reason for the development of an anomalous plasma potential also requires additional investigation.

This paper presents the results of experiments dealing with the non-classical ion and electron loss mechanism and related phenomena appearing in this context.

2. DEVICES, PLASMA DIAGNOSTICS AND EXPERIMENTAL PARAMETERS

The investigations into the plasma loss mechanism were carried out on Ogra-3 and its modification, Ogra-3B. The latter differs from Ogra-3, whose parameters are given in Ref. [8], in the field configuration of magnetic trap, i.e. instead of the magnetic coils generating the simple mirror field a superconducting baseball coil was installed, which gives rise to a 'minimum-B' magnetic field. In both mirror machines, the plasma was produced by means of 20-keV hydrogen atom injection. The maximum injection current in Ogra-3B was 0.15 eq.A. Ion trapping was provided by ionization of highly exited atoms by means of a Lorentz field. The typical injection period was 1 s. The magnetic field strength at the centre of the Ogra-3B trap was 17 kG. The mirror ratio was 2.06, the distance between the mirrors amounted to 70 cm. The radius of the plasma accumulation region was 17 cm. The angle between the injected beam and the trap axis was 79°. The initial plasma anisotropy was given by $\tau = E_{i\perp}/E_{i\parallel} = 20$. The residual gas pressure before injection pulse did not exceed 10^{-12} torr. During beam injection, the gas pressure rose to 10^{-10} torr owing to the gas flux from the injector.

The following set of diagnostics was used in the experiment:

Seven probes were installed in the horizontal plane of the trap, 40 cm from the centre, in order to measure the cold-ion flux proportional to $\int n d\ell$ on the force lines. This set of probes enabled us to calculate the radial distribution of the plasma density from r = 0 to r = 18.7 cm, where r is the plasma radius at the central trap cross-section. The projection of each probe along the field lines onto the central trap cross-section is practically a straight strip, whose height exceeds the extent of the plasma in that direction. Two grids were installed in front of the probe collectors. Application of appropriate potentials on the grids made it possible to measure the ion spectra and, hence, to obtain information on the plasma potential and its radial distribution. It was possible to bias the ion flux completely and measure the flux of electrons leaving the trap.

A probe with many grids installed 40 cm from the centre performed continuous measurements of the plasma potential. The time behaviour of the ion density in the plasma and the energy spectra of the hot ions were determined from charge-exchange neutral-atom-flux measurements.

The electron density and its axial distribution and the electron temperature and its distribution with respect to its longitudinal velocities were measured by

the absorption of super-high-frequency (SHF) electromagnetic waves at the electron cyclotron frequency. The horn emitter and receiver were placed at the trap axis on both sides of plasma. To obtain the longitudinal-velocity distribution function and the electron temperature, it was necessary to measure the dependence of the absorption coefficient on the frequency shift, $\Delta\omega = \omega_{Be}(0) - \omega_g$, where $\omega_{Be}(0)$ is the electron cyclotron frequency in the minimum of the magnetic field, and ω_g is the generator frequency [9]. When $\omega_g < \omega_{Be}(0)$, the absorption line profile is determined by the Doppler effect. When $\omega_g > \omega_{Be}(0)$, the absorption coefficient is practically independent of the electron temperature and is completely determined by the electron density and the space dependence of the magnetic field at the point of resonance [10]. Measurements of the absorption as a function of $\Delta\omega = \omega_g - \omega_{Be}(0)$ for $\omega_g > \omega_{Be}(0)$ provide information on the electron density distribution along the axis.

By a set of electrostatic antennas, it was possible to determine the spatial structure and the amplitudes and frequency spectra of oscillations in the frequency ranges of 1–500 kHz and 10–130 MHz.

The phenomena considered in this paper are investigated at peak plasma densities $\sim 10^8$ cm^{-3} in Ogra-3 and $10^9 - 2 \times 10^{10}$ cm^{-3} in Ogra-3B. In the latter device, the electron temperature attained 300 eV. The ion decay time as determined by charge exchange was 1 s after the beam had been switched off. The plasma dimensions in Ogra-3B were 14 cm and r = 7 cm in the longitudinal and radial directions, respectively.

3. EXPERIMENTAL RESULTS

Figure 1 shows the dependence of the measured plasma density on $I_{inj}\tau_{cx}$ in Ogra-3, close to the thresholds of the anisotropic ion cyclotron instability (AICI) (10^8 cm^{-3}). The product of $I_{inj}\tau_{cx}$ is obviously the plasma density expected if ion life-time is determined by charge exchange (τ_{cx} is the charge-exchange time), and the trapping efficiency of the injected current, I_{inj}, is determined by Lorentz ionization. At a density higher than the AICI threshold, fundamental-cyclotron-frequency oscillations developed. In a density range lower than the threshold of the flute instability, low-frequency (LF) oscillations were observed; their frequency increased with the density (electron drift branch of the dispersion relation). At a density higher than the threshold of the flute instability, the amplitude of the LF oscillations increased pronouncedly, and the frequency became equal to half of the ion drift frequency (if the frequency of electric drift was subtracted). With a feedback system, it was possible to suppress the LF oscillations in both regions of density, lower and higher than the threshold of the flute instability, i.e. in the whole range of densities shown in Fig.1. The suppression of the LF oscillations did not affect the development of the cyclotron instability. It was possible to suppress the cyclotron oscillations independently

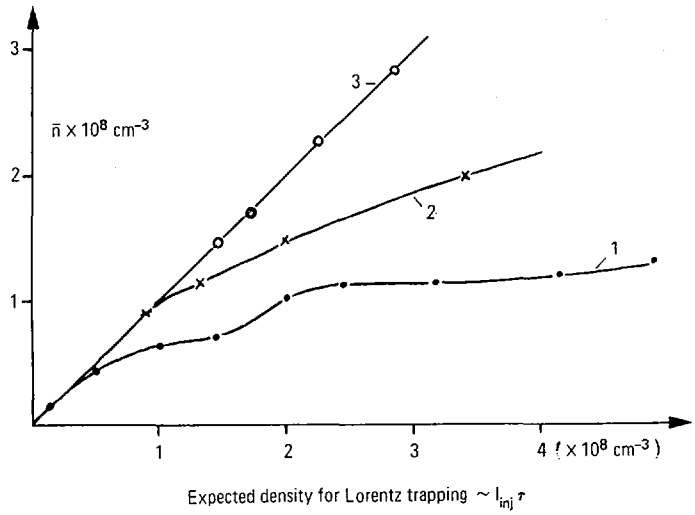


FIG. 1. Average plasma density as a function of the value expected from Lorentz trapping in Ogra-3 with simple mirror geometry. 1 – no suppression of oscillations; 2 – only cyclotron oscillations are suppressed; 3 – only drift oscillations are suppressed. B = 21.6 kG.

by the excitation of electron plasma oscillations [11]. The amplitude of the LF oscillations dropped slightly in this case, and the frequency did not change. Curve 1 in Fig. 1 shows the plasma density as a function of $I_{inj}\tau_{cx}$ when both LF and HF oscillations occur, i.e. when no means of oscillation suppression were used. Curve 2 was obtained for suppressed AICI. There was no plasma loss up to the threshold of the flute instability (1×10^8 cm^{-3}), and the density limitation in the region of the flute instability became less pronounced. Curve 3 corresponds to the case where only LF oscillations were suppressed by the feedback system in the whole density range indicated in Fig. 1. Now, the anomalous plasma loss had disappeared completely, but, as has already been mentioned, the amplitude of the cyclotron oscillation was not changed. Therefore, it is demonstrated that cyclotron activity itself does not cause plasma loss in our conditions. Additional loss of ions associated with cyclotron activity appears only in the presence of LF oscillations.

The measurement of the plasma density distribution along the trap axis had shown that this distribution was neither changed in the case of curve 1 nor in that of curve 3 (Fig. 1). In both cases, the plasma dimension along the trap axis is about 5 cm, which is much smaller than the distance between the mirrors (40 cm). This implies that additional plasma loss due to cyclotron oscillations in the presence of LF oscillations does not occur through the loss cone and, consequently, through the mirrors, but as a result of radial transport across the magnetic field.

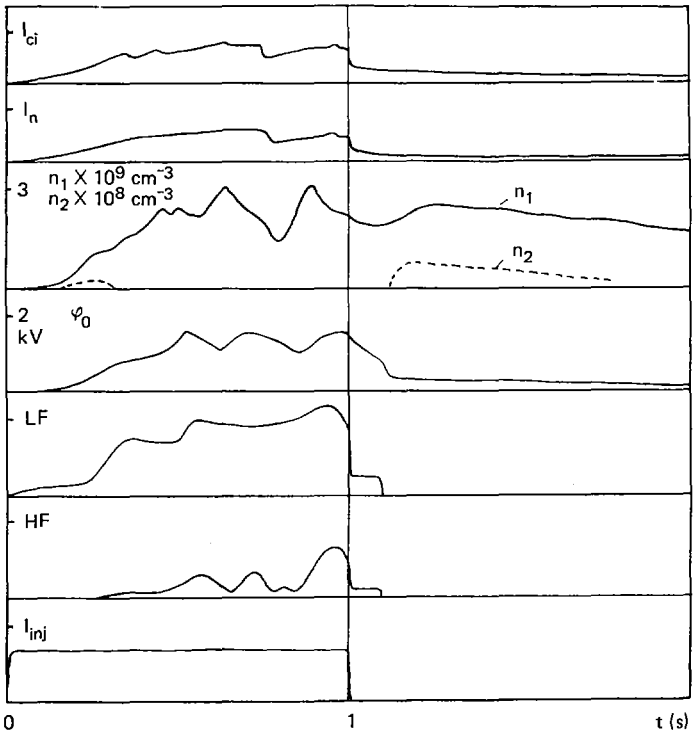


FIG.2. Typical set of oscillograms: I_{ci} – flux of cold ions at the axis; I_n – charge-exchange neutrals; n_1, n_2 – electron density at z = 3 cm and z = 7.5 cm; φ_0 – plasma potential; LF – time-averaged envelope of drift (LF) oscillations. B = 12.6 kG; HF – time-averaged envelope of ion cyclotron (HF) oscillations.

Investigations into the anomalous loss mechanism associated with the cyclotron activity were continued in the Ogra-3B device, the mirror machine with minimum-B configuration.

Figure 2 shows a typical set of signals: cold ions at the trap axis, charge-exchange neutrals, plasma density measured by means of SHF resonance electron cyclotron absorption at z = 3 cm and z = 7.5 cm, plasma potential, envelope of LF oscillations ($f \leqslant 500$ kHz), envelope of ion cyclotron oscillations (HF), and the injection current.

At the threshold of the instability development, LF and HF oscillations appear as short bursts, and the frequency of their appearance increases with the density while the amplitude of a single burst does not change significantly. The

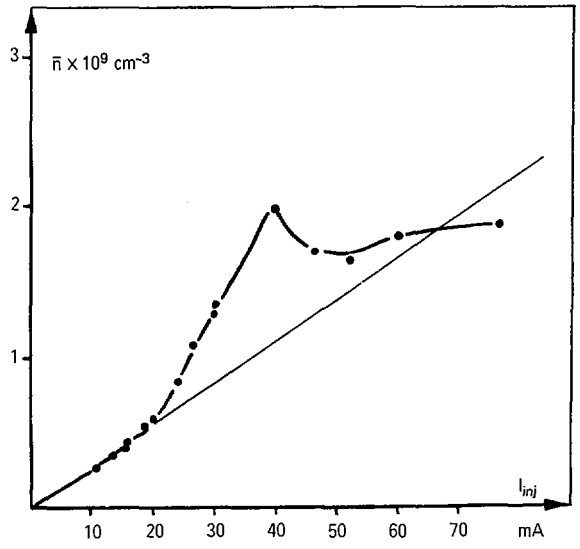


FIG. 3. Plasma density $\bar{n}$ versus beam intensity; B = 12.6 kG.

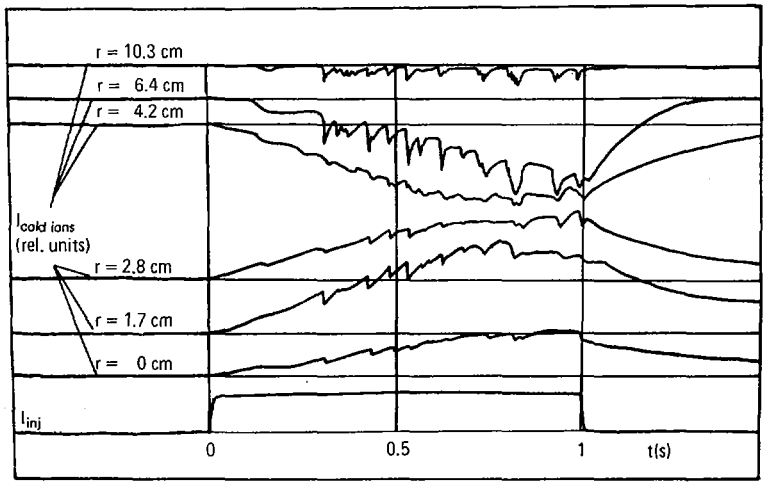


FIG. 4. Oscillograms of cold-ion flux I_{ci} at different plasma radii. B = 12.6 kG, $n \cong 2 \times 10^9$ cm^{-3}. (For the three upper curves, the vertical scale is opposite to that of the other curves.)

signal drop at the end of the injection is due to the instant drop of gas pressure. The plasma density did not drop as is seen on the oscillogram measured by the absorption of SHF wave electron density.

Figure 3 shows the average plasma density versus the injection current. The deviation from a linear dependence can be explained by an enhancement of the trapping rate due to cascade processes in the accumulated plasma [12]. At a density of 2×10^9 cm^{-3}, the cyclotron instability appears and leads to plasma losses. The threshold of this instability is proportional to the square of the magnetic field.

During the injection period when the plasma density exceeds 10^9 cm^{-3}, oscillations in the range of the drift and cyclotron frequencies are observed. Drift oscillation spectra have rather complicated structures in the frequency band of 0–500 kHz. Five harmonics of the cyclotron oscillations have been detected in the density range mentioned. Drift and cyclotron oscillations occur as short bursts with durations of typically some tens of milliseconds. As was mentioned above, the burst frequency increased with the plasma density and reached 100–200 Hz at a density of $\sim 10^{10}$ cm^{-3}.

There is a correlation between the drops of the density and the appearance of the bursts. Figure 4 shows cold-ion signals measured at different radii (all signals in Fig.4 are positive; the three upper oscillograms have been turned over for convenience) as functions of time. The drops of the density in the central part of the trap are seen to be correlated with the density peaks in the outward radial parts of plasma.

The plasma decay time measured at different radii is shown in Fig.5. The measurements were performed in conditions where both LF and HF oscillations existed after the beam had been switched off. The plasma periphery is seen to decay faster (see also Fig.4). This conclusion is also proved by a measurement of the radial distribution of $\int n d\ell$ in a quiescent plasma (Fig.6, curve 1) and in an unstable plasma (curve 2). The latter radial distribution is seen to be more peaked.

The axial plasma density distributions for quiescent ($n \cong 10^8$ cm^{-3}) and non-quiescent ($n \cong 3 \times 10^9$ cm^{-3}) regimes are shown in Fig.7. It can be seen that an instability does not change the shape of the distribution. This observation indicates that practically all losses are associated with radial transport across the magnetic field. This statement is also confirmed by peaks and drops on the abovementioned oscillograms.

Some studies on anomalous electron loss were carried out in these experiments. Observed and calculated ambipolar classical potentials versus plasma density are shown in Fig.8 (the observed value of the electron temperature used for this calculation agrees well with the classical temperature as derived from ion-electron collisions). The electron energy distribution function $f(E_{e\|})$ has been measured by using SHF wave absorption as was mentioned above. As is shown in Fig. 9 evidently, it co-incides with the Maxwellian distribution in a wide energy range.

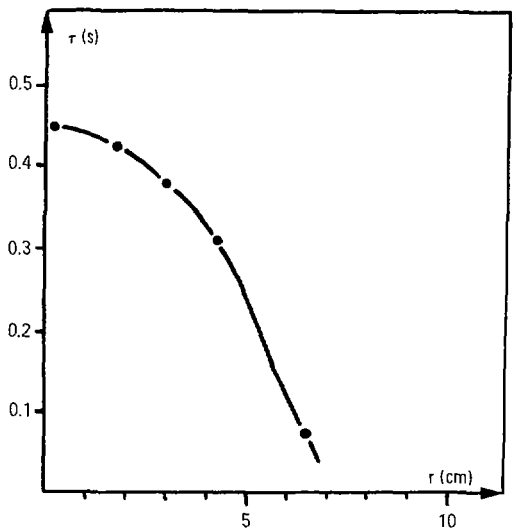


FIG. 5. Decay time of cold-ion flux at different plasma radii. B = 12.6 kG. Charge-exchange time $\tau_{cx} \cong 0.6$ s.

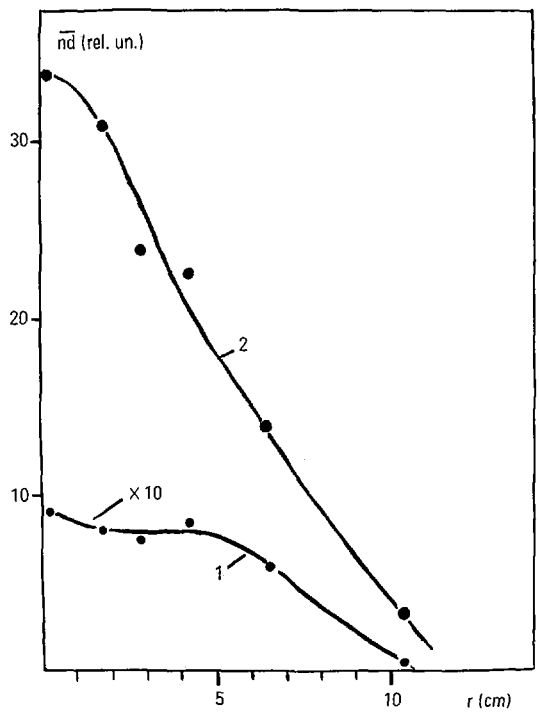


FIG. 6. Radial distribution of plasma density. (More exactly, the double-averaged plasma density

$$n(r) = \{\int [\int n(z,d)\,dh/d(z,r)]\,dz\}/\ell_z(r)$$

where $d(z,r)$ is a vertical chord in the plasma body and $\ell_z(r)$ is the plasma-body dimension along the field line). $B = 12.6$ kG. $1 - \overline{n} \cong 10^8\ cm^{-3}$, $2 - \overline{n} \cong 3 \times 10^9\ cm^{-3}$.

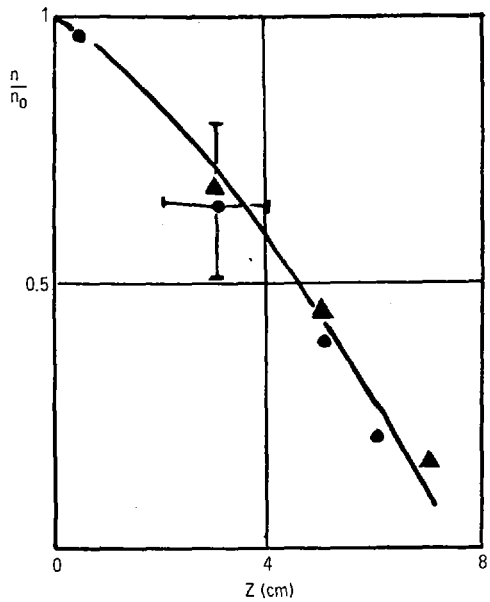


FIG. 7. Plasma density distributions along the trap axis:
● – B = 14.2 kG, $\bar{n} \cong 1 \times 10^8$ cm^{-3},
▲ – B = 15.6 kG, $\bar{n} \cong 3 \times 10^9$ cm^{-3}.

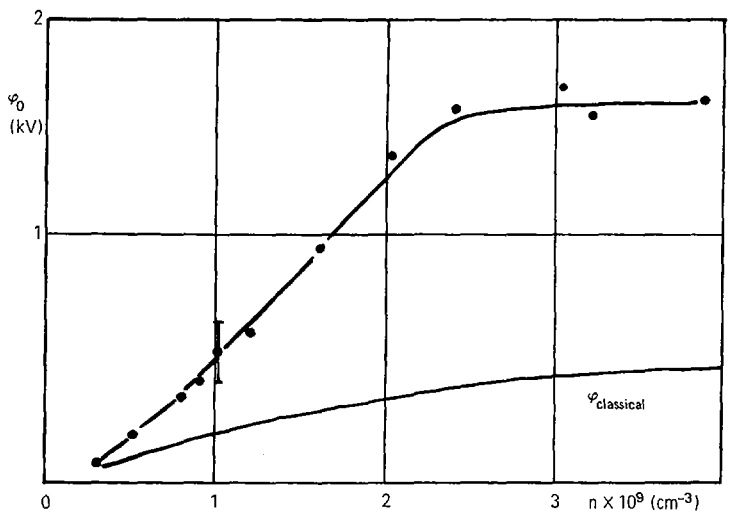


FIG. 8. Plasma potential φ_0 versus plasma density. B = 15.6 kG.

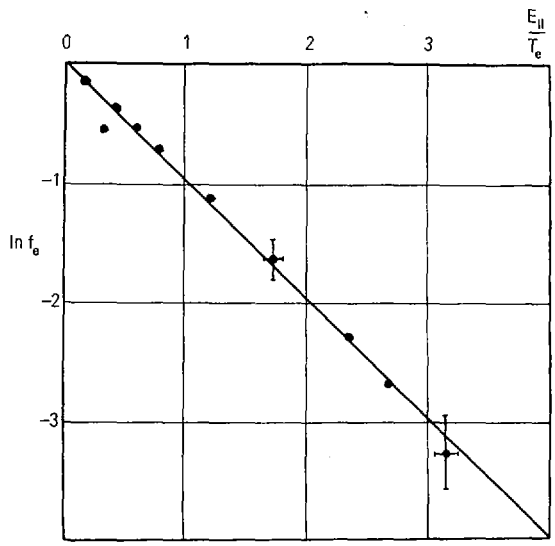


FIG. 9. Measured distribution function of electrons $f(E_{e\parallel})$, where $E_{e\parallel}$ is the longitudinal energy. $B = 12.6$ kG, $\bar{n} \cong 2 \times 10^9$ cm^{-3}.

For a calculation of the classical ambipolar potential φ_c, the condition of quasi-neutrality and Pastukhov's formula [13] were used:

$$\tau = \tau_{ee} \frac{\varphi_c}{T_e} e^{\frac{\varphi_c}{T_e}} f(R)$$

$$f(R) = \frac{\sqrt{\pi}}{4} \frac{2R + 1}{2R} \ln(4R + 2)$$

where R is the mirror ratio, τ_{ee} the electron-electron scattering time, and τ the fast-ion life-time. For our experimental conditions, $\varphi_c \approx 2.5\ T_e$; the calculated value of φ_c is shown in Fig. 8.

The measured value of the plasma potential is $\varphi \cong (5 - 7.5)\ T_e$. In a potential well like this, the flux of escaping electrons cannot exceed 1/50 of its production rate, and, in fact, measurements have proved that only a very small portion of the electrons leaves the trap along the field lines in the axial region, which means that electrons from the central plasma region are lost radially across the magnetic field.

4. DISCUSSION OF RESULTS

The results of our studies show that the appearance of ion cyclotron oscillations is followed by ion transport across the magnetic field. This transverse transport accounts for considerable ion loss from a magnetic trap. When anomalous ion loss is observed, low-frequency drift oscillations appear simultaneously with cyclotron oscillations in the plasma. As had been shown, the appearance of an anomalous potential was not associated with cyclotron activity but rather with the existence of low-frequency oscillations.

Cyclotron oscillations cannot transport ions radially, owing to their narrow frequency spectrum, but give rise to energy spreading of the initially monoenergetic ion energy distribution. Low-frequency oscillations seem to be able to induce radial drift excursions of particles in the wave field rather than to cause radial diffusion. Although oscillations with a frequency equal to that of the magnetic drift precession,

$$\omega^* = \frac{c E_{i\perp}}{eBr} \frac{\nabla B}{B}$$

could move the ions radially, in the experiment the frequencies detected did not co-incide with those just mentioned. For example in the regime illustrated in Fig.1, at densities of about 10^8 cm^{-3}, the frequency of the drift oscillations is in the range $0 - \omega^*/2$.

Putvinskij and Timofeev [14] proposed a mechanism of transverse electron transport in the field of a low-frequency wave, taking into account electron-electron Coulomb scattering. In this field with a potential ψ and a frequency ω electrons have the radial shift of

$$\xi = \frac{c}{H} \psi \frac{1}{\omega - k v_d}$$

where v_d is an electron drift velocity in an electric field of ambipolar potential φ. As practically in all cases the stationary electric field depends on Z, the average electric field affecting the electrons depends on their longitudinal energy (except for the case of a square potential well). Consequently, the average drift velocity also depends on the longitudinal energy of the electrons: $v_d = v_d (E_{e\|})$.

Since under the influence of Coulomb scattering, the energy of the electrons changes at random, the ξ-value would also change in the same manner, and the electrons would stochastically jump from one trajectory to another.

This process is an origin of radial diffusion of electrons.

Putvinskij has generalized this loss mechanism for the case of ions. The drift velocity of the ions, v_d, is the sum of magnetic and electric drift velocities. In the

case of a rarefied plasma, the ion energy change under the influence of ion collisions is negligible, but energy of the ions changes under the influence of cyclotron oscillations. Since the magnetic drift velocity depends on the particle energy we also have a reason for transverse diffusion.

The experimental results presented in this article are in qualitative agreement with theoretical predictions [14, 15], but for a quantitative comparison it would be necessary to carry out more detailed calculations and measurements.

Drift electron dispersion relation branches with positive energy which were observed both in Ogra-3 and Ogra-3B may be excited by injected beam noises, cyclotron oscillations including decay processes as considered by Arsenin [16], etc.

The anomalous transverse ion and electron diffusion in the field of harmonic oscillations as analysed in this paper does not depend on the nature of the particle energy change. The energy of the ions may change under the influence of cyclotron oscillations and Coulomb collisions, as well. In experiments with high-density plasma [17, 18], anomalous ions losses associated with rather narrow frequency spectra of cyclotron oscillations were detected. Actually, the aboveconsidered transverse loss mechanism might be operative also in the case of these experiments if, for one reason or another, low-frequency oscillations are excited.

ACKNOWLEDGEMENTS

The authors express their gratitude to V.V. Arsenin, S.V. Putvinskij, A.V. Timofeev, V.A. Chuyanov for valuable advice and also to I.N. Golovin for his support.

REFERENCES

[1] ARTEMENKOV, L.I., VASIL'EV, R.P., GALKIN, I.V., GOLOVIN, I.N., ZHIL'TSOV, V.A., et al., in Plasma Physics and Controlled Nuclear Fusion Research (Proc. 2nd Int. Conf. Culham, 1965) Vol.2, IAEA, Vienna (1966) 45.

[2] ZHIL'TSOV, V.A., KOSAREV, P.M., LIKHTENSHTEJN, V.Kh., PANOV, D.A., CHUYANOV, V.A., SHCHERBAKOV, A.G., Fiz. Plazmy 3 (1977) 37.

[3] DAMM, C.C., et al., UCRL-50002-73 (1973) 15.

[4] DAMM, C.C., FOOTE, J.H., FUTCH, A.H., Jr., GOODMAN, R.K., GORDON, F.J., et al. in Plasma Physics and Controlled Nuclear Fusion Research (Proc. 3rd Int. Conf. Novosibirsk, 1968) Vol.2, IAEA, Vienna (1969) 253.

[5] CORDEY, J.G., KUO-PETRAVIC, G., MURPHY, E.G., PETRAVIC, M., SWEETMAN, D.R., THOMSON, E., ibid., 267.

[6] AAMODT, R.E., Phys. Rev. Lett. **27** (1971) 135.

[7] TIMOFEEV, A.V., Nucl. Fusion **14** (1974) 165.

[8] ZHIL'TSOV, V.A., LIKHTENSHTEJN, V.Kh., PANOV, D.A., KOSAREV, P.M., CHUYANOV, V.A., SHCHERBAKOV, A.G., in Plasma Physics and Controlled Nuclear Fusion Research (Proc. 5th Int. Conf. Tokyo, 1974) Vol.1, IAEA, Vienna (1975) 355.

[9] SKOVORODA, A.A., TIMOFEEV, A.V., SHVILKIN, B.N., Zh. Ehksp. Teor. Fiz. **73** (1977) 526.
[10] SKOVORODA, A.A., SHVILKIN, B.N., Zh. Ehksp. Teor. Fiz. **70** (1976) 1779.
[11] ZHIL'TSOV, V.A., LIKHTENSTEJN, V.Kh., PANOV, D.A., CHUYANOV, V.A., SHCHERBAKOV, A.G., in Controlled Fusion and Plasma Physics (Proc. 7th Europ. Conf. Prague, 1977), Vol.1, Prague (1977) 100.
[12] HISKES, J.R., Nucl. Fusion 2 (1962) 1.
[13] PASTUKHOV, V.P., Nucl. Fusion **14** (1974) 3.
[14] PUTVINSKIJ, S.V., TIMOFEEV, A.V., Zh. Ehskp. Teor. Fiz. **69** (1975) 221.
[15] PUTVINSKIJ, S.V., Preprint IAEh-2628, Moscow (1976).
[16] ARSENIN, V.V., Fiz. Plazmy 2 (1976) 237.
[17] GOTT, Yu.V., IOFFE, M.S., KANAEV, B.I., MOTLICH, A.G., PASTUKHOV, V.P., SOBOLEV, R.I., in Plasma Physics and Controlled Nuclear Fusion Research (Proc. 5th Int. Conf. Tokyo, 1974) Vol.1, IAEA, Vienna (1975) 341.
[18] SIMONEN, T.G., UCR4-76115/1975.

DISCUSSION

R.E. AAMODT: One possible explanation of the enhanced electron and ion cross-field transport in the presence of both high- and low-frequency waves is that these waves may induce mutual non-linear instabilities. Have there been experimental studies of the correlation between these two types of waves and their measured saturation amplitudes?

Dzh. G. LOMINADZE: Such experiments are under way at present.

DRIFT WAVE STABILITY AND TRANSPORT THEORY IN FUSION SYSTEMS

N.A. KRALL, S. HAMASAKI, J.B. McBRIDE
Science Applications Inc.,
La Jolla, California

N.T. GLADD, P.H. NG, H.H. CHEN
University of Maryland,
College Park, Maryland

J.D. HUBA
Naval Research Laboratory,
Washington, D.C.

R.C. DAVIDSON
Office of Fusion Energy,
US Department of Energy,
Washington, D.C.

R.E. AAMODT, Y.C. LEE, C.S. LIU,
D.R. NICHOLSON, M.N. ROSENBLUTH
Science Applications Inc.,
Boulder, Colorado

D. CHERNIN
Institute for Advanced Study,
Princeton, New Jersey,
United States of America

Abstract

DRIFT WAVE STABILITY AND TRANSPORT THEORY IN FUSION SYSTEMS.

The linear properties of lower hybrid, drift cyclotron, and drift cyclotron loss-cone instabilities are calculated including shear, beta and distribution function effects. Transport runs including these effects are carried out for experiment-sized and reactor-sized devices. Non-linear effects on the DC mode due to frequency and wavenumber shifts are calculated.

1. INTRODUCTION

It is generally accepted[1] that microinstabilities affect both the heating and loss (of particles and heat) in many plasma containment devices. The modeling and prediction of the behavior of linear theta pinch, reversed field pinch (RFP), imploding liner, and magnetic mirror machines all require knowledge of the linear and nonlinear behavior of the lower hybrid (LH), ion cyclotron drift (DC), and drift cyclotron loss-cone modes (DCLC), including such realistic features as finite beta, magnetic shear, and the full set of particle and temperature gradients. In this paper, we give many of these properties (Sec. 2) and show how they affect the time evolution of various experiments (Sec. 3). Further, we formulate and examine the effects of the nonlinear frequency shift on the drift cyclotron mode (Maxwellian) and determine the spatial and temporal evolution of the spectrum of such modes in a flute approximation (Sec. 4). The latter calculation bears on mirror loss cones with a warm plasma stream.

2. LINEAR PROPERTIES OF LH, DC AND DCLC INSTABILITIES

The linear theory of these three modes have been widely discussed in the low-β, no-shear, constant temperature limit.[1] In summary, their properties in this limit are (L_n is the scale size, a_i the ion gyroradius)

$$\mathrm{LH}\left(L_n/a_i \lesssim 1\right) \quad \gamma \sim \omega_o \sim \left(\omega_{ce}\omega_{ci}\right)^{\frac{1}{2}}\left(1+\omega_{ce}^{\,2}/\omega_{pe}^{\,2}\right)^{\frac{1}{2}} \equiv \omega_H$$

$$\mathrm{LH}\left[\left(M_i/M_e\right)^{\frac{1}{4}} > L_n/a_i > 1\right] \quad \omega_o \sim \omega_H\left(a_i/L_n\right);\ \gamma \sim \omega_o\left(a_i/L_n\right)$$

$$\mathrm{DC}\left[\left(M_i/M_e\right)^{\frac{1}{2}} > L_n/a_i > \left(M_i/M_e\right)^{\frac{1}{4}}\right] \quad \omega_o \sim \ell\omega_{ci} \sim kV_D;\ \gamma \sim \omega_o\left(M_e/M_i\right)^{\frac{1}{4}}$$

In this section, we extend these conditions to include various magnetic geometries and distribution function effects, using both analytic and numerical solutions of the dispersion relation, extended for non-local effects to the form[2] $A\varphi'' + Q(\omega,k,r)\varphi = 0$, and for finite-$\beta$ effects to a 2 x 2 dispersion matrix.[2] The details of the analytic and numerical techniques, along with further graphs and results are presented elsewhere.[3-7] This section summarizes the results. The definition of shear and notation are standard.[3,6]

2.1. Lower Hybrid with Shear, Weak Inhomogeneity[3]

In the low-β limit, an analytic estimate of shear stabilization can be made. The result is LH is stable if

$$\frac{L_s}{L_n} < \frac{4L_n}{a_i}\left(1+\frac{\omega_{ce}^{\,2}}{\omega_{pe}^{\,2}}\right)^{\frac{1}{2}} \quad \text{if} \quad \frac{T_e}{T_i} \ll 1+\omega_{ce}^{\,2}/\omega_{pe}^{\,2} \tag{1}$$

$$\frac{L_s}{L_n} < \frac{L_n}{a_i}\frac{\left(1+T_e/T_i\right)^2}{T_e/T_i} \quad \text{if} \quad \frac{T_e}{T_i} >> 1+\omega_{ce}{}^2/\omega_{pe}{}^2 \qquad (2)$$

The last mode to stabilize has wavenumber $k^2a_e{}^2 = (T_e/T_i)(1+T_e/T_i + \omega_c{}^2/\omega_{pe}{}^2$

To include finite β and also the effect of strong inhomogeneities $[1 \gtrsim a_i/L_n > (m_e/m_i)^{\frac{1}{2}}]$ requires numerical analysis. We present two examples.

2.2. Lower Hybrid with Shear and Finite β_i $(T_e/T_i \to 0)$[6]

The analysis uses a fully electromagnetic, non-local, Weber-like dispersion equation to include finite ion β as well as magnetic shear. The results of numerical integration of this equation are shown in Fig. 1. Although for shear much too weak to stabilize the LH mode, increasing β_i tends to decrease the growth rate, the ultimate effect is that increasing β_i somewhat increases the shear needed to stabilize. The curve below $a_i/L_n = 1$ agrees with the analytic calculation Eq. (1).

2.3. Lower Hybrid with Shear, Strong Inhomogeneity[6]

As shown in Fig. 2, numerical integration of the β=0 dispersion Eq. shows that increasing T_e/T_i reduces the amount of shear needed to stabilize in the weak gradient limit, in agreement with Eq. (1)-Eq. (2); however, increasing T_e/T_i increases the shear for stability in the strong gradient limit.

2.4. Lower Hybrid with Temperature Gradients[4]

The problem of linear stability of the LH mode in low β can be generalized to include temperature gradients. Such a calculation has been carried out and the results are, in summary: the LH mode is unstable only for wavelengths such that ($\eta_{Tj} = d\ell nT_j/d\ell nn$)

$$1 > b_e > \frac{T_e}{2T_i}\frac{\eta_{Ti}}{1-\frac{1}{2}\eta_{Ti}}\left(1+\frac{\omega_{ce}{}^2}{\omega_{pe}{}^2}\right)^{-1} \qquad (3)$$

$$b_e{}^{\frac{1}{2}} > \frac{T_e}{T_i\sqrt{2\pi}}\,\frac{\left(1-\frac{1}{2}\eta_{Te}\right)}{\left(1-\frac{1}{2}\eta_{Ti}\right)\left(1+T_e/T_i+b_e\omega_{ce}{}^2/\omega_{pe}{}^2\right)} > 1 \qquad (4)$$

Note that whereas without ion temperature gradients ($\eta_{Ti} \to 0$) all long wavelength modes are unstable, the unstable spectrum is reduced for η_{Ti} positive. Eqs (3-4) are also necessary for the DC mode, where $\omega \approx \omega_{ci} = kV_D$ determines the wavenumber.

2.5. DC with Shear[3]

In a calculation similar to that described for the LH mode, we have obtained an analytic solution to the non-local dispersion equation, by

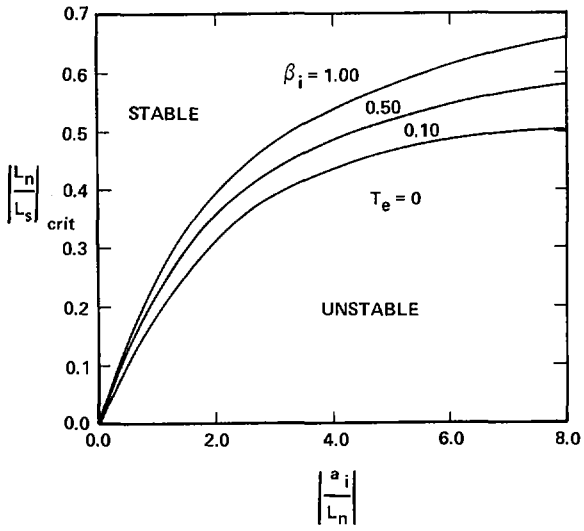


FIG. 1. Effect of magnetic shear on the LH drift instability for finite-β and cold electrons.

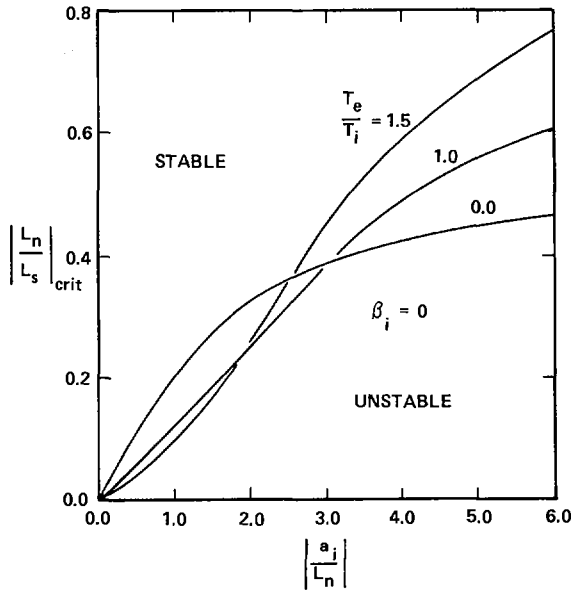


FIG. 2. Shear stabilization of LH for $\beta = 0$ and various T_e/T_i.

solving the Weber-like equation for the perturbed potential $A\varphi'' + (B-Cx^2)\varphi = 0$, where $B(x_0,\omega,k)$ is the local dispersion relation. In this case, in constrast to LH, shear reduces the growth rate rather than stabilizing the mode. The condition for shear to reduce the growth of all wavelengths of the DC modes is

$$\frac{L_s}{L_n} < \left(1 + \frac{T_e}{T_i}\right)^{\frac{1}{2}} \left(\frac{M_i}{M_e}\right)^{\frac{1}{2}} \left(\frac{a_i}{L_n}\right)^{\frac{1}{2}} \qquad (5)$$

(A somewhat weaker value of shear affects the very short wavelengths, $ka_i >> 1$.) Since the LH mode can be shown to merge with the DC mode for $(L_n/a_i) \cong (m_i/m_e)^{\frac{1}{4}}$, Eq. (5) is clearly the same as the condition for stabilizing LH modes, Eq. (1) at this value of L_n. Note also that the linear stability condition $L_n < a_i(m_i/m_e)^{\frac{1}{2}}$ bounds the righthand side of Eq. (5).

2.6. DC with Finite β[7]

A detailed numerical study of the linear dispersion matrix for DC instabilities, including electromagnetic perturbations, allows study of this mode for finite $\beta = 8\pi n(T_e+T_i)/B^2$, as well as the transition to the LH mode discussed above. The results are shown in Fig. 3 and Fig. 4. For $\beta << (m_e/m_i)^{\frac{1}{4}}$ all effects are small. For larger values, β becomes a significant stabilizing effect, due particularly to resonant ∇B orbit modifications from finite β as $\omega/kV_B \to 1$, where $V_B \cong (CT/eBL_n)\beta$. Fig. 3 and Fig. 4 show the reduction of the growth rate for T_e/T_i and for $T_e = 0$. The double curve is because $\gamma = \gamma_{max}$ for two different values of k_y, where β gets sufficiently large. As usual electromagnetic effects prevent the 'self-dug well' of the electrostatic term from stabilizing the mode. Similar though less detailed results have been obtained analytically in an earlier publication.[8] We conclude that although finite β slows the instability, it may still persist until diffusion broadens the profile to the linear stability limit $a_i/L_n \simeq (m_e/m_i)^{\frac{1}{2}}$. In a sufficiently large device, this may be unimportant compared with classical effects. More details are contained elsewhere.[7]

2.7. DCLC with Warm Plasma[5]

Although linear theory predicts that the DCLC mode in a mirror machine will be unstable over a broad band of frequency and wavenumber,[9] experimental observation indicates only narrow bands of instability at the lowest harmonics of the ion cyclotron frequency.[10] A detailed linear analysis is made of the transformation of the DCLC instability into the DC instability as the loss-cone of the ion distribution is filled by a warm Maxwellian component.[5] In particular, the loss-cone distribution is modeled by the difference of two Maxwellians with different temperatures $T_H = m_iV_H^2/2$, $T_h = m_iV_h^2/2$ and the warm component by a Maxwellian with temperature $T_w = m_i V_w^2/2$ with Δ the relative fraction of warm component. In general, it is found that the addition of warm plasma ($\Delta \neq 0$) reduces the growth rate of the DCLC and breaks the broad band wavenumber spectrum into a

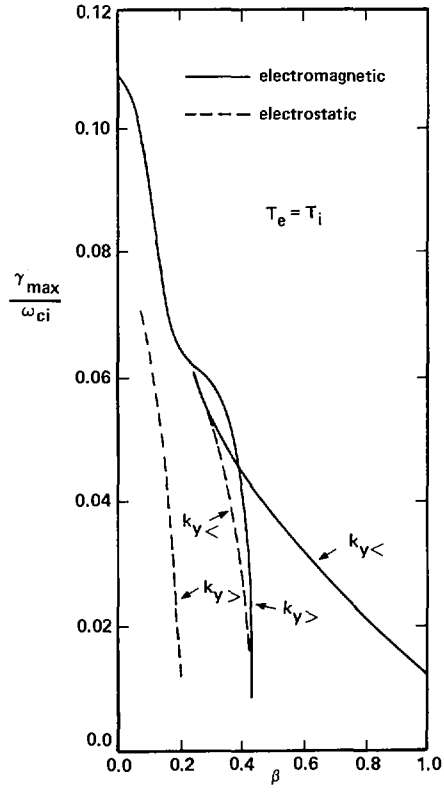


FIG. 3. Effect of finite-β on DC instability for $T_e/T_i = 1$.

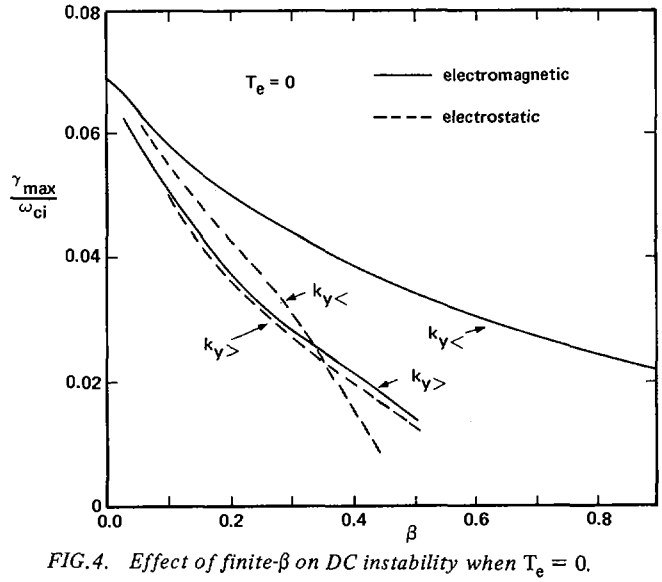


FIG. 4. Effect of finite-β on DC instability when $T_e = 0$.

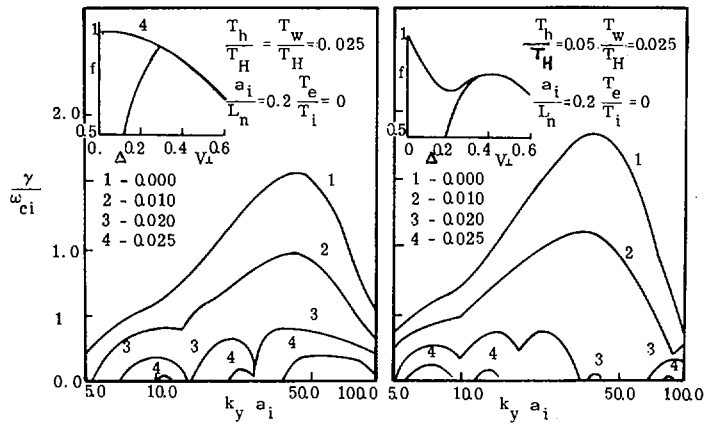


FIG.5. Warm plasma effects on DCLC instability for various ion distributions (see text).

discrete banded structure when $\gamma \lesssim \omega_{ci}$. The detailed features of the spectrum are strongly dependent on the parameters Δ, T_h/T_H, T_w/T_H characterizing the ion equilibrium. A particularly interesting result is that when the ion velocity distribution is 'double humped', some parametric combinations (e.g. $r_{LH}/L_N = .2$, $\Delta = .025$, $T_h/T_H = .05$, $T_w/T_H = .025$) result in the lowest unstable harmonic having the largest linear growth rate. This result is consistent with experimental observations and argues that these persistent observations of only the lowest harmonics may possibly be explained, linearly, by means of a partially filled loss cone. Further details, including the effects of temperature gradients and warm plasma component on the instability threshold condition, may be found in Ref. 5 (see also Fig. 5).

3. MODELING OF SHEAR- AND BETA- STABILIZED PLASMAS

In order to determine the practical importance of many of the effects discussed above, we have included those results for the LH and DC instabilities, including finite β and shear effects, in a simulation of this effect on cross field plasma diffusion. We want to determine (a) the necessity of using realistic linear stability estimates and (b) the time evolution of a system in which only part (usually the central part) of the profile is stabilized by these effects. Further, we try to show whether the instabilities will produce the same results in a large, reactor-size device as in a smaller laboratory experiment. Fig. 6 shows a plasma of experimental size which is, at t = 0, β-stabilized except near the boundary. By 1 ms the stable region has eroded away and the plasma is nearly lost, showing that finite-β stabilization is not very persistent in this configuration.

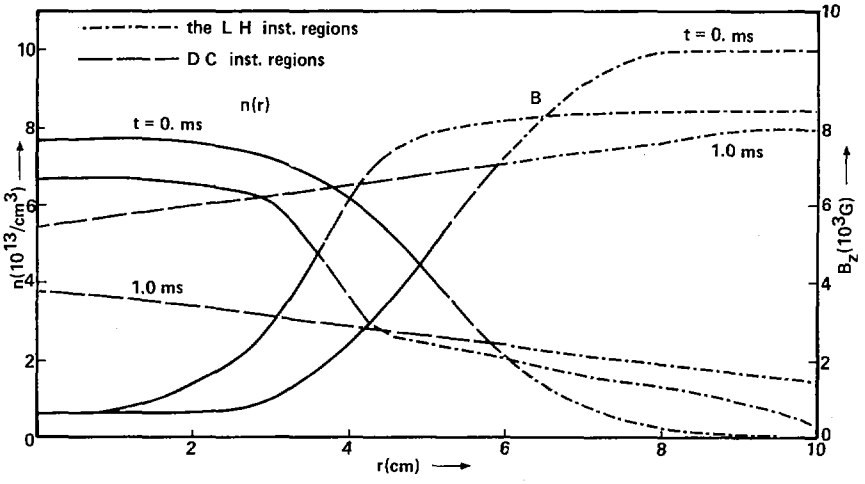


FIG.6. Time development of a (partially) β-stabilized experiment.

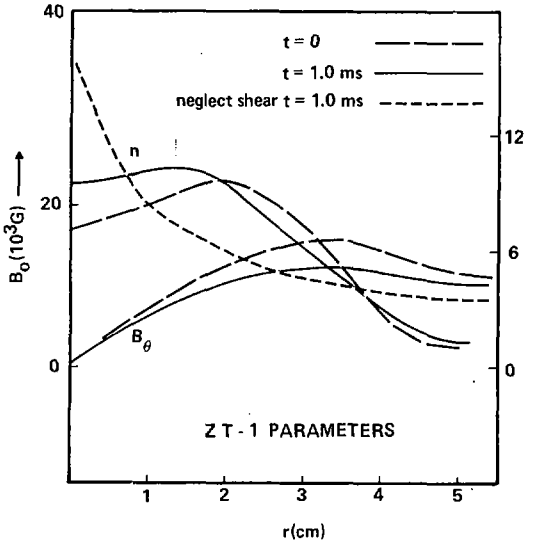


FIG.7. Time development of a (partially) shear stabilized experiment.

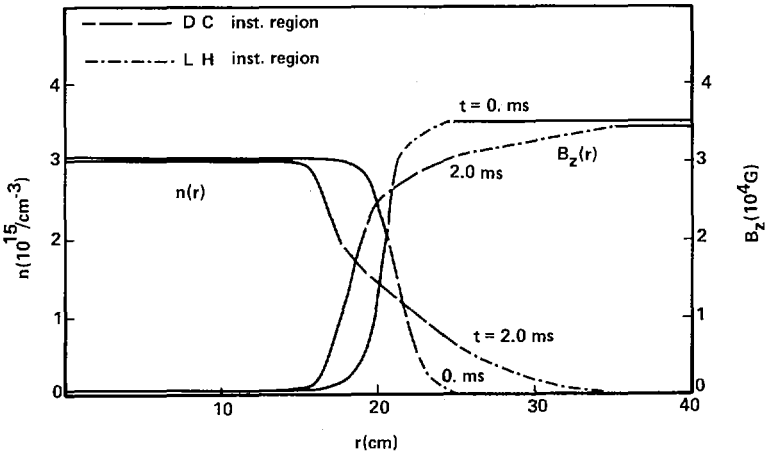


FIG.8. Time development of a β-stabilized reactor prototype.

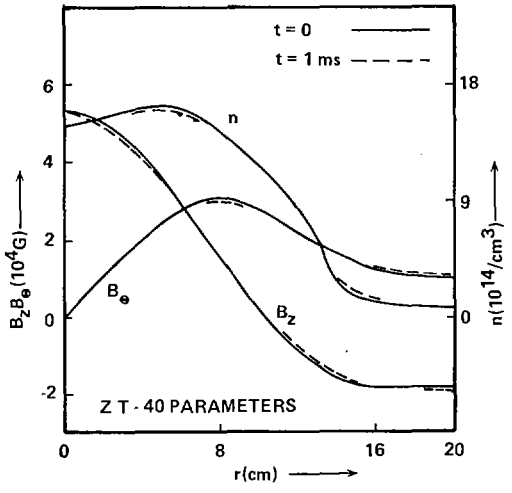


FIG.9. Time development of a shear stabilized reactor prototype.

In contrast, a partially shear stabilized case is shown in Fig. 7 of the ZT-1 type configuration, at t = 0 and at 1 ms. For contrast n(t = 1 ms) is also shown in a calculation neglecting shear stabilization. Note that shear seems a much more persistent stabilizing mechanism than finite β. The other side of the coin is that ZT cannot tolerate too much profile change without losing MHD stability. Finally, Fig. 8 and Fig. 9 show the same calculation as in Fig. 6 and Fig. 7, but on a reactor-size scale. The finite-β system (Fig. 8) is still eroding, but the rate has been considerably scaled down.

The ZT-40 example (Fig. 9) exhibits little diffusion at all on this time scale. Work in progress will include longer runs and comparison with MHD stability conditions.

4. NONLINEAR THEORY

While drift-unstable ion cyclotron waves (DC) are expected to reduce the containment properties in any magnetic configurations, they are particularly important in mirror devices where the breakdown of adiabaticity can induce rapid particle end losses and where their existence has, in fact, been observed to be correlated with containment degradation.[10, 11] As it has been established[12] that particle containment in a mirror trap including DC waves critically depends on the spectrum and amplitude, nonlinear calculations are important to obtain the saturated spectrum characteristics so that a fundamental understanding of mirror machine containment and its extrapolation to larger, hotter devices can be synthesized. In order to model the mirror loss cone plus injected warm plasma stream, we examine the effects of the nonlinear frequency shift on the DC instability (Maxwellian velocity distribution) and determine the spatial and temporal evolution of the spectrum of such modes in a strictly flute approximation.

It has been shown[13-16] that for fixed wavenumber the ion gyrofrequency is effectively nonlinearly shifted by the ion cyclotron wave which thereby detunes the resonance $\omega \cong \ell\omega_{ci} \cong kV_D$. This stabilizes the DC instability[16] when the nonlinear frequency shift is comparable to the linear growth rate. Since, however, a wave number shift might again allow the proper resonance for instability, we here determine these shifts self-consistently.

Consider the DC instability in an inhomogeneous plasma with a density profile given by $N = N_0(1 + Y/L)$. The electrostatic wave potential is assumed to be of the form $\varphi(x,t) = \Phi(x,t)\exp i(kx-\omega t)$ where Φ is the slowly varying amplitude and x is the direction of the ion diamagnetic drift $\vec{V}_D = (cT_i/eB^2N)\,\vec{B}\times\nabla N$. We examine only the resonant cases of $\omega \approx \omega_{Di} \simeq n\omega_{ci}$. To obtain the effects of the nonlinear frequency and wavenumber shift, we solve the Vlasov equation to the third order in $e\varphi$ and find the resonant ion density fluctuation is

$$n_3 = \frac{\alpha N_0 e\varphi}{T_i}\left(\frac{\omega_{xi}-n\omega_{ci}}{\omega-n\omega_{ci}}\right)\Phi^2; \quad \alpha = \frac{8n^2e^2k^2/MT}{\pi^2(\omega-n\omega_{ci})^2(4n^2-1)} \tag{6}$$

The nonresonant terms can be shown to be of order $(ka_i)^{-\frac{1}{2}}$ smaller. The only important electron nonlinearity is the usual quasilinear spatial diffusion effect which can be shown to maintain charge neutrality. The resulting nonlinear wave equation for the slowly varying $\Phi(x,t)$ can then be obtained as

$$\partial_{tt}\Phi - \partial_{xx}\Phi + \alpha|\Phi|^2\Phi - \gamma^2\Phi = 0 \tag{7}$$

where

$$\gamma = n^2\omega_{ci}\left(\frac{L}{a_i}\right)\left(\frac{m}{M}\right)^{\frac{1}{2}}\left(1+\frac{B^2}{4\pi nmc^2}\right)^{\frac{1}{2}}$$

Rescaling $\tau = \gamma t$, $X = \gamma x$ and setting $\Phi = \gamma\alpha^{-\frac{1}{2}}\Phi'$, we normalize Eq. (7) into the standard nonlinear Klein-Gordon equation.[17] For travelling-wave solutions, we may set the dependence of Φ' on τ, X only through $\zeta = X - V\tau$ and then Eq. (7) has standard elliptic function solutions. In the limit of infinite period, there are the solitary-wave solutions, which, however, are either localized but unstable:

$$\Phi = \sqrt{2}\ \mathrm{sech}\left[\zeta/\sqrt{V^2-1}\right] (V > 1)$$

or stable but not localized:

$$\tanh\left[\zeta/\sqrt{2(1-V^2)}\right] \quad (|V|<1)$$

A particular solution of physical interest is the spatially uniform solution: $\Phi'(X,\tau) = \Phi_0 \exp(-i\omega_0 t)$ with $\omega_0^2 = |\Phi_0|^2 - 1$.

Perturbing this solution with $\delta\Phi\exp[ikX - i(\delta + \omega_0)\tau]$, we find

$$\delta^2 = (\omega_0^2 + \Delta) \pm \sqrt{4\Delta\omega_0^2 + |\Phi_0|^4}$$

where $\Delta = k^2 - 1 + 2|\Phi_0|^2$. As $(\omega_0^2 - \Delta)^2 > |\Phi_0|^4$, this solution is stable to all perturbations. For $\omega_0 = 0$, this is in fact the minimum-energy state corresponding to being at the bottom of the effective potential well (see below) and we expect that the system would eventually evolve into this state through either radiation or dissipation. This is in fact borne out by the self-similar solution and numerical solution of Eq. (7). With the similarity variable $\xi = \tau^2 - X^2$, Eq. (7) becomes

$$4\xi\left(\xi\Phi_\xi\right)_\xi + \xi\left[|\Phi|^2 - 1\right]\Phi = 0 \tag{8}$$

Setting $\xi = \exp\eta$, Eq. (7) can be cast into the following oscillator equation with nonlinear and 'time-varying' spring constant:

$$\frac{d^2\Phi}{d\eta^2} = -\frac{e^\eta}{4}\left[|\Phi|^2 - 1\right]\Phi \tag{9}$$

Eq. (8) is solved numerically and the solution is shown in Fig. 10(a). Note that initially the amplitude grows exponentially with the linear growth rate; then it saturates and oscillates around $\Phi = 1$ with oscillation frequency $= \sqrt{2}$ in the present dimensionless units. The saturation amplitude for the first harmonic is found to be

$$\frac{e\Phi}{T_i} = \left(\frac{a_i}{L}\right)\left(\frac{m}{M}\right)^{\frac{1}{2}} \tag{10}$$

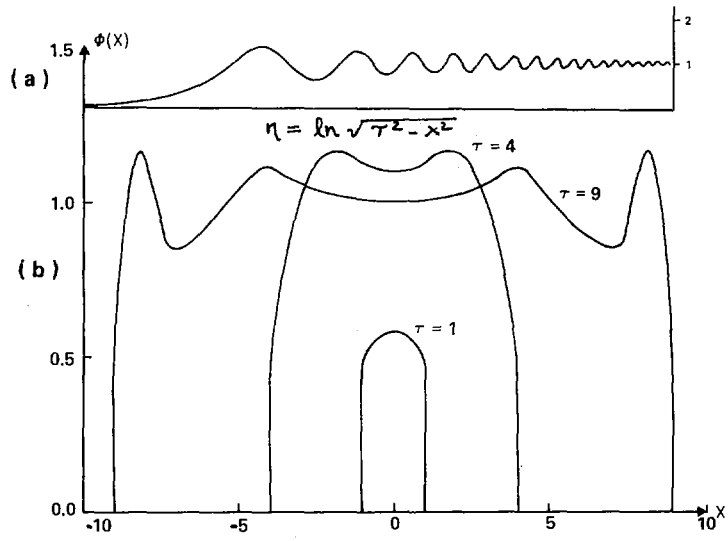


FIG. 10. (a) Self-similar solution of the non-linear Klein-Gordon equation. (b) Space-time solution of the non-linear partial differential equation.

We have also solved the full space-time equation (7) numerically, as shown in Fig. 10(b). A localized pulse is applied at x = 0 at t = 0, the pulse propagates outward with dimensionless speed 1.0. At $\tau = 1$, the response is still growing close to the dimensionless linear growth rate 1.0. However, the curves at $\tau = 4$ and $\tau = 9$ show a nonlinear saturation at the value 1.0, corresponding to the bottom of the pseudopotential well discussed above. The function $\Phi(X = 0, t)$ as observed in this numerical calculation, not shown, is found to be in precise agreement with the self-similar prediction of Fig. 10(a).

Therefore, within the framework of the assumed Maxwellian state, and for the wavenumbers in question, we have found very low amplitude saturation of the drift cyclotron waves, which is consistent with the experimental observations.[10, 11]

REFERENCES

[1] Davidson, R. C., Krall, N. A., Nuclear Fusion 17 (1977) 1313.
[2] Krall, N. A., "Drift Waves", in Advances in Plasma Physics, Vol. 1, Wiley, New York (1968).
[3] McBride, J. B., Krall, N. A., Nuclear Fusion 18 (1978) 1687.
[4] McBride, J. B., Hamasaki, S., Phys. Fluids 21 (1978) 1979.
[5] Ng, P. H., Gladd, N. T., Liu, C. S., University of Maryland Report (to be published) (DCLC finite β); Catto, P., Aamodt, R., Phys. Fluids 21 (1978) 1983.
[6] Davidson, R. C., Gladd, N. T., Goren, Y., Phys. Fluids 21 (1978) 992.

[7] Gladd, N. T., Huba, J. D., Phys. Fluids (submitted) (DC finite β).
[8] Krall, N. A., Pearlstein, L. D., Plasma Physics and Controlled Nuclear Fusion Research (Proc. 2nd Int. Conf. Culham, 1966) Vol. 1, IAEA, Vienna (1966) 735.
[9] Post, R. F., Rosenbluth, M. N., Phys. Fluids 9 (1966) 730.
[10] Turner, W. C., Powers, E. J., Simonen, T. C., Phys. Rev. Lett. 39 (1977) 1087.
[11] Coensgen, F. H., Cummins, W. F., Logan, B. G., Molvik, A. W., Nexsen, W. E., Simonen, T. C., Stallard, B. W., Turner, W. C., Phys. Rev. Lett. 35 (1975) 1051; Bagborodov, Y. T., Ioffe, M. S., Kanaev, B. I., Sobolev, R. I., Yushmanov, E. E., in Plasma Physics and Controlled Nuclear Fusion Research 1971 (Proc. 4th Int. Conf. Madison, 1971) Vol. 2, IAEA, Vienna (1972) 641.
[12] Aamodt, R. E., Phys. Rev. Lett. 27 (1971) 135; Rosenbluth, M. N., Phys. Rev. Lett. 29 (1972) 408; Timofeev, A. V., Nuclear Fusion 14 (1974) 165; Aamodt, R. E., Byers, J. A., Phys. Rev. Lett. 29 (1972) 1305.
[13] Aamodt, R. E., Bodner, S. E., Phys. Fluids 12 (1969) 1471; Aamodt, R. E., Phys. Fluids 17 (1974) 803.
[14] Nekrasov, A. K., Nuclear Fusion 14 (1974) 865.
[15] Aamodt, R. E., Lee, Y. C., Liu, C. S., Rosenbluth, M. N., Phys. Rev. Lett. 39 (1977) 1660.
[16] Zakharov, V., Shabat, A., Zh. Eksp. Teor. Fiz. 61 (1972) 118 [Sov. Phys.-JETP 34 (1972) 62]; Ablowitz, M., Kaup, D., Newell, A., Segur, H., Stud. Appl. Math. 53 (1974) 249; Makhankov, V. G., Physics Reports 35 (1978) 1.
[17] Cohen, B. I., Maron, N., Rognlien, T. D., in the proceedings of the Annual Controlled Fusion Theory Conference, Gatlinburg, Tenn. (1978), paper #OA5.

DISCUSSION

S.P. GARY: One parameter which apparently has not been studied is k_z – parallel propagation – and especially its effects on the ion-cyclotron drift instability. Our recent work with J.J. Sanderson has shown that $k_z \neq 0$ can significantly lower the threshold of this instability.

N.A. KRALL: From time to time we check back to see the effect of k_z, as in the Liewer-Krall modified two-streams study and the Krall-Fowler drift cyclotron with $k_\parallel$. The study described today did not, however, include those cases which could be modified somewhat by k_z.

J.B. TAYLOR: Your estimates of stability criteria appear to be based solely on the plane-slab model. Do you expect there to be toroidal effects on these criteria (e.g. on the existence and magnitude of shear stabilization) such as have recently been discussed in connection with drift waves?

N.A. KRALL: We have limited our applications to cases with high aspect ratio or to linear devices, such as ZT, θ-pinch, LINUS and so on, so toroidal effects can be safely neglected. Tokamak applications at high temperature would require that this whole rigmarole be repeated with trapping.

J.P. FREIDBERG: Do you believe very-low-frequency drift waves, $\omega < \omega_{ci}$, may be important in future devices, and, if so, do you plan to include them in future modelling calculations?

N.A. KRALL: Apart from systems in which end losses are a problem, the lower-frequency modes begin to dominate in even more diffuse systems (long scale lengths for the density gradient), and with lower growth rates. In larger systems they become less and less important compared with classical transport. This may discourage us from going too much lower in frequency, but we shall, at least, have gauged the possibilities and limitations of the procedure.

H.A.B. BODIN: When you were comparing shear and β-stabilization of the lower hybrid drift mode I believe you said that these become especially effective for a reactor-size machine. Did you have in mind full reactor parameters, or do you get strong effects on next-generation devices too (for example, I think there was a reference to ZT-40)?

N.A. KRALL: Yes, the ZT-40 parameters were used as 'reactor-size'. One of the main aims of a study such as ours is to determine how big a device must be before the physics characteristics of a reactor, rather than the physics of an experimental device, begin to dominate. As far as intermediate-frequency instabilities are concerned, our preliminary results indicate that a device of the ZT-40 size is 'reactor-size' in this sense.

RECENT RESULTS AND WORK ON FIELD-REVERSING E- AND P-LAYERS*

M. TUSZEWSKI[†], D.J. REJ, S.C. LUCKHARDT,
R.V. LOVELACE, D.A. LARRABEE, R.E. KRIBEL[††],
H.H. FLEISCHMANN
School of Applied and Engineering Physics
and Laboratory of Plasma Studies,
Cornell University, Ithaca, New York

A. DROBOT[#], J. GOLDEN, C.A. KAPETANAKOS,
R.A. MAHAFFEY, S.J. MARSH[##], J.A. PASOUR[+]
Naval Research Laboratory, Washington, D.C.

P.L. DREIKE, A. FRIEDMAN, M. GREENSPAN,
D.A. HAMMER, S. HUMPHRIES, Jr.[++],
A. MANKOFSKY, R.N. SUDAN
Laboratory of Plasma Studies,
Cornell University, Ithaca, New York,
United States of America

Abstract

RECENT RESULTS AND WORK ON FIELD-REVERSING E- AND P-LAYERS.

Significant progress has recently been achieved in various areas: (i) Electron ring experiments (CU-I) on RECE-Christa were successful in moving field-reversing rings from a trapping region with a high-density cloud along the tank axis into a low-density region, and subsequently compressing these rings in a rising B_z-field. The ring behaviour appears classically predictable and stable. Full-field-reversal times range up to 1.1 ms. In RECE-Berta, the earlier observed particle losses due to quadrupole fields have been traced to orbital instabilities. (ii) The proton generation capabilities of various ion sources (CU-I, NRL, CU-II) have been significantly improved. The use of such diodes for ion ring experiments is now promising. (iii) Two separate experiments have recently been initiated (NRL, CU-II), in which the injection and trapping of such proton beams are being investigated. In both experiments the

---

* Work supported by US Department of Energy, and US Office of Naval Research.

† Present address: Dept. of Electrical Engineering, University of California, Berkeley, California, USA.

†† Present address: Dept. of Physics, Auburn University, Auburn, Alabama, USA.

Permanent address: Science Appl. Inc., Arlington, Virginia, USA.

Permanent address: Sachs/Freeman Assoc., Inc., Bladensburg, Maryland, USA.

+ NRC Research Associate at NRL, USA.

++ Present address: Sandia Corporation, Albuquerque, New Mexico, USA.

beam is injected through a cusped magnetic field. Trapping is to be obtained either by a gated mirror field (NRL) or by interaction with a resistive wall structure (CU-II). Preliminary results at NRL indicate good transmission through the cusp. Pilot experiments with a smaller experiment, ANNEX, (CU-II) indicate good beam propagation. Computer simulations (NRL, CU-II) indicate that trapping efficiencies of $> 90\%$ are possible in both experimental approaches. The importance of self-magnetic fields is also evident. (iv) Equilibrium calculations (CU-I) indicate that many exponential-rigid-rotor equilibria are seriously influenced by untrapped particles. Similar calculations (CU-I) of ring compression indicate the formation of hollow current profiles particularly advantageous for plasma confinement.

INTRODUCTION

A number of fusion schemes including the well-known ASTRON [1], the Ion ring compressor [2,3], the Two-Component Reactor [4], the Field-Reversed Mirror [5], and an ion ring hybrid system [6] envision the use of field reversing rings or layers of high-energy protons. This paper is to summarize the progress recently achieved by the three U.S. groups working on the problems of field-reversing E- and P-layers.

The most important features of the present work and recent results, as enumerated in the abstract, are described separately by the three groups in more detail.

CORNELL UNIVERSITY GROUP I (CU-I) [Tuszewski, et al.]

This program involves the study of field-reversed configurations with electron and ion rings. A brief summary of very recent results is presented.

Electron Ring Experiments: Although high-energy proton rings will be needed for reactor applications, two electron ring experiments are presently being performed to determine, with less cost and simpler technology than is otherwise possible, various characteristics of field-reversed large-orbit configurations: The RECE-Christa [7] facility has recently been modified to include flux-penetrable walls, gas puff injection, two fast-pulsed coils ($t_{1/4} \approx 25$ μsec, $\Delta B/B_{zo} \approx 10\%$) providing a pulsating B_z-field to move the rings axially, and a large coil ($t_{1/4} \approx 350$ μsec, $\Delta B \leq 1.5$ kG) for adiabatic compression of the translated rings. Following the previously reported [8] successful "stacking" of separate rings, recent experiments with similar machine parameters ($E_e \approx 2.5$ MeV, $B_{zo} \approx 450$ G, $I_z \approx 50$-90 kA) produced the following results (i) Field-reversing rings have been trapped in a hydrogen cloud (few hundred mTorr), and then moved axially into a low-pressure (10-20 mTorr) region downstream. When properly handled, the rings behave stably during this process with fast-electron losses of only 10-20% (Fig. 1a). The observed translation speed and its dependence on ring strength and axial field gradient, dB_z/dz, agrees well with the results of a simple model calculation accounting for the retarding forces from the resistive wall currents. (ii) After arriving downstream, these rings ($\delta = \delta B/B_z \leq 120\%$) decay very slowly (by collisions with the low-density gas) until the decay is accelerated by the arrival of the expanding gas cloud. Again, no instabilities are observed. (iii) Using the B_z-compression coil, field-reversing rings have been compressed downstream by up to a factor 3 in B_z. Again, no instabilities or anomalous losses are observed during this process, when it is properly performed. The field-reversal factor, δ, remains constant (Fig. 1b) and the ring dimensions appear to shrink roughly proportional to $B_z(t)^{-1/2}$. Using the full sequence of trapping, moving, and compressing, field-reversing compressed rings were

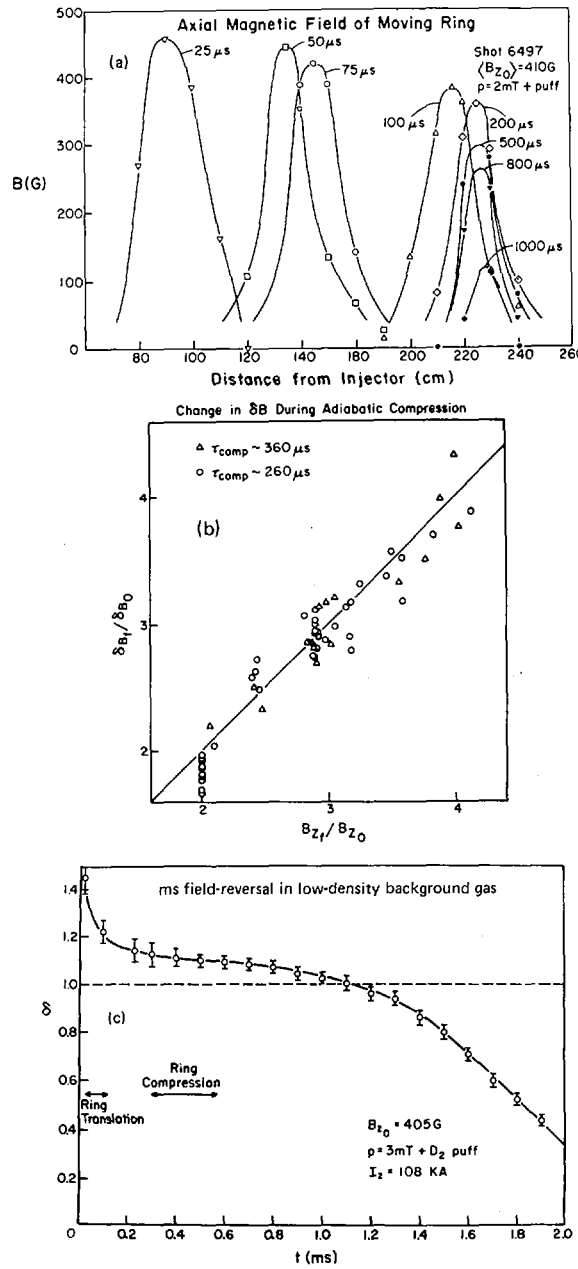


FIG.1. Results from the RECE-Christa experiment (CU-I): (a) Ring-generated axial field, δB, during ring translation; (b) Ring compression: normalized ring-induced axial field, $\delta B/\delta B_0$, at ring centre and after compression versus normalized total external field, B_z/B_{z0}. Line corresponds to δ = const. (c) Time dependence of field reversal factor, δ, for strong ring with field-reversal time of 1 ms.

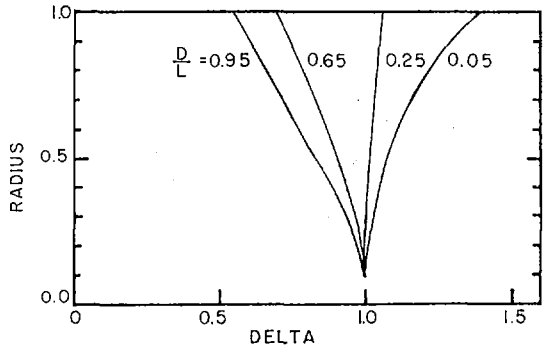


FIG. 2. Quadrupole resonances in RECE-Berta (CU-I): Radial position of 112 resonance in axially expanded Hill's vortex (D/L = diameter/length of vortex).

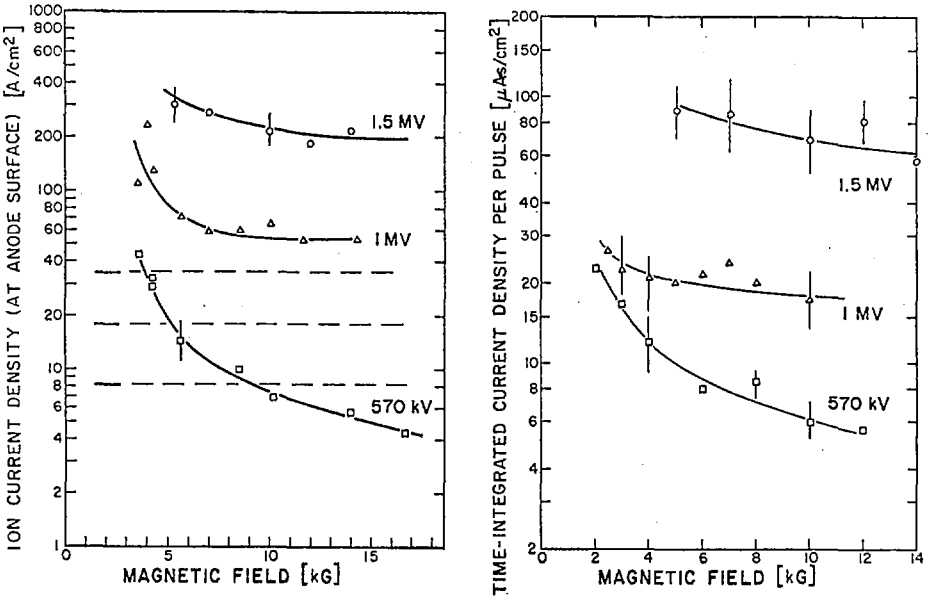


FIG. 3. Magnetically insulated diode (CU-I): Ion current density and ion yield density per pulse, 1.7-cm gap spacing for various peak voltages; voltages existing during ion emission generally are smaller (roughly 2/3).

obtained (Fig. 1c) with overall field-reversal times ranging up to 1.1 msec and $I_\theta \leq 25$ kA. Experiments with ethane puffing have just been initiated, to prepare for measurements of plasma confinement. Recent RECE-Berta [9] (400 keV, 200G) experiments on the quadrupole-induced anomalous losses reported earlier [7,10] indicate no significant emission of microwaves around the electron cyclotron frequency, a predominantly radial loss of the fast electrons, and the existence of at most two "resonances" for $\delta \leq 1$. These and the earlier results are explainable by orbital perturbations of some fast-electron groups caused by the quadrupole field. Both analytic and computer calculations with model layers performed by our group and at Livermore [11] indicate that serious perturbations can result from unstable resonances between various low-order harmonics of the radial and axial betatron frequencies and of the cyclotron frequency. Quite interestingly, our calculations for axially long layers (length/radius ≈ 3-5, as they exist in the 2XIIB experiment) predict that some important resonances will tend to occur simultaneously for a large number of particle orbits at $\delta \simeq 1$ (Fig. 2).

Ion Source Development: To prepare for future ion ring experiments in which ion cyclotron times longer than 100 nsec will exist, our earlier experiments [12] on magnetically insulated ion diodes were extended [13]: using microsecond-megavolt pulses from our RECE-Christa Marx generator, very large ion yield densities of up to 110 $\mu Asec/cm^2$ (about 70% protons) were obtained (Fig. 3) which is well within the range practically required for the generation of field-reversing ion rings. The observed ion current densities of up to 370 A/cm^2 are over 15 times larger than the Child-Langmuir ion flow expected for 1.7 cm gap and the voltages used. This enhancement appears better explained by space charge neutralization due to electrons entering the gap (e.g. along the field lines) than by the normal gap closure. This is in agreement with subsequent short-pulse experiments in which similar enhancements were observed when an electron emitting intermediate electrode was inserted just outside the gap.

Ring Theory: (i) Using a new Vlasov equilibrium code applicable to a wide range of fast-particle distributions functions, $f(H,P_\theta)$ (H - Particle energy, P_θ - canonical angular momentum) an extensive study of the physical characteristics of exponential-rigid-rotor equilibria was completed [14]. The results indicate that a significant percentage of untrapped particles exist in all such equilibria which have a sufficiently small aspect ratio to be interesting. (ii) A modification of this code was used to follow the adiabatic compression of ion rings assuming quasi-ergodic motion of the ions. Due to the existence of a new adiabatic invariant, I, it is possible to follow each ring compression by calculating only a few separate equilibria having an identical distribution function $g(P_\theta,I)$. Important results from these calculations include the appearance of hollowed-out current distributions (Fig. 4) with improved $\int d\ell/B$ stability, an increase of the relative energy spread, $\delta H/\langle H\rangle$, of particles, and also a saturation of the field-reversal factor, δ, during the compression, as it was predicted earlier [16].

NAVAL RESEARCH LABORATORY GROUP (NRL) [Drobot, et al.]

At NRL an experiment is presently underway to test the feasibility of forming a field reversing proton ring having a major radius $R \simeq 10$ cm at the midplane of the confining magnetic mirror, and an aspect ratio (=R/a, where a is the minor radius of the ring) between 2-3. The number of protons required [17] to reverse the field by such a ring is about 10^{17}. The ring will be formed in a time τ_f which is much shorter than the electron-ion collision time and thus the cancellation of ion current that is caused by the electron-ion drag [18] is avoided.

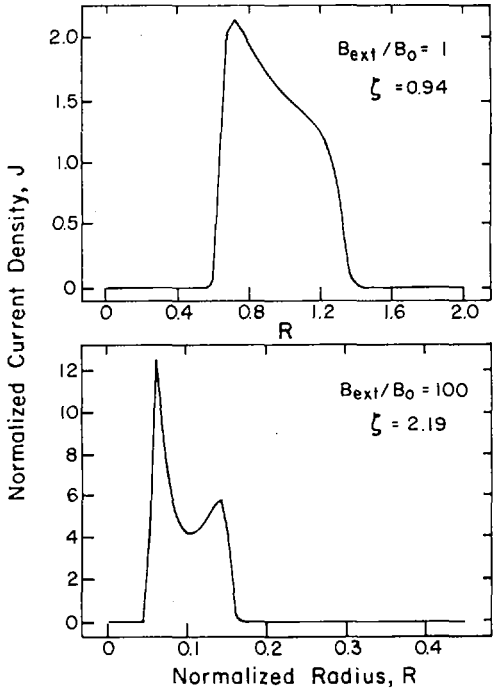


FIG. 4. Calculations of compression (CU-I): radial distribution of current density at z = 0 for Gaussian-shaped distribution function $g(P_\theta, I) = N(P_\theta - P_\theta)\exp[(I-I_0)^2/I^2]$.

A schematic of the experiment and the applied magnetic field configuration are shown in Fig. 5. The 5-meter long system consists of a low-inductance coaxial reflex tetrode [19], a magnetic cusp, a compressing static magnetic field, a gate field and a magnetic mirror. Several of the features of this experiment have been dictated by the results of a smaller experiment [20] in which a weak, propagating proton layer was formed using a 50 nsec duration, 400 keV, 3kA proton beam. For example, it was observed in that experiment [20] that only 1/3 of the protons would be transmitted through the cusp, whenever the magnetic field at the exit of the cusp was more than 40% of the critical magnetic field. The reduction of the transmission of protons through the cusp is probably associated partially with the space charge accumulation in the cusp region and partially with the radial divergence of the beam. As a consequence of these results the present experiment has been designed to operate with a value of magnetic field at the exit of the cusp that is only 1/3 of the critical field.

The 3-cm thick hollow proton beam having an average radius of 26 cm is generated by a reflex tetrode that is immersed in a uniform mangetic field. The anode of the tetrode that faces the grounded, hollow carbon cathode is made of 6-μm thick aluminized mylar foil. The second anode is placed typically 1.2 cm from the first anode and is made of 12-μm thick polyethylene foil, which is the primary source of protons The anodes are mounted on a stainless steel disc structure that is connected to the Gamble II generator, which is operated at about 1 MV positive voltage.

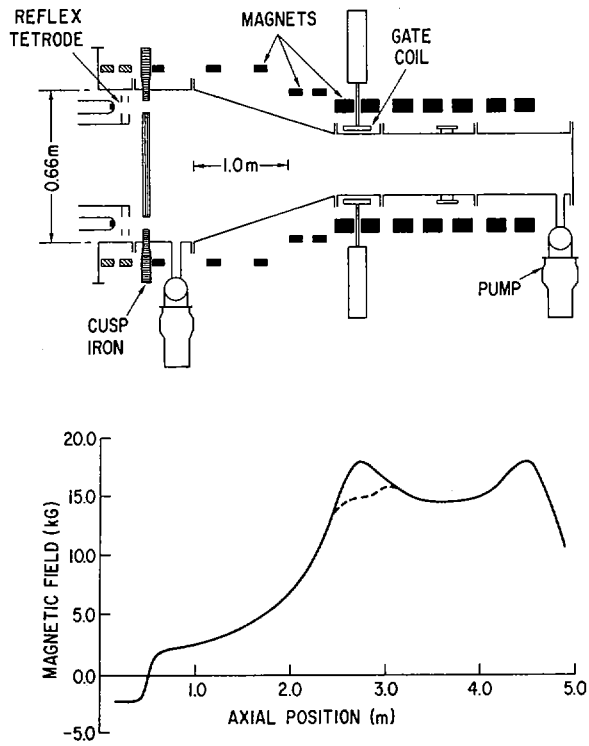


FIG. 5. Ion injection experiment (NRL): (top) A schematic of experiment. (bottom) The on-axis magnetic field as a function of axial position with (solid) and without (dashed) gate field.

Previously, reflex tetrodes [3] have been operated at the power level of 10^{10} watts. Preliminary results show that the present reflex tetrode operates well at the terawatt power level (10^{12} watts). Specifically, it is observed that the tetrode is a factor of two more efficient than a similar triode and about 85% of the tetrode proton current flows toward the virtual cathode and thus can be extracted and utilized.

After propagating for a short distance in the uniform magnetic field, the beam enters the magnetic cusp, where the protons obtain an azimuthal velocity as a result of the $aV_z B_r$ force. In agreement with the results of the previous experiment, good transmission through the cusp is observed, using nuclear activation techniques, if the magnetic field at the exit of the cusp is a fraction of the critical field.

Upon passing through the cusp, the beam enters the 2.5 meter long compressing magnetic field. As the beam propagates along this field, its radius is observed to become progressively smaller, while its azimuthal velocity increases at the expense of its translational velocity. The maximum value B_{max} of the compressing field is such that ideally the protons located at the outer edge of the beam will arrive at B_{max} with zero translational velocity. As of the present, the proton beam has been propagated to the downstream end of the compressing field. Individual

counting of delayed γ-rays emitted from small segments of carbon targets located at various locations along the compressing field shows that the hollow proton beam progressively fills in. Preliminary results show that near $B \approx B_{max}$, the beam has an almost uniform density profile. .In addition, it is observed that a large fraction of the beam is lost during the compression by the static magnetic field. Trapping with a gate field superimposed on B_{max} and confinement studies of the proton beam in the magnetic mirror will start immediately after completing the optimization of the ion source and the propagation studies of the beam through the cusp and the compressing field.

The experiment studies on the formation of ion rings are assisted by a computer simulation code [21,22]. The simulation results show that during propagation of the rotating beam in the compressing field, the self magnetic field is a function of time and the resulting inductive electric field E_θ at the front of the beam has the opposite sign to that of the azimuthal velocity V_θ. Thus, the ions in the front lose energy. In contrast, E_θ in the tail of the beam has the same sign as V_θ and thus the protons of the tail gain energy. As a consequence of this effect, the tail outruns the front and the beam executes a somersault [21]. For long-duration (>40 nsec) ion pulses, the results indicate the initial formation of two current rings oscillating through each other and achieving final trapping by "thermalization" of the ions [22]. With fast-rising gate fields, trapping efficiencies of up to 100% have been observed. The final ring is r-z stable and suffers no losses for the 550-nsec duration of the simulation. It appears that fewer protons will be needed for field-reversal if the flux-conserving wall is moved closer to the ring.

In order to describe more accurately the actual experimental situation, the computer code has recently been modified to include B_θ^{self} as well as B_z^{self}, the inductive electric fields, and the dynamics of the space charge neutralizing electrons. The B_θ^{self} acts as a magnetic piston forcing the beam to a smaller radius while the inductive electric field shortens and compresses the ring in the axial direction. As a result, the B_z^{self} is further enhanced.

CORNELL UNIVERSITY GROUP II (CU-II) [Dreike, et al.]

The experiment for the trapping of an ion ring in a mirror magnetic field, IREX, involves an annular proton beam (700 keV, 25 kA, 100 nsec) produced by a ring shaped magnetically insulated diode. The beam is injected through a cusp-like magnetic field into a solenoidal magnetic field ($B_z \approx 10$ kG, 2.5 m long). Trapping will be accomplished by a small adjustable up-stream mirror, a larger downstream mirror, and resistive rings located within the 40 cm I.D. vacuum chamber. Preliminary experiments on IREX, using an annular diode similar to that described below, are underway.

Pilot experiments have been performed using a prototype of the IREX magnetically insulated diode and the resultant rotating proton beams have been studied on a system called ANNEX (Annular Extraction Experiment). Shown schematically in Fig. 6a, the ANNEX anode consists of a cylinderically symmetric annular system; the anode emission surface is made coincident with a flux surface by properly positioning coils within the anode itself which are diamagnetic with respect to an externally applied field. The extraction cathode consists of a 65% transparent stainless steel screen. The cusp-like magnetic field in the vicinity of the diode serves to inhibit electron flow from cathode to anode (electron Hall currents flow around the anode annulus), and to impart a rotational velocity to protons as they

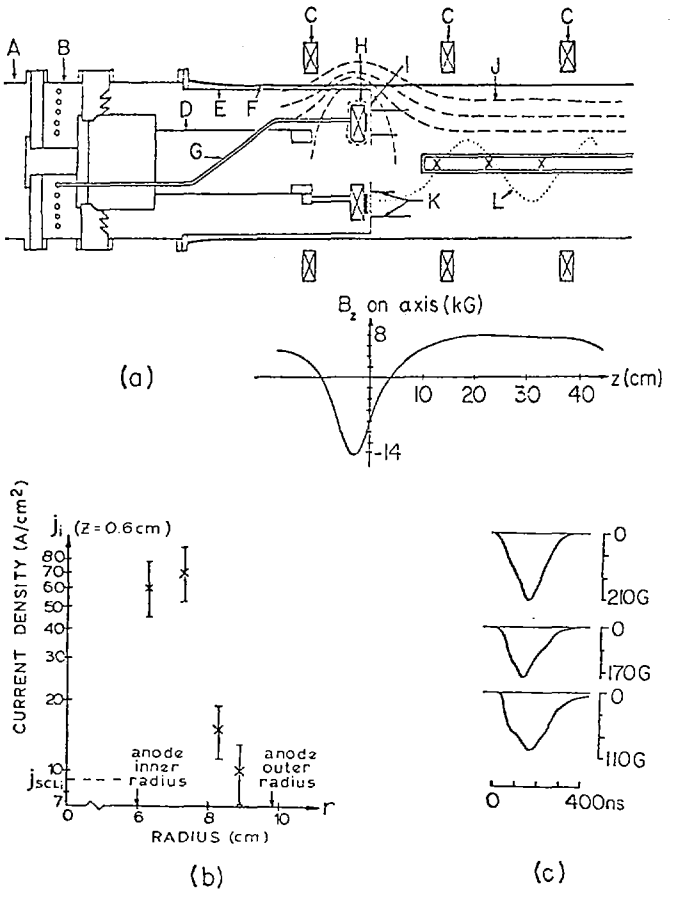


FIG. 6. ANNEX experiment (CU-II): a) Schematic: A – output end of the Omnipulse generator; B – transition section with isolation inductor for energizing the anode coil; C – solenoidal field coils; D – anode stalk; E – cathode stalk; F – glass vacuum vessel; G – cable for energizing the anode coil; H – anode; I – cathode; J – magnetic field line; K – flashboards; L – typical particle orbit. Also shown is the total axial magnetic field. b) Current density versus radius 0.6 cm behind the cathode. c) Diamagnetic signals on axis at (top to bottom) 13 cm, 23 cm, and 33 cm with mylar flashboards.

cross the anode-cathode gap and continue out into the experiment chamber. The system is operated at a pressure of 10^{-4} torr. In the absence of a proton-producing anode, diode perveance ($I/V^{3/2}$) was reduced by a factor of 60 in raising the insulating magnetic field in the accelerating gap from 0 to 7.5 kG. The gap spacing was 5.0 ± .22 mm, the diode voltage was 290 kV at 7.5 kG insulating field, and the latter field represents 1.8 B_{*}, where B_{*} is the minimum field required to produce magnetic insulation [23].

For proton beam experiments, a 185 cm annular polyethylene sheet was placed on the (metal) anode surface. This sheet has many small holes drilled in it so as to distort surface electric fields sufficiently to cause a surface

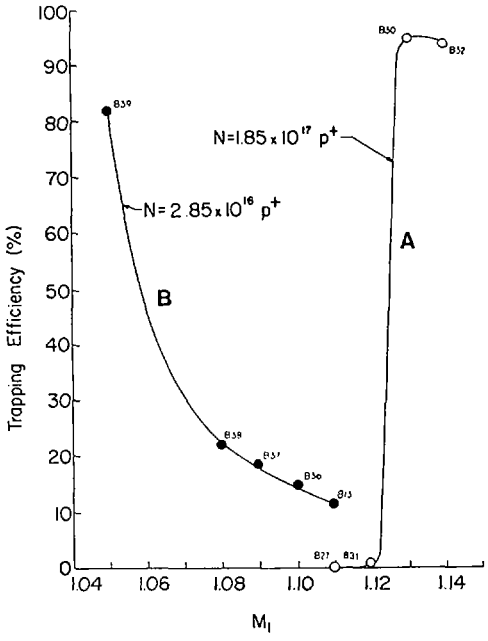


FIG. 7. Calculated trapping efficiency versus M_1 with wall resistivity η fixed (CU-II) (η = 0.72 Ω/cm).

breakdown and a copious source of ions. Again using a 5.0 mm gap, 12kA ± 3 kA average proton current was produced out of 28 kA average total diode current. Diode voltage averaged 160 kV with a pulse duration (fwhm) of about 100 nsec. This represents a proton generation efficiency of about 40%. It also represents an average enhancement of 6 over the expected space-charge limited (SCL) current [24] for the given system geometry and voltage. The average extracted proton current density as a function of radius is shown in Fig. 6b. These results, obtained using magnetically insulated Faraday cups with .002 cm^2 apertures located 0.6 cm from the cathode, are the averages of 4 azimuthal positions and several shots per position. The current densities at the two outer positions are only slightly enhanced over SCL current density, but the inner two are an order of magnitude enhanced, apparently due to electron space charge in the vicinity of the inner edge of the anode. Evidence for this is enhanced damage to that area of the anode and, in magnetic insulation experiments, an annular x-ray source coinciding with that portion of the anode. Calorimetry and witness target results both verify the intensity versus radius results just described.

Propagation experiments were performed on ANNEX using a 5.75 mm anode-cathode gap, a 6.1 kG insulating magnetic field, a 8 kG field in the propagation region, an average extracted proton current and voltage of 6 kA and 190 kV, respectively. Tests were made both with and without the passive flashboards (cylinders of metal or plastic which provide secondary electrons or breakdown to form a plasma when struck by a portion of the proton beam) located as shown in Fig. 6a. These flashboards were intended to provide a prompt source of electrons along magnetic field lines to allow rapid charge neutralization of the proton beam as it propagated across magnetic field

lines. Figure 6c shows magnetic probe signals on axis 13 cm, and 33 cm from the cathode surface for a case using mylar flashboards across the cusp region both inside and outside of the beam. An array of Faraday cups located at 23 cm and 33 cm verified that an annular beam of about 6 cm average radius and containing at least 1.0×10^{15} and 0.8×10^{15} protons respectively, reached those positions. These numbers are consistent with the $(2\pm1) \times 10^{15}$ protons estimated from magnetic probe measurements at 23 cm. They are 50% greater than results obtained without flashboards. Time of flight and pulse dispersion results indicate an axial velocity and velocity spread for the rotating proton beam of 3×10^{8} cm/sec and 1×10^{8} cm/sec, respectively, where 6×10^{8} cm/sec is the magnitude of the velocity of a 200 keV proton.

In conjunction with the experiments, numerical studies of the trapping process have been performed using a 2-d particle simulation code RINGA on a system like that shown in Fig. 6a, with the addition of an upstream magnetic mirror M_1, a downstream mirror M_2, and a resistive wall between these mirrors. Assumptions include charge neutralization, full current neutralization in the r-z plane, conservation of canonical angular momentum, and azimuthal electron currents determined by Ohm's law. Results have shown that for a sufficiently strong proton beam and a suitable choice of the upstream mirror ratio M_1, over 90% of the rotating beam can be trapped between the mirrors. This is illustrated in Fig. 7, showing that for a weaker beam (Curve B), a smaller upstream mirror must be used and that for a stronger beam (Curve A) injection efficiency is optimized a a higher value of M_1. Our results also show that a stronger ring has better defined boundaries and behaves coherently due to its self-magnetic field.

REFERENCES

[1] CHRISTOFILOS, N.C., 2nd Intern. Conf. on Peaceful Uses At. Energy, (Geneva, 1958), Vol. 32, 279; and MCNALLY, J.R., ONRL-Report ONRL-3392, 1962 (unpublished).

[2] FLEISCHMANN, H.H., Conf. Electrostat. and Electromagn, Conf. on Plasmas and Phenomenology of Relativistic Electron Beams (New York, March 1974), Ann. N.Y. Acad. Sci. 251, 472 (1975).

[3] SUDAN, R.N., OTT, E., Phys. Rev. Lett. 33, 355 (1974).

[4] CHU, K.R., KAPETANAKOS, C.A., Nucl. Fusion 15, 947 (1975).

[5] CONDIT, W.R., JR., FOWLER, T.K., POST., R.F., Lawrence Livermore Report UCRL-58002 (Feb. 1976).

[6] FLEISCHMANN, H.H., Trans. Am. Nucl. Soc. TANSAO 23, 24 (1976).

[7] DAVIS, H.A., FLEISCHMANN, H.H., LUCKHARDT, S.C., MEGER, R.A., Plasma Physics and Controlled Fusion Research, Berchtesgaden, 1976, Vol. III, p. 385.

[8] DAVIS, H.A., REJ, D.J., FLEISCHMANN, H.H., Phys. Rev. Lett. 39, 744 (1977).

[9] PHELPS, D.A., et al., Phys. Fluids 17, 2226 (1974), BZURA, J.J., et al., Phys. Rev. Lett. 29, 256 (1972).

[10] LUCKHARDT, S.C., FLEISCHMANN, H.H., Phys. Rev. Lett. 39, 747 (1977).

[11] COHEN, R.H., ANDERSON, D.V., SHARP, C., Sherwood Conf., Gatlinburg, April 1978, paper A10.

[12] LUCKHARDT, S.C., FLEISCHMANN, H.H., Appl. Phys. Lett. 30, 182 (1977).

[13] LUCKHARDT, S.C., FLEISCHMANN, H.H., KRIBEL, R.E., Cornell Report FRL-1 (Dec. 1977)

[14] LARRABEE, D.A., LOVELACE, R.V., Cornell Report FRL-3, Dec. 1977.

[15] LOVELACE, R.V., Cornell Report FRL-4 (Feb. 1978).

[16] WEIBEL, E.S., Phys. Fluids, 20, 1195 (1977).

[17] KAPETANAKOS, C.A., PARKER, R.K., CHU, K.R., Appl. Phys. Lett. 26, 284 (1975).
[18] BALDWIN, D.E., FOWLER, T.K., Lawrence Livermore Laboratory, Report UCID 17691 (1977).
[19] PASOUR, J.A., MAHAFFEY, R.A., GOLDEN, J., KAPETANAKOS, C.A., Phys. Rev. Lett. 40, 448 (1978).
[20] KAPETANAKOS, C.A., GOLDEN, J., YOUNG. F., Nucl. Fusion 16, 151 (1976)
[21] MARSH, S.J., DROBOT, A., GOLDEN, J., KAPETANAKOS, C.A., Phys. Rev. Lett. 39, 705 (1977).
[22] MARSH, S.J., DROBOT, A., GOLDEN, J., KAPETANAKOS, C.A., Phys. Fluids 21, 1945 (1978).
[23] LOVELACE, R.V., OTT, E., Phys. Fluids 17, 1263 (1974).
[24] CHILD, C.D., Phys. Rev. 32, 492 (1911); LANGMUIR, I., Phys. Rev. 2, 450 (1913).

DISCUSSION

D.R. SWEETMAN: Your electron rings appear to decay smoothly through the 'field-reversal-parameter-equals-unity' condition. Can we derive encouragement from this result that reversed field *ion* rings can be built up slowly without any catastrophic phenomena occurring?

H.H. FLEISCHMANN: I think so. In our experiments we normally do not observe any particular losses (e.g. instabilities) occurring at the field-reversal point. Thus I would certainly expect that it should be possible, in a proper arrangement, to get to field reversal with slow build-up.

REVERSED MAGNETIC FIELDS INDUCED BY A ROTATING E-BEAM*

C.W. ROBERSON[+], A. FISHER, J. HUBBARD,
W. PETER, S. ROBERTSON, N. ROSTOKER,
G. SAENZ, D. TZACH
Physics Department,
University of California,
Irvine, California

J.D. SETHIAN, K.A. GERBER, D.N. SPECTOR,
G.C. GOLDENBAUM[++], D.A. HAMMER[§], A.E. ROBSON
Naval Research Laboratory,
Washington, D.C.,
United States of America

Abstract

REVERSED MAGNETIC FIELDS INDUCED BY A ROTATING E-BEAM.

Reversed magnetic fields induced by a rotating relativistic electron beam in a plasma from a coaxial gun (University of California, Irvine) or neutral hydrogen gas (Naval Research Laboratory, Washington) are observed. At an initial plasma density of 10^{13} cm^{-3} is found a field reversal of 2 with changes in the magnetic field of 3.2 kG that last for 1 μs. Detailed agreement with measured and calculated magnetic probe responses is found at densities greater than 3×10^{13} cm^{-3}. The conductivity is found to be not classical but proportional to the plasma density. The experimental results indicate that it is necessary for the diffusion time to be less than the Alfvén time or the Alfvén time less than the beam current risetime to obtain field reversal in a preformed plasma with a rotating electron beam. Injection of a rotating beam into neutral gas has resulted in fully ionized plasmas and a field-reversed configuration with persistence time limited by the classical L/R time of the configuration (5 μs). End-on photography, radial scans with Thomson scattering and CO_2 interferometry are in agreement with an MHD equilibrium model fitted to measurements of the excluded flux and the beam-induced axial ($\Delta B/z$) and azimuthal (B_θ) fields. A reversed-field configuration has also been produced inside a closed metal tube without an applied field. The configuration persists for 18 μs and has an axial extent of 65 cm.

---

* Work support by the US Department of Energy (UCI) and the US Office of Naval Research (NRL).

[+] Present address: Naval Research Laboratory, Washington, D.C.
[++] Present address: University of Maryland, College Park, Maryland.
[§] Present address: Cornell University, Ithaca, N.Y.

A field-reversed plasma configuration has been produced with plasma currents induced by a rotating relativistic electron beam[1]. The beam is injected along an applied magnetic field into a cylindrical vacuum chamber containing plasma from a coaxial gun (UCI) or neutral hydrogen gas (NRL). The beam heats the plasma (forms the plasma as well in the gas experiment), and upon exiting the system, induces azimuthal and axial plasma currents of sufficient magnitude to reverse the applied field on axis and produce a comparable B_θ field, respectively. The resulting field structure is expected to exhibit favorable confinement properties for high-β plasmas. If the effective collision frequency is large enough to critically damp the magnetosonic modes, the plasma currents will decay with the characteristic L/R time for the configuration. Thus, a plasma confined by such a configuration, once set up, can be further heated by an imploding liquid metal liner[2](as proposed in the NRL LINUS program), or can be a target plasma in a high-Q reversed-field mirror reactor[3].

In the experiments reported here, a rotating electron beam is produced by passing an annular beam (UCI:1-1.4 MeV,50-90 kA, 60 nsec; NRL: 1.2 MeV, 50 kA, 50 nsec) through a magnetic cusp into a stainless steel interaction chamber. Field-reversed configurations are observed to persist for up to 5 μsec, with reversals in the applied field up to a factor of 2. That these fields are maintained by plasma currents, rather than trapped beam electrons, is indicated by the absence of hard X-ray signals after beam termination. Typical diagnostics in these experiments include magnetic probes, X-ray detectors, damage rods[4], Thomson scatter, CO_2 and microwave interferometry, and an image converter camera.

The theory of the interaction of a rotating beam with a plasma has received considerable attention[5]. The head of the beam induces both axial and azimuthal return currents in the plasma. If $\nu_e^2 > 4\omega_{LH}^2 (1+\omega_p^2/k^2c^2)$ the diffusion of the azimuthal return currents causes a braking of the beam and gives an effective stopping length $\ell = \gamma n_p v_\parallel^3/(2n_b v_\theta^2 \nu_e)$, where ν_e is the electron-ion collision frequency, ω_{LH} the lower hybrid frequency, ω_p the plasma frequency, k the wave number, c the velocity of light, γ the relativistic factor, n_p the plasma density, n_b the beam density, $v_\parallel$ the axial beam velocity and v_θ the azimuthal beam velocity. If ν_e is less than the critical value, the azimuthal return current is carried away by the magnetosonic mode. However, if the beam rise time is long compared to the Alfvén time the azimuthal return current does not develop[6]. Solutions of a magnetohydrodynamic model, which can be compared directly with measurements of the perturbed magnetic field, have been carried out for the UCI experiment[7].

The UCI experimental apparatus (which is similar to the NRL apparatus)is shown in Fig. 1. A rotating E-beam is produced by passing an annular beam (1 - 1.4 MeV, 50 - 90 kA, 60 nsec) through a magnetic cusp. The beam-plasma interaction chamber is filled with plasma of a density from 1×10^{13} cm^{-3} to 5×10^{14} cm^{-3} by a coaxial plasma gun or neutral hydrogen gas at pressures from 10 to 500 mTorr of H_2.

Magnetic probe measurement of the change in the axial component of the magnetic field on axis and at a radius of 7 cm are shown in Fig. 2. The on-axis signal initially goes diamagnetic and then oscillates, whereas the off-axis signal initially goes paramagnetic and oscillates. The oscillation frequency was found to be proportional to the magnetic field, as expected for a magnetosonic or compressional Alfvén mode[8]. At a density of 3×10^{13} cm^{-3} we observe a change in the magnetic field of 3.2 kG, which is a field reversal of 2 that lasts for about 1 μsec.

The calculated perturbations in the axial component of the magnetic fields are shown in Fig. 3. These calculations are for a plasma density of 10^{14} cm^{-3}, and two parameters are chosen to fit the on-axis calculated signal with the experimental. The azimuthal beam current was chosen such that the

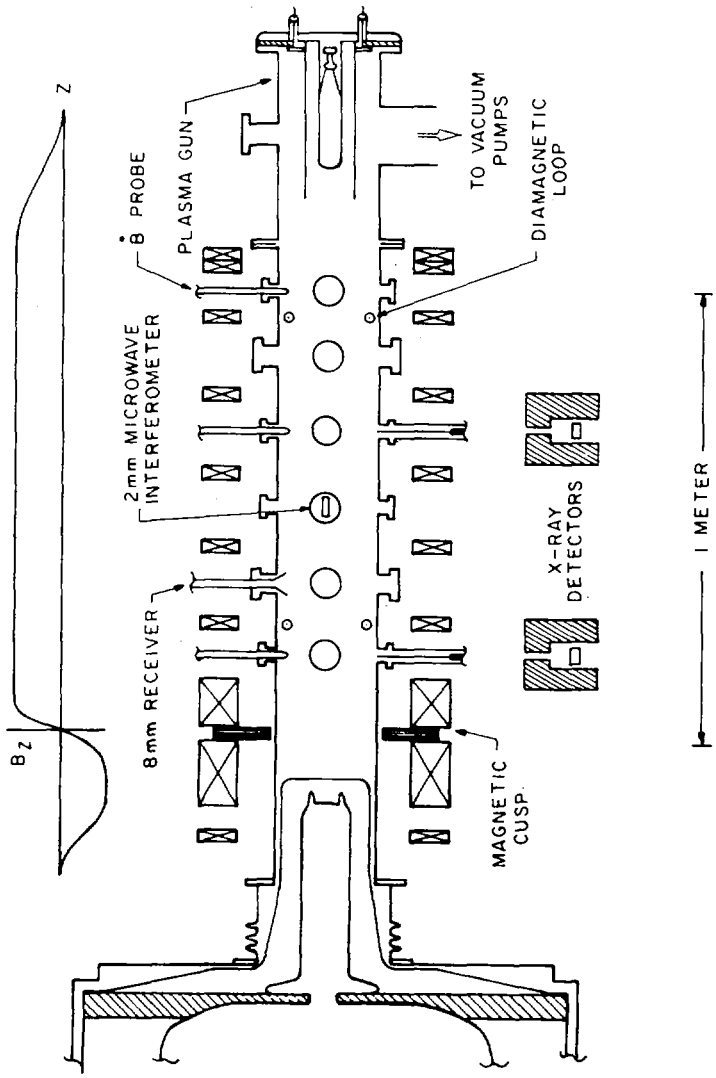


FIG.1. Experimental apparatus.

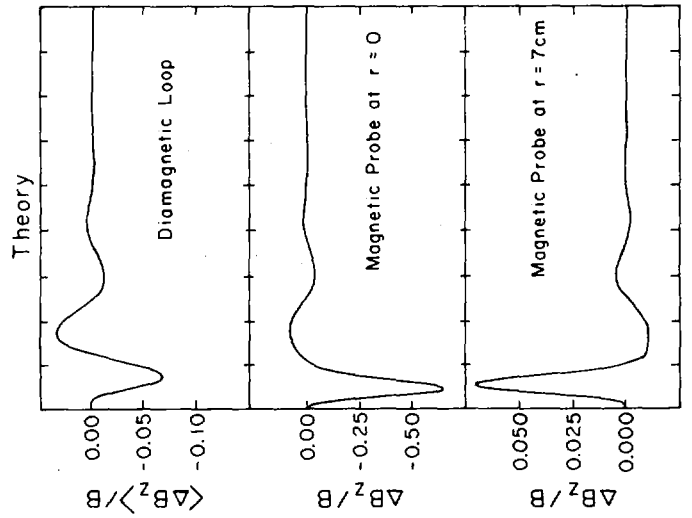


FIG.3. Calculated changes in B_z.

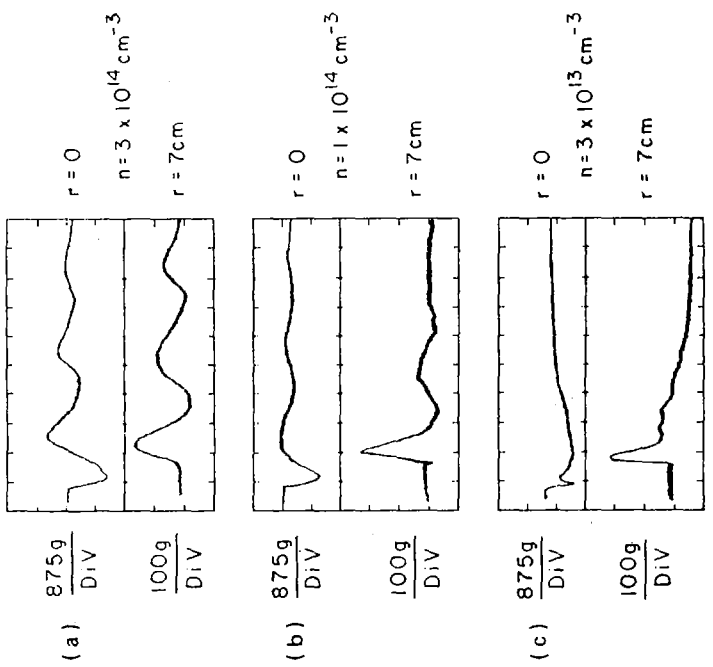


FIG.2. Magnetic probe signals versus plasma density.

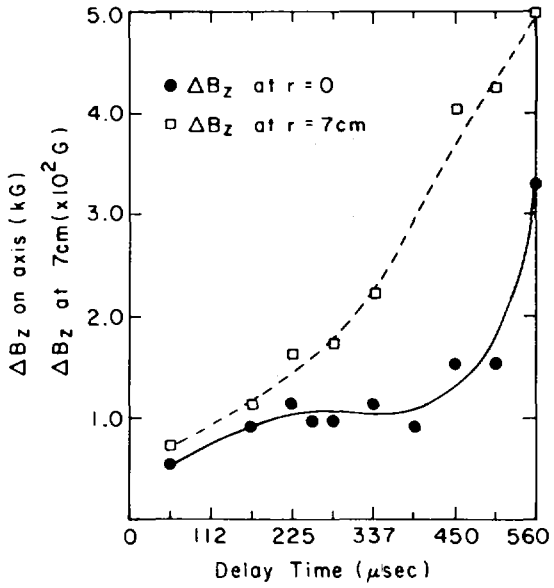


FIG.4. Peak magnetic signal versus plasma gun delay time.

magnitude of the first peak in the calculated signals matched the observed peak. The plasma conductivity in the calculations was chosen so that the damping of the waves matched the observed damping. At a density of 3×10^{13} the waves are critically damped. The conductivity required to critically damp the oscillations in the calculated curves is $\sigma = 4.5 \times 10^{11}$ sec^{-1} = $\omega_p^2/4\pi\nu_e$. From this we obtain $\nu_e = 3.7 \times 10^{10}$. This compares favorably with the value obtained from the condition for critical damping given by Molvig and Rostoker of $\nu_e = 1.3 \times 10^{10}$. Using this value of σ we find the magnetic diffusion time is $T_d = 4\pi\sigma a^2/c^2 = 640$ ns, which is approximately that observed. The effective collision frequency observed is almost two orders of magnitude higher than the Spitzer value, or that due to electron neutral collisions. Calculated curves of the perturbed magnetic field vs. density, with the conductivity constant, give less damping at the lower densities. This trend is just the opposite to that observed experimentally. However, if we adjust the conductivity to obtain calculated curves like the experimental ones, we find the effective conductivity of the plasma is proportional to the density in the range $2.5 \times 10^{13} - 5 \times 10^{14}$ cm^{-3}, or equivalently the effective collision frequency is independent of density. This technique of determining the conductivity by fitting computer solutions to the measured wave profiles gives an average over the bulk of the plasma. This is a distinct advantage over conductivity measurements in a linear device that are determined from the L/R decay of return currents, or voltage and current measurements across the plasma column. In those measurements the sheaths at the end of the device can dominate the measurements.

In Fig. 4 the amplitude of the peak of the on-axis diamagnetic signal and the off-axis (r = 7 cm) paramagnetic signal are plotted vs. the delay time between firing of the plasma gun and the beam. At a delay time

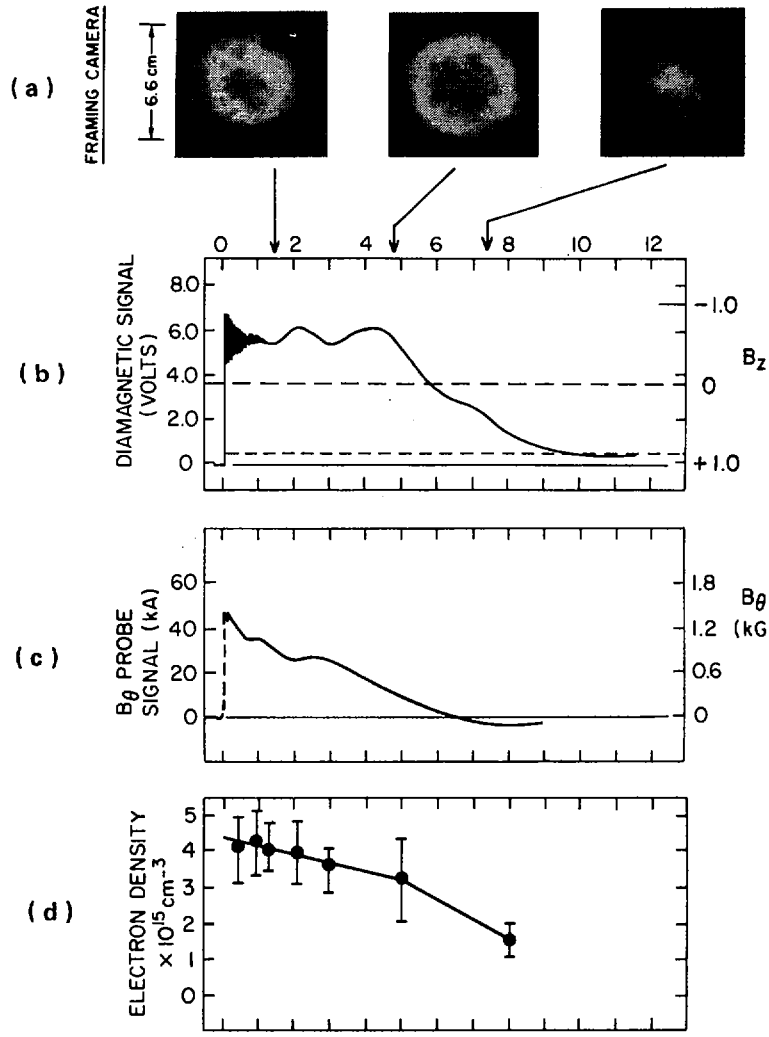


FIG.5. Experimental results showing framing photographs, diamagnetic loop signals, B_θ probe signals, and electron density.

of 170 μsec ($n_e \cong 5 \times 10^{14}$ cm^{-3}) the peak change in B_z is approximately 60% of the applied field. After the magnetosonic modes became critically damped (T_D = 337 μs, $n_e \simeq 3 \times 10^{13}$ cm^{-3}) we see a rapid rise in B_z on axis and at a density of 10^{13} cm^{-3} ($T_D \sim 560$ μs) we observe twice field reversal ($\Delta B_z = 2B_0$ = 3.2 kG) for a duration of approximately 1 μs.

To our knowledge this is the first time field reversal has been obtained in a preionized plasma with an electron beam. The field reversal is due to induced currents. These experimental results suggest the diffusion time should be less than the Alfvén time to obtain field reversal. The anomalously high collision frequencies appear to be due to beam-induced turbulence. At a density of 3 x 10^{13} cm^{-3} we measured a stopping length of 0.5 meters, which agrees with the calculated value.

We have also carried out experiments at UCI with a longer pulse beam (600 KeV, 18 kA, 1 μs) and obtained field reversal factors of 2.5 for 1 μs in plasma[9]. Although the diffusion time was longer than the Alfven time, the Alfven time was less than the beam rise time. The X-ray measurements show the field reversal is due to beam electrons in that case.

In the NRL experiment,[10] (which is similar to the UCI apparatus shown in Fig. 1), a reversed-field configuration has been produced in an initially neutral gas. The experimental results are shown in Fig. 5. End-on framing photographs (Fig. 5a) show the plasma has an annular profile and is formed away from the drift tube wall (radius 7.3 cm). At these low temperatures, the plasma is expected to be located only in the light-emitting regions, and radial scans with Thomson scattering are consistent with the framing photos.

The existence of field reversal is inferred from the output of the diamagnetic loop, Fig. 5b, which is calibrated in terms of the net field on axis. The signal depicted represents full cancellation of the applied field on axis ($B_{zi} = 0$) for approximately 6 μsec. At peak value, $B_{zi} = -.8\ B_0$. After layer formation, the diamagnetic signal displays small amplitude oscillations, which are found to correspond to magnetosonic bouncing of the plasma column. These oscillations do not grow in time, indicating the system is oscillating about a stable equilibrium. The decay of B_{zi} is concurrent with the plasma collapse, as expected.

Three diamagnetic loops placed along the drift tube axis showed the configuration contracts axially after formation. This observation can be explained by modeling the azimuthal currents as a coil which tends to maximize its self-inductance, a tendency that is balanced by the plasma pressure until it is lost.

The persistence time of the axial plasma current, indicated by a B_θ probe at 6.3 cm off axis, is shown in Fig. 5c. Note that $I_{z\text{-net}}$ = 45 kA implies the plasma currents induced by the entrance of the beam are small compared to the beam current. B_θ and B_{zi} have different decay characteristics, because the changing magnetic field cause a change in the plasma equilibrium. The decay of j_z decreases B_θ^2, changing the force balance to move the plasma outward, whereas the decay of j_θ will cause B^2_{zi} to decrease faster than B^2_{zo}, and thus move the plasma inward. Thus it is reasonable to expect a net outward motion of the plasma which compresses the (decaying) axial return flux against the wall, keeping the diamagnetic signal (which essentially measures the field outside the plasma, B_{zo}) approximately constant until B_θ has become small, at which point the plasma radius and diamagnetic signal decrease rapidly. This explanation is supported qualitatively by the framing photographs, which show plasma expansion in the first four μsec and subsequent contraction; and quantitatively by a one-dimensional model based on flux conservation and pressure balance.

In Fig.5d, the electron density from Thomson scattering (average of three shots) is plotted as a function of time. The increase in the density decay rate occurs when $B_{zi} > 0$ (i.e. field reversal is lost), consistent with a loss of axial confinement.

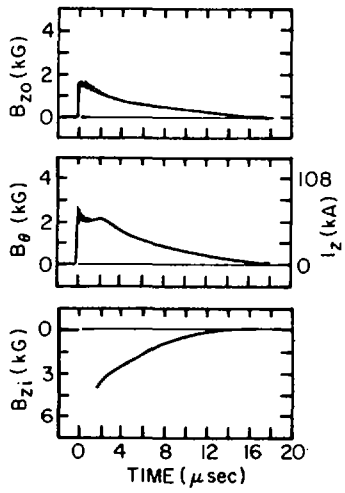


FIG. 6. Output of magnetic probes measuring B_z *(r = 6.3 cm)* $\equiv B_{zo}$; B_θ *(r = 6.3 cm); and* B_z *(r = 0 cm)* $\equiv B_{zi}$.

An MHD equilibrium model has been used to determine the configuration consistent with the experimental data. Input to the model are the flux change measured by the diamagnetic loop, and the B_{zo} and B_θ fields determined by local magnetic probes placed just inside the drift tube wall. The model output gives the radial variation of nkT_e, and is in agreement with end-on photography, radial Thomson scattering scans, and CO_2 interferometry.

The configuration has also been generated without an applied magnetic field[11]. The apparatus is similar in design to the guide field experiment, only the electron beam generator has been upgraded to produce V = 900 kV, I = 110 kA, T = 100 nsec FWHM. The beam is injected through a half cusp into a 14.6-cm-diameter stainless steel cylindrical chamber containing neutral hydrogen. The system is terminated with a transparent brass screen at z = 6.5 cm.

Typical results are shown in Fig. 6. The traces show values of B_θ at r = 6.3 cm, B_z at r = 6.3 cm (i.e. B_{zo}) and B_z on axis (i.e. B_{zi}) as measured by three magnetic probes. As B_{zo} (upper trace) is opposite to B_{zi} (lower trace), it can be seen that a field-reversed configuration has been generated with a persistence time of 12 μsec. Measurements with the B_{zi} probe removed show the configuration persists for 18-20 μsec and extends the length of the interaction chamber (65 cm). End-on framing photography shows the plasma has an annular profile with typical mean radius of r_p = 3.9 cm and annular width 1.5 cm. As the configuration decays the plasma radius does not change, unlike in the previous studies. This is to be expected, since without the applied field, all the confining fields decay with the plasma.

Both B_{zo} and B_θ play a role in plasma confinement, as they are of comparable magnitudes. This has been verified with an equilibrium model, which uses flux conservation and pressure balance to predict the mean plasma radius, r_p, as a function of B_{zo}/B_θ. The model output is shown as

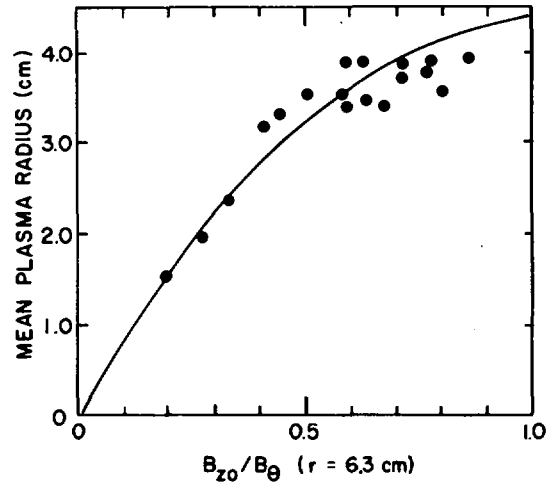


FIG. 7. B_{zo}/B_θ *versus mean plasma radius.*

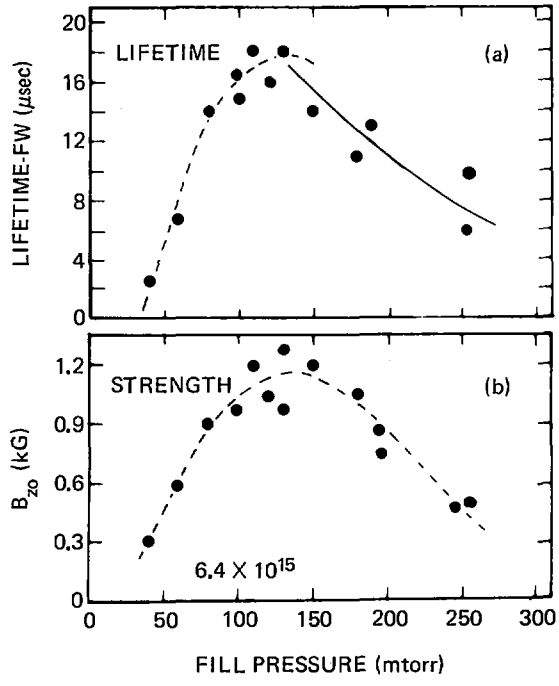


FIG. 8. Layer lifetime and strength versus fill pressure.

the solid curve in Fig. 7. The data points are obtained by varying the cusp magnetic field (which changes the pitch angle of the beam) and measuring B_{zo}/B_θ and r_p. The agreement between model and data indicates the plasma to be in radial equilibrium over a broad range of B_{zo}/B.

The configuration strength (in terms of B_{zo}), and lifetime (full width), as determined by a magnetic probe at z = 20 cm, are plotted as a function of fill pressure in Fig. 8. Both layer lifetime and strength are maximized at fill pressures between 100-150 mTorr H_2. The reduced values at pressures below 100 mTorr are attributable to a lack of sufficient plasma to achieve enough charge neutralization to allow the beam to propagate. As the pressure is increased above 150 mTorr, the energy deposited by the beam has to be shared by more particles, resulting in a lower electron temperature, T_e. Assuming classical processes, the lifetime of the configuration, τ, scales as $T_e^{3/2}$. Assuming T_e scales as $1/n$, then τ scales as $n^{-3/2}$. The solid line in Fig. 8(a) represents this $n^{-3/2}$ scaling, and can be seen to be in agreement with the data.

The elimination of the external field coils has particular advantages to a fusion reactor based on the imploding liner as the rotating beam both heats the plasma and generates the confining fields, making compression a purely mechanical process.

REFERENCES

[1] Roberson, C. W., Tzach, D., and Rostoker, N., Appl. Phys. Lett. 32 214 (1978); Hammer, D. A., Robson, A. E., Gerber, K. A., and Sethian, J. D., Phys. Lett. 60A 31 (1977).

[2] Book, D. L., et al., Plasma Physics and Controlled Nuclear Fusion Research (Proc. 6th Conf. Berchtesgaden, 1976) Vol.3, IAEA, Vienna (1977) 507.

[3] Condit, W., Fowler, T., and Post, R., LLL Report UCRL-52008 (1976).

[4] Roberson, C., Saenz, G., and Tzach, D., Rev. Sci. Inst. 48 804 (1977).

[5] Chu, K. R., and Rostoker, N., Phys. Fluids 17 813 (1974); Chu, K. R., Kapetanakos, C. A., and Clark, R., Appl. Phys. Lett. 27 185 (1975); Molvig, K., and Rostoker, N., Phys. Fluids 20 494 (1977); 20 504 (1977); Molvig, K., Rostoker, N., and Dothan, F., Plasma Physics and Controlled Nuclear Fusion Research 1974 (Proc. 5th Int. Conf. Tokyo 1974) Vol.3, IAEA, Vienna (1975) 249.

[6] Berk, H. L., and Pearlstein, D., Phys. Fluids 19 1831 (1976).

[7] Roberson, C. W., Nuclear Fusion 18 (1978) 1693.

[8] Hubbard, J., and Rostoker, N., UCI Technical Report No. 76-43 (1976).

[9] Saenz, G., and Roberson, C. W., UCI Technical Report No. 77-61 (1977).

[10] Sethian, J. D., Hammer, D. A., Gerber, K. A., Spector, D. N., Robson, A. E., and Goldenbaum, G. C., NRL Report 3648, to be in Phys. Fluids.

[11] Sethian, J. D., Gerber, K. A., Spector, D. N., and Robson, A. E., NRL Report.

DISCUSSION

H.J. HOPMAN: From the data I understand that the effective collision frequency ν_{eff} is much larger than the ion plasma frequency ω_{pi}. In turbulent heating one always observes $\nu_{eff} \approx \omega_{pi}$. Do you have an explanation for the extremely large value of ν_{eff}?

C.W. ROBERSON: Yes, it is true that the effective collision frequency is greater than ω_{pi}. We do not have a theory that explains these high collision frequencies.

Session G

PLASMA HEATING I

Chairman

F.F. CAP
Austria

LOWER HYBRID RESONANCE CONES IN TOKAMAKS

M. BRAMBILLA
Association Euratom-CEA,
Département de physique du plasma
et de la fusion contrôlée,
Service IGn, Centre d'études nucléaires,
Grenoble, France

Abstract

LOWER HYBRID RESONANCE CONES IN TOKAMAKS.

The limits are discussed of the cold plasma electrostatic description of the radiation patterns of antennas, in particular phased waveguide arrays, used to launch lower hybrid waves into a tokamak plasma. It is shown that the combined effects of electron Landau damping and of electromagnetic corrections to the phase of partial waves rapidly transform the highly inhomogeneous, localized electric field distribution prevailing near the antenna into a broad and smooth wavepacket.

As pointed out by Briggs and Parker /1/, externally launched electrostatic LH waves remain localized along characteristic patterns known as resonance cones. This behaviour is just an illustration of the fact that in a medium without spatial dispersion, like cold plasma, short wavelength quasi-electrostatic waves can propagate only at frequencies for which the Poisson equation is of the hyperbolic type /2/,/3/. Resonance cones are then the bundles of characteristics (rays) leaving the antenna. Moreover, whenever the antenna electric field has a jump (for example at the edge of a waveguide), the radiated field develops a logarithmic singularity along the rays originating at the corresponding point of the antenna. In view of the severe limitations that exceedingly large and localized electric fields, particularly near the plasma surface, could put on the efficiency of LH heating, it is worth investigating what actually limits the field amplitude.

For this purpose, we note that LH cones are not wavepackets in the usual sense of the word (if they were, the uncertainty principle would be violated) but the result of the interference of an infinitely broad ("brown") spectrum of parallel wavenumbers k_z (z and x refer here to the direction of the static magnetic field and of the density gradient, respectively). As a consequence, the peak values of the electric field will be determined by those effects which cut off the transmitted spectrum at large k_z. The most important are inefficient tunneling of short wavelengths through the underdense sheath near the antenna ($\omega_{pe} \lesssim \omega$) and Electron Landau Damping. Combined with the building up of electromagnetic corrections to the electrostatic dispersion relation, these effects rapidly attenuate the maximum electric field and destroy the localization predicted by the cold electrostatic theory.

In a slab plasma model, slow LH waves with $n_z = k_z c/\omega$ satisfying the accessibility condition are accurately described by /4/

$$\frac{d^2 E_z}{dx^2} + k_o^2 (n_z^2 - \varepsilon_{xx}) \left(-\frac{\varepsilon_{zz}}{\varepsilon_{xx}}\right) E_z = 0 \qquad (1)$$

$$E_x \simeq \frac{n_z}{(n_z^2 - \varepsilon_{xx})^{1/2}} \left(-\frac{\varepsilon_{zz}}{\varepsilon_{xx}}\right)^{1/2} E_z \qquad (2)$$

where $k_o = \omega/c$, $\varepsilon_{zz} \simeq 1 - \omega_{pe}^2/\omega^2$, $\varepsilon_{xx} = 1 + \omega_{pe}^2/\Omega_{ce}^2 - \omega_{pi}^2/\omega^2$. At sufficiently large density, $-\varepsilon_{zz} \gg 1$, $|E| \sim |E_x|$, and

$$E_x = \sum_{\sigma=\pm} \int_{n_{Acc}}^{\infty} \frac{n_z\, dn_z}{(n_z - \varepsilon_{xx})^{1/2}} \frac{q_\perp^{1/2}}{(\varepsilon_{xx})^{1/2}} A(k_z)\, e^{i\left(\sigma k_z z - k_o \int^x q_\perp\, dx\right)} \qquad (3)$$

$$q_\perp = \left(n_z^2 - \varepsilon_{xx}\right)^{1/2} \left(-\frac{\varepsilon_{zz}}{\varepsilon_{xx}}\right)^{1/2}$$

Here n_{Acc} is the lowest accessible value of n_z; the normalization is chosen so that $\omega |A(k_z)|^2/8\pi$ is the spectral density of power flux in the x direction. The two terms in the sum represent the resonance cones going to the right and to the left respectively.

From Eq.(1), one finds that $A(k_z)$ is related to the Fourier transform $\mathcal{E}_a(k_z)$ of the longitudinal component $E_z^a(z)$ of the electric field of the antenna through

$$A(k_z) = \frac{e^{5\pi i/12}}{\sqrt{\pi}} \left(\frac{3}{k_o L_n}\right)^{1/2} \frac{\mathcal{E}_a(k_z)}{(n_z^2 - 1)^{1/2}\, W_{1/3}(k_z)} \qquad (4)$$

where

$$W_{1/3}(k_z) = \begin{cases} \frac{2i}{\sqrt{3}} (\alpha^2 - 1)^{1/2} \left[J_{-1/3}(\xi) - e^{-\pi i/3} J_{1/3}(\xi)\right] & \alpha^2 > 1 \\ \frac{2i}{\sqrt{3}} \frac{1}{\Gamma(2/3)\left(x_\perp L_n/3\right)^{1/3}} & \alpha^2 = 1 \\ \frac{2i}{\sqrt{3}} (1 - \alpha^2)^{1/2} \left[I_{-1/3}(\xi) + e^{-\pi i/3} I_{1/3}(\xi)\right] & \alpha^2 < 1 \end{cases} \qquad (5)$$

Here $\xi = 2\kappa_\perp L_n (|1-\alpha^2|)^{3/2}/3$, $\kappa_\perp = (|k_z^2 - k_0^2|)^{1/2}$, $\alpha^2 = n(0)/n_{cut\,off}$ is the ratio of the plasma density at the antenna to the cut-off density, $n_{cut\,off} = 4.9 \times 10^{-7}\omega^2$ and $L_n = n_{cut\,off}\,(dn/dx)^{-1}$. $E_a(k_z)$ for an array of phased waveguides can be evaluated using the theory of Ref /5/. A selfconsistent evaluation is required since the dimensions of the antenna are comparable with the free space wavelength. The phase jump of B_y from one guide to the next induces strong currents in the edge of the wall between the guides; near these edges, localized spikes of the electric field exceed by a factor 2 or 3 the nominal field E_0, and go over continuously into the peaks along the "singular" characteristics /6/.

The electrostatic, cold plasma limit is recovered using for $W_{1/3}(k_z)$ the first of Eqs (5) with the large argument asymptotic expansion for the Bessel functions, and neglecting both unity and ε_{xx} compared with n^2_z, so that, in particular, $q_\perp$ reduces to its electrostatic form:

$$k_0 q_\perp = |k_z| \int^{x} \left(-\frac{\varepsilon_{zz}}{\varepsilon_{xx}}\right)^{1/2} dx \qquad (6)$$

This means, as expected, that this limit is a good approximation if the antenna is located at sufficiently high density, $\omega_p^2 >> \omega^2$, and is electrically short, $\langle n_z \rangle_{average} >> 1$.

In this case, the effect of ELD[1] can reasonably well be simulated by truncating the transmitted spectrum at $n_{z\,MAX} \simeq 5/\sqrt{T_e}$, where T_e is the electron temperature in keV /7/. Then the peak values of the electric field along the "singular characteristics" can be estimated to be

$$\left|\frac{E_{MAX}}{E_0}\right| \approx \frac{(-\varepsilon_{zz}(0))^{1/4}}{2\pi} \left(-\frac{\varepsilon_{zz}(x)}{\varepsilon^3_{xx}(x)}\right)^{1/4} \log(n_{zMAX}) \qquad (7)$$

At a temperature of a few tens of eV, characteristics of the tenuous plasma in the shadow of the limiter, the peaks are three to five times larger than the field of a single plane wave.

In the case of the grill, however, a low-density layer ($\varepsilon_{zz}(0) \approx 1$) with relatively steep density gradient ($10^{10} \lesssim dn/dx \lesssim 10^{12}$) is likely to exist, the guide walls playing the role of a secondary limiter. The appropriate form for $W_{1/3}(k_z)$ is then the third of Eqs (5), which shows that the transmitted spectrum is effectively truncated at $n_{MAX} \approx (k_0 L_n)^{-1}$, shorter wavelengths experiencing too strong evanescence in the underdense sheath. In this context, it is worth noting that n_{MAX} can also be reduced by rounding the edges of the antenna facing the plasma. In this case $n_{MAX} \approx (k_0 \varrho)^{-1}$, where ϱ is the radius of curvature of the edges. This rough estimation and preliminary numerical calculations suggest that this technique could be quite effective in reducing the problems associated with large electric fields near the antenna.

Further inside the plasma, the build-up of electromagnetic corrections to the phase of partial waves combines with the decrease of $n_{z\,MAX}$ to smear

---

[1] Electron Landau damping.

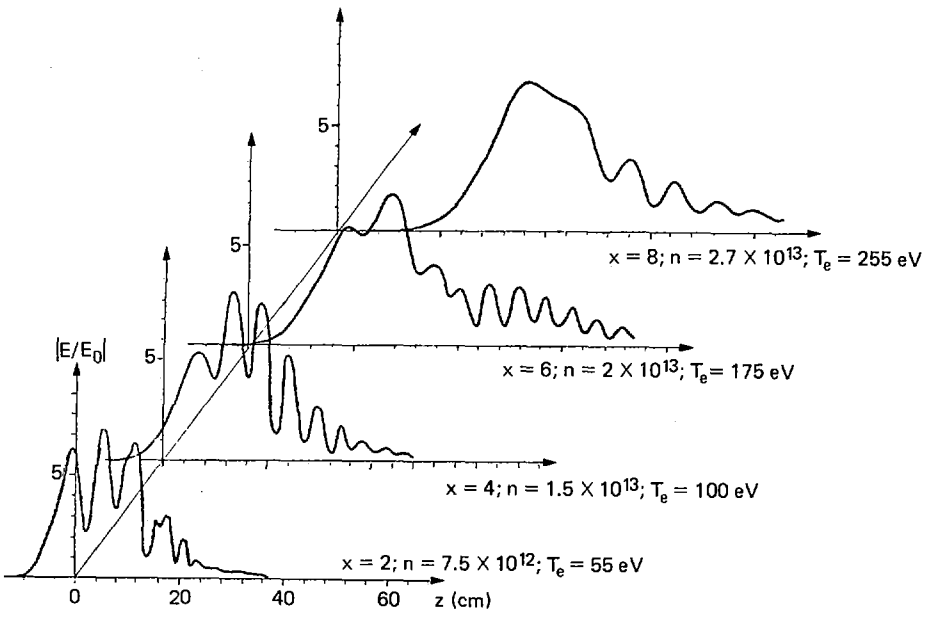


FIG.1. Electric field distribution from an array of four waveguides. The origin of the z axis is at the position of the resonance cone in the electrostatic limit. At 8 cm from the antenna only 5.3% of the incident power has been absorbed.

out the localized features of the electric field distribution. It is not difficult to show that as soon as

$$h(x) = \frac{k_0}{2}\int^{x} \left(-\varepsilon_{zz}\cdot\varepsilon_{xx}\right)^{1/2} dx \gtrsim n_{zMAX} \qquad (8)$$

the internal edges of the resonance cones are displaced farther away from the antenna by the amount $\delta z = \pm h(x) / n^2_{MAX}$ with respect to the position predicted by the electrostatic theory, while the corresponding values of the electric field become proportional to $(n_{MAX} / h)^{3/2}$. The rapid decrease of this factor with density over-compensates the WKB enhancement. Since such a reduction in the intensity is not accompanied by an important power absorption (for a well designed antenna with four guides the power associated with $n_z \gtrsim 10$ can be of the order of a few percent only), the region illuminated by the electric field must spread accordingly.

Numerical calculations of the integral (3) confirm well this qualitative discussion. As soon as condition (8) is roughly satisfied, the electric field decreases, the internal edge of the resonance cone is still acceptably well defined but penetrates radially more slowly than predicted by the electrostatic theory, while the external edge practically disappears, a wave with slowly decreasing amplitude and well defined wavelength roughly equal to the periodicity of the antenna extending for many wavelengths

along the magnetic field. From this point on, the radiation pattern can be reasonably described as a wavepacket, having lost most of the properties of the electrostatic solution (Fig. 1).

The present results should be taken into account when investigating nonlinear effects which are thought to play an important role in the power deposition of LH waves in the plasma. In particular, the broadening of the localization region can explain the success of the "uniform pump" theory of Porkolab in interpreting the spectrum of decay waves observed during the heating pulse /8/.

REFERENCES

/1/ R.J. Briggs, R.R. Parker, Phys. Rev. Lett. 29 (1972) 852.

/2/ P.M. Bellan, M. Porkolab, Phys. Fluids 17 (1974) 1592.

/3/ P.L. Colestock, Nuclear Fusion 18 (1978) 740.

/4/ M. Brambilla, Report EUR-CEA-FC 951, April 1978.

/5/ M. Brambilla, Nuclear Fusion 16 (1976) 47.

/6/ M. Brambilla, Proc. 3rd topical conf. on R.F. plasma heating, Pasadena (California) 1978, paper B1.

/7/ M. Brambilla, Nuclear Fusion 18 (1978) 493.

/8/ M. Porkolab et al., Phys. Rev. Letters 38 (1977) 230.

STOCHASTIC ION HEATING BY AN ELECTROSTATIC WAVE IN A IN A SHEARED MAGNETIC FIELD

Y. GELL, R. NAKACH
Association Euratom-CEA,
Département de physique du plasma
et de la fusion contrôlée,
Service IGn, Centre d'études nucléaires,
Grenoble, France

Abstract

STOCHASTIC ION HEATING BY AN ELECTROSTATIC WAVE IN A SHEARED MAGNETIC FIELD.

The purpose of this paper is to investigate the effects of the magnetic-field shear on the stochastic acceleration of ions by electrostatic waves in the lower-hybrid frequency range.

We consider the motion of one single particle in the presence of an electrostatic wave (generated by a lower-hybrid-type radiation) and a weakly sheared magnetic field. In order to facilitate the study of this motion in such a configuration we limit ourselves to the case of a straight-lines magnetic field and a constant-amplitude wave. Explicitly, the equation of motion is given by :

$$\frac{d\vec{v}}{dt} = \frac{e}{m} \quad (\vec{E} + \vec{v} \times \vec{B}) \qquad (1)$$

where $\vec{E} = E_0 \cos (k Y - \omega t) \vec{e}_y$

$\vec{B} = B_0 (\vec{e}_z + \frac{X}{L_s} \vec{e}_y)$

where L_s is the shear length and the other parameters have their usual meaning. Integrating the Z-component of Eq. (1), inserting the result in the X component, and normalizing time to Ω^{-1} ($\Omega = \frac{eB_0}{m}$) and length to k^{-1}, we find a system of two equations for the two remaining components

of Eq. (1) in the normalized coordinates x, y and time τ. These two equations are derivable from the following Hamiltonian :

$$h = \frac{p_x^2}{2} + \frac{p_y^2}{2} + \frac{x^2}{2}(1 + \beta u_o) + \frac{\beta^2}{8} x^4 - x p_y - \alpha \sin(y - \nu\tau) \quad (2)$$

where p_x and p_y denote, respectively, the conjugate momenta of the coordinates x and y, the shear parameter is given by $\beta = (k L_s)^{-1}$, the electrostatic perturbation parameter by $\alpha = eE_o k/m\Omega^2$, $\nu = \omega/\Omega$ and $u_o = k v_{zo}/\Omega$ where v_{zo} is a constant of integration representing the Z component velocity at the plane X = 0.

In order to study the long-time evolution of this nonlinear interaction, it is convenient to introduce action-angle variables. To this end, we perform a set of canonical transformations using the appropriate generating functions. Expanding then the periodic terms of our final Hamiltonian in Fourier series we obtain the following equivalent Hamiltonian :

$$H = I_1 + \nu I_2 + a_o(I_1, I_2) + \sum_{p=1}^{4} a_p(I_1, I_2) \cos p\theta_1 - \alpha \sum_{m=-\infty}^{+\infty} J_m(r) \sin(m\theta_1 - \theta_2) \quad (3)$$

where the action-angle variables (I, θ) are related to the previous canonical coordinates by the expressions :

$$I_1 = \frac{p_x^2}{2} + \frac{(x - p_y)^2}{2}, \quad I_2 = -p_y \quad (4)$$

$$\theta_1 = -\text{Arc tg}\frac{p_x}{x - p_y}, \quad \theta_2 = p_x - (y - \nu\tau)$$

and $J_m(r)$ is the Bessel function of order m for the argument $r = (2 I_1)^{1/2}$. Here, we will give the explicit expression only for the coefficient a_o :

$$a_o(I_1, I_2) = \frac{\beta u_o}{2}(I_2^2 + I_1) + \frac{\beta^2}{16}(2 I_2^4 + 12 I_1 I_2^2 + 3 I_1^2) \quad (5)$$

In the case where there is no shear ($\beta = 0$) the coefficients a_o and a_p vanish and the Hamiltonian (3) reduces to the Hamiltonian treated in Ref. /3/. On the other hand, the presence of the shear of the magnetic

field in such a motion introduces not only a new independent parameter (β) but also transmits a coupling between the three components of the velocity of the particle. Therefore the features of the motion will now explicitly depend on three more parameters : β, u_o, and I_{2o} where I_{2o} is the initial value of the action I_2. Physically, this reflects the fact that in our case we will have at the same time and in a nonlinear interaction the coupling of the two different physical effects which have been studied in Refs /3/, /4/ and in Ref. /5/, namely , the stochastic acceleration by an electrostatic wave propagating perpendicularly to a magnetic field /3/, /4/ and the stochastic acceleration by an electrostatic wave propagating at an oblique angle /5/.

In our study, we have considered and varied the values of the physical parameters in the following ranges : the shear parameter β was taken in the range $0{,}008 < \beta < 0{,}03$ (the upper value corresponds in fact to a rather high shear experiment), α was varied from 0,5 to 3, ν was taken a constant equal to 30. 23 as in the case treated in Ref. /3/, u_o was equal to 0, $\pm$ 1, $\pm$ 2, and I_{2o} was in the range $-40 < I_{2o} < +40$.

As can be observed and estimated, the Hamiltonian (3) contains three different types of terms, each being of different order of magnitude. The first two terms $I_1 + \nu I_2$, which are the most important in magnitude for typical values of the energy of the particle, depend linearly on the actions and correspond, therefore, to a two-dimensional linear harmonic oscillator. The "shear terms" $a_o + \sum_{p=1}^{4} a_p \cos p\,\theta_1$ are smaller than the first two terms by one order of magnitude for typical values of β and u_o but they depend nonlinearly on the actions. However, they are nonresonant terms since they depend only on one angle. Finally, the last summation term is smaller by one order of magnitude than the shear terms and represents both nonlinear and resonant terms. Only these last terms, although generally small, can lead to significant effects due to the existence of nonlinear resonances.

The nonlinear interaction of the resonant and non resonant terms causes two basic and opposite types of behavior for the particle trajectories, namelly "adiabatic" and "stochastic" motions depending on whether the resonant perturbation is respectively small or sufficiently large.

First, we consider the conditions for obtaining first order primary islands corresponding to an adiabatic motion for the particle.

In order to find these conditions, we assume that the system is subjected to one single isolated resonance and average the Hamiltonian (3) with respect to the fast variables θ_1 and θ_2 retaining only the dominant contribution due to the resonant term.

From this averaged Hamiltonian, we get for the two associated frequencies of the motion the following expressions :

$$\langle \dot{w}_1 \rangle = \left\langle \frac{d\theta_1}{dt} \right\rangle = 1 + \frac{\beta u_o}{2} + \frac{3\beta^2}{8} (I_1 + 2 I_2^2) - \alpha \frac{J_n'(r)}{r} \sin n\phi \qquad (6)$$

$$\langle \dot{w}_2 \rangle = \left\langle \frac{d\theta_2}{dt} \right\rangle = \nu + \beta u_o I_2 + \frac{\beta^2}{2} (I_2^2 + 3 I_1 I_2) \qquad (7)$$

where ϕ is the slowly varying angle $\phi = \theta_1 - \frac{\theta_2}{n}$ and n is the integer for which a commensurability condition for these two averaged frequencies is fulfilled, i.e.

$$\frac{\langle \dot{w}_1 \rangle}{\langle \dot{w}_2 \rangle} = \frac{1}{n} \qquad (8)$$

Moreover, as a consequence of the averaging process, we have the existence of an additional adiabatic invariant which in our case takes the form :

$$I_2 + \frac{I_\phi}{n} = I_o = \text{const.} \qquad (9)$$

where $I_\phi = I_1$ is the action conjugate to the angle ϕ. By using the expression (9) for the adiabatic invariant we can eliminate the action I_2 and reduce the averaged Hamiltonian to a one-dimensional Hamiltonian in the variables (I_ϕ, ϕ) depending on the additional parameter $I_o = I_{20} + \frac{I_{10}}{n}$.

So, given a set of parameters β, u_o, I_{20}, ν and I_{10}, we can find the integer n for which the condition (8) is fulfilled and give an estimate for the threshold for first-order islands by taking, in Eq. (6), $|\sin n\phi| = 1$. On the other hand, given a set of parameters, β, u_o, I_{20}, ν and n, we can find the value of the action I_ϕ corresponding to the location of the elliptic singular point ($I_\phi = I_{\phi s}$) associated with this "n" isolated primary resonances and estimate the maximum width ΔW of this resonance. This can be done by using an expansion to the first order of the expression for the frequency ω around the value of the action I_ϕ at the elliptic singular point

$$\Delta W = \left(\frac{d\omega}{dI_\phi}\right)_{I_\phi = I_{\phi s}} \cdot 2\,(\Delta I_\phi)_{max} = \left(\frac{\partial^2 \langle H \rangle}{\partial I_\phi^2}\right)_{I_\phi = I_{\phi s}} \cdot 2\,(\Delta I_\phi)_{max} \qquad (10)$$

where the derivative of the frequency with respect to the action has to be evaluated at the singular point ($I_\phi = I_{\phi s}$) and represents what is called the nonlinearity parameter of the oscillator. This nonlinearity parameter γ is given in our case by the following expressions :

$$\gamma = \left(\frac{d\omega}{dI_\phi}\right)_{I_\phi = I_{\phi s}} = \frac{\beta u_o}{n^2} + \frac{3\beta^2}{8}\left(1 + \frac{4}{n^2}\left(I_o - \frac{I_{\phi s}}{n}\right)^2 - \frac{8 I_o}{n} + 12\,\frac{I_{\phi s}}{n^2}\right) \qquad (11)$$

The expression $(\Delta I_\phi)_{max}$ appearing in Eq. (10) corresponds to the maximum of the extension of the action I_ϕ up to the value at the separatrix and is given by :

$$(\Delta I_\phi)_{max} = 2\,(\alpha J_n((2\,I_{\phi s})^{1/2})/\gamma)^{1/2} \qquad (12)$$

where γ is given by Eq. (11).

Next we establish a criterion for the onset of stochasticity. As usual, this criterion is formulated in terms of the overlap of two neighboring resonances, neglecting the secondary effets. Following Chirikov /6/, this is stated by the following expression :

$$s = \frac{\Delta W}{\Delta \omega} > 1 \qquad (13)$$

where ΔW is the maximum width of the nonlinear resonance and is given by Eqs. (10-12), and $\Delta\omega$ is the distance between two nearest neighboring resonances, $\Delta\omega = |\omega_{n+1} - \omega_n|$. The expression for ΔW and $\Delta\omega$ depends in our case on a rather large number of parameters in a fairly complicated way.

Finally, in order to check the validity of the conditions for the onset of primary islands and of the expression (13) for the criterion for the onset of stochasticity, we have solved numerically the exact equations of motion derived from the Hamilltonian (2) for various initial conditions and different values of the relevant parameters.

The observation of the orbits of the particles is conveniently realized in a cut plane, by using the well known cross-section-of-surface method.

It turns out, as a preliminary result, that if the nonlinearity parameter γ which depends both on the value of β and on the order of the primary resonance at which we are looking, is not too small or too large we have a good agreement between the numerical solutions and the theoretical predictions.

Moreover, we find that for a large class of particles the value of the electrostatic perturbation parameter α necessary for communicating an ergodic motion for these particles is reduced when compared with the one found by Karney and Bers /3/ for the case of a uniform magnetic field. This result seems to support the contention that the nonlinear interaction between resonant and nonresonant nonlinear terms in Hamiltonian systems favors the ergodicity of the motion. Thus the effect of magnetic shear is to lower the threshold for the onset of stochasticity and the possibility of subsequent ion tail formation.

The complexity of the problem prohibits the exact determination of this threshold. Thus only qualitative results are given here. This process could be investigated experimentally by varying the shear and observing the effects, if any, on ion tail formation during lower hybrid heating.

REFERENCES

/1/ - R.L. BERGER, LIU CHEN, P.K. KAW and F.W. PERKINS, Phys. Fluids, 20 11, (1977).

/2/ - M. PORKOLAB, Nucl. Fusion, 18, 3, (1978), p. 367.

/3/ - C.F.F. KARNEY and A. BERS, Phys. Rev. Lett., 39, 9, (1977).

/4/ - A. FUKUYAMA, H. MOMOTA, R. ITATANI and T. TAKIZUKA, Phys. Rev. Lett., 38, 701, (1977).

/5/ - G.R. SMITH and A.N. KAUFMAN, Phys. Rev. Lett., 34, 1613 (1975).

/6/ - B.V. CHIRIKOV, Research concerning the Theory of Nonlinear Resonances and Stochasticity, NOVOSIBIRSK (1969), C.E.R.N. Translation (1971).

DISCUSSION

ON PAPERS G-1 (A) AND G-1 (B)

G. LISITANO: My first comment is that lower hybrid heating at large RF levels has not yet been proved. One can in fact change the RF power frequency consistently without changing the absorption of RF power.

M. BRAMBILLA: On the basis of what I hear from the experimental teams I can only disagree with your comment. However, as this comment far exceeds the scope of the papers I have presented, I suggest you discuss it directly with the people involved in the experiments.

G. LISITANO: Near the plasma boundary the high-power near-field of the radiating antenna may produce strong RF turbulence effects, thus obscuring far-field interaction effects. Would you agree with that?

M. BRAMBILLA: Within the linear theory, the presence of strong fields near the antenna obviously has no influence whatever on penetration further inside the plasma. However, it is true that non-linearities and turbulence associated with the near fields can be a real nuisance, and I have tried to suggest some way (rounding the guide edges, controlling the density profile, and so on) of reducing these problems to some extent.

A. PATARAYA: You showed waves of two types – structured and unstructured. What is the reason for this? Normally these different types of waves appear only when non-linear effects are taken into account (mobile and immobile solitons).

M. BRAMBILLA: The 'wave packet' near the plasma surface contains a very broad spectrum of parallel wave numbers, in particular with $k_{\parallel}^2 c^2/\omega^2 \gg 1$. This is why it is 'structured', as you say, showing details of the antenna structure. Inside the plasma, waves with $n_{\parallel} \gtrsim 5/\sqrt{T_e}$ have been absorbed by electron Landau damping, and we find a 'narrow' packet with $n_{\parallel}$ roughly corresponding to the antenna periodicity. Such a packet is clearly structureless. No non-linear effects were included here.

C.M. SURKO: Relatively large density fluctuations have been observed at the edges of tokamak plasmas. Have you considered the effect of these flucuations on the propagation of lower hybrid waves?

M. BRAMBILLA: Interesting work has been done recently by Bellan and co-workers on this important subject (they have dealt with both theory and experimental evidence). In my work, however, these effects are not included.

OHMIC PUMPING BY MEANS OF EXTERNALLY DRIVEN TEARING MODES

M. BONNEDAL*, E. CANOBBIO
Association Euratom-CEA,
Département de physique du plasma
et de la fusion contrôlée,
Service IGn, Centre d'études nucléaires,
Grenoble, France

Abstract

OHMIC PUMPING BY MEANS OF EXTERNALLY DRIVEN TEARING MODES.

Tearing modes excited by RF currents flowing in external conductors are shown to be potentially capable of producing intense Ohmic heating near the resonant MHD singular surfaces $q(r) = -m/n$ where $q = rB_\phi/RB_\theta$ is the safety factor and the integers m and n are the poloidal and the toroidal mode numbers of the RF field. The frequencies which can be used to produce substantial additional heating are typically as low as $\lesssim$10 kHz, which allows the RF coils to be protected by stainless steel or even to be put outside the vacuum chamber. The most favourable situation is found to occur when the $q = \pm 1$ surface is present, at least marginally, in the central region of a globally stable toroidal plasma. In this case a $|m| = |n| = 1$ coil system excites the internal resistive kink mode which leaves the outer plasma layers essentially unperturbed provided that q at the plasma boundary be high enough not to couple with external helical modes through toroidal curvature and non-linear harmonics.

1. THE HEATING SCHEME

The highest plasma heating efficiency obtainable with electromagnetic fields is expected when a wave-resonance surface exists within the plasma, Below the ion gyrofrequency $\omega \ll \omega_{ci}$, such a surface is essentially the $\omega = \vec{K} \cdot \vec{v}_A$ surface, although strictly not a resonance in the cold plasma model, where $\vec{v}_A = \vec{B}_0/(4\pi\rho_0)^{1/2}$ is the Alfvén velocity vector and $\vec{K} = (0, m/r, n/R)$ is the wave vector projection on the equilibrium magnetic surfaces. In the limit $\omega \ll |\vec{K}| \cdot |\vec{v}_A|$, the above surfaces approach one of the $\vec{K} \cdot \vec{B}_0 = 0$ surfaces characteristic of MHD stability theory.

---

* Permanent address: Institute for Electromagnetic Field Theory and Euratom-Fusion Research (EUR-NE), Chalmers University of Technology, Göteborg, Sweden.

In this paper we consider this low-frequency limit of the Alfvén wave heating in more detail than was done previously [1]. The potential advantages of the present heating scheme are twofold:

(1) The frequency used is so low that the RF structures can be protected by stainless steel and actually become indistinguishable from the electrotechnical structures already present to ensure stable confinement (by feedback).

(2) The physics involved is basically the same as that of plasma confinement (equilibrium, stability and diffusion): in particular, the magnetic moment μ remains constant (apart from collisions) and the electron inertia can be neglected almost everywhere.

It is also worth mentioning that the present case is considerably simpler than the conventional Alfvén-wave heating scheme [2]. There, for a given pair of m and n values there are two distinct resonant layers, whose radii depend upon the density profile. The field divergence at these layers is weaker than in our case where the two singularities coalesce. The linear conversion of cold to warm plasma modes propagating radially [3] is inhibited by collisions at much lower frequencies.

Wave propagation and power deposition are studied in the usual tearing-mode stability scheme where the resonant singular surface is embedded in a thin resistive layer which separates two perfectly conducting plasma regions. We use the tokamak ordering and replace the torus with a straight circular cylinder of length $L = 2\pi R$. The resistive layer, whose radius is r_s and thickness δ, has as a distinguishing feature a large component of the RF electric field parallel to the static $\vec{B}$-field. The RF power dissipated into this layer is essentially

$$P_{rf} \simeq 4\pi^2 R\, r_s\, \delta \cdot E_{//} j_{//} \tag{1}$$

where $j_\parallel$, the electric current density, is mainly due to the electrons. The current flowing in the resistive layer is essentially a surface current $\vec{j}_s^{\,*} \cong j_\parallel \delta \vec{B}_0 / B_0$ which is completely determined by $\langle \vec{Q}_t \rangle_s$, the jump of the tangent components of the RF $\vec{B}$-field in the ideal MHD regions, across the layer. As shown later, the function $E_\parallel \equiv \eta_{rf} j_\parallel$ is determined by using the parallel momentum balance law for the electrons supplemented by the charge neutrality condition; $\eta_{rf} = \eta_{rf}(\omega, \nu_{coll}, \omega^*, \ldots)$ is the plasma resistivity in the presence of the RF field. It depends in general upon frequency, collision and drift frequencies, and can be larger than η_0, the DC resistivity. Then P_{rf} can be expressed in terms of the DC Ohmic power P_{oh} – which is deposited in the whole plasma volume by an essentially uniform $j_{o\phi}$ current density – as follows:

$$P_{rf} \simeq P_{oh}\, (\eta_{rf}/\eta_0) \cdot (r_s/2\delta) \cdot |\langle \vec{Q}_t \rangle_s / B_{\theta a}|^2 \tag{2}$$

where $B_{\theta a}$ is the poloidal $\vec{B}$-component at the edge of the toroidal current channel. Notice that the second of the three factors which form (P_{rf}/P_{oh}) greatly exceeds unity, while the last one has to be sufficiently smaller than unity, at least in a linear treatment.

To see whether P_{rf} can be made larger than P_{oh}, we must first calculate $\langle \vec{Q}_t \rangle$ (next section) and δ (Section 3) in terms of the characteristics of the external RF pump. This will be carried out in some detail as these considerations, which are conventional in stability theory, are not customary in the heating literature.

2. SOLUTIONS OUTSIDE THE $\vec{K} \cdot \vec{B}_0 = 0$ LAYER

We consider elementary solutions of the form $\vec{A} = \vec{A}(r) \exp i(m\theta + Kz - \omega t)$ with $K = n/R$ and $|Kr/m| \ll 1$ (the tokamak approximation) and express the e.m. field in the plasma in terms of $\xi \equiv \xi_r$, the radial MHD displacement. We find for the RF magnetic field

$$
\begin{aligned}
Q_r &= i\, F\, \xi \\
Q_\phi &= -\frac{1}{m}(F\, r\, \xi)' + \frac{K^2 r^2}{m^2}\{2\,\frac{k}{m}\,B_z \xi - \frac{F}{m}(\xi - r\,\xi')\} \\
Q_z &= \frac{Kr}{m}\frac{F}{m}(\xi - r\,\xi') - 2\,\frac{K^2 r}{m^2}\,B_z\,\xi
\end{aligned}
\tag{3}
$$

where $F = \vec{K} \cdot \vec{B}_0$; accents mark derivation with respect to r.

We suppose the $|q| = 1$ surface to be present in the plasma (some on-axis MHD activity is allowed) and we limit our analysis to the mode numbers $m = -1$, $n = 1$, corresponding to the so-called internal kink mode. Higher m values are less attractive: the field is more of a surface mode, RF coils have to be closer to the plasma or carry more current for the same power at the same location. For the $m = -n = -1$ mode, neglecting terms of order β and $\omega / |\vec{K}|\,|\vec{v}_A|$ compared to unity, ξ obeys the Euler equation [4]:

$$
(r^3 F^2\, \xi')' - g\, \xi = 0 \tag{4}
$$

with $F = K B_0 \{1 - q^{-1}\}$ and $g \cong K^2 r^3 F(3KB_z + B_\theta / r)$.

The solution of Eq.(4) is expanded in $(Kr)^2$: $\xi = \xi_0 + \xi_1 + \ldots$. ξ_0 is taken to be a constant:

$$
\begin{aligned}
\xi_0 &= \xi < \quad 0 < r < r_s \\
&= \xi > \quad r_s < r < r_a
\end{aligned}
\tag{5}
$$

The first-order solution ξ_1 is made to join the two constant solutions smoothly on each side of the $r = r_s$ surface ($r^3F^2\xi'$ is continuous across $r = r_s$):

$$r^3F^2\,\xi_1' = \xi_< \int_0^r drg \qquad 0 < r < r_s$$
$$= \xi_< \int_0^{r_s} drg + \xi_> \int_{r_s}^r drg \qquad r_s < r < r_a \tag{6}$$

The surface current at $r = r_s$ is then essentially

$$\frac{4\pi}{C} j^*_{sz} = \langle Q_\theta \rangle_s \simeq F' r_s\,(\xi_> - \xi_<) \tag{7}$$

In the vacuum ($r > r_a$) we have $\vec{Q} = \text{grad}\,\phi$, $\phi = \text{const}/r$. Therefore,

$$Q_r = i\,F_a\,\xi_>\,(r_a/r)^2$$
$$Q_\theta = -\,F_a\,\xi_>\,(r_a/r)^2 \tag{8}$$
$$Q_z = F_a\,\xi_>\,Kr_a\,(r_a/r)$$

where the constant has been determined by the continuity of Q_r.

The surface current at $r = r_a$, the externally driven pump, is given by

$$\frac{4\pi}{c} j^*_{az} = \langle Q_\theta \rangle_{r_a} = -\,F_a\,\xi_> - F_a r_a \xi' - (F_a' r_a + F_a)\xi_>$$
$$\frac{4\pi}{c} j^*_{a\theta} = -\langle Q_z \rangle_{r_a} = -\,Kr_a F_a \xi_> - 2K^2 r_a\,B_z\,\xi_> \tag{9}$$
$$+\,Kr_a F_a\,(\xi_> - r_a\xi')$$

where $F_a = F(r = r_a)$. With $J^*_{\alpha\theta} = Kr_a j^*_{az}$ we find

$$\xi_> = 0\,(r_a/R)^4 \to 0$$
$$\xi_< \simeq \frac{4\pi}{c}\,j^*_{az}\;\; r_a^2 F_a/g_1 \tag{10}$$

where

$$g_1 = \int_0^{r_s} drg \simeq - \frac{B_o^2 r_s^5 q_s'}{5R^4}$$

Thus we find, finally

$$j_{sz}^* = + j_{az}^* \; 5\left(1 + \frac{1}{q_a}\right) r_a^2 R^2 / r_s^4 \tag{11}$$

and

$$P_{rf}/P_{oh} \simeq (\eta_{rf}/\eta_{oh}) \; |\langle Q_\theta \rangle / B_\theta|_{r_a}^2 \; \frac{r_s}{2\delta} \left\{5 \frac{(q_a+1)}{q_a} \frac{r_a^2 R^2}{r_s^4}\right\}^2 \tag{12}$$

An equivalent form is

$$P_{rf}/P_{oh} \simeq (\eta_{rf}/\eta_{oh}) \; \frac{r_s}{2\delta} \left\{q_s' \; r_s \; q_a \; \frac{\xi_<}{r_a}\right\}^2 \tag{13}$$

It may also be of interest to introduce the width W of the RF magnetic island which develops inside the $q = +1$ surface. Within the linear theory

$$W \simeq 4 \; Q_r' R / B_o \; q_s' = 2 \; \xi_< \tag{14}$$

For $|m| > 1$ the islands have $W_m \propto Q_r'^{1/2}$ and encompass the corresponding singular surface.

3. THE TEARING LAYER EQUATIONS

It remains to relate δ, the width of the tearing layer, to the applied frequency ω and the other plasma parameters. Only a semiquantitative derivation is reported here, which should be sufficiently accurate for the purpose of estimating the heating rate in view of the various uncertainties inherent in the model (non-linearity, toroidicity, instability and diffusion effects have been neglected). We assume that within the layer

$$\left|\frac{A}{\rho_i^2}\right| > \left|\frac{d^2A}{dr^2}\right| >> \left|\frac{A}{r_s^2}\right| \tag{15}$$

(where ρ_i is the ion Larmor radius and A stands for the perturbed quantity) and, moreover, that

$$\nu_{ei},\ \omega \gtrsim (K_{//} v_{te})^2/\nu_{ei} \gg K_{//} v_{ti} \tag{16}$$

where $v_{t\alpha} = (2T_\alpha/m_\alpha)^{1/2}$.

Then we obtain [4] the following equations for ξ and $\phi \equiv -iq\, Q_r/q' B_\theta$:

$$(\omega\tau_A)^2 (1 - \omega_i^*/\omega) \frac{d^2\xi}{dx^2} = x\, d^2\psi/dx^2 \tag{17}$$

$$\psi = - x\, \xi + \frac{\varepsilon}{\omega\tau_A} \frac{d^2\psi}{dx^2} \tag{18}$$

where

$$x = (r - r_s)/r_s \ ;$$

$$\tau_A = - 1/v_{A\theta} q'_s \ ;$$

$$\tau_R = 4\pi r_s^2/c^2 \eta_{rf} \ ; \ \varepsilon = \tau_A/\tau_R \ll 1$$

$$\omega_\alpha^* = - c\, T_\alpha\, (d\ln n/dr)/r\, e_\alpha B_o$$

and, under conditions (16),

$$\eta_{rf} \simeq \eta_L\, (\omega + i\, \nu_{ei})/(\omega - \omega_e^*)$$

Here η_L is the classical conductivity of a Lorentz gas. Notice that η_{rf} can substantially exceed η_L only if $\omega \cong \omega_e^*$.

The 'dispersion relation' $\delta = \delta(\omega)$ is obtained by differentiating Eq.(18) twice with respect to x, multiplying the result by x, then using Eq.(17) and making

$$\frac{\partial}{\partial x} \simeq \frac{1}{x} \simeq \frac{r_s}{\delta}$$

$$\left(\frac{\delta}{r_s}\right)^4 + \left(\frac{\delta}{r_s}\right)^2 (\omega\tau_A)^2\, (1 - \omega_i^*/\omega) - \varepsilon(\omega\tau_A)\, (1 - \omega_i^*/\omega) = 0 \tag{19}$$

Since we are interested in using very low frequencies, we assume

$$(\omega\tau_A)^3 \ll |4\, \tau_A/\tau_R (1 - \omega_i^*/\omega)|$$

and find from Eq.(19)

$$\left(\frac{\delta}{r_s}\right) \simeq \left|\omega\, \tau_A^2\, (1 - \omega_i^*/\omega)/\tau_R\right|^{1/4} \qquad (20)$$

It is interesting to notice, by writing $K_\parallel \cong K'_\parallel \delta$, that

$$(K_{/\!/} v_{te})^2 \,/\nu_{ei}\omega \simeq (\rho_i/\rho)^2 < 1 \qquad (21)$$

in agreement with assumption (16).

Equations (19–20) show that δ decreases when ω decreases and, formally, $\delta \to 0$ when $\omega \to \omega_i^*$. With physically meaningful parameters $r_s/2\delta < 10^2$, which still allows for $P_{rf} \gg P_{oh}$ from Eqs (12–13). Such a conclusion, however, may well turn out to be much too optimistic, in view of the highly idealized model considered here. Finally, the question whether substantial additional heating by tearing-mode pumping can indeed be produced in practice can be answered seriously only by making experiments.

REFERENCES

[1] CANOBBIO, E., Proc. 3rd Topical Conf. on RF Plasma Heating, CALTEC, 1978, Paper F6–1.
[2] TROYON, F., in Heating in Toroidal Plasmas (Proc. Joint Varenna-Grenoble Int. Symp. Grenoble, 1978), Vol.2.
[3] HASEGAWA, A., CHEN, L., Phys. Rev. Lett. 35 (1975) 370.
[4] COPPI, B., et al., Sov. J. Plasma Phys. 2 (1976) 533.

DISCUSSION

A. HASEGAWA: It seems to me that if the finite-Larmor-radius effect were included you would be able to have collisionless heating due to electron Landau damping (ELD). Also, ω should be chosen higher than the drift wave frequency.

E. CANOBBIO: The frequency is taken to be lower than the electron collision frequency; thus ELD is excluded.

B. COPPI: I am surprised that only ω_{*i} enters into the expression for your resistive layer.

E. CANOBBIO: ω_{*e} is contained in the expression for η_{RF}. Reference to your work on this particular point is made in the text.

G. LISITANO: You have associated the bulk properties of the plasma with an internal m = 1 kink mode, but I think this may not reflect the true situation in tokamak plasmas. In other words, it may be that the tokamak kink modes are due to runaway or superthermal effects.

E. CANOBBIO: The modes we consider are excited externally. They are supposed to be stable. The heating they produce should be rather insensitive to the deviations of the plasma from its local thermal equilibrium.

H. DE KLUIVER: Would you not expect heating of the plasma to occur first at the outer resonant surfaces, since the extra pulse has to penetrate the plasma from the surface and would first make a skin there?

E. CANOBBIO: The helicity of the external RF coils is supposed to be such that no MHD resonance is encountered near the plasma boundary. Surface heating, therefore, should not be the dominant effect.

Session Q

PLASMA HEATING II

Chairman

E.S. WEIBEL
Switzerland

TRANSIT TIME MAGNETIC PUMPING IN THE PETULA TOKAMAK

R. BARDET, M. BERNARD, G. BRIFFOD, M. CLEMENT,
A. GAUTHIER, M. GREGOIRE, P. GRELOT, G. HASTE*,
F. PARLANGE, D. PINET, E. PORROT, G. REY,
B. TAQUET, J. WEISSE
Association Euratom-CEA,
Département de physique du plasma
et de la fusion contrôlée,
Service IGn, Centre d'études nucléaires,
Grenoble, France

Abstract

TRANSIT TIME MAGNETIC PUMPING IN THE PETULA TOKAMAK.

TTMP heating was successfully tested on the Petula tokamak. A substantial temperature increase could be measured. The absorbed power was thermalized, and no deleterious effects were observed during heating. The analysis of the experimental results shows good quantitative agreement with theory and the existence of the so-called non-linear regime. Starting from these considerations it is possible, by extrapolating the results, to propose TTMP heating for future machines.

1 - INTRODUCTION.

The aim of the Petula machine is to study R.F. heating at low frequency ($\omega << \omega_{ci}$) by Transit Time Magnetic Pumping. Due to technological convenience the compressional T.T.M.P. mode has been chosen. Heating experiments were performed in various plasma conditions (gas, density, magnetic field), and substantial temperature increase was observed without any pumpout or significant impurity release. The interpretation of the experimental results leads to a quantitative agreement with theory, the so-called "non-linear" regime being, however, more severe than initially predicted.

The main experimental results and the ion energy balance are reported here as well as examples of application of T.T.M.P. heating for future machines.

---

* Oak Ridge National Laboratory, Tennessee, USA.

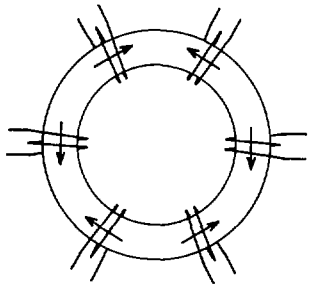


FIG.1. Oscillating magnetic-field configuration.

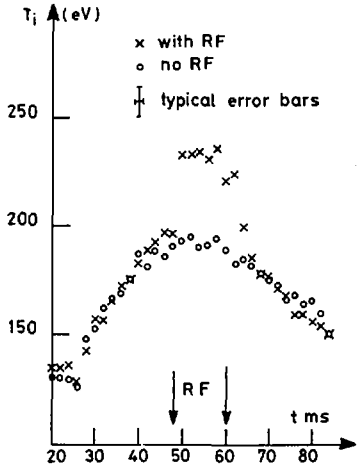


FIG.2. Typical ion temperature increase during TTMP heating.

2 - DESCRIPTION OF THE APPARATUS

The Petula Tokamak has been previously described /1/. The main parameters are the following : large radius R = 72 cm, limiter radius a = 14 cm, maximum toroidal field on the axis $R_{\emptyset}$ = 30 kG. The T.T.M.P. oscillating toroidal magnetic field is produced by a set of six R.F. coils which are connected in such a way as to produce a standing wave with three wavelengths along the toroidal direction (Fig. 1). This configuration is equivalent to two oppositely travelling waves. The frequency is chosen so that the phase velocity of the travelling waves is in the range of the ion thermal velocity. In order to avoid problems related to plasma - R.F. coil interaction the latter are located between the copper shell and the

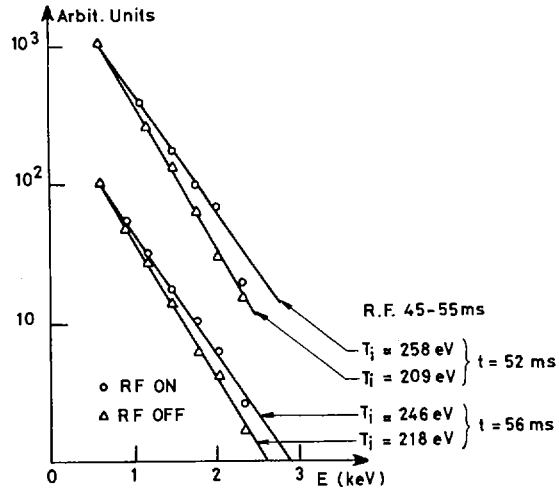


FIG.3. Typical ion energy distribution function with and without RF heating.

vacuum chamber which is made of six alumina sectors joined to the diagnostic sections : Each R.F. coil is connected to tuning capacitors so that the resonant frequency f can be varied from 90 to a few hundred kilohertz. This coupling structure is energized by a generator which can deliver 10 MW - 15 ms R.F. pulses in the above-mentioned frequency range. In these conditions the maximum oscillating magnetic field $\tilde{B}$ is given by the formula $\tilde{B} \simeq 5.10^4 f^{-1}$ (Gauss/kHz).

For the heating studies reported here, the Tokamak was operated at 13-16 kG toroidal field in hydrogen or deuterium using a gas puffing technique /2/.

3 - CHARACTERISTICS OF HEATING

Typical heating phenomenology has been described /3/. The most interesting features are the following :

- A substantial ion temperature increase is measured (Fig. 2), it shows the mean value of T_i from charge-exchange neutrals analysis for a number of shots with and without R.F.
- The energy distribution of fast charge-exchange neutrals escaping in the radial direction is true Maxwellian from .6 to 2.5 keV with no non-thermal tail observed up to 5 keV (Fig. 3). One can thus conclude that the

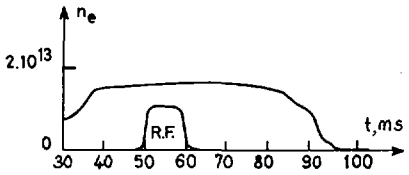


FIG.4. Electron density evolution.

energy which is given by T.T.M.P. heating in the toroidal direction is distributed and thermalized.

- The electron density does not increase appreciably during heating as is shown on Fig. 4 in which the signal of the interferometer which is perturbed during R.F. has been restored, the time derivatives of $\bar{n}$ just before and after heating being conserved.

- During R.F. pulse no significant change is observed on plasma current, loop voltage, H_β line emission and the amplitudes of CIV, OVI and OVII lines do not increase more than 10 to 15 percent so that the measured ion temperature increase can be attributed to R.F. heating effects.

4 - SUMMARY OF HEATING RESULTS

The following parameters have been varied during the experimental campaign :

- The main toroidal field : B_ϕ = 13 and 16 kG.
- The working gas : H_2 or D_2.
- The T.T.M.P. frequency : 150 and 200 kHz.
- The amplitude of the oscillating magnetic field corresponding to a modulation ratio $\frac{\tilde{B}}{B_\phi}$ for the fundamental (3 wavelengths along the torus) which ranges from $.9 \times 10^{-2}$ to 1.8×10^{-2}.
- The plasma density n_{eo} = 1.2 to $4.2 \times 10^{13} cm^{-3}$.
- The ion temperature T_{io} = 130 to 220 eV.
- Z effective from 1.5 to 4.5.

In this parameter range the R.F. power which is absorbed by the ions is always much lower than the ohmic power so that the electron temperature is constant : the ions only are significantly heated. In this situation a characteristic parameter is the ratio $y = P_{TTMP}/P_{EI}$ where P_{TTMP} and

P_{EI} are the power density given to the ions, respectively, by T.T.M.P. and collisions with electrons.

As $T_e/T_i \simeq 3$, P_{EI} is proportional to $n_e^2\, T_i^{-1/2}\, Z^* A^{-1}$, where A is the atomic mass number and Z^* a quantity which depends slightly on the impurity content.

P_{TTMP} can be written as /4/ :

$$P_{TTMP} = P_{LIN}\ \frac{1}{1 + n_c/n_i} \sim n_i T_i^{3/2}\ \frac{b^2 C}{A^{1/2} R_o}\ \frac{1}{1+n_c/n_i}$$

where :

- P_{LIN} is the expression for T.T.M.P. absorption in the linear regime and the term $\frac{1}{1 + n_c/n_i}$ represents the contribution of the so-called non-linear regime where n_c is the critical density below which the ion-ion collisions are not sufficient to ensure a Maxwellian distribution of ions :

$$n_c \sim \frac{T_i^2\, b^{3/2}\, C\, n_i}{R_o\, \log\Lambda\, Q\, n_e Z_{eff}}$$

- b is the modulation ratio $\tilde{B}/B_\phi \sim \frac{\tilde{V}}{B_\phi f}$, being $\tilde{V}$ the RF voltage on the coil.
- R_o is the large radius of the torus.
- C and Q are coefficients which depend on T_e/T_i and the quantity $x_i = \omega/KV_{thi}$, the ratio of the phase velocity of the wave to the thermal velocity of ions.

The parameter y is finally expressed as :

$$y \sim \frac{\tilde{V}^2}{B_\phi^2 f^2}\ \frac{n_i}{n_e^2}\ A^{1/2}\, T_i^2\, C\, \frac{1}{1 + \frac{n_c}{n_i}}$$

The ion temperature increase can then be evaluated from the energy balance equation in which are only considered the thermal losses in the neoclassical plateau-regime P_{NC}:

$$\frac{3}{2}\, n\, \frac{dT_i}{dt} = P_{TTMP} + P_{EI} - P_{NC}$$

Using the above-mentioned temperature dependence for P_{EI} and P_{TTMP} and the $T_i^{5/2}$ dependence for P_{NC}, the asymptotic value for $Z = T_i/T_{io} = 1 + \frac{\Delta T}{T_{io}}$ is given by the equation

TABLE I. EXPERIMENTAL DATA FOR VARIOUS WORKING CONDITIONS

Reference Number	Gas	B_ϕ(T)	$\bar{n}(10^{13})$	$\hat{n}_e(10^{13})$	$\hat{T}_{eo}$(eV)	$\hat{T}_{io}$(eV)	Z_{eff}	f_{TTMP}(khz)	b%	$\hat{\Delta T}_i$(eV)
(1)	D_2	1.6	1.8	2.8	720	175	3.5	150	1.5	61
(2)	D_2	1.6	2.	3.1	770	200	4.3	150	0.9 1.4	25 55
(3)	H_2	1.6	2.1	3.8	570	195	1.5-2	150	1.5	23
(4)	H_2	1.3	1.8	2.9	560	185	1.8	150	1.1 1.3 1.5	15 26 40
(5)	H_2	1.3	1.7	2.8	560	170	2.1	150	1.8	50
(6)	H_2	1.3	1.6	2.6	530	170	1.6	200	1.2	25

Here $\wedge$ and o refer to peak value and time before heating, respectively. The plasma current was in the range of 50-55 kA for all the above cases.

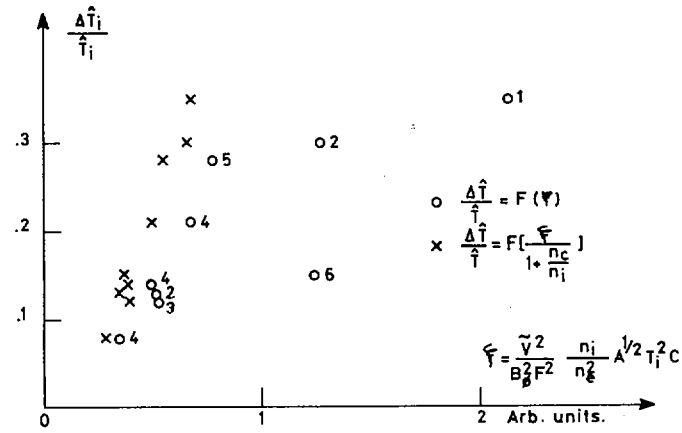


FIG. 5. Relative ion temperature increase versus experimental parameters. Numbers refer to Table II.

$$1 + \left[(1+\alpha)\, y + \alpha\right] z^2 - z^3 - \alpha z^5 = 0$$

where $\alpha = n_c/n_i$, $y = P_{TTMP}/P_{EI}$ at the beginning of heating.
For small values of α and y this equation reduces to $\Delta T/T_{io} \sim P_{TTMP}/3\, P_{EI}$.
This is also a good approximation even for y up to 1 when $0.4 < \alpha < 0.8$.

The experimental data corresponding to the various working conditions considered in this report are summarized in Table I.

The measured $\Delta T/T_{io}$ values are plotted in Fig. 5 versus the two quantities :

$$\xi = \frac{\tilde{V}_2}{B_\phi^2 f^2} \frac{n_i}{n_e^2} A^{1/2} T_{io}^2 C \sim \frac{P_{LIN}}{P_{EI}} \quad \text{and}$$

$$\xi' = \xi \frac{1}{1 + n_c/n_i} \text{ proportional to y, which takes into account}$$

non-linear effects. All quantities are evaluated on plasma axis.

From this graph, it can be concluded that $\Delta T_i/T_{io}$ has the above predicted linear dependence on y provided that the non-linear T.T.M.P. regime is included.

Since the coefficient D and consequently n_c are increasing functions of x_i, it must be remarked that the effect on the non-linear regime is essential when $x_i \gtrsim 1.6$.

5 - QUANTITATIVE INTERPRETATION

The temperature increase expected from T.T.M.P. heating can be calculated with more accuracy using a one-dimension numerical code /5/, which performs the computation of the ion temperature profile by solving the energy balance equation for the ions : $P_{EI} = P_{TTMP} + P_{TC} + P_{CX} + P_D$. P_{CX} is the charge-exchange loss term, P_D the convection one and P_{TC} represents the losses by neoclassical thermal conduction. The T.T.M.P. term is written as $P_{TTMP} = P_{LIN} \left(\frac{1}{1 + (n_c/n_i)N}\right)^{1/N}$. The calculations below have been made with N = 1.2. The coefficient Q which is essential in the evaluation of the non-linear regime is, however, calculated for $T_e/T_i = 0$. This deviation from the original formulation of Ref. /4/ is due to a new self-consistent evaluation of the electrostatic electric field component which ensures plasma charge neutrality /6/. This evaluation makes more severe the limitation of the efficiency of T.T.M.P. heating due to non-linear effects. Two expressions are considered here for the coefficient C which characterizes the linear regime ; they correspond to the two following definitions of the absorbed power :

$$P = \frac{d}{dt}\int d^3\vec{w}\ (\tfrac{1}{2}\, mw^2) f_1 \quad \text{and} \quad P = \frac{d}{dt}\int d^3\vec{w}\ \tfrac{1}{2}\, m\ (\vec{w} - \vec{v}_1)^2 f_1$$

where $\vec{w}$ is the velocity of the guiding center, f_1 and $\vec{v}_1$, respectively, the distribution function and the fluid velocity in the first order.

These two definitions can be interpreted as upper and lower limits of the absorbed power and will lead to corresponding upper and lower bounds of the computed ion temperature profile /7/.

The electron density and temperature radial dependence are taken from experimental data and supposed to be invariant. The computation is first fitted with the measured quantities $\langle Z_{eff} \rangle$ and T_i at the plasma center before RF heating is started.

This computation method was applied to the various experimental conditions and the results for the central ion temperature are plotted in Fig. 6 together with the measured values. It yields satisfactory quantitative agreement which allows us to be confident in the formulas used for T.T.M.P. absorption. The power-density, integrated power for P_{EI} and P_{TTMP} as well as the ratio $\frac{n_c}{n_i}$ and the computed ΔT_i are summarized in Table II.

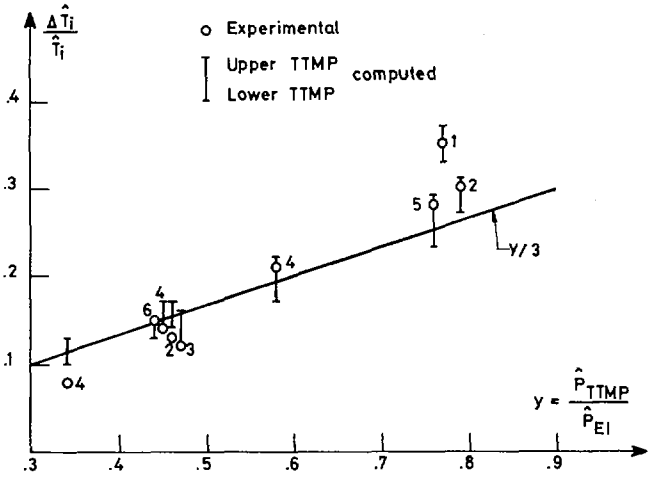


FIG.6. Computed relative ion temperature increase. Comparison with experiment. Numbers refer to Table II.

The point quoted 1 in Fig. 6 is situated well above the $\frac{1}{3}$ y curve : this can be explained by the fact that in this series of shots the thermal losses at the plasma center are less than one half of the total losses, due to an important amount of neutral gas and subsequent charge-exchange losses.

6 - APPLICATIONS TO FUTURE MACHINES

In these applications we assume that the R.F. coils are located inside the vacuum chamber of the machine. The T.T.M.P. field is produced by 12 coils, the position of which around the torus isadjusted in order to minimize the level of spatial harmonics. The number of wavelengths is chosen to be one in order to reduce the working frequency and consequently the R.F. voltage at the coil as well as the R.F. power required to produce the oscillating magnetic field $\tilde{B}$. The RF power in such a structure writes:

$$P_{RF} = F(k^2)\ \tilde{B}^2\ \ a^2\ \omega^{1/2}$$

where a is the R.F. coil radius and $F(k^2)$ the coupling coefficient which depends on the shape of the coil and its distance from the metallic vacuum chamber. In the R.F. power estimations which follow, the coupling coefficient is extrapolated from the measurements mode on a small-size model experiment of the PETULA dimension and corresponds to an upper limit.

TABLE II. CALCULATED VALUES OF ION TEMPERATURE INCREASE AND TTMP ABSORBED POWER

Reference Number	f_{KHz}	x_i	b%	$\frac{\hat{\Delta T}_i}{T_i}$ Meas.	$\frac{\hat{\Delta T}_i}{T_i}$ Calc.	n_c/n_i	$\hat{P}_{TTMP}(Wcm^{-3})$	P_{EI}(kW)	P_{TTMP}(kW)	$y = \frac{\hat{P}_{TTMP}}{P_{EI}}$
(1)	150	1.73	1.5	0.35	0.33-0.37	2.15	0.10	8.6	4.2	0.77
(2)	150	1.59	1.4 0.9	0.30 0.13	0.27-0.31 0.14-0.17	0.92 0.48	0.12 0.065	11.2 11.2	6.5 3.8	0.79 0.43
(3)	150	1.13	1.5	0.12	0.12-0.16	0.32	0.19	10.1	10.3	0.47
(4)	150	1.17	1.1 1.3 1.5	0.08 0.14 0.21	0.10-0.13 0.14-0.17 0.17-0.22	0.22 0.29 0.36	0.084 0.11 0.15	9.0 9.0 9.0	5.4 7.2 9.0	0.34 0.45 0.58
(5)	150	1.19	1.8	0.28	0.23-0.29	0.43	0.18	9.3	10.7	0.76
(6)	200	1.64	1.2	0.15	0.13-0.15	2.33	0.10	8.7	3.3	0.44

The calculated values for T.T.M.P. quantities correspond to the "optimistic" case except for $\hat{\Delta T}_i/T_i$ where both values are listed. $\hat{}$ refers to peak value.

Consider first the case of J.E.T. In this application the ratio between the R.F. coil and the vacuum chamber diameters is taken 0.75, which corresponds to a reasonable compromise between the dissipated power and the lowering of the plasma radius. The plasma radius is thus taken equal to 1 meter. The plasma parameters are those obtained with a control beam and described in Ref. /8/. The gas is hydrogen, the density $5.10^{13} cm^{-3}$ and ion temperature 1.8 keV. In this case, with a 60-MW R.F. generator which produces a modulation b = 0.7 %, at 30kHz, the absorbed power density on axis and the integrated power are, respectively, 0.16 $W \cdot cm^{-3}$ and 6.5 MW. These values are comparable to those considered in the above reference /8/ to increase the ion temperature up to 5 keV by fast-neutral injection. With a $10^{14} cm^{-3}$ electron density and the same (60-MW) R.F. generator, the total absorbed power and power density on axis are listed below for two values of T_i :

T_i kW	f_{kHz}	b %	P^o_{TTMP} W/cm^3	P^t_{TTMP} MW
6	57	0.58	0.59	23
8	66	0.56	0.55	22

For these conditions the balance between the total losses and T.T.M.P. power requires an energy replacement time of 0.48 S and 0.69 S, respectively.

The fact that the absorbed R.F. power increases with density at constant R.F. power generator makes possible to get high power absorption in the case of Ignitor-type experiment. For the following parameters: B_ϕ = 120 kG, R = 71 cm, r_p = 18 cm, and a 20-MW R.F. generator, the power absorbed on axis is :

n	T_i	f	b	P^o_{TTMP}	
6.10^{14}	1.5 keV	122 kHz	2.9×10^{-3}	1.83	W/cm^3
"	3 keV	172 kHz	2.7×10^{-3}	3.75	W/cm^3

7 - CONCLUSION

In conclusion one can point out that T.T.M.P. seems to be a satisfactorily understood R.F. heating method. The plasma stability was not altered in the PETULA Tokamak in which the applied modulation ratios are larger than those which will be necessary to heat larger machines.

T.T.M.P. offers the following advantages :

- Heating takes place in a large volume, preferentially in the hot-plasma region.
- The absorption mechanism is simple.
- Stability is preserved.
- The realization and the cost of the R.F. generators are not prohibitive.

On the other hand, the overall efficiency is poor and the problem of the realization of the coupling structure for a reactor has to be solved.

REFERENCES

/1/ - PETULA GROUP, Proceedings of the International Symposium on Plasma Wall Interaction, Jülich (1976), 105.

/2/ - PETULA GROUP, Tokamak Discharges in Petula with Alumina Chamber, 8th European Conference on Controlled Fusion, Vol. 1, Prague (1977),9.

- R. BARDET et al., Results with Alumina Limiter and Liner on the Tokamak Petula, Proceedings of the 3rd International Conference on Plasma Surface Interaction in C.F. Devices, Culham (1978), to be published in J. Nucl. Mater.

/3/ - R. BARDET et al., Recent Results of ion Heating by T.T.M.P. on Petula, 8th Eur-Conf. on Controlled Fusion, Vol. 2, Prague 1977, 242.

/4/ - E. CANOBBIO, Nucl. Fusion, 12, (1972) 561.

/5/ - M. BERNARD, EUR-CEA-FC 891 (1977).

/6/ - E. CANOBBIO, R. NAKACH, The Self-consistent Electrostatic Field induced by T.T.M.P., Proceedings of the 3rd International Symposium on Toroidal Plasma Confinement, Garching (1973), E-15.

/7/ - E. CANOBBIO, Private communication.

/8/ - A. GIBSON, M.L. WATKINS, EUR-JET-P3, (1977).

DISCUSSION

J.L. SHOHET: Can you give me some idea of the ratio of the magnetic diffusion time to the period of the RF?

M. BERNARD: The magnetic diffusion time is much longer than the period of the RF.

B. GREEN: Could you give us an idea of (i) the ion heating efficiency $(\Delta T_i)/(kW$ power to plasma) and (ii) the coupling efficiency (η) achieved in Petula?

M. BERNARD: In the Petula experiment the ion heating efficiency is 2–5 $eV \cdot kW^{-1}$ for linear TTMP cases. When the TTMP regime becomes non-linear the absorbed power is more peaked and the heating efficiency increases, but on the other hand the coupling efficiency is reduced. The coupling efficiency in Petula is of the order of 2 to 3×10^{-3}.

P.E. VANDENPLAS: What would the corresponding efficiencies be in the case of JET?

M. BERNARD: For initial conditions with $T_i = 1.8$ keV and $n = 5 \times 10^{13}$ cm^{-3}, the coupling efficiency is about 10%, but with $T_i = 6$ keV and $n = 10^{14}$ cm^{-3} it can reach 25%.

PARAMETRIC INSTABILITIES INDUCED BY A LOW-FREQUENCY HEATING WAVE IN A MAGNETICALLY CONFINED PLASMA

D. MOREAU
Association Euratom-CEA,
Département de physique du plasma
et de la fusion contrôlée,
Service IGn, Centre d'études nucléaires,
Grenoble, France

Abstract

PARAMETRIC INSTABILITIES INDUCED BY A LOW-FREQUENCY HEATING WAVE IN A MAGNETICALLY CONFINED PLASMA.

Low-frequency parametric instabilities ($\omega \ll \Omega_{ci}$) of the resonant decay type are found in an inhomogeneous plasma in the presence of an essentially electrostatic 'pump' wave simulating a transit time magnetic pumping (TTMP) wave, which propagates with finite wavelength along the equilibrium magnetic field. They involve coupling to longitudinal waves propagating almost across the magnetic field with relatively long wavelengths compared to the ion Larmor radius. This occurs in very low β plasmas ($\beta \ll m_e/m_i$, as in early TTMP experiments in small stellarators) where not only the low-frequency drift wave but also the shear Alfvén wave for almost transverse propagation is electrostatic in nature. These instabilities can produce substantial $\vec{E} \times \vec{B}$ drifts and concomitant cross-field diffusion; this is briefly discussed in relation to RF heating experiments in stellarators and tokamaks.

1. INTRODUCTION

In contrast with recent successful experiments in the Petula Tokamak /1/, early transit time magnetic pumping experiments (T.T.M.P.) in small stellarators (Proto-Cleo, WIIa) were characterized by very strong plasma losses when the heating wave was applied /2/. In most cases the "pump-out" rate was found to depend linearly on the amplitude of the r.f. fields. To explain this observation, it has been proposed that the enhanced diffusion could be produced by some low-frequency parametric instabilities /3/.

In this paper we investigate parametric processes in the case of an electrostatic pump, with frequency ω_o far below the ion cyclotron frequency, which propagates with finite wavelength along the equilibrium

magnetic field in an inhomogeneous plasma. Such a wave is an approximation of the T.T.M.P. wave which is evanescent in the radial direction, but with an attenuation length longer than the plasma radius, and has a substantial electrostatic component, parallel to the static magnetic field, which arises to ensure quasineutrality /3/, /4/.

The dispersion relation for electrostatic waves in the presence of the pump field is derived within the limits of the "local approximation" by a perturbation method somewhat similar to the one used by Aliev et al. /5/. The time-dependent "unperturbed" state consists of a Maxwellian plasma in a constant magnetic field and a low-frequency electrostatic field of amplitude E_0. However, because of the finite wavelength of the pump this state is described only linearly with respect to E_0, thus restricting the validity of the theory developed here to relatively weak pump, fields. The condition of validity, which will be specified by Eq. (3) below, is not restrictive for our problem since most of the experiments were performed in the intermediate collision regime determined by condition (3) in Section 2.

The stability of the "unperturbed" state with respect to small-amplitude electrostatic perturbations is then studied and conclusions are drawn with respect to the problem of plasma confinement during low-frequency r.f. heating. In particular, we point out that a distinction must be made between very low β plasmas (Proto-Cleo, WIIa) and higher β plasmas (Petula, future devices) as far as the nature of the excited waves is concerned. This might provide an explanation for the different plasma behaviour in the two groups of devices.

2. DISPERSION RELATION

We consider an inhomogeneous collisionless plasma in a constant magnetic field B_0 directed along the z-axis of a Cartesian coordinate system. The plasma density N(x) is supposed to vary slowly along the x direction. A low-frequency electrostatic pump field is applied along the magnetic field and has the following form :

$$\vec{E}_p = \vec{z}\, E_0 \left[e^{i(k_0 z - \omega_0 t)} + e^{-i(k_0 z - \omega_0 t)} \right] \qquad (1)$$

with $E_0 = ik_0\phi_0$ and $\mathrm{Re}\,(\phi_0) = 0$.

The equilibrium ion or electron (α = i,e) distribution function $f_{\alpha o}(\vec{r}, \vec{v}, t)$ where $\vec{r} = (x, y, z)$ and $\vec{v} = (v_x, v_y, v_z)$ is solution of the Vlasov equation. Thus any function $g_{\alpha o}(\vec{R}, \vec{V})$, where $\vec{R} = (X, Y, Z)$ and $\vec{V} = (v_\perp, \theta_o, v_{zo})$ are constants of the motion, is a solution for the equilibrium state. However, it can be shown by using a simple Krook model that $g_{\alpha o}$ would relax to the Maxwellian distribution after some collision times. Therefore we can take for the "unperturbed" distribution function of the α-species :

$$f_{\alpha o}(\vec{r}, \vec{v}, t) = g_{\alpha o}(X, v_\perp, v_{zo}) = \frac{N(X)}{(2\pi)^{3/2} v_{t\alpha}^3} \exp\left(-\frac{v_\perp^2 + v_{zo}^2}{2\, v_{t\alpha}^2}\right) \qquad (2)$$

The variables $\vec{r}$ and $\vec{v}$ can be expressed in terms of $\vec{R}$, $\vec{V}$ and t of first order in the pump amplitude E_o. Such a linear collisionless description of the "unperturbed" state of the plasma is adequate provided that the ion-ion collision frequency ν_{ii} satisfy the following condition /3/ :

$$\nu_{crit} \ll \nu_{ii} \ll \omega_o \qquad (3)$$

where ν_{crit} is some critical frequency proportional to $E_o^{3/2}$.

In order to derive the dispersion relation for electrostatic waves in the presence of the pump (1) we consider a low-frequency electrostatic perturbation of frequency ω and wave vector $\vec{k}$, which couples with the pump wave to give rise to two sidebands ($\omega \pm \omega_o$, $\vec{k} \pm \vec{k}_o$) as well as higher harmonics ($\omega + n\omega_o$, $\vec{k} + n\vec{k}_o$) where n is an integer. The potential perturbation can be Fourier-expanded as follows :

$$\delta\phi = \sum_{n=-\infty}^{+\infty} \phi^{(n)}(x)\, e^{i\left[(\vec{k} + n\vec{k}_o)\cdot\vec{r} - (\omega + n\omega_o)t\right]} \qquad (4)$$

Throughout this paper we shall consider processes which occur in a plasma layer located around $x = x_o$ where the transverse wave vector is much larger than the inverse scale length of the gradients :

$$|k_\perp| \gg |k_N| \text{ where } k_N = \left(\frac{d \ln N(x)}{dx}\right)_{x=x_o} \qquad (5)$$

This allows one to assume $\phi^{(n)}$ is independent of x in the vicinity of x_o (local approximation).

The distribution function perturbation δf_α is found from the linearized Vlasov equation by integrating along the "unperturbed" trajectories. After further integration over the velocities, the ion and electron density perturbations are found to be :

$$\delta n_\alpha = \sum_n N_\alpha^{(n)} \, e^{i\left[\vec{k}^{(n)}.\vec{r} - \omega^{(n)}t\right]} \tag{6}$$

where $\vec{k}^{(n)} = \vec{k} + n\,\vec{k}_o$, $\omega^{(n)} = \omega + n\omega_o$ and

$$N_\alpha^{(n)} = -\frac{k^{(n)2}\chi_\alpha^{(n)}}{4\pi e_\alpha}\phi^{(n)} - \frac{k_o\phi_o\omega_{p\alpha}^2}{4\pi T_\alpha \omega_o^2}\sum_\ell I_\alpha^{(\ell)} \sum_\pm \left(k_z^{(n\pm1)} A_{\alpha\mp}^{n,\ell} - k_z^{(n)} A_{\alpha\mp}^{n\pm1,\ell}\right)\phi^{(n\pm1)} \tag{7}$$

Here $\omega_{p\alpha}$ is the plasma frequency (α = e,i), $\chi_\alpha^{(n)}$ the linear susceptibility at frequency $\omega^{(n)}$ and wave vector $\vec{k}^{(n)}$ and the dimensionless coefficients $I_\alpha^{(\ell)}$ and $A_{\alpha\pm}^{n,\ell}$ are defined in terms of the modified Bessel functions of imaginary arguments I_ℓ and of the Fried-Conte plasma dispersion function Z by :

$$I_\alpha^{(\ell)} = I_\ell(b_\alpha)\, e^{-b_\alpha}, \qquad b_\alpha = \frac{k_\perp^2 v_{t\alpha}^2}{\Omega_\alpha^2} = k_\perp^2 \rho_\alpha^2 \tag{8}$$

where Ω_α is the algebraic gyrofrequency, ρ_α the mean Larmor radius and

$$A_{\alpha\pm}^{n,\ell} = \frac{(\omega^{(n)} - \omega_\alpha^*)x_{o\alpha}^2}{\sqrt{2}k_z^{(n)} v_{t\alpha}(x_\alpha^{n,\ell} - x_{o\alpha})^2}\left[\sigma^{(n)} Z(\sigma^{(n)} x_\alpha^{n,\ell}) - \sigma_o Z^\pm(\sigma_o x_{o\alpha}) + 2(x_\alpha^{n,\ell} - x_{o\alpha})\right.$$
$$\left.(1 + \sigma_o x_{o\alpha} Z^\pm(\sigma_o x_{o\alpha}))\right] - 2\, x_{o\alpha}^2\left[1 + \sigma_o x_{o\alpha} Z^\pm(\sigma_o x_{o\alpha})\right] \tag{9}$$

where $x_{o\alpha} = \omega_o/\sqrt{2}\,k_o v_{t\alpha}$, $x_\alpha^{n,\ell} = (\omega^{(n)} + \ell\,\Omega_\alpha)/\sqrt{2}\,k_z^{(n)} v_{t\alpha}$, ω_α^* is the drift frequency ($\omega_\alpha^* = k_N k_y v_{t\alpha}^2/\Omega_\alpha$), $\sigma_o = |k_o|/k_o$, $\sigma^{(n)} = |k_z^{(n)}|/k_z^{(n)}$ and the functions $Z^\pm$ are the dispersion function or its complex conjugate :

$$Z^+(x) = Z(x) \text{ and } Z^-(x) = Z(x)^* \tag{10}$$

An infinite set of coupled equations is obtained from Eq. (7) and Poisson's equation. Introducing the small parameter

$$\mu = \frac{|e|\,E_o}{\sqrt{2}\,m_i\omega_o v_{ti}} \ll 1 \tag{11}$$

which is a measure of the pump amplitude, and restricting the analysis to resonant decay processes ($\varepsilon(\omega, \vec{k}) \approx 0$), the local dispersion relation reduces to :

$$k^2\lambda_{De}^2\ \varepsilon(\omega, \vec{k}) + \mu^2 \left[\frac{A_{-1}^{+}\ A_{0}^{-}}{(\vec{k}-\vec{k}_0)^2\lambda_{De}^2 \varepsilon^{(-1)}} + \frac{A_{0}^{+}\ A_{+1}^{-}}{(\vec{k}+\vec{k}_0)^2\lambda_{De}^2\ \varepsilon^{(+1)}} \right] = 0 \qquad (12)$$

where ε stands for the dielectric constant :

$$\varepsilon^{(\pm 1)} = \varepsilon(\omega \pm \omega_0, \vec{k} \pm \vec{k}_0) = 1 + \chi_e^{(\pm 1)} + \chi_i^{(\pm 1)} \qquad (13)$$

The coupling coefficients $A_n^{\pm}$ are defined by :

$$A_n^{\pm} = \frac{m_i\ \lambda_{De}^2}{x_{oi}|e|} \sum_{\alpha=i,e} \sum_{\ell} \frac{e_\alpha}{m_\alpha \lambda_{D\alpha}^2}\ I_\alpha^{(\ell)} \left[\frac{k_z^{(n\pm1)}}{k_0}\ A_{\alpha\mp}^{n,\ell} - \frac{k_z^{(n)}}{k_0}\ A_{\alpha\mp}^{n\pm1,\ell} \right] \qquad (14)$$

We note from Eqs (9) and (14) that, if ω is real and if the imaginary Landau terms coming from $Z(\sigma^{(n)} x_\alpha^{n,\ell})$ can be neglected, the following symmetry relation holds :

$$A_{n+1}^{-} = -\ (A_n^{+})^{*} \qquad (15)$$

so that the coupling coefficients $A_{-1}^{+}\ A_0^{-}$ and $A_0^{+}\ A_{+1}^{-}$ appearing in Eq. (12) are real and negative.

3. ANALYSIS OF THE DISPERSION RELATION

We shall now discuss Eq. (12) for three-wave parametric decay, e.g. $\varepsilon(\omega, \vec{k}) \approx 0$, $\varepsilon(\omega + \omega_0, \vec{k}+\vec{k}_0) \approx 0$, while the term containing $\varepsilon(\omega-\omega_0, \vec{k}-\vec{k}_0)$ can be neglected as non-resonant. For this we assume that in the absence of the pump there exist two normal modes $\omega_1(\vec{k})$ and $\omega_2(\vec{k}+\vec{k}_0)$ which satisfy the resonance condition :

$$\omega_1(\vec{k}) + \omega_0 - \omega_2(\vec{k}+\vec{k}_0) \equiv \Delta \approx 0 \qquad (16)$$

Now by writing

$$\omega = \omega_1(\vec{k}) + x + i\gamma \qquad (17)$$

where x is the frequency shift due to the pump and γ the growth rate of the oscillations, and by Taylor-expanding the dielectric functions around their

respective roots $\omega_1 + i\gamma_1$ and $\omega_2 + i\gamma_2$, we obtain the following equation for γ, valid when Eq. (15) holds true :

$$(\gamma-\gamma_1)(\gamma-\gamma_2)\left[1+\frac{\Delta^2}{(2\gamma-\gamma_1-\gamma_2)^2}\right] = -\frac{\mu^2\,|A_o^+|^2}{k^2(\vec{k}+\vec{k}_o)^2\lambda_{De}^4\,(\frac{\partial\varepsilon_R}{\partial\omega})_{\omega_1}\cdot(\frac{\partial\varepsilon_R}{\partial\omega})_{\omega_2}} \qquad (18)$$

This equation, in which ε_R means $Re(\varepsilon)$, shows that the influence of the pump is maximum when the frequency mismatch Δ vanishes and that this influence is destabilizing only if the product $(\frac{\partial\varepsilon_R}{\partial\omega})_{\omega_1}\cdot(\frac{\partial\varepsilon_R}{\partial\omega})_{\omega_2}$ is negative. However this result requires that Eq. (15) hold true and also that the imaginary parts coming from $\partial Im(\varepsilon)/\partial\omega$ can be neglected, which is not always the case. Eq.(18) also shows that if γ_1 and γ_2 are small (weak linear damping) the growth rate increases linearly with respect to the pump amplitude.

We shall now specify the eigenmodes ω_1 and ω_2 which can be coupled in two cases :

1) Ion sound waves and low-frequency drift waves in a strongly non-isothermal plasma ($T_e >> T_i$)

In the presence of a density gradient, the ion sound waves are modified into two branches /6/, namely :

An accelerated ion acoustic mode which becomes the usual drift wave when the parallel wavenumber is small;
A retarded ion acoustic mode which is weakly damped only if $T_e >> T_i$.

Coupling between these two modes and the pump defined in Eq. (1) gives rise to a parametric instability. However, this is not of great interest in laboratory plasmas where the ion and electron temperatures have the same order of magnitude.

2) Drift waves and shear Alfvén waves in a very low β plasma ($\beta << m_e/m_i$)

In a very low β plasma there exists another branch of longitudinal oscillations which is the continuation of the shear Alfvén wave for propagation almost normal to the magnetic field. This wave is referred to as a low-frequency electron sound wave /7/ or as a hybrid mode which joins the

shear Alfvén wave and the intermediate frequency electro-acoustic wave /8/. When the Alfvén speed is much larger than the electron thermal speed ($\beta << m_e/m_i$) the shear Alfvén wave becomes longitudinal for almost transverse propagation, even at frequencies much below the ion cyclotron frequency. Its frequency in an homogeneous plasma is given by

$$\omega \approx \Omega_i \cos\theta \sqrt{\frac{m_i}{m_e}} \qquad (19)$$

when the transverse wavelength greatly exceeds the mean ion Larmor radius ($k_\perp \rho_i << 1$) and if $\cos\theta << \sqrt{m_e/m_i}$, where θ is the angle between $\vec{k}$ and $\vec{B}_o$.

This wave is very weakly damped because of its large phase velocity along the magnetic field. Our numerical calculations show that it can lead to a strong instability by coupling with low-frequency drift waves (Fig. 1). In the case where $k_o = 0$ (which was shown in Ref. /1/ to produce the strongest "pump-out") the growth rate of the instability is rapidly as large as the drift wave frequency for moderate values of μ. The order of magnitude of the parameter μ defined by Eq. (11) is the modulation rate of the magnetic field, $b = \tilde{B}/B_o$, produced by the T.T.M.P. wave, which is indeed a few percent in most of the experiments.

4. CONCLUSION

The numerical results which have been obtained up to now suggest that the new parametric instabilities described in this paper might be at the origin of the enhanced diffusion which was observed during r.f. heating experiments in small stellarators. These devices were indeed operating in the very low β regime whereas the Petula Tokamak, in which no anomalous transport has been observed during T.T.M.P. heating, has $\beta \approx m_e/m_i$. However, it remainsto be shown that there is no other instability involving electromagnetic waves in the large - β devices.

A detailed study of the enhanced transport induced by parametric instabilities would be necessary for a better understanding and assessment of the "pump-out". Yet this transport can be roughly evaluated from quasi-linear theories which yield a diffusion coefficient proportional to the

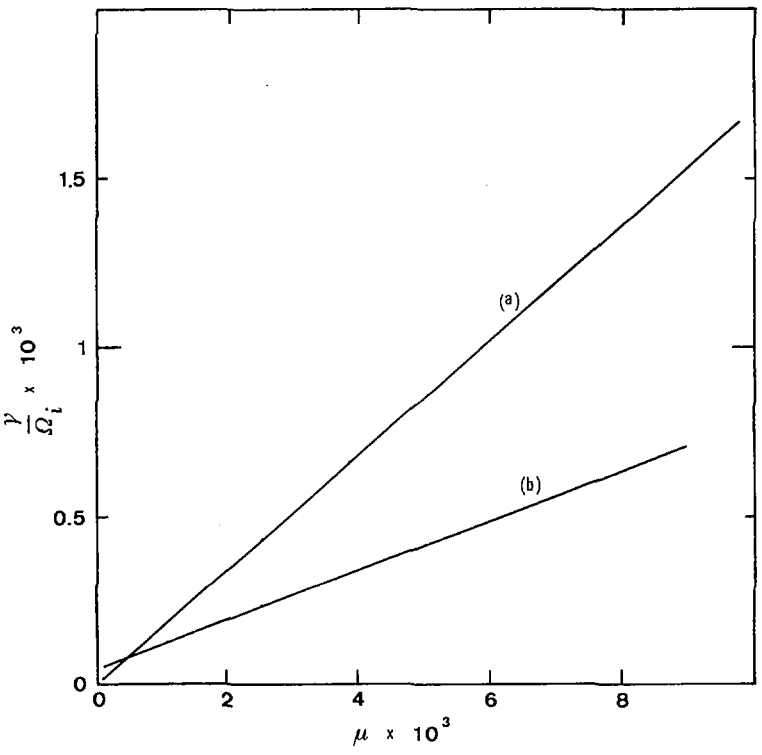


FIG.1. Growth rate γ versus μ obtained from numerical solution of Eq. (12) for a hydrogen plasma; a and R being respectively the small and large plasma radii, the parameters are:

(a) $k_0 = 0$; $ak_\perp = ak_y = 5$; $k_z R = 2 \times 10^{-2}$; $a/R = 0.2$; $\omega_1/\Omega_i = -3.7 \times 10^{-2}$; $\omega_2/\Omega_i = 2 \times 10^{-3}$.

(b) $k_0 R = 1$; $ak_\perp = ak_y = 22.5$; $k_z R = 10^{-3}$; $a/R = 0.1$; $\omega_1/\Omega_i = -9 \times 10^{-3}$; $\omega_2/\Omega_i = 7.5 \times 10^{-3}$.

In both cases, $\omega_0 = \omega_2 - \omega_1$; $\omega_{pi}^2/\Omega_i^2 = 2 \times 10^3$; $\rho_i/a = 2 \times 10^{-2}$; *and* $ak_N = -1$.

growth rate of the most violent fluctuations and to the square of the fluctuating potential $\tilde{\phi}$ /9/ :

$$D \approx \frac{\gamma}{k_N^2} \left(\frac{e\tilde{\phi}}{T_e}\right)^2 \qquad (20)$$

This is consistent with the experimental observations in the stellarators since γ is itself linearly dependent on the amplitude of the heating wave while $|e\tilde{\phi}/T_e|$ was found to be large and roughly independent of the modulation b. For the numerical case described in Section 3 (2) and taking the

fluctuation level measured in Proto-Cleo, we obtain from Eq. (20) a diffusion coefficient as large as 10^3 times the plateau value of neoclassical theory.

In future machines of larger size the fluctuation level is expected to remain low so that parametric processes due to T.T.M.P. waves should not affect plasma confinement.

ACKNOWLEDGEMENTS

The author is indebted to Drs E. CANOBBIO and M. BRAMBILLA for useful discussions and to Dr. O. DE BARBIERI for his help in doing the numerical calculations.

REFERENCES

/1/ PETULA GROUP, Physics Letters 63 A (1977) 97.

/2/ W. MILLAR, Report CLM-R-144 (1975) ; H.D. PACHER, C. MAHN and G. CATTANEI, Bull. Am. Phys. Soc. 18 (1973) 1353.

/3/ E. CANOBBIO, "Plasma Physics and Controlled Nuclear Fusion Research 1974 (Proc. 5th Int. Conf. Tokyo, 1974) Vol. 3, IAEA, Vienna (1975) 333; III Symp. on Plasma Heating in Toroidal Devices, Varenna (1976) p. 165.

/4/ J.M. DAWSON and M.F. UMAN, Nucl. Fus. 5 (1965) 242.

/5/ Y.M. ALIEV, V.P. SILIN, C. WATSON, Sov. Phys.-JETP 23 (1966) 626.

/6/ N.A. KRALL, in Advances in Plasma Physics (A. SIMON, W.B. THOMPSON, Eds), Vol. I, p. 183.

/7/ A.I. AKHIEZER, I.A. AKHIEZER, POLOVIN, SITENKO and STEPANOV, Plasma Electrodynamics, Pergamon Press (1975).

/8/ T.E. STRINGER, Plasma Physics (Journal of Nuclear Energy Part C) 5 (1963) 89.

/9/ E. MAZZUCATO, Phys. Fluids 21 (1978) 1063.

DISCUSSION

A. HASEGAWA: In TTMP the applied field is primarily magnetic. This being so, could you explain why you chose an electrostatic pump field?

D. MOREAU: J.M. Dawson first showed that, in a plasma with finite electron temperature, a TTMP wave has a substantial electrostatic component which ensures quasi-neutrality. Furthermore, the force exerted by this low-frequency wave on the particles, $\mu\nabla B$, although energy-dependent, can be assimilated to the electrostatic force I used in my paper.

PROGRESS IN HEATING OF FUSION PLASMAS WITH ALFVÉN WAVES AND MAGNETOACOUSTIC OSCILLATIONS

J.L. SHOHET*, J.N. TALMADGE*
The University of Wisconsin-Madison, Madison, Wisconsin

J.A. TATARONIS**, W. GROSSMANN**
Courant Institute, New York University, New York, New York

A. HASEGAWA
Bell Laboratories, Murray Hill, New Jersey

L. CHEN
Plasma Physics Laboratory, Princeton University,
Princeton, New Jersey,
United States of America

E. HOLZHAUER, G. JANZEN, F. MOSER, G. MÜLLER,
E. RÄUCHLE, E. SCHNEIDER, P.G. SCHÜLLER
Institut für Plasmaforschung der Universität Stuttgart,
Stuttgart, Federal Republic of Germany

Abstract

PROGRESS IN HEATING OF FUSION PLASMAS WITH ALFVÉN WAVES AND MAGNETOACOUSTIC OSCILLATIONS.

A summary of theoretical and experimental developments regarding the use of both Alfvén and magnetoacoustic waves for plasma heating is presented. New theoretical advances related to Alfvén wave heating of toroidal plasmas allow the analysis of general non-axisymmetric configurations such as stellarators. As an explanation for the experimentally observed enhanced transport in stellarators heated by Alfvén waves, the formation of magnetic islands about rational magnetic surfaces is proposed. Various linear and non-linear heating mechanisms associated with the kinetic Alfvén wave are given. In a high-β plasma produced by a linear Θ-pinch, efficient absorption of $k = 0$, $m = 0$ magnetoacoustic waves was demonstrated for the collisionless case.

* Supported by the National Science Foundation under Grant ENG-77-14820.
** Supported by the US Department of Energy Contract No. EY-76-C-02-3077.

I. Introduction

The purpose of this paper is to provide a summary of recent theoretical and experimental developments regarding the use of Alfvén waves and magnetoacoustic oscillations to heat magnetically confined plasmas. Our goal in this work is fourfold: (1) to describe new theoretical advances related to Alfvén wave heating of toroidal plasmas, with specific emphasis on stellarators; (2) to present an explanation of the enhanced transport obtained in these toroidal experiments; (3) to analyze the kinetic aspects of Alfvén wave heating in terms of the kinetic Alfvén wave; and (4) to show the efficient absorption of radially propagating magnetoacoustic waves in a collisionless high-ß plasma.

II. Alfvén Wave Heating in General Toroidal Geometry (NYU, Wisconsin)

Alfvén wave heating is based on the existence of spatial singularities which are predicted by the equations of ideal MHD [1,2,3]. As an example, the radial component v_r of the linearized velocity of a linear screw pinch possesses a logarithmic singularity, $v_r \sim \ln(r-r_o)$, about surfaces where the applied frequency ω of the heating source equals the local frequency of an Alfvén wave, $\omega_A(r)$, i.e. $\omega = \omega_A(r_o)$. The question to be asked here is what the equivalent relation might be between ω and the singular points or surfaces in more complicated geometries.

For the particular case of an axial-symmetric toroidal configuration, Pao [4] has shown that there exists a system of ordinary differential equations, defined on each magnetic surface ψ = const., which must be solved for its eigenvalues Ω as a function of ψ. The singular surfaces ψ_o = const., i.e. those about which energy absorption and local heating can be predicted, satisfy $\omega = \Omega(\psi_o)$. In cases where the equilibria possess no axis of symmetry, such as toroidal stellarators, we show in this section that the corresponding equations for $\Omega(\psi)$ form a system of partial differential equations defined on each magnetic surface.

The ideal linearized MHD equations are written as follows, assuming a time dependence of $\exp(i\omega t)$:

$$i\omega\rho\vec{v} = (\vec{B}\cdot\nabla)\vec{b} + (\vec{b}\cdot\nabla)\vec{B} - \nabla p^* \tag{1}$$

$$i\omega\vec{b} = (\vec{B}\cdot\nabla)\vec{v} - (\vec{v}\cdot\nabla)\vec{B} - \vec{B}\nabla\cdot\vec{v} \tag{2}$$

$$i\omega p_1 = -\vec{v}\cdot\nabla P - \gamma P\nabla\cdot\vec{v} \tag{3}$$

where $\vec{b}$ is the linearized magnetic field, $\vec{B}$ is the equilibrium magnetic field, $\vec{v}$ is the plasma velocity, P is the equilibrium pressure, γ is the ratio of specific heats, and p^* has been written in place of the total linearized pressure $p_1 + \vec{B}\cdot\vec{b}$. We now introduce three variables in place of the spatial coordinates: $\psi(\vec{r})$, $\alpha(\vec{r})$ and $\beta(\vec{r})$ where α = const. and and ß = const. are surface variables which span the ψ = const. surfaces, and ψ satisfies $B\cdot\nabla\psi = 0$. In terms of these new variables, we have $\vec{B}\cdot\nabla = (\vec{B}\cdot\nabla\alpha)\partial/\partial\alpha + (\vec{B}\cdot\nabla\beta)\partial/\partial\beta$, i.e.

the operator $\vec{B}\cdot\nabla$ contains only derivatives with respect to the surface variables. In terms of (ψ, α, β), we obtain, from eqs. (1)-(3),

$$\frac{\partial \vec{X}}{\partial \psi} = \vec{\vec{A}}\cdot\vec{X} + \vec{\vec{C}}\cdot\vec{Y} \tag{4}$$

$$\vec{\vec{\chi}}\cdot\vec{Y} = \vec{\vec{K}}\cdot\vec{X} \tag{5}$$

where $\vec{X}$ and $\vec{Y}$ are vectors defined by

$$\vec{X} = \begin{bmatrix} v^1 \\ \\ p^* \end{bmatrix}, \qquad \vec{Y} = \begin{bmatrix} v^2 \\ v^3 \\ b^2 \\ b^3 \end{bmatrix} \tag{6}$$

$\vec{\vec{A}}$, $\vec{\vec{C}}$, $\vec{\vec{\chi}}$, and $\vec{\vec{K}}$ are matrices whose elements are linear first-order differential operators with respect to the surface variables, α and β, but <u>not</u> with respect to ψ, and $v^1 = \vec{v}\cdot\nabla\psi$, $v^2 = \vec{v}\cdot\nabla\alpha$, $v^3 = \vec{v}\cdot\nabla\beta$, $b^2 = \vec{b}\cdot\nabla\alpha$ and $b^3 = \vec{b}\cdot\nabla\beta$. The nature of the solutions of eqs. (4) and (5) for $\vec{X}$ and $\vec{Y}$ depends on whether the operator $\vec{\vec{\chi}}$ possesses an inverse for a given ψ and ω. If the inverse exists, then the system can be integrated to obtain analytic solutions. However, if the inverse does not exist, i.e. if there exists for some $\omega = \omega_0$ and $\psi = \psi_0$ a non-trivial function $\vec{\Phi}(\psi_0, \alpha, \beta)$ such that $\vec{\vec{\chi}}\cdot\vec{\Phi} = 0$, then singular solutions may exist about the given surface $\psi \equiv \psi_0 \equiv$ const. To demonstrate this, assume the following forms for $\vec{X}$ and $\vec{Y}$:

$$\vec{X} = \vec{f}\,\ln(\psi-\psi_0) + \vec{g} \tag{7}$$

$$\vec{Y} = \frac{\vec{h}}{\psi-\psi_0} + \vec{s}\,\ln(\psi-\psi_0) + \vec{u} \tag{8}$$

where the vectors $\vec{f}$, $\vec{g}$, $\vec{h}$, $\vec{s}$ and $\vec{u}$ are analytic functions of ψ, α and β that we expand in a power series in ψ about $\psi = \psi_0$ in the form,

$$\vec{f} = \vec{f}_0(\alpha,\beta) + \vec{f}_1(\alpha,\beta)(\psi-\psi_0) + \vec{f}_2(\alpha,\beta)(\psi-\psi_0)^2 + \ldots$$

The coefficients of $(\psi - \psi_0)^n$ are derived by substituting eqs. (7) and (8) in eqs. (4) and (5) and setting the coefficients of $(\psi-\psi_0)^m$ and $(\psi - \psi_0)^n \ln(\psi - \psi_0)$ equal to zero. To lowest order one obtains,

$$\vec{\vec{\chi}}_0\cdot\vec{h}_0 = 0 \qquad \text{(periodic boundary conditions)} \tag{9}$$

where the operator $\vec{\vec{\chi}}_0$, defined by $\vec{\vec{\chi}} = \vec{\vec{\chi}}_0 + (\psi - \psi_0)\vec{\vec{\chi}}_1 + \ldots$, contains partial derivatives only with respect to α and β. All other coefficients appearing in the power series expansions can be expressed in terms of $\vec{h}_0$ by solving equations of the form $\vec{\vec{\chi}}_0 \cdot \vec{q} = \vec{u}$, subject to a compatibility condition, $\langle \vec{\phi}^+, \vec{u} \rangle = 0$ where $\vec{\phi}^+$ is a null vector of the operator adjoint to $\vec{\vec{\chi}}_0$. The eigenvalues of eq. (9) are $\Omega(\psi)$ which define the singular surfaces $\omega = \Omega(\psi_0)$. The conclusion we draw from this development is that if the compatibility condition is satisfied, v^1 and p^* can possess logarithmic singularities in space while the singularities of v^2, v^3, b^2, b^3 are of the type $(\psi - \psi_0)^{-1}$. If the compatibility condition were not satisfied, then other forms of singularities would appear.

The singularities of $\underset{\sim}{X}$ and $\underset{\sim}{Y}$ present in eqs. (7) and (8) correspond to resonance phenomena which imply energy absorption and accumulation, analogous to that of the screw pinch geometry [1]. The analytic continuation across the singular surface,

$$\vec{f} \ln(\psi - \psi_0) \rightarrow \vec{f} \ln(\psi_0 - \psi) \pm i\pi\vec{f}$$

gives rise to an imaginary part of $\vec{X}$, which in turn implies that the effective impedance of an external coil exciting the plasma possesses a resistive part. We point out that resonance between the coil and a singular surface can occur only if the α and β dependence of the fields excited by the coil is compatible with the eigenfunctions of $\vec{\vec{\chi}}_0$, i.e. with h_0.

III. Alfvén Wave Heating of Stellarators (Wisconsin)

Several experiments have been performed attempting to heat plasmas confined in toroidal magnetic systems by means of rf at low frequencies, typically well below the ion cyclotron frequency [7,8,9,10,11]. The basic motivation for these experiments came from theoretical work predicting absorption of Alfvén waves in inhomogeneous plasmas [1,2,3]. The experiments have all been performed in stellarator or stellarator-type devices. While significant heating has been observed in all of these experiments, they have also been characterized by significant loss of plasma during the heating (pump-out). The loss of confinement in one experiment, Proto-Cleo at Wisconsin, has been studied in detail [8]. It was found that the loss of confinement was directly proportional to the amplitude of the modulating field. Examination of the Kharkov Uragon II stellarator results shows a similar, but not quantitatively measured behavior [9].

It is the purpose of this section to propose an explanation of the enhanced transport. It is based on the formation of magnetic islands due to the interaction of the magnetic field produced by the heating coil with the confining field. Figure 1 shows a diagram of the stellarator together with the launch coil. Proto-Cleo is operated as an $\ell = 3$, 7 field period device. The launch coil is an $\ell = 3$, 1 field period winding. This winding, being made of a single conductor, behaves not like a true stellarator, but rather like a torsatron. It thus generates a vertical field, which can move the magnetic axis of the confining field configuration, much like a vertical field does in the case of a tokamak. Since the toroidal multiplicities of the Alfvén winding

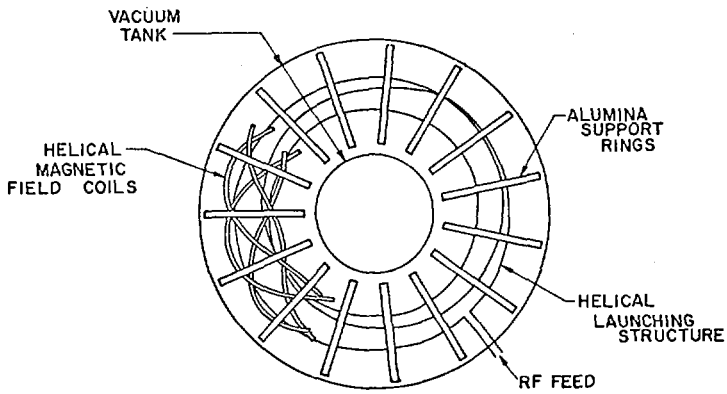


FIG.1. Proto-Cleo stellarator with its launch coil.

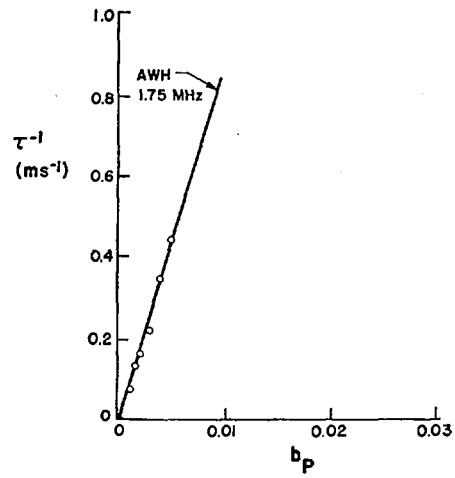


FIG.2. Pump-out versus modulation.

and the confining winding differ, it is quite likely that magnetic islands would form at appropriate resonant regions. In addition, if the heating frequency is low, as is the case for Alfvén waves, it might be expected that the perturbations of the magnetic field structure would be able to penetrate into the body of the plasma.

Figure 2 shows the relationship between rf pump-out time and modulation amplitude of the confining field by the Alfvén wave launch coil. In order to present data due to the presence of the rf alone, the following relationship was used:

$$\frac{1}{\tau_{RF}} = \frac{1}{\tau_{Net}} - \frac{1}{\tau_{No\ RF}} \qquad (10)$$

The net confinement time was measured by observing the value of the plasma density at the end of the rf heating pulse and comparing it to that observed at the same instant of time with no rf present and fitting an exponential between this value and the density at the beginning of the pulse. It can be seen from Fig.2 that the reciprocal of the rf decay time τ_{RF} is linearly proportional to the modulation amplitude.

Previous attempts to explain the transport based on diffusion processes have been complicated by this linear dependence, since crossfield diffusion due to the presence of rf fields would most likely exhibit a quadratic dependence on the rf amplitude. However, the linear dependence on confinement can be obtained by considering the possibility of formation of magnetic islands by the interactions of the modulating field and the confining field. Transport is then increased, typically because the step size for diffusion becomes the island width.

The island width Δ_{mn} is given by the following approximate expression [12,13]:

$$\Delta_{mn} \sim 4\left[2R \left|\frac{b_{mn}(r)}{B_T} \left(\frac{d\iota}{dr}\right)^{-1}\right|_{r=r_{mn}}\right]^{1/2} \tag{11}$$

In equation (11), b_{mn} is the amplitude of the perturbing magnetic field, m and n are the poloidal and toroidal mode numbers, B_T is the toroidal field, R is the major radius, and $\left(\frac{d\iota}{dr}\right)$ is the derivative of the rotational transform of the confining field at the point where it is resonant with the mode structure of the perturbing field (r_{mn}), i.e. at the mnth rational surface. For this particular launch coil [14], an infinite set of modes are generated, with the relation,

$$\text{mode number} = p(\theta - \tfrac{1}{3}\phi) \tag{12}$$

p is an integer, θ is the poloidal angle and ϕ is the toroidal angle. Thus, m and n form an infinite set, e.g. (m=1, n=1/3), (m=2, n=2/3), (m=3, n=1), etc. Islands can form whenever the condition for resonance with the confining field is satisfied by any of the modes that can be excited by the launch coil.

In order to test this assumption, the vacuum magnetic surfaces for Proto-Cleo were calculated numerically by following magnetic field lines around the torus. Figure 3 shows computer-generated plots of the vacuum magnetic surfaces under three conditions. The top drawing shows the surfaces with no modulation. The middle drawing shows the surfaces with approximately 1.5 % modulation, and the bottom drawing with identical modulation but with the current in the launch coil reversed. During an actual experiment, the magnetic surfaces should continuously deform from one set to the other, limited only by the rate of diffusion of the magnetic field lines through the plasma. Several islands are identified in the bottom two drawings. They are of rather high multiplicity. The surfaces near the magnetic axis, where the transform is small, do not appear to be closed, but this is because computation was stopped before the entire surface was generated.

Since a vertical field is also generated by the launch coil, a shift in the location of the magnetic axis is seen, although no major shift in the location of the last closed magnetic surface

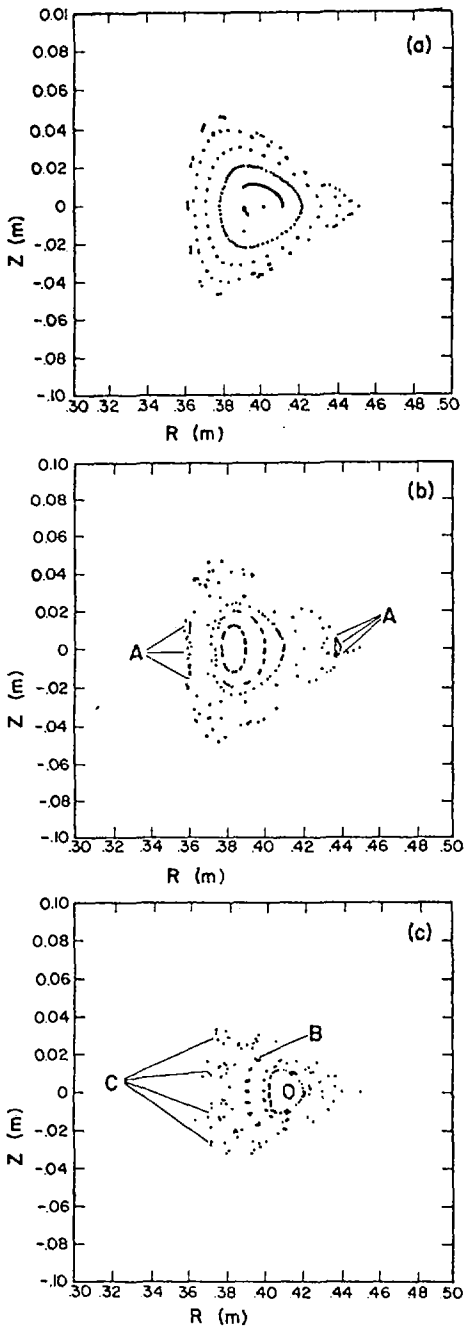


FIG. 3. Magnetic surfaces. Islands are seen at points labelled A, B, C. Island A is of toroidal multiplicity 2.

is noticeable. Ergodicity of the magnetic field lines is present near the outside of the closed surfaces. Since the fields from the launch coil are strongest near the coil itself, it is to be expected that the magnetic surfaces near the axis tend to be preserved. That is, as minor radius increases, the surfaces should first form islands, then a region of ergodicity should appear, and finally a new set of islands should form at the outside of the ergodic region. Evidence of this is seen in Fig. 3.

Equation (11) shows that the width of the islands is proportional to the square root of the modulation. In order for enhanced particle transport to occur, the collision frequency must be of the order of the transit time of the electrons around the torus. Near the outer boundaries of the magnetic islands, the rotational transform is high and thus the step size is, in effect, of the order of the island width. As a result, the diffusion, being proportional to the square of the step size, will be directly proportional to the modulating field amplitude. Such conditions are satisfied in Proto-Cleo, along with magnetic diffusion times of the order of the r.f. period or less.

In order to determine whether Alfvén wave heating would be effective in other experiments, or with other launch coils, a similar analysis of the magnetic field structure must be made. In particular, if a launching structure could be made with no superfluous harmonics, it would only couple to the magnetic surface at one location for Alfvén wave heating and then it would not be as likely to generate magnetic islands throughout the plasma volume as in the case with the launching structure used in Proto-Cleo.

IV. Kinetic Alfvén Wave (Bell Laboratories, Princeton)

Kinetic theory is used in this section to calculate the heating rate of plasma species both in the linear [5] and nonlinear [6] regimes.

First, it is identified that the resonant absorption found in the ideal MHD analyses [1, 3] is a manifestation of a resonant mode conversion of the MHD wave to a kinetic wave whose dispersion relation is given by,

$$\omega^2 = k_{\parallel}^2 v_A^2 (1 + k_{\perp}^2 \rho_s^2)$$

where $\rho_s^2 = (T_e + 3\,T_i/4)/(m_i \omega^2)$

and $k_{\parallel}$ and $k_{\perp}$ are parallel and perpendicular wave numbers, T_e and T_i are electron and ion temperatures, m_i the ion mass, v_A the Alfvén speed and ω_{ci} is the ion cyclotron frequency. We call this the kinetic Alfvén wave. The plasma is heated by the damping of the kinetic Alfvén wave. The kinetic Alfvén wave is found to propagate toward the higher density side, which is favorable for the core heating.

For a supplementary heating, we must assume the plasma to be collisionless. In the linear regime, the heating occurs due to the Landau damping. We note that because the kinetic Alfvén wave accompanies electrostatic perturbation, it faces the Landau resonances. In a low beta plasma: $\beta << 1$, the electron Landau

damping dominates, hence electrons are predominantly heated at a rate given by [5],

$$n_0 \frac{dT_e}{dt} \approx \omega \left(\frac{m_e}{m_i \beta} \right)^{1/2} \frac{|\tilde{B}_\theta|^2}{2\mu_0}$$

where m_e is the electron mass and $\tilde{B}_\theta$ is the poloidal component of the wave magnetic field and ω is the applied frequency. We note that $\tilde{B}_\theta$ is enhanced over the external (MHD) magnetic field by a factor of $(a/\rho_s)^{1/2} \approx 30$ (where a is the minor radius) due to the resonant mode conversion. If $\beta \gtrsim 0.2$, the ion Landau damping also becomes appreciable.

Nonlinear heating is also expected because of the enhanced amplitude of the kinetic Alfvén wave. If $T_e \lesssim 3T_i$, the nonlinear Landau damping of the kinetic Alfvén wave heats ions. The heating rate is given by [6]

$$n_0 \frac{dT_i}{dt} \approx \frac{\omega_A}{10\beta} \frac{|\tilde{B}_0|^2}{B_0^2} \frac{\omega_{ci}}{\omega} (k_\perp \rho_s)^2 \frac{|\tilde{B}_\theta|^2}{2\mu_0}$$

The threshold value of the wave amplitude $|B_\theta|$ for the nonlinear heating is $\approx 10^{-2}$ x toroidal magnetic field B_0. However, in terms of the MHD wave amplitude, which roughly corresponds to the externally applied field intensity, it corresponds only to the order of 10 Gauss.

V. Absorption of Magnetoacoustic Waves (Stuttgart)

The use of magnetoacoustic oscillations to heat magnetically confined plasmas was studied on a cylindrical collisionless high-ß plasma. In the more collisional regime absorption of magnetoacoustic waves in a high-ß plasma has already been observed [15].

In order to study the absorption process a radially propagating m = 0, k = 0 magnetosonic wave of low amplitude was excited. The energy transfer from this wave to the plasma was low compared to the energy losses of the plasma so that direct heating could not be observed in this mode of operation.

The cylindrical high-ß plasma was produced by fast magnetic compression of a preionized plasma in a 2 m θ-pinch coil. The filling gas was hydrogen at 2 m Torr filling pressure. The attained plasma parameters in the post-implosion phase (4 μs after compression) were measured with magnetic probes and interferometry in the visible and infrared. Fig. 4 shows the radial profiles of the axial magnetic field B_{0z} and density n_e. From these profiles one calculates a value of 100 eV for $T_e + T_i$. Magnetoacoustic waves of type m = 0, k = 0 were excited by modulating the external confining magnetic field. The modulating pulse had a frequency spectrum from 0.8 to 1.5 MHz. The degree of modulation was about 15 %. The propagation of the magnetic component of the wave was followed by magnetic probes at different radial positions. The density modulation on axis was measured by time resolved interferometry. Figure 5 shows the radial profile of amplitude and phase of the wave field for the spectral component at f = 1 MHz. The wave pulse propagates inward from the

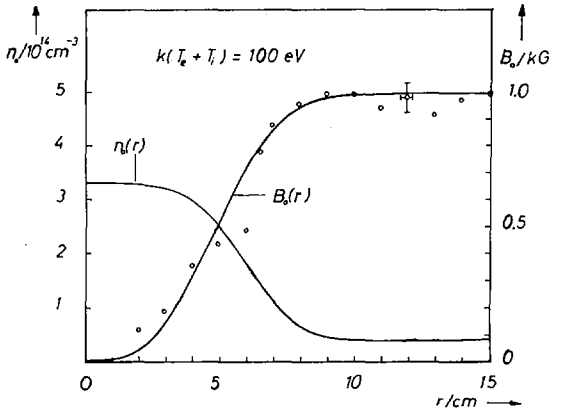


FIG. 4. Radial profiles of axial magnetic field B_{0_z} and density n_0.

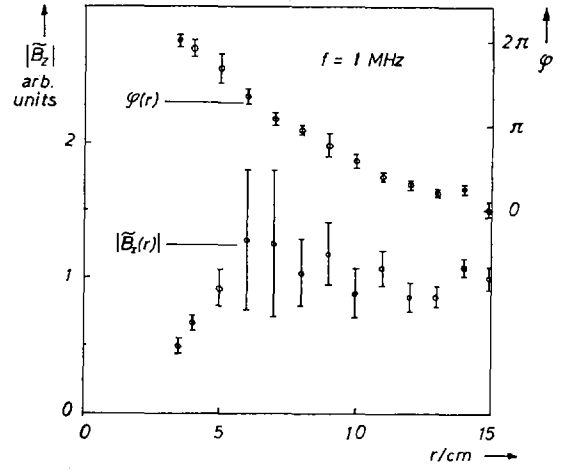


FIG. 5. Measured radial profiles of amplitude and phase of the wave field $\tilde{B}_z$.

dense plasma boundary at r = 6 cm with a phase velocity of about 10^7 cm/s carrying an energy density flux of about

$10^3 \frac{J}{cm^2 \cdot s}$ to the plasma core.

This means that the power transfer to the plasma centre is about 10 MW, which is equivalent to an energy gain of about 5 eV/μs per particle. By measuring the resistive loading induced on the wave launching coil by the plasma a power input of the same order as the power transfer to the plasma centre could be measured. The characteristic behavior of magnetosonic waves in this high-β plasma is a mode conversion from a MHD-wave to a

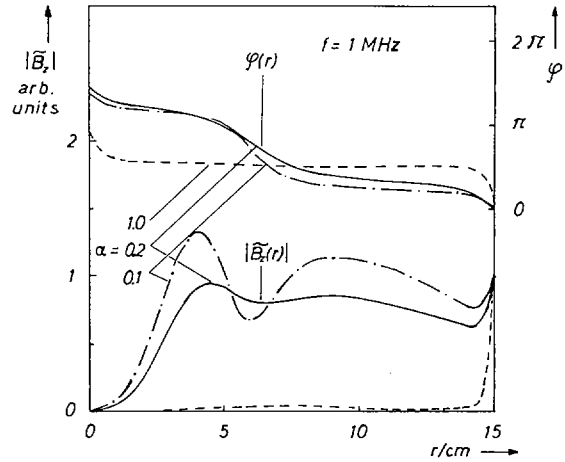


FIG. 6. Computed radial profiles of amplitude and phase of the wave field $\tilde{B}_z$ for various values of $\alpha = \nu_{effective}/\nu_{classical}$ (ν = viscosity coefficient).

pure ion-sonic wave which propagates in the magnetic-field-free plasma core. A density modulation of about 30 % could be observed on axis.

The theoretical analysis of the problem has been done initially through numerical integration of the linearized MHD equations. The measured radially inhomogeneous plasma parameters were used in these computations. In the temperature range of the plasma, the ion viscosity is the dominant damping mechanism. At higher filling pressures and thus smaller ion temperatures a highly reduced viscous damping was observed. Figure 6 shows computed radial profiles of the amplitude and phase of the wave field for different values of the classical ion viscosity coefficient. A comparison with the measured values of Fig. 5 indicates that a viscosity coefficient between 0.1 and 0.2 times the classical value of the plasma must be assumed to explain the experimental results.

The difference between the classical model and the experimental results could be due to the fact that the conditions implicit in the MHD model are not satisfied throughout the plasma, especially in the centre. Moreover, the radial distribution of the ion temperature, on which the viscosity has a sensitive dependence, was assumed to be uniform for the compressed part of the plasma.

The experiment has shown that magnetoacoustic waves are efficiently absorbed even in the collisionless case. However, in this case, an exact theory must include ion kinetic effects in order to explain the observed phenomena.

References

[1] TATARONIS,J.A., GROSSMANN,W., Z.Phys.261 (1973) 203 and 217; Nucl.Fusion 16 (1976) 667

[2] TATARONIS,J.A., J. Plasma Phys. 13 (1975) 87

[3] HASEGAWA,A., CHEN,L., Phys.Rev.Letts.32 (1974) 454; Phys.Fluids 17 (1974) 1399

[4] PAO,Y.P., Nucl.Fusion 15 (1975) 631

[5] HASEGAWA,A., CHEN,L., Phys.Rev.Letts. 35 (1975) 370

[6] HASEGAWA,A., CHEN,L., Phys. Fluids 19 (1976) 1924

[7] GOLOVATO,S.N., SHOHET,J.L., TATARONIS,J.A., Phys.Rev.Letts. 37 (1976) 1272

[8] GOLOVATO,S.N., SHOHET,J.L., Phys.Fluids, to be published

[9] DIKIJ,A.G. et al., Plasma Physics & Controlled Fusion Research (IAEA, Vienna, 1977), Vol.II, p. 129

[10] UO,K.,et al., Plasma Physics & Controlled Fusion Research (IAEA, Vienna,1977), Vol.II, p. 103; OBIKI,T. et al., Phys.Rev.Letts. 39 (1977) 812

[11] DEMIRKHANOV,R.A., et al., Plasma Physics & Controlled Fusion Research (IAEA, Vienna,1977), Vol.III, p. 31

[12] RECHESTER,A.B., ROSENBLUTH,M.N., Phys.Rev.Letts.40 (1978) 38

[13] CALLEN,J.D., Phys.Rev.Letts. 39 (1977) 1540

[14] GOLOVATO,S.N., SHOHET,J.L., TATARONIS,J.A., IEEE Trans. on Plasma Sci., PS-5 (1977) 952

[15] JACOBSON,A.R.,et al., Phys.Rev.Letts 37 (1976) 897.

DISCUSSION

C.N. WATSON-MUNRO: Have you obtained or can you obtain from your stellarator any direct experimental evidence of magnetic islands?

J.L. SHOHET: To measure the island structure, we would need an electron beam and a d.c. current in the Alfvén wave winding. The winding was not cooled sufficiently to allow this. However, we believe that the indirect evidence, namely the vacuum field calculations and the enhanced transport proportional to the first power of the modulating field, is most striking.

C.W. ROBERSON: Have observations of the decay of the Alfvén waves into ion-acoustic waves been made?

J.L. SHOHET: No; the enhanced transport, being linearly proportional to the RF field amplitude, exhibited no threshold. That is, no matter how small the RF field was, the enhanced transport remained. No change in the linearity appeared over the range of RF field amplitudes permitted by the experiment.

M. BRAMBILLA: Does the 'island' mechanism also explain the fact that the pump-out rate appears to have a strong dependence on the applied frequency in Proto-Cleo?

J.L. SHOHET: We have not calculated the island structure for the low-frequency TTMP experiments done in Proto-Cleo. However, it must be noted that, in the case of d.c., the presence of islands does not appear to affect the transport. Thus higher frequencies should – as is the case in Proto-Cleo – result in greater transport for the same RF field amplitude until the magnetic diffusion time becomes longer than an RF period. In the Petula tokamak, for example, the magnetic diffusion time is longer than an RF period, so no enhanced transport occurs.

A. PATARAYA: Did you, in your study of heating by low-frequency waves, take into account the dispersion of low-frequency linear waves? We know that in a situation like this involving a finite wave amplitude, non-linear waves (solitons or wave-packets) can be generated. Did you allow for the formation of such waves?

J.L. SHOHET: No; because of the absence of any threshold of the amplitude on the transport, no non-linear effects were anticipated. That is, the linear effect on the pump-out extended down to zero amplitude.

FAST-MAGNETOSONIC-WAVE EXCITATION IN LARGE-TOKAMAK PLASMAS

A.V. LONGINOV, K.N. STEPANOV, V.A. TSURIKOV
Kharkov Physicotechnical Institute of the Ukrainian SSR
Academy of Sciences,
Kharkov, Union of Soviet Socialist Republics

Abstract

FAST-MAGNETOSONIC-WAVE EXCITATION IN LARGE-TOKAMAK PLASMAS.

An analysis is performed of the peculiarities of fast-magnetosonic-wave (FMSW) excitation with frequencies less than or of the order of the ion cyclotron frequency in plasmas of large tokamaks. As a function of wave frequency, damping rate and plasma dimensions, three excitation regimes of these waves are possible: eigenmode resonances of the toroidal plasma cavity, multimode resonances (radiation regimes in an endless plasma cylinder), and the radiation regime in the plasma half-space.— Apart from the eigenmode resonances of separate toroidal modes, the eigenmode resonance of paired modes is shown to be possible; its use allows the solution to the problem of electric breakdown of the coupling structure to be simplified. – The characteristic behaviour of the current layer impedance is investigated in the presence of a metal screen; it is shown that RF power can be coupled effectively to the plasma in all three regimes. – The results of a numerical treatment of FMSW excitation in the T-10 tokamak are presented; and it is demonstrated that a regime may exist where the current loop impedance changes slightly when the density changes, which permits the use of fixed-frequency sources for plasma heating. – The advantages are noted of using multi-mode resonance and radiation – in the half-space regimes for plasma heating in large systems with reactor parameters.

1. INTRODUCTION

Fast magnetosonic waves (FMSW) are among the most promising candidates for RF heating of plasmas in toroidal traps with tokamak reactor parameters [1–3]. The problem of powerful sources (f = 1–100 MHz) for this purpose can already be solved now. Effective mechanisms of FMSW absorption by plasma particles are in existence. Finally, it is possible to solve the problem of effective coupling of RF power to the plasma.

The excitation of FMSW in a toroidal plasma cavity is performed by using special coupling structures (antennas) placed, as a rule, in the vicinity of the plasma boundary. The finiteness of the plasma column, the dimensions of the coupling structure, and the damping rate of the waves play an important role in

wave excitation. Various excitation regimes can be realized, depending on the wave frequency and damping rate, and the dimensions of the plasma and the coupling structure. In this paper, results are presented of an analysis of the peculiarities of FMSW excitation in large toroidal traps.

In Section 2, the general picture of FMSW excitation in a plasma torus of large dimensions is presented. Resonant excitation of a separate toroidal eigenmode is shown to be possible in a region of weak damping as well as the resonant excitation of paired eigenmodes. With increasing damping, multi-mode resonances appear, and in the region of strong damping a regime of radiation into half-space is realized. In Section 3, the peculiarities of FMSW excitation by a current layer in the presence of a metal screen (vacuum chamber) are discussed. In Section 4, results are presented of a calculation of excitation and damping of FMSW with a frequency of $\omega \approx 2\omega_{Bi}$ in a T-10 tokamak. Finally, in Section 5, advantages and drawbacks of using different regimes of FMSW excitation for plasma heating in tokamaks of various dimensions are discussed.

2. GENERAL PICTURE OF FMSW EXCITATION IN LARGE TORI

Let us illustrate the peculiarities of electromagnetic wave excitation by taking an FMSW with $\omega \sim \omega_{Bi}$ as an example. The frequency of FMSW is related to the wave number by

$$\omega \sim k\bar{v}_A \tag{2.1}$$

where $\bar{v}_A = B_0/(4\pi\,\bar{n}\,m_i)^{1/2}$ and $\bar{n}$ are the average values of Alfvén velocity and plasma density, respectively, and $k = (k_r^2 + k_\vartheta^2 + k_\chi^2)^{1/2}$ is the wavenumber,

$$k_r = \frac{n\pi}{a}, \qquad k_\vartheta = \frac{m}{r}, \qquad k_\chi = \frac{\ell}{R}$$

with a as the plasma radius and n the radial mode number. The wavelength in the plasma, $\lambda \sim 1/\bar{k}_A = \bar{v}_A/\omega$, appears, in large tokamaks for $\omega \sim \omega_{Bi}$, to be small compared to the plasma radius; therefore, the FMSW field can be represented in the WKB-approximation:

$$E(r,t) = \sum_{\ell,m} E^{(\ell,m)} \left(\exp\left(-i\int^r k_r dr\right) + \rho^{(\ell,m)} \exp\left(i\int^r k_r dr\right)\right) \exp(im\vartheta + i\ell\chi) \tag{2.2}$$

where χ and ϑ are the large and small azimuthal angles, and $\rho^{(\ell,m)} = |\rho|\exp(-i\psi)$ is the complex reflection coefficient. The quantity $|\rho| = \exp(-\tau)$ and the phase ψ are determined by the relations

$$\tau = 2\int_{r_1}^{r_2} \mathrm{Im}\, k_r\, dr \tag{2.3}$$

$$\psi = 2\int_{r_1}^{r_2} k_r dr \sim 2\bar{k}_A a \tag{2.4}$$

where Im k_r is the absorption coefficient, the integration over r is performed over the region $r_1 < r < r_2$, where $k_r^2 > 0$.

In the following, waves are considered that propagate almost perpendicularly to the magnetic field ($k_r \approx \bar{k}_A = \omega/\bar{v}_A \gg k_{\vartheta,\chi}$) because it is only they that penetrate well into a plasma of large dimensions ($\bar{k}_A a \gg 1$) since the zone of wave evanescence is very narrow for them.

The eigenmode frequencies $\omega^{(\ell,m,n)}$ are very close to each other for large ℓ, m, n. Therefore, the changes in the average density, $\Delta\bar{n}$, or magnetic field, ΔB, corresponding to a frequency change $\Delta\bar{\omega}$, where $\Delta\bar{\omega}$ is the average distance between the eigenmode frequencies, are also very small:

$$\frac{\Delta\bar{n}}{\bar{n}} \sim 2\frac{\Delta B}{B} \sim 2\frac{\Delta\bar{\omega}}{\omega} \sim \frac{1}{\ell m n} \ll 1$$

(A similar expression for $\Delta\bar{\omega}/\omega$ has been obtained in Ref. [4].)

The radiation intensity of the coupling structure essentially depends on the spectral characteristics of the 'exciting' electric field on the antenna surface (or 'exciting' electric current in the antenna):

$$E_0(\vartheta,\chi) = \sum_{\ell,m} E_0^{(\ell,m)} \exp(im\vartheta + i\ell\chi - i\omega t) \tag{2.5}$$

i.e. on how the $E_0^{(\ell,m)}$ depend on ℓ and m. The resonant mode power (ℓ, m, n) absorbed in a plasma contains the resonant denominator:

$$P^{(\ell,m)} \propto \frac{|E_0^{(\ell,m)}|^2}{(\bar{n}-\bar{n}^{(\ell,m,n)})^2 + (\delta\bar{n})^2} \tag{2.6}$$

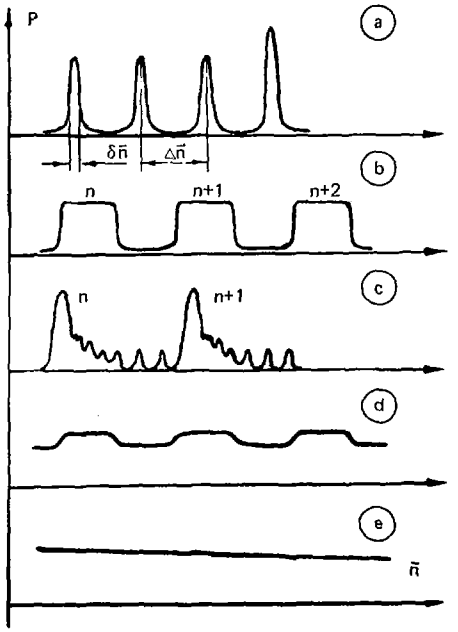


FIG.1. Radiated power versus plasma density for various excitation regimes:
a) eigenmode resonance regime for separate and paired modes;
b) multi-mode resonance regime with excitation of a separate radial mode;
c) multi-mode resonance regime and eigenmode regime for separate modes for the broad spectrum of the exciting field;
d) multi-mode resonance with excitation of several radial modes;
e) regime of radiation into half-space.

where $\bar{n}^{(\ell,m,n)}$ is the value of the plasma density $\bar{n}$ for which the external-source frequency is equal to the resonant frequency, $\omega = \omega^{(\ell,m,n)}$. The density deviation from the resonant value corresponding to the half-width of the resonant-damping curve is equal to

$$\frac{\delta\bar{n}}{\bar{n}} \sim \frac{\tau}{\bar{k}_A a} \sim \frac{\tau}{\pi n} (\tau \ll 1) \tag{2.7}$$

where τ is the optical thickness of the plasma expression (2.3).

If the distance between the resonances $\Delta\bar{n}$ is considerably larger than the half-width of the resonance $\delta\bar{n}$, then the total power absorbed

$$P = \sum_{\ell,m} P^{(\ell,m)} \tag{2.8}$$

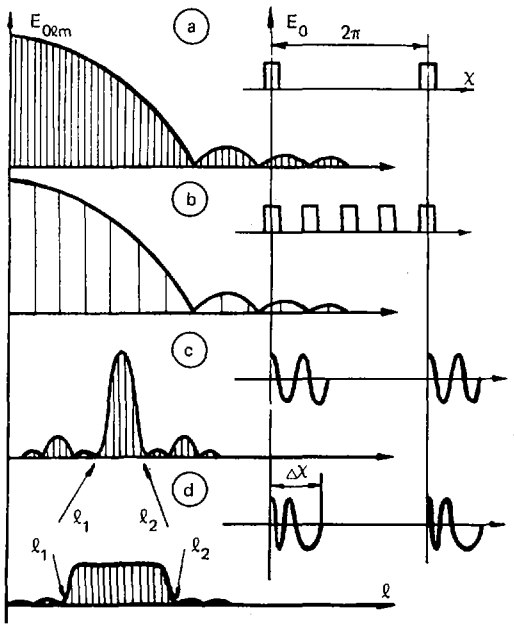


FIG.2. Spectral intensity of the exciting field versus longitudinal number ℓ for four typical distributions of the exciting field.

will be determined by the resonant term only. In the case where the density $\bar{n}$ (or the magnetic field B) changes in time, the quantity P will be of the form shown in Fig.1a, i.e. it will show separate high narrow peaks of width $\delta\bar{n}$ with distances $\Delta\bar{n}$ between them. (Note that all previously reported experiments on RF plasma heating in tokamaks by FMSW were based on using the eigenmode resonances [5–8].)

If the distance $\Delta\bar{n}$ between the resonances becomes less than the half-width $\delta\bar{n}$ of the resonance, then overlap of neighbouring resonances occurs, and the power P absorbed in the plasma and other energy characteristics of the radiation system assume smoother shapes than that depicted in Fig.1a.

The radiation regime of an antenna depends on its spectral characteristics, i.e. on the exciting field distribution over ϑ and χ. Let us consider the most characteristic cases:

1) Let the field $E_0(\vartheta,\chi)$ = const on the radiating surface with dimensions $L_\parallel = R\Delta\chi$ along the column axis and $\Delta\vartheta$ over the small azimuth. In this case (Fig.2a,b),

$$E_\delta^{(\ell,m)} \propto \frac{\sin\frac{1}{2}\,\ell\Delta\chi}{\ell}\,\frac{\sin\frac{1}{2}\,m\Delta\vartheta}{m} \qquad (2.9)$$

so that the spectral width of the exciting field is determined by the expressions

$$\Delta\ell \sim \frac{R}{L_\parallel}, \quad \Delta m \sim \frac{2\pi}{\Delta\vartheta} \tag{2.10}$$

2) It is possible to "squeeze" the spectral width by taking several, e.g. p, of such exciting fields and spacing them over the large azimuth along the torus with $\Delta\chi' = 2\pi/p$ between them. In this case (Fig.2b), the spectral width is diminished p times compared to relation (2.10), $\Delta\ell \sim (R/L_\parallel)/(1/p)$.

3) If the exciting field on the radiating surface does not depend on ϑ in the $\Delta\vartheta$ range and has the shape of the sinusoidal section in the χ-direction (Fig.2c)

$$E_0(\vartheta,\chi) \propto \cos k_{\parallel 0} R\chi \qquad (0 \leqslant \chi \leqslant \Delta\chi) \tag{2.11}$$

where $k_{\parallel 0}\, R \gg 1$, then we have

$$E_0^{(\ell,m)} \propto \left[\frac{\sin \frac{1}{2}(\ell-\bar{\ell})\Delta\chi}{\ell-\bar{\ell}} + \frac{\sin \frac{1}{2}(\ell+\bar{\ell})\Delta\chi}{\ell+\bar{\ell}} \right] \frac{\sin \frac{1}{2} m\Delta\vartheta}{m} \tag{2.12}$$

where $\bar{\ell} = k_{\parallel 0}\, R \gg 1$, and the spectral width is determined, as before, by the expression (2.10). However, in the spectrum over ℓ, the harmonics with small ℓ will be strongly damped as compared to expression (2.9): the amplitude (2.12) is markedly different from zero only for those ℓ that are close to the average value $\bar{\ell}$.

4) It should be noted that, for a given length $L_\parallel$ of the radiating surface, we can, in principle, broaden the spectrum $\Delta\ell$, which may, as will be shown below, substantially affect the operating regime of the exciting system. The spectrum of the system for which

$$E_0(\chi) \propto \cos \int k_0(\chi)\, R\, d\chi \qquad (0 \leqslant \chi \leqslant \Delta\chi) \tag{2.13}$$

where $k_0(\chi)$ is a weak function of $\chi (|dk_0/d\chi| \ll k_0^2\, R)$, is an example of such "broadened" spectrum.

For a linear profile,

$$k_0(\chi) = k_0 + k_0'\chi \quad (k_0'/k_0^2\, L_\parallel^2 \gg 1) \tag{2.14}$$

we obtain that the spectral density is a 'step' with a width

$$\Delta\ell = \ell_2 - \ell_1 \qquad (\ell_1 = k_0 R < \ell < \ell_2 = k_0 R + k_0' L_\parallel)$$

and the 'step' width $\Delta\ell = k_0' L_\parallel$ is considerably larger than the spectral width of the finite section of a sinusoid, $\Delta\ell = R/L_\parallel$.

Let us now consider the radiation of an exciting system of finite dimensions. For these systems, in the weak-damping case ($\tau \ll 1$), three operating regimes are characteristic. In the following, we shall restrict ourselves to the excitation of modes with fixed azimuthal number m.

2.1. Eigenmode resonances of separate or paired modes

The distance $\Delta\bar{n}^{(\ell)}$ between resonances with longitudinal numbers ℓ and $\ell + 1$ and fixed radial number n is equal to

$$\frac{\Delta\bar{n}^{(\ell)}}{\bar{n}} \sim \frac{2\ell + 1}{\bar{k}_A^2 R^2} \left(1 + \frac{\omega^2}{\omega_{Bi}^2}\right) \tag{2.15}$$

For not too large values of ℓ ($\ell < \ell_{max} \sim \bar{k}_A R$), the condition of excitation of a separate mode with this ℓ, $\Delta\bar{n}^{(\ell)} > \delta\bar{n}$, takes the form

$$2\ell \gg \left(\frac{R}{a}\right)^2 \bar{k}_A a \tau \left(1 + \frac{\omega^2}{\omega_{Bi}^2}\right)^{-1} \tag{2.16}$$

For large devices, this condition holds when the damping τ is sufficiently weak or the wave frequency ($\bar{k}_A = \omega/\bar{v}_A$) is small and modes with not too high $n \sim \bar{k}_A a$ are excited.

Note that condition (2.16) has a simple meaning: the damping decrement of a given eigenmode is significantly less than the distance between neighbouring frequencies. The condition for the existence of a paired-mode resonance, i.e. a resonance where modes with longitudinal numbers ℓ and $\ell + 1$ are excited simultaneously, coincides with expression (2.16).

2.2. Radiation regime in an endless cyclinder (multi-mode resonance regime)

If condition (2.16) is not fulfilled, the separate resonances overlap. If the antenna creates a broad oscillation spectrum ($\Delta\ell \gg 1$), excitation of a large number of modes with close ℓ-values takes place simultaneously so that these regimes may be called multi-mode (over ℓ) resonances. In this case, the electromagnetic waves propagating along the plasma column are damped at a distance from the

antennas less than the large radius of the torus so that this regime may also be called the radiation regime in an endless plasma cylinder.

For the multi-mode (over ℓ) resonance regime under consideration, two cases may be realized: In one of them, all resonantly excited modes have the same radial number n, in the other one, a group of modes with close values of n is excited.

a) Let us consider the first case. The resonant-curve width in the multi-mode resonance $\delta\bar{n}$ is considerably larger than that for separate-mode excitation, and for the exciting-field spectrum for which $\Delta\ell = \ell_2 - \ell_1 < \ell_1$ (see Fig.2c, d), it is determined by the spectral width $\Delta\ell$:

$$\frac{\delta\bar{n}}{\bar{n}} \sim 2\left(1 + \frac{\omega^2}{\omega_{Bi}^2}\right)\frac{\ell\Delta\ell}{\bar{k}_A^2 R^2} \tag{2.17}$$

Obviously, $\delta\bar{n}$, (2.17), should be smaller than the density change $\Delta\bar{n}^{(n)} \sim \bar{n}/\bar{k}_A a$, for which the next, (n + 1)-th radial mode is excited. This implies the following condition for the existence of the multi-mode (over ℓ) resonance with a fixed number n:

$$\frac{\Delta\ell}{\ell} < \frac{1}{2}\left(\frac{R}{a}\right)^2 \frac{\bar{k}_A a}{\ell^2} \left(1 + \frac{\omega^2}{\omega_{Bi}^2}\right)^{-1} \tag{2.18}$$

limiting the spectral width $\Delta\ell$ of the exciting field. The condition may be written in the following form by taking into account expression (2.10):

$$L_\parallel > \frac{k_\chi}{\bar{k}_A} a\left(1 + \frac{\omega^2}{\omega_{Bi}^2}\right) \tag{2.19}$$

This inequality has a simple meaning: resonant excitation of a separate radial mode takes place when the electromagnetic wave performs many oscillations between the column centre and the exciting system placed near the column boundary before it is emitted with a group velocity of

$$v_{g\parallel} = \frac{\partial\omega}{\partial k_\chi} \sim \frac{k_\chi}{\bar{k}_A^2} \omega\left(1 + \frac{\omega^2}{\omega_{Bi}^2}\right) \tag{2.20}$$

and leaves the antenna region.

Figure 1b shows, as an example, the power pumped into the plasma versus the density change in the case of a multi-mode resonance with a fixed radial number n for a current loop with a spectrum of the type represented in Fig.2c,d.

As will be seen from these figures, the power pumped into the plasma has the form of wide resonances corresponding to a sequential excitation of modes with radial numbers n, n + 1, ... (note that this excitation regime was investigated in Ref.[9] for the particular case of n = 1 and a spectrum similar to that of Fig.2c for an endless plasma cylinder). In the case of an exciting-field spectrum for which $\Delta\ell \gg \ell_1$ (see Fig.1a), condition (2.16) for the existence of eigenmode resonances may hold for sufficiently large values of ℓ, while it may break down for small values of ℓ. In this case, for a density corresponding to the condition of the mode resonances with small ℓ, the regime of overlapping resonances where, as at other densities, the eigenmodes will be excited will be present. Figure 1c shows a qualitative picture of such a regime.

b) The second case is realized when conditions (2.16) and (2.18) break down. Then groups of resonant modes with close values of ℓ from the interval $\bar{\ell} - \frac{1}{2}\Delta\ell < \ell < \bar{\ell} + \frac{1}{2}\Delta\ell$ and with various values of n are excited in the plasma. The energy pumped into the plasma depends weakly on the density (Fig.1d) because of overlap of resonances with neighbouring n. In this case, a condition opposite to inequality (2.19) holds, i.e. waves with different n have time enough to leave the antenna with a group velocity of $v_{g_\parallel}$ along the column before performing one oscillation along the radius.

The regime of multi-mode resonance when the spectrum over azimuthal numbers m is finite, may resemble these two regimes. In this case, the effect of changes in the plasma parameters on the antenna loading is weakened because of the simultaneous presence of several multi-mode (over ℓ) resonances for modes with different m.

2.3. Regime of radiation into half-space

Let us, finally, note one further possible operating regime of the exciting system, i.e. when wave damping occurs at a distance less than the plasma radius ($\tau > 1$). In this case, there are no reflection and interference effects leading to eigenmode resonances, and the coupling structure operates in a radiation regime similar to the radiation regime of the antenna in the infinite, or, more strictly, half-infinite medium (Fig.1e). Such a regime is realized for FMSW in large tori with sufficiently strong damping of these waves. (Excitation of FMSW with $\omega \sim \omega_{Bi}$ in this regime is discussed in Refs [1, 2].)

The power absorbed in the plasma is least sensitive, of all quantities, to changes in the plasma parameters. Therefore, in the radiation regime the demands on the excitation system and the RF power source may be simplified substantially.

3. EXCITATION OF FMSW BY CURRENT SHEATH

Let us consider the excitation of FMSW by a narrow current sheath placed in the vicinity of the plasma between the plasma and a metal screen. The current density in the loop is equal to

$$j_y = j_0 \delta(x-d) \qquad \left(|z| < \frac{L_\parallel}{2}\right) \tag{3.1}$$

where $L_\parallel$ is the loop width in the direction of the magnetic field ($L_\parallel \ll a$), d is the distance between loop and screen, and $j_0 = |j_0|\exp(-i\omega t)$ is the current per unit length of the loop (the total current in the loop $J = |j_0|L_\parallel$). Such loops are installed periodically along the Z-axis at the distance of $\Delta z = 2\pi R - L_\parallel$ from one another. (This system is a model for the excitation of axially symmetric waves by a single loop in a torus with a large radius R, $r \to -x$, $y \to r\vartheta$, $z \to R\chi$.)

Expanding j_y and the FMSW field in Fourier series and solving the Maxwell equations we easily obtain the impedance per unit length (along the y-axis) of the current sheath:

$$Z = Z_1 + iZ_2 = \frac{1}{j_0} E_y|_{x=d} \qquad |z| < \frac{1}{2} L_\parallel \tag{3.2}$$

The expression for Z has the form

$$Z = \sum_{\ell=-\infty}^{\infty} (Z_1^{(\ell)} + i Z_2^{(\ell)}) e^{ik_\parallel z} \tag{3.3}$$

where $k_\parallel = \ell/R$ and

$$Z_1^{(\ell)} = \frac{4\pi a_e}{cN_\perp} \frac{\tau(1+\cos\psi) + (1/2)\tau^2}{[(1+\cos\psi + \frac{1}{2}\tau^2)\eta - \sin\psi]^2 + \tau^2} \tag{3.4}$$

$$Z_2^{(\ell)} = \frac{4\pi a_e}{cN_\perp} \frac{(1+\cos\psi + (1/2)\tau^2)\eta - \sin\psi}{[(1+\cos\psi + \frac{1}{2}\tau^2)\eta - \sin\psi]^2 + \tau^2} \tag{3.5}$$

$$N_\perp = \frac{ck_{r0}}{\omega}, \qquad \eta = \frac{k_\parallel}{k_{r0}} \operatorname{cth} k_\parallel d, \qquad a_e = \frac{1}{\pi\ell} \sin\frac{\ell L_\parallel}{2R}$$

Here k_{r0} is the value of radial wave number at the plasma boundary. For narrow loops ($|k_\parallel z| \ll 1$), the impedance Z does not depend on the z-co-ordinate.

We have, for simplicity, assumed that plasma has a sharp boundary $a = r_2$ and $k_{r0}^2 > 0$. For an inhomogeneous plasma with a zone of wave evanescence, where $k_r^2 < 0$ and the width is given by

$$\Delta r \cong a - r_2 \sim \frac{k_\parallel^2 \bar{v}_A^2}{\omega^2} a \ll a$$

the analysis carried out here remains valid, by order of magnitude, for modes with $k_\parallel \Delta r < \pi$ (which penetrate well into the plasma) if in expressions (3.4) and (3.5) k_{r0} is replaced by

$$k_{r0} \equiv \bar{k}_A (\bar{k}_A a)^{-1/3}$$

Let us introduce the quality of the loop, i.e. the ratio of the oscillating (reactive) power to the power radiated by the loop, which can be expressed through the impedance

$$Q = \frac{Z_2}{Z_1} \tag{3.6}$$

The quantity Q vanishes at the resonance $Z_2 = 0$.

Consider the changes experienced by $Z_{1,2}^{(\ell)}$ because of a change in the plasma density $\bar{n}$. For $\bar{k}_A a \gg 1$, even a small change $\sim \bar{n}/\bar{k}_A a$ of the average plasma density leads to a change $\delta\psi \sim 1$ in ψ. Other quantities determining $Z_{1,2}^{(\ell)}$ depend on $\bar{n}$ more weakly. Therefore, we obtain the dependence of $Z_{1,2}^{(\ell)}$ on $\bar{n}$ considering how these quantities depend on ψ.

The quantity $Z_2^{(\ell)}$ vanishes and $Z_1^{(\ell)}$ is maximum when

$$\psi = \psi_{res} + 2\pi n \text{ for}$$

$$\sin\psi = \eta(1 + \cos\psi + \frac{1}{2}\tau^2) \tag{3.7}$$

This case corresponds to the resonant excitation of the mode with numbers $\ell = \ell_{res}$ and n. Then,

$$Z_1^{(\ell)} = \frac{4\pi a_e}{c N_\perp} \frac{1 + \cos\psi}{\tau} \tag{3.8}$$

When the density change is $\sim \bar{n}/(\bar{k}_A a)$ the impedance $Z_1^{(\ell)}$ diminishes $1/\tau^2$ times, and the resonance width $\delta\bar{n}$ is determined by formula (2.7).

If the non-overlap condition of separate resonances (2.16) holds, the separate mode $\ell = \ell_{res}$ (and $\ell = -\ell_{res}$) is excited so that the total impedance of the system is active and determined by the value (3.8), $Z \approx 2 Z_1^{(\ell_{res})}$. Near the resonance, the quantity Q can be small, $Q \lesssim 1$.

If the current in the loop j_0 is given, then under the conditions of the resonance considered, the power absorbed by the plasma is maximum:

$$P_{max} \propto Z_1^{(\ell_{res})} |j_0|^2 \propto \frac{|j_0|^2}{\tau} \tag{3.9}$$

On changing $\bar{n}$, P appears to consist of narrow peaks with widths $\delta\bar{n}$; P_{max} is $1/\tau$ times larger than the average value $\bar{P}$.

If the electric field intensity on the loop E_0 rather than current in the loop is given, the value of power pumped into the plasma

$$P \propto \frac{Z_1 |E_0|^2}{Z_1^2 + Z_2^2} \tag{3.10}$$

approaches its maximum on changing $\bar{n}$ at the resonance $Z_2 = 0$, when Z_1 is minimum. The equation $Z_2 = 0$ has, if condition (2.16) is fulfilled, the solution $\psi = \psi'_{res} + 2\pi n$, where ψ'_{res} is close to ψ_{res}. In this case, the two modes with $\ell = \ell_{res}$ and $\ell = \ell_{res} + 1$ are the largest in the sum over ℓ (other harmonics add only little) and

$$Z_1 = \frac{64\pi a_e}{c N_\perp} \frac{\tau}{(\Delta\psi)^2} \qquad (\eta < 1) \tag{3.11}$$

where $\Delta\psi = \psi(\ell_{res+1} + 1) - \psi(\ell_{res}) \sim 2(k_\parallel/\bar{k}_A)\,(a/R) < \pi$. Thus, in the case considered, all toroidal modes are excited; two modes have, however, the largest amplitudes; so it is natural to call this resonance a paired-mode resonance. In this case, the amplitude of the electric-field intensity assumes the smallest value on the loop, approaching its maximum on the opposite side of the torus. (The amplitude of the magnetic field intensity, on the contrary, approaches its maximum on the loop and its minimum on the side of the torus opposite to the loop.) This fact simplifies the problem of electrical insulation of the exciting antenna.

If the condition opposite to condition (2.16) holds, then, if

$$[(1 + \cos\psi + \frac{1}{2}\tau^2)\,\eta - \sin\psi]^2 \lesssim \tau^2 \tag{3.12}$$

is fulfilled, a large number of harmonics, $\ell_{res}-\delta\ell \lesssim \ell \lesssim \ell_{res}+\delta\ell$, where

$$\delta\ell \sim \tau \frac{R}{a}\frac{\bar{k}_A}{k_\parallel} \gg 1 \tag{3.13}$$

are excited simultaneously. These waves are damped at a distance from the exciting antenna less than R, and the distance between the natural frequencies appears to be smaller than the damping rate of the toroidal mode.

The contribution of the resonant modes to the impedance is given by

$$Z_{1\,res} \approx \frac{8\pi^2 a_e}{cN_\perp}\frac{1+\cos\psi}{1+\omega^2/\omega_{Bi}^2}\frac{R}{a}\frac{\bar{k}_A}{k_\parallel} \tag{3.14}$$

(The non-resonant harmonic contribution is small compared to (3.14)).

Figure 1c shows the behaviour of the impedance versus the density: the maximum of $Z_{1\,res}$ corresponds to the excitation of a group of modes with small ℓ_{res}. When the density increases, modes with large ℓ_{res} are excited, and $Z_{1\,res}$ diminishes proportionally to $1/\ell_{res}$; besides (see relation (2.16)), at sufficiently large ℓ_{res}, the overlap condition may break down; in this case, Z_1 will have sparse, narrow maxima (Fig.1c); a further increase in $\bar{n}$ will lead to the excitation of the $n+1-$th radial mode with small ℓ_{res} (second peak in Fig.1c) and so on. Such a picture is valid when $(a/R)\sqrt{n} < 1$. When $(a/R)\sqrt{n} > 1$, the harmonics n-1, n-2, ... contribute to the impedance Z_1, and the quantity Z_1 changes on increasing $\bar{n}$ more smoothly than is shown in Fig.1c (see Fig.1d).

If the damping is strong, the current sheath radiates into the plasma as if it were a half-infinite medium ($\rho = 0$). In this case, the impedance $Z_{1,2}^{(\ell)}$ is equal to

$$Z_1^{(\ell)} = \frac{4\pi a_e}{cN_\perp}\frac{1}{1+\eta^2} \tag{3.15}$$

$$Z_2^{(\ell)} = \frac{4\pi a_e}{cN_\perp}\frac{\eta}{1+\eta^2}$$

where $\eta = (k_\parallel/k_{r0})\,\mathrm{cth}\, k_\parallel d$. The quality of the loop for the ℓ-th harmonic is equal to

$$Q^{(\ell)} = \frac{Z_2^{(\ell)}}{Z_1^{(\ell)}} = \eta \tag{3.16}$$

With increasing density $n_0 = n_{|x=d|}$, the quantity $Z_1^{(\ell)}$ grows for $\eta > 1$, approaches maximum for $\eta \sim 1$ and diminishes for $\eta < 1$. The quantity $Z_2^{(\ell)}$

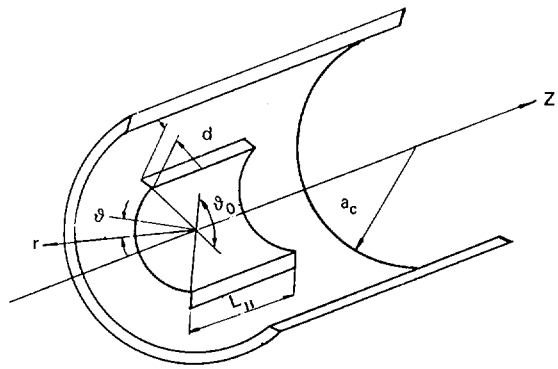


FIG.3. Exciting-current layer inside the vacuum chamber.

depends weakly on n_0 for $\eta > 1$ and diminishes proportionally to n_0 at $\eta \ll 1$. The quantity $Q^{(\ell)}$ diminishes monotonically with increasing n_0.

It is important that the quantities $Z_{1,2}^{(\ell)}$ and $Q^{(\ell)}$ are not too sensitive to changes in density: to change them twice, the change in density of $\delta\bar{n} \sim \bar{n}$ is required.

The presence of the screen leads to an increase in loop quality, and, for $k_{r0}d \ll 1$, the quality $Q^{(\ell)}$ is high; but for $k_{r0}d \gtrsim 1$, the quality is low, $Q^{(\ell)} \lesssim 1$, even if the conductive screen is present.

4. NUMERICAL TREATMENT OF FMSW EXCITATION BY A CURRENT SHEATH IN AN INHOMOGENEOUS PLASMA CYLINDER

In this section, results are presented of numerically treating FMSW excitation by a current sheath of finite dimensions along Z as well as along the azimuthal angle ϑ in an inhomogeneous plasma cylinder surrounded by a metal screen (Fig.3). Dimensions plasma and chamber correspond to the T-10 Tokamak: plasma radius a =35.5 cm, chamber radius a_c = 39 cm. The density profile is chosen in the form $n(r) = n_0(1-r^2/a^2)$. The magnetic field B = 40 kG and the frequency $\omega = 3.832 \times 10^8\ s^{-1}$ correspond to the resonance $\omega = 2\omega_{Bi}$ for deuterium. The current sheath width $L_\parallel$ = 50 cm, the azimuthal dimension $\vartheta_0 = \Delta\vartheta = 110°$, and the distance between current sheath and chamber d = 2.5 cm. The distance between the neighbouring atennas, $L = 2\pi R$, was assumed to be equal to 942.5 cm (one single antenna in the torus). In the calculations, a model of a solenoidal current sheath was used for which $\mathrm{div}\vec{j} = 0$.

Cyclotron absorption of RF oscillations in a plasma taking place in the resonant layer in a toroidal plasma under the condition $|\omega - 2\omega_{Bi}| < k_\parallel v_{Ti}$ was

simulated by using a dielectric permeability tensor in which only absorption due to collisions between electrons and ions was taken into account [14]. The value of ν_{ei} was chosen such that the value of τ (2.3) (by order of magnitude, $\tau \sim (m_e/m_i)/(\nu_{ei}/\omega)\bar{k}_A a$) corresponds to τ (5.1) for cyclotron absorption at the $\omega = 2\omega_{Bi}$ resonance, toroidal effects having been taken into account. In the following, all results are given for the case $\nu_{ei}/\omega = 10$, which is equivalent to taking account of ion cyclotron absorption in a toroidal plasma at $T_i \sim 1$ keV.

The electromagnetic field was calculated as a superposition of Fourier components,

$$E_\vartheta(r,\vartheta,z) = \sum_{m=-m_0}^{m=m_0} \sum_{\ell=0}^{\ell=\ell_0} E^{(\ell,m)}(r) e^{im\vartheta} \cos\frac{2\pi\ell}{L} z$$

where the function $E^{(\ell,m)}(r)$ was found by numerical integration of the second-order differential equation describing the propagation of the fast branch [12] of FMSW with fixed longitudinal and azimuthal wavenumbers, $k_\parallel = 2\pi\ell/L$ and m, respectively. In the present calculations, $\ell_0 = 100$, $m_0 = 9$, which corresponds to 1919 modes taken into account. The current density j_ϑ on the current layer was assumed to have no dependence on z and ϑ. The specific impedance of the current surface was calculated from the expression

$$Z = Z_1 + iZ_2 = \frac{1}{j_0}\left[E_\vartheta(z_1\vartheta) + \frac{2d}{r}\frac{\partial E_r(z,\vartheta)}{\partial\vartheta}\right]\Bigg|_{r=a_c-d} \qquad (4.1)$$

The average impedance is a convenient characteristic of the exciting current surface, this impedance being determined by the following expression:

$$\bar{Z}_{1,2} = \frac{1}{S}\int Z_{1,2}(z,\vartheta)dS \qquad (4.2)$$

where S is the antenna area.

Figures 4–7 show some results of the calculations. Figure 4 shows the density dependence of longitudinal and azimuthal mode numbers giving maximum contribution to the RF energy flux radiated into the plasma (resonant modes or modes close to the natural resonance). It follows from Fig.4 that, on varying the density from $n_0 = 5 \times 10^{13}$ cm^{-3} to $n_0 = 8.5 \times 10^{13}$ cm^{-3}, the radial number of resonant modes existing in a plasma grows from n = 4 at $n_0 > 5 \times 10^{13}$ cm^{-3} to n = 5 at $n_0 > 8 \times 10^{13}$ cm^{-3}. On increasing the density, the resonant modes

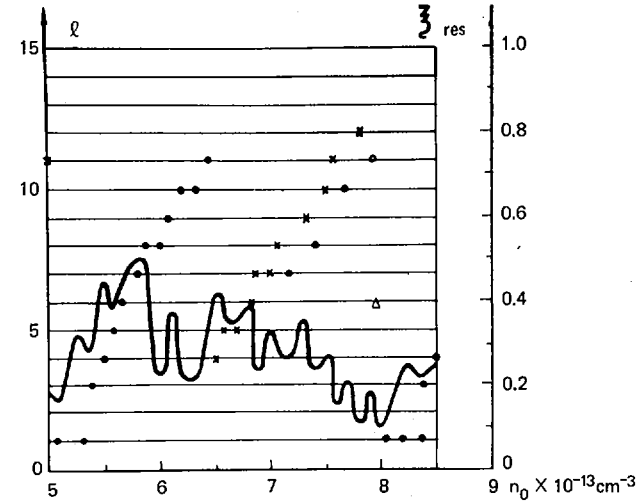


FIG.4. Resonant ℓ and ξ_{res} (ratio of absorbed power corresponding to the resonant mode to the total absorbed power) versus density n_0.
● – $m = 0$, × – $m = 1$, ○ – $m = -1$, Δ – $m = 2$.

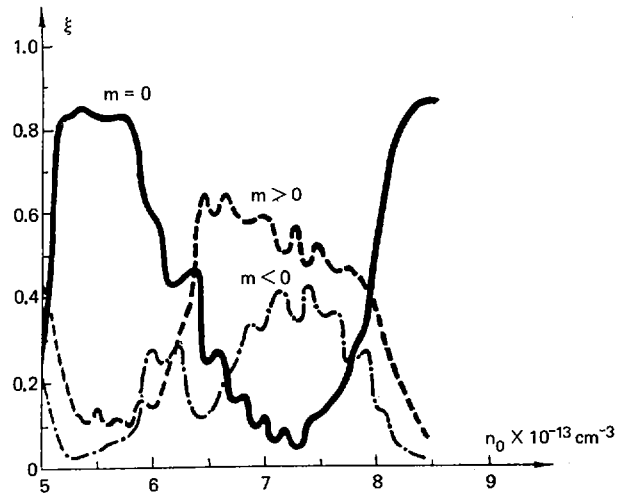


FIG.5. Total power of modes versus density: $m > 0$ (- - -), $m = 0$ (——), and $m < 0$ (– · – · –), in per cent of total power.

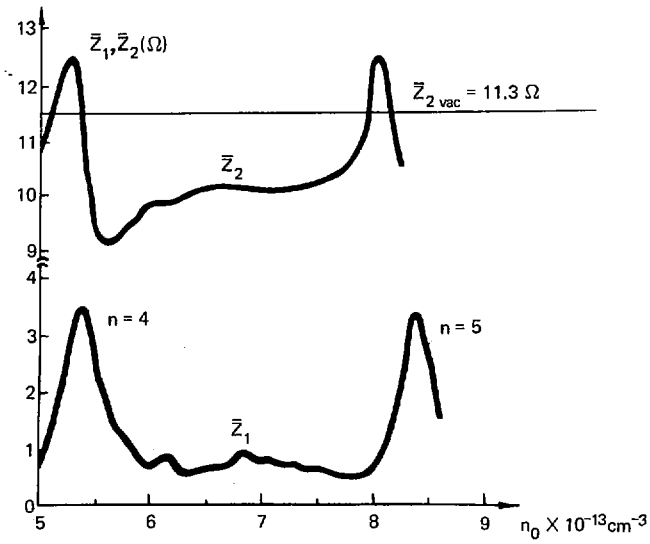


FIG.6. Impedances $\bar{Z}_1$ and $-\bar{Z}_2$ (in ohms) versus density (straight line corresponds to impedance of current layer when plasma is absent).

with given radial number n are excited first for symmetric oscillations (m = 0) and then for asymmetric ones (m ≠ 0). The relative power flux of the 'maximum' resonant mode divided by the total power flux is also presented here versus density. It is seen from Fig.4 that the energy flux of the maximum resonant mode does not exceed 40% of the total flux in the whole range of density variation, which indicates the multi-mode character of the excitation in this case.

Figure 5 shows a similar dependence of the relative total fluxes for all modes with m = 0, m > 0 or m < 0 on density. The maximum flux for modes with a given azimuthal number m occurs when the resonance for modes with small longitudinal wavenumber ℓ takes place, which agrees with formula (3.14). It is interesting that the power flux for modes with m > 0 is higher in the whole range of plasma density variation and at some densities it is even much higher than that for m < 0. In particular, this effect gives rise to azimuthal forces acting on the plasma column and leading to its rotation [15,16].

Figure 6 shows the values of active and reactive average impedances $\bar{Z}_1$ and $-\bar{Z}_2$ versus density. It also shows the vacuum value of the average impedance. As seen from Fig.6, we do not observe resonant effects in the behaviour of $\bar{Z}_{1,2}$ dut to the excitation of separate resonant modes. In particular, the reactive

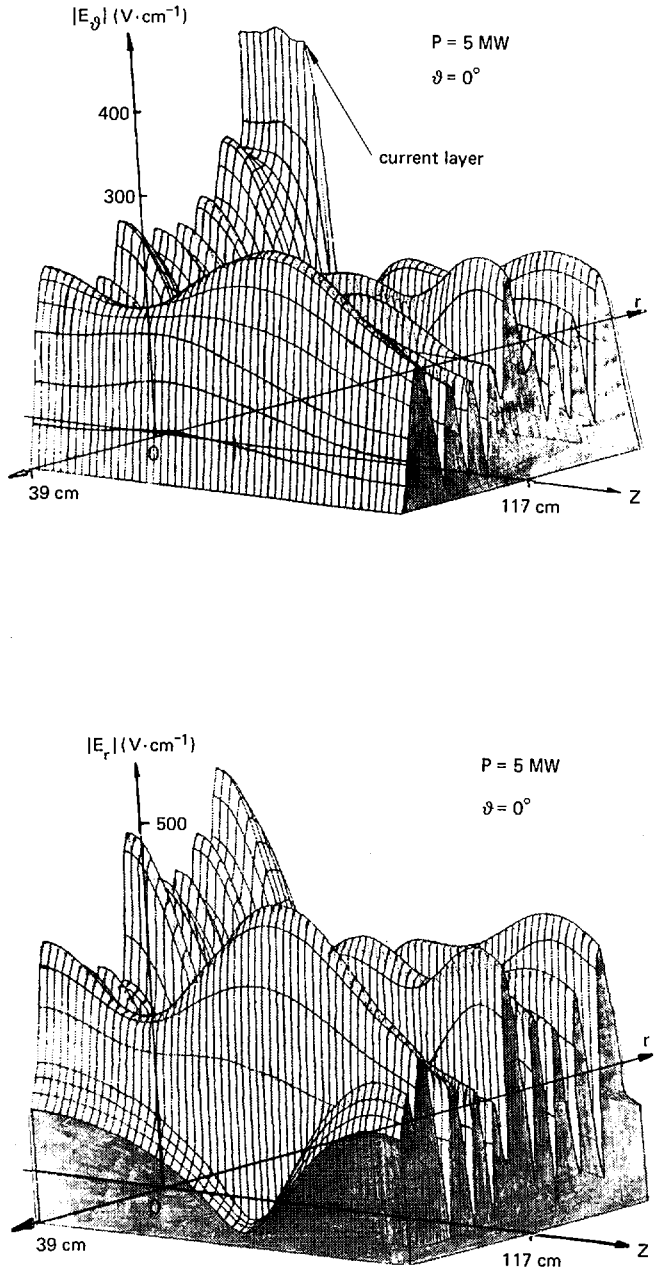


FIG. 7. Amplitude distributions of fields E_ϑ (a) and E_r (b) in the cross-section of the plasma column at $\vartheta = 0$ in the excitation system region for $n_0 = 7 \times 10^{13}$ cm^{-3} and $P = 5$ MW.

impedance $\bar{Z}_2$ remains positive (inductive) in the whole range of density variation. The appearance of a maximum in the behaviour of $\bar{Z}_1$ corresponds to the case of symmetric modes being resonant (m = 0) with low values of longitudinal wavenumbers ℓ ($|\ell| = 0, 1, 2, 3$). This case is similar to the excitation of the multi-mode resonance discussed earlier (Fig.1c). This case is, however, different essentially in that a finite spectrum over azimuthal wavenumbers m is also present. As a result of this, (1) the neighbouring resonances overlap in the whole range of density variation, (2) in a rather wide range of density variation, active and reactive impedances change relatively slightly, which allows us to establish a sufficiently steady load for the RF energy source when the density varies and the frequency is kept fixed. Note also that the quality, $Q = Z_2/Z_1 \sim 10$, is sufficiently small, which allows effective pumping of RF power under the conditions considered.

In Fig.7, as an example, the isometric pictures are shown of the field component distribution of E_ϑ (Fig.7a) and of E_r (Fig.7b) over the plasma column cross-section for the azimuthal angle $\vartheta = 0$ and the plasma density $n_0 = 7.1 \times 10^{13}$ cm^{-3} over the plasma column length from z = 0 to z = 117 cm (or over 1/8 from the plasma column perimeter for the T-10 tokamak). The field amplitudes correspond to power level of 5 MW pumped into the plasma. In Fig.7a, we observe an increase of the field amplitude E_ϑ on the exciting-current surface compared to the field in the plasma. However, the fields in the plasma and on the current surface differ not too much (approximately 1.7 times), and the maximum amplitude of the electric-field intensity on such a surface equal to $E_\vartheta = 433$ V·cm^{-1} is sufficiently low despite a rather high level of power going into the plasma, which is mainly due to the use of an extended exciting-current surface.

For the distributions presented, the complicated interference picture of the plasma fields is a characteristic feature indicating a multiplicity of excited oscillation modes. For the plasma density assumed ($n_0 = 7.1 \times 10^{13}$ cm^{-3}) mainly asymmetric modes with azimuthal numbers m = +1 and m = −1 are excited (Fig.5). This fact, in particular, leads to a highly advantageous field distribution from the point of view of localizing the absorption of RF power in the centre of the plasma column. (The amplitudes of the field components E_ϑ and E_r in the central area have relatively high values.)

Thus, the results numerically treating the FMSW excitation at $\omega = 2\omega_{Bi}$ for deuterium show that, under the conditions of the T-10 tokamak, the use of a current loop with finite longitudinal and azimuthal dimensions results in an overlap of separate-mode resonances; therefore, it is possible to carry out the RF power pumping at sufficiently steady parameters of the exciting system, a fact which relieves us of having to re-tune the frequency of the RF source during the heating pulse.

5. DISCUSSION OF THE RESULTS

As was shown above, the character of the FMSW excitation regime depends on the magnitude of τ. For a high-temperature plasma in tokamaks, the following types of FMSW damping are important: cyclotron damping at the fundamental frequency ($\omega = \omega_{Bi}$) and the first harmonic ($\omega = 2\omega_{Bi}$) [1–3], electron Cherenkov damping [10] and cyclotron resonance for a small addition of ions [11–13]. By using well-known expressions for the FMSW damping rates, it is not difficult to show that for cyclotron damping [1, 2]

$$\tau \sim \beta_i \bar{k}_A R \qquad (\omega = 2\omega_{Bi}) \tag{5.1}$$

$$\tau \sim \beta_i \bar{k}_A R \left(\frac{k_\parallel}{\bar{k}_A}\right)^2 \qquad (\omega = \omega_{Bi}) \tag{5.2}$$

where $\beta_i = 4\pi \bar{n} T_i / B^2$. The electron Cherenkov damping contribution to τ is equal to [10]

$$\tau \sim \beta_e \bar{k}_A a\, z_e e^{-z_e^2} \qquad \left(z_e = \frac{\omega}{\sqrt{2}\, k_\parallel v_{T_e}} \lesssim 1\right) \tag{5.3}$$

where $\beta_e = 4\pi \bar{n} T_e / B^2$. When there is a small group of resonant ions of density $\bar{n}' \ll \bar{n}$ in the plasma, we have [13]:

$$\begin{aligned} \tau &\sim \frac{\bar{n}'}{\bar{n}}\, \bar{k}_A R \qquad (\bar{n}' < \bar{n}'_{cr}) \\ \tau &\sim \frac{\bar{n}}{\bar{n}'} \left(\frac{k_\parallel v'_T}{\omega}\right)^2 \bar{k}_A R \qquad (\bar{n}' > \bar{n}_{cr}) \end{aligned} \tag{5.4}$$

where v'_T is the thermal velocity of the resonant ions, $\bar{n}'_{cr} \sim \bar{n}\, k_\parallel v'_T / \omega$.

The estimates (5.1) – (5.4) and the formulas from Sections 2 and 3 allow us to determine the conditions for FMSW excitation in the torus.

Since $\tau \propto a$ or $\tau \propto R$, the eigenmode resonance regime requiring small τ is, first of all, characteristic of small and the radiation regime of large systems. At the same time, for systems with intermediate parameters lying in a wide band it is, in principle, possible – in the same device – to achieve various regimes of wave excitation.

In a plasma with two ion species ($\bar{n}' \sim \bar{n}$), for an FMSW with a frequency between the cyclotron frequencies of the ions, a conversion of the fast mode into a slow one with a subsequent transformation of the slow mode into a plasma mode is possible [10]. If for these waves $\omega/k_{\parallel} \lesssim v_{Te}$, then in a plasma of large dimensions ($\bar{k}_A a \gg 1$) these waves are totally absorbed in the area where the fast wave is converted into a slow one ($\tau > 1$) so that in this case a regime of radiation into half-space is established.

This regime can also be realized when the plasma is heated by cyclotron resonance with 'impurity' ions, even in relatively small devices at $\bar{n}' \sim \bar{n}'_{cr}$.

When the $\omega = 2\omega_{Bi}$ resonance and electron Cherenkov damping are used in traps with reactor parameters, as a rule, the regime of overlapping resonances is formed ($a \sim 1$ m, $T_{i,e} = 1-5$ keV, $B \sim 50$ kG, $\bar{n} = 10^{13} - 10^{14}$ cm^{-3}), the radiation regime being possible in this case only for very large systems.

As $(k_{\parallel}/k_A)^2 \ll 1$ for large traps, then, at $\omega = \omega_{Bi}$, for resonances to overlap, considerably higher values R and T_i are required than at $\omega = 2\omega_{Bi}$.

In small system with $\omega \sim \omega_{Bi}$, it is possible to achieve regimes of excitation of a separate mode or of paired-mode resonances. In large systems, for these regimes to be realized, it is necessary to design exciting antennas with narrow spectra.

Our considerations allow us to draw the following conclusions:

1) The excitation resonances enable highly effective coupling of RF power to the plasma even if the excitation system is weakly coupled to the plasma cavity (e.g. for a small distance between the conductive chamber and the current loop and a large width of the evanescent zone between the loop and the dense-plasma region).

Use of the eigenmode resonance of the paired modes, apart from a high efficiency of excitation, allows us to obtain a low value of the loop impedance and, consequently, facilitates the solution to the problem of electric breakdown near the antenna.

A drawback of this regime is the necessity of changing, with time, the generator frequency, in line with the variations in the plasma parameters.

If sufficiently strong damping of waves with $\omega \sim \omega_{Bi}$ occurs, this regime cannot be established in large devices.

2) The resonance overlap regime (the radiation regime in an endless cylinder) is, first of all, achieved in devices with large perimeters, when a local excitation system generating a wide spectrum in ℓ and m numbers is used (it is also possible to use an extended excitation system of special type with a broadened spectrum, see relations (2.13) and (2.14)).

In this regime, the problem of resonance frequency tracking is greatly simplified, and for the multi-mode resonance over radial numbers there is no problem, at all.

3) The radiation regime in half-space occurs in systems with high values of $\bar{n}$, a and R when damping is sufficiently strong ($\tau > 1$). For this regime, it is almost unnecessary to track the frequency.

4) For the two last regimes, especially for the regime of radiation into half-space, it is more difficult to achieve high efficiency of the excitation system (low value of quality). (Perhaps, for this region the absence of excitation resonances on increasing the damping, e.g. in a plasma with two kinds of ions, is considered dramatic in the problem of RF plasma heating in large systems by FMSW for $\omega \sim \omega_{Bi}$.) However, as follows from the calculations presented, effective effective excitation is possible in these regimes, too. In these cases, the regimes mentioned prove to be even more useful than the regime of eigenmode resonances.

Thus, the investigation performed shows that FMSW in the frequency range $\omega \sim \omega_{Bi}$ can be coupled to the plasma with high efficiency in a device of small dimensions as well as in a reactor tokamak. In the latter case, regimes with multimode resonances and with radiation into half-space are preferred.

ACKNOWLEDGEMENTS

The authors would like to acknowledge many helpful discussions with V.V. Chechkin and V.D. Egorenkov.

REFERENCES

[1] GRIGOR'EVA, L.I., LONGINOV, A.V., PYATAK, A.I., SIZONENKO, V.L., SMERDOV, B.I., STEPANOV, K.N., CHECHKIN, V.V., in Plasma Physics and Controlled Nuclear Fusion Research (Proc. 4th Int. Conf. Madison, 1971) Vol. 3, IAEA, Vienna (1971) 573.

[2] LONGINOV, A.V., STEPANOV, K.N., Preprints KhFTI 72-1, 72-2, Kharkov (1972).

[3] ADAM, J., SAMAIN, A., Report EUR-CEA-FC-579, Fontenay-aux-Roses (1971) 29.

[4] STIX, T., in Plasma Heating in Toroidal Devices (Proc. 3rd Symp. Varenna, 1976), Bologna (1976) 156.

[5] IVANOV, N.V., KOVAN, I.A., LOS', E.V., Pis'ma Zh. Ehksp. Teor. Fiz. **14** (1971) 212.

[6] VDOVIN, V.L., RUSANOV, V.D., SHAPOTKOVSKIJ, N.V., Pis'ma Zh. Ehksp. Teor. Fiz. **14** (1971) 410.

[7] ADAM, J., CHANCE, M., EUBANK, H., GETTY, W., HINNOV, E., HOOKE, W., HOSEA, J., JOBES, F., PERKINS, F., SINCLAIR, R., SPERLING, J., TAKAHASHI, H., in Plasma Physics and Controlled Nuclear Fusion Research (Proc. 5th Int. Conf. Tokyo, 1974) Vol.1, IAEA, Vienna (1975) 65.

[8] EQUIPE TFR, in Plasma Physics and Controlled Nuclear Fusion Research (Proc. 6th Int. Conf. Berchtesgaden, 1976) Vol.3, IAEA, Vienna (1977) 39.

[9] STIX, T.H., The Theory of Plasma Waves, McGraw-Hill, New York (1962).

[10] KLIMA, R., LONGINOV, A.V., STEPANOV, K.N., Nucl. Fusion **15** (1975) 1157.

[11] LONGINOV, A.V., A Method of Heating Deuterium or Deuterium-Tritium Plasma, Author's Statement, N 342560, with a priority of 14 January, 1971, OIPOTZ N5 (1975).
[12] ADAM, J., Report EUR-CEA-FC-711, Fontenay-aux-Roses (1973);
[13] KLIMA, P., LONGINOV, A.V., STEPANOV, K.N., Zh. Tekh. Fiz. **46** (1976) 704.
[14] AKHIEZER, A.I., LAPSHIN, V.I., STEPANOV, K.N., Zh. Ehksp. Teor. Fiz. **70** (1976) 81.
[15] DOLGOPOLOV, V.V., Preprint KhFTI, 77-16, Kharkov (1977).
[16] NEMOV, V.V., Preprint KhFTI, 77-33, Kharkov (1977).

DISCUSSION

B. GREEN: In your numerical calculations you used a separation of 1 cm between coupling structure and plasma. How does the power coupling efficiency depend on this separation? And what would the separation be in a large, reactor-size tokamak?

K.N. STEPANOV: Coupling of high-frequency energy into the plasma remains effective as long as $k_{\parallel} d \leqslant 1$, where d is the plasma-antenna separation. In large tokamaks d could well reach values of several tens of centimeters (for small $k_{\parallel}$).

R.R. WEYNANTS: You mentioned in your talk the fear expressed by some authors in the past that the overlapping of the modes would lead to destructive interference in the plasma centre. Could you please repeat what it is in your calculations that prevents such a thing from happening?

K.N. STEPANOV: It is true that the effect of strong growth of the electric field due to interference was not found in our case. This strong growth of the electric field near the antenna, for a given transfer of power into the plasma, occurs in the case of narrow windings, as A.V. Longinov and V.A. Tsurikov have shown. With narrow windings there are a great number of harmonics with large ℓ which hardly penetrate the plasma at all because the zone of opacity is large for them: their field is concentrated near the antenna. The plasma is well penetrated by the field of a small number of harmonics with low values of ℓ, which must then provide the specified power coupling. It is this circumstance which leads to an increase of the overall field near the antenna.

K.V. ROBERTS: There would appear to be a useful analogy here with the interaction of particles such as neutrons with nuclei, where in some circumstances one can get strong individual resonances, and in other circumstances one can get many overlapping resonances and a smooth cross-section $\sigma(E)$ as a function of energy. Have you looked at the theory from this point of view?

K.N. STEPANOV: The smooth $\sigma(E)$ and $p(\overline{n})$ relations are in fact quite similar phenomena, and I think you are right that the analogy with neutron scattering might be useful.

Session Y

PLASMA HEATING III

Chairman

T. CONSOLI
France
Papers Y-4-1 and Y-4-2 were presented
by H. De Kluiver as Rapporteur

PLASMA PRODUCTION AND HEATING BY GLASS-CO_2-HYBRID LASER SYSTEM FOR MAGNETIC TRAPS

K.N. SATO, S. OKADA, T. SEKIGUCHI*,
T. FUKAGAWA
Institute of Plasma Physics,
Nagoya University,
Chikusa, Nagoya

M. AIZAWA, H. YASUDA
Department of Physics,
University of Tokyo,
Bunkyo, Tokyo

R. YOSHINO, H. SAITO
Department of Electrical Engineering,
University of Tokyo,
Bunkyo, Tokyo,
Japan

Abstract

PLASMA PRODUCTION AND HEATING BY GLASS-CO_2-HYBRID LASER SYSTEM FOR MAGNETIC TRAPS.

As an extension of a previous series of studies on filling a magnetic trap with pellet-initiated laser-produced plasma, preliminary experiments are performed on glass-CO_2-hybrid laser heating, in an attempt to produce plasmas with greater total ion number and higher ion energy. First, a comparison is made of the properties of plasmas produced by each laser pulse with identical laser parameters (except wavelength) in the absence and presence of external magnetic field. Then, the combined heating effect by, successively, irradiated glass and irradiated CO_2 (also CO_2-glass) laser pulse is examined by varying the time separation and output energy ratio of the two laser pulses. It is found that such a new method of laser heating is promising for future development as a hot plasma source.

---

* Also at Dept. of Physics and Dept.of Electrical Engineering, University of Tokyo, Bunkyo, Tokyo.

1. INTRODUCTION

A series of systematic studies has been reported by some of the present authors on laser-produced plasmas as a unique hot plasma source for magnetic traps. They include:

(a) production of hot plasmas with ion energy of keV range from a solid pellet (including deuterium ice) by pulsed Nd-glass laser beam(s) [1–3];
(b) physical processes involved in the interactions between rapidly expanding laser-produced plasma and surrounding magnetic fields [4];
(c) application of the studies of plasma confinement properties of magnetic traps (in particular, spindle cusp for high-β plasmas [5, 6] as an immediate application); and
(d) related theoretical problems, including computer simulations [7,8].

For this hot plasma source to be applicable to magnetic traps with a large effective plasma volume of interest to nuclear fusion, production of plasmas with much greater total ion number and higher temperature is required. In this connection, hot deuterium plasmas with initial electron temperature of nearly 500 eV (the ion kinetic energy of keV range) and total ion number of about 2×10^{17} have been achieved by a Nd-glass laser system with output energy ~70 J and pulse width ~20 ns [3]. However, when an increase in total ion number is attempted with a fixed output energy of a glass laser (by decreasing the peak power and increasing the pulse width, and thus resulting in lower ion energy), spatial anisotropy of plasma becomes unavoidably greater and this in turn decreases the trapping rate of plasma particles by magnetic fields.

The present paper reports two efforts undertaken to substantially improve this unsatisfactory situation:

(1) Comparison of the properties of plasmas produced by glass laser (1.06 μm) with those produced by CO_2 laser (10.6 μm) under nearly identical laser conditions;
(2) Effects of plasma production and heating by a glass-CO_2-hybrid laser system.

2. EXPERIMENTAL ARRANGEMENT

The experimental set-up is shown schematically in Fig.1. A pair of coils of 10 cm inner diameter are placed inside the vacuum container and produce an almost uniform magnetic field (B = 1.5 T maximum).

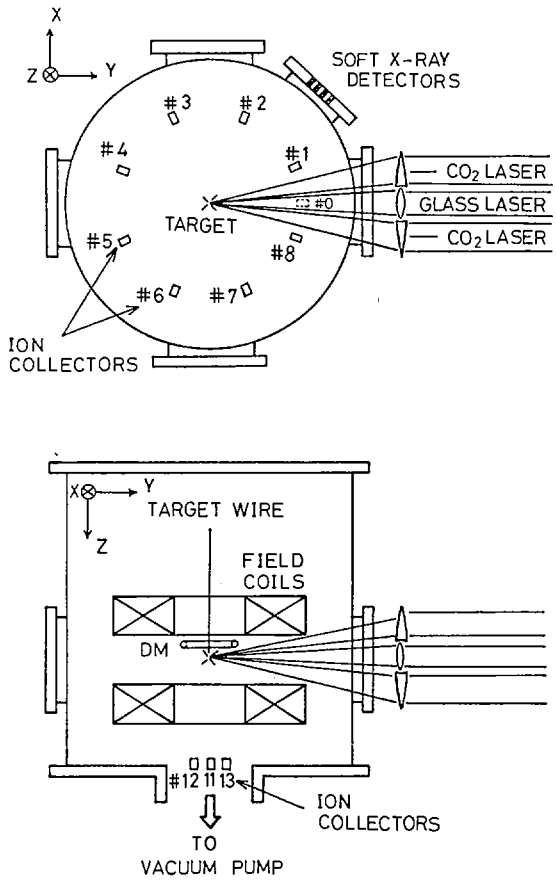


FIG.1. Experimental arrangement.

The laser target is either beryllium or aluminium wire of 50–150 μm diameter, suspended in a vacuum. The plasma is produced by means of a Nd-glass laser system and a CO_2 laser system, separately or simultaneously. The glass laser can deliver 100 J at 10–20 ns pulse width, and the CO_2 laser has an output of nearly 50 J in the first peak with 50 ns pulse width. To facilitate the comparison, however, identical laser parameters have been chosen for the two laser systems in the present series of experiments (30 J, 50 ns). The beam spot diameter of the glass laser is fixed at ~0.2 mm for the target size of 50 μm, while that of the CO_2 laser varies in the range of 0.2–3 mm. In the case of hybrid laser heating, as shown in Fig.1, both laser beams irradiate a tip of target wire from the same direction so that the glass laser beam propagates inside the hollow CO_2 laser beam.

TABLE I. TYPICAL RESULTS OF GLASS, CO_2 AND HYBRID-LASER HEATING

	A	B	C	D	E
	Nd glass only (30 J)	CO_2 only (30 J)	Hybrid Mixture Mode (15 J + 15 J)[a]	Hybrid Pre-Pulse Mode (3 J + 30 J)[b]	Reference for Pre-Pulse Mode[c] [CO_2 only, Y≠0]
T_e [keV] (by soft X-ray)	0.5	0.3(1.5)	0.5 ~ 0.7	–	–
$\bar{E}_i$ [keV]	1.2	0.23	0.71	–	–
E_i (#1)	1.2	0.28	1.24		
E_i (#11)	0.21	0.07	0.12		
σ_{E_i} (X-Y) (by ion collectors)	0.53	0.31	0.30		
N_e	3.2×10^{16}	2.3×10^{16}	6.7×10^{16}	1.2×10^{16}	1.0×10^{16}
N_e (#1)	6.0×10^{16}	3.4×10^{16}	7.0×10^{16}	1.5×10^{16}	1.4×10^{16}
N_e (#11)	0.37×10^{16}	1.2×10^{16}	6.4×10^{16}	0.5×10^{16}	0.2×10^{16}
σ_N (X-Y) (by ion collectors)	0.37	0.25	0.31	0.17	0.28
$N_i\bar{E}_i$ [J][d]	1.6	0.21	1.9	–	–
$N_i\bar{E}_i$ (#1)	3.2	0.38	3.5		
$N_i\bar{E}_i$ (#12)	0.03	0.04	0.33		
N_eT_e [J]	2.6	1.1	5.4 ~ 7.5	–	–

[a] $\tau_d = \tau_d$(opt.)

[b] E_L(Nd) = 3 J, $E_L(CO_2)$ = 30 J, $\phi_s(CO_2)$ = 1 mm, τ_d = 100 ns

[c] $E_L(CO_2)$ = 30 J, $\phi_s(CO_2)$ = 1 mm

[d] $N_i = N_e/Z$, Z = 4

For plasma diagnostics, a 4-channel soft X-ray absorption method determines the initial electron temperature (T_e). Many ion collectors are provided around the origin of plasma formation, as shown in Fig.1, to measure both the ion kinetic energy (by time of flight) in the absence of magnetic field and the ion flux density in the presence of magnetic field. A one-turn diamagnetic loop 8 cm in diameter is placed 2 cm away from the plasma origin, as seen in Fig.1. High-speed framing photography monitors possible particle escape across the magnetic field lines owing to plasma instabilities. However, no violent particle escape was observed in this series of experiments.

3. COMPARISON OF PROPERTIES OF PLASMAS PRODUCED BY GLASS-CO_2 LASER

3.1. Comparison in the absence of B

The experiments were performed under conditions of laser parameters such that the target material employed cannot be completely 'burned' (ionized) by the glass laser or CO_2 laser alone.

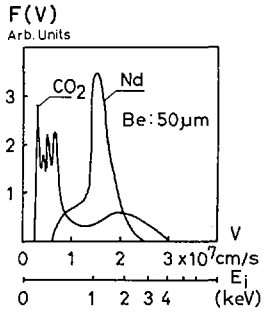


FIG.2. Difference of velocity distribution function of plasmas by two laser systems with beryllium target.

Typical results of experimentally determined velocity (energy) distributions of expanding ions produced are shown in Fig.2 for the two laser frequencies for a beryllium target 50 μm in diameter. Large discrepancies are seen in the form of the distribution functions as well as in the average ion energy $\bar{E}_i$ (see columns A and B in Table I). The simultaneously determined values of T_e are also shown in Table I). The simultaneously determined values of T_e are also shown in Table I, which indicates that the initial T_e value of glass-laser plasma is higher than that of CO_2 plasma, although the latter has a high energy component.

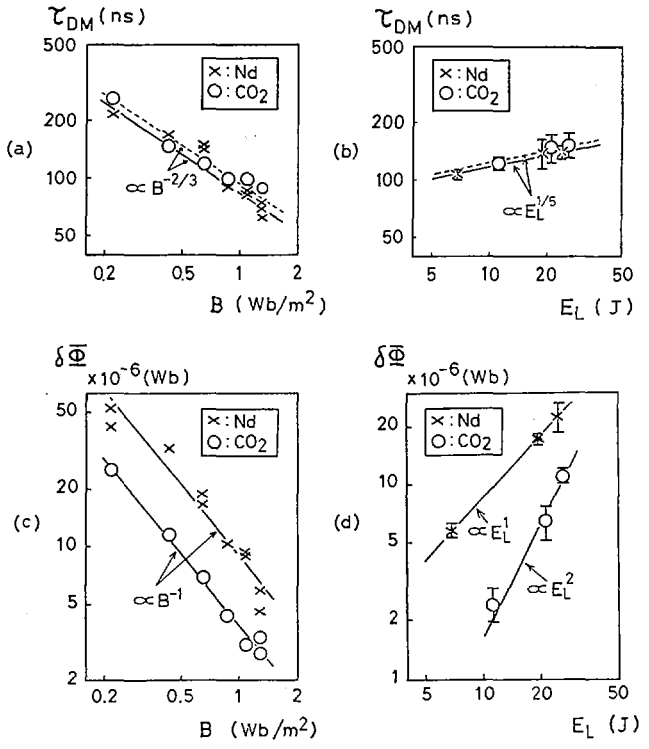


FIG.3. Variations of typical interaction time (τ_{DM}) and the excluded magnetic flux ($\delta\Phi$) versus B and E_L, respectively.

The total particle numbers $N_e = ZN_i$ (Z is the ion charge number) are also shown in Table I; the N_e values for the two cases are comparable. The overall laser energy absorption for the glass laser is therefore much higher than for the CO_2 laser.

The spatial isotropy in both particle number and energy in the case of the glass laser is found to have much decreased from that of the CO_2 laser. In Table I, the quantities $E_i(\#1)$ and $N_e(\#1)$ are the ion energy and time-integrated ion flux, both measured, respectively, by the collector #1 (see Fig.1); $E_i(\#11)$ and $N_e(\#11)$ are those measured by the collector #11. In Fig.1, σ stands for the standard deviation divided by the average value of the signals from collectors located in the X-Y plane. The suffixes N and E represent the particle number and energy, respectively.

3.2. Comparison in the presence of B

The laser-produced plasma expands very rapidly in the initial phase until the plasma pressure decreases to the same order of magnitude as the magnetic pressure. The radius of the plasma blob across the B-field then stops increasing and begins to decrease. The time that elapses until the plasma radius becomes maximum is denoted by τ_{DM}, which has been determined by the diamagnetic loop measurements. The variations of τ_{DM} versus B and versus E_L (laser energy) are shown in Fig.3(a) and (b), respectively. Similarly, those of the magnetic flux ($\delta\Phi$) excluded from the diamagnetic loop versus B and versus E_L are given in Fig.3(c) and (d), respectively.

No discrepancy has essentially been found for the functional dependences between the two wavelength cases for Fig. 3(a) – (c). The $B^{-2/3}$ dependence in Fig.3(a) is consistent with the result of other experiments [9] as well as with the theoretical result based on our simplified oscillation model. However, the same theoretical model predicts $\tau_{DM} \propto E_L^{1/12}$, while the experimental result indicates $\tau_{DM} \propto E_L^{1/5}$ (Fig.3(b)). The excluded magnetic flux $\delta\Phi$, which is proportional to nTS/B (S is the cross-sectional area normal to B), should be proportional to $B^{-1/3}E_L^{1/3}$, whereas the corresponding experimental dependence is seen to be nearly $B^{-1}E_L^{\alpha}$ ($\alpha \gtrsim 1$) (see Fig.3(c) and (d)). In addition, the functional dependence of $\delta\Phi$ on E_L is different between the two wavelength cases (Fig.3 (d)). These remain to be clarified.

4. EFFECTS OF GLASS-CO_2-LASER HYBRID HEATING

Here, two different modes of laser operation are considered for hybrid-laser heating, referred to hereafter as *mixture-mode operation* and *prepulse-mode operation*, respectively. In the former, both the laser output energy (E_L) and focal beam diameter (ϕ_s) of the glass laser are taken to be nearly identical with those of the CO_2 laser (E_L = 30 J and $\phi_s \sim 0.2$ mm in these experiments), while in the latter the conditions E_L (glass) $< E_L$ (CO_2) and ϕ_s (glass) $\ll \phi_s$ (CO_2) are chosen (ϕ_s (glass) ~ 0.2 mm, ϕ_s (CO_2) = 1 $\sim$ 3 mm).

4.1. Results of mixture-mode operation

(a) In the absence of magnetic field, as shown in columns A and B of Table I, both the energy and particle number of ions produced in the X-Y plane (Fig.1) are very different from those in the Z-direction (compare E_i (#1) and N_e(#1) with E_i (#11) and N_e (#11), respectively), and this spatial anisotropy is more pronounced in the glass laser. This tendency also persists in hybrid-laser heating.

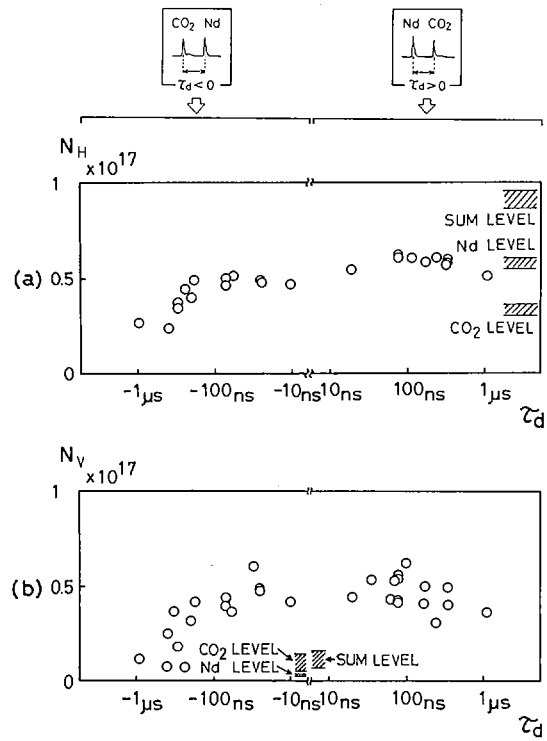


FIG.4. Dependence of the ion particle numbers on the time separation of two laser pulses (τ_d).
(a) Ion number in the X-Y plane (N_H) by #1 collector versus τ_d.
(b) Ion number in the Z-direction (N_V) by #11 collector versus τ_d.

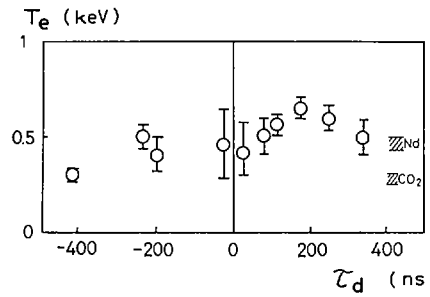


FIG.5. Electron temperature by soft X-ray measurement versus τ_d.

The effect of hybrid-laser heating is shown in Fig.4, where the ion particle number in the X-Y plane (measured by #1 collector, denoted by N_H in Fig.4(a)) as well as that in the Z-direction (measured by #11 collector, denoted by N_V in Fig.4(b)) is given as the function of the time separation (τ_d) between the glass-CO_2 laser pulse for fixed laser energies (E_L(glass) $\cong$ E_L(CO_2) $\sim$ 30 J). As indicated in Fig.4, the value of τ_d is taken positive when the glass-laser pulse precedes the CO_2-laser pulse. The horizontal shaded level, labelled 'Nd level' or 'CO_2 level', indicates the N-value corresponding to the glass-laser or CO_2-laser irradiation alone, and 'sum level' means the simple sum of these two levels.

The experimental results shown in Fig.4 indicate that no anomaly occurs in the variation of N_H with τ_d, approaching the CO_2 level and the Nd level at the negative and positive end of τ_d respectively, and varying only gradually between those ends (Fig.4(a)). This is not the case for N_V, i.e. a large relative enhancement of the N_V-value is seen to occur in the hybrid laser irradiation (Fig.4(b)). As seen in Table I, the total ion number produced (N_i) increases by a factor of 2–3.

In this hybrid laser irradiation, the initial T_e-value (obtained by soft X-ray measurement) also exhibits a slight increase in a narrow region of τ_d (= +100 – 300 ns) (from 0.3 – 0.5 keV to 0.5 – 0.7 keV; see Fig.5 and Table I).

(b) In the presence of magnetic field. The results of diamagnetic loop measurements are shown in Fig.6. The two separate diamagnetic signals corresponding to each laser shot are observed in the range of $|\tau_d| \gtrsim 50$ ns. In the negative τ_d region, the two signal levels do not differ essentially from those obtained from each laser shot alone (indicated again as 'Nd level' and 'CO_2 level').

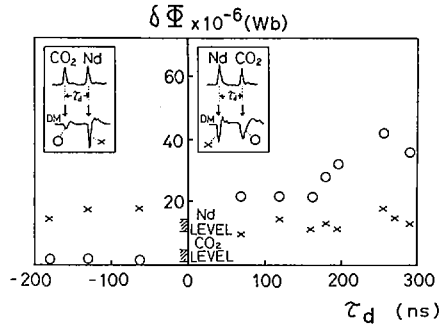


FIG.6. The results of diamagnetic measurements; excluded magnetic flux versus τ_d.

An anomaly does arise in the positive τ_d region, i.e. although the level of diamagnetic signal corresponding to the preceding glass-laser pulse is almost identical with the Nd level, the one corresponding to the subsequent CO_2-laser

pulse increases astonishingly by a factor of 10–20 in a wider region of τ_d. It is interesting to note that the region of $\tau_d = +150 - 300$ ns, where the signal enhancement is particularly pronounced, coincides with the τ_d region where an increase in the T_e value is observed (Fig.5).

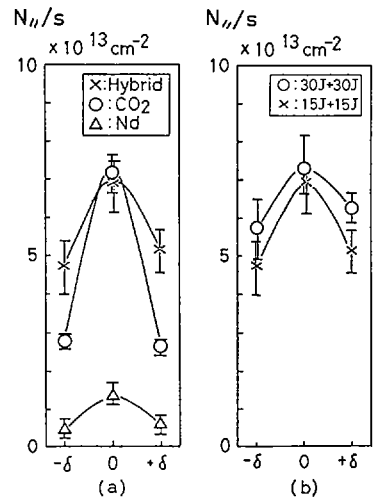


FIG.7. Spatial distribution of the time-integrated ion flux density ($N_{\parallel}/S$) measured by ion collectors #11–13.

Figure 7 shows the time-integrated flux density of ions ($N_{\parallel}/S$) streaming along the magnetic field lines (B) which has been measured by the ion collectors #11–13 (Fig.1). One result seen from Fig.7(a) is that for individual laser shots the relation $N_{\parallel}$ (glass) $\ll N_{\parallel}$ (CO_2) holds, and this appears to reflect a stronger spatial anisotropy of plasmas produced in the glass laser case in the absence of B (Table I). When plasma is produced by the hybrid-laser shots, the value of $N_{\parallel}/S$ near the central region of the ion stream remains almost the same as the value produced by the CO_2 laser shot alone, but an increase is seen to occur in the outer region of the plasma stream, implying an increase in the radius of the plasma stream. An estimate indicates that the total particle number flowing in both directions of the B-field in this case increases remarkably and approaches the total number of particles produced in the absence of B.

Figure 7(b) shows the effect of the energy level of the hybrid-laser system on $N_{\parallel}/S$ for a beryllium target wire 50 μm in diameter, as an example. It is seen that the difference between the case of E_L (glass) = E_L (CO_2) ~ 15 J (total ~ 30 J) and that of E_L (glass) = E_L (CO_2) ~ 30 J (total ~ 60 J) is minor, and this suggests that a total laser energy of nearly 100 J is required to achieve almost complete burning of the target material in this case.

(c) Summary of preliminary experiments for the mixture-mode operation of hybrid-laser heating: (i) If the time separation (τ_d) between the glass-CO_2-laser pulse is properly chosen ($\tau_d = -0.2 - +1$ μs) in the absence of magnetic field, the total number of particles produced becomes larger than the simple sum of that for each laser shot. Simultaneously, an existing strong spatial anisotropy, which is particularly pronounced for the glass laser, is considerably diminished and approaches an isotropic plasma expansion; and (ii) although the average ion energy remains almost the same as that in the glass-laser shot alone, the trapping rate of particles by magnetic fields (and thus the total ion number streaming along the B-field lines) substantially increases for the reasons mentioned in (i) above. The results obtained are summarized in Table I.

The following possible interpretations for these phenomena may be considered: the preceding glass-laser pulse produces a weakly ionized plasma or dense neutral gas or a certain spatial distribution of plasma parameters which are appropriate for the subsequent longer-wavelength CO_2-laser pulse to ionize and heat to very high temperature. Detailed studies for the physical mechanisms involved have yet to be performed.

4.2. Results of prepulse-mode operation

In the present experiments, the following conditions have been chosen for the prepulse mode of operation: E_L (glass) $\sim$ 3 J; E_L (CO_2) $\sim$ 30 J; ϕ_s (glass) $\sim$ 0.2 mm; ϕ_s (CO_2) $\sim$ 1 mm. The τ_d value has been varied only in the range of $\tau_d > 0$. The results so far obtained indicate that both the N_V value (Fig.4(b)) and the total ion number N_e increase slightly in the region $\tau_d = 0 - 3$ μs (Table I), but these effects are less significant than in the case of the mixture-mode operation for the experimental conditions. This mode of operation appears to deserve further exploration by varying the combination of laser parameters.

5. CONCLUDING REMARKS

As a candidate for producing laser plasmas with greater total ion number and higher ion energy, glass-CO_2-hybrid laser heating has been adopted and preliminary experiments performed. The combination of laser parameters and the size of the wire target have been intentionally chosen such that the target material is not completely 'burned' (ionized) by each laser system alone.

First, the property of plasmas produced by each laser system has been compared, and the results indicate that the glass laser is better than the CO_2 laser for producing plasmas with higher initial temperature and ion energy, but gives rise to a pronounced spatial anisotropy. The contrary is the case for the CO_2 laser. Consequently, in the presence of magnetic field, the total particle number

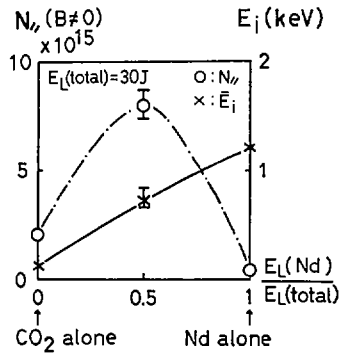


FIG.8. Average ion kinetic energy (E_i) in the absence of B and the total ion number flowing along B-lines $N_{\parallel}$ ($B \neq 0$) estimated by the measured values by collectors #11–13 with various laser heating systems.

contained in the plasma stream along the field lines is much larger for the CO_2 laser than the glass laser.

The hybrid-laser system can combine the merits of both systems, and the results of preliminary experiments have revealed that, for a fixed total laser energy, the hybrid-laser system may produce plasmas with larger particle number, better spatial isotropy and ion energy as high as in the glass laser alone. As a result, the total particle number contained in the plasma stream along magnetic field lines has increased substantially. The results are summarized in Fig.8.

The problem of plasma production and heating by a many-directional multi-beam hybrid-frequency laser system and a nearly spherical target pellet ought to be addressed in the future.

REFERENCES

[1] TANIMOTO, T., et al., J. Phys. E **5** (1972) 27.
[2] KITZUNEZAKI, A., et al., Plasma Phys. **17** (1975) 875.
[3] SATO, K.N., et al., Proc. 9th Symp. on Fusion Technology (Garmisch-Partenkirchen, 1976, p. 879; Proc. 3rd Int. Mtg. on Heating of Toroidal Plasmas, Grenoble, 1976, CEA-CR-10, CEA, Paris (1976) Vol.2, p.367; Plasma Physics and Controlled Nuclear Fusion Research 1976 (Proc. 6th Int. Conf. Berchtesgaden, 1976) Vol.2, IAEA, Vienna (1977) 567; Laser Interaction of Related Plasma Phenomena (Proc. 4th Workshop, Troy, N.Y., 1976), Plenum, N.Y. (1977) Part A, p.333.
[4] SUDO, S., et al., J. Phys. D **11** (1978) 389.
[5] KITZUNEZAKI, A., et al., Phys. Fluids **17** (1974) 1875.
[6] KOGOSHI, S., et al., J. Phys. D **11** (1978) 1057.
[7] OHWADANO, Y., et al., Jpn. J. Appl. Phys. **16** (1977) 1025.
[8] YOSHINO, R., et al., J. Phys. Soc. Jpn. **44** (1978) 1694.
[9] HAUGHT, A.F., et al., Phys. Fluids **13** (1970) 2842.

DISCUSSION

F.R. SCHWIRZKE: Is it possible that self-generated magnetic fields cause the anisotropy in the plasma produced by the Nd-laser? What in fact do you think is the influence of self-generated magnetic fields on the results?

K.N. SATO: We have run separate experiments on self-generated magnetic fields, thin-wire targets and plane targets. In the case of the plane target, the spatial profile of the plasma produced appears to be affected, to some extent, by a self-generated magnetic field. However, it has been observed that this effect tends to be less pronounced in the case of the thin-wire target (with the laser focal-spot diameter greater than the target diameter). For our purposes, at any rate, we intend to employ multilaser beams to obtain further improvement in the spatial isotropy (which is important for efficient plasma trapping by magnetic fields); the effects of self-generated magnetic fields should then not be serious.

H.J. HOPMAN: How does the number of trapped ions vary with laser power density (10^{12} W · cm^{-2} in your case) at constant laser energy?

K.N. SATO: There are two parameters which can be manipulated to vary the laser power density at constant laser energy: one can vary the pulse width or the laser spot size. The situation is accordingly somewhat complicated, but we have observed that there are optimum values for both parameters. For example, making the pulse width very short or the laser spot size large decreases the number of particles produced, and the opposite conditions lead to a pronounced anisotropy of plasma expansion. The trapped-particle number depends not only on the particles produced but also on the spatial isotropy of plasma expansion.

L.L. LENGYEL: As you know, our group at Garching has investigated the same question (multi-pulse heating of pellets) both theoretically and experimentally. Results of computations on pellet heating of hybrid frequencies were presented two years ago in Berchtesgaden. Your results are in general in agreement with the results of our studies, except in two respects: you observe higher maximum temperatures and worse plasma homogeneity at the Nd wavelength. Since the critical density for the CO_2 laser wavelength is two orders of magnitude lower than that corresponding to an Nd laser, you heat a low-density layer with a CO_2 laser; thus the peak temperature should be higher than in the case of an Nd laser. By the same token (i.e. by heating the plasma far away from the high-density core) the homogeneity of the temperature should be worse in the case of the CO_2 laser pulse. How do you explain these phenomena?

K.N. SATO: We believe that these are the first experimental results reported which give a precise comparison of heating effects obtained with glass lasers and CO_2 lasers as well as laser heating by means of the hybrid-wavelength laser system. As we have mentioned, the experiments were carefully designed in the sense that we intentionally chose identical laser parameters (laser total output energy, pulse duration and focal spot size, though not wavelength) and target parameters. Now,

in response to your questions, I must say that the experimental facts we have observed are just opposite to what you are saying; in point of fact the glass laser produces higher ion energy together with pronounced spatial anisotropy, whereas the contrary is true in the case of the CO_2 laser. Your theoretical inference is understandable, and the absorption length in the glass laser case is shorter than that in the CO_2 laser case, so that the laser energy is deposited within a more limited plasma volume in the glass laser case than in the CO_2 laser case. This tends to counterbalance the absorption mechanisms which you were referring to. Anyhow, I think we can conclude that further detailed studies will have to be made before we can arrive at a satisfactory interpretation.

INVESTIGATION OF PLASMA HEATING BY POWERFUL RELATIVISTIC ELECTRON BEAMS

A.V. ARZHANNIKOV, A.V. BURDAKOV, B.N. BREJZMAN,
A.S. BURMASOV, L.N. VYACHESLAVOV, V.S. KOJDAN,
V.V. KONYUKHOV, V.A. KORNILOV, Eh.P. KRUGLYAKOV,
V.N. LUK'YANOV, K.I. MEKLER, A.A. PODYMINOGIN,
A.I. ROGOZIN, D.D. RYUTOV
Institut of Nuclear Physics,
Novosibirsk, Union of Soviet Socialist Republics

Abstract

INVESTIGATION OF PLASMA HEATING BY POWERFUL RELATIVISTIC ELECTRON BEAMS.

The results of investigations on plasma heating by relativistic electron beams, conducted at the Institute of Nuclear Physics, which are an integral part of the programme of investigating the possibility of creating a thermonuclear reactor based on solenoid systems, are outlined. The results of experiments on the interaction of high-current relativistic electron beams and a plasma, carried out on the GOL-1 and INAR devices, are presented. – Experiments on beam transport in a plasma ($n_e \cong 10^{14}$ cm^{-3}) in two magnetic-field configurations: homogeneous (L = 7.5 m) and multi-mirror (L = 3.5 m), were carried out on the GOL-1 device. No macroscopic beam instabilities were found. The interaction of the beam with the plasma was investigated simultaneously with the beam transport ($n_e \cong 10^{14}$ cm^{-3} and H_0 = 13 kOe). Approximately 5% of energy per metre is released in the plasma at j_b = 1 kA·cm^{-2}. – A series of experiments was carried out on the INAR device, whose purpose it was to clarify the possibility of heating a plasma with a density of $n \sim 10^{15}$ cm^{-3}. It is shown that a decrease in the angular spread of the injected beam by reducing the thickness of the input foil and also the use of a strong magnetic field lead to an increase in the energy release in the plasma column; the most effective heating is observed, in this case, at the beam input into the plasma. At H_0 = 25 kOe, j_b = 1 kA·cm^{-2} and at an input foil thickness of 6 μm (Ti), the relative beam energy losses in a plasma with density of $n = 4 \times 10^{14}$ cm^{-3} amounted to 20% on a length of 240 cm. A plasma heating efficiency of 10–15% of the total beam energy at a density of $n = 3 \times 10^{15}$ cm^{-3} was achieved with an increase in the beam current density of up to 5 kA·cm^{-2}. The strong dependence of the energy release in the plasma on the angular beam spread as well as its non-uniformity over the length of the device indicate that a beam instability should play the main role.

1. INTRODUCTION

Investigations of plasma heating by relativistic electron beams, carried out at the Institute of Nuclear Physics, are an integral part of the programme for the development of a physical model of a thermonuclear reactor based on solenoid (specifically, multi-mirror) devices.

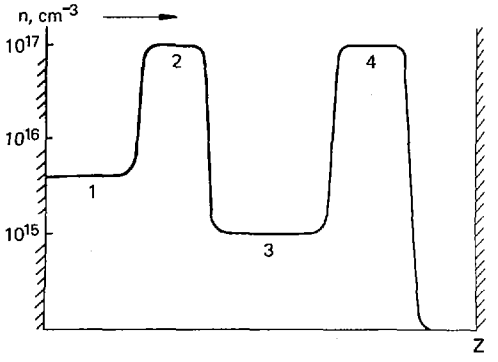


FIG.1. Plasma density distribution along the device with 'two-stage' heating scheme: 1) transport section; 2) and 4) dense plasma bunches; 3) energy release zone. Dashed line denotes ends of device and arrow shows direction of beam injection.

We assume that a dense plasma ($n \sim 10^{17}-10^{18}$ cm^{-3}) (see Fig. 1) will be created in the central part of such device. Our present ideas imply that the simplest method of solving problems of beam transport towards this plasma and of energy release in it is the use of a 'two-stage' heating scheme [1]. Its essence is that a zone with relatively low density ($n \sim 10^{15}$ cm^{-3}), where the beam loses its energy owing to a beam instability and from where the energy is transferred to the denser plasma by electron thermal conductivity, is created between two bunches of dense plasma.

It has now been established rather dependably (both theoretically [1] and experimentally [2]) that the plasma heating efficiency decreases as its density increases if the beam densities are not high enough ($n_b/n < 10^{-3}$). Therefore, the beam will interact with the plasma mainly in section 3 where the density is minimum in the density profile shown in Fig. 1. By choosing the length of this section in the manner required, one may be certain that the relativistic electrons leave a significant fraction of their energy on it. With regard to the transport section (1), the losses here will be significantly less, since $n_1 \gg n_3$ (it is only necessary to provide macroscopic beam stability during the transport). It is natural that the plasma density in section 1 should be much lower than that in sections 2 and 4 since otherwise the dense plasma would rapidly cool down owing to the electron thermal conductivity to the ends. We note that heating of only a small portion of the electrons rather than of all of them is permitted in section 3. This is quite acceptable if the length of the free path of the "hot" electrons in zones 2 and 4 is less than the length of these zones. Heating the main mass of the plasma is thus provided by pair collisions, which removes the rather rigid constraints on the beam parameters existing in collective methods of dense-plasma

heating. Since the transit time of a "hot" electron through zone 3 is short compared to the beam duration, the situation in this zone should be quasi-steady: energy release compensates the outflow of heat caused by the departure of "hot" electrons to zones 2 and 4.

The following problems must be solved for a successful functioning of this scheme in application to a multi-mirror reactor: 1) provide beam transport with a current up to 200 kA in a uniform and multi-mirror magnetic field; 2) provide release of beam energy in a plasma with a density of the order of 10^{15} cm^{-3}. A report is given below on investigations conducted at the Institute of Nuclear Physics in this direction.

2. TRANSPORT OF RELATIVISTIC ELECTRON BEAMS AND HEATING IN GOL-1

2.1. Description of device

A diagram of the GOL-1 device [3] is presented in Fig. 2. The source of relativistic electron beams in the device is the 'Vodyanoj' high-current accelerator [4]. The accelerator diode is separated from the vacuum chamber of the device by a titanium anode foil 50-μm thick. The beam at the input into the chamber has the following parameters: total energy Q up to 1 kJ, current I_b up to 55 kA, half-width of the current pulse $\Delta t_{1/2}$ = 35 ns and cross-section S_b = 45 cm^2.

The vacuum chamber with an inner diameter of 13 cm is made of stainless steel 3 mm thick and has more than 60 windows for measuring the beam and plasma parameters. The total length of the chamber is $L \cong 7.5$ m.

A hydrogen plasma was created by three oscillating high-voltage (up to 50 kV) discharges with ring-shaped electrodes (the inner diameter of the electrodes was 9 cm). The plasma density distribution along the radius and the length was first investigated by double Langmuir probes. The plasma density in experiments with relativistic electron beams was measured by three Michelson interferometers at a wavelength of λ = 10.6 μm [5]. With the indicated method of preparation, it was possible to create a plasma with a maximum density of up to 2×10^{14} cm^{-3} and a radial inhomogeneity of the order of 10 percent.

The total current in the system was measured by several wall shunts and magnetic probes. The current distribution of the relativistic electron beams over the cross-section was monitored by movable Faraday micro-cylinders. The energy content of the plasma was determined by diamagnetic measurements using probes located at a number of points along the length of the device. A graphite calorimeter, joined to the beam current collector, was located at the output end of the system. The collector-calorimeter was separated from the plasma by a 12-μm thick titanium foil.

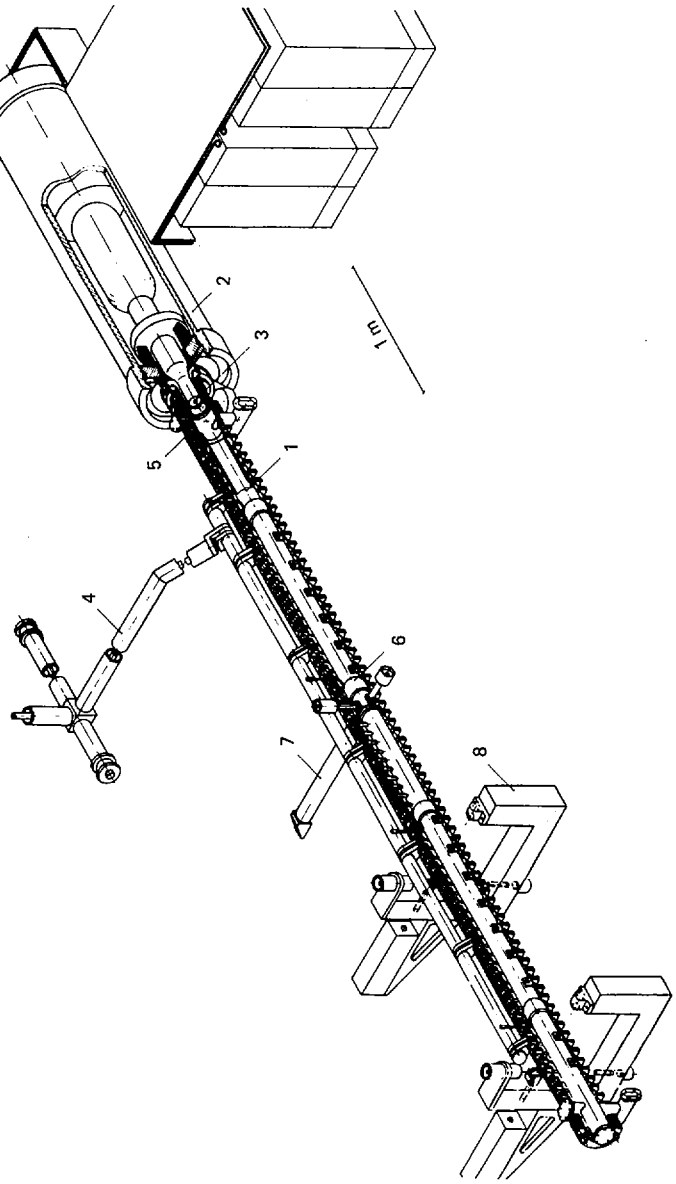


FIG.2. GOL-1 device: 1) vacuum chamber; 2) relativistic electron beam generator; 3) accelerator diode; 4) and 5) conductor and magnetic system; 6) one of wall shunts; 7) location of laser beam input for recording Thompson scattering; 8) Michelson interferometer ($\lambda = 10.6$ μm).

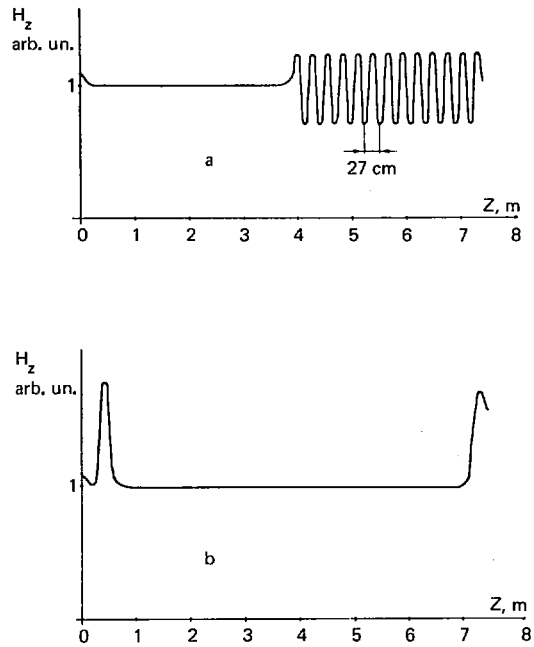


FIG.3. Longitudinal configurations of the magnetic field. H_z = 1 corresponds to 13 kOe. The beam is injected at z = 0.

The magnetic system of the device consists of 85 series-connected loops of red-hot bronze (the outer diameter of the loops is 30 cm, the inner diameter is 20 cm, and the thickness is 2.5 cm) and is powered from a capacitor bank with an energy reserve of up to 1 MJ. The length of the first current half-period in the magnetic system is 7 ms.

All the experiments to be described below were conducted at a fixed plasma density of $n \cong 10^{14}$ cm^{-3}.

2.2. Transport of relativistic electron beams

The magnetic-field configurations used in the experiments are shown in Fig. 3. The intensity is equal to 13 kOe in the zones where the magnetic field is uniform. In the absence of corrugation (Fig. 3b), the beam passed through a system with charge conservation; the charge losses amounted to 30% at all values of beam current (I_b = 25–55 kA) when a configuration with a corrugated-field section (Fig. 3a) was used. These losses are due to aperture restrictions in the

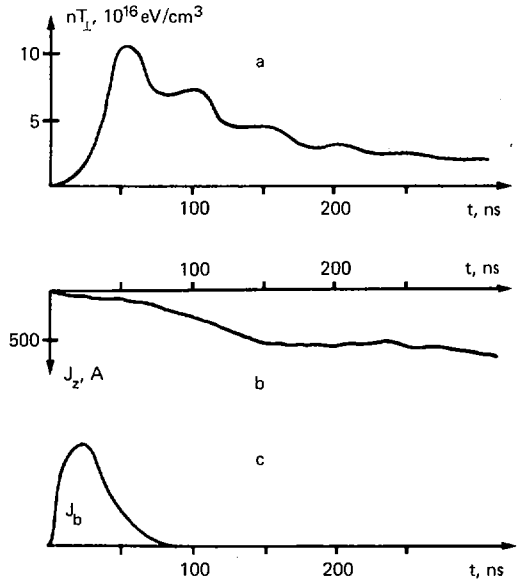


FIG.4. a) Plasma diamagnetism in the z = 207 cm plane ($j_b \cong 1.2$ kA·cm^{-2}). The beam current collector is installed at the output from the device behind corrugated-field section (see Fig. 3a); b) total current in z = 207 cm plane; c) shape of beam current at output from the device.

section with corrugated field. The fact that the transport efficiency does not depend on the current points to the absence of macroscopic beam instabilities when the beam moves along the multi-mirror magnetic configuration.

2.3. Plasma heating

Plasma heating was investigated simultaneously with beam transport. The experimental results given below are related mainly to the magnetic-field configuration shown in Fig. 3a. A typical diamagnetic signal from a probe placed at a distance of z = 207 cm from the anode foil of the accelerator is presented in Fig. 4a. The total current in the plasma measured at the same point is presented below (Fig. 4b). The shape of the beam current recorded by the end collector is shown in Fig. 4c for comparison. It is obvious from Fig. 4 that the duration of the diamagnetic signal appreciably exceeds that of the beam. Considerably shorter diamagnetic signals were observed in the case when the end collector was installed in front of the corrugated section at a distance of z = 400 cm from the accelerator. The corresponding signal is shown in Fig. 5a. The diamagnetic signal from the same probe (z = 207 cm), related to the case of plasma heating in a long mirror (see Fig. 3b), is presented alongside it (in Fig. 5b).

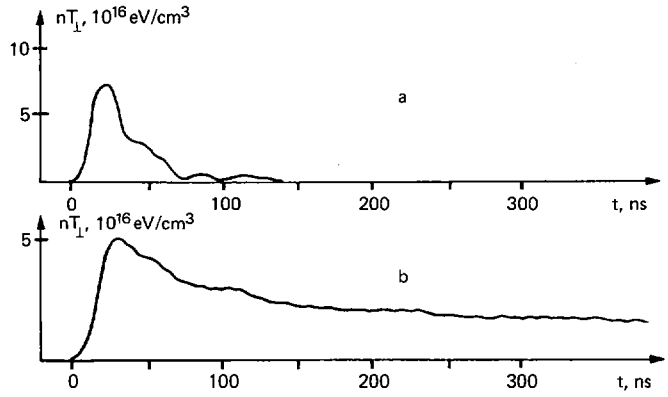


FIG.5. a) Plasma diamagnetism in the z = 207 cm plane ($j_b \cong 1$ kA·cm^{-2}). The collector is installed before corrugation section ($z \cong 400$ cm) in a uniform magnetic field; b) plasma diamagnetism in the z = 207 cm plane ($j_b \cong 0.8$ kA·cm^{-2}). The collector is installed in a magnetic mirror at the output from the device. The field configuration is shown in Fig. 3b.

The rapid drop of diamagnetism in the absence of mirrors at the ends of the system is naturally related to plasma cooling due to electron thermal conductivity. The mean energy of hot electrons ($\epsilon \sim 10$ keV) can be roughly estimated from the cooling time ($\tau \sim L/v_{te}$), while the electron density can be assessed from the amount of diamagnetism. These estimates show that the fraction of hot electrons amounts to several percent of the total number of plasma electrons.

The total beam energy losses in the plasma were determined by the difference of the calorimeter readings at z = 0 and z = 400 cm. The dependence of these losses on the beam current is shown in Fig. 6. It is shown in the same figure how the energy content of the plasma, calculated from data of diamagnetic measurements on the assumption that heating is isotropic, depends on the current. It is obvious from the figure that measurements of total plasma energy and beam energy losses are in good agreement with each other. Under the conditions of our experiments (H = 13 kOe, $n \cong 10^{14}$ cm^{-3} and $j_b \cong 1$ kA·cm^{-2}), the relativistic electron beam leaves approximately 5% of the energy per metre in the plasma. This energy release can only be explained by the development of a beam instability and is, as is well-known, not related to plasma heating by the reverse current. The latter statement follows from the high degree of current neutralization existing in our experiments.

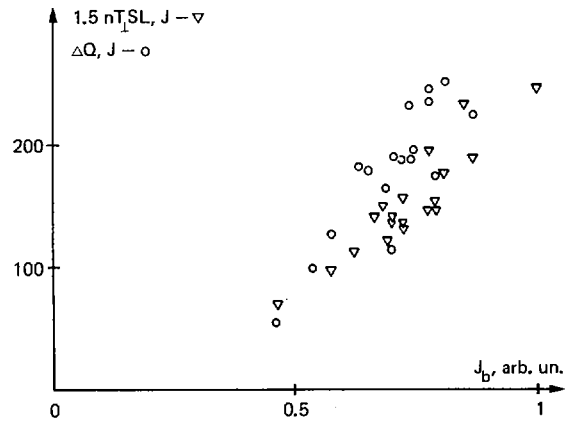


FIG.6. Energy content of plasma calculated from diamagnetic measurements (▽) and by beam energy losses (○) on length of $\Delta z \cong 400$ cm.

3. EXPERIMENTS ON THE INAR DEVICE

3.1. Purpose of experiments

The main purpose of the experiments, which were conducted recently on the INAR device, was to find effective methods of beam heating of a plasma with a density of $n \sim 10^{15}$ cm^{-3}. According to existing theoretical concepts [1], the power contributed by the beam to the plasma should increase as the beam spread decreases and as its density increases and also as the external magnetic field intensity increases.

The losses of relativistic electron energy in the anode foil are small. Therefore, the beam at the input to the plasma may be regarded as monoenergetic at each instant of time; the particle energy is determined by the voltage on the accelerator diode. With regard to the angular electron distribution, besides by scattering in the foil, it is affected by the own magnetic field of the beam, H_φ, and, partially, by the non-collinarity of the electric and magnetic fields in the inter-electrode gap in the diode. There is no field H_φ in the plasma because of neutralization of the beam current. Therefore, the line of force on the anode foil has a break, and the electrons intersecting the foil acquire a transverse (with respect to the magnetic field) component of momentum ($p_\perp/p_\parallel = H_\varphi/H_z$). The angular beam distribution found with regard to this effect is shown in Fig. 7. The calculation was made on the assumption that the mean square angle of electron scattering in the anode foil is equal to 0.1 and the ratio of the beam's own magnetic field H_φ to the external longitudinal field H_z is also equal to 0.1. Since the field

H_φ increases in a radial direction, the width of the distribution function on the beam periphery is greater than that in the near-axial part. It is remarkable that the position of the maximum distribution function is also shifted somewhat, owing to a break in the line of force.

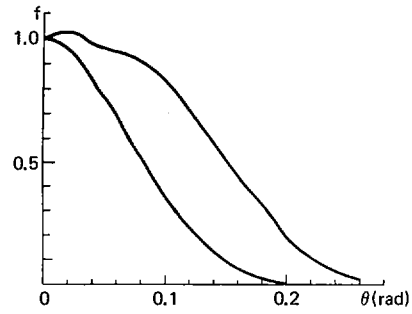


FIG. 7. Angular relativistic electron beam distribution at INAR input; upper curve refers to beam periphery (r = 1 cm) and lower curve to the near-axial zone (r = 0). The distribution function is normalized to its own value at θ = 0.

According to the concepts outlined above, we began to use thinner anode foils than previously (down to 6 μm Ti) in our experiments to reduce the angular spread of the beam. The longitudinal magnetic field was increased simultaneously: up to H_0 = 25 kOe on the uniform section and up to H_z = 42 kOe in the mirrors, in one of which the accelerator anode was located. We note that we have already previously observed an increase in the relativistic electron beam energy contribution to the plasma with an increasing magnetic field [6].

3.2. Influence of angular beam spread on plasma heating effectiveness

The principle of the device and the methods of measurement are described in Refs [2, 6–9]. The relativistic electron beam in this series of experiments had the following parameters: electron energy 0.8–1.0 MeV, beam current 20–25 kA, duration ~ 50 ns, beam diameter at input 2–4 cm, and total beam input energy 0.5–0.6 kJ. The measurements were performed in the range of preliminary-plasma densities of $n = 3 \times 10^{14}$–8×10^{15} cm^{-3}.

Diamagnetic measurements showed that a decrease in the angular beam spread by reducing the thickness of the anode foil leads both to a significant increase in total energy release in the plasma and to a significant non-uniformity in the energy release along the plasma column. Typical oscillograms of signals

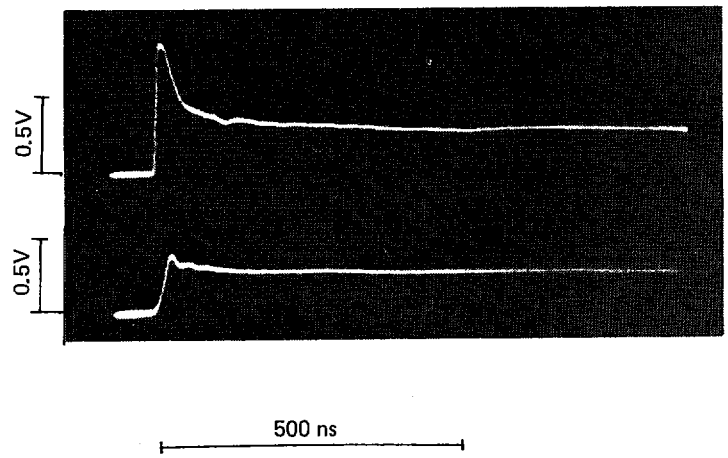


FIG.8. Oscillograms of signals from diamagnetic probes placed at $z_1 = 25$ cm (upper oscillogram) and $z_2 = 85$ cm (lower oscillogram). The regime is $I_b \cong 20$ kA, thickness of titanium anode foil is $d = 10$ μm; $n \cong 4 \times 10^{14}$ cm^{-3} and $H_0 = 25$ kOe.

from diamagnetic probes upon injection of a beam 4 cm in diameter into the plasma with $n = 4 \times 10^{14}$ cm^{-3} are shown in Fig. 8. It is obvious that the initial signal amplitudes differ substantially; as time passes on, however, the diamagnetism is equalized along the device. The transverse plasma energy distributions $nT_\perp S$ over the device with different anode foil thicknesses, plotted from these oscillograms, are shown in Fig. 9. The experimental points are shown for a moment of time that corresponds to maximum diamagnetic signals. It is obvious that the plasma energy near the beam input ($z_1 = 25$ cm) increases more than tenfold with a decrease of anode foil thickness from 50 to 6 μm[1] (the mean square angular beam spread decreases from 24° to 7°, in this case). The value of $nT_\perp S$ also increases, although to a lesser extent, at larger distances. On the whole, variation of the input foil length from 50 to 6 μm leads to an approximately sevenfold increase of the total energy release in the entire plasma column ($L = 240$ cm).

The dependence of the relativistic electron beam energy release in the plasma on the anode foil thickness d, found by diamagnetic measurements, agrees with the results of calorimetric measurements of the total beam energy losses. These measurements were made by the same graphite calorimeter covered with a $d = 10$ μm thick titanium foil, which was alternately installed either directly on the anode foil or at the output of the device. The results of these measurements

[1] The amplitude of the injected current increases in this case by only several percent.

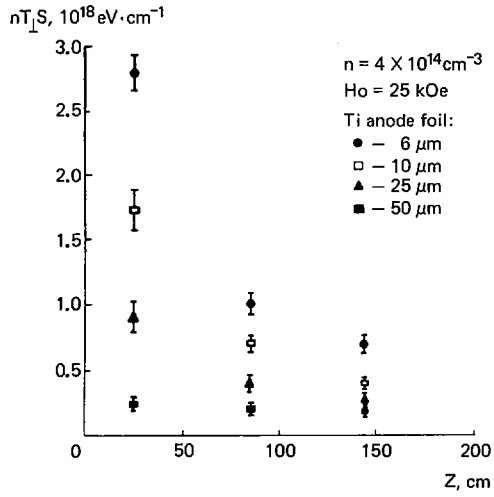


FIG.9. Transverse plasma energy distribution along plasma column at different anode foil thicknesses.

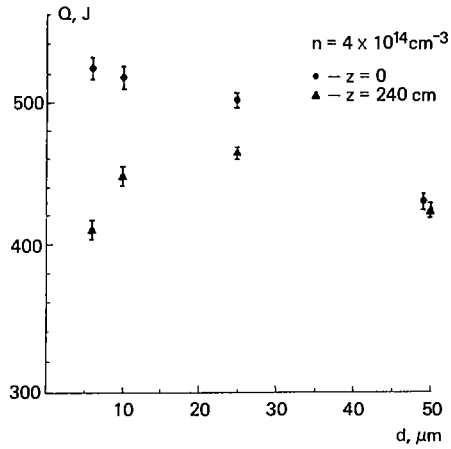


FIG.10. Results of measuring input and output beam energies at different anode foil thicknesses. The regime is $I_b \cong 20$ kA, $D_b = 4$ cm and $n = 4 \times 10^{14}$ cm^{-3}.

are shown in Fig. 10. It is obvious that a decrease in the anode foil thickness from 50 to 6 μm leads to some increase of the total beam energy at the input (the energy increases by almost 20% mainly because of better passage of the low-energy part of the beam pulse through the thin foils). With regard to the calorimeter at the plasma output, the output energy first increases somewhat and then decreases appreciably with the indicated variation of the value of d. This is explained in the following manner: The injected energy increases rather significantly (by 70 J) with variation of d from 50 to 25 μm, while the effectiveness of beam interaction with the plasma increases slightly. Therefore, the increase of beam energy losses in the plasma is less than the increase of injected energy. With a further decrease of input foil thickness, the increase of injected energy is insignificant while the beam interaction with the plasma increases very significantly. For example, it is obvious that the input energy increases by only 20 J with variation of d from 25 to 6 μm, whereas the output energy decreases by 55 J and thus the total beam energy losses in the plasma reach 110 J at d = 6 μm. This indicates directly that the increase of the total beam energy losses in the plasma with decreasing input foil thickness does not occur because of the low-energy part of the beam, but is brought about by an increase in the effectivity of beam interaction with the plasma with a decrease in its angular spread.

In the investigated regime, the total charge of the beam was conserved when it passed through the plasma so that the beam energy losses recorded by the calorimeter are due to deceleration rather than to beam particle losses. Thus, the energy release in the plasma reaches $\Delta Q/Q_0 \cong 20\%$ at a plasma density of $n = 4 \times 10^{14}$ cm^{-3} and a plasma column length of L = 240 cm with a beam current density of 1 kA$\cdot$cm^{-2} and an angular spread of $\theta \sim 0.1$ rad.

As was shown previously [8], total compensation of the beam not only in current and charge but also in current density is observed at $n \gtrsim 2 \times 10^{14}$ cm^{-3}. Beam compensation was always total in the experiments described. Therefore, the observed beam-to-plasma energy transfer is not due to dissipation of reverse-current energy. The strong dependence of energy release in the plasma on the angular beam spread and also its non-uniformity along the device indicate that beam instability should play the main role.

3.3. Dense-plasma experiments

Since the effectiveness of beam plasma interaction was rather high at $n = 4 \times 10^{14}$ cm^{-3}, a transition to the range of still higher plasma densities was interesting. In this context, some changes were introduced into the system for creation of a foreplasma. An increase of the anode voltage of a Penning discharge up to 60 kV made it possible to achieve a preliminary plasma density up to 8×10^{15} cm^{-3} at an initial hydrogen pressure of approximately 0.3 mm Hg and a magnetic field of $H_0 = 25$ kOe. This value was determined by a Michelson interferometer at a wavelength of $\lambda = 10.6$ μm, described in Ref. [5].

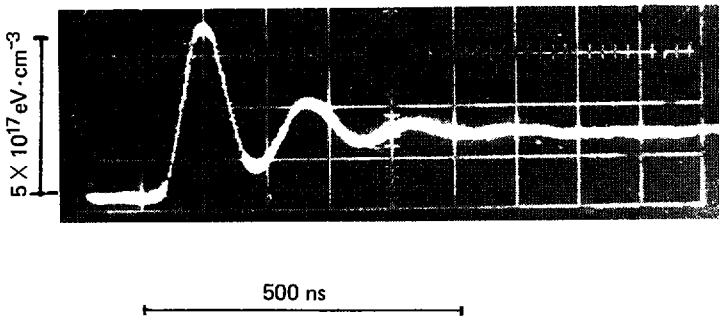


FIG.11. Oscillogram from diamagnetic probe (z = 60 cm) at n = 3 X 10^{15} cm^{-3}, j_b = 5 kA/cm^2 and H_0 = 25 kOe.

A series of experiments on the injection of relativistic electron beams into a plasma whose density increased successively from 4 X 10^{14} to 8 X 10^{15} cm^{-3} was conducted. It was established that a density increase leads to some decrease in the effectiveness of the relativistic electron beam interaction with the plasma, but it may still be rather high up to n = (3–5) X 10^{15} cm^{-3}. As noted above, the effectiveness of the interaction should increase as the beam density increases. An increase in beam current density to j_b = 5 kA·cm^{-2} was accomplished by reducing the beam diameter from 4 to 2 cm. This made it possible to achieve an energy contribution at a level of 10–15% of the total beam energy to a plasma with a density of (3–5) X 10^{15} cm^{-3} when a relativistic electron beam was injected through a thin foil.

A typical oscillogram of a signal from a diamagnetic probe (z = 60 cm) upon injection of a beam with n_b = 10^{12} cm^{-3} through a Ti-foil with d = 6 μm into a plasma with n ≅ 3 X 10^{15} cm^{-3} in a magnetic field of H_0 = 25 kOe is shown in Fig. 11. The signal fluctuations were caused by radial magnetoacoustic fluctuations of the plasma column (they were first observed in the experiments of Ref. [6]). The plasma density, for known geometric dimensions of the plasma column and magnetic field intensity, may be estimated from the period of these oscillations. The density determined in this manner is in satisfactory agreement with the value found from processing of the interferograms.

In determining the specific energy content of the plasma, $nT_\perp$ S, the oscillatory nature of the diamagnetic signals was taken into account and the necessary corrections in determining the true plasma pressure were made. It can be seen from the oscillogram that the transverse plasma energy decreases comparatively slowly in time after completion of the relativistic electron beam injection (τ_{inj} ≅ 50 ns).

As is shown in Refs [9, 10], plasma heating occurs in the zone occupied by the beam at n > 2 X 10^{14} cm^{-3} when there is beam compensation not only

in current but also in current density. Therefore, one may find from the oscillogram that the plasma pressure has a value of $nT_\perp \cong 3 \times 10^{17}$ eV·cm^{-3} (at $n \cong 3 \times 10^{15}$ cm^{-3}) after relativistic electrom beam injection.

Thus, the use of relativistic electron beams with small angular spread and high current density makes it possible to heat a plasma with a density of up to $(3-5) \times 10^{15}$ cm^{-3} with sufficiently high efficiency in a strong magnetic field.

4. SUMMARY

1. Transport of a beam with a current of up to 55 kA (current density of 1 kA·cm^{-2}) in a multi-mirror magnetic field without any indication of a development of macroscopic instabilities was accomplished experimentally in the GOL-1 device. Practically total beam current neutralization occurs at a plasma density of $n = 10^{14}$ cm^{-3}. The beam releases up to 20% of its energy in the plasma on a length of 4 m.

2. An increase in the magnetic field up to 25 kOe (up to 42 kOe in the mirrors) and a decrease in the anode foil thickness down to 6 μm made it possible to achieve 20%-effectiveness of energy transfer from the relativistic electron beam with a current density of $j_b \cong 1$ kA·cm^{-2} to a plasma with a density of 4×10^{14} cm^{-3} at plasma column length of L = 240 cm on the INAR device.

Comparable energy releases at a plasma density up to $(3-5) \times 10^{15}$ cm^{-3} can be achieved with an increase of beam current density to 5 kA·cm^{-2}.

3. The derived results indicate the possibility of achieving the regimes required for operation of a solenoid reactor as described in the introduction.

REFERENCES

[1] BREJZMAN, B.N., RYUTOV, D.D., Nucl. Fusion **14** (1974) 874.

[2] ABRASHITOV, Yu.I., KOJDAN, V.S., KONYUKHOV, V.V., LAGUNOV, V.M., LUK'YANOV, V.N., MEKLER, K.I., Pis'ma Zh. Ehksp. Teor. Fiz. **18** 11 (1973) 675.

[3] BUDKER, G.I., DANILOV, V.V., KORNILOV, V.A., KRUGLYAKOV, E.P., LUK'YANOV, V.N., MIRNOV, V.V., RYUTOV, D.D., Plasma Physics and Controlled Nuclear Fusion Research (Proc. 5th Int. Conf. Tokyo, 1974) Vol. 2, IAEA, Vienna (1975) 763.

[4] BOYARINTSEV, E.L., KAPITONOV, V.A., KORNILOV, V.A., Dokl. Akad. Nauk SSSR, **217** (1974) 4.

[5] BURMASOV, V.S., KRUGLYAKOV, E.P., PODYMINOGIN, A.A., Fiz. Plazmy **4** 1 (1978) 140.

[6] ABRASHITOV, Yu.I., KOJDAN, V.S., KONYUKHOV, V.V., LAGUNOV, V.M., LUK'YANOV, V.N., MEKLER, K.I., RYUTOV, D.D., Zh. Ehksp. Teor. Fiz. **66** 4 (1974) 1324.

[7] ARZHANNIKOV, A.V., BREJZMAN, B.N., VYACHESLAVOV, L.N., KOJDAN, V.S., KONYUKHOV, V.V., RYUTOV, D.D., in Plasma Physics and Controlled Nuclear Fusion Research (Proc. 5th Int. Conf. Tokyo, 1974) Vol. 3, IAEA, Vienna (1975) 257.
[8] ARZHANNIKOV, A.V., KOJDAN, V.S., in Phenomena in Ionized Gases (Proc. 12th Int. Conf., Eindhoven, 1975) 278.
[9] KOJDAN, V.S., ROGOZIN, A.I., Zh. Ehksp. Teor. Fiz. **71** 5 (1976) 1837.
[10] BURDAKOV, A.V., KOJDAN, V.S., MATSUKAWA, E., Rep. 2nd Conf. Diagnostics of High-Temperature Plasma (Khar'kov, 1977).

DISCUSSION

H. HORA: Did you compare the penetration length of the electrons through the plasma with the classical (Fokker-Planck-type) values, and was there a deviation for your high currents (anomalous stopping power)?

D.D. RYUTOV: The typical penetration length at $n \sim 10^{14}\,cm^{-3}$ and $E = 1$ MeV is several hundreds of kilometres.

T. KAWABE: Have you made any measurements of fluctuations during beam injection or after?

D.D. RYUTOV: At plasma densities of $\sim 10^{15}\,cm^{-3}$, Langmuir oscillations, which are supposed to be responsible for the effects observed, have frequencies in a range which is very inconvenient for measurement purposes, so we have not tried to detect them.

B.G. LOGAN: Did you observe any radial spreading or radial diffusion of the electron beam propagating in the GOL-1 experiment?

D.D. RYUTOV: No, if there is good current neutralization we never detect radial spreading.

PLASMA HEATING BY CURRENT-DRIVEN TURBULENCE IN THE TOKAMAK TORTUR I*

H. DE KLUIVER, C.J. BARTH, H.J.B.M. BROCKEN,
J.J.L. CAARLS, B. DE GROOT, H.W. KALFSBEEK,
H.W. PIEKAAR, A. RAVESTEIN, W.R. RUTGERS,
B. DE STIGTER, H.W.H. VAN ANDEL†, H.W. VAN DER VEN
Association Euratom-FOM,
FOM-Instituut voor Plasmafysica,
Rijnhuizen, Nieuwegein, Netherlands

Abstract

PLASMA HEATING BY CURRENT-DRIVEN TURBULENCE IN THE TOKAMAK TORTUR I.

The heating of plasmas in toroidal devices by excitation of turbulence in a current skin layer is the subject of this paper. Expressions are derived for the additional heating power that can be achieved by multiple pulsing. The experimental results of the effect of one heating pulse are presented. It is shown that about 800 J have been deposited within a single heating pulse of 4 μs duration in the plasma volume of the tokamak TORTUR I.

1. Introduction

The heating of plasmas in toroidal devices by excitation of turbulence in a current skin is investigated. In section 2 expressions for the expected amount of energy dissipation from one or a sequence of current pulses superposed on the bias current of a tokamak, provoking weakly ion-acoustic waves in the skin, are derived. An expression for the anomalous conductivity in the skin is compared with results of detailed computer calculations. In section 3 the experimental device TORTUR I and the diagnostics used are described. In section 4 heating results are presented and compared with analytical and computational results.

2. The energy dissipation in a toroidal plasma from one or a number of turbulent heating pulses

When the local current density is sufficiently high, the electrons obtain a drift velocity $v_d > c_s$ and ion-acoustic instabilities establish a weakly turbulent state at the plasma surface. A skin region, of width

$$\delta = \frac{\sqrt{3}\, c}{\omega_{si}\sqrt{\gamma(\gamma-1)(1-\alpha)}}$$

is formed, in which strong energy dissipation occurs [1]. Here α denotes the fractional loss of energy out of the skin during turbulent dissipation due to transport to the wall as well as to the interior of the plasma column, $\gamma = v_d/c_s$ is the ratio of drift velocity to ion-sound speed, $c_s = (kT_e/m_i)^{\frac{1}{2}}$,

---

* This work was performed under the Euratom-FOM Association agreement with financial support from ZWO and Euratom.

† Département de physique, Université de Montréal, Montreal, Canada.

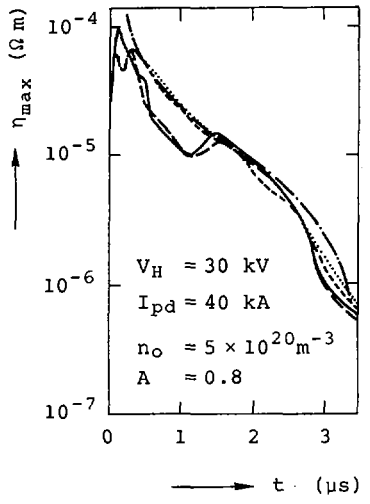


FIG. 1. Peak value of skin resistivity η as function of time for four saturation mechanisms. The density is assumed to be $n(r) = n_0\{1-A(r/a)^2\}$. *– – – – Ion trapping; . . . . electron-cyclotron effect; — — non-linear Landau damping; —— ion-resonance broadening. The — · — · — · curve is inferred from relation (1).*

and ω_{si} is the ion plasma frequency in the skin. This region of anomalous dissipation can be maintained as long as the time rate of change of the skin current $(\partial I_{sk}/\partial t)/I_{sk}$ is high enough to keep the plasma skin in a state of turbulence. The plasma conductivity can then be derived to be

$$\sigma(t) = \frac{1}{\mu_o \delta^2} \frac{I_{sk}}{(\partial I_{sk}/\partial t)} \quad (<< \sigma_{classical}) \tag{1}$$

The above relation has been compared with computer results on the resistivity in the skin derived from a one-dimensional, two-fluid MHD code [2], where, based on the marginal stability concept [3], a number of mechanisms for the saturation of the ion-acoustic instability have been tested (Fig. 1). It is to be noted that the marginal stability concept does not need the exact dynamics of the turbulence. It can be seen that expression (1) closely follows the simulation results. Apparently, a detailed following on a microscopic scale of the evolutions in time of the turbulence seems not to be necessary. A time dependence as suggested by (1) with $\sigma << \sigma_{class}$ can also occur for other types of instabilities - as for instance a current-driven transverse electrostatic ion-cyclotron wave - with its own threshold $\gamma = v_d/c_s$. It is easily shown that (1) is equivalent to a relation between the induced electric field in the skin, E_{sk}, and $\partial I_{sk}/\partial t$:

$$E_{sk} = \frac{\mu_o \delta}{2\pi a} \frac{\partial I_{sk}}{\partial t} \tag{2}$$

where $I_{sk} = 2\pi a \delta e n_{ps} v_d$ has been used; a is the minor radius of the torus and n_{ps} is the average density in the skin.

The amount of energy dissipated in the skin due to superposition of a current $I_{sk}(t) = \hat{I}_{sk}\sin(\omega t)$ is:

$$W_p(t) = 2\pi R_T \int_0^t E_{sk} \cdot I_{sk}\, d\tau = \frac{1}{2}\mu_o \delta \frac{R_T}{a} \hat{I}_{sk}^2 \sin^2(\omega t) \qquad (3)$$

for $t < \pi/2\omega$ with R_T as the major radius.

Realizing that a fraction $(1-\alpha)$ of the dissipated energy in (3) is heating the electrons in the skin volume $4\pi^2 R_T a \delta$, the electron temperature in the skin, T_{es}, is found to be:

$$T_{es} = \frac{\mu_o (1-\alpha)(\gamma-1)\, \hat{I}_{sk}^2}{12\pi^2 a^2 n_{ps} e \gamma} \qquad (4)$$

(temperatures are expressed in volt) where we have taken $(T_{es} + T_{is}) = \frac{\gamma}{\gamma-1} T_{es}$ from quasi-linear theory.

The process of heating the plasma core by one or more additional current pulses is only effective as long as $T_{es} \geq T_{ec}$. Furthermore, for q-safety reasons, $\hat{I}_{sk}$ should be smaller than the toroidal ohmic heating current I_{OH}. Since the temperature of the plasma core ($T_{ec} = T_{ic}$) is related to its beta poloidal (β_{pc}) by

$$T_{ec} = \frac{\mu_o I_{OH}^2 \beta_{pc}}{16\pi^2 a^2 n_{pc} e}$$

β_{pc} is limited to:

$$\beta_{pc} \leq \frac{4}{3} \frac{n_{pc}}{n_{ps}} (1-\alpha)\left(\frac{\gamma-1}{\gamma}\right) \qquad (5)$$

With sufficiently high toroidal fields ignition temperatures may be reached at safe q-values by superposing a series of pulses on the confinement current I_{OH}.

Let τ be the time between two heating pulses, and τ_H the total heating time for N pulses: $\tau_H = N\tau$. Assume a partition of the fractional energy losses from the skin, α, into a fraction α_w - losses to the wall - and into a fraction α_i, beneficial for heating the plasma interior: $\alpha = \alpha_w + \alpha_i$. With these assumptions an upper bound for the heating power, P_T, defined as $P_T \tau_H = N W_p$, can be found by imposing condition (5) for the maximal achievable beta poloidal. When N pulses are required to reach this state, it can be shown that:

$$P_T \leq \frac{n_{pc}}{n_{ps}} \left(\frac{\gamma-1}{\gamma}\right)\left(\frac{1-\alpha}{1-\alpha_w}\right)\left(\frac{R_T \mu_o I_{OH}^2}{2\tau_H}\right) \frac{N}{\sum_{n=0}^{N-1} e^{-(N-n)\tau/\tau_E}} \qquad (6)$$

where τ_E is the energy confinement time, assumed to be independent of the temperature. For $\tau_H \geq \frac{2}{3}\tau_E$, the summation can be adequately represented by

$$\sum_{n=0}^{N-1} e^{-(N-n)\tau/\tau_E} = N \frac{\tau_E}{\tau_H}\left[1 - 0.39\left(\frac{\tau_E}{\tau_H}\right)^{1.28}\right]$$

An example is given for the Frascati tokamak. Let 26 pulses be added in $\tau_H (= 5\,\tau_E) = 0.175$ s and assume $\gamma = 3.6$; $\alpha = 0.5$, $\alpha_w = 0.15$, $n_{pc} = n_{ps}$, $I_{OH} = 1$ MA, while $R_T = 0.85$ m and $a = 0.21$ m. Insertion of these numbers into (6) leads to a supplementary heating power of $P_T = 6.6$ MW, giving $T_e = 5{,}4$ keV at $n_p = 10^{20} m^{-3}$.

In section 4 the heating of the TORTUR I plasma will be compared with the expressions of this section and with computational results.

3. The TORTUR I device and the diagnostics used

The measurements were done on the TORTUR I tokamak ($R_T = 0.46$ m, $a = 0.09$ m) at toroidal magnetic fields up to 1.8 tesla [4]. The toroidal electric fields

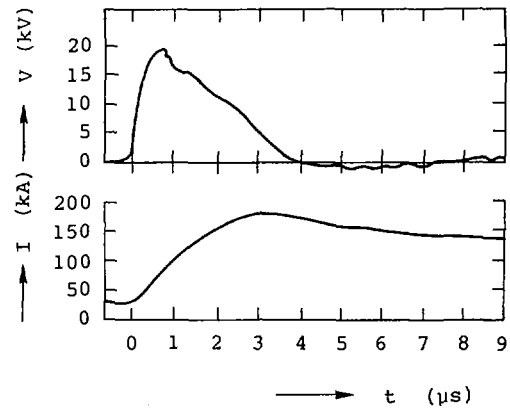


FIG. 2. Plasma current due to inductively applied voltage versus time.

for containment and heating are induced by discharging capacitor banks through the copper shell enveloping the quartz vacuum vessel. The initial hydrogen plasma is fully ionized with $T_e \approx 10$-20 eV, at densities adjustable between 3×10^{19} m^{-3} and 2×10^{20} m^{-3}.

For the turbulent heating pulse a 125 kJ, 50 kV, 70 kHz bank ($\frac{1}{4}T = 3.5$ μs) is used, causing electric fields on the plasma surface up to approximately 10 kV/m. With a capacitor bank voltage $V_c = 32$ kV a skin current of 150 kA is superposed on a bias current of 30 kA. The heating current can be crowbarred at chosen times. In Fig. 2 a voltage-current trace vs time is presented. For a more detailed description of the experiment and previous results the reader is again referred to Ref. [4].

Apart from the usual measurements, as the measurement of the loop voltage, the total current, the diamagnetism etc., a number of specialized diagnostics have served to analyze the penetration processes and the local dissipation. The radial profiles of the poloidal and toroidal magnetic field components are measured with a multicoil magnetic probe. The probe consists of an array of 6 pairs of miniature pick-up coils, spaced 3.4 cm apart [2].

The system records during one shot B_θ and B_ϕ as a function of time at 6 locations. To deduce current densities as well as electric fields, the profile is scanned at 4 mm intervals taking 5 shots per position. Samples have been taken in the horizontal median plane as well as in a 2 cm off-axis vertical direction. From these profiles magnetic and electric energy densities may be inferred, assuming no toroidal dependence of the plasma parameters.

Another diagnostic comprises electron temperature and density measurements by laser-light scattering at two radial positions. Electron temperatures have also been deduced from the emission of soft X-rays (100 eV < T_e < 1 keV). The thermal plasma radiation at various harmonics of the electron-cyclotron frequency, f_{ce}, has been measured by means of a far-infrared spectrometer [5] as functions of time. Analysis of the black-body radiation at 2 f_{ce} yields the radial distribution of electrons having energies in excess of approx. 300 eV. These measurements also indicate superthermal emission near f_{pe} during turbulence. Superthermal plasma radiation in the frequency range from 8-40 GHz has been extensively investigated with a multiplexer microwave analyzer put to our disposal by courtesy of the UKAEA-laboratory at Culham [6]. Measurements of radiation due to plasma oscillations below f_{pi} have been carried out with a broad-band antenna.

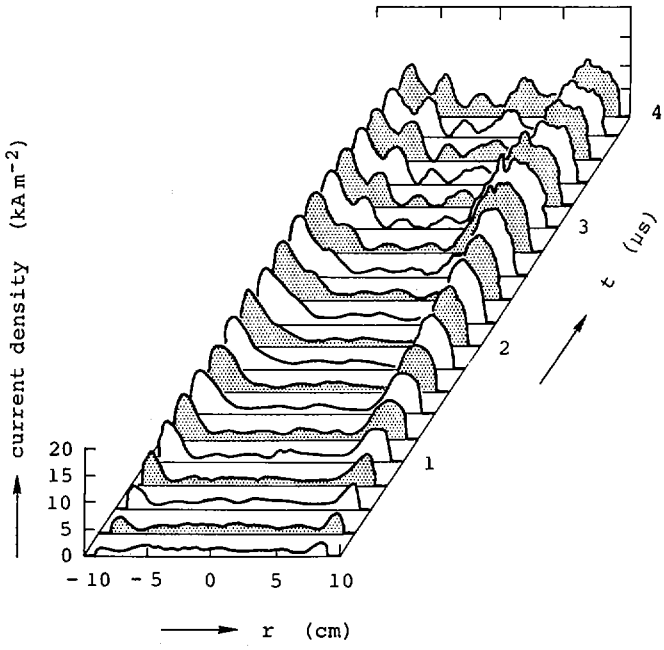


FIG.3. Toroidal current density profiles versus time.

The energy spectrum of charge-exchange neutrals has been analyzed with a calibrated, 8-channel electrostatic analyzer. Integral charge-exchange fluxes have also been monitored by a molybdenum secondary emission detector.

The plasma line density can be monitored at 2 cords by means of a CO_2-laser interferometer. A vacuum UV-spectrometer has been used for registering the continuous emission between 100 and 400 Å. From these data the electron temperature in the plasma afterglow can be roughly determined.

All data were processed in a 20-channel data acquisition system.

4. Results of plasma heating in TORTUR I

The heating of a plasma with an initial density $n \sim 1\times10^{20}$ m^{-3}, a temperature $T_e = T_i \sim 10$ eV, a volume 0.07 m^3, and carrying a toroidal bias current of 30-40 kA, is investigated experimentally. At the start the plasma thus contains an energy, defined as $3/2\ n\,e\,(T_e+T_i)$, of 30 J.

During the application of the high-voltage high-current pulse (up to 150 kA), various stages of the turbulent heating process can be recognized experimentally, as shown in Fig. 3, where radial profiles of $j_\phi(r)$ as measured with the magnetic probe array, are given.

Within 0.5 μs the current establishes a skin layer. This layer stays grossly unchanged until 2 μs. Then the inner side of the skin starts to penetrate into the plasma interior. When $(\partial I/\partial t)/I$ becomes too small, i.e. near 3.5 μs, the skin layer can no longer be maintained and the current is distributed across the plasma body. The occurrence of the skin-like current profiles has been reported in other toroidal and linear experiments [7].

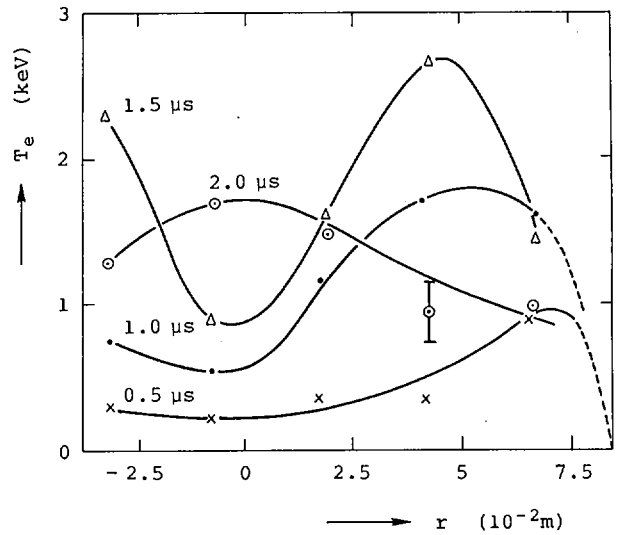


FIG.4. Electron temperature derived from intensity of $2f_{ce}$ as function of space and time. $B_T = 1.7$ T, $n_e = 0.6 \times 10^{20}$ m^{-3}.

During the first 2 μs the probe signals are fairly reproducible from shot to shot. Computer calculations (see Sec. 2) can satisfactorily describe the current transport and the intense energy dissipation [2]. Assuming saturation of the current-driven ion-acoustic mode near $\gamma = 6$-7, it is to be expected that if a non-thermal distribution is formed, an equivalent of 30% of the electrons is heated up to 3 keV. Indeed during the first microsecond the start of turbulence is revealed by short bursts (~ 20 ns) of X-rays (energies 4-6 keV) which have completely disappeared at 2 μs. The presence of an electron population heated up to temperatures between 2 and 3 keV is manifest from cyclotron emission near the second harmonic from 1-3 μs and from soft X-ray emissions in the overlapping ranges 1 keV-100 eV between ~ 2 and ~ 4 μs. From synchrotron emission data [5] (Fig. 4) it is inferred that a rapid transport of energy across the magnetic field (1-2×10^5 m/s) takes place. The distribution with an average temperature of 1.8 keV is already flattened at 2 μs. From the laser-scattering measurements it is concluded that besides the above-mentioned hot electrons, the electron population consists of a colder part with temperatures of 120 eV near the skin and 100 eV near the axis.

A fast energy transport from a hot skin to the inner part of the plasma has been reported earlier in linear as well as in toroidal configurations [8]. Oblique ion-acoustic waves ($k_\perp \neq 0$, $c_s \approx 5.5\times10^5$ m/s) driven by the energetic tail electrons, refracted on the temperature gradient [9] are likely candidates. This, however, is by all means not the only possible mechanism for fast energy transport as e.g. also fast unstable electron drift waves can occur in the skin due to opposite gradients of the temperature and the density, giving rise to considerable cross-field transport [10].

Evidence for ion-acoustic waves as a principal instability mechanism in the skin - apart from the skin width $\approx c/\omega_{pi}$ - are heavy plasma oscillations below f_{pi} [4]. From the energy density dissipated in the skin and the observed

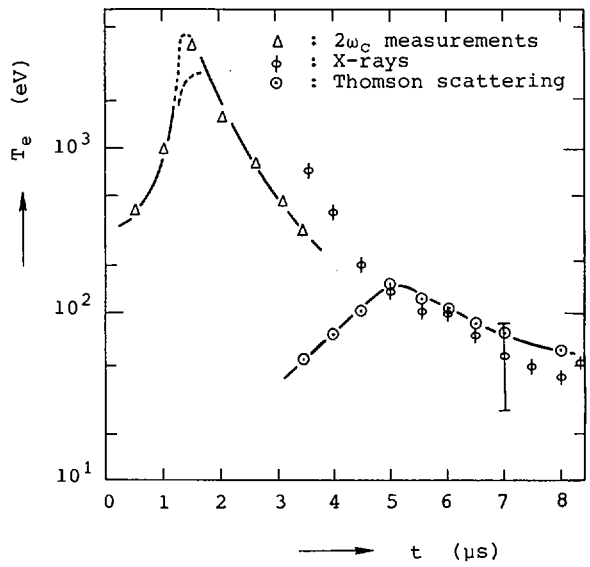


FIG. 5. Electron temperatures versus time.

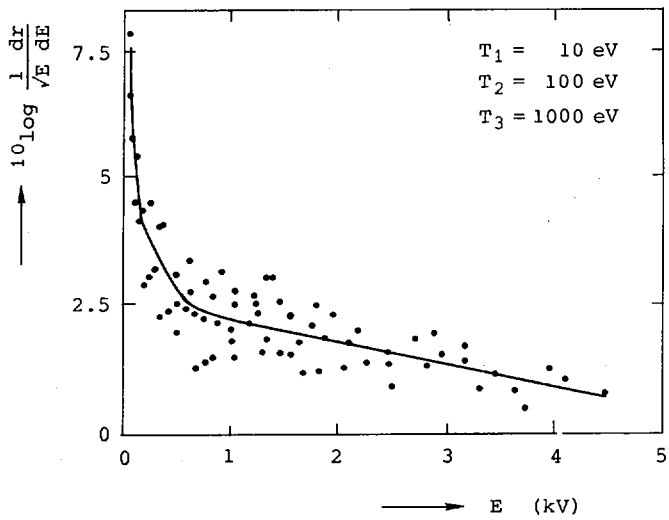


FIG. 6. Energy spectrum of flux r of charge-exchange neutrals emitted from the plasma at t = 3 μs. Each datum is the average of 5 shots. The drawn line is a least-squares fit of a three-Maxwellian function of the three temperatures listed in the figure.

current densities it is found that γ settles near 3-4 (rather than 6-7), indicating lower threshold values for the critical current density. Excitation of turbulence at lower drift velocities and lower ratios of T_e/T_i is possible for current-driven transverse electrostatic ion-cyclotron modes [11]. Besides evidence of the above-mentioned ion-acoustic types of turbulence, we have evidence of a beam-plasma type of interaction during the first 2 μs. A strong non-thermal emission spectrum is then present in the frequency range 9 GHz < $f \leq f_{ce}$ [6]. The quasi beams are presumably high-energy tail electrons not caught by the ion-acoustic microfields, their energy being effectively depleted in beam-plasma interactions.

After 2 μs and up to 3.6 μs the skin region can still be identified. However, the current penetration at the inner edge takes place in an erratic way indicating the local occurrence of MHD instabilities. The presence of tearing modes has to be assumed. The deduction of electric fields from the probe data near the centre are less reliable during this period, possibly because of unknown toroidal derivatives. However, in the outer skin the flux surfaces, deduced from the combined horizontal and vertical probe measurements, remain undamaged. A further heating of the bulk of the electrons and the ions is indicated in Figs. 5 and 7. The electron temperature, as indicated by the laser scattering system, increases up to 150 eV at 3.5 μs. Also the ion energies are rapidly increasing. At a time of 3.5 μs, two Maxwellian populations of 110 eV and 1000 eV are observed by the multichannel charge-exchange neutral analyzer (Fig. 6). From the time-behaviour of the various energetic ion components it seems that the 1100 eV population is located exclusively in the skin region, whereas the colder (100 eV) group is present throughout the plasma volume.

A straightforward deduction of the absolute densities of the heated ions was not possible, due to the building up of a dense mantle plasma (typically 10^{21} m^{-3}) of lower temperature ($T_e \sim 20$ eV), formed by ionization of the flux emitted by the strongly outgassing quartz wall, leading to an effective energy degrading and shielding, and yielding an intense flux of low energy neutrals with a characteristic temperature of about 10 eV.

After 3.5 μs the turbulence dies out and the flux surfaces fill up the inner region with a speed of approximately 4×10^4 m/s. The collapse leads by a redistribution of magnetic surfaces to a distribution with less energy.

Next the heat balance up to 3.5 μs will be discussed. In Fig. 7 the total energy dissipation during turbulence as deduced from the probe measurements is given as a function of time (trace 1). It is to be noted that some 1200 J are supplied in 3.5 μs. This dissipation is compared with expression (3) of section 2, taking $\gamma = 3.6$, $n_{ps} = 1.2\times10^{20}$ m^{-3}, and $\alpha = 0.5$ (trace 2). It can be seen that formula (3) slightly overestimates the dissipation. It may be realized that in reality turbulence is not always and everywhere effective in the skin volume. Compare to this end the analytical expression $\eta(t)$ with the computational result in Fig. 2, revealing large fluctuations around a lower average. The result of the computer calculations is shown in trace 3. As discussed before, in the numerical model, a relatively high threshold value for the onset of the instability is taken (γ ='6-7). It is anticipated that the computer code will show an appreciable increase in dissipated energy after insertion of the value $\gamma \approx 3$, as deduced from the experiments.

In Fig. 8 the partition of dissipated energy amongst various categories of heated electrons and ions is given vs time. The sum (trace 4) should be compared with the traces in Fig. 7, keeping in mind that the input energy should be multiplied by the factor $(1-\alpha_w)$. It is to be noted that the absolute accuracy of the energy of the hot component of the electrons is known no better than a factor of 1.5 (trace 1). The accuracy of the colder electrons ($\sim$ 100 eV) is about 30% (trace 2).

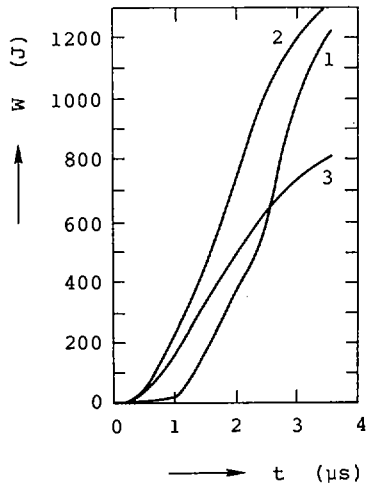


FIG. 7. Total energy input as deduced from the probe measurements (trace 1); as calculated from Eqs (3), $\gamma = 3.6$, $\alpha = 0.5$ (trace 2); and as found with the two-fluid, one-dimensional MHD code, $\gamma = 6.8$ (trace 3).

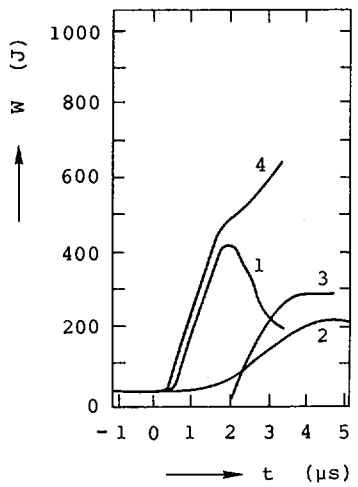


FIG. 8. Partition of dissipated energy amongst various categories of heated electrons and ions versus time.

As argued before, absolute number densities for the two ion populations were only indirectly available. However, from the relative populations of the emitted 10 eV, 110 eV, and 1000 eV ions, together with information on thickness, density and temperature of the mantle plasma, we could conclude to the presence of some 70 J of 100 and 1000 eV ions in the skin.

Another important contribution to the ion energy can be found near the plasma centre (trace 3). It is postulated that a major part of the rapid decrease in energy of the hot electrons (trace 2) between 2 and 3 μs is transferred to the ions by some form of damping process, e.g. by ion-Landau damping or ion-cyclotron damping. (Normal thermalization needs at least 10 μs). The presence of such a heated group of ions near the centre is greatly supported by a charge-exchange emission which is present as long as the hot core plasma is not cooled down by the broadening plasma mantle (typically in 100 μs).

It is concluded that the energy deposited in a skin region during weakly turbulent processes of current-driven ion-acoustic types can be accounted for by the heating of ions and electrons of the original plasma, showing that large enhanced losses out of the plasma are not present.

After replacement of the quartz wall by a thin stainless-steel liner [12], the effect of the superposition of a number of pulses, of longer duration and at lower voltages, will be investigated experimentally.

References

[1] HIROSE, A., PIEKAAR, H.W., SKARSGARD, H.M., Nucl. Fusion 16 (1976) 963; PIEKAAR, H.W., KLUIVER, H. DE, Phys. Lett. 62A (1977) 413.

[2] KALFSBEEK, H.W., Proc. Joint Varenna-Grenoble Int. Symp. on Heating in Toroidal Plasmas, Grenoble, 1978.

[3] MANHEIMER, W.M., BORIS, J.P., Comments on Plasma Physics and Contr. Fusion 3 (1977) 15.

[4] KLUIVER, H. DE et al., Phys. Lett. 62A (1977) 157.

[5] VAN ANDEL, H.W.H., RUTGERS, W.R., submitted for publication in Plasma Physics.

[6] VAN ANDEL, H.W.H., (1978) Rijnhuizen Report RR 78-109, FOM-Instituut voor Plasmafysica, Nieuwegein, The Netherlands.

[7] MASCHERONI, P.L., Phys. Fluids 20 (1977) 634.
HUTCHINSON, I.H., MORTON, A.H., Nucl. Fusion 16 (1976) 447.

[8] ARANCHUK, L.E. et al., JETP-Lett. 15 (1972) 22.
NISHIDA, Y. et al., Phys. Rev. Lett. 38 (1977) 653.

[9] NISHIDA, Y., HIROSE, A., Plasma Physics 19 (1977) 447.

[10] HASEGAWA, A., Plasma Instabilities and Non-Linear Effects, Berlin, Springer Verlag (1975).

[11] DRUMMOND, W.E., ROSENBLUTH, M.N., Phys. Fluids 5 (1962) 1507.
KINDEL, J.M., KENNEL, C.F., J. of Geophys. Res. 76 (1971) 3055.

[12] PIEKAAR, H.W., KLUIVER, H.DE, (1977) Rijnhuizen Report RR 77-102, FOM-Instituut voor Plasmafysica, Rijnhuizen, Nieuwegein, The Netherlands.

EXPERIMENTS ON HOT-ION PRODUCTION IN TOROIDAL PLASMAS BY APPLYING PULSED ELECTRIC FIELDS ALONG AND ACROSS THE TOROIDAL MAGNETIC FIELD

T. ISHIMURA, N. HOSOGANE, S. OHI, T. YAMAMOTO*
Plasma Physics Laboratory,
Faculty of Engineering,
Osaka University, Osaka

M. ICHIMURA+, N. INOUE, K. YAMAZAKI+, Y. OGAWA,
M. KIKUCHI, A. OZAKI, T. UCHIDA
Department of Nuclear Engineering,
University of Tokyo, Tokyo,
Japan

Abstract

EXPERIMENTS ON HOT ION PRODUCTION IN TOROIDAL PLASMAS BY APPLYING PULSED ELECTRIC FIELDS ALONG AND ACROSS THE TOROIDAL MAGNETIC FIELD.

Results are given of experiments in ion heating by strong pulsed electric fields. Experiments have been carried out with tokamaks TORIUT-3 at the University of Tokyo and OT-1 at Osaka University. In TORIUT-3, new experimental results were obtained when a high-voltage theta pinch was applied to a part of the torus. Although the amplitude of the pulsed field at the opposite side of the theta-pinch coil is about one order of magnitude smaller than that under the coil, the emission of fast neutral particles was observed simultaneously all around the torus as in the case of full torus application. The production of hot ions was observed to be accompanied by the appearance of a strong radial electric field, whose presence can give rise to the acceleration of ions and/or the occurrence of turbulent heating due to cross-field instability. In OT-1, the turbulent heating experiment on a hydrogen plasma was carried out by applying the pulsed electric field along the toroidal magnetic field. The intensity of the radially emitted fast neutral flux does not depend so remarkably on the position of observation along the torus. Hot ions with velocity perpendicular to the toroidal field were therefore seen to be produced throughout the torus. However, from observation of a tangentially emitted fast neutral flux, it becomes clear that hot ions with velocity parallel to the toroidal field are produced non-uniformly and the region of their production is restricted to the neighbourhood of the limiter. These results imply that two kinds of ion heating process occur in the plasma simultaneously.

---

* Institute of Scientific and Industrial Research, Osaka University.

\+ Present address: Institute of Plasma Physics, Nagoya University, Nagoya.

1. INTRODUCTION

Heating experiments by use of strong electric fields across the magnetic field have already been carried out with some toroidal machines [1–3]. In particular, for rapid further heating of a tokamak plasma a high-voltage theta pinch has been applied to the TORIUT-3 (previously called PT-II) tokamak plasma [2, 4, 5]. In these experiments rapid production of keV ions and sudden alteration of the behaviour of runaway electrons were observed. No serious disruption of the current ring has been observed since the pulse duration is shorter than the poloidal Alfvén time.

Here we describe the experiment on the application of the high-voltage theta pinch to a part of the tokamak plasma. Hot ion production and the generation of a strong radial electric field were observed at the opposite side of the theta-pinch section.

Turbulent heating experiments by applications of a pulsed electric field along the torus have also been carried out with some toroidal machines [6–9] as well as linear machines. In toroidal turbulent heating experiments, it is generally considered that the heating occurs uniformly along the torus, since the pulsed electric field is uniformly applied to the plasma by electromagnetic induction. Moreover, ion heating in these experiments is considered to be isotropic if a few results obtained in the linear turbulent heating experiments are referred to [10, 11]. However, isotropic ion heating has not been examined in any toroidal machine because of the difficulty of diagnostic arrangement. We describe here an experiment to re-examine the propriety of these conjectures. Ion heating is investigated in two directions perpendicular and parallel to the magnetic field by applying turbulent heating to the OT-1 tokamak plasma.

2. EXPERIMENT WITH PULSED ELECTRIC FIELD ACROSS THE TOROIDAL FIELD

2.1. Experimental set-up

Experiments in the TORIUT-3 tokamak have confirmed that tokamak plasma can be heated by applying a high-voltage theta pinch all round the torus. For further comprehension of the heating mechanism in these experiments, we applied the theta-pinch pulse to a part of the torus. Details of the experimental device are described in Ref.[12] and typical experimental parameters just before pulsed heating are given in Table I.

The theta-pinch coil, which is also used as a stabilizing conductive shell, is divided into eight parts. To each part a pulsed current is fed from a Blumlein line charged up to a maximum value of 100 kV. The duration of the magnetic pulse generated with one theta-pinch coil is about 0.75 μs and almost

TABLE I. PARAMETERS OF TORIUT-3 TOKAMAK PLASMA JUST BEFORE APPLICATION OF THE PULSED ELECTRIC FIELD

R_p	25 cm	n_e	2×10^{13} cm^{-3}
a_p	8 cm	T_e	20 eV (laser)
B_t	2 kG		

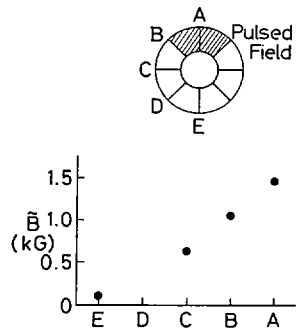


FIG. 1. Variations of the amplitude of the pulsed magnetic field along the torus.

the same as that with eight coils. Figure 1 shows the spatial variation of the pulse amplitude along the torus when the magnetic pulse is applied to a 1/4 section of the torus. The amplitude of the pulsed magnetic field observed under the theta-pinch coils is about 1.5 kG, while the pulse amplitude at the opposite side of the coils on the torus is about one order of magnitude smaller than that under the coils.

2.2. Results and discussion

Time variations of parameters obtained when the pulse was applied to a 1/8 section of the tokamak are shown in Fig.2, in which signals of the left-hand column (A) were observed under the theta-pinch coil and those of the right-hand column (B) at the opposite side of the coil. The pulsed magnetic field is anti-parallel to the bias magnetic field, the magnitude of which is 1 kG. Radial electric field (E_r), charge-exchange neutrals (N_{cx}) and soft X-rays (I_{sx}) were measured with carefully balanced high-impedance double probe, 8-channel neutral particle analyser and Ge-diode detector, respectively. Any serous disruption of the plasma ring due to the pulse application was not observed, as in the case of the full-torus application.

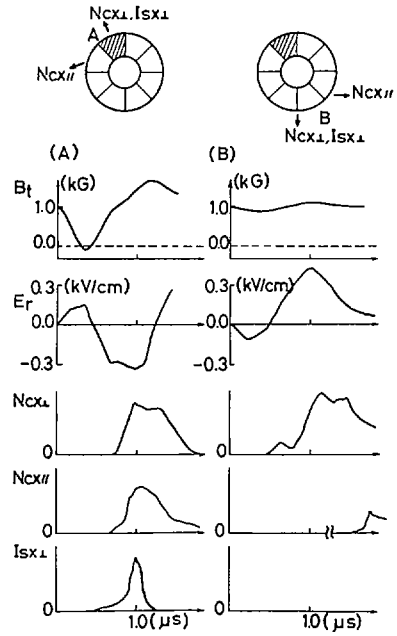


FIG. 2. Time variations of the toroidal magnetic field B_t, the radial electric field E_r, charge-exchange neutral flux emitted perpendicularly to the toroidal field $N_{cx\perp}$, charge-exchange neutral flux emitted tangentially to the toroidal field $N_{cx//}$, and the radiation intensity of X-rays observed at positions A and B.

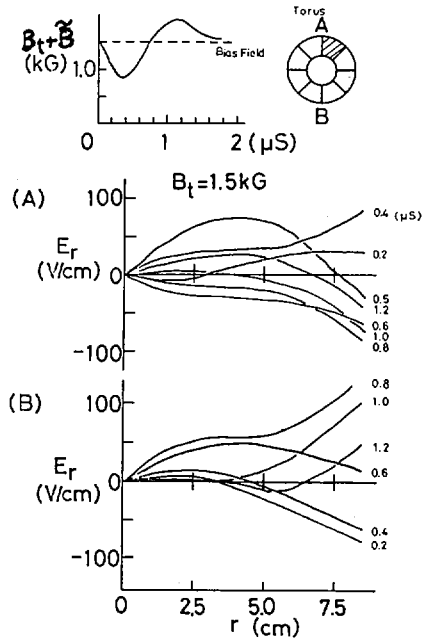


FIG. 3. Spatial distributions of the radial electric field as a function of time measured at positions A and B.

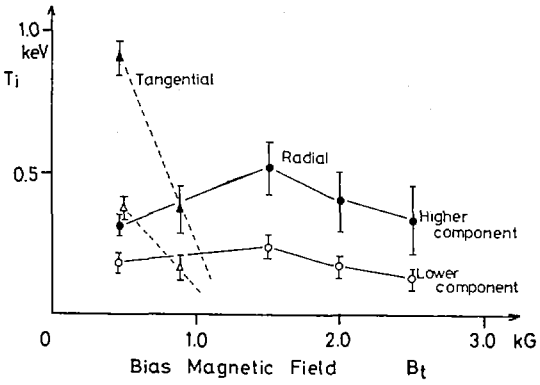


FIG. 4. Dependence of perpendicular and parallel ion temperatures on the bias magnetic field.

The time-of-flight analysis confirmed that the radial emission of charge-exchange neutrals due to the theta pinch is produced simultaneously all round the torus. On the other hand, as seen in Fig.2, the tangential emission of charge-exchange neutrals and the radiation of soft X-rays are observed under the coil only when the pulsed magnetic field cancels the bias field. The electron temperature estimated from the Be-foil absorption method is about 0.7 keV. Tangential hot ions and hot electrons are possibly generated by the turbulent heating due to the induced pulsed current along the poloidal field, since the toroidal field becomes small under the pinch coil.

It should be noted that the direction of the E_r-field at position A is inverse to that at position B. The production of hot ions at position B is ascribed to the appearance of a strong electric field, the time and spatial variations of which are shown in Fig.3. The radial electric field is induced by the following mechanisms. Under the theta-pinch coil, charge separation occurs by the rapid change of the magnetic field since ions behave like unmagnetized particles, and electrons like magnetized fluid, in our experimental conditions. These radially pumped-out electrons flow along the magnetic field line and produce the radial electric field all round the torus. The presence of the radial electric field can give rise to the acceleration of ions and/or the occurrence of turbulent heating due to cross-field instability.

Figure 4 shows the ion temperature deduced from the neutral particle measurements in the radial and tangential directions as a function of the bias magnetic field in the case of application of the magnetic pulse antiparallel to the bias field. The energy•spectrum of the hot ions has two temperature components as in the case of the full-torus application. Figure 4 suggests that the heating mechanisms depend on the ratio of the pulsed field amplitude to the bias field strength. Ion heating parallel to the bias magnetic field, and electron

heating, occur only when the bias magnetic field is weak, in which case a steep magnetic sheath appears. Presumably the turbulent heating due to the steep magnetic sheath occurs under the theta-pinch coil.

For the confinement of the hot ions produced by the pulse application, the main part of the hot ions escape in a burst as a result of the toroidal orbit displacement, since the toroidal magnetic field of the present device is weak and the poloidal Larmor radius for a keV ion is nearly equal to the minor radius. A small fraction remaining in the torus during a few tens of μs is lost by the charge-exchange process. To confine the hot ions produced, higher toroidal magnetic field and lower neutral particle density will be required.

2.3. Conclusions

The high-voltage theta pinch was applied to a part of the tokamak plasma, and production of hot ions was observed all round the torus. Under the theta-pinch coil, hot ion production is attributed to the turbulent process due to poloidally induced current and/or to the ion reflection due to the strong magnetic sheath, while, at the opposite side of the pinch coil, hot ion production is caused by the occurrence of the strong radial electric field.

3. EXPERIMENT WITH PULSED ELECTRIC FIELD ALONG THE TOROIDAL FIELD

3.1. Experimental set-up and initial plasma

A schematic diagram of the tokamak OT-1 (Osaka Torus-1) used in this experiment is shown in Fig.5. The vacuum chamber is a glass tube of 30 cm major radius and 7 cm minor radius. The radius of the limiter is 5.5 cm and the toroidal magnetic field is 13 kG. The copper shell serves as the primary of the transformer to induce the pulsed electric field along the toroidal magnetic field. The initial tokamak plasma is produced by discharging hydrogen gas. The high voltage for turbulent heating is applied to the plasma when the mean electron density reaches 1×10^{13} cm^{-3}. The plasma current is then 5 kA and the conductivity temperature is about 30 eV, if $Z_{eff} = 2$ is assumed.

3.2. Experimental results

As shown in Fig.6(a), the fast-rising current for turbulent heating is superimposed on the initial plasma current and is sustained constant by the power-crowbar method [13]. The time variations of typical signals in the turbulent heating phase are shown in Fig. 6(b)–(e). The mean electron drift velocity at the current peak

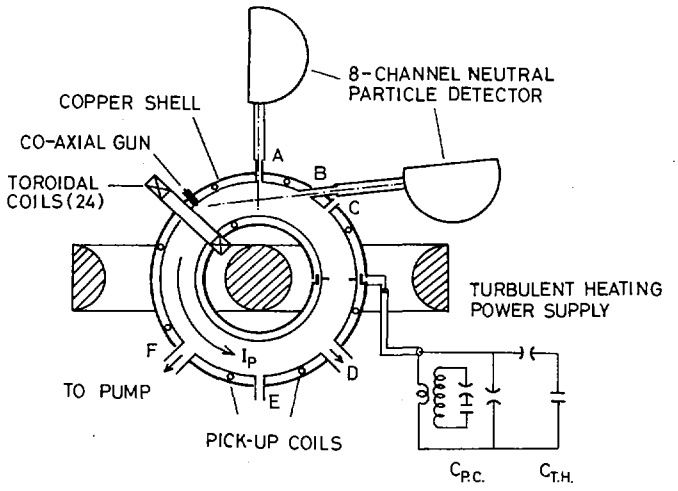


FIG.5. Schematic diagram of OT-1.

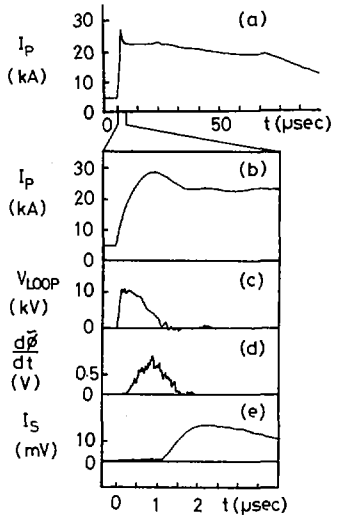


FIG.6. Time variations of typical signals: (a) and (b) plasma current; (c) one-turn loop voltage; (d) magnetic fluctuation; and (e) charge-exchange neutral flux measured by secondary electron detectors (SED).

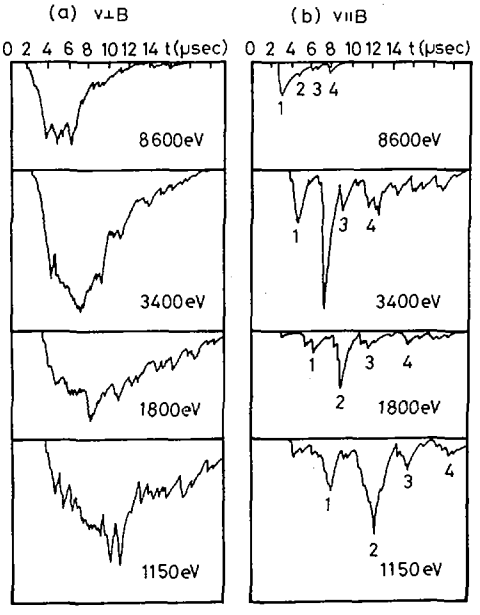


FIG. 7. Signal waveforms of charge-exchange neutral fluxes emitted in the directions perpendicular (a) and parallel (b) to the toroidal magnetic field.

is 2×10^8 cm·s^{-1}, which is large enough to excite ion-sound instability. The fluctuation of the magnetic field is observed from 0.2 μs to 1.5 μs, when hot ions are produced vigorously.

Figure 7(a) and (b) shows the signal waveforms of charge-exchange neutral fluxes measured by an 8-channel neutral particle detector (NPD) attached alternately to the ports A and B. From signal waveforms shown in Fig. 7(a) it is deduced that the hot ions with velocity perpendicular to the magnetic field (hot ions with v⊥B), the energy spectrum of which is a two-temperature Maxwellian of 150 eV and 630 eV in lower and higher temperatures respectively, are produced in 1 μs, and decay probably owing to charge-exchange loss. The signal waveforms shown in Fig. 7(b) imply that the hot ions with v//B are produced non-uniformly along the torus and circulate several times along the toroidal magnetic field, because the time differences between two adjacent peaks are almost equal to the flight time necessary for one circulation.

The position of maximum hot ion production is found by analysing the orbits of the hot ions with v//B corresponding to each peak. The orbits are shown in Fig. 8. Each orbit is a straight line expressed by the equation $z = v_{//}(t_0 - t)$, where z is the distance from the NPD to the position of the particle at t along the torus, $v_{//}$ the particle velocity, and t_0 the time of arrival of the

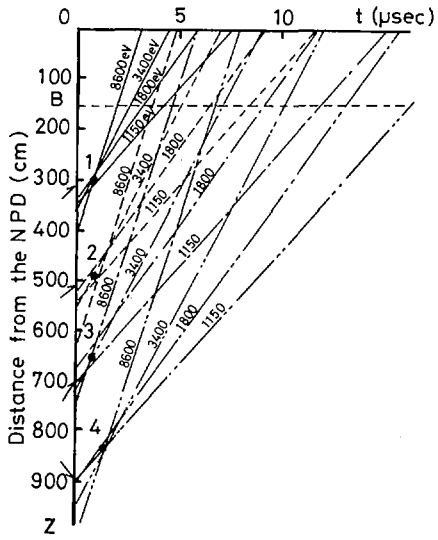


FIG. 8. Orbits of the ion with v//B corresponding to the peaks. Orbits of the ion corresponding to the first, second, third and fourth peaks of each waveform are shown by solid, broken, single-dotted-broken and double-dotted-broken lines, respectively. Arrows show the positions of the limiter, and B shows the position of the port B.

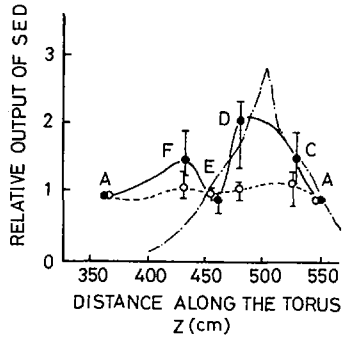


FIG. 9. Spatial variations of charge-exchange neutral fluxes at 2.5 μs (●) and 4.0 μs (○), and spatial distribution of the hot ions with v//B (dotted-and-dashed line). A, C, D, E and F show the positions of the measurements.

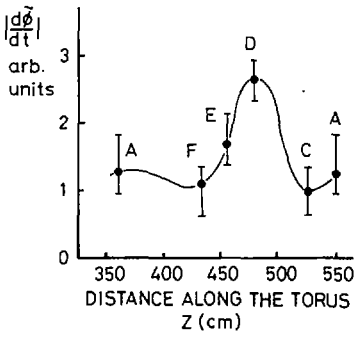


FIG.10. Spatial variations of the relative fluctuation amplitude of the poloidal magnetic field along the torus at 0.6 μs. A, C, D, E and F show the positions of the measurements.

particle at the NPD. Here, we assume the velocity $v_{//}$ does not change during travel. The hot ions are apparently produced at about 1 μs at four positions spaced at intervals of nearly 188 cm, i.e. the circumference of the torus. Of course, all these positions in Fig.8 correspond to the same position, which lies between the limiter and the port D. The spatial distribution of the production of these hot ions is given by expressing the abscissa of each waveform in terms of $z(= v_{//}(t_1 - t)$, where $t_1 = 1$ μs). Using this procedure, it becomes clear that the half-width of the distribution is 50–80 cm. The curve drawn by the dotted-and-dashed line in Fig.9 shows the distribution obtained from the second peak of the waveform for 1150 eV.

The spatial distribution of hot ions with $v \perp B$ along the torus is investigated by secondary electron detectors (SED). Figures 6(e) and 9 show the time variation of the charge-exchange neutral flux and its spatial variations at 2.5 μs and 4.0 μs, respectively. The spatial variation becomes uniform after 3 μs. It is apparent from Fig.9 that the spatial distribution of the hot ions with $v \perp B$ does not agree with that of the hot ions with $v // B$. This discrepancy implies further that the ion heating is not isotropic.

Fluctuation of the poloidal magnetic field in the frequency range of $f > 50$ MHz is measured with a magnetic probe set alternately at points 1 cm away from the plasma surface. The spatial variation of the amplitude of the fluctuation along the torus at 0.6 μs is shown in Fig.10. The amplitude is large at the port D around which the hot ions with $v // B$ are mainly produced. This also implies that the instability is excited non-uniformly and, consequently, that ion heating is induced non-uniformly.

3.3. Discussion and conclusion

Our experimental results conflict with the conjectures described in Section 1 and therefore, to interpret our results tentatively, we make up a simple model. We decompose the spatial distribution of the fluctuation shown in Fig.10 into a uniformly distributed fluctuation and a fluctuation distributed only round the port D, and assume that each of them is excited by each kind of instability, one of which is current-driven, excited uniformly along the torus. Ion heating due to this instability occurs in the direction perpendicular to the magnetic field, otherwise the hot ions with v//B would be distributed throughout the torus. The ion-sound wave propagating almost perpendicular to the magnetic field, which was observed in another experiment [14], is probably responsible for this ion heating, because the drift velocity of the electron is large enough to excite ion-sound instability, and the direction of the associated electric field is perpendicular to the magnetic field. The other instability is that excited round the port D. It causes the production of the hot ions with v//B and the excess hot ions with v⊥B distributed around the port D. As this instability is excited in the neighbourhood of the limiter, certain effects of the limiter on the plasma are probably responsible for it.

In conclusion, the current-driven instability is excited uniformly along the torus and causes ion heating only in the direction perpendicular to the magnetic field. The production of the hot ions with v//B is restricted around the limiter and is caused by some instability originating from the interaction between the plasma and the limiter.

ACKNOWLEDGEMENTS

The TORIUT-3 group wishes to thank Prof. S.Nagao of Tohoku University for his encouragement and Dr. H.Nihei, Mr. T.Kobata and Mr. J.Morikawa for useful discussions. The OT-1 group wishes to thank Prof. H.Itô, Prof. S.Nagao of Tohoku University and Prof. T.Amano for their encouragement, and Prof. K.Watanabe, Prof. K.Adati of Nagoya University, Dr.T.Uyama and Dr. H.Kishimoto of Japan Atomic Energy Research Institute for useful discussions.

REFERENCES

[1] SÖLDNER, F., STEUER, K.-H., Plasma Physics and Controlled Nuclear Fusion Research 1976 (Proc. 6th Int. Conf. Berchtesgaden, 1976) Vol.3, IAEA, Vienna (1977) 89.
[2] INOUE, N., et al., ibid. 3.
[3] CHEN, Y.G., et al., Phys. Rev. Lett. 38 (1977) 1400.

[4] ICHIMURA, M., et al., Controlled Fusion and Plasma Physics (Proc. 8th Europ. Conf. Prague, 1977) Vol.1 (1977) 3.
[5] YAMAZAKI, K., et al., Plasma Wall Interaction (Proc. Int. Symp. Jülich, 1976), Pergamon (1977) 619.
[6] HAMBERGER, S.M., JANCARIK, J., Phys. Fluids **15** (1972) 825.
[7] HIROSE, A., SKARSGARD, H.M., IEEE Trans. Plasma Sci. PS-5 (1977) 66.
[8] BENGTSON, R.D., et al., Phys. Fluids **18** (1975) 710.
[9] DeKLUIVER, H., et al., Phys. Lett. **62A** (1977) 157.
[10] WHARTON, C., et al., Plasma Physics and Controlled Nuclear Fusion Research 1971 (Proc. 4th Int. Conf. Madison, 1971) Vol.2, IAEA, Vienna (1971) 25.
[11] SUPRUNENKO, V.A., SOKHOMLIN, E.A., TOLOK, V.T., Plasma Phys. **12** (1970) 627.
[12] INOUE, N., et al., Rev. Sci. Instrum. **47** (1975) 735.
[13] KITAGAWA, S., HIRANO, K., Rev. Sci. Instrum. **45** (1974) 962.
[14] AMAGISHI, Y., et al., Phys. Lett. **63A** (1977) 31.

DISCUSSION

ON PAPERS Y-4-1 AND Y-4-2

D. DOBROTT: Could you comment on the applicability of turbulent heating to high-beta or reactor-type tokamak plasmas where it seems that flux surface shaping and current density profiles are so important in determining stability?

H.DE KLUIVER: Turbulent heating might be a viable method of heating reactor-type tokamak plasmas, as has been argued here. We would expect from the experimental evidence that, given a number of additional current pulses, preferably with time intervals shorter than the energy confinement time, it should be possible to heat a large plasma volume to ignition temperature. From the scaling laws it seems that this should be possible at conveniently low loop voltages. The extra current added should not – need not – alter the radial q-profile to a dangerous form. On the contrary, a proper addition of current and heat near the periphery, avoiding two large gradients, could be benefical for plasma stability and help to control the radial temperature profile.

T. KAWABE: What is the thermal conduction across the magnetic field?

H. DE KLUIVER: The question of thermal conduction across the magnetic field has not yet been solved, and more experiments are needed. We do, however, already have a few favourable indications of rapid heat transport towards the axis of the discharge by waves (reported by Nishida and co-workers and by Aranchuk and co-workers). In the Dutch experiment there do not appear to be any large energy losses towards the vessel wall during the heating; furthermore, the current in the skin re-distributes rapidly at the end of turbulence. Certainly, the question of thermal conduction during and after turbulence is of major importance.

SUMMARY ON INFORMAL MEETINGS ON STELLARATORS, PLASMA FOCUS AND TANDEM MIRRORS

1. STELLARATORS

(G. Grieger)

1. Status

At this meeting experimental results were available from five stellarator devices:

CLEO (Culham, UK)
L-2 (Moscow, USSR)
W VII-A (Garching, FRG)
HELIOTRON D and DM (Kyoto, Japan)
R-0 (Sukhumi, USSR)
PROTO-CLEO (Madison, USA)

Unfortunately, results were missing from URAGAN, etc. (Kharkov, USSR) and, as they are just about going into operation, from JIP-TII (Nagoya, Japan), and WEGA-Stellarator (Grenoble/Garching, France/FRG).

2. Results

It now seems to be well established that helical fields improve the confinement properties of Ohmically sustained discharges.

In the presence of external helical fields the energy confinement time of Ohmically heated plasmas can be increased by factors of 2–10 above that of comparable tokamaks.

If more than about 25% of the edge rotational transform are produced by external helical fields, disruptions can reliably be avoided.

When avoiding the disruptive instability the density limit can be increased above what is observed in tokamaks until the radiation losses from the small impurity concentrations can no longer be balanced by the available heating power.

For helium plasmas the ion heat conductivity is neoclassical. At higher densities ion and electron temperatures are so close to each other that the difference is within the accuracy of the measurement.

Stellarator fields allow the immediate inclusion of a limiter or divertor if the separatrix is placed in the appropriate position.

With sufficient external field and heating current, the $q = 1$ surface can extend to about 2/3 of the plasma radius, leading to flat profiles within it and to steep, stable gradients in the outer confining regions (W VII-A). On the other hand, with strong shear of the helical field, the sequence of $q = 1$, $q = 2$, and $q = 3$ surfaces can be reversed and, if desired, the $q = 1$ surface can even be located outside the plasma (CLEO, L-2).

In this respect, it is essential to note that in addition to the scaling laws of global energy confinement – as favourable as they are – a detailed consideration of the radial dependence of the transport is necessary.

Many of these observations have direct relevance for tokamaks, e.g. the observation of a new radiative density limit.

3. Current-free operation

The above results strongly suggest the transition to current-free operation of stellarators. In this respect the role of shear of the magnetic field is of particular interest; is it necessary for achieving stable configurations, or should one avoide it in order to avoide the effect of magnetic resonances and only rely on favourable V'' properties?

In this respect, the three machines, W VII-A, L-2, and CLEO have basically different properties of their vacuum field configuration (Fig.1):

W VII-A has almost vanishing shear;

In CLEO, iota vanishes on the magnetic axis and increases strongly with radius;

L-2 combines the properties of the preceding devices, i.e. a non-vanishing iota on the axis with a strong increase towards the edge.

Therefore, it should be possible to answer this question experimentally. But a necessary prerequisite for such experiments is the availability of heating schemes other than Ohmic ones. RF-heating (CLEO and L-2), neutral injection (CLEO and W VII-A) and laser-pellet injection (CLEO, L-2, W VII-A) will be tried. The application of Alfvén-wave heating to PROTO-CLEO has, however, not yet been

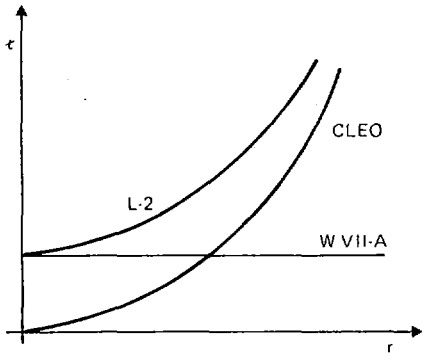


FIG.1. Iota versus radius in three experiments.

successful because of enhanced transport. This has probably to do with the low temperature of the plasma and, therefore, the repetitive formation of islands because the magnetic diffusion time was comparable with the RF-period.

4. Future

The promising results of the moderate-size stellarators operating at present underline the need for an extension of the studies of hotter and larger plasmas. One step will be done by Heliotron E which is expected to go into operation in 1980. Future large stellarators will require innovative construction designs in order to get rid of the interactive forces between the helical windings and the main field coils. This could be achieved by producing all the essential parts of the stellarator field by one set of coils alone. Two approaches are available – one can either start from the main field coils and twist them (Wobig-Rehker) or start from the helix and cancel the return currents (torsatron). The latter method might even lead to nearly force-free systems.

Recently, there has been a renewal of interest in stellarators in the USA, and two experiments comparable to PLT in size are being designed: WISTOR, a steady-state, superconducting $\ell = 3$ torsatron is being designed at the University of Wisconsin, and TOREX-4, a pulsed $\ell = 4$ torsatron with cryogenically cooled copper coils is being designed at MIT.

2. PLASMA FOCUS

(G. Decker, T. Oppenländer, J.P. Rager)

Plasma Focus research and development efforts today proceed along three main directions simultaneously. The first one is related to the derivation of scaling laws for the design of high-energy Plasma Focus devices, while the last two are related to the understanding of the basic physics and physical processes occurring during either the long-timescale phenomena (current sheath dynamics during build-up, run-down and implosion) or the short-timescale phenomena accompanying the neutron production (anomalous effect, nature and role of macroscopic and microscopic instabilities, mechanism of neutron production and beam generation).

1. Scaling laws for the design of large PF devices

Despite the existence of extensive diagnostic programmes in many a laboratory concerned with plasma focus (PF) research, the amount of knowledge in that field is still insufficient for the derivation of realistic and tractable optimization criteria. However, the phenomenological observation that the neutron yield Y_n scales as I_p^4 (I_p is the current flowing in the plasma at pinch time) is an important milestone on this way, and is used by a majority of laboratories as a justification for achieving a compromise between highest possible maximum current and magnetic energy.

a) Electrotechnical considerations

To achieve the highest possible maximum discharge current out of a focus device with fixed energy W, initial current rise-time I and load $\dot{L}$, it is necessary to choose the proper voltage. An analytical model leads, with these assumptions, to an optimum voltage and to a scaling $Y_N \sim W^{8/3}$ assuming $\dot{I} \sim W$ and $Y_N \sim I^4$. In this model, 15% to 20% of the initial energy appears as kinetic energy. Considering also the given quarter period of the discharge and the typical run-down velocity of about 10^7 cm·s^{-1}, the length of the gun is fixed and for given radii the filling pressure P_0 can be predicted within a factor 2. For the radius scaling R_0, it seems favourable to use small radius and small pressures to minimize current losses along the insulator surface, but the empirical condition $P_0 R_0^2 \sim W$ also has to be satisfied. This condition has been checked for different devices and holds well. To fulfil these conditions, it can be necessary to increase the neutral density in front of the electrode by gas puffing. In these considerations restrike along the insulator or repetitive-focusing operation, as observed in slow devices, is not included. Restrikes in the back during the compression phase may possibly not

affect the power supply of the pinch because a rather high fraction of the initial energy is already stored inductively in the gun itself (compare L_g/R_p characteristic time with the coherence time of the short timescale where L_g is the gun inductance and R_p the anomalous pinch-resistance).

b) Physical considerations and observations

The main problem in scaling up the neutron yield with current or energy is now recognized to be problems in the $Y_n \sim I_p^4$ scaling due to a change in physical mechanisms. It seems that for every device there exists an upper energy limit at which the neutron yield abruptly leaves this scaling and remains too low. This limit is usually met by increasing the energy via increasing the voltage only. The energy level where the scaling is left is specific for each device (e.g. ≈500 kJ in the Frascati 1-MJ device, ≈40 kJ in the DPF 78, Stuttgart). The decrease of neutron yield for higher energies is accompanied by changes in break-down and run-down behaviour of the discharge as well as by changes in the neutron spectra. So, long-and short-timescale phenomena eventually related to each other play a role. The Frascati group will do further research on these problems.

2. Plasma focus as beam generator

Neutron production in plasma focus devices has certainly also to be regarded in connection with fast-ion beams. The Limeil group reports about ½ TW electron and ion beam (each). But a direct matching between the current and the filling pressure seems also important as the conditions for beam optimization and neutron production optimization differ to some extent. The Limeil programme will essentially deal with these problems in the future. Beams with ion energies up to 1 MeV have been observed by the Hoboken group. These beams appear to be subdivided into several channels of 5 ... 100 μm diameter. The beam energy was reported to be up to 10% (!) of the initial energy in the device. Speaking of beams it would be useful to distinguish two different classes: 'beams' which might have large diameters and divergence as a mechanism for producing neutrons and, on the other hand, beams of small diameter and divergence. The energies of the ion and electron beam scale with the current I. When I is increased the anomalous resistivity in the pinch (derived through indirect measurements) remains constant, so the voltage increases ahdn, hence, the energy of the particles. Thus, the anomalous resistivity ($R_p \approx 0.3 - 0.5\ \Omega$, Limeil Group) is found to be constant over two orders of magnitude of the current.

3. Correlations

To gain further understanding of the physical mechanism of neutron production correlations between various parameters, measurements and the neutron

yields Y_N have been discussed. With the limitation that some of the correlations listed are valid only for specific devices, Y_N correlates with

the suprathermal scattering signal amplitude (strongly);
the amplitude of the time derivative of a magnetic probe signal ($\partial^2 B/\partial t^2$) during the instability phase;
the IR yield;
the hard-X-ray yield but possibly with the restriction that a correlation only between the intensity of the hard X-rays and the appearance of fast neutrons (and not with the total yield) has been observed by the Frascati group. Furthermore, it is known from the works published by the Kurchatov and Livermore groups that there was no correlation between very fast deuterons and the total Y_N;
the directed soft-X-ray emission ($\approx$1 keV, $\delta\theta \leqslant 100$ mrad) which has been observed by the Darmstadt group only.

Furthermore, there arises the question of whether the enhanced resistivity is correlated with an enhanced scattering. To explain the high value of the anomalous resistivity mentioned above the suprathermal scattering signal is estimated to be approximately 10^3 times higher than the thermal one. The amplitude of the scattered signals was measured to be the same in the high density region in the pinch and in the low-density zone around it where most of the current flows. A physical mechanism for the high value of the anomalous resistivity has not been given as yet. It was argued that the strongest instability to enhance resistivity, the ion-acoustic mode, merely yields an enhancement factor of 10. Then, it was questioned whether the ion-acoustic mode appears at all, as it requires $T_e \gg T_i$ and cannot appear in regions of E⊥B. However, as the ion temperature is not definitely known, the Limeil group will perform scattering experiments to resolve this open question.

From the correlation of Y_N with the B probe signal it seems to be important to have, first, an intense classical Z-pinch with an explosive growing of $m = 0$ instabilities leading to anomalous effects during the decay of the plasma. The correlation of Y_N with the directed soft-X-ray emission may point to current-driven microinstabilities, which was also proposed by the Darmstadt group.

4. Sheath structure

Experiments on the influences of different insulator materials on the sheath structure have shown that mainly the current density distribution changes in width and amplitude. Furthermore, the sheath structure can vary depending on external parameters like geometry, vacuum, etc.

No direct correlation of the measured sheath parameters (i.e. electron density, current density distribution) to the neutron yield could be found. Differing from

the 'normal' sheath structure (i.e. maximum current density behind the maximum electron density) magnetic-probe measurements done at the Filippov device at the Lebedev institute showed, in general, double current density peaks and current loops in the sheath.

5. Conclusions

The state of the art indicates that, to further optimize the existing plasma focus devices, the voltage must be increased to some optimal value which allows a more intense current to be drawn from the source at a given energy level.

However, the main problem in scaling up the neutron yield is to overcome the break in the W^2 or I_p^4 scaling which apparently is not fundamentally linked to either the use of high voltage or to reaching a high energy level of operation. In this direction, a simple stop-gap exists: the decoupling of the gas filling requirements by gas puffing in front of the anode top; it would satisfy independently the conditions for a good current sheath dynamics during the long timescale, as well as the pinch particle-content condition at that energy level. As far as the mechanisms for neutron production and beam generation are concerned, some progress has been made in the understanding of the role, location and quantitative aspects of the instabilities and the turbulence, for different types of experiments (Mather and Filippov geometries).

The existence of several neutron production mechanisms is being documented and the research of their connections with the nature of the instabilities and turbulences is being actively pursued.

3. TANDEM MIRROR

(T. Kawabe,
B.G. Logan,
D.D. Ryutov)

The main object of the meeting was to exchange information among those who are doing research on tandem mirrors and those who are interested in this field of research. The speakers were:

D.D. Ryutov (Novosibirsk): Construction of an ambipolar mirror and theoretical studies of radial transport.
B.G. Logan (LLL): Construction of TMX.

D. Baldwin (LLL): Radial transport theory.
R. Conn (University of Wisconsin): Construction of RF tandem mirror and theoretical study of radial transport.
T. Kawabe (University of Tsukuba): Present status of Tsukuba programme on GAMMA-6 and GAMMA-10 experiments.
T. Kammash (University of Michigan): Computer simulation of impurity problems in tandem mirror.
W. Horton (University of Texas): Theoretical studies of drift wave and radial transport.

CHAIRMEN OF SESSIONS

Session A	R.S. PEASE	UK
Session C	K.A. RAZUMOVA	USSR
Session N	S. MORI	Japan
Session T	H.P. FURTH	USA
Session F	B.B. KADOMTSEV	USSR
Session K	M.N. ROSENBLUTH	USA
Session O	B. LEHNERT	Sweden
Session P	D. PFIRSCH	FRG
Session W	P.E. VANDENPLAS	Belgium
Session E	H. DREICER	USA
Session U	R. TOSCHI	Italy
Session H	D. PALUMBO	CEC
Session L	R. WIENECKE	FRG
Session J	F. ENGELMANN	Netherlands
Session S	V.O. JENSEN	Denmark
Session G	F.F. CAP	Austria
Session Q	E.S. WEIBEL	Switzerland
Session Y	T. CONSOLI	France
Session B	C. YAMANAKA	Japan
Session D	M.V. BABYKIN	USSR
Session M	J.P. WATTEAU	France
Session V	C.M. STICKLEY	USA
Session X	C.N. WATSON-MUNRO	Australia
Session I	P.E. REBUT	CEC
Session R	J.F. CLARKE	USA
Summary Session	R.J. BICKERTON	UK

SECRETARIAT OF THE CONFERENCE

Scientific Secretaries:	J.A. PHILLIPS V.S. VLASENKOV	Division of Research and Laboratories, IAEA
Administrative Secretary:	Caroline DE MOL VAN OTTERLOO	Division of External Relations, IAEA
Editors:	J.W. WEIL Miriam LEWIS	Division of Publications, IAEA
Records Officer:	S.A. EDMINSTER	Division of Languages, IAEA

The following conversion table is provided for the convenience of readers and to encourage the use of SI units.

FACTORS FOR CONVERTING SOME OT THE MORE COMMON UNITS TO INTERNATIONAL SYSTEM OF UNITS (SI) EQUIVALENTS

NOTES:

(1) SI base units are the metre (m), kilogram (kg), second (s), ampere (A), kelvin (K), candela (cd) and mole (mol).

(2) ▶ indicates SI derived units and those accepted for use with SI;
▷ indicates additional units accepted for use with SI for a limited time.
[*For further information see The International System of Units (SI), 1977 ed., published in English by HMSO, London, and National Bureau of Standards, Washington, DC, and International Standards ISO-1000 and the several parts of ISO-31 published by ISO, Geneva.*]

(3) The correct abbreviation for the unit in column 1 is given in column 2.

(4) ✻ indicates conversion factors given exactly; other factors are given rounded, mostly to 4 significant figures.
≡ indicates a definition of an SI derived unit: [ ] in column 3+4 enclose factors given for the sake of completeness.

Column 1 *Multiply data given in:*	Column 2	Column 3 *by:*	Column 4 *to obtain data in:*	
Radiation units				
▶ becquerel	1 Bq	(has dimensions of s^{-1})		
disintegrations per second (= dis/s)	1 s^{-1}	≡ 1.00×10^{0}	Bq	✻
▷ curie	1 Ci	= 3.70×10^{10}	Bq	✻
▷ roentgen	1 R	[= 2.58×10^{-4}	C/kg]	✻
▶ gray	1 Gy	[≡ 1.00×10^{0}	J/kg]	✻
▷ rad	1 rad	= 1.00×10^{-2}	Gy	✻
sievert *(radiation protection only)*	1 Sv	[= 1.00×10^{0}	J/kg]	✻
rem *(radiation protection only)*	1 rem	[= 1.00×10^{-2}	J/kg]	✻
Mass				
▶ unified atomic mass unit ($\frac{1}{12}$ of the mass of ^{12}C)	1 u	[= $1.660\,57 \times 10^{-27}$	kg, approx.]	
▶ tonne (= metric ton)	1 t	[= 1.00×10^{3}	kg]	✻
pound mass (avoirdupois)	1 lbm	= 4.536×10^{-1}	kg	
ounce mass (avoirdupois)	1 ozm	= 2.835×10^{1}	g	
ton (long) (= 2240 lbm)	1 ton	= 1.016×10^{3}	kg	
ton (short) (= 2000 lbm)	1 short ton	= 9.072×10^{2}	kg	
Length				
statute mile	1 mile	= 1.609×10^{0}	km	
nautical mile (international)	1 n mile	= 1.852×10^{0}	km	✻
yard	1 yd	= 9.144×10^{-1}	m	✻
foot	1 ft	= 3.048×10^{-1}	m	✻
inch	1 in	= 2.54×10^{1}	mm	✻
mil (= 10^{-3} in)	1 mil	= 2.54×10^{-2}	mm	✻
Area				
▷ hectare	1 ha	[= 1.00×10^{4}	m^2]	✻
▷ barn *(effective cross-section, nuclear physics)*	1 b	[= 1.00×10^{-28}	m^2]	✻
square mile, (statute mile)^2	1 $mile^2$	= 2.590×10^{0}	km^2	
acre	1 acre	= 4.047×10^{3}	m^2	
square yard	1 yd^2	= 8.361×10^{-1}	m^2	
square foot	1 ft^2	= 9.290×10^{-2}	m^2	
square inch	1 in^2	= 6.452×10^{2}	mm^2	
Volume				
▶ litre	1 l *or* 1 ltr	[= 1.00×10^{-3}	m^3]	✻
cubic yard	1 yd^3	= 7.646×10^{-1}	m^3	
cubic foot	1 ft^3	= 2.832×10^{-2}	m^3	
cubic inch	1 in^3	= 1.639×10^{4}	mm^3	
gallon (imperial)	1 gal (UK)	= 4.546×10^{-3}	m^3	
gallon (US liquid)	1 gal (US)	= 3.785×10^{-3}	m^3	
Velocity, acceleration				
foot per second (= fps)	1 ft/s	= 3.048×10^{-1}	m/s	✻
foot per minute	1 ft/min	= 5.08×10^{-3}	m/s	✻
mile per hour (= mph)	1 mile/h	= 4.470×10^{-1} = 1.609×10^{0}	m/s km/h	
▷ knot (international)	1 knot	= 1.852×10^{0}	km/h	✻
free fall, standard, g		= 9.807×10^{0}	m/s^2	
foot per second squared	1 ft/s^2	= 3.048×10^{-1}	m/s^2	✻

This table has been prepared by E.R.A. Beck for use by the Division of Publications of the IAEA. While every effort has been made to ensure accuracy, the Agency cannot be held responsible for errors arising from the use of this table.

Column 1 *Multiply data given in:*	Column 2	Column 3 *by:*	Column 4 *to obtain data in:*
Density, volumetric rate			
pound mass per cubic inch	1 lbm/in^3	= 2.768 X 10^4	kg/m^3
pound mass per cubic foot	1 lbm/ft^3	= 1.602 X 10^1	kg/m^3
cubic feet per second	1 ft^3/s	= 2.832 X 10^{-2}	m^3/s
cubic feet per minute	1 ft^3/min	= 4.719 X 10^{-4}	m^3/s
Force			
▶ newton	1 N	[≡ 1.00 X 10^0	m·kg·s^{-2}]*
dyne	1 dyn	= 1.00 X 10^{-5}	N *
kilogram force (= kilopond (kp))	1 kgf	= 9.807 X 10^0	N
poundal	1 pdl	= 1.383 X 10^{-1}	N
pound force (avoirdupois)	1 lbf	= 4.448 X 10^0	N
ounce force (avoirdupois)	1 ozf	= 2.780 X 10^{-1}	N
Pressure, stress			
▶ pascal	1 Pa	[≡ 1.00 X 10^0	N/m^2] *
▷ atmosphere[a], standard	1 atm	= 1.013 25 X 10^5	Pa *
▷ bar	1 bar	= 1.00 X 10^5	Pa *
centimetres of mercury (0°C)	1 cmHg	= 1.333 X 10^3	Pa
dyne per square centimetre	1 dyn/cm^2	= 1.00 X 10^{-1}	Pa *
feet of water (4°C)	1 ftH_2O	= 2.989 X 10^3	Pa
inches of mercury (0°C)	1 inHg	= 3.386 X 10^3	Pa
inches of water (4°C)	1 inH_2O	= 2.491 X 10^2	Pa
kilogram force per square centimetre	1 kgf/cm^2	= 9.807 X 10^4	Pa
pound force per square foot	1 lbf/ft^2	= 4.788 X 10^1	Pa
pound force per square inch (= psi)[b]	1 lbf/in^2	= 6.895 X 10^3	Pa
torr (0°C) (= mmHg)	1 torr	= 1.333 X 10^2	Pa
Energy, work, quantity of heat			
▶ joule (≡ W·s)	1 J	[≡ 1.00 X 10^0	N·m] *
▶ electronvolt	1 eV	[= 1.602 19 X 10^{-19}	J, approx.]
British thermal unit (International Table)	1 Btu	= 1.055 X 10^3	J
calorie (thermochemical)	1 cal	= 4.184 X 10^0	J *
calorie (International Table)	1 cal$_{IT}$	= 4.187 X 10^0	J
erg	1 erg	= 1.00 X 10^{-7}	J *
foot-pound force	1 ft·lbf	= 1.356 X 10^0	J
kilowatt·hour	1 kW·h	= 3.60 X 10^6	J *
kiloton explosive yield (PNE) (≡ 10^{12} g·cal)	1 kt yield	≃ 4.2 X 10^{12}	J
Power, radiant flux			
▶ watt	1 W	[≡ 1.00 X 10^0	J/s] *
British thermal unit (International Table) per second	1 Btu/s	= 1.055 X 10^3	W
calorie (International Table) per second	1 cal$_{IT}$/s	= 4.187 X 10^0	W
foot-pound force/second	1 ft·lbf/s	= 1.356 X 10^0	W
horsepower (electric)	1 hp	= 7.46 X 10^2	W *
horsepower (metric) (= ps)	1 ps	= 7.355 X 10^2	W
horsepower (550 ft·lbf/s)	1 hp	= 7.457 X 10^2	W
Temperature			
▶ temperature in degrees Celsius, t where T is the thermodynamic temperature in kelvin and T_0 is defined as 273.15 K	$t = T - T_0$		
degree Fahrenheit	$t_{°F} - 32$	X (5/9) gives	t *(in degrees Celsius)* *
degree Rankine	$T_{°R}$		T *(in kelvin)* *
degrees of temperature difference[c]	$\Delta T_{°R}$ (= $\Delta t_{°F}$)		ΔT (= Δt) *
Thermal conductivity[c]			
1 Btu·in/(ft^2·s·°F) *(International Table Btu)*		= 5.192 X 10^2	W·m^{-1}·K^{-1}
1 Btu/(ft·s·°F) *(International Table Btu)*		= 6.231 X 10^3	W·m^{-1}·K^{-1}
1 cal$_{IT}$/(cm·s·°C)		= 4.187 X 10^2	W·m^{-1}·K^{-1}

[a] atm abs, ata: atmospheres absolute; atm (g), atü: atmospheres gauge.

[b] lbf/in^2 (g) (= psig): gauge pressure; lbf/in^2 abs (= psia): absolute pressure.

[c] The abbreviation for temperature difference, deg (= degK = degC), is no longer acceptable as an SI unit.

HOW TO ORDER IAEA PUBLICATIONS

An exclusive sales agent for IAEA publications, to whom all orders and inquiries should be addressed, has been appointed in the following country:

UNITED STATES OF AMERICA UNIPUB, 345 Park Avenue South, New York, NY 10010

In the following countries IAEA publications may be purchased from the sales agents or booksellers listed or through your major local booksellers. Payment can be made in local currency or with UNESCO coupons.

ARGENTINA	Comisión Nacional de Energía Atomica, Avenida del Libertador 8250, RA-1429 Buenos Aires
AUSTRALIA	Hunter Publications, 58 A Gipps Street, Collingwood, Victoria 3066
BELGIUM	Service du Courrier de l'UNESCO, 202, Avenue du Roi, B-1060 Brussels
CZECHOSLOVAKIA	S.N.T.L., Spálená 51, CS-113 02 Prague 1 Alfa, Publishers, Hurbanovo námestie 6, CS-893 31 Bratislava
FRANCE	Office International de Documentation et Librairie, 48, rue Gay-Lussac, F-75240 Paris Cedex 05
HUNGARY	Kultura, Hungarian Trading Company for Books and Newspapers, P.O. Box 149, H-1389 Budapest 62
INDIA	Oxford Book and Stationery Co., 17, Park Street, Calcutta-700 016 Oxford Book and Stationery Co., Scindia House, New Delhi-110 001
ISRAEL	Heiliger and Co., Ltd., Scientific and Medical Books, 3, Nathan Strauss Street, Jerusalem
ITALY	Libreria Scientifica, Dott. Lucio de Biasio "aeiou", Via Meravigli 16, I-20123 Milan
JAPAN	Maruzen Company, Ltd., P.O. Box 5050, 100-31 Tokyo International
NETHERLANDS	Martinus Nijhoff B.V., Booksellers, Lange Voorhout 9-11, P.O. Box 269, NL-2501 The Hague
PAKISTAN	Mirza Book Agency, 65, Shahrah Quaid-e-Azam, P.O. Box 729, Lahore 3
POLAND	Ars Polona-Ruch, Centrala Handlu Zagranicznego, Krakowskie Przedmiescie 7, PL-00-068 Warsaw
ROMANIA	Ilexim, P.O. Box 136-137, Bucarest
SOUTH AFRICA	Van Schaik's Bookstore (Pty) Ltd., Libri Building, Church Street, P.O. Box 724, Pretoria 0001
SPAIN	Diaz de Santos, Lagasca 95, Madrid-6 Diaz de Santos, Balmes 417, Barcelona-6
SWEDEN	AB C.E. Fritzes Kungl. Hovbokhandel, Fredsgatan 2, P.O. Box 16356, S-103 27 Stockholm
UNITED KINGDOM	Her Majesty's Stationery Office, P.O. Box 569, London SE 1 9NH
U.S.S.R.	Mezhdunarodnaya Kniga, Smolenskaya-Sennaya 32-34, Moscow G-200
YUGOSLAVIA	Jugoslovenska Knjiga, Terazije 27, P.O. Box 36, YU-11001 Belgrade

---

Orders from countries where sales agents have not yet been appointed and requests for information should be addressed directly to:



Division of Publications
International Atomic Energy Agency
Kärntner Ring 11, P.O. Box 590, A-1011 Vienna, Austria

79- 03696

INTERNATIONAL
ATOMIC ENERGY AGENCY
VIENNA, 1979

SUBJECT GROUP: III
Physics/Plasma Physics, Fusion
PRICE: Austrian Schillings 970,–